



HAL
open science

Crystal chemistry of vanadium phosphates as positive electrode materials for Li-ion and Na-ion batteries

Édouard Boivin

► **To cite this version:**

Édouard Boivin. Crystal chemistry of vanadium phosphates as positive electrode materials for Li-ion and Na-ion batteries. Other. Université de Picardie Jules Verne, 2017. English. NNT: 2017AMIE0032. tel-03648931

HAL Id: tel-03648931

<https://theses.hal.science/tel-03648931>

Submitted on 22 Apr 2022

HAL is a multi-disciplinary open access archive for the deposit and dissemination of scientific research documents, whether they are published or not. The documents may come from teaching and research institutions in France or abroad, or from public or private research centers.

L'archive ouverte pluridisciplinaire **HAL**, est destinée au dépôt et à la diffusion de documents scientifiques de niveau recherche, publiés ou non, émanant des établissements d'enseignement et de recherche français ou étrangers, des laboratoires publics ou privés.



Thèse de Doctorat

Mention chimie

Spécialité Chimie des Solides et Sciences des Matériaux

présentée à l'Ecole Doctorale en Sciences Technologie et Santé (ED 585)

de l'Université de Picardie Jules Verne

Édouard BOIVIN

pour obtenir le grade de Docteur de l'Université de Picardie Jules Verne

***Crystal Chemistry of Vanadium Phosphates as Positive
Electrode materials for Li-ion and Na-ion Batteries***

Soutenue le 24/11/2017, après avis des rapporteurs, devant le jury d'examen :

M. Alain Demourgues , Directeur de Recherches, CNRS, ICMCB, Bordeaux	Rapporteur
M^{me}. Christine Martin , Directrice de Recherches, CNRS, CRISMAT, Caen	Rapporteur
M. Florent Boucher , Directeur de Recherches CNRS, IMN Nantes	Examineur
M. Olivier Mentré , Directeur de Recherches CNRS, ENSC Lille	Examineur
M^{me}. Montse Casas-Cabanas , Chargée de Recherches, CIC-energigune, Bilbao	Examineur
M^{me}. Laurence Croguennec , Directrice de Recherches CNRS, ICMCB, Bordeaux	Examineur
M. Christian Masquelier , Professeur, UPJV, Amiens	Examineur
M. Jean-Noël Chotard , Maître de Conférences, UPJV, Amiens	Examineur



*à Aurore,
pour m'avoir supporté pendant ces longs mois de rédaction*

« On fait la science avec des faits, comme on fait une maison avec des pierres; mais une accumulation de faits n'est pas plus une science qu'un tas de pierres n'est une maison. »

Henri Poincaré, *La Science et l'hypothèse* (1908)

Publications

The material presented in this thesis is an expanded version of the material that was published in the following papers:

E. Boivin, J.-N. Chotard, M. Ménétrier, L. Bourgeois, T. Bamine, D. Carlier, F. Fauth, E. Suard, C. Masquelier, L. Croguennec, Structural and Electrochemical Studies of a New Tavorite Composition: LiVPO_4OH . *Journal of Materials Chemistry A* (**2016**), *4*, 11030–11045.

E. Boivin, J.-N. Chotard, M. Ménétrier, L. Bourgeois, T. Bamine, D. Carlier, F. Fauth, C. Masquelier, L. Croguennec, Oxidation under Air of Tavorite LiVPO_4F : Influence of Vanadyl-Type Defects on Its Electrochemical Properties. *Journal of Physical Chemistry C* (**2016**), *120*, 26187–26198.

T. Bamine, E. Boivin, F. Boucher, R. J. Messinger, E. Salager, M. Deschamps, C. Masquelier, L. Croguennec, M. Ménétrier, D. Carlier, Understanding Local Defects in Li-Ion Battery Electrodes through Combined DFT/NMR Studies: Application to LiVPO_4F . *Journal of Physical Chemistry C* (**2017**), *121* (6), 3219–3227.

E. Boivin, C. Masquelier, L. Croguennec, J.-N. Chotard, Crystal Structure and Lithium Diffusion Pathways of a Potential Positive Electrode Material for Lithium-Ion Batteries: $\text{Li}_2\text{V}(\text{H}_{0.5}\text{PO}_4)_2$. *Inorganic Chemistry* (**2017**), *56* (12), 6776–6779.

E. Boivin, J.-N. Chotard, T. Bamine, D. Carlier, P. Serras, V. Palomares, T. Rojo, M. Ménétrier, A. Iadecola, L. Dupont, L. Bourgeois, F. Fauth, C. Masquelier, L. Croguennec, Vanadyl-type defects in Tavorite-like NaVPO_4F : from the average long range structure to local environments. (**2017**) accepted in *Journal of Materials Chemistry A*

Table of Contents

RÉSUMÉ DE LA THÈSE	1
CHAPTER I: GENERAL INTRODUCTION.....	17
I-1. Energetic context	19
I-2. Li- and Na-ion batteries	21
<i>I-2a. Fundamentals of batteries</i>	<i>22</i>
<i>I-2b. Negative electrode materials</i>	<i>26</i>
<i>I-2c. Electrolyte</i>	<i>27</i>
<i>I-2d. Positive electrode materials</i>	<i>28</i>
I-3. Vanadium phosphates as cathodes for Li- or Na-ion batteries	31
<i>I-3a. NASICON and anti-NASICON $A_xV_2(PO_4)_3$ ($A = Li, Na$).....</i>	<i>32</i>
<i>I-3b. $Na_3V_2(PO_4)_2F_3$.....</i>	<i>37</i>
<i>I-3c. Tavorite A_xVPO_4Y.....</i>	<i>40</i>
<i>I-3d. Discussion</i>	<i>46</i>
I-4. Aims of this work.....	51
CHAPTER II: INFLUENCE OF VANADYL-TYPE DEFECTS ON THE STRUCTURE AND ON THE ELECTROCHEMICAL PROPERTIES OF $LiVPO_4F$	55
II-1. $LiVPO_4F$, a well-known material?	57
<i>II-1a. $LiVPO_4F$: Syntheses, structure and defects</i>	<i>57</i>
<i>II-1b. Phase diagram of Li_xVPO_4F and redox processes involved.....</i>	<i>64</i>
<i>II-1c. Summary and prospects</i>	<i>76</i>
II-2. Oxidation under air of $LiVPO_4F$	78
<i>II-2a. Synthesis of oxidized samples.....</i>	<i>78</i>
<i>II-2b. Average long range structure & microstructure.....</i>	<i>81</i>
<i>II-2c. Growing of vanadyl-type environments</i>	<i>86</i>
<i>II-2d. Electrochemical properties</i>	<i>93</i>
<i>II-2e. Summary and prospects</i>	<i>95</i>
II-3. Extended $LiVPO_4F_{1-y}O_y$ solid solutions, from the long range average structure to the local environments.....	97

II-3a. A non Vegard's law behavior.....	97
II-3b. Average long range structure and microstructure	102
II-3c. Characterization of V^{3+} -F/ V^{4+} =O disorder	107
II-3d. Summary and prospects.....	119
II-4. Impact of vanadyl-type defects on electrochemical performance, on phase diagram and on redox mechanisms.....	120
II-4a. High voltage region, an optimal vanadyl-type defects' concentration	120
II-4b. Low voltage region, a probe for the local environments around vanadium.....	140
II-4c. Summary and prospects	150
CHAPTER III: FURTHER INVESTIGATION OF THE TAVORITE PHASE DIAGRAM	153
III-1. A new tavorite-type composition: NaVPO ₄ F	155
III-1a. Syntheses, structure and defects	155
III-1b. Study of electrochemical inactivity	166
III-1c. Summary and prospects	171
III-2. LiVPO ₄ OH, a new type of two electrons system	173
III-2a. Syntheses and structure of LiVPO ₄ OH.....	173
III-2b. Electrochemical properties and redox mechanism.....	189
III-2c. Summary and prospects	199
III-3. A potential high voltage two electrons system: Li ₂ V(H _{0.5} PO ₄) ₂	202
III-3a. Influence of Hydrogen on the Lithium diffusion path	207
III-3b. Summary and prospects.....	208
CONCLUSION AND PERSPECTIVES	211
ANNEX.....	217
BIBLIOGRAPHY	264

Résumé de la thèse

Le développement de nouveaux matériaux d'électrodes positives pour des batteries Lithium-ion à haute densité d'énergie est l'un des principaux enjeux de la recherche dans le domaine, à la fois au niveau académique et industriel. Des matériaux tels que les oxydes lamellaires $\text{LiM}^{1-x-y}\text{M}^2_x\text{M}^3_y\text{O}_2$ avec $\text{M} = \text{Co}, \text{Ni}, \text{Mn}, \text{Al} \dots$ (LiCoO_2 ,¹ $\text{LiNi}_{0.80}\text{Co}_{0.15}\text{Al}_{0.05}\text{O}_2$ ² et $\text{LiNi}_{1/3}\text{Mn}_{1/3}\text{Co}_{1/3}\text{O}_2$ ³ ...) montrent de bonnes performances et sont déjà industriellement développés. LiCoO_2 est par exemple le matériau le plus rencontré dans les batteries Li-ion d'appareils mobiles, depuis 1991. Cependant, son prix et sa stabilité thermique limitée à l'état chargé de la batterie⁴ ont favorisé le développement des matériaux d'électrode positive à charpentes polyanioniques fournissant une stabilité thermique à long terme, essentielle pour le cyclage répété et la sécurité du dispositif.

Les composés polyanioniques sont un assemblage d'octaèdres MO_6 ($\text{M} =$ métal de transition) et de polyèdres XO_n ($\text{X} = \text{P}, \text{S}, \text{Si}, \text{B} \dots$), offrant une variété de réseaux bi ou tridimensionnels avec des espaces interstitiels disponibles pour une diffusion aisée d'ions alcalins. Dans ces matériaux, le remplacement des anions Oxygène des oxydes par des groupements polyanioniques XO_n augmente la masse électrochimiquement inactive et tend à diminuer la capacité massique. Toutefois, la forte covalence de ces groupements tend à augmenter la ionicité de la liaison métal-oxygène antagoniste et ainsi, par effet inductif, augmenter le potentiel vs. Li d'un couple oxydant réducteur donné comparé à celui obtenu dans des oxydes. De plus, il est possible de moduler d'avantage ce potentiel en changeant la nature du groupement polyanionique comme démontré, par Goodenough, dans la structure de type NASICON, $\text{A}_3\text{M}_2(\text{XO}_4)_3$ ($\text{A} = \text{Li}, \text{Na}$; $\text{M} = \text{Fe}, \text{Ti}, \text{V} \dots$; $\text{X} = \text{P}, \text{W}, \text{Mo}, \text{S} \dots$), passant du phosphate au tungstate au molybdate et au sulfate⁵. La grande variété d'arrangements atomiques qu'ils peuvent adoptés avec des possibilités de substitutions cationiques et anioniques permet d'adapter leurs propriétés à l'application ciblée.

Les recherches sur les composés polyanioniques comme matériaux de cathodes ont, dans un premier temps, été dominées par celles sur la triphylite LiFePO_4 ⁶⁻¹⁰ (structure de type olivine). Cependant, malgré le haut potentiel pour un couple $\text{Fe}^{2+}/\text{Fe}^{3+}$ délivré par LiFePO_4 (*i.e.* 3.45 V vs. Li^+/Li), il reste plutôt faible comparé à celui des oxydes à base de Cobalt, Manganèse ou Nickel, conduisant à une densité d'énergie plus faible. Une manière d'augmenter le potentiel du couple $\text{Fe}^{2+}/\text{Fe}^{3+}$ est de d'avantage tirer profit de l'effet inductif en utilisant des composés contenant du fluor et/ou des groupements sulfates. En effet, LiFeSO_4F adoptant soit une structure Tavorite soit une structure Triplite délivre une tension plus haute pour le couple

$\text{Fe}^{2+}/\text{Fe}^{3+}$ comparé à celui observé pour LiFePO_4 (*i.e.* respectivement 3.6 et 3.9 vs. Li^+/Li contre 3.45 V vs. Li^+/Li pour LiFePO_4)^{11,12}.

La structure Tavorite est l'un des systèmes structuraux les plus adaptés pour tirer avantage de l'effet inductif. En effet, comme montré dans la **Figure 1**, la grande flexibilité de ce réseau permet d'ajuster le potentiel de travail des matériaux Tavorites LiMXO_4Y en modulant la nature du métal de transition (avec $\text{M} = \text{V}, \text{Fe}, \text{Mn}, \text{Ti}$), du groupement polyanionique (XO_4 avec $\text{X} = \text{P}$ or S) ou de l'anion pontant (avec $\text{Y} = \text{O}, \text{F}, \text{OH}, \text{H}_2\text{O}$).

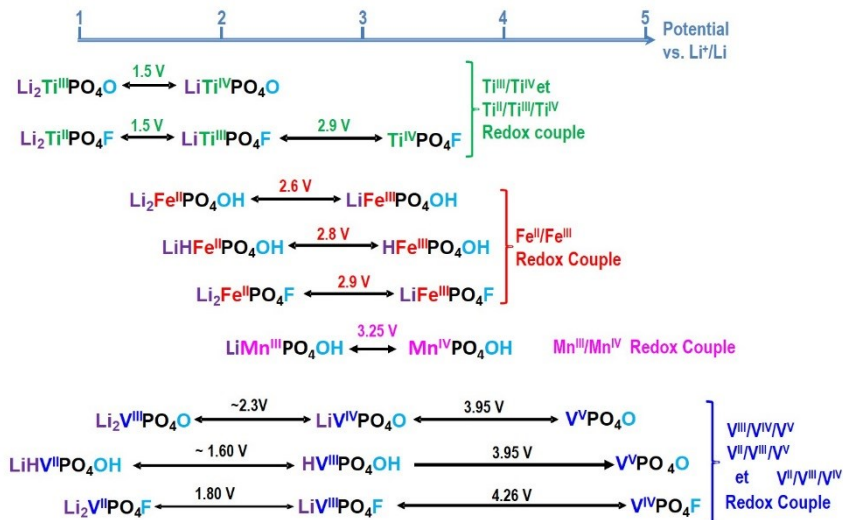


Figure 1: vue d'ensemble des compositions $\text{Li}_x\text{MPO}_4\text{Y}$ adoptant la structure Tavorite et les voltages correspondant (adapté depuis la réf. ¹³)

Dans cette structure, les octaèdres MO_4Y_2 sont liés par l'anion pontant Y et forment des chaînes infinies connectées entre elles par des tétraèdres XO_4 . Cet arrangement cristallographique génère un réseau tridimensionnel et des canaux pour la diffusion des ions alcalins. Les phosphates de Vanadium adoptant la structure Tavorite sont très attractifs du fait de leur haut potentiel de fonctionnement, ils délivrent une densité d'énergie compétitive avec celle de matériaux déjà commercialisés tels que LiFePO_4 : densité d'énergie de 655 et 620 Wh/Kg pour respectivement LiVPO_4F et LiVPO_4O vs. 586 Wh/Kg pour LiFePO_4 . Dans ces matériaux, au-delà de l'effet inductif, un autre facteur agit de manière significative sur le potentiel: la liaison vanadyle $\text{V}^{4+}=\text{O}$, fortement covalente, qui tend à réduire le potentiel du couple $\text{V}^{4+}=\text{O}/\text{V}^{5+}=\text{O}$ correspondant. En effet, dans LiVPO_4O , l'extraction de lithium se produit à 3.95 V vs Li^+/Li alors que, dans LiVPO_4F , exempt de liaison vanadyle, malgré le plus faible degré d'oxydation du Vanadium, cette extraction a lieu à un potentiel plus haut (*i.e.* à la tension moyenne de 4.26V vs Li^+/Li pour le couple redox $\text{V}^{3+}/\text{V}^{4+}$).

LiVPO₄F montre de très bonnes performances même à des régimes élevés^{14,15} ainsi qu'une stabilité vis-à-vis de l'air, de l'humidité dans son état original ainsi que dans son état chargé,¹⁶⁻¹⁸ des caractéristiques essentielles pour sa production à grande échelle comme matériau d'électrode positive pour batteries Li-ion. Ce matériau présente ainsi de nombreuses qualités mais aussi des « défauts »... Défauts structuraux récemment mis en évidence par RMN 2D dans un échantillon semblant pur et stœchiométrique du point de vue de la diffraction.¹⁹ Quelle est la nature de ces défauts? Quelle est leur influence sur la structure à l'échelle locale et moyenne? Comment ces défauts impactent les performances électrochimiques, les mécanismes redox et le diagramme de phases observés au cours des réactions d'extraction ou d'insertion du Lithium? De plus, bien que le diagramme de phases Li_xVPO₄F ait déjà été étudié en profondeur dans notre groupe, certains mystères persistent concernant la phase intermédiaire Li_{2/3}VPO₄F.

Ordres complexes dans Li_{2/3}VPO₄F

De nouvelles informations sur les mécanismes redox et les transitions de phases mis en jeu pendant le cyclage de LiVPO₄F ont été données dans ce manuscrit. Par des expériences d'absorption des rayons X conduites *operando* au seuil K du vanadium, l'activation réversible et asymétrique du couple V³⁺/V⁴⁺ a été mise en évidence. Ceci est en bon accord avec les travaux précédemment menés dans notre groupe, révélant une transition de phase à la composition Li_{0.67}VPO₄F pendant la charge de la batterie, transition qui n'est pas observée au cours de la décharge.²⁰

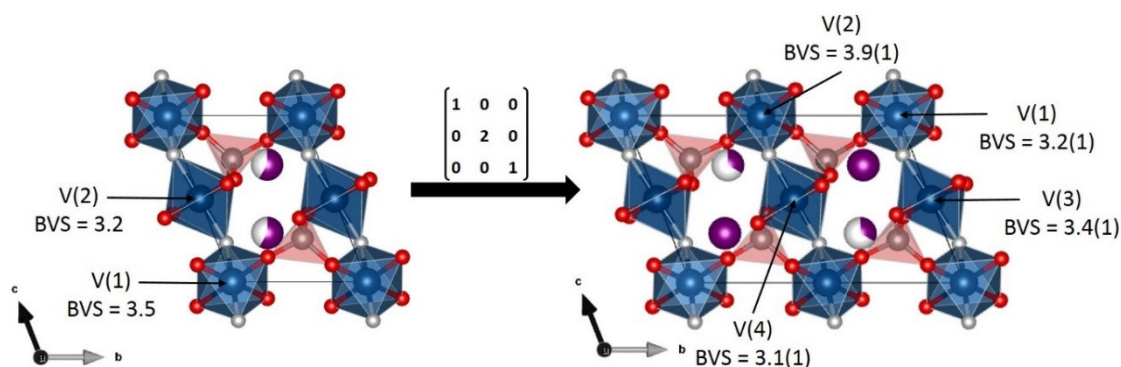


Figure 2: projection le long de la direction $[100]$ de la structure de $Li_{0.67}VPO_4F$ obtenue à partir de l'affinement Rietveld dans un modèle avec $Z=2$ (gauche) et dans un modèle $Z=4$ (droite): les octaèdres VO_4F_2 sont représentés en bleu, les tétraèdres PO_4 en rouge et le lithium en violet.

La caractérisation plus en profondeur de cette phase réalisée par diffraction des rayons X (DRX) synchrotron a révélé, pour la première fois, un ordre complexe. En effet, les contributions de faibles intensités observées par DRX nécessitent un doublement de la maille pour être prises en compte, répartissant le Lithium, présent dans un unique site occupé à deux-

tiers dans la maille moyenne, dans deux sites remplis de manière inhomogène ($\tau(\text{Li}(1))=1$ et $\tau(\text{Li}(2))=0.33$). De plus, l'analyse des BVS (Bond Valence Sum) suggère également l'établissement d'un ordre de charges partiel $\text{V}^{3+}/\text{V}^{4+}$ avec des cations vanadium montrant un fort caractère V^{3+} ou V^{4+} et d'autres une valence mixte ($\text{V}^{3+}/\text{V}^{4+}$) (voir la **Figure 2**).

Du point de vue de l'EXAFS (Extended X-ray Absorption Fine Structure), la première sphère de coordination autour du vanadium peut être décrite comme une combinaison d'environnements de type V^{4+} (*i.e.* VPO_4F -type) et de type V^{3+} (*i.e.* LiVPO_4F -type) et ne diffère d'un mélange $\text{LiVPO}_4\text{F}/\text{VPO}_4\text{F}$ (dans des proportions 0.67/0.33) que pour des sphères de coordination éloignées. Ceci soutient l'ordre de charge partiel suggéré par l'étude BVS. A première vue, la Résonance Magnétique Nucléaire (RMN) du ^7Li nous est apparue comme la technique la plus pertinente pour décrire cet ordre complexe, mais, sans calculs théoriques de type DFT (Density Functional Theory), la signature RMN n'a pas pu être complètement interprétée.

Défauts de type vanadyles dans LiVPO_4F

La nature des défauts précédemment mis en évidence par RMN dans $\text{LiVPO}_4\text{F}^{19}$ (repérés par ∇ à la **Figure 3a**) a été partiellement élucidée. La première approche calculatoire considérée des défauts de type « vanadyle » selon deux modèles: $\text{LiVPO}_4\text{F}_{0.96}\text{O}_{0.04}$ (modèle I) and $\text{Li}_{0.96}\text{VPO}_4\text{F}_{0.96}\text{O}_{0.04}$ (modèle II) illustrés à la **Figure 3b**.

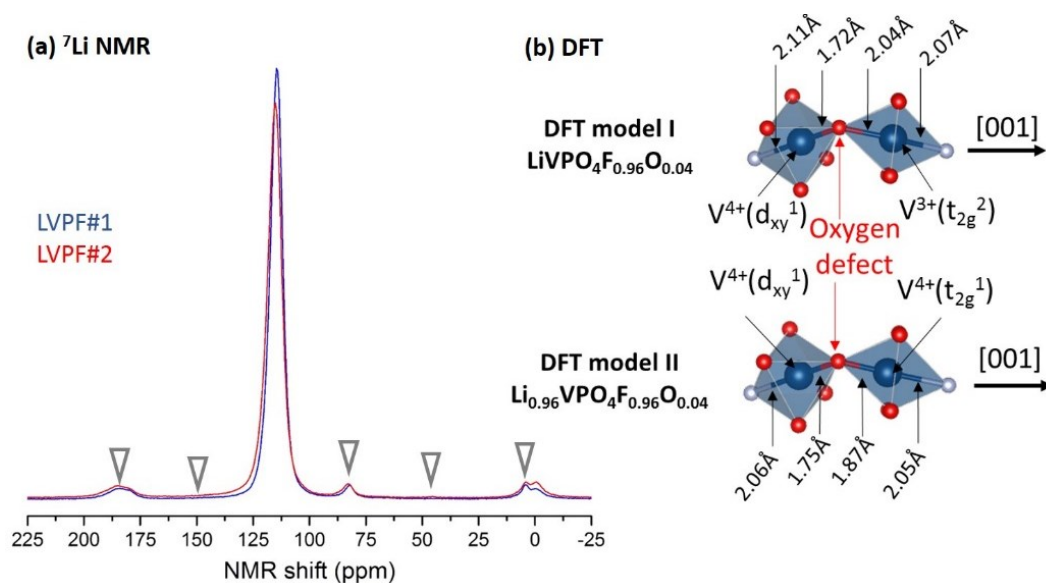


Figure 3: (a) spectres RMN du ^7Li de deux échantillons de LiVPO_4F (LVPF#1 et LVPF#2), les contributions des défauts sont notés avec ∇ . (b) représentation schématique des modèles considérés pour les calculs DFT permettant d'identifier la nature des défauts.

Le modèle I impliquant la substitution partielle du fluor par l'oxygène et la formation locale de la liaison vanadyle (liaison $V^{4+}=O$ covalente) prédit, entre autres, une contribution dont le déplacement est négatif, non observée expérimentalement. Dans le modèle II, des lacunes de lithium sont générées au voisinage des défauts de type vanadyle conduisant à la formation de paires de V^{4+} à l'intérieur des chaînes d'octaèdres riches en V^{3+} . Les déplacements RMN prédits par ce modèle II sont en bon accord avec le spectre expérimental, en particulier au regard de l'absence de signal dans la région négative.²¹

Expérimentalement, la présence de défauts de type vanadyle a été mise en lumière par XANES au travers d'une faible contribution dans le pré-seuil à 5469.7 eV, signature typique des $V^{4+}=O$ (vs. 5469.4 eV pour $LiV^{4+}PO_4O$). Cependant, nous sommes, pour le moment, dans l'incapacité de valider le modèle II, car pour de si faibles concentrations de défauts, les lacunes de lithium ne peuvent être décelées par diffraction. De plus, la différence de signature XANES attendue pour ces deux modèles étant inconnue, sans simulation théorique des spectres, il n'est pas possible de valider le modèle II. Ces défauts de type vanadyle pourraient influencer la structure et les propriétés électrochimiques, mais les étudier en de si faibles concentrations est compliqué. La stratégie adoptée a été d'augmenter la quantité de défauts dans $LiVPO_4F$ par différents moyens afin de tenter d'élucider leur nature ainsi que leur influence sur la structure et les propriétés électrochimiques.

La substitution partielle du fluor par l'oxygène peut en effet se produire soit durant le traitement thermique (traces d'oxygène dans le four rempli sous Ar) ou pendant la trempe à azote liquide de l'échantillon à la fin de la synthèse ou au cours de son stockage. Ce matériau s'est révélé être extrêmement stable dans les conditions ambiantes ce qui invalide la dernière hypothèse.

- Dans un premier temps, les échantillons obtenus par recuit sous air de $LiVPO_4F$ à des températures contrôlées ont été examinés afin d'étudier l'effet d'une oxydation qui aurait eu lieu entre la sortie du four et la plongée de l'échantillon dans l'azote liquide.
- Dans un deuxième temps, une gamme de compositions $LiVPO_4F_{1-y}O_y$ a été obtenue via une unique étape de synthèse simulant la formation de défauts générés pendant la synthèse de " $LiVPO_4F$ ".

Oxydation sous air de LiVPO_4F

L'oxydation sous air de LiVPO_4F a été étudiée afin de prendre connaissance des différents types de défauts qui pourraient s'être formés dans des conditions de synthèses non contrôlées. Cette méthode a démontré la possibilité de préparer des oxy-fluorures de compositions $\text{LiVPO}_4\text{F}_{1-y}\text{O}_y$ avec une valence mixte $\text{V}^{3+}/\text{V}^{4+}$. Toutefois, il apparaît que les domaines de solutions solides formées à des températures de recuits modérées (*i.e.* $T < 525^\circ\text{C}$) sont limités (à 10% de la substitution maximale). Les mélanges entre des phases riches en fluor et riches en oxygène sont obtenus à des températures plus élevées. L'analyse de la microstructure a révélé la présence d'effets de contraintes dans tous les matériaux $\text{LiVPO}_4\text{F}_{1-y}\text{O}_y$, probablement du fait de la large différence de nature entre les séquences de liaisons $\text{O}\dots\text{V}^{\text{IV}}=\text{O}$ et $\text{F}-\text{V}^{\text{III}}-\text{F}$ qui rend difficile leur mélange homogène/statistique le long des chaînes d'octaèdres. En plus de la description structurale moyenne donnée par DRX, les spectroscopies RMN et IR apparaissent comme les techniques complémentaires les plus adéquates pour mener à une caractérisation en profondeur des environnements locaux.

Bien que la spectroscopie vibrationnelle ait révélé que la nature des défauts formés par recuit de LiVPO_4F sous air est similaire à ceux présents dans le matériau original dans des concentrations plus élevées, leur distribution apparaît être complètement différente, du point de vue de la RMN. En effet, La RMN a montré que les pics attribués aux défauts dans LiVPO_4F tendent à disparaître alors qu'une contribution de type LiVPO_4O (différente mais proche de celle observée pour LiVPO_4O) croît en intensité avec l'oxydation du matériau (**Figure 4**).

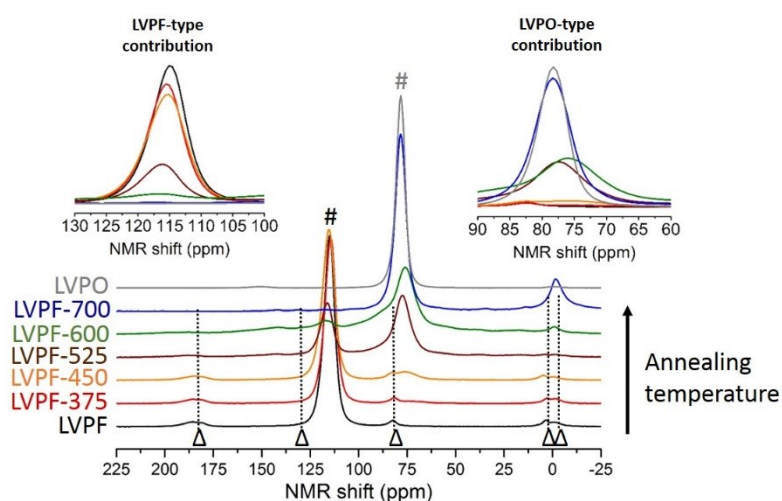


Figure 4: Spectres RMN du ^7Li normalisés (selon la masse d'échantillon) de LVPF, LVPF-375, LVPF-450, LVPF-525, LVPF-600, LVPF-700, and LVPO. En insert, agrandissements des signaux isotropes associés aux différentes contributions principales. Les pics isotropes sont notés par # et les contributions additionnelles par Δ.

Par conséquent, les défauts dans le matériau LiVPO_4F original pourraient faire office de sites de nucléation pour des domaines de types LiVPO_4O plus étendus dont la taille croît avec l'augmentation de la température de recuit. A faible température (*i.e.* $T < 525^\circ\text{C}$), la taille de ces domaines étant trop petite, la DRX ne les détecte pas comme des phases distinctes. Toutefois, au regard du profil de tension délivrée par ces échantillons « monophasés » (*i.e.* monophasés à l'échelle de la diffraction), une contribution de type LiVPO_4O est détectée à 4.0 V vs. Li^+/Li . L'électrochimie étant une sonde locale, cette contribution révèle la présence de domaines de type LiVPO_4O étendus et non des défauts ponctuels/isolés. Donc, le recuit sous air de LiVPO_4F semble ne pas générer de nouveaux sites ponctuels de défauts mais étend les régions défectueuses conduisant ainsi à une distribution locale $\text{V}^{3+}\text{-F}/\text{V}^{4+}\text{=O}$ différente de celle obtenue pour LiVPO_4F .

La RMN et les tests électrochimiques ont révélé que cette stratégie ne reproduit pas les défauts observés dans LiVPO_4F et n'est donc pas pertinente pour étudier l'impact des défauts ainsi générés sur les propriétés électrochimiques. Pour cette raison, l'étude de solutions solides étendues $\text{LiVPO}_4\text{F}_{1-y}\text{O}_y$ obtenues via une unique étape de synthèse a été conduite.

Solutions solides étendues $\text{LiVPO}_4\text{F}_{1-y}\text{O}_y$

La synthèse en une étape des phases Tavorite $\text{LiVPO}_4\text{F}_{1-y}\text{O}_y$ a été réalisée en contrôlant le taux de substitution fluor/oxygène. En faisant varier l'excès de carbone utilisé comme réducteur du précurseur V^{5+} , des échantillons de valences mixtes $\text{V}^{3+}/\text{V}^{4+}$ ont été obtenus. Le degré d'oxydation moyen du vanadium, déterminé par des mesures de susceptibilités magnétiques, sont en bon accord avec la formation de matériaux à valences mixtes. Dans ces matériaux, une distribution désordonnée des anions F^-/O^{2-} et des cations $\text{V}^{3+}/\text{V}^{4+}$ le long des chaînes d'octaèdres a été décelée. Le champ cristallin induit par ce désordre conduit à une déviation significative à la loi de Végard corrélée à de forts effets de contraintes anisotropes. L'EXAFS explique partiellement cet écart à la loi de Végard, prédisant la contraction des octaèdres de V^{4+} dans un environnement mixtes fluor/oxygène conduisant à une contraction du paramètre de maille lié à la direction de propagation des chaînes d'octaèdres (*i.e.* \vec{c} voir **Figure 5**). Ce comportement a été attribué à la compétition entre l'ionicité de la liaison $\text{V}^{3+}\text{-F}$ et la covalence de la liaison $\text{V}^{4+}\text{=O}$ qui génère de forts effets de contraintes au sein de la structure.

Du point de vue de l'EXAFS, ces matériaux peuvent être décrits comme une combinaison de 3 sortes d'environnements pour le vanadium, dont les proportions varient

d'une composition à l'autre, comme représentés à la **Figure 5**. Du fait du désordre, la diffraction prédit la présence d'octaèdres de vanadium purement centrosymétriques alors que les spectroscopies XANES (X-ray Adsorption Near Edge Structure) et Raman ont clairement mis en lumière des distorsions locales de types vanadyle. La RMN a révélé une signature complexe avec des contributions apparentées à celles des défauts locaux observés dans LiVPO_4F . Cependant, l'ICP-OES (spectrométrie d'émission optique à plasma induit) et la DN (diffraction des neutrons) ont révélé l'absence de lacunes de lithium, contrairement aux prédictions des calculs DFT pour le modèle retenu précédemment (modèle II voir **Figure 3b**). Des calculs DFT et des expériences de RMN 2D sont en cours afin de mieux comprendre la signature RMN et de déceler d'éventuels ordres locaux $\text{V}^{3+}/\text{V}^{4+}$ malgré l'apparent désordre à longue distance qui permettraient d'expliquer ces contradictions.

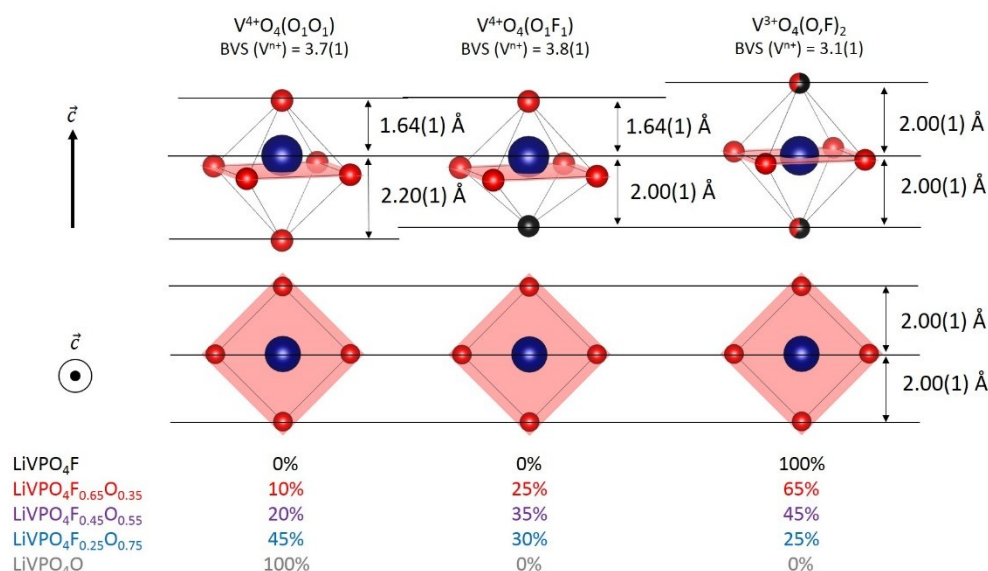


Figure 5: résumé des interprétations de l'EXAFS expliquant la déviation à la loi de Vegard le long de la direction propagation des chaînes d'octaèdres.

L'étude spectroscopique de ces matériaux a mis en évidence que les défauts impactent fortement la structure électronique des orbitales des éléments présents dans le matériau vanadium et *a fortiori* les propriétés électrochimiques. Par conséquent, l'influence de la concentration en défauts de types vanadyle sur l'électrochimie des matériaux $\text{LiVPO}_4\text{F}_{1-y}\text{O}_y$ a été étudiée.

Influence de la concentration des défauts de type vanadyle sur les performances électrochimiques et mécanismes impliqués.

Nous suspectons que tous les matériaux LiVPO_4F reportés dans la littérature présentent une quantité variable de défauts de type vanadyle. Les performances électrochimiques dépendent probablement de leur concentration/distribution, mais aussi de la nature du revêtement de carbone ou de la taille des particules. Dans la région haut potentiel (*i.e.* 3.0-4.6V vs Li^+/Li), les matériaux $\text{LiVPO}_4\text{F}_{1-y}\text{O}_y$ montrent des propriétés proches de celles de LiVPO_4F mais avec une augmentation de la tension de travail à mesure que le taux de fluor augmente et, à bas régimes, une capacité et une polarisation plus faibles pour les phases présentant une valence mixte. A plus hauts régimes, alors que la capacité délivrée par LiVPO_4F diminue fortement, celles des matériaux $\text{LiVPO}_4\text{F}_{1-y}\text{O}_y$ apparaissent plus importantes spécialement pour les échantillons riches en fluor (**Figure 6**). Par conséquent, il semblerait qu'une concentration optimale de défauts de type vanadyle existe, améliorant les propriétés de transport et ainsi les performances électrochimiques à hauts régimes.

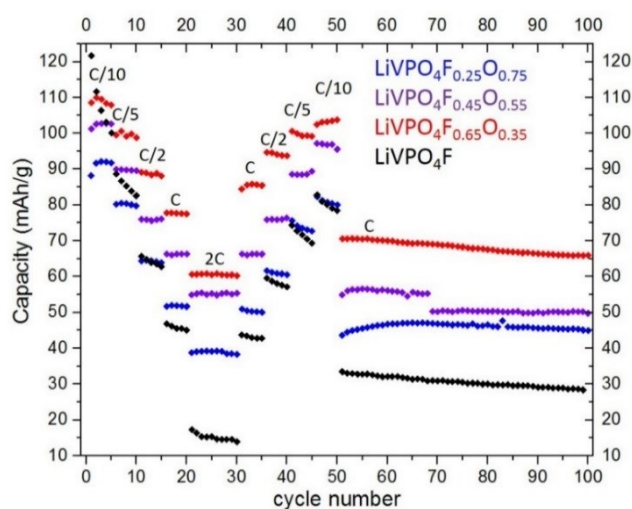


Figure 6: Evolution de la capacité de décharge des matériaux $\text{LiVPO}_4\text{F}_{1-y}\text{O}_y$ à différents régimes (depuis C/10 jusqu'à 2C) en fonction du nombre de cycles.

Afin de comprendre l'origine de cette concentration optimale de défauts de types vanadyle, l'étude des propriétés de diffusion du lithium (par cyclages galvanostatiques en mode GITT), du mécanisme structural (par DRX synchrotron *operando*) et des processus redox (par XAS *operando*) a été menée au cours du cyclage des matériaux $\text{LiVPO}_4\text{F}_{1-y}\text{O}_y$.

Les expériences XAS *operando* ont clairement mis en évidence l'activation du couple $\text{V}^{4+}=\text{O}/\text{V}^{5+}=\text{O}$ pendant la première étape de la charge de la batterie et du couple $\text{V}^{3+}/\text{V}^{4+}$ dans un environnement riche en fluor conduisant à la formation de matériaux de valences mixtes

V^{5+}/V^{3+} . L'étude *operando* par DRX a révélé que cette première étape correspond à un large domaine de solution solide où la structure moyenne semble figée. La compétition entre la grande covalence de la liaison vanadyle ($V^{4+}=O$ et ensuite $V^{5+}=O$) et la forte ionicité de la liaison $V^{3+}-F$ empêche la contraction de la structure le long des chaînes d'octaèdres. La delithiation plus profonde se produit selon deux processus pseudo-biphasés consécutifs avec une transition de phase à la composition correspondante à un ratio V^{3+}/V^{4+} approximatif de 2 quel que soit la quantité de défauts $V^{4+}=O$ dans le matériau de départ (**Figure 7**).

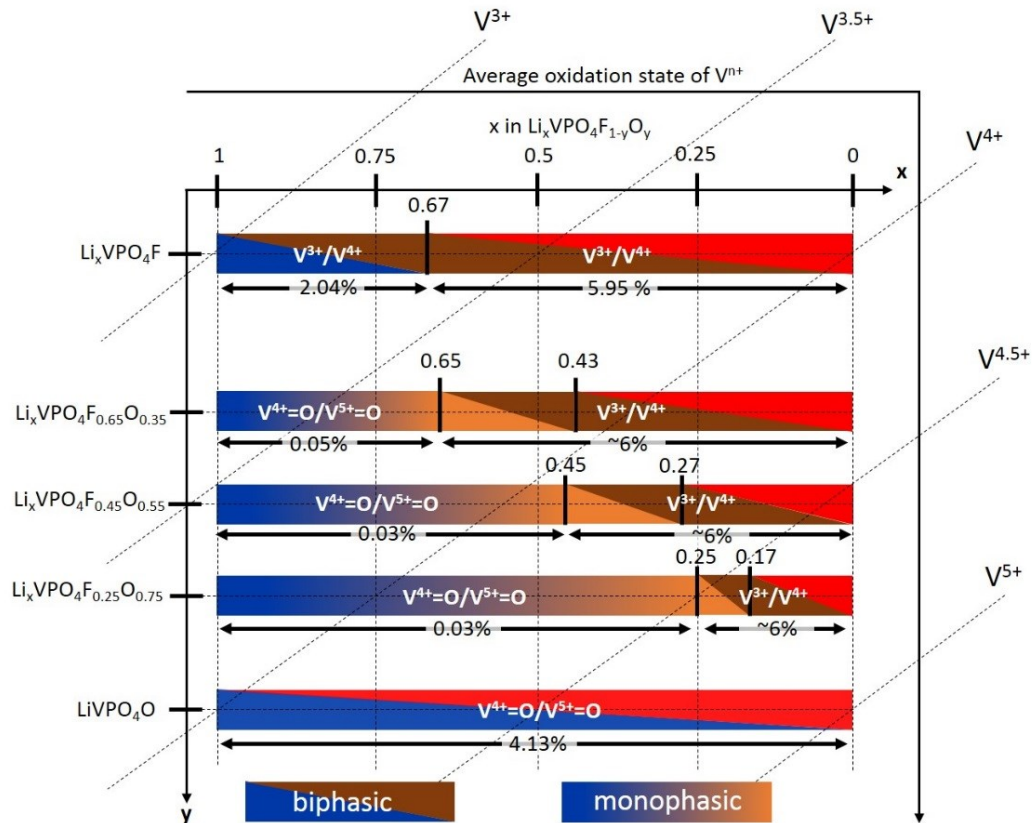


Figure 7: diagramme de phases et processus redox schématisés du système $Li_xVPO_4F_{1-y}O_y$.

Le diagramme de diffraction correspondant au matériau complètement délithié obtenu *ex-situ* contient 2 phases. L'hypothèse que nous avons proposée est de considérer la séparation en deux phases, l'une riche en fluor, l'autre riche en oxygène. Notons que cette « démixtion » résulte probablement de la clusterization partielle des domaines V^{3+}/V^{4+} (et F/O^{2-}) observée dans le matériau initial et que les plus fortes contraintes imposées par le champ cristallin à l'état chargé la mettent en lumière. Toujours est-il que, dans les phases $LiVPO_4F_{1-y}O_y$, l'activation du couple V^{3+}/V^{4+} conduit à une contraction globale de la structure et à un rétrécissement de la taille des chemins de diffusion du lithium. L'effet bénéfique des défauts vanadyle sur la stabilité en cyclage et sur les performances en régime pourrait provenir de l'équilibre entre les deux processus décrits (*i.e.* $V^{4+}=O/V^{5+}=O$ vs. V^{3+}/V^{4+}). En effet, la structure

semble figée durant l'activation du couple $V^{4+}=O/V^{5+}=O$ et la délithiation plus profonde conduit à des changements de volumes similaires quel que soit le taux de substitution O^{2-}/F^- (voir **Figure 5**). Par conséquent, pour les phases riches en oxygène (ayant un large domaine $V^{4+}=O/V^{5+}=O$) la structure subit de forts changements dans un domaine de composition étroit alors que pour les phases riches en fluor (ayant un étroit domaine $V^{4+}=O/V^{5+}=O$), ces changements sont étalés sur un domaine de composition plus large. Les évolutions structurales plus douces observées pour les matériaux riches en fluor ont un effet bénéfique sur la stabilité en cyclage et sur les performances en régime.

Le profil de potentiel observé durant l'insertion de Lithium dans ces matériaux peut être décrit comme une combinaison entre des signatures de types $LiVPO_4O$, au-dessus de 1.9 V, $LiVPO_4F$, entre 1.6 et 1.9 V et une troisième contribution à plus bas potentiel (*i.e.* 1.4 V vs. Li^+/Li) dans des proportions relatives évoluant en fonction du taux de substitution O^{2-}/F^- . En effet, les expériences XAS menées *operando* au seuil K du vanadium ont révélé la réduction du $V^{4+}=O$ en $V^{3+}-O$ durant la première étape de lithiation. Ceci induit la formation d'une phase purement V^{3+} avec la persistance d'une distorsion « vanadyle » qui a été mise en évidence à la fois par XANES et par EXAFS. La lithiation plus profonde conduit à l'activation du couple V^{3+}/V^{2+} avec l'atténuation de cette distorsion et une forte augmentation des longueurs de liaisons autour du vanadium. Ceci confirme l'interprétation visuelle faite sur la base de l'électrochimie qui, étant une sonde locale, permet d'approximer la quantité de défauts de types vanadyle dans " $LiVPO_4F$ " sans avoir recours à des techniques de caractérisations lourdes qui ne sont pas disponibles pour tous (en particulier la RMN du solide et le XAS).

Substitutions des sites alcalins et anioniques dans la structure Tavorite.

La prospection vers la stabilisation de nouvelles phases potentiellement intéressantes à l'électrode positive de batteries Li et Na-ion est un des principaux enjeux dans le domaine. Par conséquent, la substitution des sites anioniques et alcalins dans la structure Tavorite a été réalisée. Les processus électrochimiques engendrés par les nouveaux matériaux ainsi obtenus ont révélé d'autres aspects fascinants de la liaison vanadyle.

Structures locales et moyennes de NaVPO_4F et étude de son inactivité électrochimique.

Nous reportons pour la première fois la synthèse d'une phase riche en V^{3+} à base de sodium cristallisant dans une structure de type Tavorite. Ce matériau a été obtenu dans des conditions hydrothermales, conduisant à la formation de particules en formes d'aiguilles et à une large distribution de tailles. Sa structure cristalline a été déterminée par une combinaison de plusieurs techniques couvrant la diffraction des RX sur poudre et des électrons ainsi que les spectroscopies infra rouge, RMN et d'absorption des RX. Les calculs de BVS et les mesures de susceptibilité magnétique ont révélé un degré d'oxydation moyen pour le vanadium légèrement supérieur à V^{3+} , suggérant la présence de défauts de types vanadyle (proche de 15%) et ainsi une composition approximative $\text{NaVPO}_4\text{F}_{0.85}\text{O}_{0.15}$. Des effets microstructuraux ont été identifiés via des élargissements anisotropes des raies de diffraction. En effet, de telles contraintes sont en accord avec la présence d'environnements de types vanadyle en tant que défauts, qui génèreraient localement un rétrécissement des distances V-F(O) le long des chaînes d'octaèdres $\text{VO}_4(\text{F},\text{O})_2$. Des techniques spectroscopiques telles que l'IR et le XAS ont été utilisées pour étudier ces environnements locaux. En effet, la signature caractéristique de la contribution de type vanadyle a été clairement identifiée alors que la présence de groupements OH a été exclue. Ce matériau est électrochimiquement (quasi) inactif malgré une morphologie adéquate et des défauts de type vanadyle qui peuvent améliorer les performances (tout du moins pour l'analogue lithié). En effet, l'étude par BVEL (Bond Valence Energy Landscape) et par DRX *operando* de LiVPO_4F cyclé vis à vis du sodium ont révélé que les performances électrochimiques de ce matériau sont inhibées par la faible mobilité intrinsèque du sodium dans la charpente Tavorite.

LiVPO_4OH : Vers un nouveau de type de système à deux électrons.

Un nouvel hydroxyle phosphate à base de vanadium adoptant la structure Tavorite a été obtenu pour la première fois, par voie hydrothermale à environ 250°C . Il peut être préparé à partir d'au moins 3 précurseurs de vanadium (VCl_3 , V_2O_5 et VPO_4) conduisant à des matériaux avec des morphologies différentes. Toutefois, quel que soit le précurseur utilisé, des impuretés de différentes natures persistent. Parmi celles-ci, une impureté de type Tavorite, proche mais différente de LiVPO_4O , a été obtenue. La structure de LiVPO_4OH a été déterminée grâce aux affinements combinés de données de diffraction des neutrons et des rayons X synchrotron révélant la formation d'une phase Tavorite. Sa structure est très similaire à celle de LiVPO_4F (remplacement de F par OH) avec des distances légèrement plus longues autour du vanadium et avec la formation d'une liaison hydrogène au travers du canal hexagonal de la structure

Tavorite. Des preuves additionnelles de la présence de groupements hydroxyles influencés par leurs environnements ont été données par la spectroscopie IR via un large signal d'élongation des OH, typique pour un groupement hydroxyle impliqué dans une liaison hydrogène. Malgré la grande similarité entre les structures de LiVPO_4OH et LiVPO_4F , l'étude BVEL a révélé que cette liaison hydrogène pouvait gêner la mobilité du Lithium et imposer des chemins de diffusion différents dans LiVPO_4OH .

L'insertion de lithium dans LiVPO_4OH se produit en deux étapes : un processus de solution solide jusqu'à atteindre la composition $\text{Li}_{1.25}\text{VPO}_4\text{OH}$ et ensuite une réaction biphasée jusqu'à former la phase $\text{Li}_2\text{V}^{\text{IV}}\text{PO}_4\text{OH}$. La structure de cette dernière a été résolue grâce à des données de DRX synchrotron. La symétrie du réseau polyanionique adopté par $\text{Li}_2\text{VPO}_4\text{OH}$ est liée à celle de $\text{Li}_2\text{VPO}_4\text{O}$ alors que les longueurs de liaisons autour du vanadium sont proches de celles observées pour $\text{Li}_2\text{VPO}_4\text{F}$ (2.14 vs. 2.13 Å pour $\text{Li}_2\text{VPO}_4\text{F}$), en bon accord avec le degré d'oxydation commun du vanadium dans ces deux phases. Une combinaison de cartes de Bond Valence et de carte de Fourier différence ont permis de proposer 4 sites pleinement occupés pour le Lithium dans $\text{Li}_2\text{VPO}_4\text{OH}$, qui doivent encore être confirmés par diffraction des neutrons et des expériences de RMN du ^7Li .

Dans la région à haut potentiel, malgré des pauvres performances, cette nouvelle phase révèle un mécanisme original. En effet, les mesures GITT (**Figure 8**) ont révélé que l'oxydation du vanadium se produit à un potentiel d'équilibre constant de 3.95 V vs Li^+/Li jusqu'à atteindre l'état V^{5+} .

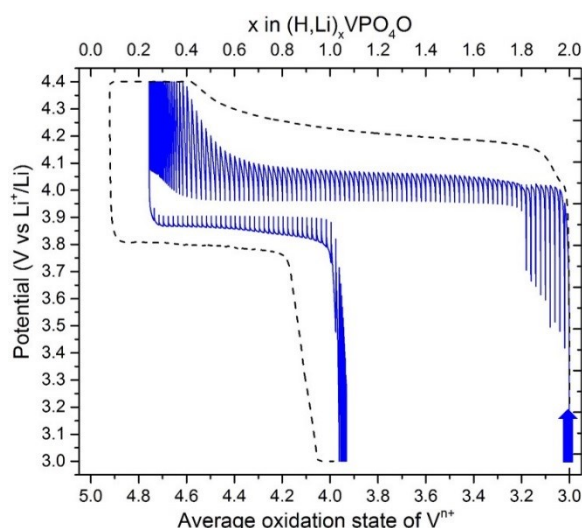


Figure 8: profile GITT de LiVPO_4OH cyclé entre 3.0 et 4.4V vs. Li^+/Li (i.e. région à haut potentiel).

Des expériences de XANES menées *operando* au seuil K du vanadium ont mis évidence la croissance continue d'une forte contribution $V^{5+}=O$ dans le pré-seuil, suggérant l'activation du couple $V^{3+}-O/V^{5+}=O$ pour ce mécanisme. De plus, la DRX synchrotron *operando* a révélé que l'oxydation de $LiV^{III}PO_4OH$ se produit en un unique processus biphasé conduisant à la formation de V^VPO_4O à l'état chargé. Par conséquent, aucune phase riche en V^{4+} n'a pu être détectée pendant le cyclage alors que l'extraction de lithium aurait dû induire la formation de la phase intermédiaire, V^IVPO_4OH . Nous suspectons que cette dernière est instable. Notre hypothèse concernant l'instabilité de V^IVPO_4OH , conduisant à l'extraction de Li^+ et de H^+ , est de considérer la compétition entre la liaison $V^{4+}=O$ d'un côté et la liaison O-H de l'autre (**Figure 9**): la séquence V^IV-O-H est ainsi déstabilisée le long des chaînes d'octaèdres. Afin de satisfaire à la valence de l'oxygène impliqué dans les deux liaisons, un affaiblissement de la liaison OH se produit conduisant à l'extraction concomitante des cations Li^+ et H^+ .

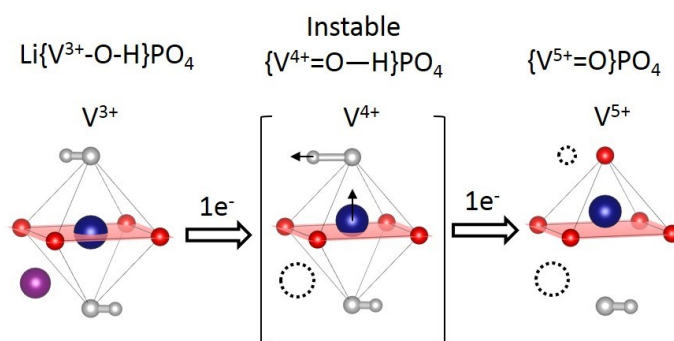


Figure 9: illustration schématique du processus d'oxydation de $LiVPO_4OH$

Finalement, cette étude révèle que la versatilité de la chimie du vanadium avec un large nombre de degrés d'oxydations stables (depuis V^{2+} à V^{5+}), stabilisés dans des environnements très différents (depuis des environnements très réguliers jusqu'à d'autres très irréguliers), ouvre la voie vers la formation de nouveaux matériaux dont les contraintes imposées par le champ cristallin donnent des propriétés électrochimiques attractives.

Chapter I: General introduction

Table of Contents

I-1. Energetic context	19
I-2. Li- and Na-ion batteries	21
<i>I-2a. Fundamentals of batteries</i>	22
<i>I-2b. Negative electrode materials</i>	26
<i>I-2c. Electrolyte</i>	27
<i>I-2d. Positive electrode materials</i>	28
I-3. Vanadium phosphates as cathodes for Li- or Na-ion batteries	31
<i>I-3a. NASICON and anti-NASICON $A_xV_2(PO_4)_3$ ($A = Li, Na$)</i>	32
<i>I-3b. $Na_3V_2(PO_4)_2F_3$</i>	37
<i>I-3c. Tavorite A_xVPO_4Y</i>	40
<i>I-3d. Discussion</i>	46
I-4. Aims of this work	51

I-1. Energetic context

At the origin, human beings used biomass as the only energy resource and its environmental impact through CO₂ release was limited because the photosynthesis reabsorbed the quasi totality of these emissions. This equilibrium persisted until the end of the 18th century and the beginning of the massive use of fossil energy needed to supply some recently discovered technologies. Indeed, in 1782, the steam engine (*i.e.* first device able to convert thermal energy into a mechanical one) was designed by James Watt. This historic fact marked the beginning of the 1st industrial revolution which was followed by several new discoveries such as the combustion engine and the access to electricity at the end of the 19th century. Then, the increase of energy consumption per capita has never stopped and the major part of this energy doesn't originate from renewable sources.

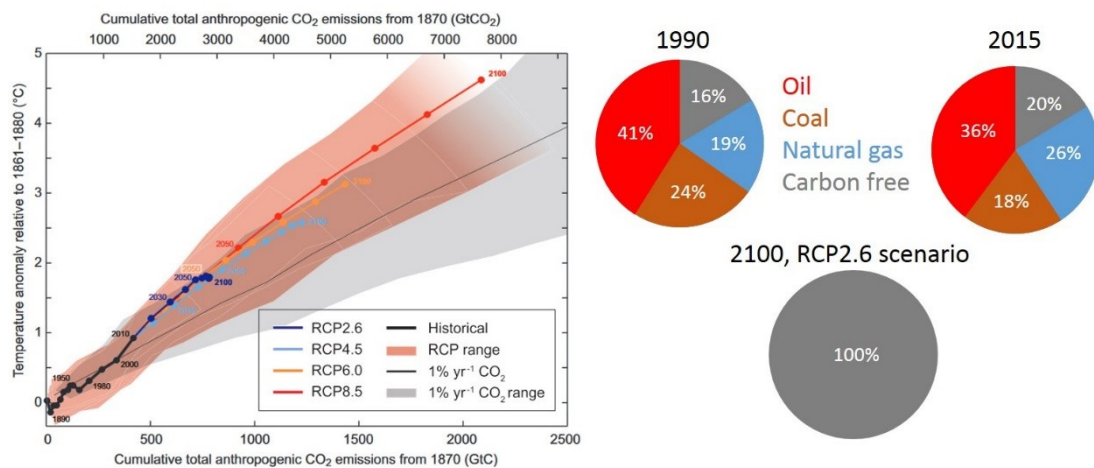


Figure I-1: Projection of the evolution of cumulative CO₂ emission and corresponding anomaly temperature according to several scenarios from the more pessimistic (RCP8.5) to the more optimistic (RCP2.6, allowing to limit the raising of temperature at 2°C in 2100). These scenarios are described in ref. ²² (left). The fraction of energy sources of the world energy consumption in 1990, 2015 and 2100 (according to the RCP2.6 scenario) (right). The carbon free term gathers nuclear and renewables sources (solar, wind, tidal, biomass and geothermal).

Indeed, at the world scale, around 80% of the energy consumed comes from fossil sources (coal, gas and oil), the remaining part being produced from nuclear reactions (4%), renewable sources (4%) and biofuels (12%)^{22,23} (**Figure I-1**). Estimations including the growth of consumption and the decrease of resources discovered predict that the reserves have a lifespan which doesn't exceed 60 years for gas, uranium and oil²⁴. Only two centuries were sufficient to consume a huge part of resources which were formed since hundred millions of years. The combustion of these carbonated compounds leads to the release of a important amounts of CO₂ which tends to increase the concentration of this greenhouse gas in the atmosphere. Even if the photosynthesis carries on, it becomes insufficient to overcome the

massive emission of CO₂ and the global warming becomes unstoppable (**Figure I-1**). The consequences are tragic for the eco-systems with an increase of temperature leading to ice melt and thus the increase of the sea level which, due to the raise of CO₂ concentration inside, becomes more and more acid²².

Considering the increase of the population (around 7 billion people today and 9 billion projected for 2050), the situation will become insurmountable if nothing is done at the technological level. Several strategies are in development to inverse the CO₂ emission curves, such as decrease of energy consumption of devices, increase of renewable energy part or CO₂ sequestration/valorization. These approaches are the subject of intense research both at academic and industrial levels. Science has the occasion to take up the biggest challenge of our age. The solar, wind, tidal, biomass or geothermic energy can deliver enough to satisfy the growing energy demand. Indeed, the sun, on its own, sends in 90 minutes enough energy to satisfy the annual worldwide consumption but its exploitation needs a solution allowing efficient conversion to electricity. The inherent disadvantage of renewable energies (solar, wind...) resides in their intermittence which causes large fluctuations of delivered energy incompatible with the steady demand of our society (**Figure I-2**). It is therefore peremptory to design new energy storage technologies that can be adapted either to network applications or to on-board ones and batteries could satisfy to these requirements.

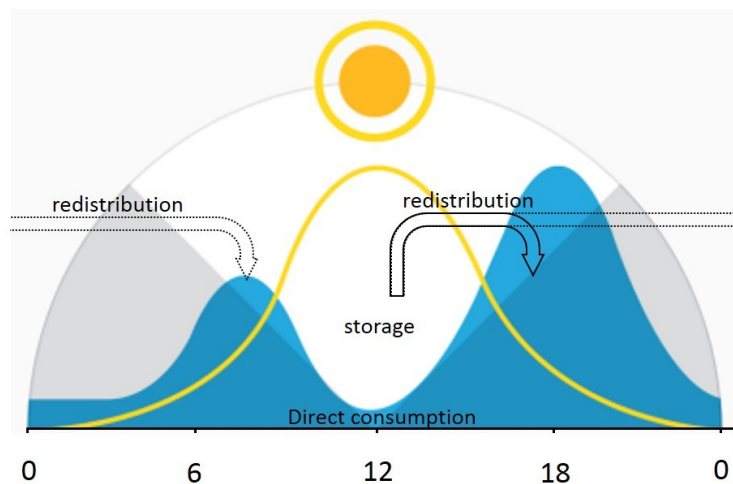


Figure I-2: Mismatching between typical profile of energy demand of households (represented in blue) and solar energy production (represented in yellow) (adapted from ref²⁵). The electrochemical energy storage and redistribution could overcome this mismatching.

The combination of batteries with electric vehicles dates from 1889 and the production, by the general company of Belgian transport, of the first car equipped with a lead-acid battery having an autonomy of 89km and a maximum speed up to 100Km/h. Following these performances few electric vehicles were designed (Detroit electric in 1911, Peugeot VLV in

1941, Tama electric in 1949...) until the oil crisis of 1973. This historic fact marks the beginning of the real interest of industrial players for battery technology whereas the academic research on this topic has never stopped but never really raised. In 1996 the development of electric vehicles at a larger scale started, but the performances provided by Ni-MH battery used in the EV1 commercialized by general motor didn't satisfy the consumers' expectations and the production has quickly stopped. Hundred years have been needed to multiplied by only 3 the energy density stored in batteries from 1859 (discovery of lead-acid battery by Gaston Planté) until 1960's (Battery Ni-MH) whereas the performances of thermal vehicles reach records. The main reasons of this two-tier development is the abundance, low cost and conveniences of fossil fuel which motivated industrial players to neglect the electric vehicles at the expense of thermal ones offering better autonomy for lower price and higher safety. Still today, these limitations persist even with the emergence of new electrochemical devices such as fuel cells, supercapacitors and new generations of batteries.

Since 1789 and the discovery of the chemical generation of electricity by Volta, numerous technologies have been developed: Lead-acid, Nickel-Cadmium, Ni-Metal Hydride, Lithium ion, Lithium air, Lithium sulfur and their sodium analogs (Na-ion, Na-air and Na-S)... The Lithium and, to a lesser extent, Sodium based technologies are those providing the best performances due to the strong electropositivity (high voltage difference) of these alkaline metals and their small weight (high gravimetric capacity). Among them, Li-ion and Na-ion chemistries are the main candidates besides the promising theoretical performances of more recently developed ones such as Li-air and Li-S, currently at an immature state of development. The discovery of Li-ion technology at the academic level precedes of only about 10 years its first commercialization (respectively 1980 by Goodenough and 1991 by Sony). This very fast industrialization process reflects the technological breakthrough offered by Li-ion batteries.

I-2. Li- and Na-ion batteries

The operating principle of all batteries is based on the conversion of chemical to electric energy through redox reactions occurring at both electrodes (**Figure I-3**). The Li-ion batteries vary from the other technologies in the insertion/extraction of the mobile (Li^+) entities in/from a host network. During charge, at the positive electrode, the extraction of the alkaline cations from the host structure is accompanied by the oxidation of the transition metal ions inside. Due to the electric field generated by the external system, the Li^+ cations migrate across the electrolyte and the negative electrode material is reduced. During the following discharge, the battery returns to its equilibrium state involving the inverse phenomena and the migration of

cations is now driven by the electric field induced by the voltage difference between the anode and the cathode. By misuse of language, the positive electrode is called cathode (seat of reduction) and the negative one, anode (seat of oxidation) due to the spontaneous reactions occurring during this discharge.

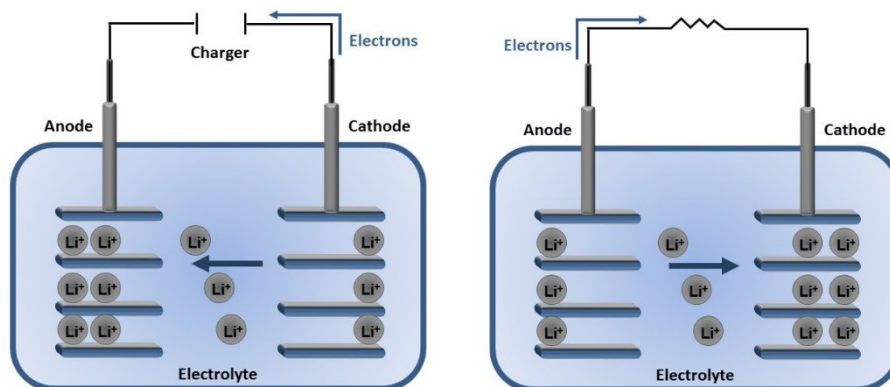


Figure I-3: schematic of Li-ion batteries during charge (left) or discharge (right) (adapted from ref.²⁶)

In the following, a quick overview for the basic understanding of Li-ion batteries will be given while the introduction of this manuscript doesn't aim to provide an exhaustive review of the chemistry of batteries. However, if more details are required a rich literature is available about this topic^{27–29}.

I-2a. Fundamentals of batteries

The gravimetric capacity Q_m (mAh/g) corresponds to the amount of electric charge that can be stored/delivered per unit of mass of active material in an electrode. It is deduced from the following relation:

$$Q_m \text{ (mAh/g)} = \frac{x \cdot F}{3,6 \cdot M}$$

with x = number of electrons theoretically exchange

F = the Faraday's constant ($F=96500$ C/mol)

M = the molar weight of the active material (g/mol)

The open circuit voltage (equilibrium voltage, also called OCV or V_{OC}) of the cell is dictated by the difference of Fermi level (ΔE_F) between an electron localized in the 1s orbital of Lithium and another one in the antibonding "nd*" orbital of the transition metal in the cathode. A confusion is often done, because the chemical potential of electrons in the anode material, μ_A (in eV or Joule), is higher than μ_C whereas the redox potential of Li⁺/Li (anode) is lower than Mⁿ⁺/M⁽ⁿ⁺¹⁾⁺ (cathode) (expressed in Volt).

$$FV_{OC} = -\Delta E_F = \mu_A - \mu_C \quad \text{with } F \text{ is the Faraday's constant}$$

The difference of energy between the electron localized in the anode and in the cathode materials doesn't only depend on the nature of the transition metal and on its oxidation state. For a given redox couple, as the chemical potentials are directly related to the stability of the phases at the charged/discharged states, the voltage depends heavily on the crystal structure of the electrode material. The most famous mechanism impacting the redox potential, the inductive effect, was theorized and experimentally demonstrated by Goodenough^{5,30} (**Figure I-4**).

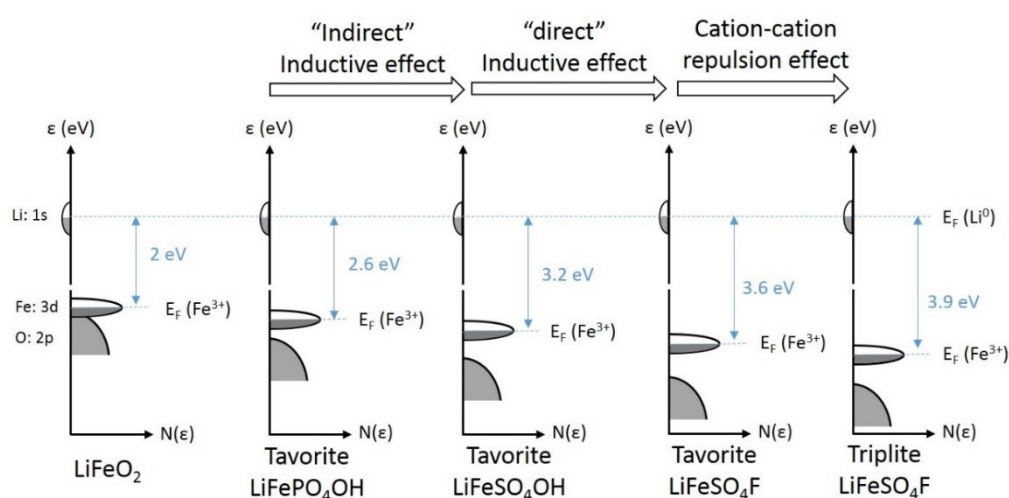


Figure I-4: Schematic density of state of Li and Fe orbitals in different materials highlighting the “indirect” inductive effect, the “direct” inductive effect (moving from phosphate to sulfate and from hydroxide to fluoride, respectively) and the cation-cation repulsion effect in FeO_4F_2 corner sharing (Tavorite) versus in partial FeO_4F_2 edge sharing (Triplite). Adapted from ref. ¹³

According to this theory the potential of a given redox couple ($M^{n+}/M^{(n+1)+}$) is governed by the ionic-covalent character of the bonds formed by M and its ligands. Indeed, an increase of the M-L (metal-ligand) bond's ionicity tends to stabilize the antibonding 3d orbitals of the transition metal and thus increase the difference of fermi levels between the anode and the cathode materials. The quantification of this effect was demonstrated in the iron containing NASICON framework, $Fe_2(XO_4)_3$. In this structure, moving from X = Mo to W and then S, the difference of electronegativity with the oxygen atoms is decreased (*i.e.* $\Delta\chi = 1.5, 1.32$ and 1.1 respectively) that leads to strengthen the covalent character of the X-O bonds. Thus, in order to satisfy to the valence oxygen involved in the X-O-Fe sequence, the Fe-O becomes more ionic and the voltage of the Fe^{2+}/Fe^{3+} redox couple varies from 3.0 to 3.6 V vs Li^+/Li .

Another way to increase the ionicity of the M-L bond is to directly modify the nature of the ligand. Indeed, when moving from L = OH to F in tavorite LiFePO_4L , an increase of voltage is observed (~ 0.3 V), F being more electronegative than the OH group^{11,31}. Another factor influencing the voltage is the $\text{M}^{n+}/\text{M}^{n+}$ repulsion at delithiated state which was demonstrated in LiFeSO_4F crystallizing either in tavorite (corners shared FeO_4F_2 octahedra, $d_{\text{Fe-Fe}} \sim 3.6$ Å) or in triplite (both corners and edges shared FeO_4F_2 octahedra, $3.1 < d_{\text{Fe-Fe}} < 3.4$ Å) structures in which the voltage varies from 3.6 to 3.9 V vs Li^+/Li ³².

The profile of V_{oc} (*i.e.* at equilibrium) in function of the chemical composition of the electrode materials is guided by the Gibbs free energy, $G(x)$, and the variance rules³³:

$$V_{oc} = -\frac{1}{F} \left(\frac{dG(x)}{dx} \right) + cst$$

$$V = C + 2 - P$$

The variance, V , is the number of the thermodynamic freedom's degrees of the system (*i.e.* temperature, pressure and voltage), C the number of components and P the number of phases in equilibrium between them. This is relevant to Li-ion batteries because during (de)intercalation the system is composed of 2 components (Lithium and the host structure) and P is either 1 or 2 depending of the kind of reaction occurring: monophasic or biphasic. The monophasic reaction (also called solid solution reaction) involves the complete miscibility of Lithium inside the host structure. Therefore, only one phase (α , β or γ at the **Figure I-5**) is present in all the particles of the material ($P = 1$). With constant pressure and temperature, for each composition, the only degree of freedom remaining is the voltage. Upon electrochemical cycling, the voltage-composition profile of a material showing a single-phase reaction will be curved. For biphasic reactions, α and β (or β and γ in the **Figure I-5**) phases are present with a ratio depending of the state of charge/discharge, thus $P = 2$ and $V = 2$ as well. Two degrees of freedom are "used" by temperature and pressure, and therefore the value of the voltage must be fixed in the whole composition's domain of the insertion/extraction reaction. During a two-phase reaction the voltage-composition profile will be constant.

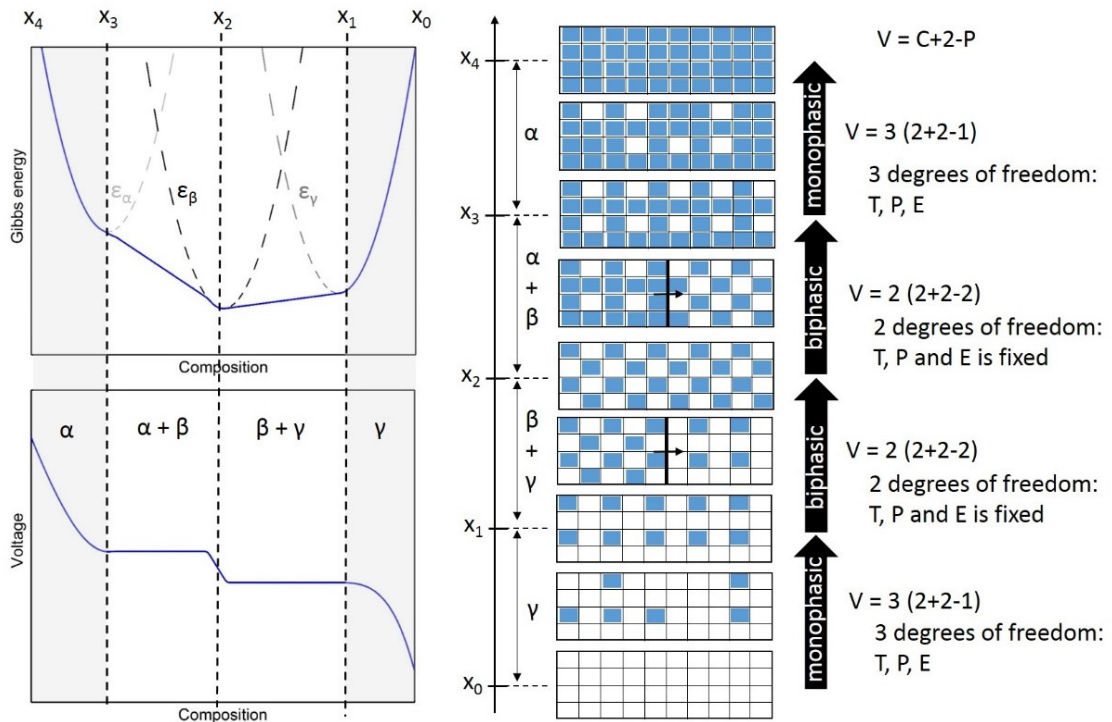


Figure I-5: Relation between the Gibbs free energy of the α , β and γ phases, the voltage profile in function of the lithium content, x , and the Lithium insertion mechanism

For a pure biphasic reaction the energy density is the product of the V_{OC} and specific gravimetric capacity ($E = V_{OC} * Q_m$) but in the other cases (most of the cases, actually) as the voltage isn't constant during alkaline insertion/extraction, the general formula must be expressed as:

$$E \text{ (Wh/kg)} = \int_{x_{min}}^{x_{max}} \frac{F \cdot Voc(x)}{3.6 \text{ Mw}} dx$$

The energy density is independent of the time required to store/deliver electrons whereas this factor is very important to evaluate the performances of batteries for specific applications requiring fast charge/discharge processes. By convention the rate is denoted as C/n (or nC) which means that the full capacity is theoretically achieved within n hours (or $1/n$ hour). This definition is incomplete because the factors impacting the kinetic of transport phenomena in batteries materials is, actually, the current density, j ($\text{mA} \cdot \text{cm}^{-2}$) which is related to n as follows:

$$j \text{ (mA/cm}^2\text{)} = \frac{Q_m \cdot m}{n \cdot S}$$

where Q_m is the theoretical capacity (as defined above), m is the mass of active material in the electrode, n is the time required for a full charge/discharge of the battery and S is the surface of the electrode in contact with the current collector. Typically, an increase of current will impact the polarization (difference between voltage measured during battery operation and the one at the equilibrium state), the capacity and thus the real energy density delivered by the battery.

I-2b. Negative electrode materials

The high chemical potential of metallic Lithium and its low molar weight (6.94 g.mol^{-1}) make it the most convenient anode material for high energy density batteries (theoretical gravimetric capacity of Li metal: 3.86 Ah.g^{-1}). However, during charge of the battery (deposition of Li^0 on the anode side) this metal forms dendrites which involve high risks of short circuit and thermal runaways³⁴. Moreover, alkali metals are unstable towards essentially all electrolytes, reacting with both organic solvents and inorganic salts used as electrolytes in the battery. That leads to the formation of insulating solid electrolyte interfaces (SEI) detrimental for performances³⁴. Due to these safety issues and to the formation of the insulating SEI, most of the commercial batteries use graphite as the anode material, despite its lower capacity and lower fermi energy (and hence smaller voltage difference vs. the cathode). Indeed, graphite reversibly intercalates Li to form LiC_6 (theoretical capacity of 372 mAh.g^{-1}) at approximately 0.15 V vs. Li^+/Li . While this material prevents the formation of dendrites, the SEI formation on the graphite-electrolyte interface is essential to maintain its good performances³⁵. Indeed, at the pristine state, the structure of graphite can be exfoliated by the co-insertion of lithium and solvent molecules between layers. The surface reaction of graphite with electrolyte under controlled conditions prevents the exfoliation thanks to the formation of a passivating layer. This step is essential for the long life cyclability of graphite anode.

Another approach to overcome the detrimental effect of SEI formation is the development of “high voltage anodes” which typically operate above 1.0 V vs. Li^+/Li and thus avoid Lithium plating. This material class has been deeply investigated with the spinel $\text{Li}_4\text{Ti}_5\text{O}_{12}$, which reversibly intercalates about 150 mAh.g^{-1} at 1.55 V .^{36–38} Nevertheless, the limited capacity remains the main drawback of graphite and $\text{Li}_4\text{Ti}_5\text{O}_{12}$ anodes, and thus Silicon, providing a theoretical capacity around 3600 Ah/g is a serious candidate to their replacement. Most of the efforts currently devoted regarding the improvement of performances of silicon anodes tend to limit the capacity fading due to the huge volume expansion between Si and $\text{Li}_{15}\text{Si}_4$ (end of discharge phase)³⁹. Moreover, the problem of very high volumetric capacity

anode materials such as Silicon (*i.e.* up to 1500 mAh/cm³) is that the thickness of the negative electrode, with a gravimetric capacity equivalent to the one of the positive electrode, is very weak (*i.e.* about 10 times thinner than the cathode). At the technological level, the manufacturing of such thin film is tricky. The trend to overcome the huge volume expansion and the need of very thin films is towards the study of graphite/Silicon composites as anode material.⁴⁰

I-2c. Electrolyte

The electrolyte plays the role of electrical separator and ionic connector between the anode and the cathode (**Figure I-6**).

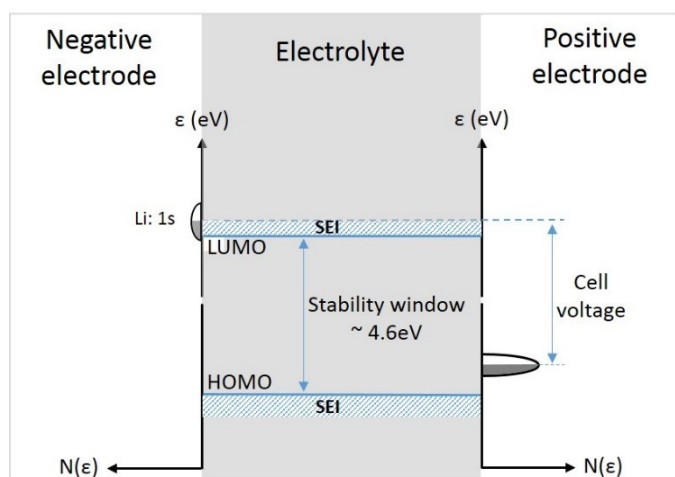


Figure I-6: Schematic density of states for electrode materials revealing the stability windows of the electrolyte and the solid electrolyte interface (SEI) formation.

A purely ionic conductivity is thus required for this component of the battery. Moreover the chemical compatibility with both electrodes and the intrinsic electrochemical stability in a wide voltage windows must be ensured. The chemical compatibility criteria differ according to the couple electrode/electrolyte. Indeed, as mentioned in the previous section the surface reaction between the graphite electrode and the electrolyte is essential to its performances whereas it is detrimental to those of lithium anode. In order to ensure the reversibility of reactions along the cell operation, the electrochemical potentials of the anode and cathode must be within the potential window defined by the lowest unoccupied and highest occupied molecular orbitals (LUMO and HOMO) of the electrolyte.

Several solutions exist to fulfill these requirements, among them a lithium salt dissolved in a mixture of organic solvents, an ionic liquid, a polymer or ceramic ionic conductor ...

According to the kind of electrolyte used, the corresponding technology will be called as Lithium-polymer, All solid state battery (ASSB, for ceramic) or Li-ion battery (for liquid electrolyte). Despite its relative toxicity, flammability and the risk of leaks, the most used electrolyte consists in a LiPF_6 salt dissolved in an equi-volumetric mixture of ethylene carbonate (EC) and dimethyl carbonate (DMC). Considerable efforts were devoted to the optimization of electrolyte compositions via the use of different solvent molecules and additives that help to increase its stability⁴¹. Indeed, the liquid electrolyte is the weak point of Li-ion batteries and the development of high voltage electrolytes is highly desirable in order to increase the voltage and thus the energy density of batteries.

All solid-state batteries (*i.e.* with solid inorganic electrolyte) were considered in order to overcome numerous issues of liquid electrolytes. Indeed, the stability voltage range of a ceramic electrolyte is generally larger but their ionic conductivity is significantly lower compared to their liquid analogues⁴². In 2011, Kamaya *et al.*⁴³ reported a new material, $\text{Li}_{10}\text{GeP}_2\text{S}_{12}$, presenting the highest Li^+ conductivity achieved in a solid electrolyte with $12 \text{ mS}\cdot\text{cm}^{-1}$ at room temperature and an excellent electrochemical stability in a wide potential windows (~ 1 to 5V). The improvement of ionic conductivity (both at room temperature and at high temperature), the chemical stability (reaction at the interface with electrode) and the electrochemical stability are the main challenges for the development of safe, high voltage, long life all solid state batteries.

I-2d. Positive electrode materials

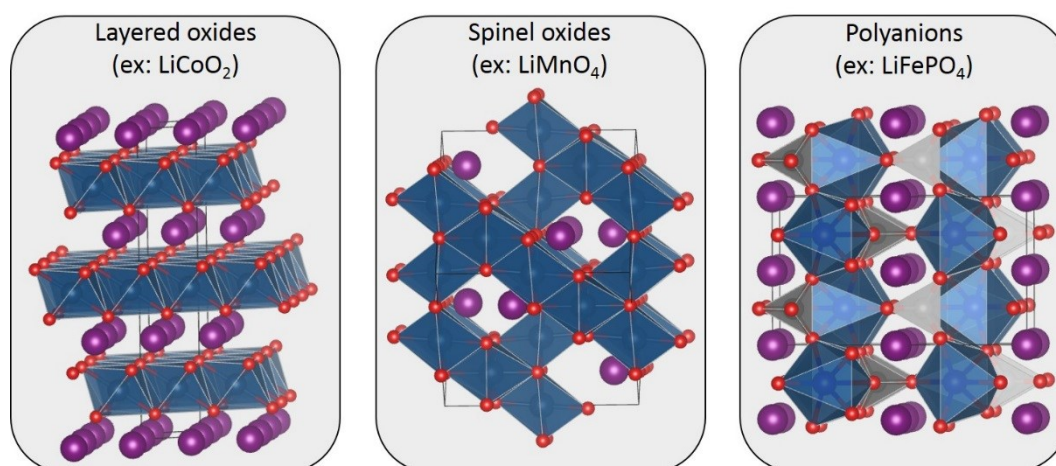


Figure I-7: Structural frameworks of the most common positive electrode materials: layered oxide LiCoO_2 (left), spinel oxide LiMn_2O_4 (middle) and polyanionic olivine LiFePO_4 (right)

A wide range of materials may be potentially used as positive electrode in Li-ion batteries and several of them are indeed commercially produced for various applications and specifications. The numerous possible materials reported in literature are commonly classified in three groups: Layered oxides (2D frameworks), spinel oxides and polyanionic materials (3D frameworks) (**Figure I-7**).

i. Layered oxides

The layered materials, with general formula A_xMO_2 (with M a transition metal and A an alkaline cation) were first studied by Goodenough as positive electrodes for Li-ion batteries. Their structures are clearly suitable for lithium insertion/extraction, as they are stacked into layers of close-packed transition metal octahedra leaving large empty spaces between them in which alkaline cations can easily diffuse. Among these compositions, $LiCoO_2$ was widely studied and is now commercialized in the major part of mobile devices on the market. With a working voltage of 3.9V for the Co^{3+}/Co^{4+} redox couple and a theoretical capacity of 275mAh/g, its practical performances are very good¹ even though only 0.5 Li^+ can be reversibly extracted/inserted. Nevertheless, the price and toxicity of cobalt motivated the investigation of other compositions. Nickel was proposed as a good option⁴⁴⁻⁴⁶ but the stoichiometry of $LiNiO_2$ is challenging to control. Indeed, in this material, a part of Ni^{2+} cations occupy the interlayer space and disrupt the lithium diffusion inside⁴⁷. The compounds containing Ni^{3+} , Co^{3+} and additives such Al^{3+} or Mn^{3+} present interesting characteristics, especially $LiNi_{0.70}Co_{0.15}Al_{0.15}O_2$ ² and $LiNi_{0.33}Co_{0.33}Mn_{0.33}O_2$ ³ but are thermally instable at the charged state with O_2 release involving irreversible structural changes and safety issues.

In the 2000's, Dahn and coworkers incorporated Lithium into the transition metal layers, leading to $Li(Li,Ni,Mn)O_2$ -type materials which revealed an unexpected quasi-reversible overcapacity (considering only the redox of transition metals) at 4.5V vs. Li^+/Li ⁴⁸. This overcapacity was later assigned to the activation of the oxygen redox. In this kind of materials contrary to the classical layered oxide where O_2 is released inducing safety issues, the instability at high voltage of O^{2-} entities leads to the reversible formation of O_2^{n-} species⁴⁹. In Li-rich NMC (*i.e.* $Li(Li,Ni,Mn,Co)O_2$ -type materials), both phenomena seem to occur and a fast voltage fading is observed during electrochemical cycling. Currently, huge efforts are devoted to reach the full reversibility of this mechanism. It has been demonstrated only in 4d and 5d transition metal oxides⁵⁰ (*i.e.* Ru and Ir-rich oxide) but the high weight (conferring a low gravimetric capacity) and the cost of these metals prohibit their industrial developments revealing the need to return to real system with lighter and cheaper 3d metals.

ii. Spinel oxides

In order to overcome the structural instability of 2D structures, the 3D oxides were widely investigated. The spinel-type composition, $\text{Li}(\text{Mn}^{\text{III}}\text{Mn}^{\text{IV}})\text{O}_4$, operates at 4.1V vs Li^+/Li for the $\text{Mn}^{3+}/\text{Mn}^{4+}$ redox couple upon Li^+ extraction for a capacity of 150mAh/g or 3.0V vs Li^+/Li upon Li^+ insertion for the same redox couple.⁵¹ In this structure, MnO_6 octahedra are connected to each other through edge-sharing and define a three-dimensional network of conduction paths for lithium motion. Nevertheless, the LiMn_2O_4 Spinel has shown a lack of robustness in its cycle life and undergoes irreversible loss of capacity that becomes faster at elevated temperatures. This phenomenon has been assigned either to (i) the disproportionation of Mn^{3+} at the surface of the particles in the presence of traces of H^+ into Mn^{2+} and Mn^{4+} and the dissolution of the divalent cation inside organic electrolyte⁵² or to (ii) the strong Jahn-teller effect observed for Mn^{3+} cations inducing huge volume change during electrochemical cycling⁵³. Whatever the mechanism, Mn^{3+} cations seem to be at the origin of the capacity fading. That was overcome by the partial substitution of Mn^{3+} by Ni^{2+} leading to the Mn^{3+} free $\text{LiNi}^{2+}_{0.5}\text{Mn}^{4+}_{1.5}\text{O}_4$ composition which delivers better cyclability compared to LiMn_2O_4 and a higher working voltage at around 4.7V vs Li^+/Li for the $\text{Ni}^{2+}/\text{Ni}^{3+}$ redox couple⁵⁴. Nevertheless, the lack of stable electrolytes at this voltage is the limiting factor for the development of this chemistry in real batteries. Another way explored to avoid the capacity fading is the stabilization of over-lithiated ($\text{Li}_{1+x}\text{Mn}_{2-x}\text{O}_4$) compositions that also improves the cycling life⁵³.

iii. Polyanionic materials

Polyanionic compounds are built of MO_6 octahedra (M = transition metal) and XO_n polyhedra (X = P, S, Si, B ...), with a variety of bi- or three-dimensional frameworks with open interstitial spaces available for easy alkali ions diffusion. As discussed before, the replacement of oxygen anions in oxides by XO_n groups in polyanionic compounds increases the electrochemically inactive weight per mol of electron exchanged, and thus tends to decrease the gravimetric energy density of these materials. However, the high covalency of these polyanionic groups tends to increase the ionicity of the metal-oxygen bonds and thus, by inductive effect, increase the operating voltage vs. Li for a given redox couple versus that observed in oxides. Furthermore, it is possible to tune further this potential by changing the nature of the polyanionic group as nicely demonstrated in NASICON-type structures $\text{A}_3\text{M}_2(\text{XO}_4)_3$ (A = Li, Na; M = Fe, Ti, V ...; X = P, W, Mo, S ...) moving from phosphate, tungstate and molybdate to sulfates⁵. The huge variety of atomic arrangements and crystal structures that they can adopt with an extreme versatility towards cation and anion substitutions allows

to tune the properties for a targeted application. Moreover, the frameworks provide long-term structural stability, essential for extensive electrochemical cycling and safety issues.

Research on polyanionic compounds as cathode materials were first dominated by those on the triphylite LiFePO_4 ⁶⁻¹⁰ (olivine-type structure). Nevertheless, despite the high voltage for the $\text{Fe}^{2+}/\text{Fe}^{3+}$ redox couple delivered in LiFePO_4 (*i.e.* 3.45 V vs. Li^+/Li), it remains pretty low compared with layered and spinel oxides, leading to a lower theoretical energy density. The intrinsic low voltage provided by the $\text{Fe}^{2+}/\text{Fe}^{3+}$ redox couple was first compensated by the partial replacement of iron by manganese in triphylite $\text{LiFe}_{1-x}\text{Mn}_x\text{PO}_4$, but as the Manganese content in the material increases its kinetic limitations are exacerbated^{55,56}.

Another way to increase the voltage of iron compositions is to further make use of the inductive effect using fluorine and/or sulfate containing materials. Indeed, LiFeSO_4F compositions adopting either a Tavorite or a Triplite arrangement deliver higher redox voltage for $\text{Fe}^{2+}/\text{Fe}^{3+}$ redox couple than the one observed in LiFePO_4 (*i.e.* 3.6 and 3.9 vs Li^+/Li respectively against 3.45 V vs Li^+/Li in LiFePO_4)^{11,12}. The voltage of the $\text{Fe}^{2+}/\text{Fe}^{3+}$ redox couple in $\text{Li}_2\text{Fe}^{\text{II}}\text{SiO}_4$ is pretty low (*i.e.* 3.0V vs Li^+/Li) compared to LiFePO_4 but this lowering affects also the $\text{Fe}^{3+}/\text{Fe}^{4+}$ redox couple which becomes reachable in classical electrolytes (*i.e.* 4.7 V vs Li^+/Li) and thus increases the energy density⁵⁷. Nevertheless, the strong structural changes involved are detrimental to the long-term performances of $\text{Li}_2\text{FeSiO}_4$. To the best of our knowledge, this material is the only one providing multi-electron mechanism (*i.e.* exchange of more than 1 electron per transition metal) for Iron compounds whereas vanadium phosphate based materials offer numerous examples.

Therefore my work is focused on the study of vanadium phosphate materials at the positive electrode for Li and Na-ion batteries. The state of the art of the crystal chemistry will be detailed in the following part.

I-3. Vanadium phosphates as cathodes for Li- or Na-ion batteries

Vanadium phosphate compositions provide a very rich crystal chemistry thanks to the wide range of oxidation states reachable for vanadium cations (V^{2+} , V^{3+} , V^{4+} and V^{5+}) and the wide panel of environments that they can adopt (regular octahedra, distorted octahedra, square pyramids, trigonal bipyramids and tetrahedra) (**Figure I-8**). These crystallographic features confer to vanadium phosphate materials very interesting catalytic, magnetic and electrochemical properties. The relation between structure and catalytic as well as magnetic

properties has already been reviewed by Raveau's group in 2000.⁵⁸ Despite the existence of several reviews on polyanionic structures in Li and Na-ion batteries^{13,39,59,60}, none of them are focused on the electrochemical properties and their relations with crystallographic structure in vanadium phosphates. The introduction of this manuscript is thus the opportunity to do it. In this part we will discuss mainly about the link between crystallographic arrangements and electrochemical properties (structural evolutions, redox mechanisms and their associated voltage, electronic and ionic conductivities ...).

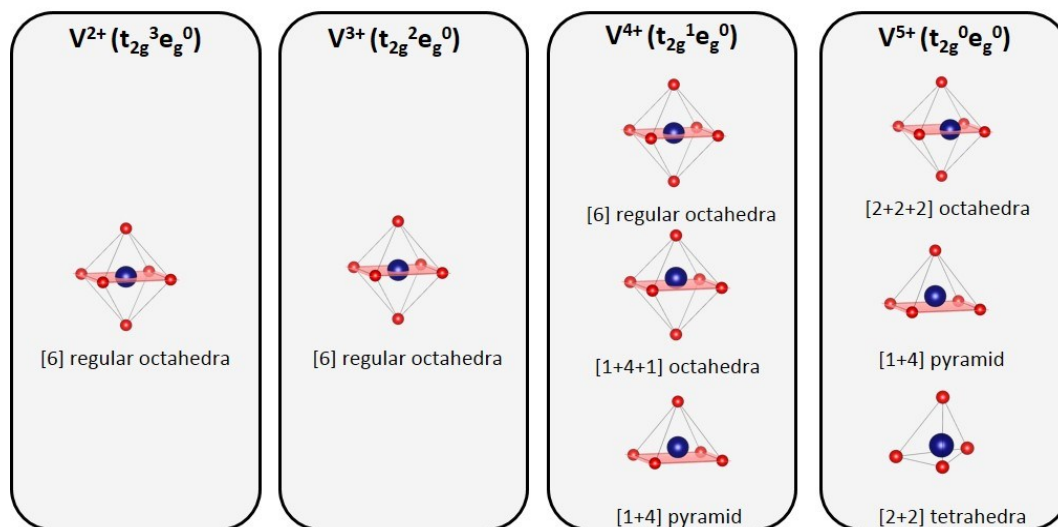


Figure I-8: stable environments of vanadium according to its oxidation state, adapted from ref. ⁵⁸

I-3a. NASICON and anti-NASICON $A_xV_2(PO_4)_3$ ($A = Li, Na$)

The NASICON (Na-super ionic conductor) and anti-NASICON structures have the general formula $A_xM_2(XO_4)_3$ (with $M = Fe, Ti, Sc, Hf, V, Ti, Zr, \dots$ or mixture of them and $X = W, P, S, Si, Mo$ or mixture of them),^{61,62}. These highly flexible structures in terms of composition provide a great playground for solid state chemists. For instance, Goodenough demonstrated experimentally the inductive effect which modulates the voltage of the Fe^{3+}/Fe^{2+} redox couple inside this framework⁵ and subsequently is at the origin of the research on polyanionic materials as cathodes for alkaline-ion batteries. Due to their high ionic conductivity, wide range of potential stability and low thermal expansion, NASICON materials were mainly studied as ceramic electrolytes for all solid state batteries⁶² but some compositions are of interest as electrode materials for classical Li and Na-ion batteries. That is, actually, the case of vanadium phosphate based compositions. The crystallographic arrangements of NASICON and anti-NASICON are closely related. Indeed, they are built on a three-dimensional framework of VO_6 octahedra sharing all their corners with PO_4 tetrahedra and vice versa. The basic repeating

units, formed by three tetrahedra and two octahedra (*i.e.* $V_2(PO_4)_3$), commonly named “lantern unit”, are linked to 6 others in the NASICON structure and with 8 in the anti-NASICON one (**Figure I-9**). This diversity of lantern units’ arrangements generates different ion conduction paths and vanadium environments leading to quite different electrochemical properties

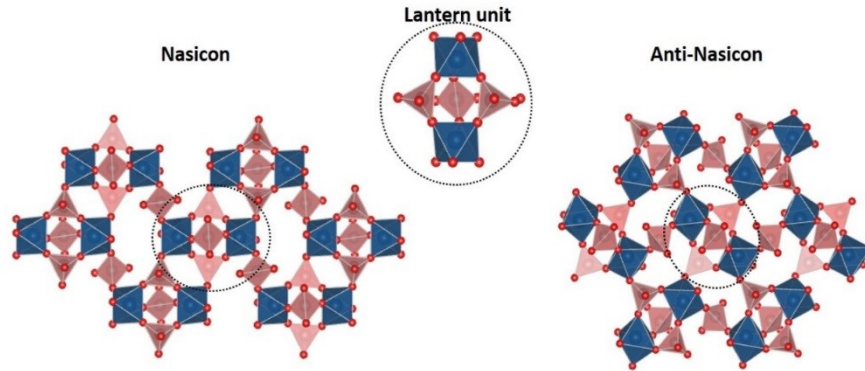


Figure I-9: structural relationship between Nasicon (left) and anti-Nasicon (right) structure adapted from ref. ¹³

i. Anti-NASICON $Li_3V_2(PO_4)_3$

The crystal structure of the anti-NASICON polymorph of $Li_3V_2(PO_4)_3$ has been determined from single-crystal X-ray diffraction by Huang⁶³ and from combined X-ray synchrotron/neutron diffraction data by Patoux⁶⁴. In this structure, the lithium ions fully occupy three crystallographic sites (one tetrahedral Li(1)O₄ and two pseudo tetrahedral Li(2)O₄O and Li(3)O₄O sites) ⁶⁵. The electrochemical extraction of lithium from $Li_3V_2(PO_4)_3$ occurs according to several biphasic reactions involving the V^{3+}/V^{4+} redox couple at 3.6, 3.7 and 4.1 V vs Li^+/Li and then the V^{4+}/V^{5+} one at 4.5V vs Li^+/Li . The voltage profile of lithium reinsertion strongly depends on the activation or not of this V^{4+}/V^{5+} redox couple during charge (**Figure I-10**).

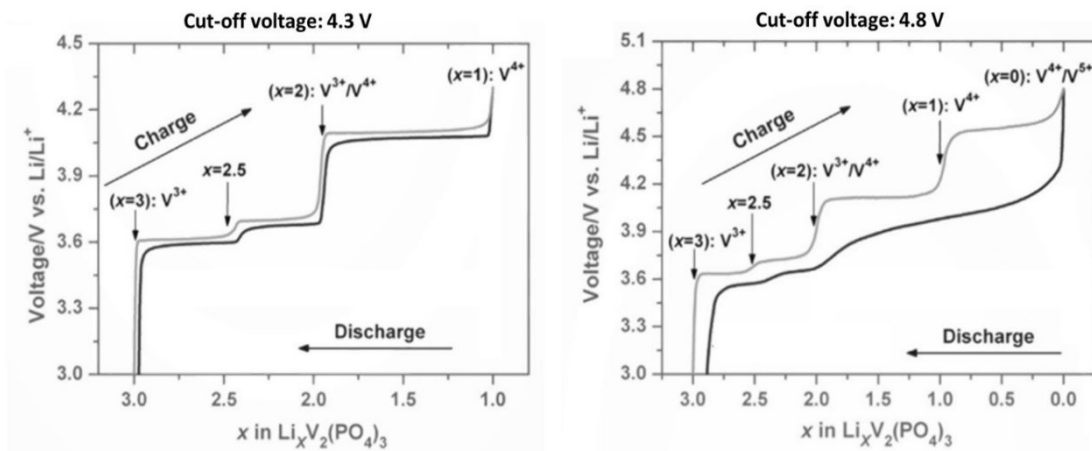


Figure I-10: Electrochemical signature of $Li_3V_2(PO_4)_3$ cycled between (a) 3.0 and 4.3V or between (b) 3.0 and 4.8V vs. Li^+/Li adapted from ref. ⁶⁶

Nazar and coworkers⁶⁵ studied the complex phase diagram involved during lithium extraction from $\text{Li}_3\text{V}_2(\text{PO}_4)_3$ through diffraction (XRD and ND) and NMR, (summarized in **Figure I-11**). The chemically obtained intermediate phases $\text{Li}_{2.5}\text{V}^{\text{III}}\text{V}^{\text{IV}}_{0.5}(\text{PO}_4)_3$, $\text{Li}_2\text{V}^{\text{III}}\text{V}^{\text{IV}}(\text{PO}_4)_3$, $\text{LiV}^{\text{IV}}_2(\text{PO}_4)_3$ and the fully delithiated one $\text{V}^{\text{IV}}\text{V}^{\text{V}}(\text{PO}_4)_3$ were thus investigated. The first delithiation step leads to the formation of $\text{Li}_{2.5}\text{V}_2(\text{PO}_4)_3$ with partial depopulation of pseudo tetrahedral (Li(3)O₄O) site and a complex short range ordering of $\text{V}^{3+}/\text{V}^{4+}$ cations⁶⁷. The following delithiation step affects only the remaining Li(3) to yield the $\text{Li}_2\text{V}^{\text{III}}\text{V}^{\text{IV}}(\text{PO}_4)_3$ with a lithium/vacancies and a $\text{V}^{3+}/\text{V}^{4+}$ ordering suggested by diffraction ($\text{V}(1)\text{-O} = 1.91\text{\AA}$ and $\text{V}(2)\text{-O} = 1.99\text{\AA}$ in average on 6 inequivalent V-O bonds in each octahedron leading to BVS of 4.1 and 3.2 respectively). The further oxidation of vanadium allows to reach the V^{4+} -rich $\text{LiV}_2(\text{PO}_4)_3$ phase in which only one Li site remains as fully occupied. At this stage, there are two crystallographic vanadium sites which are very similar ($\text{V}(1)\text{-O} = \text{V}(2)\text{-O} = 1.91\text{\AA}$ in average). The last process leading to the $\text{V}_2(\text{PO}_4)_3$ composition seems to be the more kinetically limited with a quite big polarization (around 500mV).⁶⁵ At this state of charge, the environments of vanadium (with a mixed valence $\text{V}^{4+}/\text{V}^{5+}$) become more distorted but the average V-O distances are similar to those observed in V^{IV} -rich $\text{LiV}_2(\text{PO}_4)_3$ phase. This extraction/insertion process is asymmetrical as the lithium ordering observed for $\text{LiV}_2(\text{PO}_4)_3$ during charge isn't observed during discharge. A disordered Lithium re-intercalation is detected until the $\text{Li}_2\text{V}_2(\text{PO}_4)_3$ composition is reached⁶⁸. This dissymmetrical mechanism isn't observed for lower cut-off voltage (*i.e.* 4.3 V when the $\text{V}^{4+}/\text{V}^{5+}$ redox couple isn't activated, see **Figure I-10**). Under this cycling conditions the charge and discharge processes are similar and the polarization becomes smaller.⁶⁹

That was tentatively explained in ref. ⁶⁵ by the Lithium/vacancies ordering observed in $\text{LiV}_2(\text{PO}_4)_3$ which involves an ordered depopulation of Lithium cations whereas from the disordered fully delithiated phase the lithium is free to be inserted randomly until yield the $\text{Li}_2\text{V}_2(\text{PO}_4)_3$ composition. More recently, *operando* XANES at V K-edge investigation of this irreversible mechanism revealed the formation of anti-site Li/V defects at high voltage (**Figure I-11**) providing to V^{5+} a more stable tetrahedral environment than the initial octahedral one⁷⁰.

The lithium insertion into $\text{Li}_3\text{V}_2(\text{PO}_4)_3$ reveals as well a complex series of reaction to reach $\text{Li}_5\text{V}^{\text{II}}_2(\text{PO}_4)_3$ involving the $\text{V}^{2+}/\text{V}^{3+}$ redox couple⁷¹. The whole lithium insertion process into $\text{Li}_{3+x}\text{V}_2(\text{PO}_4)_3$ is comprised of four consecutive two-phase regions to reach $\text{Li}_5\text{V}_2(\text{PO}_4)_3$. Approximately 0.5 Li^+ is inserted at every potential plateau around 1.95, 1.86, 1.74 and 1.66 V vs Li^+/Li , corresponding to the following composition changes: $\text{Li}_3\text{V}^{\text{III}}_2(\text{PO}_4)_3 \rightarrow \text{Li}_{3.5}\text{V}^{\text{III}}\text{V}^{\text{II}}_{1.5}(\text{PO}_4)_3 \rightarrow \text{Li}_4\text{V}^{\text{III}}\text{V}^{\text{II}}(\text{PO}_4)_3 \rightarrow \text{Li}_{4.5}\text{V}^{\text{III}}\text{V}^{\text{II}}_{0.5}(\text{PO}_4)_3 \rightarrow \text{Li}_5\text{V}^{\text{II}}_2(\text{PO}_4)_3$.⁶⁴ To

the best of our knowledge, the crystallographic details of this complex mechanism have never been fully studied yet.

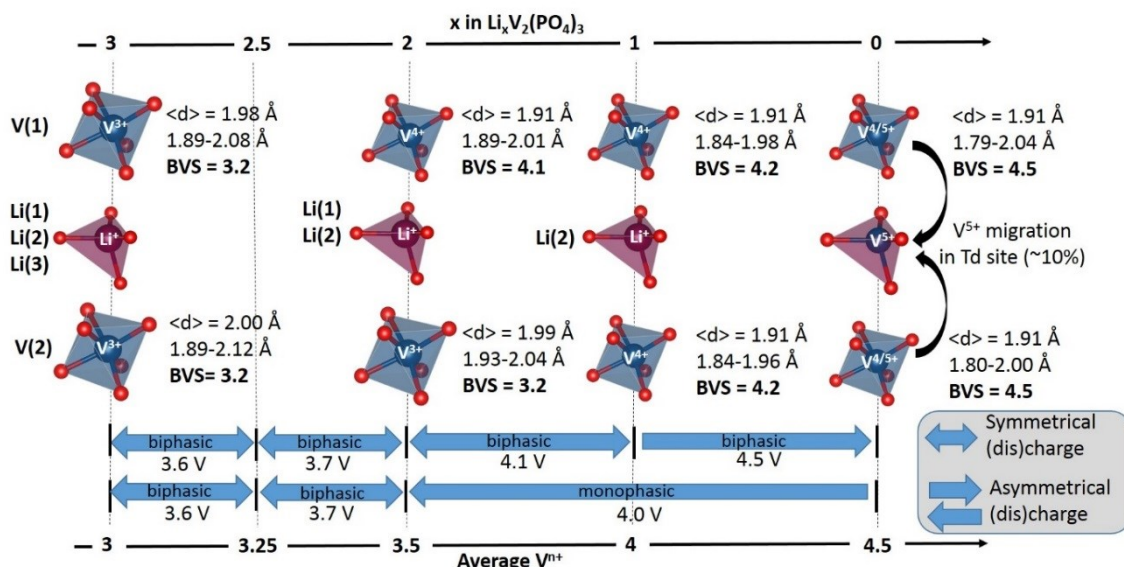


Figure I-11: structural evolution during Lithium extraction/insertion from/into $\text{Li}_3\text{V}_2(\text{PO}_4)_3$ ^{65,70}

In phosphate-type cathode materials, the electronically insulating phosphate groups isolate the valence electrons of transition metals within the lattices resulting in low intrinsic electronic conductivities. Therefore, the use of carbon coating or/and doping elements are required to improve the electrochemical performances, all works applying these strategies are reviewed in ref⁶⁶. The fact remains that the major part of these studies reports good performances in the small voltage range (*i.e.* 3.0-4.3 V vs Li^+/Li , in which only the $\text{V}^{3+}/\text{V}^{4+}$ is activated). Indeed, due to the strong distortion of vanadium environments and the Li/V anti-site defects generated, the kinetic limitations of the $\text{V}^{4+}/\text{V}^{5+}$ process seems difficult to overcome.

The anti-NASICON form of $\text{Li}_3\text{V}_2(\text{PO}_4)_3$ described just before is the thermodynamically stable polymorph but Gaubicher *et al.*⁷² obtained the NASICON form by Na^+/Li^+ ionic exchange from $\text{Na}_3\text{V}_2(\text{PO}_4)_3$ in a saturated aqueous solution of LiNO_3 . This material reveals a similar electrochemical signature compared to the one of $\text{Na}_3\text{V}_2(\text{PO}_4)_3$ with a single plateau until the $\text{LiV}_2(\text{PO}_4)_3$ composition at 3.7V vs Li^+/Li .

ii. NASICON $\text{Na}_3\text{V}_2(\text{PO}_4)_3$

The crystal structure of $\text{Na}_3\text{V}_2(\text{PO}_4)_3$ was originally reported by Delmas *et al.*⁷³ 40 years ago using the standard rhombohedral unit cell, S.G. $R\bar{3}c$. Since then, $\text{Na}_3\text{V}_2(\text{PO}_4)_3$ has always been reported to adopt the rhombohedral symmetry with a partial occupancy of both Na(1) (6*b* Wyckoff position) and Na(2) (18*e* Wyckoff position) sodium sites. Nevertheless, a recent article reveals that a $C2/c$ space group is more appropriated for describing this structure at room temperature and below due to Sodium-vacancies ordering⁷⁴ within five sites (one 4*a* and four others 8*f*) fully occupied. Several transitions between -10 and 230°C involving 4 distinct phases (α ordered, β and β' with incommensurate modulations and γ disordered) was reported. The transition between the α and β forms occurs close to the ambient temperature, at 27°C. This phase transition might impact the sodium diffusion and *a fortiori* the electrochemical performances. The vanadium environment isn't really impacted by the space group used to describe $\text{Na}_3\text{V}_2(\text{PO}_4)_3$. In both cases the VO_6 entities are slightly distorted with distances ranging between 1.97 and 2.03 Å for the rhombohedral description (2.00 Å in average on one vanadium site) or 1.94 and 2.06 Å for the monoclinic one (2.00 Å in average on the three vanadium sites).

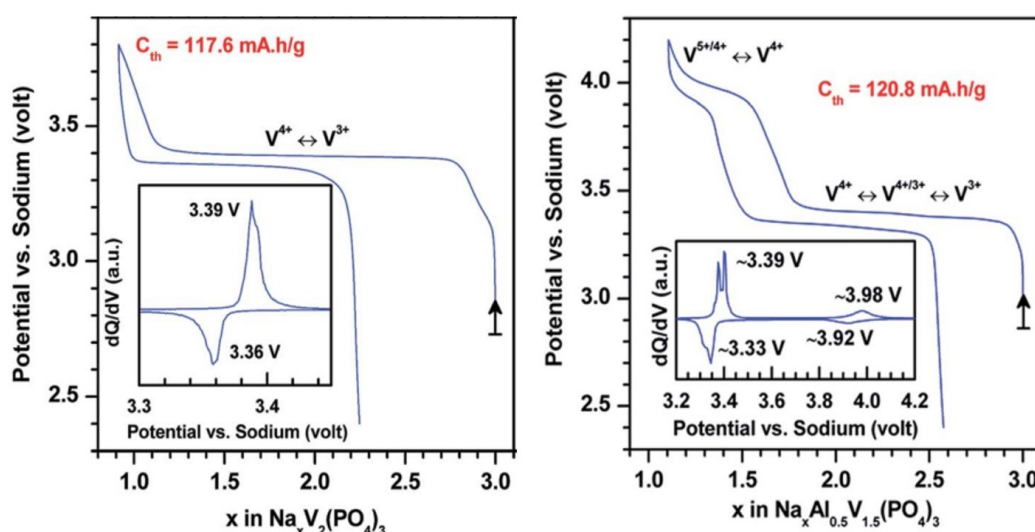


Figure I-12: high voltage signature of Nasicon $\text{Na}_3\text{V}_2(\text{PO}_4)_3$ and $\text{Na}_3\text{V}_{1.5}\text{Al}_{0.5}(\text{PO}_4)_3$, adapted from ref. ⁷⁵

The electrochemical sodium extraction from $\text{Na}_3\text{V}^{\text{III}}_2(\text{PO}_4)_3$ occurs at a 3.4 V vs Na^+/Na according to a biphasic reaction until the $\text{NaV}^{\text{IV}}_2(\text{PO}_4)_3$ composition is reached (**Figure I-12**). The structure of this V^{4+} phase, reported by Jian *et al.*⁷⁶, keeps a NASICON framework (Rhombohedral, $R\bar{3}c$) with only one Sodium site (6*b* Wyckoff site) quasi-fully occupied (0.95). During the sodium extraction, the V-O distances in VO_6 octahedra undergo an inequivalent shortening leading to distorted VO_6 octahedra (with 3 V-O distances at 1.86 Å and 3 others at

1.95 Å). The remaining sodium was reported by Gopalakrishnan *et al.*⁷⁷ to be extracted chemically, to yield the new mixed-valence (V^{5+} and V^{4+}) composition $V_2(PO_4)_3$ but its formation has never been reported electrochemically since then..

Even if the third sodium cation in $Na_3V_2(PO_4)_3$ doesn't seem electrochemically removable, the V^{4+}/V^{5+} redox couple in the NASICON was reported to lie at around 4 V vs Na^+/Na thanks to the partial substitution of a part of Vanadium by Aluminum⁷⁵, Iron⁷⁸ or Chromium⁷⁹. The Aluminum substituted material presents two advantages as it allows to increase the capacity due to lower weight of Aluminum compared to Vanadium (and also iron and Chromium) as well as to reach the mixed valence V^{4+}/V^{5+} state at rather high voltage (*i.e.* 4.0V vs Na^+/Na , see **Figure I-12**). Another strategy was reported by Goodenough's group⁸⁰ who synthesized sub-micron sized particles of $Na_4M^{2+}V^{3+}(PO_4)_3$ with $M = Fe^{2+}, Mn^{2+}$. The substitution of part of vanadium, which can't be oxidized in V^{5+} , by another transition metal operating on the M^{2+}/M^{3+} redox, enhances the energy density. In these materials, the electrochemical extraction of sodium involves the V^{3+}/V^{4+} (at 3.4V vs Na^+/Na) and Mn^{2+}/Mn^{3+} (at 3.7V vs Na^+/Na) or Fe^{2+}/Fe^{3+} (at 2.6V vs Na^+/Na) with very good capacity at 1C (100 mAh/g for the Manganese substituted phase and 105 mAh/g for the iron one) with high capacity retention over 1000 cycles (around 90% of the initial capacity).

The apparent replacement of a PO_4 group in $Na_3V_2(PO_4)_3$ by 3 fluorine atoms leads to the $Na_3V_2(PO_4)_2F_3$ composition, often wrongly named as a "NASICON composition" as its crystal structure is totally different.

I-3b. $Na_3V_2(PO_4)_2F_3$

The first physico-chemical investigation of the $Na_3M_2(PO_4)_2F_3$ family was conducted 20 years ago by Le Meins *et al.*⁸¹ They demonstrated a great flexibility of this framework which can accommodate many trivalent cations in octahedral sites ($M = Al, V, Cr, Fe$ and Ga). The structure of the vanadium phase was first proposed in a tetragonal system using the $P4_2/mnm$ space group. According to this description the sodium occupies two $8i$ sites, one fully occupied and the other half occupied. Later, a combined synchrotron X-ray and neutron diffraction investigation conducted by Bianchini *et al.*⁸² revealed a slight orthorhombic distortion at room temperature. The *Amam* space group (*i.e.* *S.G.* #63, *Cmcm*) used leads to a different sodium distribution in the cell with three Na sites, one $4c$ fully occupied and two $8f$ partially occupied (approximately distributed as 1/3 : 2/3) (**Figure I-13**). The new description proposed doesn't impact significantly the host structure which is built by $V_2O_8F_3$ bi-octahedra with a common F atom (and two "free" V-F bonds) aligned along the [001] direction and connected to each other

through PO_4 tetrahedra belonging to the (001) plane (**Figure I-13**). The VO_4F_2 octahedra in this structure are non-centrosymmetric and vanadium doesn't occupy the gravity center. Indeed a displacement along the c direction leads to two slightly different V-F bonds ($\text{V-F}(1) = 1.968(6)$ Å and $\text{V-F}(2) = 1.981(2)$ Å).

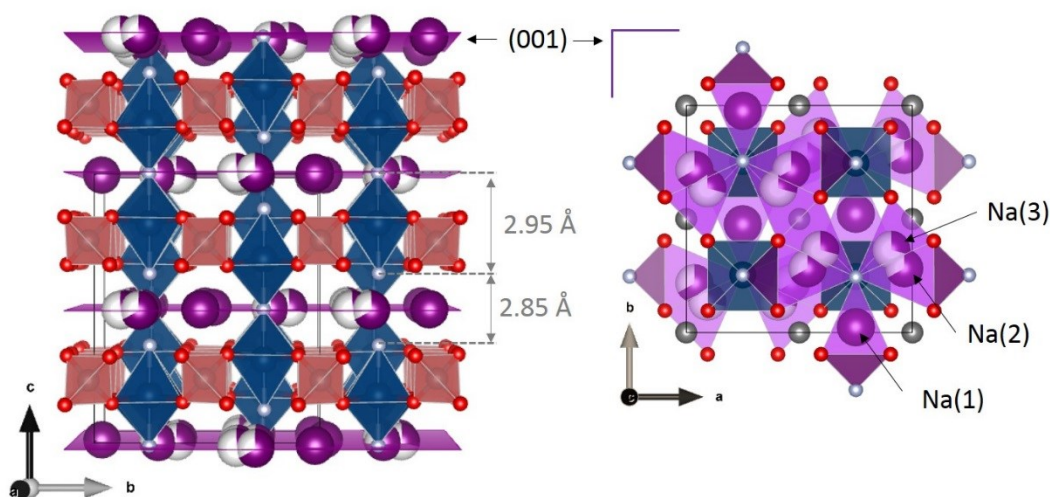


Figure I-13: Structure of $\text{Na}_3\text{V}_2(\text{PO}_4)_2\text{F}_3$ (left) and sodium distribution (right) adapted from ref. ⁸²

Slow electrochemical galvanostatic cycling shows the presence of four distinct reversible voltage-composition features at 3.68, 3.70, 4.16 and 4.19 V vs Na^+/Na (**Figure I-14**) suggesting a complex phase diagram upon sodium extraction/reinsertion⁸³.

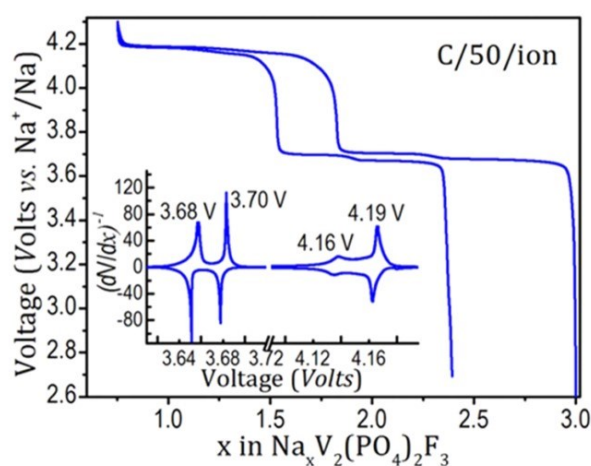


Figure I-14: Galvanostatic electrochemical cycling of a $\text{Na}_3\text{V}_2(\text{PO}_4)_2\text{F}_3$ at C/50 per exchanged ion and the corresponding derivative curve in inset adapted from ref ⁸⁴

The in-depth *in operando* synchrotron XRD investigation conducted by Bianchini *et al.*⁸⁴ is summarized in **Figure I-15**. The phase diagram involves several intermediate phases of compositions $\text{Na}_x\text{V}_2(\text{PO}_4)_2\text{F}_3$ with $x = 2.4, 2.2, 2, 1.8$ and 1.3 before reaching the $\text{NaV}_2(\text{PO}_4)_2\text{F}_3$.

During extraction of the first sodium an alternation between ordered and disordered phases (Na^+ /vacancy and/or $\text{V}^{3+}/\text{V}^{4+}$ ordering and disordering) is observed. The superstructure peaks observed for the $\text{Na}_{2.4}\text{V}_2(\text{PO}_4)_2\text{F}_3$ disappear for $\text{Na}_{2.2}\text{V}_2(\text{PO}_4)_2\text{F}_3$ and the diffraction pattern of $\text{Na}_2\text{V}_2(\text{PO}_4)_2\text{F}_3$ reveals the reappearance of a series of additional contributions non indexed in the tetragonal cell. In the V^{3+} -rich phase, both symmetrically inequivalent V-F are very similar and as the oxidation of vanadium is increased, two kinds of bonds gradually appear as a short one at 1.88 Å and a longer one at 1.94 Å whereas the equatorial V-O bonds decrease uniformly (from 1.99 to 1.95 Å). The extraction of the second sodium involves also intermediates phases at $x=1.8$ and $x=1.3$ accompanied by the disappearance of the superstructure peaks and finally leads to the formation of $\text{NaV}_2(\text{PO}_4)_2\text{F}_3$. This phase contains a single Na site and two vanadium sites conferring to vanadium cations two very different environments despite an average oxidation state of V^{4+} . Indeed, the BVS calculation suggests actually the formation of a V^{3+} - V^{5+} pair in bi-octahedra at this composition (**Figure I-15**).

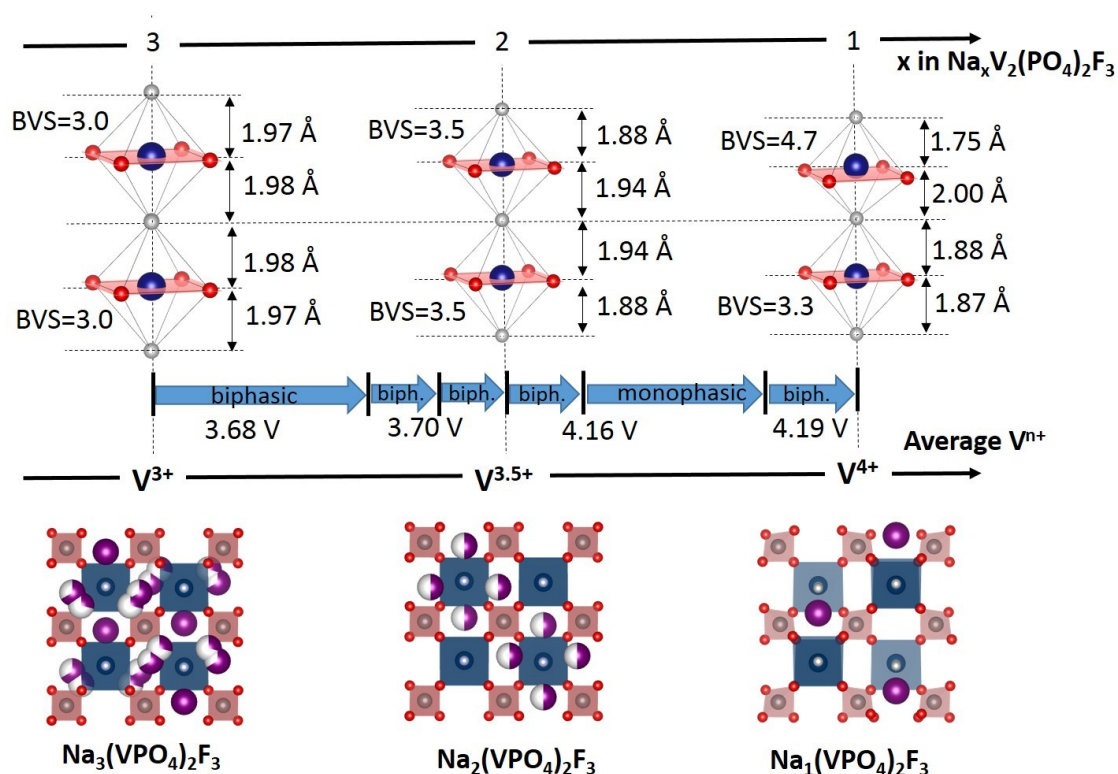


Figure I-15: structural evolution during Sodium extraction/insertion from/into $\text{Na}_3(\text{VPO}_4)_2\text{F}_3$ adapted from ref.⁸⁴ and ⁸⁵

The precise investigation of the redox phenomena involved during sodium extraction was conducted by Broux *et al.*⁸⁶ through *operando* XANES at V K-edge. Their conclusions are in good agreement with the observations made previously by XRD. Indeed, thanks to principal component analysis, three main contributions were found and assigned to $\text{V}^{\text{III}}-\text{V}^{\text{III}}$, $\text{V}^{\text{III}}-\text{V}^{\text{IV}}$ and

V^{III} - V^V pairs of vanadium in bi-octahedra. The V^{IV} disproportionation at the approximate $Na_2V_2(PO_4)_2F_3$ composition accounted for the high voltage of the second plateau which could correspond actually to the V^{4+}/V^{5+} redox couple until the $NaV^{III}V^V(PO_4)_2F_3$ composition is reached. The mixed valence $V^{IV}V^V(PO_4)_2F_3$ phase has never been reported experimentally, indeed Kang and coworkers predicted that the corresponding Na^+ extraction could occur at very high voltage⁸⁷ (*i.e.* up to 5V vs Na^+/Na) unreachable in classical sodium electrolyte available (whose limit of voltage stability is around 4.3 V vs Na^+/Na).

Most of the $Na_3V_2(PO_4)_2F_3$ materials reported as stoichiometric in the literature could present various amounts of vanadyl-type defects which could impact on the electrochemical signature. Several authors indeed studied in details the crystallographic changes generated by the partial substitution of Fluorine for Oxygen in $Na_3V_2(PO_4)_2F_{3-x}$ (with $0 \leq x \leq 0.5$ ⁸⁵, $0 \leq x \leq 2$ ⁸⁷ and $x=1.6$ ^{88,89}). This oxidation has strong effects on the local environments of vanadium and on the sodium distribution whereas only slight changes are observed for cell parameters. Indeed, the local formation of vanadyl bonds was spotted by the strong pre-edge contribution of the V K-edge XANES spectra. The Na^+ distribution in the framework presents similarities with the high temperature form of $Na_3V_2(PO_4)_2F_3$ ($T > 400K$).^{82,85}

The partial substitution of fluorine for oxygen is beneficial for enhancing the charge rates of the battery. Indeed, Several works report very good high rate performance (for both charge and discharge) on partially substituted $Na_3V_2(PO_4)_2F_{3-x}O_x$. Kang's group⁸⁸ was actually the first to investigate the performance of $Na_3V_2(PO_4)_2F_{1.4}O_{1.6}$ (*i.e.* $V^{3.8+}$) as a cathode material and reported high charge and discharge rate capabilities until 20C, assigned to a pretty low activation energy for Na^+ diffusion (~ 350 meV) inside the framework and despite the poor electronic conductivity ($\sim 2.4 \times 10^{-12}$ S.cm⁻¹). The cycling stability at 1C was attributed to the small volume change during sodium extraction/insertion ($\sim 3\%$). The same group published one year later a promising result about the computed voltage for the extraction of the third sodium around 4.7V for $Na_3V_2(PO_4)_2F_{1.5}O_{1.5}$ ⁸⁷ (lower than the one computed up to 5V in $Na_3V_2(PO_4)_2F_3$), maybe reachable in available electrolyte.

I-3c. Tavorite A_xVPO_4Y

Tavorite-type compositions of general formula A_xMXO_4Y are a third class of very interesting polyanionic structures. A is an alkaline cation (*i.e.* Li, Na and $0 \leq x \leq 2$), M is a metal (*i.e.* Mg, Al, Ti, V, Fe, Mn, Zn or mixture of them). The polyanionic group, XO_4 , is either PO_4 or SO_4 and the bridging anion, Y, is an halide, hydroxide, oxygen, H_2O group or a mixture of them¹³. These materials benefit in particular from the inductive effect of both phosphate (or

sulphate) and Y anion. The multiple redox center added to this double inductive effect brings a strong interest at both practical and fundamental aspects as it allows to scan a wide range of working voltages, from 1.5 V for $\text{Ti}^{3+}/\text{Ti}^{4+}$ in $\text{LiTiPO}_4\text{O}^{90}$ to 4.26 V for the $\text{V}^{3+}/\text{V}^{4+}$ redox couple in $\text{LiVPO}_4\text{F}^{91}$ (Figure I-16). The high voltage provided by the $\text{V}^{3+}/\text{V}^{4+}$ and $\text{V}^{4+}/\text{V}^{5+}$ redox couples confers high theoretical energy densities to the vanadium-based Tavorite compositions.

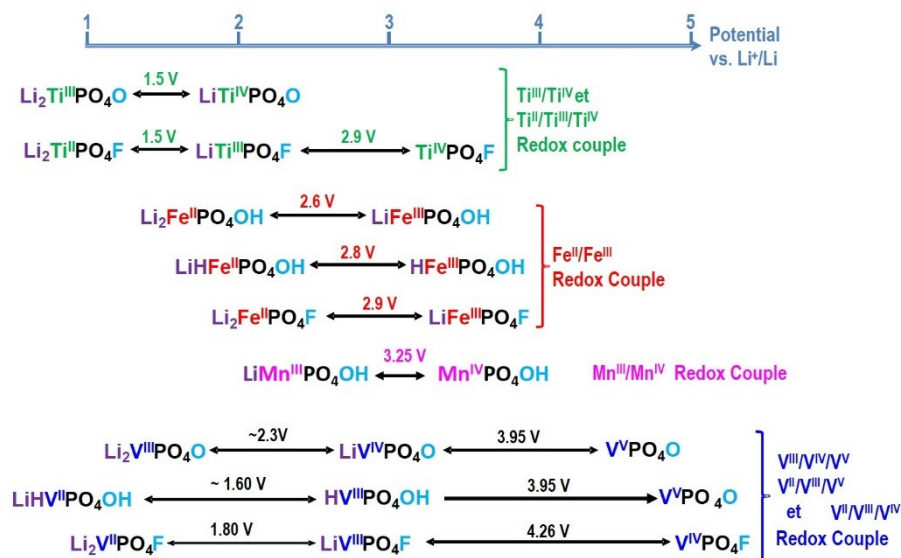


Figure I-16: Overview of Tavorite compositions $\text{Li}_x\text{MPO}_4\text{Y}$ and their corresponding voltage adapted from ref. 13

The crystal structure of Tavorite materials can be described using either triclinic ($P-1$, with $Z=2$ or $Z=4$) or monoclinic ($C2/c$ or $P2_1/c$) crystalline systems^{92–94}. The term “Tavorite structure” is thus a misuse of language and regroups actually Tavorite (triclinic, LiFePO_4OH mineral) and Montebrazite (monoclinic, LiAlPO_4OH mineral) ones. The crystallographic arrangements are very similar in both cases and can be described as vanadium octahedra (VO_4Y_2) sharing a bridging anion Y in order to form infinite chains $[-\text{Y} - \text{VO}_4 - \text{Y}-]_{\infty}$. These chains are connected to each other through PO_4 tetrahedra sharing their 4 oxygen atoms with 4 vanadium octahedra belonging to 3 different chains. The 3 dimensional framework thus generated accommodates alkaline cations in hexagonal channels. The symmetry of vanadium octahedra is dictated by the nature of the V-Y bond. Indeed, in $\text{LiV}^{\text{III}}\text{PO}_4\text{F}$ and $\text{HV}^{\text{III}}\text{PO}_4\text{OH}$, the vanadium is located on an inversion center of the VO_4Y_2 octahedra whereas in $\text{NaV}^{\text{IV}}\text{PO}_4\text{O}$ and $\text{LiV}^{\text{IV}}\text{PO}_4\text{O}$ a deviation from the centrosymmetry is allowed by the space group. In the V^{3+} -rich phase, the nature of the bridging anion impacts significantly the bond length in VO_4Y_2 octahedra. Indeed, between $\text{LiVPO}_4\text{F}^{92}$ and $\text{HVPO}_4\text{OH}^{93}$ the V-Y bond varies from 1.99 to 2.15 Å whereas a more ionic bond is expected for V-F compared to V-OH₂. Actually the covalency of the H-O-H group leads to a longer antagonist V-O bond in order to satisfy the valence of the bridging oxygen. In the Tavorite-like structure, for an oxidation state of

vanadium superior to +3, vanadium can form the vanadyl bond. This strongly covalent V=O bond can be formed only with oxygen atoms which aren't already involved in a covalent PO₄ group. Therefore only the bridging oxygen fulfils these requirements and thus in the V⁴⁺ compounds an ordering between short and long bonds takes place along the chains leading to -O=V⁴⁺--O=V⁴⁺--O- sequences. This ordering generates a change of space group (*P2₁/c* for NaVPO₄O⁹⁴) or a doubling of the cell size (*Z=4* for LiVPO₄O⁹²) (**Figure I-17**).

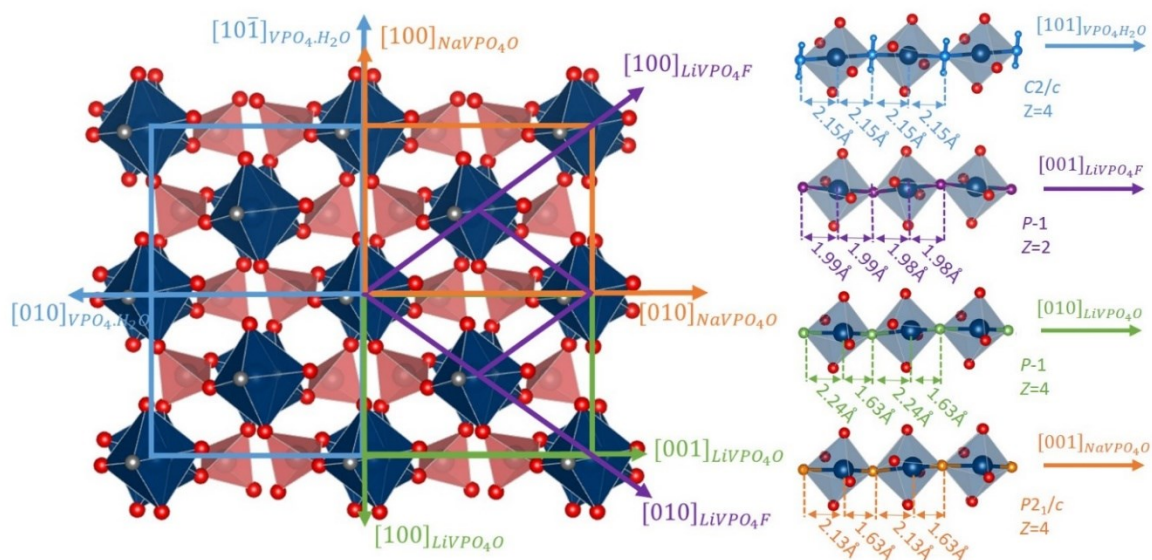


Figure I-17: Structural relationships between Tavorite-type materials

i. NaVPO₄O

Only one study reports on the electrochemical properties of tavorite-type NaVPO₄O⁹⁵. The synthesis was conducted via a sol-gel assisted carbo-thermal reduction of (NH₄)VO₃ by citric acid and the material thus obtained presents pretty large particles (around 10µm). In order to overcome the kinetic limitation involved by these large particles, a ball-milling with acetylene black is necessary. Indeed, at 10mA/g between 2.0 and 4.4V vs Na⁺/Na, the ball-milled powder provides a capacity of 90mAh/g (60% of theoretical) at a voltage located around 3.8 V vs Na⁺/Na. This material seems kinetically limited and since the publication of this paper, no study dealing either with understanding of the mechanisms leading to these poor electrochemical properties or with the investigation of new Na-based Tavorite-like compositions was published.

ii. LiVPO_4O

Tavorite-type $\text{Li}_x\text{VPO}_4\text{O}$ was much more studied. The lithium content in this material varies from 0 to 2, corresponding to V^{5+} and V^{3+} respectively. Nevertheless, the important difference between the average voltage for oxidation of V^{4+} into V^{5+} (*i.e.* 3.95 V vs Li^+/Li) and the reduction of V^{4+} to V^{3+} (around 2.3 V vs Li^+/Li) does not permit its use in a real multi-electron battery system (**Figure I-18**).

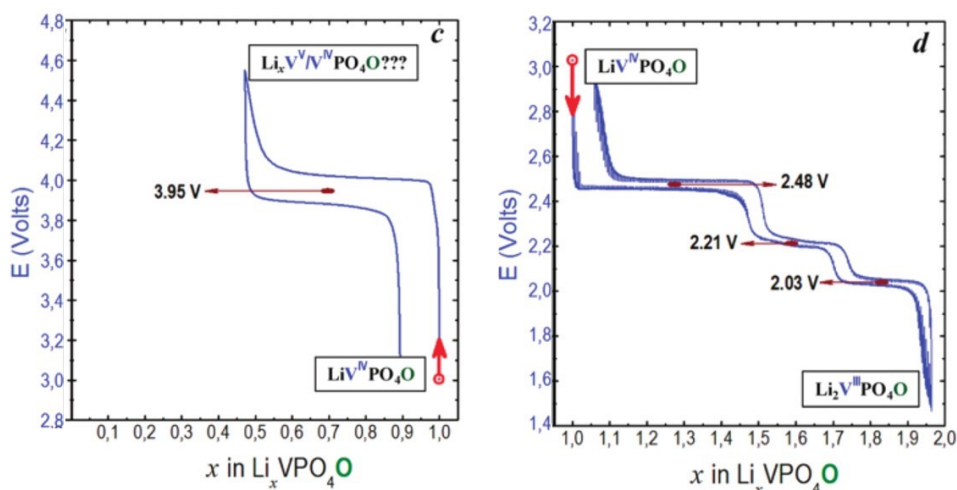


Figure I-18: voltage profile of $\text{Li}_x\text{VPO}_4\text{O}$ cycled between 3.0-4.6 V vs. Li^+/Li (left) and between 3.0 and 1.5 V vs. Li^+/Li in GITT mode (right) adapted from ref. ⁹²

In the high voltage region (*i.e.* 3.0 – 4.6 V vs. Li^+/Li involving the $\text{V}^{4+}/\text{V}^{5+}$ redox couple), the oxidation process occurs via a biphasic mechanism between $\text{LiV}^{\text{IV}}\text{PO}_4\text{O}$ and $\text{V}^{\text{V}}\text{PO}_4\text{O}$.⁹² The crystal structure of this V^{5+} -containing phase (ϵ - VPO_4O) is described in a Cc space group allowing the formation of vanadyl bonds which is more covalent than the one observed in LiVPO_4O (*i.e.* 1.59 vs 1.67 Å, **Figure I-20**). Conversely, the antagonist V^{5+} —O bond along the chains becomes longer passing from 2.2 Å in LiVPO_4O to 2.5 Å in VPO_4O leading to a small increase of the cell volume during lithium extraction ($\Delta V/V = 4.1\%$) and the breakage of the chains⁹⁶. The low voltage region signature is less interesting for performance due to the low voltage delivered but offers a very rich crystal chemistry. Indeed, 3 voltage plateaus (2.45, 2.21 and 2.04 V vs. Li^+/Li) are observed involving 2 intermediate phases, $\text{Li}_{1.5}\text{VPO}_4\text{O}$ and $\text{Li}_{1.75}\text{VPO}_4\text{O}$, before reaching the $\text{Li}_2\text{VPO}_4\text{O}$ composition and the disappearance of the vanadyl entity⁹⁷. Although, this V^{3+} -rich composition is described in a triclinic ($P-1$, $Z=4$) system allowing the formation of a vanadyl-type distortion along the chains, the refined V-O distances don't reveal significant differences between them⁹⁶.

Lin *et al.*⁹⁸ studied in more details the structural evolutions at the local scale during the lithium insertion in $\text{Li}_{1+x}\text{VPO}_4\text{O}$ by a combination of *operando* PDF, *ex-situ* XAS and DFT. They concluded to the disappearance of vanadyl bonds for the $\text{Li}_{1.5}\text{V}^{3.5+}\text{PO}_4\text{O}$ and to the persistence of the antagonist longer one until the $\text{Li}_{1.75}\text{VPO}_4\text{O}$ in good agreement with the phase transitions observed (**Figure I-18**).

iii. LiVPO_4F

The investigation of LiVPO_4F started in 2003 with a series of studies conducted by Barker and co-workers^{91,99,100}. The promising performance of this material made it one of the most studied favorite compositions. Indeed, the high voltage delivered for the Lithium extraction (4.25 V vs. Li^+/Li for the $\text{V}^{3+}/\text{V}^{4+}$ redox voltage, **Figure I-19**) and a capacity very close to the theoretical one even at high C-rate confer to this material an higher energy density compared to the ones of LiFePO_4 and LiCoO_2 (655 vs. 585 and 525 Wh/kg respectively).

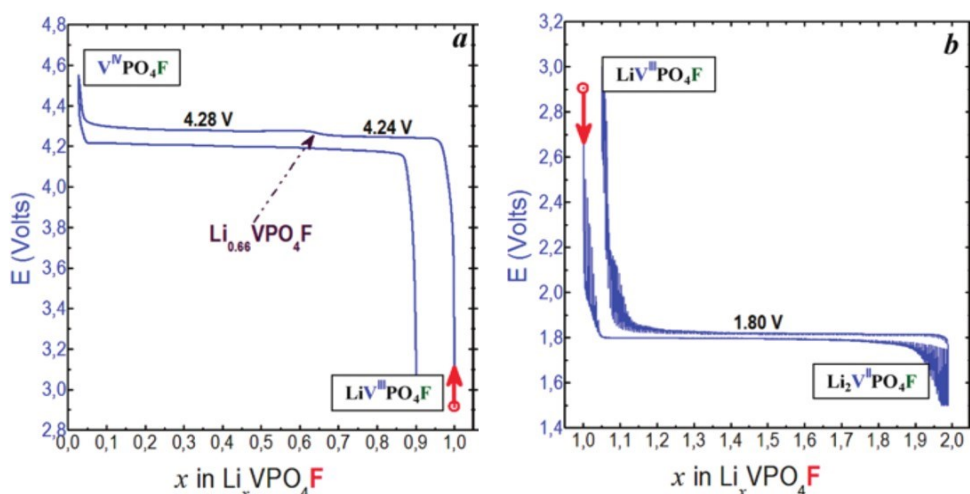


Figure I-19: voltage profile of $\text{Li}_x\text{VPO}_4\text{F}$ cycled between 3.0-4.6 V vs. Li^+/Li (left) and between 3.0 and 1.5 V vs. Li^+/Li in GITT mode (right) adapted from ref.⁹²

The Lithium extraction from LiVPO_4F involves an intermediate phase, $\text{Li}_{2/3}\text{VPO}_4\text{F}$ and then VPO_4F through two biphasic reactions. The crystal structure of VPO_4F was reported by Ellis *et al.*¹⁰¹, its $C2/c$ space group involving centrosymmetric vanadium octahedra with V-F distances of 1.95 Å (**Figure I-20**) whereas the structure of the $\text{Li}_{2/3}\text{VPO}_4\text{F}$ has never been reported. This intermediate phase is not formed during discharge where a biphasic reaction between the end-members compositions VPO_4F and LiVPO_4F takes place²⁰. This asymmetric charge/discharge mechanism isn't really understood for the moment even if it was first attributed by Ellis *et al.* to the presence of two lithium sites partially occupied (0.8/0.2) in the

starting LiVPO_4F . Nevertheless, this hypothesis was ruled out later by Ateba Mba *et al.* who localized Lithium in a single site fully occupied. Piao *et al.*¹⁰² conducted *operando* V-K edge XANES in order to probe the redox mechanism during delithiation of LiVPO_4F . By a principal component analysis they used 3 components to fit the series of spectra recorded upon charge suggesting at least a $\text{V}^{3+}/\text{V}^{4+}$ ordering for $\text{Li}_{2/3}\text{VPO}_4\text{F}$. The lithium insertion into LiVPO_4F occurs at low voltage, typical for the $\text{V}^{3+}/\text{V}^{2+}$ redox couple (*i.e.* 1.8V vs. Li^+/Li) through a biphasic reaction leading to the formation of $\text{Li}_2\text{VPO}_4\text{F}$ (**Figure I-19**). The structure of $\text{Li}_2\text{VPO}_4\text{F}$ is described in a $\text{C2}/c$ space group with vanadium occupying a 4b site involving centrosymmetric VO_4F_2 octahedra with V-F distances at 2.15 Å and equatorial V-O ones at 2.13 Å in average¹⁰¹ (**Figure I-20**). Lithium atoms are distributed between two 8f Wyckoff sites half occupied in LiO_3F_2 environments.

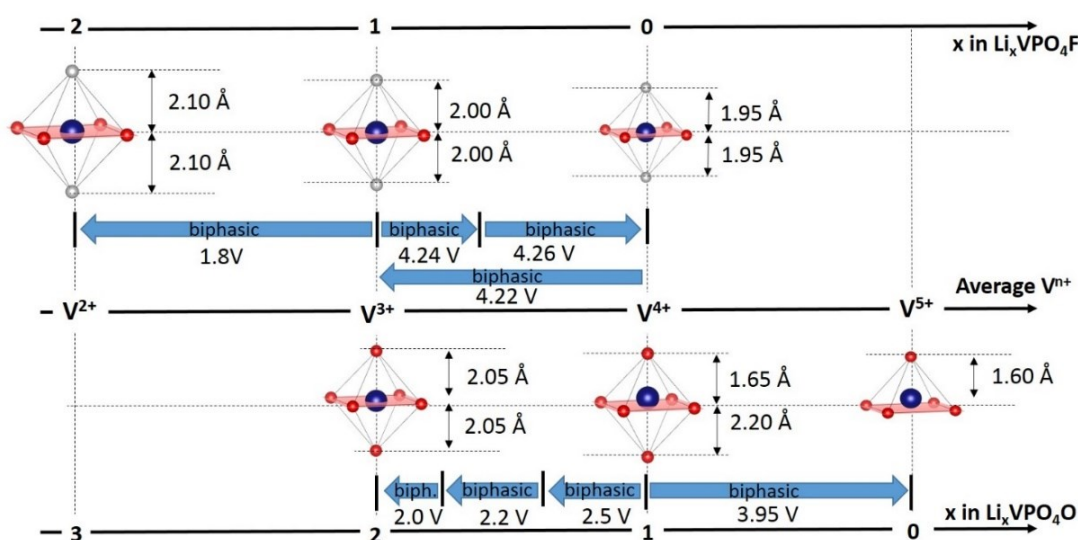


Figure I-20: structural evolution during Lithium extraction/insertion from/into LiVPO_4F ²⁰ and LiVPO_4O ^{96,98}

Various chemical routes to obtain polycrystalline powders of Tavorite LiVPO_4F were reported: sol-gel assisted carbo thermal reduction (CTR)^{103–105}, ionothermal¹⁰⁶... The major part of these reports highlights the difficulty to obtain pure powders (*i.e.* without anti-NASICON $\text{Li}_3\text{V}_2(\text{PO}_4)_3$ due to the volatilization of VF_3) or vanadyl free compounds (without vanadyl-type defects or LiVPO_4O as impurity). Indeed, a series of recent papers demonstrated, by ^7Li NMR (and its 2D analogue) and DFT calculations, the presence of various amounts of vanadyl-type defects in crystallographically pure LiVPO_4F ^{19,21}. Recently, Kang and co-workers¹⁵ reported on an ingenious trick to avoid the fluorine loss during annealing, using PTFE as an additional fluorine source. The material thus obtained reveals very impressive electrochemical performance at high C-rate with a stable discharge capacity of 120 mAh/g at 10C during 500 cycles. The same group published also for the first time the electrochemical properties of the

mixed valence $\text{LiV}^{3+/4+}\text{PO}_4\text{F}_{0.25}\text{O}_{0.75}$ obtained from $\text{V}^{5+}_2\text{O}_5$, $\text{NH}_4\text{H}_2\text{PO}_4$ and LiF without reducing agents, combining ball milling in water and annealing under argon flow¹⁰⁷. This strategy aimed to decrease the difference of voltage between insertion and extraction, conferring to the material a very high energy density (*i.e.* 820 Wh/kg) in a reduced voltage range (*i.e.* 2.0-4.5 V vs. Li^+/Li) with the activation of the $\text{V}^{3+}/\text{V}^{4+}$ and $\text{V}^{4+}/\text{V}^{5+}$ redox couples.

I-3d. Discussion

Many other vanadium phosphates (and diphosphates, see **Table I-1**) have been stabilized and studied as positive electrode materials for Li(Na)-ion batteries.^{86,92,108–122} The introduction of this manuscript doesn't aim to provide an exhaustive review of all of them but the systems that we chose to describe carefully just before now allow us to generalize and predict a part of their properties (especially working voltages, redox mechanisms and structural evolutions) from the consideration of their crystal structures in their pristine state.

Vanadium-containing compounds present interesting electrochemical performance due to the ability of vanadium to be stabilized in various oxidation states (*i.e.* from V^{2+} to V^{5+}) and thus provide multi-electron systems (exchange of more than 1 electron per transition metal). Combined with the rather high voltage of $\text{V}^{3+}/\text{V}^{4+}$ and $\text{V}^{4+}/\text{V}^{5+}$, vanadium phosphate materials have impressive theoretical energy densities. Nevertheless only a minor part of these compositions can really be termed as a high voltage multi-electron material. Indeed, the voltage difference between both electrons per transition metal in multi-electron systems must be low. For instance this difference between $\text{V}^{3+}/\text{V}^{4+}$ ($\sim 2.4\text{V}$ vs. Li^+/Li) and $\text{V}^{4+}/\text{V}^{5+}$ ($\sim 3.95\text{V}$ vs. Li^+/Li) in Tavorite $\text{Li}_{1\pm x}\text{VPO}_4\text{O}$ being around 1.7 V and the one between $\text{V}^{2+}/\text{V}^{3+}$ (1.8V vs. Li^+/Li) and $\text{V}^{3+}/\text{V}^{4+}$ (4.26V vs. Li^+/Li) in $\text{Li}_{1\pm x}\text{VPO}_4\text{F}$ being around 2.4V are too large.

Thus, among the vanadium phosphate discussed here, only the anti-NASICON $\text{Li}_3\text{V}_2(\text{PO}_4)_3$ and NASICON $\text{Na}(\text{V},\text{Al})_2(\text{PO}_4)_3$ (and also $\text{Li}_9\text{V}_3(\text{P}_2\text{O}_7)_4(\text{PO}_4)_2$ and $\text{Li}_5\text{V}(\text{PO}_4)_2\text{F}_2$, see **Table I-1**) are real high voltage multi-electron systems (with the activation of $\text{V}^{3+}/\text{V}^{4+}$ around 4.0V and of the $\text{V}^{4+}/\text{V}^{5+}$ around 4.5V vs. Li^+/Li) but this second redox process is often kinetically limited and/or irreversible. In this discussion we will try to understand the huge differences of voltage observed for the $\text{V}^{3+}/\text{V}^{4+}$ redox couple according to the structures as well as the kinetic limitations and the irreversibility of the $\text{V}^{4+}/\text{V}^{5+}$ one. Then we will discuss about new strategies to tend towards high voltage multi-electron systems and the main approaches to favor faster transport properties.

Table I-1: list of the vanadium phosphate materials and their redox voltage and corresponding practical capacity. The values of voltage are reported vs. Li^+/Li even for those obtained in Na-cell (according to $E(\text{Na}^+/\text{Na}) = 0.3 \text{ V vs. Li}^+/\text{Li}$), in that case the voltage are marked by *. More details about the classification of these materials (Type I, II or III) are provided in the text.

	initial V^{n+}	V/P ratio	$\text{V}^{2+}/\text{V}^{3+}$		$\text{V}^{3+}/\text{V}^{4+}$		$\text{V}^{4+}/\text{V}^{5+}$		Ref.
			E (V vs. Li^+/Li)	Capacity (mAh/g)	E (V vs. Li^+/Li)	Capacity (mAh/g)	E (V vs. Li^+/Li)	Capacity (mAh/g)	
type I materials									
$\text{Na}_3\text{V}_2(\text{PO}_4)_3$	V^{3+}	0.67	1.9*	59	3.7*	118	/	/	75
$\text{Na}_3\text{V}_{1.5}\text{Al}_{0.5}(\text{PO}_4)_3$	V^{3+}	0.67	1.9*	60	3.7*	85	4.3*	28	75
$\text{r-Li}_3\text{V}_2(\text{PO}_4)_3$	V^{3+}	0.67	/	/	3.7	131	/	/	72
$\text{m-Li}_3\text{V}_2(\text{PO}_4)_3$	V^{3+}	0.67	1.8	131	3.9	131	4.5	33	65
LiVP_2O_7	V^{3+}	0.5	2	116	4.3	95	/	/	108,109
$\text{Na}_7\text{V}_4(\text{P}_2\text{O}_7)_3(\text{PO}_4)_2$	V^{3+}	0.5	/	/	4.2*	90	/	/	110
$\text{Na}_7\text{V}_3\text{Al}_1(\text{P}_2\text{O}_7)_3(\text{PO}_4)_2$	V^{3+}	0.5	/	/	4.2*	77	4.5	46	111
$\text{Li}_9\text{V}_3(\text{P}_2\text{O}_7)_4(\text{PO}_4)_2$	V^{3+}	0.3	/	/	3.7	55	4.5	55	112
$\text{Na}_7\text{V}_3(\text{P}_2\text{O}_7)_4$	V^{3+}	0.375	/	/	4.3*	80	/	/	113
type II materials									
LiVPO_4F	V^{3+}	1	1.8	156	4.2	156	/	/	92
$\text{Na}_3\text{V}_2(\text{PO}_4)_2\text{F}_3$	V^{3+}	0.67	1.5*	64	4*	64	4.5*	64	86,121
$\text{Li}_5\text{V}(\text{PO}_4)_2\text{F}_2$	V^{3+}	2	/	/	4.15	85	4.5	85	114
type III materials									
$\alpha\text{-LiVPO}_4\text{O}$	V^{4+}	1	/	/	2.4	155	3.95	150	92,122
$\beta\text{-LiVPO}_4\text{O}$	V^{4+}	1	/	/	2.2	155	4	130	115
$\beta\text{-NaVPO}_4\text{O}$	V^{4+}	1	/	/	/	/	3.6*	58	116
$\gamma\text{-LiVPO}_4\text{O}$	V^{4+}	1	/	/	2	80	4	150	117
$\text{Li}_4\text{VO}(\text{PO}_4)_2$	V^{4+}	0.5	/	/	2	94	4.1	94	118
$\text{Na}_4\text{VO}(\text{PO}_4)_2$	V^{4+}	0.5	/	/	/	/	3.8*	77	119
$\text{Li}_2\text{VOP}_2\text{O}_7$	V^{4+}	0.5	/	/	/	/	4.1	64	120

The huge divergences in the $\text{V}^{3+}/\text{V}^{4+}$ redox voltages can't be attributed to the inductive effect or to the cation-cation repulsions which are two main parameters impacting the voltage.^{30,32} Indeed, the voltage for the $\text{V}^{3+}/\text{V}^{4+}$ redox couple in the favorite system $\text{Li}_x\text{VPO}_4\text{Y}$ (with $\text{Y} = \text{O}$ or F) varies from 2.4 V for $\text{Li}_{1+x}\text{VPO}_4\text{O}$ to 4.26 V in $\text{Li}_{1-x}\text{VPO}_4\text{F}$. This is attributed to the effect of the highly covalent vanadyl bond which is observed for oxidation states of vanadium superior to 3+ in $\text{Li}_{1-x}\text{VPO}_4\text{O}$ and in $\text{Na}_3\text{V}_2\text{O}_{2x}(\text{PO}_4)_2\text{F}_{3-2x}$. These structures present a common crystallographic feature: at least one oxygen around vanadium isn't involved in a covalent P-O bond. In the other structures, the VO_6 octahedra share all their oxygen atoms with PO_4 (or P_2O_7) groups. The structure of the delithiated or desodiated V^{4+} corresponding phase are

vanadyl free with VO_6 octahedra slightly distorted. The corresponding vanadyl free $\text{V}^{3+}/\text{V}^{4+}$ redox couple is thus located at 3.9 V in monoclinic $\text{Li}_{3-x}\text{V}_2(\text{PO}_4)_3$ and 4.2 V in $\text{Li}_{1-x}\text{VP}_2\text{O}_7$ at an higher voltage than the $\text{V}^{3+}/\text{V}^{4+}$ couple in tavorite $\text{Li}_{1+x}\text{VPO}_4\text{O}$ (around 2.3 V vs. Li^+/Li).

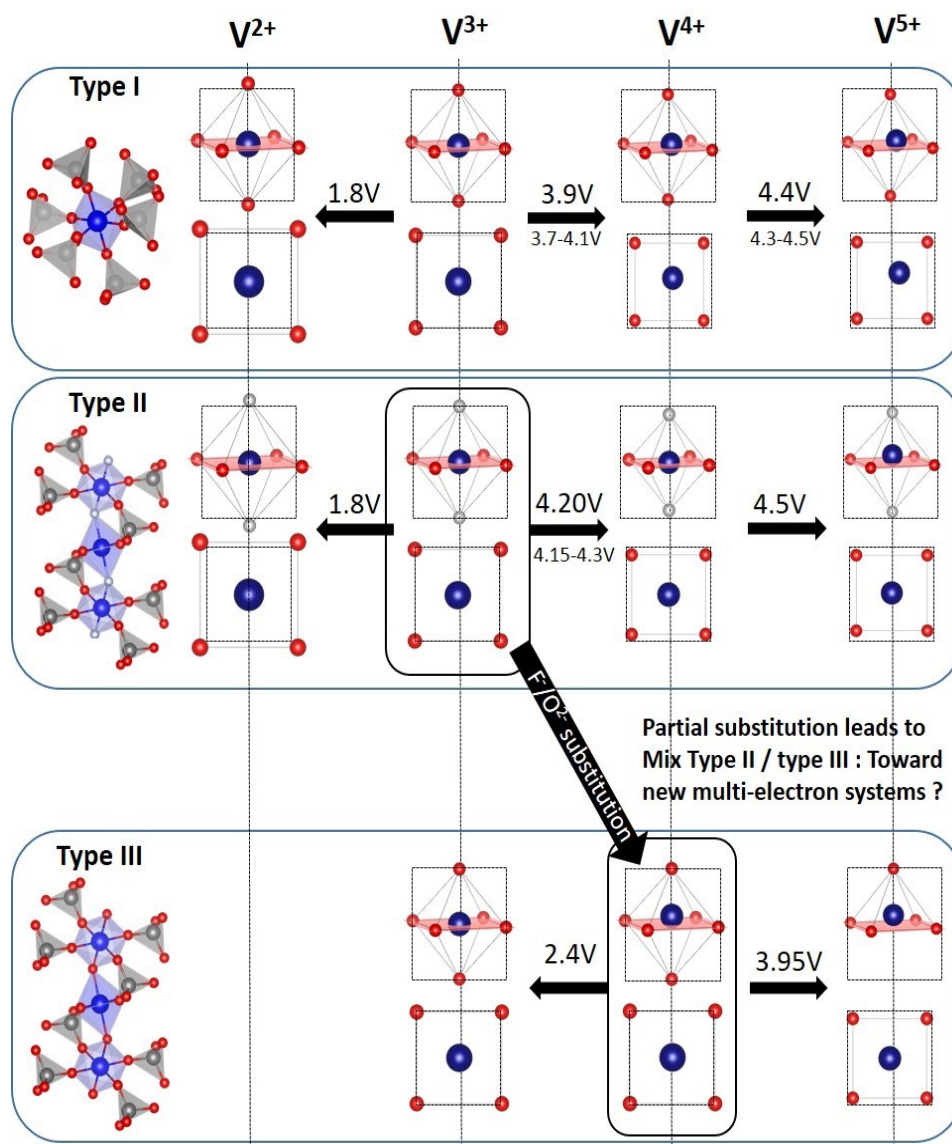


Figure I-21: Typical evolution of vanadium environments according to the oxidation state of vanadium for type I, type II and type III materials.

Therefore, as proposed by Boudin *et al.*⁵⁸, a classification into several groups according to the crystallographic features adopted by vanadium phosphates can be done to explain these differences. They proposed three groups classified according to the size of the “clusters” of vanadium polyhedra ($[\text{VO}_x]_n$ with $1 < n < \infty$). This classification is relevant to discuss about catalytic or magnetic properties of vanadium phosphates but doesn’t really make sense for the discussion about electrochemical properties. Therefore, the way that we chose to sort these structures is to consider vanadyl-forbidden (type I and type II) and vanadyl-allowed (type III)

structures. In type I materials the formation of a vanadyl bond is prevented by the fact that all oxygen belonging to VO_6 octahedra are shared with PO_4 -type entities, thus no oxygen are available to form a second covalent bond. In type II materials, at least one of the ligands around vanadium is unshared with a phosphate group, but in that case, it's the nature of this ligand (F^- instead of O^{2-}) which prevents the formation of the vanadyl bond. Type III gathers the structures having at least one oxygen belonging to VO_6 octahedra available to form the covalent vanadyl bond.

This classification makes further sense regarding the structural evolution during alkaline insertion/extraction (summarized in **Figure I-21**).

- For type I materials, in which the vanadyl bond cannot appear due to the involvement of each oxygen atom of VO_6 octahedra in a PO_4 -type entity, the typical evolution of the vanadium environment upon oxidation (from V^{2+} to V^{5+}) follows a quasi-homogeneous shortening of V-O bonds from V^{2+} to V^{4+} and a strong increase of VO_6 distortion to reach the V^{5+} state.
- In type II materials, the vanadyl bond formation is prevented by the presence of fluorine and the vanadium environment follows similar evolution.
- Type III materials, in which the vanadyl bond is formed for the oxidation of vanadium at higher degrees than 3+, follow a different mechanism. The V^{3+} environments are quasi undistorted. As the oxidation state of vanadium is increased through alkaline extraction the vanadium leaves the gravity center of the VO_6 octahedra to get closer to one of its oxygen ligands in order to form the vanadyl bond. The migration of vanadium atom along dz^2 orbitals of vanadium leads to the formation of distorted $\text{V}^{\text{IV}}\text{O}_6$ octahedra (with typical distances ranging between 1.6 and 2.4 Å along and quasi equivalent equatorial distances around 2 Å) and then to $\text{V}^{\text{IV}}\text{O}_5$ pyramids (in which the short V=O bond is about 1.6 Å and a shortening of the other distances is observed around 1.8-1.9 Å).

The activation of the $\text{V}^{4+}/\text{V}^{5+}$ redox couple in type III materials occurs around 4V whereas this redox couple is activated at around 4.5 V in type I and type II ones. The $\text{V}^{4+}/\text{V}^{5+}$ redox is often kinetically limited and/or irreversible most probably due to the structural rearrangements required to provide to V^{5+} cations a satisfying environment. Indeed, the V^{5+} cations are stable either in a pyramidal symmetry (1+4 coordination) or in a tetrahedral one (2+2 coordination) or even in a very distorted octahedral one (2+2+2 coordination)⁵⁸. In each case, at least one covalent bond must be formed and this formation isn't privileged by the crystallographic arrangements adopted by type I and II materials. Beyond their kinetic limitations, the $\text{V}^{4+}/\text{V}^{5+}$ redox couple is mostly irreversible in type I materials. An hypothesis

often proposed to explain this irreversibility is the formation of Li/V anti-site defects providing to V^{5+} cations a more stable tetrahedral environment than its initial octahedral one.⁷⁰

Type II materials are crystallographically pseudo type III ones in which the oxygen involved in the vanadyl bond is replaced by Fluorine, which prevents its formation. Thus, by substitution (partial or total), of this fluorine by oxygen, type II materials become type III. That was carefully investigated in the $Na_3V_2(PO_4)_2F_{3-x}O_x$ ^{85,87-89} and more recently in the $LiV^{3+x}PO_4F_{1-x}O_x$ ($x=0.75$).¹⁰⁷

- For $LiV^{3+x}PO_4F_{1-x}O_x$ the reversible insertion/extraction involves around 1.6 electron per vanadium conferring a high energy density (*i.e.* 800 Wh/kg) in a reduced voltage range (*i.e.* 2.0-4.8V vs. Li^+/Li).
- For $Na_3V_2(PO_4)_2F_{3-x}O_x$ the partial substitution of Fluorine by oxygen tends to decrease the voltage of extraction of the third Na^+ cations⁸⁷ (from 5V to 4.7V vs. Na^+/Na from pure fluoride to oxy-fluoride) leading to the reversible exchange of 1.2 electron per vanadium.

Another strategy frequently reported to theoretically enhance both capacity and the redox voltage is the substitution of a part of “inactive” vanadium for Aluminum. Indeed, Al^{3+} can't be oxidized and for compensation this requires an increase of oxidation state of V^{n+} at a higher degree than the one observed in the Aluminum free compound, for the same total number of Na^+ extracted. To the best of our knowledge, this strategy was a success only for the NASICON ($Na_3(V,Al)_2(PO_4)_3$) framework with the reversible activation of the V^{4+}/V^{5+} redox couple at 4.0 V vs. Na^+/Na .⁷⁵ More recently, Yamada and coworkers¹²³ investigated the partial substitution of polyanionic groups in Alluaudite $Na_xFe_y(SO_4)_{3-2z}(PO_4)_z$ compositions, with the aim of enhancing the Na/Fe ratio and thus the theoretical capacity. To the best of our knowledge, this strategy has never been reported for vanadium materials and combined with transition metal substitution could be a good strategy to improve electrochemical properties in the highly flexible structures adopted by vanadium phosphates.

In phosphate-type cathode materials, the electronically insulating phosphate groups tend to isolate the valence electrons of the transition metals within the lattices resulting in low intrinsic electronic conductivities. Thus, type I materials are expected to be less electronically conductive due to the topology around vanadium octahedra, separated by PO_4 groups whereas in type II and III materials, VO_6 octahedra share corners. For V^{n+} compositions ($n=2, 3, 4$ or 5) the e_g orbitals (pointing towards the ligands) are empty and the electron conduction paths

aren't obvious to describe. Several approaches have been developed to enhance the transport properties of these materials, through carbon coating for instance. Indeed, the best performance reported for Vanadium phosphate materials have been achieved thanks to narrow contacts between a carbon conductive matrix and the active material.^{14,15,124,125} The decrease of particles' sizes using innovative synthesis routes tends also to enhance the transport properties by decreasing the length of electronic (and cationic) conduction paths. Another strategy, often combined with the first ones, is to dope either the alkaline site or the transition metal sites so as to decrease the band gap and/or to increase the alkaline diffusion in the bulk.

Currently, the major part of the efforts devoted to vanadium phosphates as cathodes for Li-ion batteries deals with enhancing the performance of already existing ones. Indeed, the search for new phases shade off since few years. The stabilization of new promising compositions and the in-depth understanding of the mechanisms involved during alkaline insertion/extraction have to remain a "hot topic" in the perspective of high voltage two electron systems. Beyond this practical interest, the very rich crystal chemistry offered by vanadium phosphate materials is of interest for a fundamental point of view, and could reserve many good surprises.

I-4. Aims of this work

The previous section has demonstrated that vanadium phosphate materials offer both practical and fundamental interests. Nevertheless, many compositions were up to now unexplored. Therefore, this PhD work aimed at exploring new Tavorite-type materials and at revisiting some of the well-known ones. Our approach to achieve ours targets followed this typical procedures:

i) The synthesis of a targeted composition using various ways (all solid state, hydrothermal, sol-gel assisted ceramic, ball milling) in order to stabilize eventual metastable phases and tune the microstructure impacting strongly the electrochemical performance of such polyanionic materials.

ii) The in-depth description of materials at the pristine state from the long range average structure, thanks to diffraction techniques (SXRPD, ND and/or single crystal XRD), to the local environments, using spectroscopy techniques (solid state NMR, XAS, IR and/or Raman).

iii) The fine inspection of the phase diagram and the redox mechanisms involved during electrochemical operation of the materials thanks to *operando* techniques (SXRPD and XAS).

The in-depth understanding of the mechanisms involved during electrochemical cycling allows to highlight the reasons of the electrochemical limitations. Then the synthesis of new materials (composition, structure and microstructure) was developed to overcome these limitations and tend toward better performance. The complex phenomena observed in batteries required the use of complementary techniques in order to probe the materials at different scales. The fundamental of these techniques and the experimental conditions used are briefly described in the Annex section.

LiVPO_4F is a widely studied material as positive electrode for Li-ion (over 150 articles deal with). Nevertheless, some mysteries persist about the mechanisms involved during Lithium extraction/insertion from/into LiVPO_4F that we will try to resolve in a first part (**I-1**). Moreover, recently, vanadyl-type defects have been detected in a crystallographically pure LiVPO_4F .^{19,21} These defects might impact the electrochemical performance as a similar way that a good coating or particle size decrease. In the following we will study the influence of the vanadyl-type defects' concentration on the structure (**sections I-2 and I-3**) and electrochemical performance, as well as on the structural and redox mechanisms (**section I-4**). The stabilization of new Tavorite compositions remains also a part of my PhD work. The synthesis, the structural study from long average structure to local environments, the electrochemical properties as well as the structural and redox mechanisms of new phases such as NaVPO_4F (**II-1**), LiVPO_4OH (**II-2**) highlight other aspects of the fascinating vanadyl bond properties. Beyond Tavorite structure, the vanadium phosphate materials offer a wide range of crystallographic arrangements which prevent the formation of the vanadyl bond leading to quite different properties. Among them, the new $\text{Li}_2\text{V}(\text{H}_{0.5}\text{PO}_4)_2$ phase crystalizing in Marinite-like (*i.e.* $\text{Li}_2\text{Fe}(\text{SO}_4)_2$) structure has been structurally studied and the lithium diffusion pathways inside will be compared with those of its Marinite related phase (**II-3**).

Chapter II: Influence of vanadyl-type defects on the structure and on the electrochemical properties of LiVPO_4F

Table of contents

II-1. LiVPO_4F , a well-known material?	57
<i>II-1a. LiVPO_4F: Syntheses, structure and defects</i>	57
<i>II-1b. Phase diagram of $\text{Li}_x\text{VPO}_4\text{F}$ and redox processes involved</i>	64
<i>II-1c. Summary and prospects</i>	76
II-2. Oxidation under air of LiVPO_4F	78
<i>II-2a. Synthesis of oxidized samples</i>	78
<i>II-2b. Average long range structure & microstructure</i>	81
<i>II-2c. Growing of vanadyl-type environments</i>	86
<i>II-2d. Electrochemical properties</i>	93
<i>II-2e. Summary and prospects</i>	95
II-3. Extended $\text{LiVPO}_4\text{F}_{1-y}\text{O}_y$ solid solutions, from the long range average structure to the local environments	97
<i>II-3a. A non Vegard's law behavior</i>	97
<i>II-3b. Average long range structure and microstructure</i>	102
<i>II-3c. Characterization of $\text{V}^{3+}\text{-F}/\text{V}^{4+}=\text{O}$ disorder</i>	107
<i>II-3d. Summary and prospects</i>	120
II-4. Impact of vanadyl-type defects on electrochemical performance, on phase diagram and on redox mechanisms	121
<i>II-4a. High voltage region, an optimal vanadyl-type defects' concentration</i>	121
<i>II-4b. Low voltage region, a probe for the local environments around vanadium</i>	142
<i>II-4c. Summary and prospects</i>	152

II-1. LiVPO₄F, a well-known material?

Vanadium based phosphate Tavorite compounds are very attractive because of their high potential and theoretical energy density, at least competitive with the already commercialized LiFePO₄¹³: 655Wh/Kg for LiVPO₄F vs. 586Wh/Kg for LiFePO₄. Among the articles which report on an apparently pure LiVPO₄F (over 100), obvious discrepancies are noticed in lattice parameters and electrochemical properties. In parallel, a study performed recently in our groups in collaboration with the CEMHTI Laboratory in Orléans has revealed that apparently pure and stoichiometric LiVPO₄F powders (as determined from X-ray and neutron diffraction as well as high resolution transmission electron microscopy) contain a series of local defects detected by ⁷Li Magic Angle Spinning Nuclear Magnetic Resonance spectroscopy (MAS NMR) and identified as defects within the LiVPO₄F crystal structure by 2D ⁷Li{⁷Li} exchange spectroscopy¹⁹. Moreover, even if the Li_xVPO₄F phase diagram has already been investigated²⁰, several questions remain. In this section, new insights about the nature of these defects, the phase diagram as well as the redox processes involved during electrochemical cycling of LiVPO₄F will be given thanks to numerous diffraction and spectroscopy techniques (electrochemical test in half cells, Synchrotron X-Rays Diffraction, Neutrons Diffraction, Magic Angle Spinning Nuclear Magnetic Resonance, X-ray Absorption Near Edge Spectroscopy and Extended X-ray Absorption Fine Structure). The principle, the experimental conditions and the references used for each technique are carefully described in the section Annex-I.

II-1a. LiVPO₄F: Syntheses, structure and defects

i. Average structure of LiVPO₄F

Two supposedly identical LiVPO₄F samples (LVPF#1 and LVPF#2) were synthesized, according to a two steps carbothermal reduction reaction, as described previously⁹². V₂O₅ (Sigma-Aldrich, > 98%) is reduced by a small excess of C_{SP} carbon (*i.e.* a highly divided soot) in the presence of NH₄H₂PO₄ (Sigma-Aldrich, > 99%). A thermal treatment at 800°C under argon flow leads to the formation of VPO₄/C, in which the vanadium phosphate particles are surrounded by residual carbon nanoparticles localized in the grain boundaries¹²⁶. After the addition of a stoichiometric amount of LiF to VPO₄/C, the mixture is annealed at 800°C during 1h under argon flow and quenched in liquid nitrogen to form LiVPO₄F. Even if the amount of carbon in the composite VPO₄/C is measured by TGA before the addition of LiF (Sigma-Aldrich, > 99%), the VPO₄/LiF stoichiometry isn't totally under controlled as tiny amounts of LiF are observed as impurity in both samples LVPF#1 and LVPF#2.

Table II-1: Cell parameters and the estimated amount of LiF impurity determined from Rietveld refinement of SXRPD patterns recorded for LVPF#1 and LVPF#2, with the corresponding chemical analyses performed by ICP (Li, V and P, P being fixed to 1) or CHNS (C).

	LVPF#1	LVPF#2
S.G.	<i>P</i> -1	<i>P</i> -1
<i>a</i> (Å)	5.1689(1)	5.1689(1)
<i>b</i> (Å)	5.3086(1)	5.3089(1)
<i>c</i> (Å)	7.2622(1)	7.2619(1)
α (°)	107.590(1)	107.599(1)
β (°)	107.971(1)	107.986(1)
γ (°)	98.396(1)	98.372(1)
<i>V</i> (Å ³)	174.285(3)	174.287(3)
<i>Z</i>	2	2
wt.% LiF	<2	<2
Molar ratio Li/V/P	1.02(5) / 0.97(5) / 1	1.02(5) / 0.99(5) / 1
wt.% C	5.65	5.15

Table II-1 summarizes the results of the chemical analysis and the cell parameters determined for both samples. The compositions of the samples obtained using ICP-AES (for the Li, V, and P contents) and gas chromatography (CHNS) (for the C content) are in good agreement with those expected for the final products (see **Table II-1**). The synchrotron XRD patterns of the two samples are compared in the **Figure II-1a**. Both diffraction patterns are very similar, suggesting thus that this synthesis is very reproducible. As the refinement results are pretty similar for both samples, only the structure of LVPF#1 is carefully described.

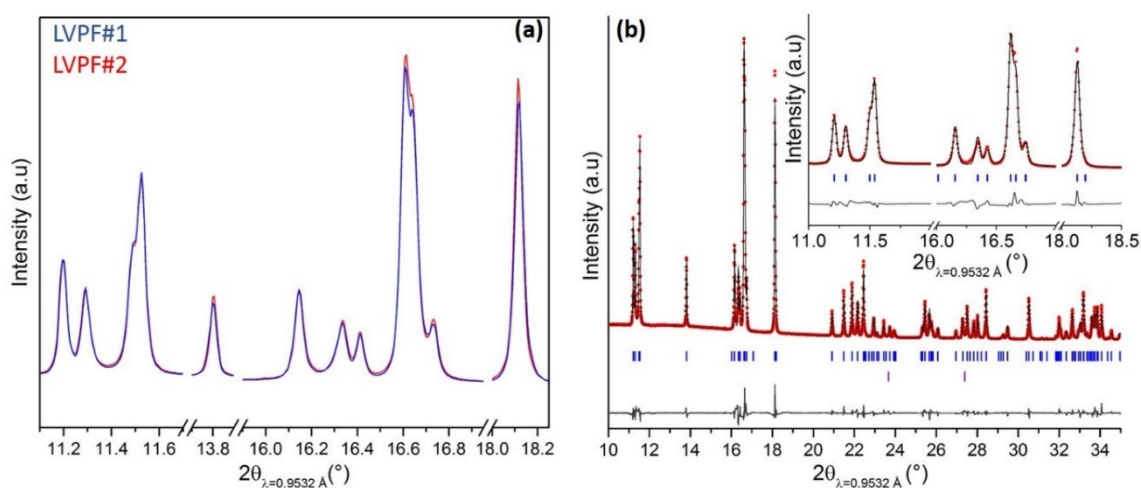


Figure II-1: (a) Comparison of selected 2θ regions of the SXRPD patterns of LVPF#1 and LVPF#2, recorded at ALBA synchrotron (Barcelona) in collaboration with Dr. François Fauth (b) Rietveld refinement of the LVPF#1 SXRPD pattern. The observed intensities are plotted as red points, the theoretical Bragg positions are plotted as blue (LiVPO_4F) or purple (LiF) marks, calculated intensities and the difference between observed and calculated intensities are plotted as black lines.

The SXRPD pattern of LVPF#1 can be indexed with a P-1 triclinic unit cell ($a = 5.1689(1)$ Å, $b = 5.3086(1)$ Å, $c = 7.2622(1)$ Å, $\alpha = 107.590(1)^\circ$, $\beta = 107.971(1)^\circ$, $\gamma = 98.396(1)^\circ$, $V/Z = 87.142(6)$ Å³). The Rietveld refinement shown in **Figure II-1b** was performed considering the structural model $(\text{Li}(1))_{2i}(\text{M}(1))_{1a}(\text{M}(2))_{1b}\{(\text{P})_{2i}[\text{O}_{2i}]_4\}\text{F}_{2i}$ already used in reference⁹². The Bond Valence Sums (BVS) were calculated using the Zachariasen formula $[V_i = \sum_j s_{ij} = \sum \exp\{(d_0 - d_{ij})/0.37\}]$, with the parameter d_0 which characterizes a typical cation–anion distance taken from Brown et al.¹²⁷ The BVS allowed to differentiate oxygen and fluorine atoms despite their close scattering factors. Indeed the BVS value associated with the bridging anion was found to be smaller (1.17(2)) than those of the four others (in average close to 1.95(4)). This result is in good agreement with the structure already reported for other existing Tavorite phases, with the fluorine anion bridging adjacent MO₄F₂ octahedra along the chains (**Figure II-2**).⁹² Moreover, the BVS values for both vanadium sites were found close to 3 (3.06(2) and 3.11(2)), in good agreement with the formation of a V³⁺-rich phase. The cell parameters, atomic positions and distances thus determined are given in **Table II-2** and in **Table II-3**.

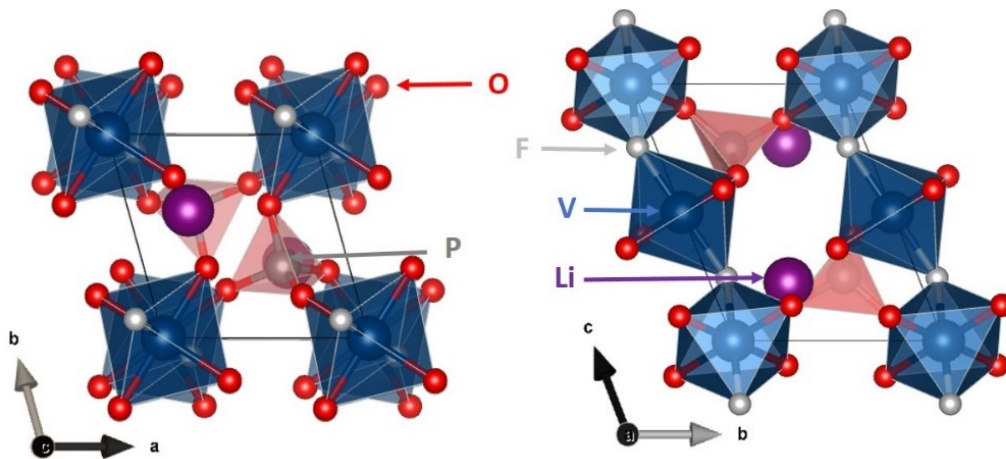


Figure II-2: Structure of LiVPO₄F along the [001] (left) and the [100] (right) directions: VO₄F₂ octahedra in blue, PO₄ tetrahedra in red and lithium in purple.

As illustrated in **Figure II-2**, the crystal structure of LiVPO₄F is built up by VO₄F₂ octahedra sharing a common fluorine atom to form $\cdots\text{V}(1)\cdots\text{F}\cdots\text{V}(2)\cdots\text{F}\cdots\text{V}(1)\cdots$ infinite chains running along $[001]_{p-1}$. These chains of octahedra are connected to each other via PO₄ tetrahedra forming $\cdots\text{V}\cdots\text{O}\cdots\text{P}\cdots\text{O}\cdots\text{V}\cdots$ sequences. These corner-sharing polyhedra generate a three-dimensional network within which lithium atoms occupy the tunnels along the $[100]_{p-1}$ direction. The phosphorus atom lies within a tetrahedron with P–O distances in the range of 1.525(9)–1.543(9) Å. Vanadium occupies the inversion center of VO₄F₂ octahedra with a narrow range of V–O distances, 1.943(6)–2.001(5) Å, V–F distances being of 1.986(5) Å and 1.977(6) Å for the octahedra centered on the V(1) and V(2) atoms respectively. The V(1)O₄F₂ octahedron is slightly less distorted than the V(2)O₄F₂ octahedron ($\Delta = 6.5 \times 10^{-6}$ and $\Delta = 1.5 \times 10^{-4}$

respectively). The unique Li(1) site observed in LiVPO₄F is surrounded by four oxygen and one fluorine atoms, in a distorted LiO₄F polyhedron with Li-O distances ranging between 1.90(3) and 2.29(3) Å ($\Delta = 6.0 \times 10^{-3}$) conferring a BVS value associated with Li(1) rather close to 1 (*i.e.* 0.92(3)).

Table II-2: Structural parameters obtained by Rietveld refinement of the structure of LVPF#1.

LiVPO ₄ F (LVPF#1)							
SG : <i>P</i> -1		$a = 5.1689(1) \text{ \AA}$		$\alpha = 107.590(1)^\circ$			
Z = 2		$b = 5.3086(1) \text{ \AA}$		$\beta = 107.970(1)^\circ$		$\chi^2 = 23.8$	
LiVPO ₄ F : 99.4(1) wt.%		$c = 7.2622(1) \text{ \AA}$		$\gamma = 98.396(1)^\circ$		$R_{\text{Bragg}} = 3.30 \%$	
LiF : 0.6(1) wt.%		$V = 174.285(3) \text{ \AA}^3$		$V/Z = 87.143(3) \text{ \AA}^3$			
Atoms	Wickoff position	X	y	z	Occupancy	Biso	BVS
V(1)	1 <i>a</i>	0	0	0	1	0.395(7)	3.06(2)
V(2)	1 <i>b</i>	0	0	½	1	0.358(6)	3.11(2)
P(1)	2 <i>i</i>	0.323(1)	0.646(1)	0.249(1)	1	0.531(9)	4.99(6)
O(1)	2 <i>i</i>	0.374(2)	0.238(2)	0.589(1)	1	0.35(1)	1.96(3)
O(2)	2 <i>i</i>	0.110(2)	0.670(2)	0.359(1)	1	0.53(1)	1.89(4)
O(3)	2 <i>i</i>	0.694(2)	0.656(2)	0.862(1)	1	0.68(1)	2.03(3)
O(4)	2 <i>i</i>	0.265(2)	0.791(2)	0.095(1)	1	0.79(1)	1.92(4)
F(1)	2 <i>i</i>	0.887(1)	0.087(1)	0.245(1)	1	0.69(1)	1.17(2)
Li(1)	2 <i>i</i>	0.709(7)	0.374(6)	0.228(5)	1	3.4(2)	0.92(3)

Table II-3: Significant bond length lengths (Å) of LiVPO₄F obtained from Rietveld refinement of SXRPD data.

$$\text{Polyhedral distortion is calculated as } \Delta = \frac{1}{N} \sum_{i=0}^N \frac{(d_i - \langle d \rangle)^2}{\langle d \rangle^2}.$$

	V(1)	V(2)	P(1)	Li(1)
coordination	6 (Oh)	6 (Oh)	4 (Td)	4 (Td)
O(1)	/	1.943(6)	1.532(9)	2.27(2)
O(1')	/	1.943(6)	/	/
O(2)	/	2.001(5)	1.543(9)	2.15(2)
O(2')	/	2.001(5)	/	/
O(3)	1.974(5)	/	1.543(9)	1.95(3)
O(3')	1.974(5)	/	/	/
O(4)	1.977(6)	/	1.525(9)	2.29(3)
O(4')	1.977(6)	/	/	/
F(1)	1.986(5)	1.977(6)	/	1.90(3)
F(1')	1.986(5)	1.977(6)	/	/
Average	1.979(5)	1.974(6)	1.536(9)	2.11(3)
Δ	6.5×10^{-6}	1.5×10^{-4}	2.5×10^{-5}	6.0×10^{-3}

As previously mentioned, some defects in LiVPO₄F¹⁹ has been detected by NMR but SXRPD did not allow us to confirm their presence, especially in such low concentration. Spectroscopy techniques (NMR and XAS) are more appropriate to probe such local defects and thus elucidate their nature.

i. The local environments in LiVPO₄F

⁷Li MAS NMR spectroscopy experiments were performed on both LVPF#1 and LVPF#2 samples in order to probe the local environments of Lithium and especially the nature of the paramagnetic elements around it (V³⁺ or V⁴⁺). The NMR spectra of the two LiVPO₄F samples, shown in the **Figure II-3a**, present more obvious differences than the corresponding XRD patterns.

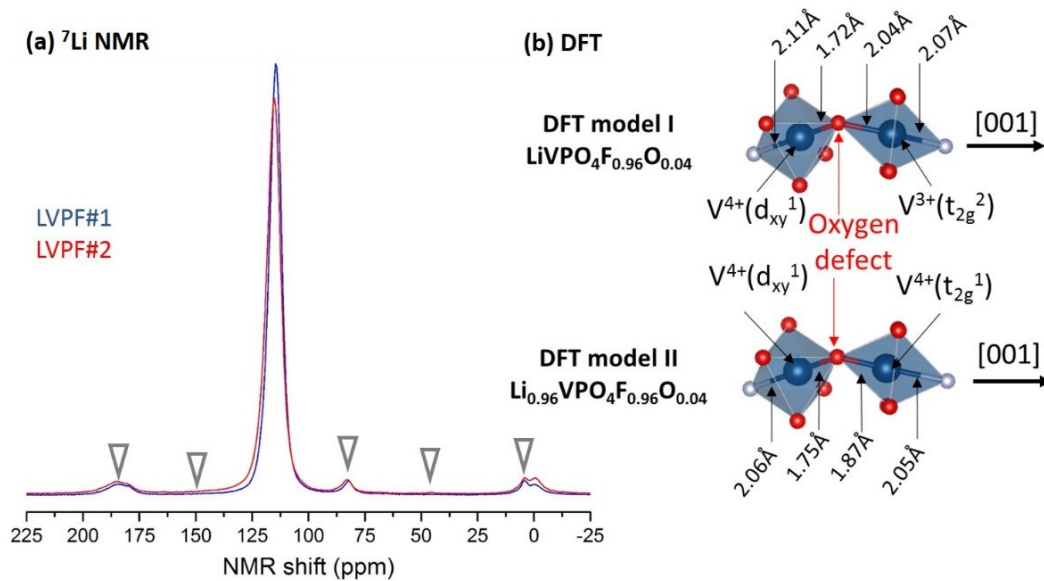


Figure II-3: (a) ⁷Li MAS NMR spectra of LVPF#1 and LVPF#2, the defects contributions are noted with ▽. (b) The schematic representation of the models considered for DFT calculations to try to identify the nature of the defects.

Indeed, although the isotropic signal is located at 115 ppm in both cases, the width and the intensity of this contribution varies from one sample to another. The negatively shifted contribution (*i.e.* -1 ppm) is assigned to the diamagnetic LiF impurity whose amount seems slightly higher in LVPF#2. Moreover, some additional signals are detected at 4, 45, 82, 150 and 183 ppm (marked as ▽ in the **Figure II-3a**): they correspond to those detected by Messinger *et al.* in ref. ¹⁹. The intensities of these additional signals are slightly higher for the LVPF#2 sample which is also the sample presenting the larger isotropic peak (at 115 ppm). In order to get more insight into these additional signals, DFT calculations were performed by Dr Tahya Bamine-Abdessalam (PhD obtained in ICMCB under the supervision of Dr Dany Carlier and Dr Michel Ménétrier). In the following, we will give only a quick summary of these results, but more details are provided in her PhD manuscript¹²⁸.

As the NMR shift for paramagnetic materials is governed by the Fermi contact interaction (see **section Annex I-4**), DFT calculations, through rebuilding 3D spin density maps, allow to predict the position of NMR signals. Our hypothesis concerning the nature of the defect is the partial substitution of oxygen for fluorine leading locally to the formation of V⁴⁺=O vanadyl-type bonds for charge compensation. Two models have been investigated: LiVPO₄F_{0.94}O_{0.06} (model I) and Li_{0.94}VPO₄F_{0.94}O_{0.06} (model II), both considering 2a x 2b x 2c cells (*i.e.* Z=16). **Figure II-3b** summarizes the local symmetry around vanadium cations and their electronic configuration in the vicinity of the defects. In the first case, the environment of vanadium being close to an oxygen defect presents a vanadyl-type distortion (*i.e.* F-V^{IV}=O-V^{III}-F entities located in a V^{III}-rich chain with distances of 2.11, 1.72, 2.04 and 2.07 Å respectively). In the second case, a lithium vacancy has been created in the neighboring of the oxygen defect leading to the formation of V^{IV} - V^{IV} pairs in a V^{III}-rich chain (*i.e.* F-V^{IV}=O-V^{IV}-F with distances of 2.06, 1.75, 1.87 and 2.05 Å respectively). Regarding the electronic configuration of the vanadium cations, all V³⁺ (even those close to defects) are t_{2g}² with a homogenous distribution of the two electrons in the three orbitals, whereas all the V^{IV} cations involved in a vanadyl bond adopt a d_{xy}¹ configuration with the d_{xy} orbitals pointing towards Li through the common edge shared by VO₄OF with the LiO₄F environments. The electronic configuration of the V^{IV} cations generated to compensate for Li vacancies is more ambiguous. Indeed, some of them are similar to those observed in model I whereas others exhibit a single occupied orbital pointing toward the center of the octahedra faces that might result from a recombination of the t_{2g} orbitals due to different local symmetry.

The model without lithium vacancy (model I) provides among others a negatively shifted NMR contribution at -35 ppm which is in disagreement with the experimental spectrum, whereas the creation of V^{IV}-V^{IV} pairs by introducing lithium vacancies (model II) seems to provide a better description of the system. Indeed, the negatively shifted contribution is not observed anymore and the shifts predicted are in better agreement with the experimental spectrum²¹. Nevertheless, using diffraction techniques, it was not possible to validate neither the hypothesis of the vanadyl-type defects (due to similar interaction of oxygen and fluorine with X-rays or neutrons) nor the small deficiency in lithium ($\Delta\tau(\text{Li}^+) = 0.04$), which would be of the same order of magnitude than the accuracy given by the technique itself. Therefore, the investigation of the local electronic structure of vanadium by XAS was expected to provide relevant experimental proof to validate the hypothesis of vanadyl-type defects. The Vanadium K-edge XANES spectra of both LiVPO₄F samples are shown in the **Figure II-4**.

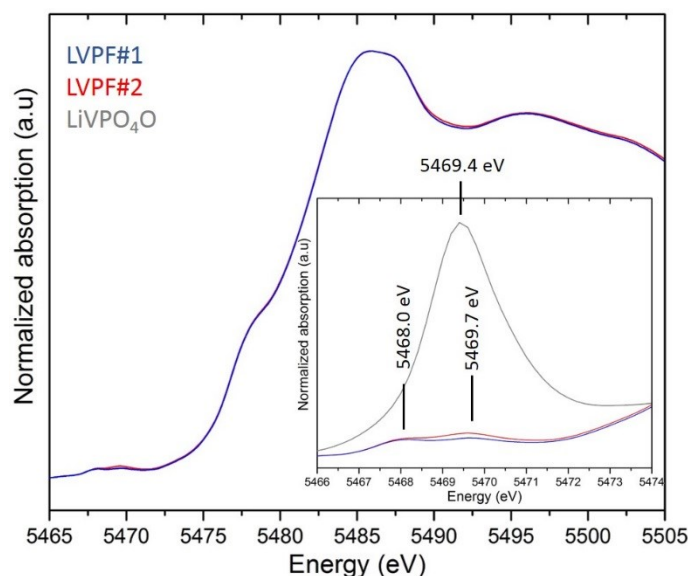


Figure II-4: The XANES spectra of the two LiVPO_4F samples whose pre-edge regions are compared in inset to that of the LiVPO_4O spectrum. The spectra were recorded at Soleil synchrotron in collaboration with Dr. Antonella Iadecola.

XANES spectra exhibit a pre-edge absorption feature (located between 5466.0 and 5474.0 eV shown in inset of the **Figure II-4**) followed by the absorption edge (located between 5474.0 and 5485.0 eV). This strong peak is assigned as the dipole-allowed transition $1s$ to $4p$,¹²⁹ and the pre-edge feature as the transition $1s$ to $3d$.¹²⁹ That latter is strictly forbidden in perfectly regular Vanadium octahedra but becomes dipole allowed due the distortion of the local symmetry around the absorber. That leads to a $3d$ - $4p$ orbital mixing and thus to an overlap of the metal $3d$ orbitals with the $2p$ orbitals of the ligand¹²⁹. This pre-edge region thus probes local distortions around vanadium and could give insights into the nature of the defects. Actually, two weak contributions are detected in the pre-edge for LVPF#1 and LVPF#2 with relative intensities slightly different. At a first sight, these peaks can be assigned to the $1s$ - t_{2g} transition at 5468.0 eV and $1s$ - e_g one at 5469.7 eV resulting from the vanadium's orbitals splitting a crystal field of 1.7 eV. However, that latter is located close to the contribution of a covalently bonded V^{4+} through a vanadyl-type bond^{85,129} with a slight shift (*i.e.* 0.3 eV) compared to the contribution of $\text{V}^{4+}=\text{O}$ bond in LiVPO_4O (*i.e.* 5469.4 eV in inset of **Figure II-4**). Therefore, the slight intensity differences observed in this region could arise from the vanadyl defects, in different concentrations in both samples.

Combining DFT calculations and spectroscopies, the nature of the defects observed in LiVPO_4F has been only partially elucidated. These vanadyl-type defects have for sure, considering the difference between LiVPO_4F and LiVPO_4O electrochemical signatures, an impact on the electrochemical properties of LiVPO_4F even through for a tiny amount of defects

it is difficult to conclude between the actual impact of the defects or slight differences in the electrode formulation for instance. The strategy that we adopted and which will be detailed in the section II-2, II-3 and II-4 of this manuscript is to increase - on purpose - the amount of defects in LiVPO_4F by different ways.

As a further support to understand the impact of higher defects' concentration in LiVPO_4F , we decided to carry on the study undertaken by Dr. Jean-Marcel Ateba Mba^{20,126} and Dr. Matteo Bianchini¹³⁰ in our groups on the phase diagram involved during electrochemical cycling of LiVPO_4F and to investigate the corresponding redox processes. The results will be presented in details for LVPF#1, the sample showing the smaller amount of defects.

II-1b. Phase diagram of $\text{Li}_x\text{VPO}_4\text{F}$ and redox processes involved

i. Electrochemistry

In order to investigate separately the high voltage region (involving the $\text{V}^{\text{III}}/\text{V}^{\text{IV}}$ redox couple) and low voltage region (involving $\text{V}^{\text{III}}/\text{V}^{\text{II}}$ redox couple), LiVPO_4F was cycled in lithium cells, either in galvanostatic mode between 3.0 and 1.5 V vs. Li^+/Li or in GITT conditions between 3.0 and 4.6 V vs Li^+/Li at C/50 (**Figure II-5**).

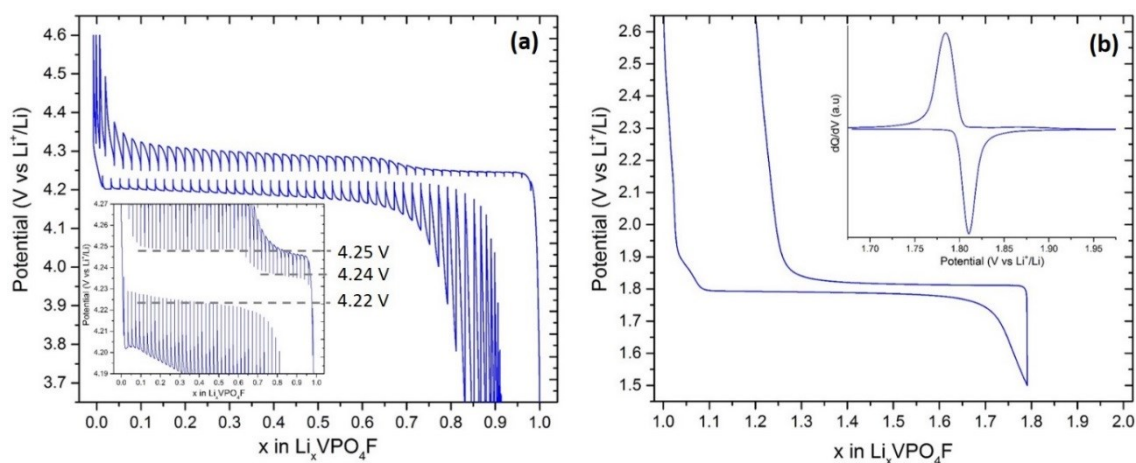


Figure II-5: Electrochemical cycling of LVPF#1: (a) between 3.0 and 4.6V vs. Li^+/Li at C/50 in GITT conditions (galvanostatic pulse of 1h followed by a relaxation period until the voltage variation becomes inferior to 4mV/h) and (b) between 3.0 and 1.5V vs. Li^+/Li at C/50 with the corresponding derivative curve in inset.

The lithium extraction from LiVPO_4F corresponds to the oxidation of V^{III} to V^{IV} involving two plateaus at 4.24 V and then 4.25V vs Li^+/Li . The transition between the first and the second plateaus occurs at the $\text{Li}_{0.67}\text{VPO}_4\text{F}$ composition and a significant increase of the polarization is observed after this phase transition. The following discharge occurs at 4.22V vs Li^+/Li as a

biphasic process between the lithium-free and the fully lithiated phases with a capacity of 140 mAh/g and doesn't involve the intermediate phase observed during the charge^{20,130}. In the low voltage region (*i.e.* 3.0 - 1.5 V vs Li⁺/Li), the lithium insertion-extraction into/from LiVPO₄F occurs at 1.8 V involving the V^{III}/V^{II} redox couple with a reversible capacity of 94 mAh/g. The corresponding phase diagram has been already studied²⁰ through *operando* X-ray diffraction. In the following the redox mechanisms and the local structure around vanadium are presented as deduced by *operando* XANES at the V K-edge at Rock beamline, Soleil Synchrotron (the details of the experimental set up and the references spectra are provided in the section Annex I-6).

ii. The asymmetrical V³⁺/V⁴⁺ mechanism in Li_{1-x}VPO₄F

An *operando* XANES experiment was performed at the V K-edge during the electrochemical cycling of the Li // LiVPO₄F battery in the potential range 3.0-4.6 V vs Li⁺/Li. Further details about the experimental setup (the cell, the electrode formulation, the characteristics of the X-rays beam...) and the spectra of Tavorite reference are provided in the section Annex I-6. The results are given in **Figures II-6** and **Figure II-8**, for the charge at C/10 and for the next discharge at C/5 respectively (in each case, the scans are acquired during 5 minutes every 15 minutes corresponding to 1 scan every 0.02 Li⁺ and 0.04 Li⁺ respectively).

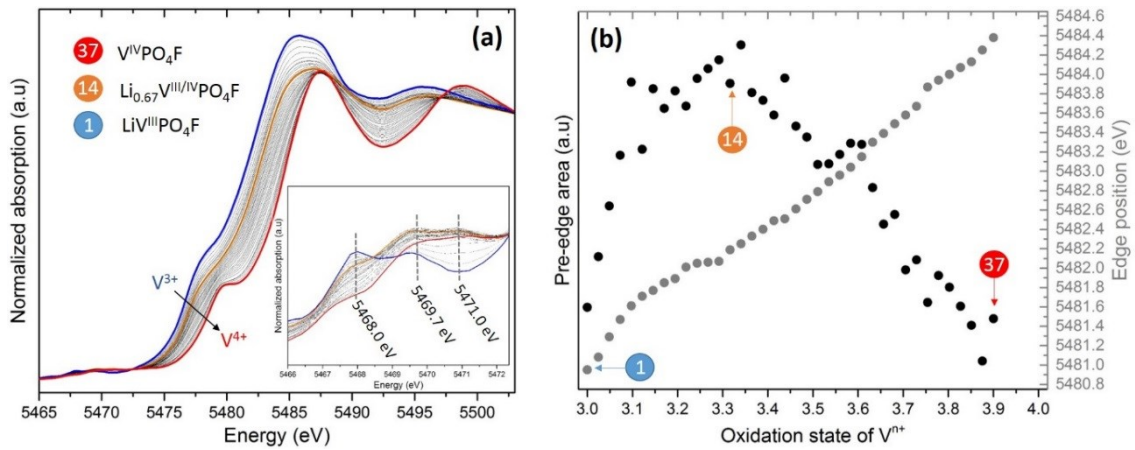


Figure II-6: (a) XANES spectra recorded *operando* during Lithium extraction from LiVPO₄F, the enlargement of the pre-edge region is given in inset. The colored spectra (#1, #14 and #37) corresponds to specific compositions previously highlighted in ref.²⁰ (b) The evolution of the pre-edge area and edge position as a function of the average oxidation state of vanadium (calculated from the electrochemistry).

As mentioned previously, the pre-edge feature provides information about the local environment around vanadium and its distortion. **Figure II-6b** shows the evolution of this region as well as the edge shift as a function of the average oxidation state of vanadium. During the charge, the energy of the edge gradually increases from 5481.0 eV to 5484.4 eV in good

agreement with the raise of the average oxidation state of vanadium, whereas the pre-edge region evolves differently, in two steps. Indeed, the global intensity of the pre-edge features increases during the first third of the charge (*i.e.* until the approximate $\text{Li}_{0.67}\text{VPO}_4\text{F}$ composition) and then decreases, suggesting that the local environment of vanadium in $\text{Li}_{0.67}\text{VPO}_4\text{F}$ is more distorted than those observed in the two end members LiVPO_4F and VPO_4F .

In order to fit the data set and extract the main information, the principal component analysis (PCA) combined with multivariate curves resolution (MCR) was applied to the whole series of spectra. This method was carefully described and discussed in the references^{131–134} and a brief summary of this technique is provided in the section **Annex I-7**. The results obtained are shown in **Figure II-7**.

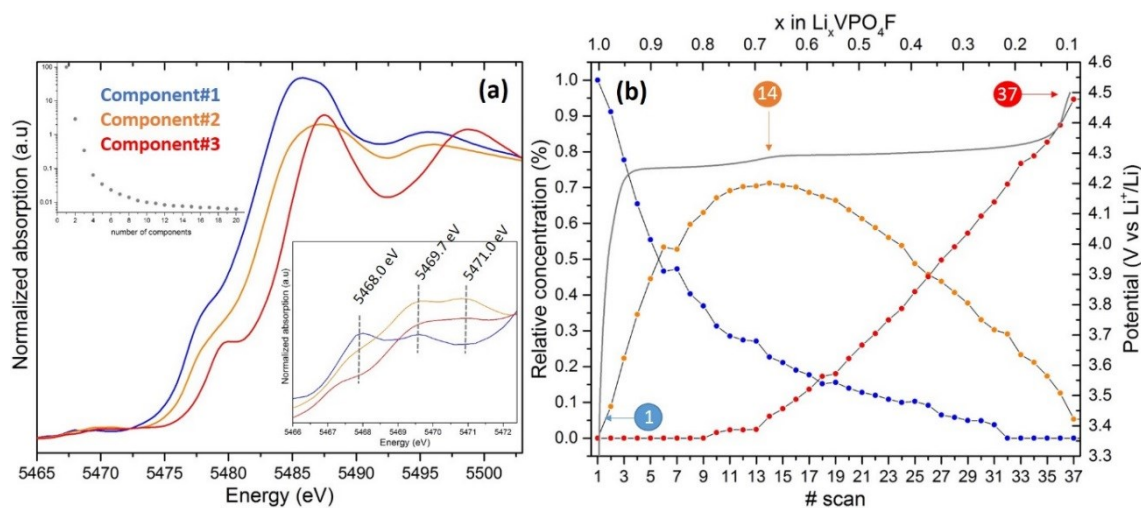


Figure II-7 : (a) The components obtained thanks to the principal component analysis, the variance plot justifying the use of three components and the enlargement of the pre-edge region being shown in inset. (b) The evolution of the relative concentration of each component as a function of the scan number and of x in $\text{Li}_x\text{VPO}_4\text{F}$.

The variance plot (in inset of **Figure II-7a**) reveals that 99.86% of the XAS signal can be described using 3 components, the residual part being supposedly due to the experimental noise. **Figure II-7** represents the 3 components thus computed and the evolution of their relative concentrations as a function of the state of charge. The evolution of the concentration of the component#2 seems to be correlated to that of the pre-edge area (shown at the **Figure I-6b**). Indeed, during the first third of the charge the contribution of Component#1 decreases at the expense of Component#2, and then upon further Lithium extraction that latter decreases at the expense of Component#3. It is important to notice that spatial inhomogeneities were already observed by X-ray diffraction performed *operando* during electrochemical cycling of the $\text{Li} // \text{LiVPO}_4\text{F}$ cells and even *in situ* in relaxed conditions in ref^{20,130}. As a consequence, the relative concentration of the intermediate component never

reaches 100%. Here, its maximum reaches 72% which corresponds approximately to the Li_{0.67}VPO₄F composition, with in addition a concentration of 21% and 7% for the components #1 and #3 respectively. The component#1 is very similar to the spectrum of the pristine material. The edge shifts from 5481.0 eV for the component#1 to 5482.2 eV for the component#2 and then to 5484.4 eV for the component#3.

The pre-edge region gives insight into the local environment around vanadium. As mentioned before, the starting material presents a tiny amount of vanadyl-type defects which would be associated with the contribution at 5469.7 eV (5469.4 eV for the Tavorite-like LiV⁴⁺PO₄O, see **Figure Annex-I-11**), the other intensity at 5468.0 eV is typical for vanadium at the V³⁺ state in a slightly distorted octahedra.⁸⁵ For the component#2 a decrease of the V³⁺ contribution is observed. In parallel, the contribution at 5469.7 eV increases, as well as a new one around 5471.0 eV which is typical for a vanadium at a V⁵⁺ oxidation state covalently bonded through a vanadyl bond (as that observed for the tavorite-like V⁵⁺PO₄O at 5470.7 eV see **Figure Annex-I-11**). The appearance of this contribution could be due to the electrochemical activity of vanadyl-type defects. Indeed, the operating voltage of the V⁴⁺=O/V⁵⁺=O couple in LiVPO₄O is located at lower voltage than the V³⁺/V⁴⁺ couple in LiVPO₄F (*i.e.* 3.95 for V⁴⁺/V⁵⁺ in LiVPO₄O and 4.24 V for V³⁺/V⁴⁺ in LiVPO₄F). The further extraction of lithium leads to a decrease of the global intensity of the pre-edge with the loss of the V³⁺ contribution (*i.e.* at 5468.0 eV), the vanadium octahedra in the intermediate Li_{0.67}VPO₄F phase would be more distorted than those of the end-member phase.

Figure II-8a shows the spectra collected during the following discharge at C/5 (the scans are acquired during 5 minutes every 15 minutes corresponding to 1 scan every 0.04 Li⁺).

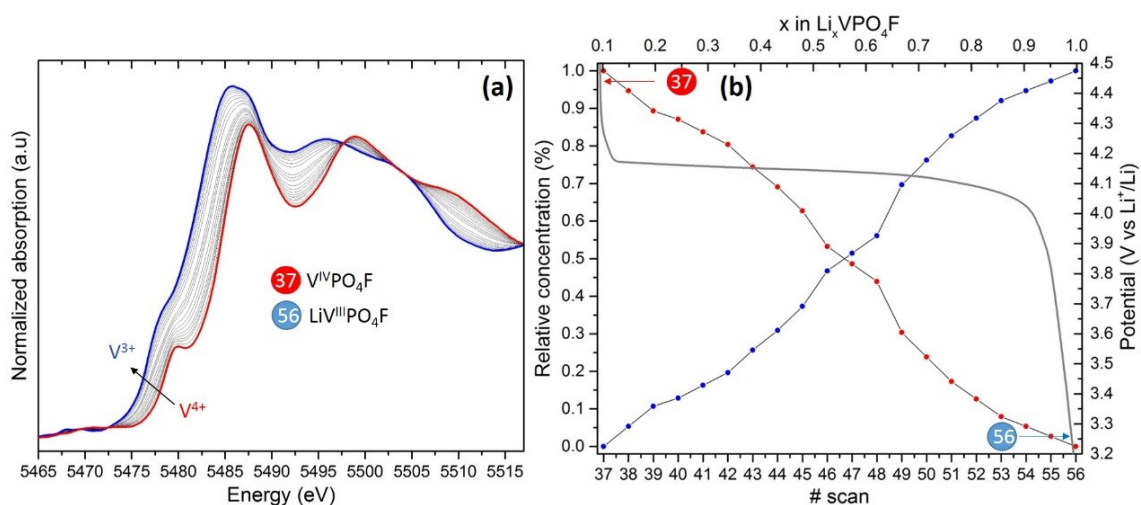


Figure II-8: (a) XANES spectra acquired operando during Lithium reinsertion in VPO_4F and (b) the corresponding voltage profile and the relative concentration of the LiVPO_4F and VPO_4F contributions obtained by linear combination of the 37th and 56th spectra are shown in inset.

During the discharge a simple linear combination between the first and the last spectra is sufficient to fit all the series of spectra (**Figure II-8b**). Indeed, as expected by the electrochemical signature (and also by *in-situ* XRD²⁰) there is no intermediate phase involved in this mechanism. It's thus interesting to compare the component of the charge corresponding the $\text{Li}_{0.67}\text{VPO}_4\text{F}$ phase (*i.e.* component#2) with its discharge analogue ($\text{Li}_{0.67}\text{VPO}_4\text{F}$ (dis), spectrum#13).

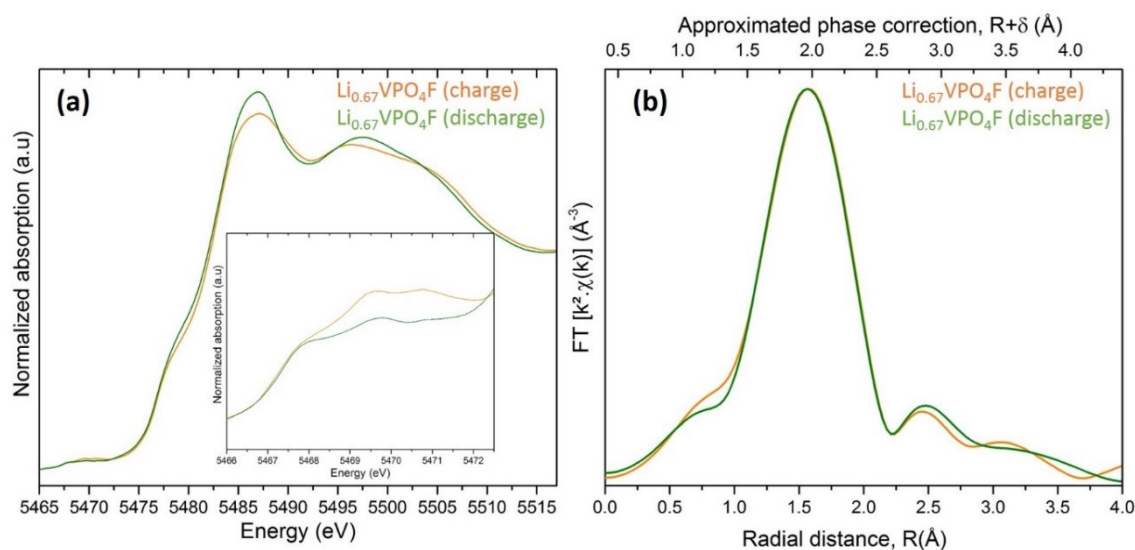


Figure II-9: The XANES spectra (a) and EXAFS spectra (b) observed during charge (orange) and during discharge (green) both at the $\text{Li}_{0.67}\text{VPO}_4\text{F}$ composition are compared.

Figure II-9a shows that only a small shift is observed in the edges' position (0.2 eV), whereas the pre-edge regions are significantly different. The intensity of the pre-edge is stronger upon charge than upon discharge. Actually, as LiVPO_4F and $\text{Li}_{0.67}\text{VPO}_4\text{F}$ are described in a $P-1$ space group whereas VPO_4F adopts a monoclinic symmetry (*i.e.* $S.G.$ $C2/c$), the lower symmetry in $\text{Li}_{0.67}\text{VPO}_4\text{F}$ could induce stronger distortion of the vanadium and thus a stronger pre-edge feature compared to a mixture containing 67% LiVPO_4F and 33% VPO_4F . **Figure II-9b** compares their EXAFS oscillations and clearly highlights that considering only the first ligand shell (*i.e.* 1.0-2.2 Å around vanadium), there is no significant difference in the average ligand distribution (nature and distances) between the charge and the discharge, whereas some differences appear at higher distances. Nevertheless, despite several attempts, we were only able to fit properly the EXAFS oscillations associated with the first coordination sphere.

The fit of the EXAFS oscillations of each component extracted using PCA and the spectrum corresponding to the $\text{Li}_{0.67}\text{VPO}_4\text{F}$ composition during discharge are represented in

Figure II-10a and the results are gathered in **Table II-4**. The reverse Fourier transform of the signal in R-space, allowing to select only the V-X contributions being enclosed in the first coordination sphere around the absorbing element (in our case 1-2.2 Å corresponding to the first shell of ligands X), is also shown in **Figure II-10b**.

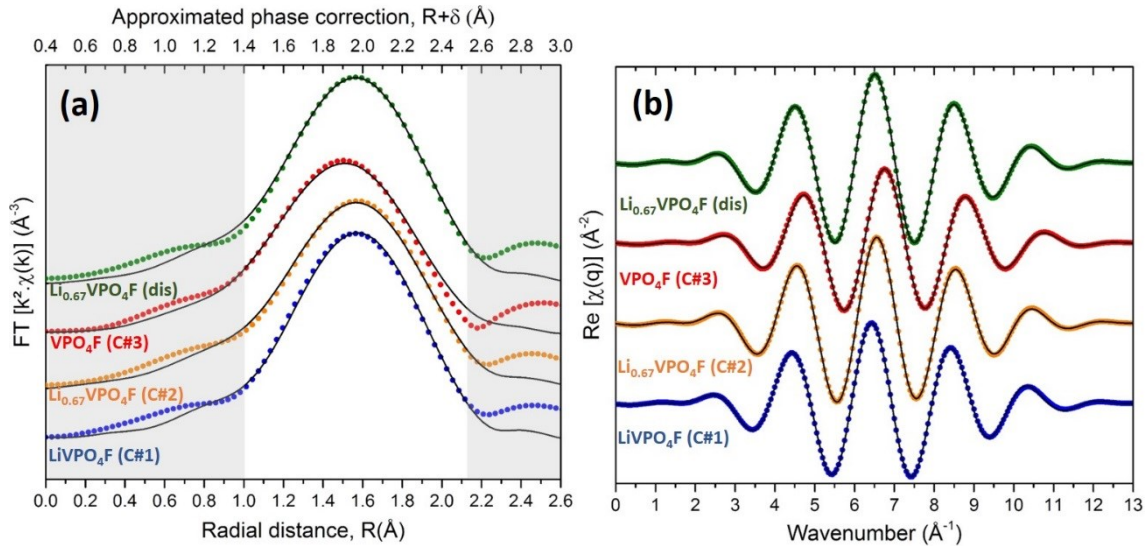


Figure II-10: (a) Fit of the k^2 -weighted V K-edge EXAFS spectra Fourier transform (k -range: 3.7 - 11.0 \AA^{-1} , sine window) in the R space (R range: $1.0 - 2.05 \text{ \AA}$, $dR = 0.1 \text{ \AA}$) for the components #1, #2 and #3 obtained thanks to the PCA during charge and for the spectrum corresponding to the $\text{Li}_{0.67}\text{VPO}_4\text{F}$ composition obtained during discharge. (b) The corresponding fit of the real part of $\chi(q)$ corresponding to the reverse Fourier transform of the spectra given in (a), considering only a limited R -range ($1.0 - 2.05 \text{ \AA}$, $dR = 0.1 \text{ \AA}$). The circles represent the experimental data and the solid lines represent the result of the fit. The parameters thus extracted are provided in Table II-4.

Component#1 corresponding to the LiVPO_4F composition can be fitted considering a regular octahedron with 6 V-L distances equal to $2.00(1) \text{ \AA}$ (*i.e.* 4 oxygen and 2 fluorine atoms) and a Debye Waller factor, $\sigma^2 = 0.004 \text{ \AA}^2$. As fluorine and oxygen interact similarly with X-rays, it's impossible to distinguish them and thus to consider the presence of a tiny amount of oxygen defects in LiVPO_4F . The lengths determined for the V-L distances from the analysis of the EXAFS data are in very good agreement with those calculated from XRD ($\langle d_{\text{V-L}} \rangle_{\text{XRD}} = 1.972(6) \text{ \AA}$ in centrosymmetric octahedra, see **Table II-3**), and the resulting BVS is also very close to the theoretical one (*i.e.* $2.92(8)$ vs $3.09(3)$ in average for the two vanadium sites as obtained from XRD). For Component#3, corresponding to the VPO_4F composition, a similar model has been used (*i.e.* regular octahedra) with V-L (L being O or F) distances of $1.93(1) \text{ \AA}$ (and a twice bigger $\sigma^2 (= 0.008 \text{ \AA}^2)$) conferring a BVS in good agreement with the oxidation state of vanadium (*i.e.* $3.85(9)$ vs 4.00 theoretically). Component#2 (*i.e.* $\text{Li}_{0.67}\text{VPO}_4\text{F}$) can be fitted considering a model corresponding to 67% of LiVPO_4F and 33% of VPO_4F (*i.e.* 4 V-L distances at $2.00(1)$ with $\sigma^2 = 0.006 \text{ \AA}^2$ and 2 at $1.93(1) \text{ \AA}$ with $\sigma^2 = 0.009 \text{ \AA}^2$) with bigger Debye-

Waller factors higher than those observed for the components #1 and 2. As σ^2 can be conceptualized as the disorder parameter, the distances found by EXAFS are actually distributed around the mean value and a larger σ^2 highlights a stronger distortion/disorder of the vanadium environment and could explain the higher pre-edge intensity observed for Li_{0.67}VPO₄F. From the EXAFS point of view, the first coordination sphere around vanadium in the intermediate phase Li_{0.67}VPO₄F is similar to a mixture of 2/3 LiVPO₄F and 1/3 VPO₄F and *a fortiori* is similar to the corresponding composition during discharge (*i.e.* a biphasic material containing 2/3 LiVPO₄F and 1/3 VPO₄F). Indeed, the fit of its spectrum leads to similar distances to Li_{0.67}VPO₄F (C#2) but with a weaker Debye Waller factor ($\sigma^2 = 0.005$). It means that the local environments observed around vanadium in the single phase Li_{0.67}VPO₄F obtained in charge are similar to those observed in LiV^{III}PO₄F and in V^{IV}PO₄F, and in a proportion 2:1 similar to that observed in the biphasic compound of average composition Li_{0.67}VPO₄F obtained in discharge.

Table II-4: Structural Parameters obtained from fit of the k^2 -weighted V K-edge EXAFS spectra Fourier transform. The parameters marked by * for a same sample have been refined together. The XRD distances reported in this table are average ones and are compared to the average distances found by EXAFS and to the associated BVS.

sample	V ⁿ⁺ -X	coordination number, N	R (Å)	σ^2 (10 ⁻³ Å ²)	BVS
LiVPO₄F (C#1)	V ³⁺ -F	2	2.00(1)	0.004(1)	2.92(8)
	V ³⁺ -O	4	2.00(1)	0.004(1)	
	Average EXAFS	6	2.00(1)	0.004(1)	/
	Average XRD	6	1.972(6)	/	3.09(2)
Li_{0.67}VPO₄F (C#2)	V ^{3/4+} -X	4	2.00(1)	0.006(1)	3.23(9)
	V ^{3/4+} -X	2	1.93(1)	0.009(1)	
	Average EXAFS	6	1.98(1)	0.007(1)	/
	Average XRD	6	1.95(3)	/	3.4(1)
VPO₄F (C#3)	V ⁴⁺ -F	2	1.93(1)	0.008(1)	3.85(9)
	V ⁴⁺ -O	4	1.93(1)	0.008(1)	
	Average EXAFS	6	1.93(1)	0.008(1)	4.21(8)
	Average XRD	6	1.90(1)	/	/
Li_{0.67}VPO₄F (dis)	V ^{3/4+} -X	4	2.00(1)	0.006(1)	3.23(9)
	V ^{3/4+} -X	2	1.93(1)	0.009(1)	
	Average EXAFS	6	1.98(1)	0.007(1)	/
	Average XRD	6	/	/	/

iii. $\text{Li}_{0.67}\text{VPO}_4\text{F}$: Lithium/vacancy and $\text{V}^{3+}/\text{V}^{4+}$ ordering?

In-order to further understand the nature of the intermediate phase, several attempts to obtain it as a pure phase were carried out. Previous works highlight the difficulty to obtain this phase as a single phase even under *operando* conditions at rather low cycling rates and the authors suggested the existence of spatial inhomogeneities in the electrode^{20,130}. In order to overpass the possible kinetic limitations at the origin of these inhomogeneities, a very low C-rate (C/200) was applied until reaching the voltage of this transition (*i.e.* 4.245 V vs Li^+/Li). The XRD pattern of the material obtained is compared to that of the pristine LiVPO_4F in **Figure II-11**.

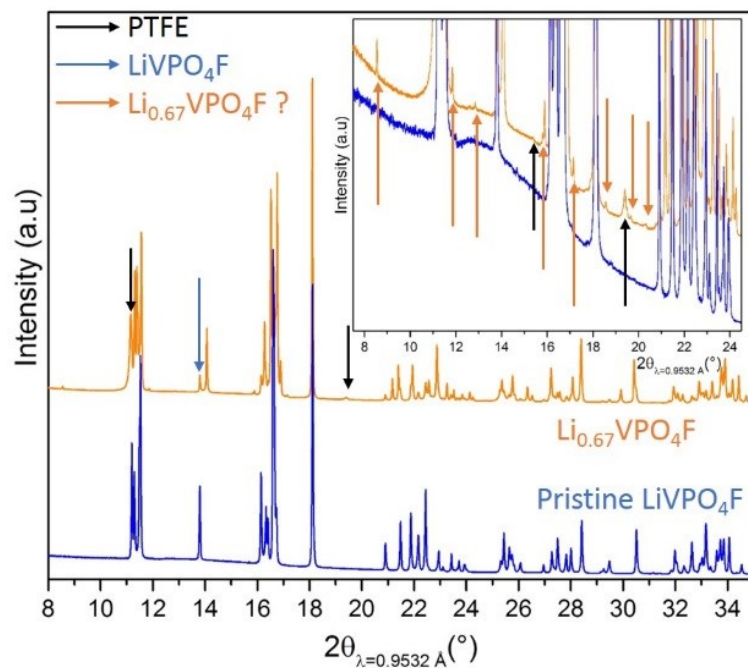


Figure II-11: Comparison of the SXRPD patterns of $\text{Li}_{0.67}\text{VPO}_4\text{F}$ (orange) obtained by electrochemical delithiation of the pristine material LiVPO_4F (blue). In that former, Additional contributions arise from the binder (PTFE, black arrows), the pristine material (LiVPO_4F , many contributions but only one highlighted with a blue arrow) and the possible superstructure peaks (orange arrows).

Despite the precautions taken, some remaining intensities associated with the pristine material are observed. Moreover some additional wide peaks are detected at 2θ values of 11.15, 15.88 and 19.40° which match with the binder contribution (PTFE). Another series of additional peaks that cannot be indexed in a LiVPO_4F -type unit cell is also observed at 2θ values of 11.85, 12.84, 15.81, 17.01, 18.56, 19.66, 20,76° ... which could correspond to superstructure peaks induced by peculiar $\text{V}^{3+}/\text{V}^{4+}$ and/or $\text{Li}^+/\text{vacancies}$ ordering. All the main peaks of the SXRPD pattern recorded for $\text{Li}_{0.67}\text{VPO}_4\text{F}$ have been first indexed with a P-1 triclinic unit cell ($a =$

5.1693(1) Å, $b = 5.2234(1)$ Å, $c = 7.2752(1)$ Å, $\alpha = 107.499(1)^\circ$, $\beta = 109.486(1)^\circ$, $\gamma = 96.906(1)^\circ$, $V/Z = 85.613(2)$ Å³ and $Z=2$). The Rietveld refinement is shown in **Figure II-12a**.

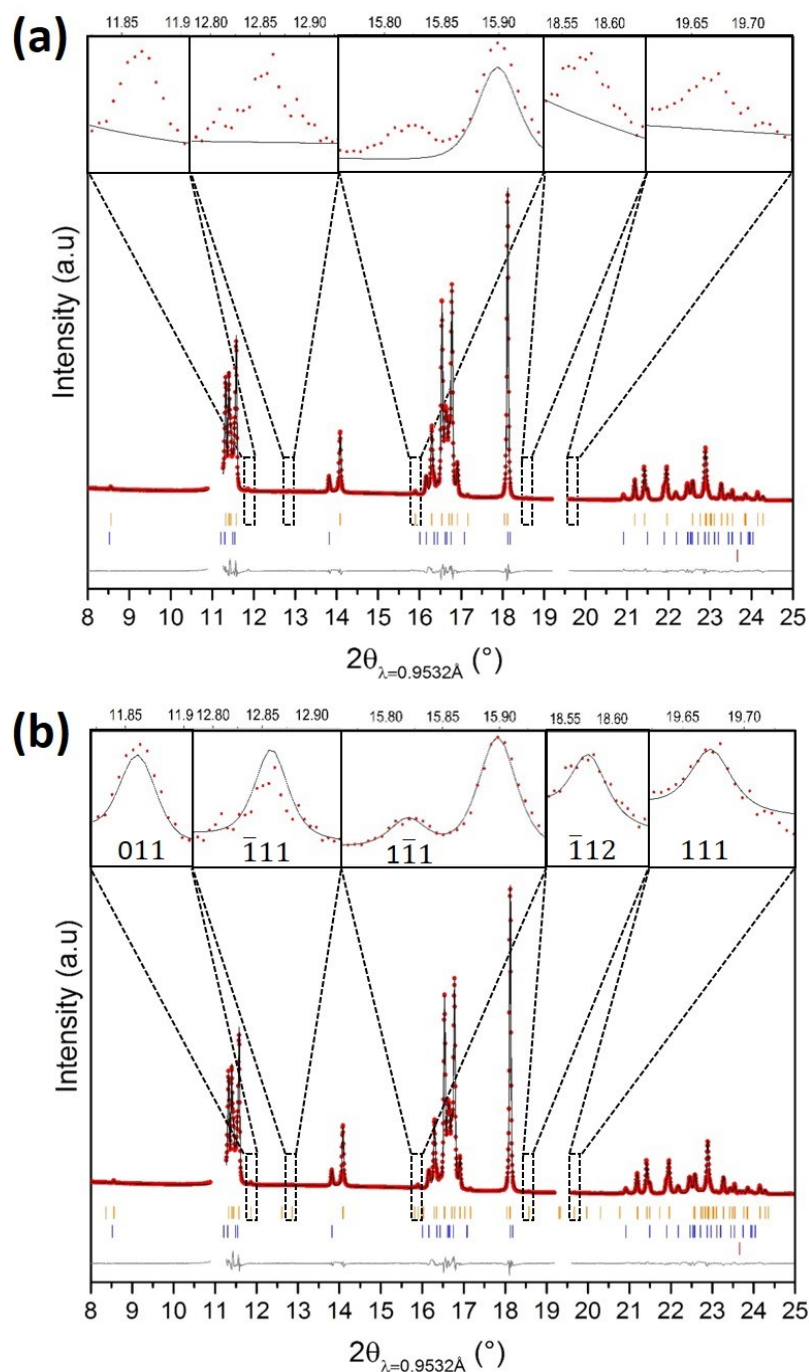


Figure II-12: Rietveld refinement of the $\text{Li}_{0.67}\text{VPO}_4\text{F}$ structure based on SXRPD data using a $Z=2$ model (LiVPO_4F -type model) (a) and using a $Z=4$ model (ax_2bxc) (b). The observed intensities are plotted as red points, the theoretical Bragg positions are plotted as orange ($\text{Li}_{0.67}\text{VPO}_4\text{F}$), blue (LiVPO_4F) and red (LiF) marks, calculated intensities and the difference between observed and calculated intensities are plotted as black lines. In the inset the enlargement of selected 2θ regions shows that some tiny contribution aren't indexed in the $Z=2$ cell whereas they are using the $Z=4$ cell.

The refinement of the average structure of Li_{0.67}VPO₄F was performed considering the same model than the one used to describe LiVPO₄F, but with a partial occupancy of the Lithium site ($\tau(\text{Li}) = 0.64(3)$) with a huge Debye Waller factor (*i.e.* 6.2(4) Å²). It might suggest that the Lithium site could in fact be splitted in two rather close sites, and this ordered distribution of the Li⁺ ions could be at the origin of the additional peaks as superstructure lines. The other main difference with the structure of the pristine material resides in the V(1) environment. Indeed, the average distance around V(1) is 1.933(3) Å (vs 1.98 Å for LiVPO₄F) whereas the V(2) environment doesn't seem to be modified by the extraction of 1/3 of the Li⁺ ions from the host structure. The BVS of these vanadium cations are 3.53(5) and 3.19(5) for V(1) and V(2) respectively, against 3.06(3) and 3.11(3) in LiVPO₄F. This result suggests a V³⁺/V⁴⁺ ordering, and hence Leball refinements by doubling or tripling the unit cell parameter(s) of the pristine material LiVPO₄F were also performed. Even if the stoichiometry of the Li_{0.67}V^{3.33+}PO₄F phase might suggest, for a full V³⁺/V⁴⁺ ordering, a three-fold multiplicity, the better fit of the tiny intensities was obtained for the doubling of b. Therefore, only a partial V³⁺/V⁴⁺ ordering and/or an inhomogeneous distribution of lithium in the two sites induced by the doubling of the unit cell along the b axis would occur at this composition. In order to check for this hypothesis, Rietveld refinement in the Z=4 cell (**Figure II-12b**) was carried out keeping the profile function and all the parameters related to the secondary phases as refined in the Z=2 cell, and constraining the distances in the phosphate groups ($d_{\text{P-O}} = 1.55 \pm 0.05$ Å). This structural model is characterized by 4 Vanadium and 2 Lithium (the structural parameters and the vanadium and lithium environments as determined are provided in **Tables II-5** and **Table II-6**).

Table II-5: Significant bond length lengths (Å) of Li_{0.67}VPO₄F obtained from Rietveld refinement of SXRPD data.

Polyhedral distortion is calculated as $\Delta = \frac{1}{N} \sum_{i=0}^N \frac{(d_i - \langle d \rangle)^2}{\langle d \rangle^2}$.

coordination	V(1) 6 (Oh)	V(2) 6 (Oh)	V(3) 6 (Oh)	V(4) 6 (Oh)	Li(1) 5	Li(2) 5
O(1)	/	/	1.87(3)*2		/	2.09(9)
O(2)	/	/	/	1.97(3)	2.10(9)	/
O(3)	/	/	1.93(2)*2		2.34(9)	2.12(9)
O(4)	/	/	/	2.01(3)	2.13(9)	2.51(9)
O(5)	/	1.86(3)*2	/		/	2.38(9)
O(6)	1.95(2)*2	/	/		2.10(9)	/
O(7)	/	1.90(3)*2	/		/	/
O(8)	1.96(3)*2	/	/		/	/
F(1)	1.92(3)*2	/	2.02(3)*2		1.85(9)	/
F(2)	/	2.00(3)*2	/	1.93(3)*2	/	1.84(9)
Average	1.94(3)	1.92(3)	1.94(3)	1.97(3)	2.18(9)	2.19(9)
Δ	1.5x10 ⁻⁴	1.9x10 ⁻³	1.9x10 ⁻³	5.4x10 ⁻⁴	2.0x10 ⁻²	2.5x10 ⁻²
BVS	3.2(1)	3.9(1)	3.5(1)	3.1(1)	0.9(2)	0.9(2)

The refinement of the Lithium positions and of the associated B_{iso} was first performed considering an homogeneous occupancy of both sites ($\tau(\text{Li}(1)) = \tau(\text{Li}(2)) = 0.67$), and then such as their sum corresponds to an average occupancy of 0.67. The Li(1) site is found to be quasi fully occupied ($\tau(\text{Li}(1)) = 0.99(5)$) whereas the Li(2) site is only one-third occupied ($\tau(\text{Li}(1)) = 0.34(5)$), in good agreement with at least a partial ordering of the Li⁺ ions within the tunnels of the structure.

Table II-6: Structural parameters obtained by Rietveld refinement of the structure of Li_{0.67}VPO₄F using the Z=4 model.

Li _{0.67} VPO ₄ F							
SG : <i>P-1</i>		$a = 5.1693(1) \text{ \AA}$		$\alpha = 107.495(1)^\circ$			
Z = 4		$b = 10.4465(1) \text{ \AA}$		$\beta = 107.487(1)^\circ$		$\chi^2 = 33.1$	
LiVPO ₄ F : 27.3(1) wt.%		$c = 7.2751(1) \text{ \AA}$		$\gamma = 98.905(1)^\circ$		$R_{Bragg} = 3.65 \%$	
LiF : <2 wt.%		$V = 342.443(3) \text{ \AA}^3$		$V/Z = 85.611(3) \text{ \AA}^3$			
atoms	Wickoff position	x	Y	z	Occupancy	B iso	BVS
V(1)	1 <i>a</i>	0	0	0	1	1.17(4)	3.2(1)
V(2)	1 <i>c</i>	0	0.5	0	1	1.73(4)	3.9(1)
V(3)	1 <i>b</i>	0	0	0.5	1	1.80(4)	3.5(1)
V(4)	1 <i>g</i>	0	0.5	0.5	1	1.72(5)	3.1(1)
P(1)	2 <i>i</i>	0.337(5)	0.323(2)	0.264(3)	1	1.34(5)	5.3(3)
P(2)	2 <i>i</i>	0.327(5)	0.821(2)	0.257(3)	1	1.78(5)	5.0(3)
O(1)	2 <i>i</i>	0.353(8)	0.121(5)	0.598(6)	1	2.06(9)	2.3(2)
O(2)	2 <i>i</i>	0.372(7)	0.625(4)	0.590(5)	1	1.18(9)	2.3(2)
O(3)	2 <i>i</i>	0.173(8)	0.851(3)	0.407(4)	1	1.29(6)	2.2(2)
O(4)	2 <i>i</i>	0.111(5)	0.332(3)	0.355(4)	1	1.87(9)	1.9(2)
O(5)	2 <i>i</i>	0.713(7)	0.338(3)	0.840(5)	1	1.93(9)	2.2(2)
O(6)	2 <i>i</i>	0.707(7)	0.827(3)	0.861(4)	1	2.08(9)	2.4(2)
O(7)	2 <i>i</i>	0.252(8)	0.393(4)	0.096(5)	1	2.12(9)	2.1(2)
O(8)	2 <i>i</i>	0.263(9)	0.895(5)	0.109(6)	1	2.13(9)	2.3(2)
F(1)	2 <i>i</i>	0.881(8)	0.036(3)	0.229(5)	1	1.83(9)	1.1(2)
F(2)	2 <i>i</i>	0.877(8)	0.531(4)	0.240(4)	1	1.45(9)	1.3(2)
Li(1)	2 <i>i</i>	0.728(9)	0.187(7)	0.280(9)	0.99(3)	2.0(5)	0.9(2)
Li(2)	2 <i>i</i>	0.789(9)	0.701(7)	0.301(9)	0.64(3)	2.0(5)	0.9(2)

Considering the BVS of vanadium atoms (*i.e.* 3.2 (1), 3.9(1), 3.5 (1) and 3.1(1) for V(1), V(2), V(3) and V(4) respectively, and 3.4(1) in average vs. 3.33 theoretically), the same conclusion can be made with at least a partial charge ordering on vanadium. Indeed, the V(2) site has a strong V⁴⁺ character, the V(1) and V(4) sites a strong V³⁺ character and the V(3) site seems to be alternatively occupied by V³⁺ and V⁴⁺ (see **Figure II-13**). Nevertheless, the doubling of the a parameter (or c parameter), allowing the alternation of V³⁺/V⁴⁺ cations along the [100] direction (or within the (100) plane) for this site, generates many unobserved theoretical contribution without providing a more relevant fit. Therefore a disordered distribution of V³⁺ and V⁴⁺ cations at the V(3) (statistical distribution or local ordering) seems to take place.

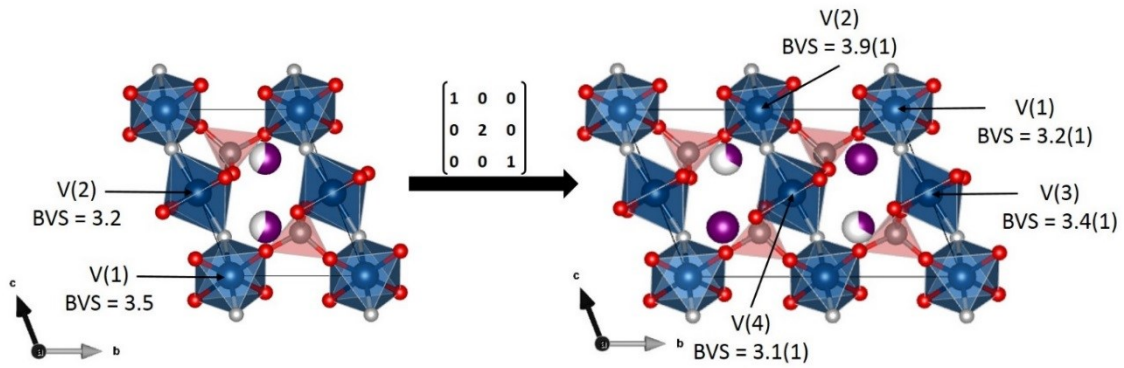


Figure II-13: projection along the $[100]_{P-1}$ direction of the structure of $\text{Li}_{0.67}\text{VPO}_4\text{F}$ obtained from Rietveld refinement in the $Z=2$ model (left) and in the $Z=4$ model (right): VO_4F_2 octahedra are represented in blue, PO_4 tetrahedra in red and lithium in purple.

In order to get more insights into the Lithium environment in $\text{Li}_{0.67}\text{V}^{3+/4+}\text{PO}_4\text{F}$, ^7Li NMR experiment was also carried out. The NMR spectra of this sample, shown in **Figure II-14**, contains 4 shifted contributions at 38, 113, 134 and 162 ppm. The peak centered at 113 ppm (denoted as peak#2 in **Figure II-14**) is asymmetric, most probably due to the presence of residual LiVPO_4F (isotropic signal at 115 ppm), and the contribution close to 0 ppm (peak#0) is a diamagnetic contribution assigned to the LiF impurity and/or residual electrolyte salt (LiPF_6).

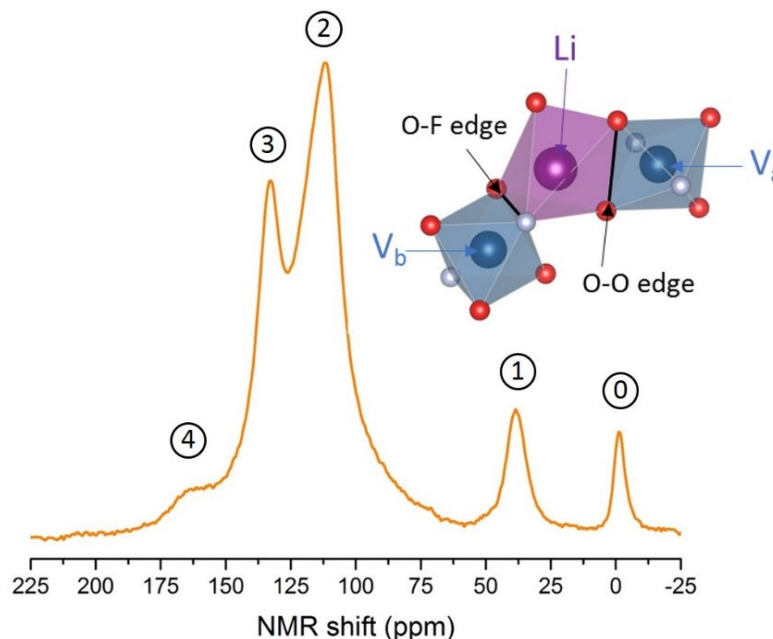


Figure II-14: ^7Li MAS NMR spectrum of $\text{Li}_{0.67}\text{VPO}_4\text{F}$ and the schematic Lithium environment simplified based on the hypothesis that only the VO_4F_2 octahedron sharing an edge with LiO_4F can provide a spin transfer.

As observed in LiVPO_4F , the lithium polyhedra in $\text{Li}_{0.67}\text{VPO}_4\text{F}$ share two edges and two vertices with the vanadium octahedra. The e_g orbitals of vanadium (either V^{3+} or V^{4+}) being empty, only edge sharing between LiO_4F and VO_4F_2 polyhedra can lead to significant spin transfer via t_{2g} orbitals. Thus only 2 vanadium atoms (labelled V_a and V_b in inset of **Figure II-14**)

contribute significantly to the shift observed in the ⁷Li NMR signals (V_a sharing an O-O edge and V_b sharing an O-F edge with LiO₄F polyhedra, inset **Figure II-14**). Therefore, considering the number of lithium sites and the (dis)order of V^{3+}/V^{4+} cations, the number of theoretical contributions in the NMR spectra can be predicted. In our case two crystallographic lithium sites have been identified by diffraction. If they are different enough to be differentiated by NMR, they should lead to 8 signals (in the case of a statistical distribution of V^{3+}/V^{4+} cations around them), whereas the NMR spectra reveals the presence of only 4 shifted contributions. Therefore, either these lithium sites are too similar to be separated considering the large width of the signals, or a peculiar V^{3+}/V^{4+} ordering (not fully identified yet, as detailed just before) generates a smaller number of possible interactions (and thus of NMR contributions). Considering the first hypothesis (i.e. two undifferentiated Li sites and a statistical distribution of V^{3+}/V^{4+} around them), the relative intensity of the signals observed should be distributed as follows: 0.44:0.22:0.22:0.12 respectively for Li in interaction with V_a^{3+}/V_b^{3+} , V_a^{3+}/V_b^{4+} , V_a^{4+}/V_b^{3+} and V_a^{4+}/V_b^{4+} . Nevertheless, the fit of the NMR signal thanks to a pseudo-Voigt function (taking into account the spinning side bands which aren't depicted in **Figure II-14**) contradicts this hypothesis. It supports thus also the presence of a partial ordering of V^{3+}/V^{4+} . Nevertheless, without further investigations of the NMR signature by DFT calculations, it will not be possible to get more in-depth information on the nature of this ordering.

II-1c. Summary and prospects

In summary, new insights about the redox processes and phase transitions involved during the electrochemical cycling of LiVPO₄F are proposed. Thanks to *operando* XANES experiments performed at the vanadium V K-edge, the asymmetrical and reversible activation of the V^{3+}/V^{4+} redox couple has been highlighted. That is in good agreement with the previous works conducted in our groups, revealing that during electrochemical extraction of Li⁺ from LiVPO₄F, a phase transition occurs at the Li_{0.67}VPO₄F composition which isn't observed during discharge.²⁰ Further characterization of this phase has been performed by SXRPD and revealed, for the first time, a complex ordering. Indeed, the tiny contributions observed by XRD require the use of a Z=4 model to be fitted, splitting the single Li site occupied at two-thirds into two very similar sites inhomogeneously filled ($\tau(\text{Li}(1))=1$ and $\tau(\text{Li}(2))=0.33$). However, Li⁺ being a weak scatterer in XRD, the lithium distribution between both sites has to be confirmed by ND. Moreover, the BVS study suggests a partial charge ordering of V^{3+}/V^{4+} cations, with some vanadium cations showing either a strong V^{3+} or V^{4+} character or a mixed valence state (V^{3+}/V^{4+}). From the EXAFS point of view, in this phase the first ligands' shell around vanadium can be described as a combination of V^{4+} -type (i.e. VPO₄F-type) and V^{3+} -type (i.e. LiVPO₄F-type)

environments and differs with a mixture of LiVPO₄F/VPO₄F (0.67/0.33) only for far shells supporting the local charge ordering suggested by the BVS. At a first sight, ⁷Li NMR appears as the most relevant technique to describe this partial ordering, but, without DFT calculations, the signature could not be fully understood yet. This work remains a preliminary crystallographic study of the ordering observed in Li_{0.67}VPO₄F which requires further investigations to be fully elucidated. For instance, DFT and electron diffraction, which have been shown for instance to be tools of choice for the understanding of the ordering observed in Na_{2/3}FePO₄,¹³⁵ could confirmed our hypotheses. Indeed, DFT would allow to predict the more stable orderings and their NMR signatures and TEM could support our proposition for the supercell, in order to reach the chemical driving force for this ordering and for this asymmetry between charge and discharge upon electrochemical cycling (the single phase Li_{0.67}VPO₄F being observed only during charge).

Furthermore, the nature of the defects previously highlighted by NMR in LiVPO₄F¹⁹ has been partially elucidated. The first computational approach considered vanadyl-type defects according to two models: LiVPO₄F_{0.96}O_{0.04} (model I) and Li_{0.96}VPO₄F_{0.96}O_{0.04} (model II). The model I involving partial substitution of oxygen for fluorine and the local formation of the vanadyl bond (covalent V⁴⁺=O bond) predicts, among other, a negatively shifted contribution not observed experimentally. In model II, lithium vacancies are generated in the neighboring of vanadyl-type defects leading to the formation of V⁴⁺ pairs inside V³⁺-rich chains of octahedra (see **Figure II-3**). The NMR shifts predicted by this model II are in very good agreement with the experimental spectrum of LiVPO₄F especially regarding the absence of negatively shifted component.²¹ Experimentally, the presence of vanadyl-type defects have been clearly highlighted by XANES through a weak pre-edge contribution at 5469.7 eV, typical signature of V⁴⁺=O (vs. 5469.4 eV for LiVPO₄O). Nevertheless, we weren't able to validate the second model either, as for such a weak concentration of defects the lithium vacancies cannot be detected by diffraction techniques. Moreover, the difference in the V K-edge XANES spectra expected for the two models being unknown, without any theoretical simulation of the corresponding spectra it isn't actually possible to validate definitely this second model. The strategy that we adopted was thus to increase the amount of defects in LiVPO₄F by different ways in order to try to elucidate their nature. In the following of this chapter the ways explored will be described in details and the impact of the defects generated on the structural and electrochemical properties as well as on the structural and redox mechanisms observed upon electrochemical cycling will be investigated.

II-2. Oxidation under air of LiVPO₄F

In the previous section, the nature of the defects observed in LiVPO₄F have been partially elucidated combining DFT calculations and spectroscopy. These vanadyl-type defects could impact the structure and electrochemical performance but the study of their direct influence in such weak amounts is challenging. The strategy that we adopted was to increase the amount of defects by different ways in order to better characterize them. The partial substitution of fluorine by oxygen could occur either during the thermal treatment (trace of oxygen in furnace) or during the quenching of the sample in liquid nitrogen at the end of the synthesis or during storage of the materials. This material has revealed itself to be extremely stable under ambient conditions which invalidate the last hypothesis. In the first time, samples obtained by annealing LiVPO₄F under air will be investigated in order to study the effect of an oxidation which would occur between the removal of the sample out of the oven and the immersion in the liquid nitrogen.

II-2a. Synthesis of oxidized samples

As already discussed in section II-1, LiVPO₄F (the LVPF#1 sample) was obtained pure: all the diffraction lines could be indexed in a typical Tavorite unit cell described in the *P-1* space group with $a = 5.1689(1) \text{ \AA}$, $b = 5.3086(1) \text{ \AA}$, $c = 7.2622(1) \text{ \AA}$, $\alpha = 107.590(1)^\circ$, $\beta = 107.971(1)^\circ$, $\gamma = 98.396(1)^\circ$ and $V/Z = 87.143(3) \text{ \AA}^3$. The TGA data obtained for the thermal treatment of LiVPO₄F under air is shown in **Figure II-15**.

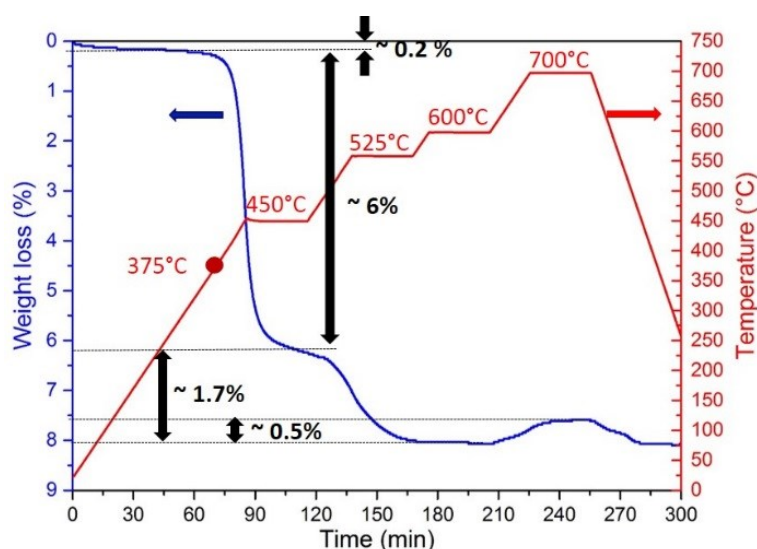


Figure II-15: TGA curve obtained under air for the pristine LVPF as function of time and plotted as a blue line and the corresponding temperature vs. time curve plotted as a red line. The heating/cooling rate is $\pm 5^\circ\text{C}/\text{min}$ and the temperature plateau is maintained during 30 minutes.

The TGA data highlights three main weight-loss domains:

- The first one, between 25°C and 100°C, matches with the evaporation of the adsorbed water and corresponds to about 0.2 wt.%.
- The second one starts at 375°C and is associated with a weight loss of 6 wt. % (until 450°C) that may correspond to the elimination of the surrounded carbon through the formation of CO₂ (*i.e.* approximately to the 5 wt.% of carbon remaining from the synthesis).
- The third transition occurs near 525°C and generates a loss of 1.7 wt. % of the initial mass, which would correspond to the weight loss expected for a complete substitution of oxygen for fluorine. Note that the oxidation of LiVPO₄F may begin at lower temperature.

A small weight gain occurs (around 0.5 wt.%) upon heating from 600°C to 700°C that is lost upon cooling. The XRD pattern of the material recovered at the end of this thermal treatment under air corresponds to that of the Tavorite phase LiV^{IV}PO₄O with Li₂V^VPO₆ present as a minor impurity (most probably at the origin of this reversible weight gain). In order to get more insight into the nature of the materials successively formed during the thermal treatment under air, a series of controlled thermal treatments of the pristine material, LiVPO₄F, was performed under air during 30 minutes at various annealing temperatures. The six samples thus obtained are called in the following LVPF-T (with T= 375, 450, 525, 600 and 700°C). Selected 2θ domains of Synchrotron XRD patterns of these samples are compared in **Figure II-16**, with the corresponding SEM images given in inset.

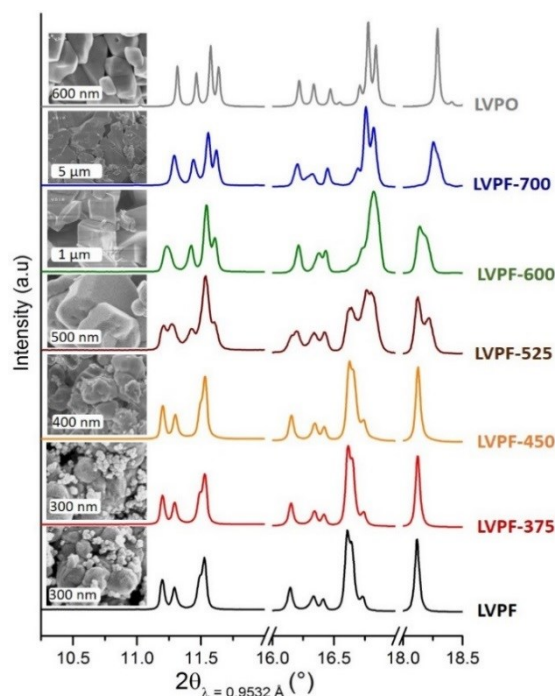


Figure II-16: Synchrotron XRD patterns of the pristine materials (LVPF and LVPO) and the annealed samples (LVPF-375, LVPF-450, LVPF-525, LVPF-600 and LVPF-700). Corresponding SEM images are shown in inset.

A rather continuous evolution of the diffraction patterns is observed. Contrary to the results obtained by Ma *et al.*¹⁷, a clear phase separation is observed for samples thermally treated at 525°C and above. For the lower temperature treated samples (*i.e.* up to 450°C), no obvious significant change of the diffraction pattern is observed and a very narrow solid solution domain seems to be formed. For the high temperatures processed samples, the XRD patterns could appear as combinations of LVPF and LVPO ones. The SEM images associated with LVPF reveals the formation of aggregates made of 300-600 nm primary particles with 20 nm divided carbon at their surface (the latter appearing as bright small particles in **Figure II-16**). The SEM images also highlight the almost complete disappearance of carbon nanoparticles at 450°C, in good agreement with the TGA analysis. Furthermore, a significant increase of the particles size is observed from 300 - 600 nm for the pristine LVPF material to 1000 - 5000 nm for LVPF-700. Curiously, this growth of particles is not accompanied by a narrowing of the diffraction lines. In fact, the formation of highly disordered materials and/or the separation into phases very close in compositions are likely at the origin of strain inducing peaks broadening.

Table II-7: Results of CHNS and ICP-OES chemical analyses carried out on all samples. Their color varies according to the weight percentage of carbon and to the oxidation state of vanadium. The average particle sizes are obtained thanks to SEM images given in inset in the figure II-16.

Samples	colors	CHNS C (w%)	ICP-OES			Particle sizes (nm)
			Li/V	Li/P	V/P	
LVPF	Black	5.65	0.98	1.02	1.04	300 – 600
LVPF-375	Black	4.29	1.02	1.01	0.99	300 – 600
LVPF-450	Dark grey	1.09	0.99	1.01	1.02	300 – 600
LVPF-525	Brown	0.22	0.97	0.99	1.03	500 – 1000
LVPF-600	Brown	/	1.03	1.06	1.03	500 – 2000
LVPF-700	Dark green	/	1.05	1.04	0.99	1000 – 5000
LVPO	Green	/	0.99	1.02	1.03	500 – 1000

ICP-OES and CHNS analyses of these samples were carried out in order to titrate the Li, P and V contents on one side and the remaining carbon on the other side, and to check for the chemical composition of these materials. **Table II-7** summarizes the results obtained. As expected by TGA results, a volatilization of remaining carbon as CO_2 is observed mostly between LVPF-450 and LVPF-525. This observation is supported by the change in the color of the different samples, from dark grey for LVPF-375 to brown for LVPF-525 and green for LVPF-700. Contrary to the results reported by Ma *et al.*¹⁷, no significant variation of the Li/V ratio from 1/1 is observed (neither for the Li/P ratio nor for the V/P ratio) suggesting that the stoichiometry LiVPO_4Y ($\text{Y} = \text{F}_{1-x}\text{O}_x$) is maintained.

II-2b. Average long range structure & microstructure

In order to ascertain the nature of the materials formed following our in-air thermal treatment, corresponding XRD patterns were analyzed and structural models were refined by the Rietveld method considering either a single or two Tavorite-type phases : LiVPO₄F-type or/and LiVPO₄O-type. The main difference between LiV^{III}PO₄F and LiV^{IV}PO₄O lies in the distances observed along the chains of octahedra⁹²: they are constant and equal to 1.98 Å in LiVPO₄F, whereas there is an alternation between a short bond (the vanadyl bond around 1.7 Å) and a longer one (around 2.2 Å) in LiVPO₄O (**Figure II-17**).

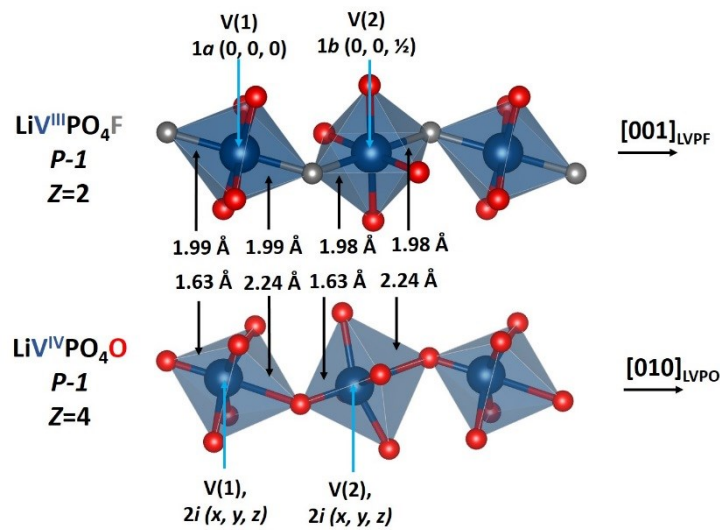


Figure II-17: Comparison of bond lengths along the chains of octahedra for tavorite-like structure: LiV^{III}PO₄F (P-1, Z=2, V(1) in 1a and V(2) in 1b sites) and LiV^{IV}PO₄O (P-1, Z=4, both vanadium in 2i sites)

In LiVPO₄F the vanadium cations are thus sitting at the center of the VO₄F₂ octahedra, in special positions (0, 0, 0) and (0, 0, 1/2). In order to allow the displacement of the vanadium cations from the center of the octahedra along the chains, and the possible formation of oxy-fluoride LiVPO₄F_{1-y}O_y solid solutions, Rietveld refinements were performed considering a LiVPO₄O-type model, and thus the doubling of the unit cell according to the following matrix:

$$\begin{bmatrix} \vec{a} \\ \vec{b} \\ \vec{c} \end{bmatrix}_{LVPO} = \begin{bmatrix} 1 & 0 & 1 \\ 0 & 1 & 0 \\ 0 & 1 & 0 \end{bmatrix} * \begin{bmatrix} \vec{a} \\ \vec{b} \\ \vec{c} \end{bmatrix}_{LVPF}$$

This model predicts superstructure peaks related to the ordering of the vanadyl-type distortion, therefore it isn't the most appropriate one for describing LiVPO₄F-type materials (for which the local vanadyl-type distortions are expected to be absent). However it allows to compare all phases generated by partial substitution of oxygen for fluorine all along the

oxidation process. Refined in a LiVPO₄O-type model, the cell parameters of LiVPO₄F are $a = 6.84751(3) \text{ \AA}$, $b = 7.26212(3) \text{ \AA}$, $c = 7.93166(3) \text{ \AA}$, $\alpha = 89.931(4)^\circ$, $\beta = 91.544(5)^\circ$, $\gamma = 117.854(4)^\circ$ and $V/Z = 87.18 \text{ \AA}^3$. The results of the refinements are summarized in **Table II-8** and in **Figures II-18, II-19 and II-20**.

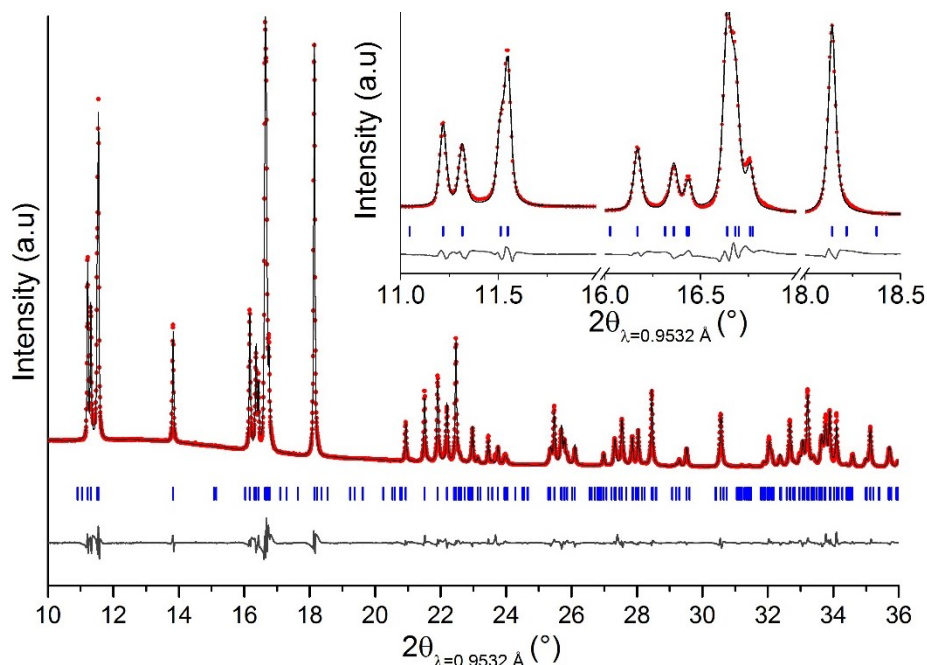


Figure II-18: Rietveld refinements obtained for the samples LVPF-450 taking into account the structural model of LiVPO₄O. The observed intensities are plotted as red points, the theoretical Bragg positions are plotted as blue marks, calculated intensities and the difference between observed and calculated intensities are plotted as black lines. In inset, an enlargement of the 2θ domain 11 - 18.5°.

The patterns of LVPF-375 and LVPF-450 (as highlighted for the latter in **Figure II-18**) can be refined using a single phase model, close to LVPF but significantly different, revealing that a solid solution domain exists below 450°C. For instance, the V/Z values obtained for LVPF-375 and LVPF-450 are 87.12 \AA^3 and 87.05 \AA^3 respectively, versus 87.18 \AA^3 for LVPF. In order to estimate the substitution level in these materials the Vegard's law was applied on their volumes. The vanadium average oxidation states would be 3.02 and 3.05 in LVPF-375 and LVPF-450 respectively, versus 3 for LVPF, hence their compositions would be LiVPO₄F_{0.98}O_{0.02} and LiVPO₄F_{0.95}O_{0.05}. Note that the individual cell parameters don't follow this law and a strong deviation is observed, especially for a and b. As reported before in ref ¹³⁶, single crystals with LiVPO₄F_{1- γ} O _{γ} compositions also don't adopt a linear evolution of their cell parameters with the substitution ratio whereas the cell volume does (this non-Vegard behavior will be carefully examine and partially explained in the **section II-3**). From 525°C two phases are observed in each sample, and must be considered for the Rietveld refinement to determine their structure (as highlighted for LVPF-525 in **Figure II-19**).

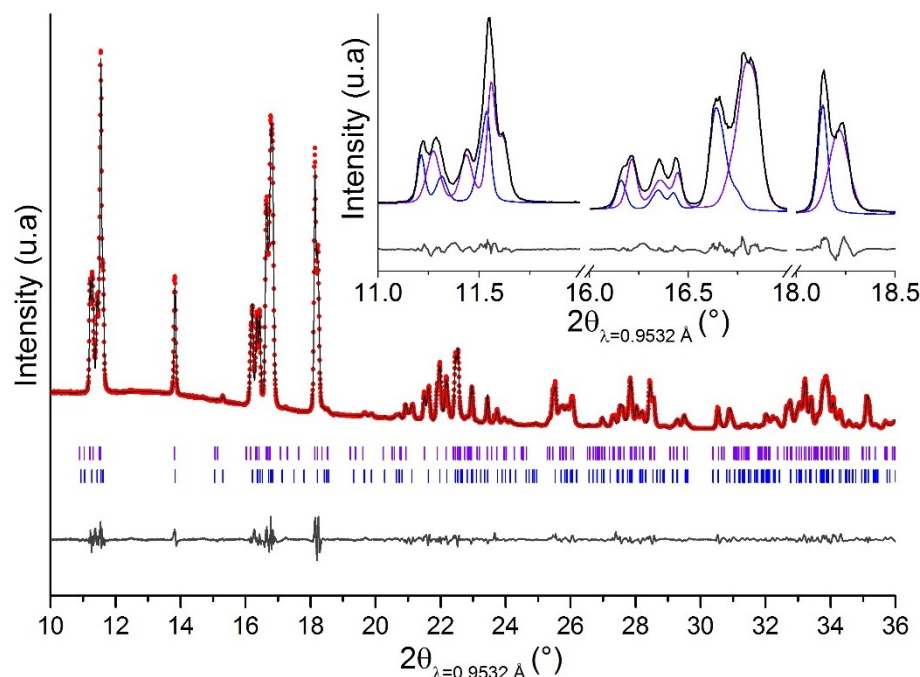


Figure II-19: Rietveld refinements obtained for the samples LVPF-525 taking into account the structural model of LiVPO_4O . The observed intensities are plotted as red points, the theoretical Bragg positions are plotted as purple (LiVPO_4F -type phase) or blue (LiVPO_4O -type phase) marks, calculated intensities and the difference between observed and calculated intensities are plotted as black lines. In inset, a zoom between 11 and 18.5° in which the contribution of each phase is represented.

Both Tavorite-type phases belong to the $\text{LiVPO}_4\text{F}_{1-y}\text{O}_y$ phase diagram: one is close to LVPF whereas the other is close to LVPO. Their compositions are $\text{LiVPO}_4\text{F}_{0.90}\text{O}_{0.10}$ and $\text{LiVPO}_4\text{F}_{0.08}\text{O}_{0.92}$ respectively (*i.e.* based on the Vegard's law applied on their cell volumes). The refinements of LVPF-600 and LVPF-700 confirm the persistence of the phase separation, but at higher treatment temperatures the Tavorite-type phases formed are really close to LVPO (*i.e.* $\text{LiVPO}_4\text{F}_{0.11}\text{O}_{0.89}$ and $\text{LiVPO}_4\text{F}_{0.03}\text{O}_{0.97}$ for LVPF-600 and $\text{LiVPO}_4\text{F}_{0.04}\text{O}_{0.96}$ and $\text{LiVPO}_4\text{F}_{0.01}\text{O}_{0.99}$ for LVPF-700). The global compositions calculated for each sample, taking into account the composition and weight percentage determined for each phase, are continuously enriched in oxygen with the increase of the annealing temperature moving from $\text{LiVPO}_4\text{F}_{0.96}\text{O}_{0.04}$ for LVPF-375 to $\text{LiVPO}_4\text{F}_{0.02}\text{O}_{0.98}$ for LVPF-700. Moreover, as the substitution of oxygen for fluorine increases, the average oxidation state of vanadium increases and the difference between the short and the long V-X bonds increases along the chains, from 0.04 Å for LVPF to 0.65 Å for LVPF-700 (Table II-8 and Figure II-20a), in good agreement with the growing of vanadyl-type environments.

Due to an inhomogeneous line broadening, all these patterns were refined using an anisotropic strain broadening model, corresponding to a *P*-1 space group and provided in the Fullprof software^{137,138}. By drawing the so called Williamson-Hall plot (*i.e.* $\beta_{\text{obs}} \cdot \cos\Theta$ as function of $\sin\Theta$), the size and strain effects can be separated. **Figure II-20** shows the evolution of the width of the microstrains' distribution ($\epsilon_{\text{hkl}} = \Delta d_{\text{hkl}}/d_{\text{hkl}}$) along peculiar directions ([100], [010], [001] and in average along all [hkl] directions) for all samples. **Table II-8** summarizes the microstructure parameters (D_{hkl} (= the apparent crystallite size) and ϵ_{hkl}).

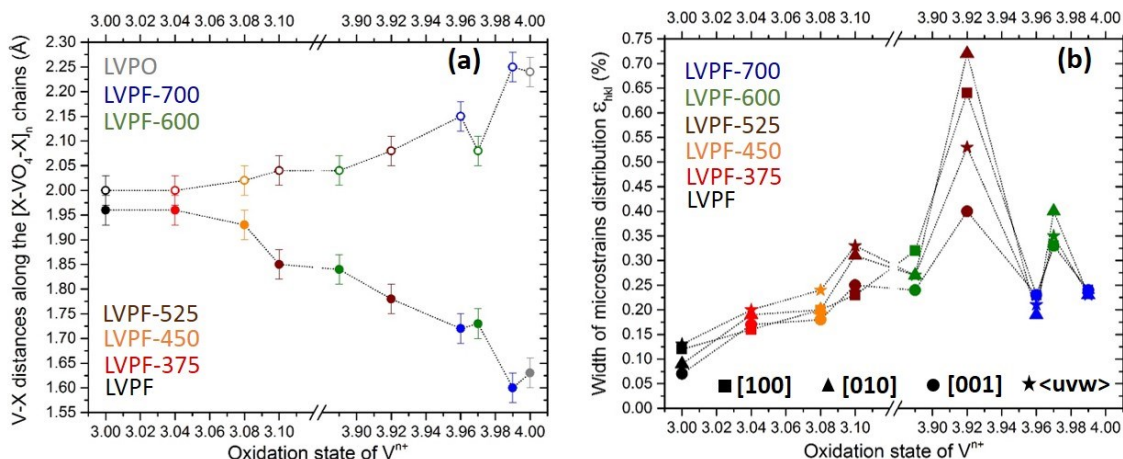


Figure II-20: (a) evolution of the shorter and longer V-X distances along the $[X-VO_4-X]_n$ chains as function of the vanadium oxidation state. The empty circles represent the long V-X distances and full circles the short V-X distances. (b) The width of the microstrains' distribution along [100] (square), [010] (triangles), [001] (circles) directions and the average on all [uvw] (stars) directions.

The analysis of the microstructure reveals that the strains along these three directions increase until 525°C and then decrease. Partial oxidation of the pristine material leads to the formation of vanadyl-type defects that would generate strains at the local scale, relaxed then thanks to the phase separation between a fluorine-rich phase and an oxygen(vanadyl)-rich phase. Moreover, the strains appear more extended along the [100] and [010], this latter corresponding to the vanadyl bond propagation direction. Indeed, the substitution of a part of fluorine by oxygen, leads to the formation of vanadyl bonds at the local scale (as dilute defects for small substitution ratios) which may disrupt the antagonist V-F bonds and generates small variations in the lattice parameters from one unit cell to another, especially along the b axis. The coherent diffraction size domains obtained from the microstructure analysis are consistent, from the pristine LVPF to LVPF-450, with the particles sizes observed by SEM and thus with a particles' growth most probably due to the effect of sintering. Then, a decrease of the apparent crystallites sizes is observed for samples treated from 450°C to 525°C, in parallel to a strong increase of microstrains, whereas an obvious particles' growth is observed by SEM. The intergrowth of different phases (here two, in a ratio close to 40:60 in LVPF-525 as reported in **Table II-8**) inside the particles would induce the formation of multiple domains and

boundaries resulting in the lowering of apparent crystallites sizes and in a strong increase of microstrains. After treatment at higher temperature, the narrowing of the diffraction lines is due to the combined effect of the decrease in microstrains and the increase in crystallites domain sizes generated by the sintering.

Table II-8: Summary of the parameters obtained thanks to the Rietveld refinement. The vanadium average oxidation state in each phase and the global composition of each sample were obtained applying the Vegard's law applied to the unit cell volume. The width of microstrains' distribution along the [100], [010], [001] directions and in average for all [uvw] directions ($\epsilon = \Delta d_{hkl}/d_{hkl}$) and also the crystallites domain size are given (* means no size broadening detected).

	wt. %	V/Z (\AA^3)	Vanadium average oxidation state	Global composition	Distances along the chains (\AA)		Width of microstrains distribution ϵ_{hkl} (%) along				Crystallites' domain size D (nm)
					the longer V-X	the shorter V-X	[100]	[010]	[001]	In average, <uvw>	
LVPF	100	87.18(1)	3	LiVPO ₄ F	2.00(3)	1.96(3)	0.12	0.09	0.07	0.13	256.2
375	100	87.12(1)	3.04	LiVPO ₄ O _{0.04} F _{0.96}	2.00(3)	1.96(3)	0.16	0.19	0.17	0.20	466.1
450	100	87.05(1)	3.08	LiVPO ₄ O _{0.08} F _{0.92}	2.02(3)	1.93(3)	0.20	0.20	0.18	0.24	607.4
525	35(1)	87.01(2)	3.10	LiVPO ₄ O _{0.65} F _{0.35}	2.04(3)	1.85(3)	0.23	0.31	0.25	0.33	173.8
	65(1)	85.63(2)	3.92		2.08(3)	1.78(3)	0.64	0.72	0.40	0.53	227.1
600	47(2)	85.69(2)	3.89	LiVPO ₄ O _{0.93} F _{0.07}	2.04(3)	1.84(3)	0.32	0.27	0.24	0.27	*
	53(2)	85.56(2)	3.97		2.08(3)	1.73(3)	0.33	0.40	0.33	0.35	767.6
700	41(2)	85.58(1)	3.96	LiVPO ₄ O _{0.98} F _{0.02}	2.15(3)	1.72(3)	0.23	0.19	0.23	0.21	*
	59(2)	85.52(2)	3.99		2.25(3)	1.60(3)	0.24	0.23	0.24	0.23	1276.0
LVPO	100	85.51(1)	4	LiVPO ₄ O	2.24(3)	1.63(3)	/	/	/	/	/

These results demonstrate the possibility to prepare phosphate Tavorite-type materials LiVPO₄F_{1-y}O_y, being mixed oxy-fluorides and showing thus mixed V³⁺/V⁴⁺ valences. Nevertheless, it appears that, at least by this synthesis method (*i.e.* an oxidation under air of LiVPO₄F at various temperatures), the solid solution domains are limited (with 10% of maximum substitution). The microstructure analysis reveals the presence of size and strains effects in all these LiVPO₄F_{1-y}O_y, materials probably due to the large difference in nature between the bond sequences O...V^{IV}=O and F-V^{III}-F that makes difficult to mix them homogeneously/statistically along the chains. In addition to the average long range structural description given by X-ray diffraction, MAS NMR, XAS and IR spectroscopy appear as the most suitable complementary techniques to get an in-depth characterization of the local scale.

II-2c. Growing of vanadyl-type environments

i. Vibrational spectroscopy

The Mid-IR diffuse reflectance spectra recorded between 450 and 4000 cm^{-1} for all the annealed samples are compared to those of LVPF and LVPO in **Figure II-21**. The assignment of the main vibrational bands is given in **Table II-9**. The spectra obtained for all the intermediate phases cannot be explained by a simple linear combination of the spectra recorded for the extreme phases LiVPO_4F and LiVPO_4O . That is in good agreement with the results obtained by XRD revealing the formation of solid solution type phases $\text{LiVPO}_4\text{F}_{1-y}\text{O}_y$ which are significantly different from LiVPO_4F and LiVPO_4O .

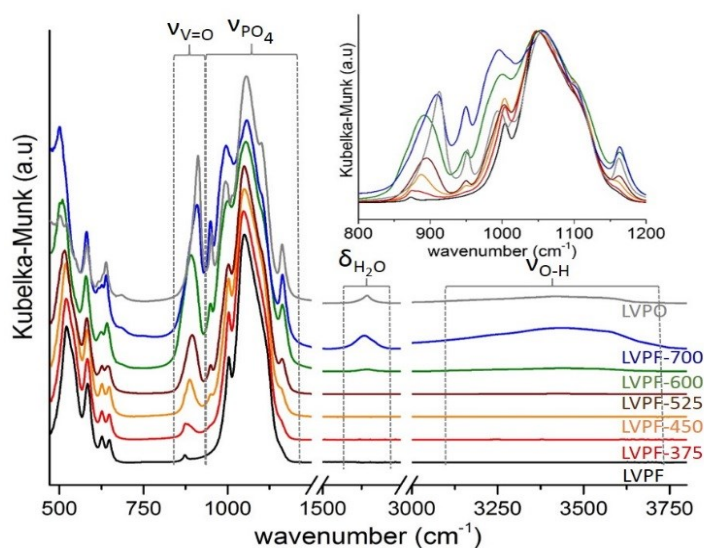


Figure II-21: diffuse reflectance infrared spectra of LVPF, LVPO and the LVPF-T samples in the $475 - 3800\text{ cm}^{-1}$ range and, in inset, the $800 - 1200\text{ cm}^{-1}$ region assigned to the stretching vibration of PO_4 groups and V=O bond. The Spectra were recorded at ISM in collaboration with Dr. Lydie Bourgeois

In the $3000 - 4000\text{ cm}^{-1}$ region, no contribution was detected in the LVPF spectrum whereas a very broad signal is observed for LVPO. This band is assigned to the adsorbed water stretching vibration in good agreement with the presence of the corresponding H-O-H bending vibration at 1635 cm^{-1} .¹³⁹ When the annealing temperature is increased, these two signals appear from 525°C and gradually grow until 700°C . The amount of adsorbed water is thus obviously increased for samples that had been previously treated at higher temperature, despite the decrease of the specific surface area of the powder. Actually, this unexpected result can be explained considering the disappearance of the carbon coating with the formation of CO_2 during the annealing in air. That carbon coating would act as a protective layer against the moisture adsorption: without it, the affinity of the material with water is

obviously increased. Otherwise, the vanadyl ($\{V=O\}^{2+}$) stretching vibration mode, in LVPO, is located at 915 cm^{-1} (**Table II-9**). This band is not expected in LVPF which is theoretically a V^{3+} -rich fluorophosphate and a vanadyl-free composition. Nevertheless, a tiny peak is observed at 874 cm^{-1} (shifted versus the vanadyl stretching vibration mode observed in LVPO) which could match with the presence of localized vanadyl-type defect in LVPF as already discussed here but also previously in ¹⁹. Moreover, as the annealing temperature is increased, a high wavenumber shift, an increase intensity and a significant broadening of this vanadyl-type vibration are observed. As already reported, there is a correlation between the length of the V=O bond and the wavenumber of the associated stretching mode¹⁴⁰. Basically, the shorter the V=O bond, the higher the wavenumber is. These results obtained by interpretation of IR data are in very good agreement with the structural descriptions reported before, *i.e.* the decrease of the V=O bond length whereas the antagonist V-O bond length increases with temperature (see **Figure II-20**). Furthermore, due to the alternation between shorter and longer V-X distances along the chains with the increase of temperature, the vanadium ions do not occupy anymore the central position of the VO₄X₂ octahedra leading to an increase of the equatorial V-O bond lengths (between $1.965(3)\text{ \AA}$ in average for LVPF and $1.986(3)\text{ \AA}$ in average for LVPO). This elongation has a direct influence on the gradual shift of the δ_{O-V-O} vibrations from 632 to 627 cm^{-1} and 650 to 642 cm^{-1} by increasing the average oxidation state of vanadium in the material.

Table II-9: Wavenumbers of different vibrations observed by diffuse reflectance IR spectroscopy and their assignment.

Wavenumber (cm^{-1})							Assignment	ref
LVPF	LVPF-375	LVPF-450	LVPF-525	LVPF-600	LVPF-700	LVPO		
/	/	/	3400	3400	3400	3400	V _{O-H}	139
/	/	/	1650	1650	1650	1650	δ_{H_2O}	139
/	/	1163	1165	1166	1165	1165	VPO ₄	141
1120	1121	1113	1104	1104	1104	1103	VPO ₄	141,142
1051	1048	1051	1050	1055	1056	1056	VPO ₄	141,142
1007	1007	1006	1006	1001	998	998	VPO ₄	141,142
/	/	953	953	951	952	953	VPO ₄	141
874	877	889	896	895	912	915	V _{V=O}	141

The PO₄ stretching region is located between 950 and 1200 cm^{-1} .^{141,142} A single crystallographic site exists for phosphorus in LiVPO₄F, whereas two sites are identified in LiVPO₄O due to the lower symmetry (*i.e.* doubling of the unit cell). This is shown by the increase in the number of components in the PO₄ stretching region (**Table II-9**). With the increase of temperature, from 375°C , some vibration bands characteristic of LiVPO₄O-type appear around 950 and 1165 cm^{-1} and gradually shift and grow in intensity suggesting that LVPF is oxidized to LVPO through the formation of LiVPO₄F_{1-y}O_y phases.

In short, the combination of Synchrotron X-ray powder diffraction and FTIR spectroscopy allows to demonstrate the formation of vanadyl-type defects in LVPF through its thermal treatment in air. Upon increase of temperature, $\text{LiVPO}_4\text{F}_{1-y}\text{O}_y$ phases are formed, in limited composition ranges with y either smaller than 0.1 (of LVPF-type) or higher than 0.9 (of LVPO-type). In order to probe the defects formed within their environments through their vicinity to vanadium cations (V^{3+} or V^{4+}), ^7Li , ^{31}P and ^{19}F nuclei, MAS NMR spectroscopy experiments were conducted.

ii. NMR

^7Li , ^{31}P and ^{19}F MAS NMR experiments were carried out on LiVPO_4F , LiVPO_4O and all the annealed samples. This technique is sensitive to the local environment of the probed atom (nucleus) and proved to be a powerful tool to detect vanadyl-type defects¹⁹. **Figure II-22** shows the ^7Li MAS NMR spectra recorded for all samples.

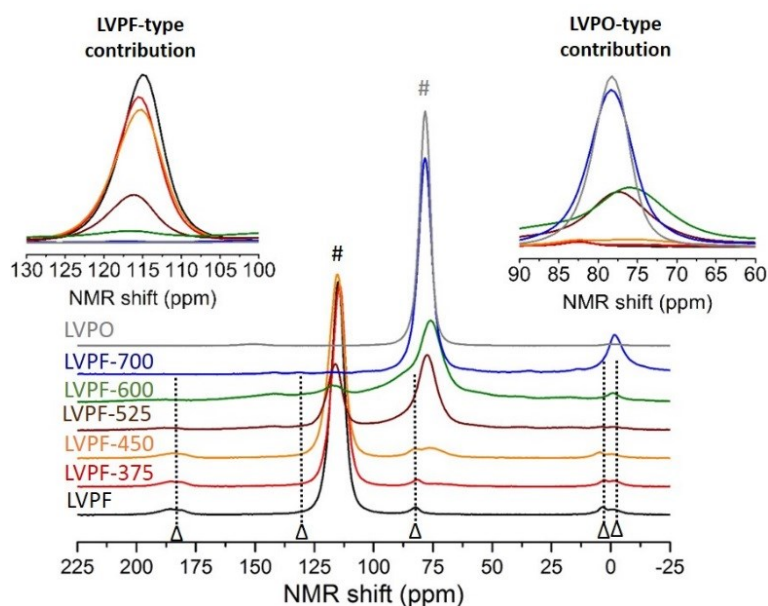


Figure II-22: ^7Li normalized (according to the mass of the sample) MAS NMR spectra of LVPF, LVPF-375, LVPF-450, LVPF-525, LVPF-600, LVPF-700, and LVPO. In inset, zooms of the isotropic signals associated with the different contributions. The isotropic peaks are noted by # and additional contributions by Δ.

A rather sharp signal centered at 115 ppm is observed for LiVPO_4F , which is close to that published previously as corresponding to the unique Li site identified by diffraction^{126,128}. The spectrum for the LVPF sample also exhibits a weak signal at -1 ppm assigned to the presence of residual LiF and others additional signals at 4, 84 and 186 ppm. 2D dipolar homonuclear correlation NMR experiments recently performed by Messinger et al.¹⁹ have shown that all these additional signals are correlated to the main one, and correspond thus to

Li⁺ ions in the same material, that would be located nearby V ions with altered oxidation and/or spin states. All paramagnetic materials (such as Vanadium based Tavorite-like compounds discussed in this section) lead to NMR spectra dominated by interactions between nuclear and electron spins (hyperfine interactions). The Fermi contact shift, which governs the position of the NMR signal of such compounds, corresponds to the presence of some density of electron spin at the nucleus probed. Indeed, the value of the Fermi contact shift is proportional to the spin density at the site of the probed nucleus and to the magnetic susceptibility of the compound.¹⁴³ Modelling (using DFT) the defect in LiVPO₄F by considering the presence of oxygen replacing fluorine locally in the structure, leads to a rather satisfactory ⁷Li NMR signal assignment²¹.

The investigation of the NMR spectrum of LVPO shows a single sharp peak at 79 ppm, less shifted than in LiVPO₄F (115 ppm) due to the higher oxidation state of vanadium. Indeed, V⁴⁺ ($t_{2g}^1e_g^0$) provides less spin transfer towards the Li nuclei than V³⁺ ($t_{2g}^2e_g^0$), in the same structural environment. In LiVPO₄O, there are two crystallographic sites for Lithium^{126,128}. So, two ⁷Li MAS NMR peaks would have been expected whereas only one is detected, due to the strong structural and electronic similarity between the two sites as confirmed by the calculated shifts for the Li in the structure¹²⁸.

The effect of the annealing treatment under air is detected as soon as 375°C. Indeed, for this sample, a small decrease in intensity of the LiVPO₄F-type main signal is observed, with the appearance of a tiny peak at 75 ppm. This latter contribution seems to match with a LiVPO₄O-type environment for Lithium. This trend is confirmed with an increase of the annealing temperature (*i.e.* 450°C and 525°C). Indeed, the intensity of the LiVPO₄F-type signal decreases at the benefit of the LiVPO₄O-type one. The NMR shifts are highly sensitive to the local environment of the probed nuclei and highlights thus here that only one additional environment can be detected for lithium, slightly different from that of LiVPO₄O with an NMR shift 5 ppm smaller. Note that the LiVPO₄F-type contribution is slightly more shifted (116 ppm against 115 ppm for the pristine LVPF), that could originate from a shortening of the Li-V distance in the vicinity of LVPF-type local environments. Note also that there is a strong modification of the ⁷Li MAS NMR spectra between LVPF-450 and LVPF-525, in good agreement with the results obtained by SXRPD which highlight a weak substitution level of oxygen for fluorine in LVPF-450 (less than 10%) and a larger one for LVPF-525 with a global composition of LiVPO₄O_{0.65}F_{0.35}. For this latter and especially for LVPF-600, several new peaks appear and a significant broadening is observed. This is likely due to the formation of a series of different (V⁴⁺, V³⁺) environments for the Li⁺ ions in these materials highly disordered. Note that the

appearance of these new contributions is done at the expense of those existing in the pristine material (*i.e.* 4 and 186 ppm), the latter being associated with localized vanadyl-type defects¹⁹. Nevertheless, the correlation between these NMR shifts and the nature of the defects formed due to a partial oxidation of LVPF is not trivial and would require DFT calculations.

The ^{31}P MAS NMR spectra of the end-members phases are compared to those of the series of LVPF-T samples in **Figure II-23**.

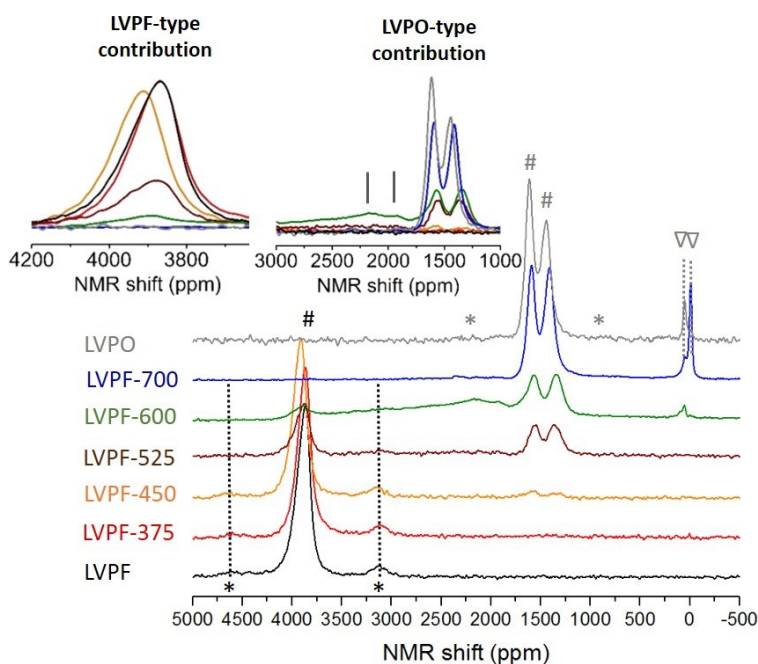


Figure II-23: ^{31}P normalized (according to the mass of the sample) MAS NMR spectra of LVPF, LVPF-375, LVPF-450, LVPF-525, LVPF-600, LVPF-700, and LVPO. In inset, zooms of the isotropic signals associated with the different contributions. The isotropic peaks are noted by #, their spinning side bands by * and additional contributions by ∇. The contributions which can be assigned to a ^{31}P in interaction with both V^{3+} and V^{4+} cations are noted by |.

The LVPF sample exhibits a single relatively sharp ^{31}P MAS NMR signal at 3868 ppm in agreement with the unique phosphorous site present in the structure. The two signals at 1593 ppm and 1418 ppm observed for LiVPO_4O confirm the existence of two different types of phosphorus, in agreement with the two crystallographic sites. Furthermore, especially, due to the smaller number of electrons in $\text{V}^{4+} t_{2g}$ orbitals of LVPO compared to that in $\text{V}^{3+} t_{2g}$ orbitals of LVPF, the isotropic signals in LVPO are less shifted than in LVPF. The effects of annealing on the ^{31}P MAS NMR spectra of the different samples is detected from 375°C with a slight decrease of the LiVPO_4F -type signal without any modification of its shift. At this temperature no new signal is observed. A small LiVPO_4O -type contribution is detected only from 450°C, with an NMR shift smaller than those observed for LVPO (1365 and 1580 ppm against 1443 and 1614 ppm for LVPO). In this sample, the shift of the LVPF-type contribution is also affected, it

increases from 3868 ppm for the pristine phase LVPF to 3911 ppm for LVPF-450. At 525°C, in the LVPO region, a new broad signal is observed around 2100 ppm. The shift of this peak is very different from those of LVPO and may correspond to a strongly disordered LVPO-type phase. This trend is amplified with the increase of the annealing temperature: at 600°C this new contribution is even more intense with two components identified at 1930 and 2185 ppm, besides a broad contribution also observed up to 3000 ppm. These signals are probably due to phosphorus nuclei in interaction with several distribution of V^{3+} and V^{4+} cations in their environment. The ^{31}P NMR spectrum of the sample annealed at 700°C is very close to that of LVPO, but it differs slightly in the shift (1413 and 1593 ppm versus 1443 and 1614 ppm for LVPO) and in the relative intensity of each signal. The diffraction analysis has shown that this material is a biphasic one, with two phases very close to each other, which could not be separated by ^{31}P MAS NMR. Furthermore, the signal corresponding to phosphorus in diamagnetic compound grows at -9 and 52 ppm from 600°C.

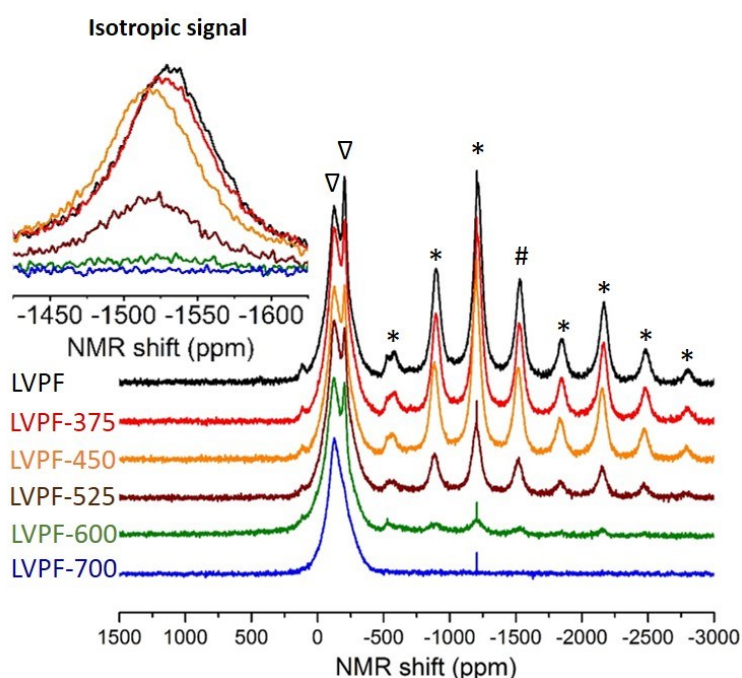


Figure II-24: ^{19}F normalized (according to the mass of the sample) NMR spectra of LVPF, LVPF-375, LVPF-450, LVPF-525, LVPF-600, LVPF-700, and LVPO. In inset, zoom of the isotropic signals. The isotropic peaks are noted by #, their spinning side bands by * and additional contributions by ∇.

The comparison of the ^{19}F MAS NMR spectrum of LVPF with those of the series of samples LVPF-T is given in **Figure II-24**. The ^{19}F MAS NMR spectrum of LVPF exhibits a strong parasitic contribution from the probe (which contains Teflon) around 150 ppm, and a non-shifted signal assigned to residual LiF. The isotropic peak is located at -1500 ppm. All other signals are assigned to spinning side bands. From 375°C, the global intensity of the signal decreases gradually until 700°C due to the replacement of oxygen for fluorine. Nevertheless,

surprisingly, no others peaks which would be assigned to Fluorine atom in interaction with a V^{4+} can be detected. The large number of spinning sidebands and the narrow solid solution domains (with less than 10% of oxygen substitution for fluorine (and vice versa) in $\text{LiVPO}_4\text{F}_{1-y}\text{O}_y$) could make difficult the observation of the contributions expected. Furthermore, the intensity of the non-shifted signal assigned to LiF decreases gradually with the temperature whereas ^7Li MAS NMR suggests an increase amount of the diamagnetic phase(s). LiF is also affected by the annealing and probably react with water contained in air to form LiOH and HF. Indeed, ^1H MAS NMR experiments were performed and highlight an increase of diamagnetic signal with the increase of temperature, which can be assigned to LiOH signature.

This MAS NMR study appears as fully consistent with the diffraction results discussed just before, and especially with the microstructure analysis that highlighted strong strains effects within the $\text{LiVPO}_4\text{F}_{1-y}\text{O}_y$ phases. The analysis of the corresponding ^7Li and ^{31}P MAS NMR spectra supports the formation of solid solutions in narrow compositions domains (*i.e.* close in compositions either to LVPF or to LVPO), as NMR signals close but different from those of LVPF and LVPO were observed. These signals are often slightly shifted (of few ppm) and broadened, suggesting a distribution of environments containing either mainly V^{3+} (in LVPF-type phases) or mainly V^{4+} (in LVPO-type phases) as local defects around the probed nuclei. Although, the annealing under air of LiVPO_4F generates an increase of the concentration of vanadyl type environments, NMR highlighted that the defects generated by this way seem to be different to those observed in the pristine material. Indeed, the peaks assigned to the defects' contributions in LiVPO_4F tend to disappear whereas a LVPO-type contribution grows in intensity upon oxidation of the material. Therefore, the defects in the pristine LiVPO_4F could constitute some nucleation sites for LiVPO_4O -type domains whose size grows with the rise of annealing temperature until to be detected as separated phases by SXRPD. However, It is interesting to mention the case of LVPF-600 which revealed intermediate NMR signals (*i.e.* between those typical of LVPF and those typical of LVPO) suggesting that, for this sample, environments more largely mixed in V^{3+} and V^{4+} are formed at the local scale. The electrochemical signature of these mixed environment have thus to be compared with those of the end-members phases.

II-2d. Electrochemical properties

i. High voltage signatures

In order to investigate separately the high voltage region (involving the $\text{V}^{\text{III}}/\text{V}^{\text{IV}}/\text{V}^{\text{V}}$ redox couples) and low voltage region (involving $\text{V}^{\text{IV}}/\text{V}^{\text{III}}/\text{V}^{\text{II}}$ redox couples), the pristine materials (*i.e.* LVPF and LVPO) and all LVPF-T samples were cycled in lithium cells between 3.0 and 1.5 V vs. Li^+/Li and between 3.0 and 4.6 V vs. Li^+/Li at a C/50 rate. The resulting galvanostatic and their derivative curves are given in **Figures II-25** (for LVPF, LVPO, LVPF-525, LVPF-600 and in the Annex part in **Figures Annex-II-1** for all the samples).

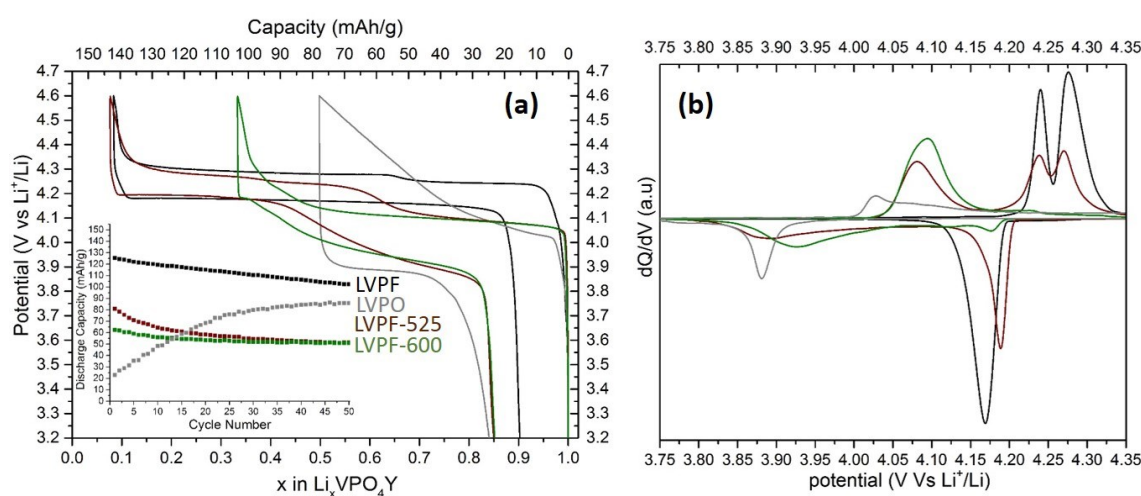


Figure II-25: (a) Galvanostatic curves obtained versus Lithium at a C/50 rate for LVPF, LVPO, LVPF-525 and LVPF-600 in the high voltage domain (*i.e.* between 3.0 and 4.6 V vs. Li^+/Li). The corresponding derivative curves are given in (b). The evolution of the discharge capacity at C/10 is given in inset of (a).

The lithium extraction from LiVPO_4F (*i.e.* here 0.96 Li^+) corresponds to the oxidation of V^{III} to V^{IV} , observed here at 4.24 V and then 4.28 V vs. Li^+/Li (equilibrium values at 4.24 and 4.25 V, given in section II-1). The transition between the first and the second plateaus occurs at the $\text{Li}_{0.67}\text{VPO}_4\text{F}$ composition. Actually, the charge mechanism is a two steps biphasic process between LiVPO_4F , $\text{Li}_{0.67}\text{VPO}_4\text{F}$ and VPO_4F .²⁰ The following discharge is seen at 4.17 V vs. Li^+/Li as a biphasic process between the lithium-free and the fully lithiated phases, with a reversible capacity of 120 mAh/g, and does not involve the intermediate phase. The lithium extraction from the LVPO composition occurs at a lower potential than from LVPF (3.95 V vs. Li^+/Li) even if the $\text{V}^{\text{IV}}/\text{V}^{\text{V}}$ redox couple is apparently involved. Due to the presence of vanadyl bonds the redox couple actually involved is $\{\text{V}=\text{O}\}^{2+}/\{\text{V}=\text{O}\}^{3+}$. As synthesized, the reversible capacity of LVPO is about one third of the theoretical one (55 vs. 156 mAh/g).

The diffraction and spectroscopic results of this study have highlighted the possibility to substitute partially fluorine by oxygen, and to form partial solid solutions $\text{LiVPO}_4\text{F}_{1-y}\text{O}_y$ by the annealing LVPF in air. This oxidation induces the appearance from 375°C of a plateau at around 4.1 V vs. Li^+/Li whose length grows as the annealing temperature is increased. According to **Figure II-25a** and **Figure Annex-II-1a**, from 525°C, the annealing affects greatly the reversible capacity that decreases, but below this temperature the reversible capacities observed for the LVPF-T samples remain close to that of the pristine LVPF. This decrease in capacity could be explained either by deteriorated transport properties for the oxidized compositions due to the sintering of the particles or to the loss of carbon as conductive additive within the active mass during the annealing, as highlighted by SEM images and CHNS chromatography results. The evolution of the discharge reversible capacity obtained at a C/10 rate (inset in **Figure II-25a**) shows a strong and continuous decrease in capacity as the annealing temperature is increased. Furthermore, as described above, the phase diagram observed during the charge of LiVPO_4F presents the formation of an intermediate phase corresponding to the $\text{Li}_{0.67}\text{VPO}_4\text{F}$ composition. The derivative curves given in the **Figure II-25b** and **Figure Annex-II-1b** show that the presence of this intermediate phase persists at least until the $\text{LiVPO}_4\text{F}_{0.90}\text{O}_{0.10}$ composition corresponding to the highly fluorinated phase in LVPF-525.

ii. Low voltage signature

In the low voltage region (*i.e.* 3.0 - 1.5 V vs. Li^+/Li), the lithium insertion/extraction into/from LVPF occurs at 1.8 V according to a biphasic process between LiVPO_4F and $\text{Li}_2\text{VPO}_4\text{F}$ involving the $\text{V}^{\text{III}}/\text{V}^{\text{II}}$ redox couple (**Figure II-26** and **Figure Annex-II-2**).

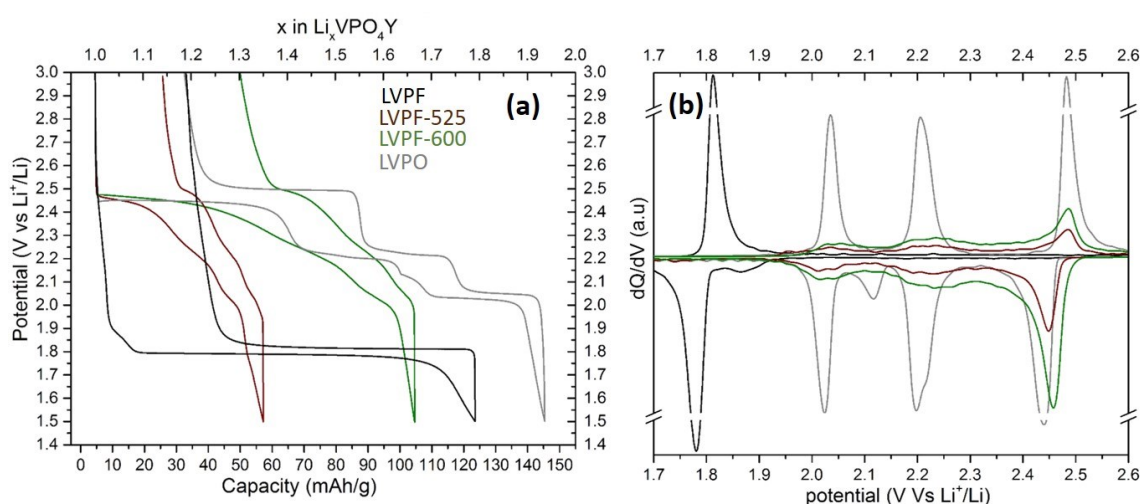


Figure II-26: (a) Galvanostatic curves obtained versus Lithium at a C/50 rate for LVPF, LVPO, LVPF-525 and LVPF-600 in the low voltage domain (*i.e.* between 3.0 and 1.5 V vs. Li^+/Li). The corresponding derivative curves are given in (b).

The lithium insertion into LVPO leads to the reduction of V^{IV} to V^{III} and occurs at 2.48 V, 2.20 V then 2.03 V vs. Li⁺/Li, to reach the Li₂V^{III}PO₄O composition at the end of the discharge with a reversible capacity close to the theoretical one (143 vs. 159 mAh/g). This mechanism involves several intermediate phases Li_{1.5}VPO₄O and Li_{1.75}VPO₄O according to a three steps biphasic mechanism⁹⁶. Coming back to the LVPF-T samples, the electrochemical signature of LVPO appears and grows with the temperature. At 375°C several shoulders appear at 2.45, 2.20 and 2.00 V vs. Li⁺/Li and the length of the plateau at 1.8 V, related to LiVPO₄F-type phase, strongly decreases (as clearly shown by the derivative curves given in the **Figure Annex-II-2b**). For LVPF-450 and LVPF-525 the electrochemical signature of LVPF disappears whereas XRD revealed the persistence of a fluorine-rich phase at these temperatures. Everything happens as if the LiVPO₄F-type phase does not participate in the insertion-extraction processes involved in the low potential region. The strong decrease in capacity in the low voltage domain when fluorine is partially replaced by oxygen in LiVPO₄F_{1-y}O_y even for small values of y, may results from the crystal field.

In our point of view there is a destabilization of V^{II} in an asymmetrical environment (*i.e.* F-V^{II}-O). Indeed, there are significant structural differences between the phases previously mentioned (*i.e.* LVPF, LVPO and the corresponding intercalated compositions), especially concerning the V-X bond length along the chains of VO₄X₂ octahedra. In the V^{III} phases (*i.e.* LiVPO₄F and Li₂VPO₄O) this V-X bond length are almost homogeneous (1.98 Å and 1.95 Å respectively). In Li₂V^{II}PO₄F, the V-F are longer (2.12 Å) and also constant because V²⁺ is preferentially stabilized in a symmetrical environment due to its electronic configuration (t_{2g}³). The insertion of Lithium in a fluorine-rich compound (V^{(3+ε)+}) involves theoretically mainly the reduction of V³⁺ in V²⁺. Nevertheless, V²⁺ may be destabilized in a distorted environment induced by the presence in its first coordination sphere of oxygen and fluorine along the chain, this could explain why a small amount of oxygen in a LiVPO₄F-type phase leads to a strong decrease in capacity. Inversely, the lithium insertion in an oxygen-rich phase would be promoted as suggested by the comparison of LiVPO₄F and Li₂VPO₄O. Actually, in the pristine material the average oxidation state of vanadium is V^{(3+ε)+} and the strains highlighted by SXRPD measurement would be relaxed thanks to insertion of lithium involving the reduction of V^{IV} to V^{III} and leading to an overall homogenization of the distances V-X along the chains.

II-2e. Summary and prospects

The oxidation under air at controlled temperature of the promising positive electrode material, LiVPO₄F, was investigated in order to get a good knowledge of the different types of defects or compositions which can be formed under uncontrolled synthesis conditions. A

combination of high resolution synchrotron powder X-ray diffraction, with infrared and MAS NMR spectroscopies was proved to be the tools of choice to characterize the materials thus formed. Their complex composition, microstructure and defects induced by the annealing treatment impact hugely their electrochemical properties in comparison to those of LVPF and LVPO. Below 450°C , solid solutions $\text{LiVPO}_4\text{F}_{1-y}\text{O}_y$ are formed with less than 10% of oxygen substitution for fluorine and still limited impact on the electrochemical performance at high potential. Above 450°C the effect is drastic, moving from a LVPF-type electrochemical signature to that of LVPO-type, with a decrease of the average discharge potential, a larger hysteresis between the charge and the discharge, a decrease of the reversible capacity etc. In the low voltage region, the effect of the oxygen defects is even more pronounced, everything happens as if the presence of vanadyl-type defects would prevent the formation of V^{2+} during lithium intercalation in the mixed valence $\text{V}^{\text{III}}/\text{V}^{\text{IV}}$ pristine materials, $\text{LiVPO}_4\text{F}_{1-y}\text{O}_y$: very rapidly, already with a small amount of oxygen substitution for fluorine, only the LiVPO_4O 's electrochemical signature is detected.

Although, vibrational spectroscopy revealed that the nature of the defects formed by annealing LiVPO_4F under air are similar to those of the pristine material and in higher concentration, their distribution appears to be clearly different. Indeed, NMR has shown that the peaks assigned to the defects' contributions in LiVPO_4F tend to disappear whereas a LVPO-type contribution grows in intensity upon oxidation of the materials. Therefore, the defects in the pristine LiVPO_4F could constitute some nucleation sites for more extended LiVPO_4O -type domains whose size grows with the rise of annealing temperature. At low temperature, the size of these domains being too small, SXRPD doesn't detect them as separated phases. But, regarding the voltage profile of the monophasic (at least from the SXRPD point of view) samples (LVPF-375 and LVPF-450), an LiVPO_4O -type contribution appears at 4.0V vs. Li^+/Li . Solid state electrochemistry being a local probe, this contribution reveals the presence of extended LiVPO_4O -type domains and not punctual/isolated vanadyl-type defects. The annealing under air of LiVPO_4F doesn't generate new defects' site but extends the defected regions leading to a different $\text{V}^{3+}\text{-F}/\text{V}^{4+}=\text{O}$ distribution. Therefore, this strategy doesn't reproduce the defects observed in LiVPO_4F and thus doesn't seem relevant to study the impact of these defects on the electrochemical performance. Thus, the defects might arise from the synthesis (trace of oxygen in the furnace filled under Ar) and not from an uncontrolled quenching. We will try to demonstrate that in the following part through the investigation of extended $\text{LiVPO}_4\text{F}_{1-y}\text{O}_y$ solid solutions obtained from a single step synthesis.

II-3. Extended $\text{LiVPO}_4\text{F}_{1-y}\text{O}_y$ solid solutions, from the long range average structure to the local environments.

II-3a. A non Vegard's law behavior

The mixed valence (*i.e.* $\text{V}^{\text{III}}/\text{V}^{\text{IV}}$) phases were obtained through one-step solid state syntheses. First, V_2O_5 , LiF and H_3PO_4 are dissolved in magnetically stirred distilled water at room temperature during 1h. After water evaporation at 80°C overnight, an excess of C_{sp} carbon (*i.e.* a highly divided soot) is added to the mixture. During the heating treatment (700°C , 1h under Argon) the carbon acts as a reducer agent of the V^{5+} to give $\text{V}^{(3+x)+}$ phases. Therefore, the excess of carbon introduced in the reaction medium is expected to affect the oxidation state of vanadium in the final product. The samples obtained will be, in a first step, called LVPF- ϵ with ϵ referring to the molar excess of Carbon used for the syntheses, their SXRPD patterns are shown in the **Figure II-27**.

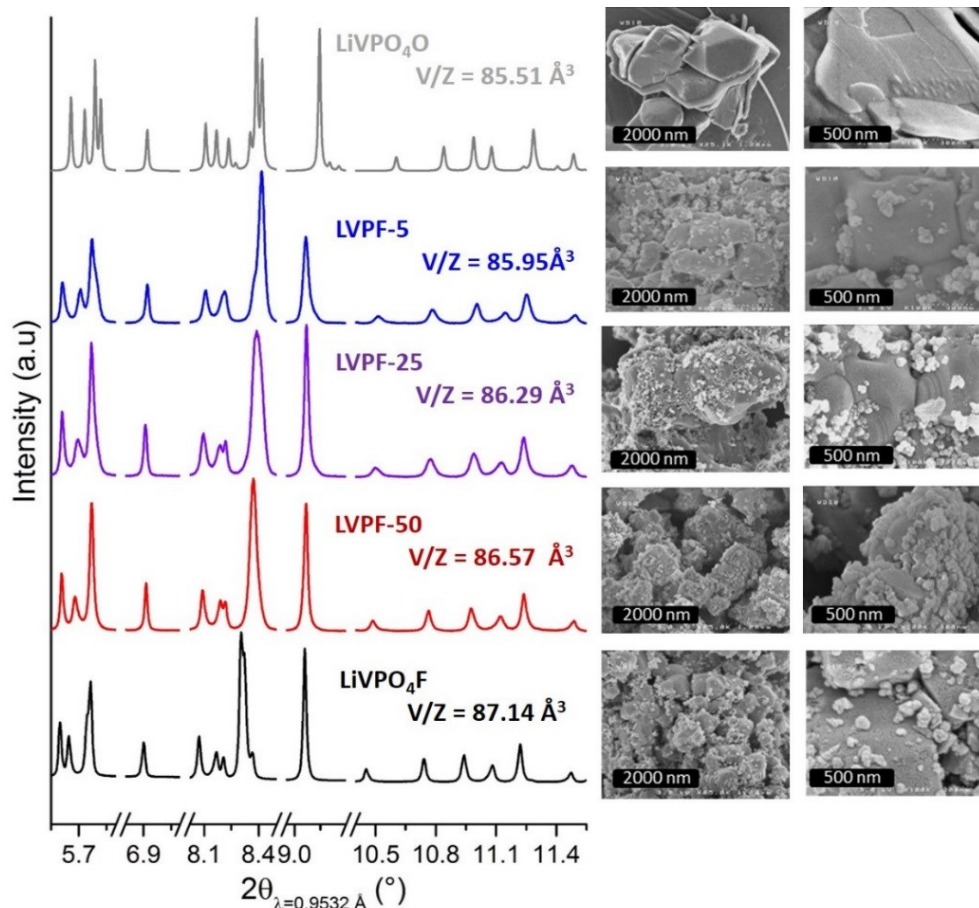


Figure II-27: Synchrotron XRD patterns of the $\text{LiVPO}_4\text{F}_{1-y}\text{O}_y$ series of materials and the corresponding SEM images are shown in inset.

The SEM images obtained for all samples discussed in this section are given in the inset of **Figure II-27**. The primary particles of the mixed valence materials and LiVPO₄F are smaller compared to those of LiVPO₄O (*i.e.* 500-1000 nm against 1000-3000 nm) most probably due to the presence of carbon which for the former prevents the sintering of particles during the annealing treatment. These primary particles are aggregated in larger agglomerates, with small grains of carbon (50-100 nm) in the grain boundaries coming from the excess of carbon used during the syntheses.

Table II-10: cell parameters determined from full pattern matching refinement of Synchrotron XRPD patterns with the corresponding chemical analyses performed by ICP-OES (Li, V and P) or TGA-MS (C and F) and magnetic parameters

	LVPO	LVPF-5	LVPF-25	LVPF-50	LVPF
Cell parameters, P-1					
a (Å) =	6.7320(1)	5.1568(2)	5.1626(1)	5.1651(1)	5.1689(1)
b (Å) =	7.1942(1)	5.2871(2)	5.2946(1)	5.2995(1)	5.3087(1)
c (Å) =	7.9204(1)	7.1722(2)	7.1899(2)	7.2147(1)	7.2621(1)
α (°) =	89.843(1)	107.145(2)	107.224(1)	107.357(1)	107.591(1)
β (°) =	91.272(1)	107.578(2)	107.608(2)	107.801(1)	107.973(1)
γ (°) =	116.886(3)	98.611(2)	98.664(1)	98.499(1)	98.394(1)
V/Z (Å ³) =	85.510(9)	85.952(9)	86.286(6)	86.576(3)	87.141(6)
Z =	4	2	2	2	2
Estimated compositions (Vegard's law)	LiVPO ₄ O	LiVPO ₄ F _{0.27} O _{0.73}	LiVPO ₄ F _{0.48} O _{0.52}	LiVPO ₄ F _{0.65} O _{0.35}	LiVPO ₄ F
Chemical composition					
Molar ratio Li/V/P =	1.02(5) / 0.97(5) / 1	1.02(5) / 1.04(5) / 1	1.04(5) / 1.02(5) / 1	1.05(5) / 1.04(5) / 1	1.04(5) / 1.02(5) / 1
C (wt%) =	/	2.58	5.95	7.06	5.97
F (wt% / mol%) =	/	0.52 / 0.29	0.90 / 0.51	1.35 / 0.77	1.57 / 0.90
Magnetic properties					
$\chi_m T$ (emu/mol) =	0.375 (theoretical)	0.529	0.663	0.779	1.000 (theoretical)
Average oxidation state of V ⁿ⁺	4	3.75	3.55	3.35	3
Estimated compositions (Magnetism)	LiVPO ₄ O	LiVPO ₄ F _{0.25} O _{0.75}	LiVPO ₄ F _{0.45} O _{0.55}	LiVPO ₄ F _{0.65} O _{0.35}	LiVPO ₄ F

Thanks to ICP-OES chemical analyses, the molar ratios Li/V/P were determined for all samples. The results, given in the **Table II-10**, are in good agreement with the expected compositions LiVPO₄(O,F) (*i.e.* with 1Li:1V:1P). Nevertheless, the O/F ratio isn't reachable by ICP. A way to estimate this ratio is TGA coupled with MS performed under air. Indeed, as highlighted in **section II-2-a**, under particular conditions, it is possible to separate the weight losses assigned to carbon volatilization and substitution of fluorine by oxygen in carbon coated LiVPO₄F.

In the TGA data shown in **Figure II-28**:

- a first weight loss assigned to adsorbed water evaporation occurs below 200°C and corresponds to less than 1% in each sample.
- Between 200 and 500°C a second loss is measured accompanied by a signal on the CO_2 channel (*i.e.* $m/z=44$) whereas no significant HF release ($m/z=20$) is detected (**Figure II-28b**). Thus, only the carbon departure can be assigned to this weight loss and the carbon contents in each sample studied is reported in **Table II-10**.
- Then, during the temperature plateau applied at 500°C for 1h, a third weight loss occurs accompanied by the detection of HF without carbon release. Therefore, the weight percentage obtained corresponds to the weight fraction of fluorine in the materials (also reported in **Table II-10**).

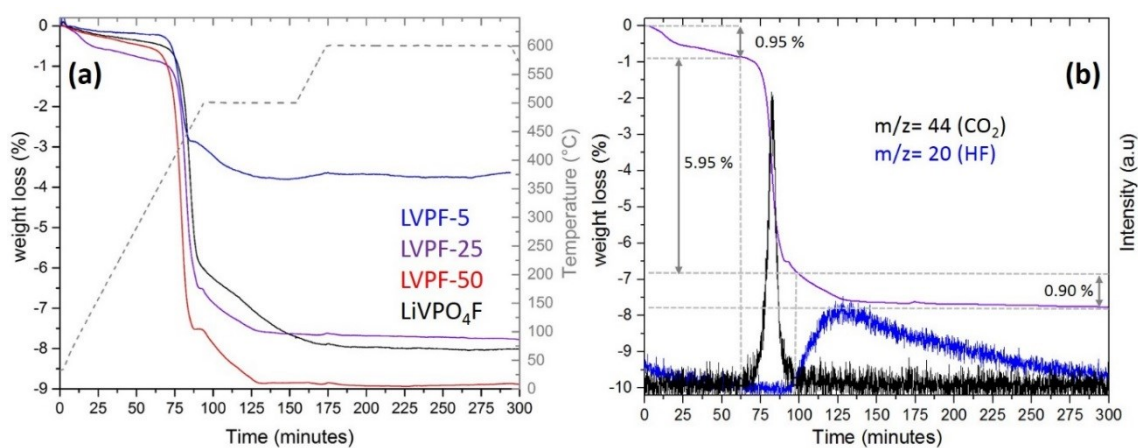


Figure II-28: (a) TGA data obtained under air for all the $\text{LiVPO}_4\text{F}_{1-y}\text{O}_y$ samples, (b) TGA-MS data obtained for the LVPF-25 (*i.e.* $\text{LiVPO}_4\text{F}_{0.45}\text{O}_{0.55}$) material in function of time (purple line) and the corresponding MS intensities (blue line for HF and black line for CO_2).

In order to confirm the fluorine content thus obtained which is, assuming the $\text{LiVPO}_4\text{F}_{1-y}\text{O}_y$ composition, related to the average oxidation state of vanadium, the magnetization of all materials were measured in function of temperature in the paramagnetic domain (**Figure II-29**). For V^{3+} ($3d^2$) cations an important spin-orbit coupling is often observed impacting significantly the effective magnetic moment according to the crystal field strength. However, for the $\text{LiVPO}_4\text{F}_{1-y}\text{O}_y$ Tavorite system, the spin-orbit coupling can be considered to be negligible¹³⁶ thus the Curie-Weiss' law, estimating the magnetic susceptibility according to the electronic configuration transition metals, can be apply. The average oxidation states of vanadium in each sample (reported in the **Table II-10**) are in good agreement with the compositions proposed thanks to TGA-MS and with the formation of mixed $\text{V}^{3+}/\text{V}^{4+}$ valence materials: 3.75, 3.55 and 3.35 using respectively a molar excess of citric acid of 5%, 25% and

50%. The compositions of the materials LVPF-5, LVPF-25 and LVPF-50 were thus assigned to $\text{LiVPO}_4\text{F}_{0.25}\text{O}_{0.75}$, $\text{LiVPO}_4\text{F}_{0.45}\text{O}_{0.55}$ and $\text{LiVPO}_4\text{F}_{0.65}\text{O}_{0.35}$ respectively and have to be confirmed by the diffraction study. In the following the materials will be named as their corresponding compositions.

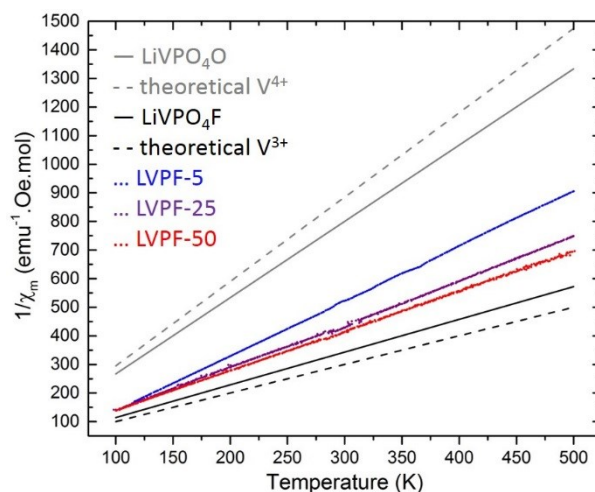


Figure II-29: Temperature dependence of the inverse of the magnetic susceptibilities for the $\text{LiVPO}_4\text{F}_{1-y}\text{O}_y$ materials: experimental as continuous lines, theoretical considering vanadium at the trivalent state as black dot line and theoretical considering vanadium at the tetravalent state as grey dot line.

The three samples thus obtained, whose SXRPD patterns are compared in **Figure II-27** to those of the end member phases $\text{LiV}^{\text{IV}}\text{PO}_4\text{O}$ and $\text{LiV}^{\text{III}}\text{PO}_4\text{F}$, crystallize in Tavorite-type structures described in triclinic ($P-1$) unit cells. The cell volumes obtained by Le bail refinements follow a continuous evolution from $\text{LiV}^{\text{IV}}\text{PO}_4\text{O}$ ($V/Z = 85.51 \text{ \AA}^3$) to $\text{LiV}^{\text{III}}\text{PO}_4\text{F}$ ($V/Z = 87.14 \text{ \AA}^3$) with the increasing oxidation state of vanadium. The cell parameters thus determined are reported in **Table II-10**. Note that the increase of carbon excess up to 50% doesn't allow to obtain a pure V^{3+} phase and the decrease down to 5% leads to the formation of a LiVPO_4O -type phase as secondary phase.

LiVPO_4F and LiVPO_4O are not described in the same model. Indeed, due to the presence of V^{4+} and the formation of the vanadyl bond (*i.e.* short $\text{V}^{\text{IV}}=\text{O}$ bond), the cell of LiVPO_4O is twice larger. Thus described, the cell parameters cannot be compared. In order to allow this comparison, **Figure II-30** illustrates the evolution of the cell parameters of all samples (and others vanadium oxy-fluorophosphates Tavorite materials reported in literatures^{107,136} and in the previous section) in the LiVPO_4O 's model as a function of the average oxidation state of vanadium determined by magnetic measurements.

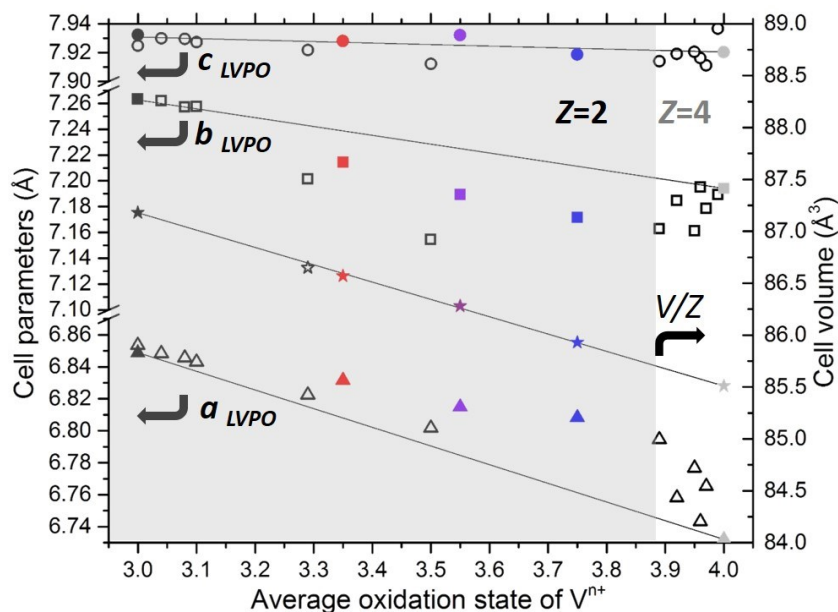


Figure II-30: Evolution of cell parameters (*a*: circles, *b*: squares and *c*: triangles) in a LiVPO_4O -type ($Z=4$) model and cell volume (V/Z : stars) in function of the average oxidation state of vanadium for the whole series of $\text{LiVPO}_4\text{F}_{1-y}\text{O}_y$ compositions discussed in this section (filled markers) and those reported in literature (refs ¹³⁶ and ¹⁰⁷) or in the previous section are depicted as empty markers. The grey area corresponds to the range of composition for which the cell is a LiVPO_4F -type one ($Z=2$, centrosymmetric vanadium octahedra) and the white area represents the appearance of superstructure peaks due to the ordered deviation from centrosymmetry for the octahedra (LiVPO_4O -type cell, $Z=4$).

Figure II-30 highlights that, contrarily to the cell volume, the cell parameters (especially a_{LVPO} and b_{LVPO}) don't follow the Vegard's law. The shape of the evolution of *a* and *b* parameters in function of V^{n+} is linear until an average oxidation state of 3.90 for vanadium and shows a significant deviation from linearity for higher oxidation states. Moreover, the phase transition between the cell with a multiplicity of 2 (LiVPO_4F -type) and 4 (LiVPO_4O -type) required to describe the ordering of vanadyl-type distortion coincides with the composition for which the deviation from linearity is maximum and such as the average oxidation state of vanadium is 3.9. Actually, the crystal field imposed by the highly ionic V-F bonds seems to prevent the formation of the vanadyl environments (*i.e.* $\text{O}=\text{V}^{4+}-\text{O}$) along the chains of octahedra (*i.e.* \vec{b}_{LVPO} or \vec{c}_{LVPF}). That could probably be at the origin of the deviation from the Vegard's law. In order to overcome the framework shrinking induced by the compaction of the chains, an elongation occurs along the \vec{a}_{LVPO} (or $(\vec{a} + \vec{b})_{\text{LVPF}}$) direction whereas no significant deviation has been detected along \vec{c}_{LVPO} (or $(\vec{a} - \vec{b})_{\text{LVPF}}$).

In the following part, the in-depth characterization of the average structure from synchrotron and neutron diffraction data will be carried out in order to understand this deviation from the Vegard's law.

II-3b. Average long range structure and microstructure

The profile and structure refinements have been done combining ND and SXRPD data. Actually, both techniques are required to fully solve the structure especially to localize the lithium atoms and to perform a careful microstructure analysis. Indeed, even if the resolution of ND is lower compared to the SXRPD one, the higher scattering factors at high angle allows to make a more accurate difference between size and strain broadening.

All Bragg peaks observed for $\text{LiVPO}_4\text{F}_{0.45}\text{O}_{0.55}$ can be indexed with a $P-1$ triclinic unit cell in $Z=2$ model (LiVPO_4F -type model), with $\text{Li}_3\text{V}_2(\text{PO}_4)_3$ crystallizing in anti-NASICON structure as minor impurity (<2 wt.%) and without superstructure peaks showing the disordered distribution of O/F (as well as $\text{V}^{3+}/\text{V}^{4+}$) along the chains. This disorder should generate locally some differences of interatomic distances from one cell to another and thus leads to strains which would induce diffraction lines broadening. Indeed, the profile of all these patterns are governed by a strong anisotropic strain broadening and must be refined using the corresponding model provided in the Fullprof software¹³⁸. The **Figure II-31** compares the width of microstrains' distribution (ϵ_{hkl}) with the deviation from Vegard's law in specific directions for the whole series of compositions.

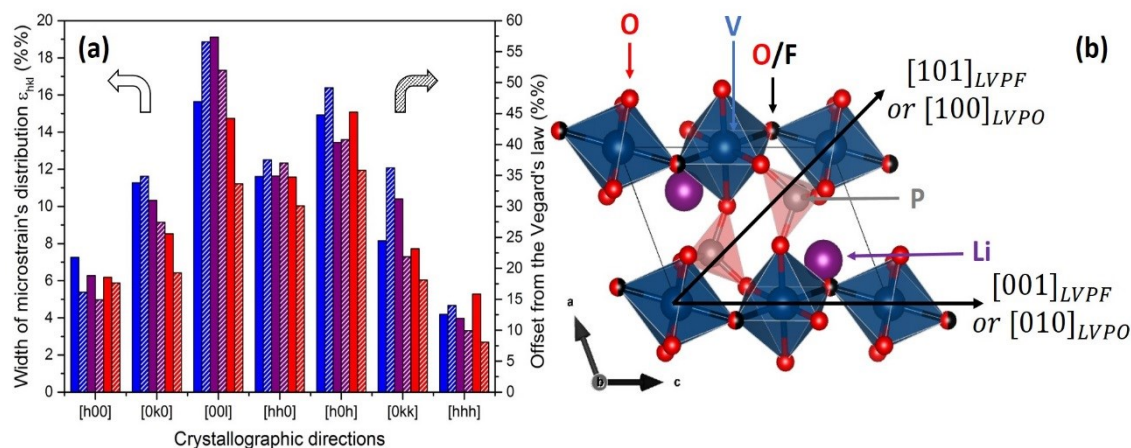


Figure II-31: (a) comparison between the width of microstrains distribution (without hatched lines) and the amplitude of the deviation from the Vegard's law (with hatched lines) obtained from the profile matching of the SXRPD patterns in the LiVPO_4F -type model along selected directions for the 3 mixed valence samples ($\text{LiVPO}_4\text{F}_{0.25}\text{O}_{0.75}$: blue, $\text{LiVPO}_4\text{F}_{0.45}\text{O}_{0.55}$: purple and $\text{LiVPO}_4\text{F}_{0.65}\text{O}_{0.35}$: red) (b) relation between the LiVPO_4O -type and the LiVPO_4F model showing the direction of the max strains and of the maximum offset from the Vegard's law in both model.

Figure II-31 suggests a link between the width of microstrains' distribution and the amplitude of the deviation from the Vegard's law. Indeed, the highest offset is found to take place along the propagation direction of the chains of octahedra (*i.e.* $[001]$ in the LiVPO_4F 's

model) and this direction corresponds to the maximum of strains induced by the disordered $\text{V}^{3+}\text{-F}/\text{V}^{4+}=\text{O}$ distribution which is most probably at the origin of the deviation from Vegard's law. Moreover, the second maximum of strains takes place along the $[101]_{\text{LVPF}}$ corresponding to $[100]_{\text{LVPO}}$ along which a significant gap from the Vegard's law is observed.

Rietveld refinements were performed considering the structural model $\text{Li}_{2i}(\text{M}(1))_{1a}(\text{M}(2))_{1b}\{(\text{P})_{2i}[\text{O}_{2i}]_4\}\text{X}_{2i}$ already used to describe LiVPO_4F . For $\text{LiVPO}_4\text{F}_{0.45}\text{O}_{0.55}$, the comparisons of the experimental and calculated diffraction patterns (SXRPD and ND) are given in **Figure II-32**. The cell parameters, atomic positions and distances thus determined are given in **Table II-11** and in **Table II-12**.

Table II-11: Structural parameters obtained by combined Rietveld refinement of the structure of $\text{LiVPO}_4\text{F}_{0.45}\text{O}_{0.55}$ based on synchrotron XRD and Neutron powder Diffraction Data.

LiVPO ₄ F _{0.45} O _{0.55}							
SG : <i>P</i> -1		<i>a</i> = 5.1633 (1) Å	α = 107.236 (1)°		Synchrotron X-rays:	χ^2 = 27.0 %	
<i>Z</i> = 2		<i>b</i> = 5.2967 (1) Å	β = 107.629 (1)°			R_{Bragg} = 2.58 %	
		<i>c</i> = 7.1969 (1) Å	γ = 98.662 (1)°		neutrons:	χ^2 = 1.83 %	
		<i>V</i> = 172.800 (6) Å ³	<i>V/Z</i> = 86.400 (6) Å ³			R_{Bragg} = 3.46 %	
atoms	Wickoff position	<i>x</i>	<i>y</i>	<i>z</i>	Occupancy	B iso	BVS
V(1)	1 <i>a</i>	0	0	0	0.99(1)	0.977	3.15(1)
V(2)	1 <i>b</i>	0	0	1/2	1.00(1)	1.298	3.36(1)
P(1)	2 <i>i</i>	0.323(1)	0.647(1)	0.250(1)	1.00(1)	0.756	4.95(1)
O(1)	2 <i>i</i>	0.372(2)	0.240(1)	0.590(1)	1.00(1)	1.128	1.94(1)
O(2)	2 <i>i</i>	0.110(2)	0.671(1)	0.360(1)	1.00(1)	0.927	1.94(1)
O(3)	2 <i>i</i>	0.690(2)	0.656(2)	0.862(1)	1.00(1)	1.055	1.96(1)
O(4)	2 <i>i</i>	0.266(1)	0.795(1)	0.095(1)	1.00(1)	0.539	1.92(1)
O(5)	2 <i>i</i>	0.894(2)	0.081(1)	0.590(1)	0.55	0.389	1.42(1)
F(1)	2 <i>i</i>	0.894(2)	0.081(1)	0.590(1)	0.45	0.389	1.24(1)
Li(1)	2 <i>i</i>	0.723(6)	0.380(6)	0.232(6)	0.97(4)	3.739	0.89(1)

Their crystal structures can be described as VO_4X_2 (with X= O or F) octahedra sharing common corner forming $[\text{X} - \text{VO}_4 - \text{X}]_{\infty}$ chains along $[001]$ direction. These chains of octahedra are connected to each other via PO_4 tetrahedra in such a way that each oxygen atom belonging to the VO_4 square plane of the VO_4X_2 octahedra is involved in a different phosphate group. The three-dimensional network thus generated accommodates lithium atoms within the tunnels along the $[010]$ direction. Oxygen and fluorine cannot be differentiated either by X-ray or neutron diffraction and Bond valence sums (BVS) were thus calculated. It allowed to determine the nature of the atoms which link the octahedra between them: indeed the BVS value associated with the bridging anion was systemically found to be smaller (*i.e.* the BVS values of F(1)/O(5) are 1.37(2)/1.60(2), 1.24(1)/1.42(1), 1.22(1)/1.40(1) respectively for $y=0.75$, 0.55 and 0.35 in $\text{LiVPO}_4\text{F}_{1-y}\text{O}_y$) than those of the four other oxygen atoms (in average 1.94(2),

1.94(1), 1.91(1)). This result is in agreement with the structure already reported for other existing Tavorite-like fluoride phosphate phases, with the fluorine atom bridging adjacent MO_4F_2 octahedra along the chains.

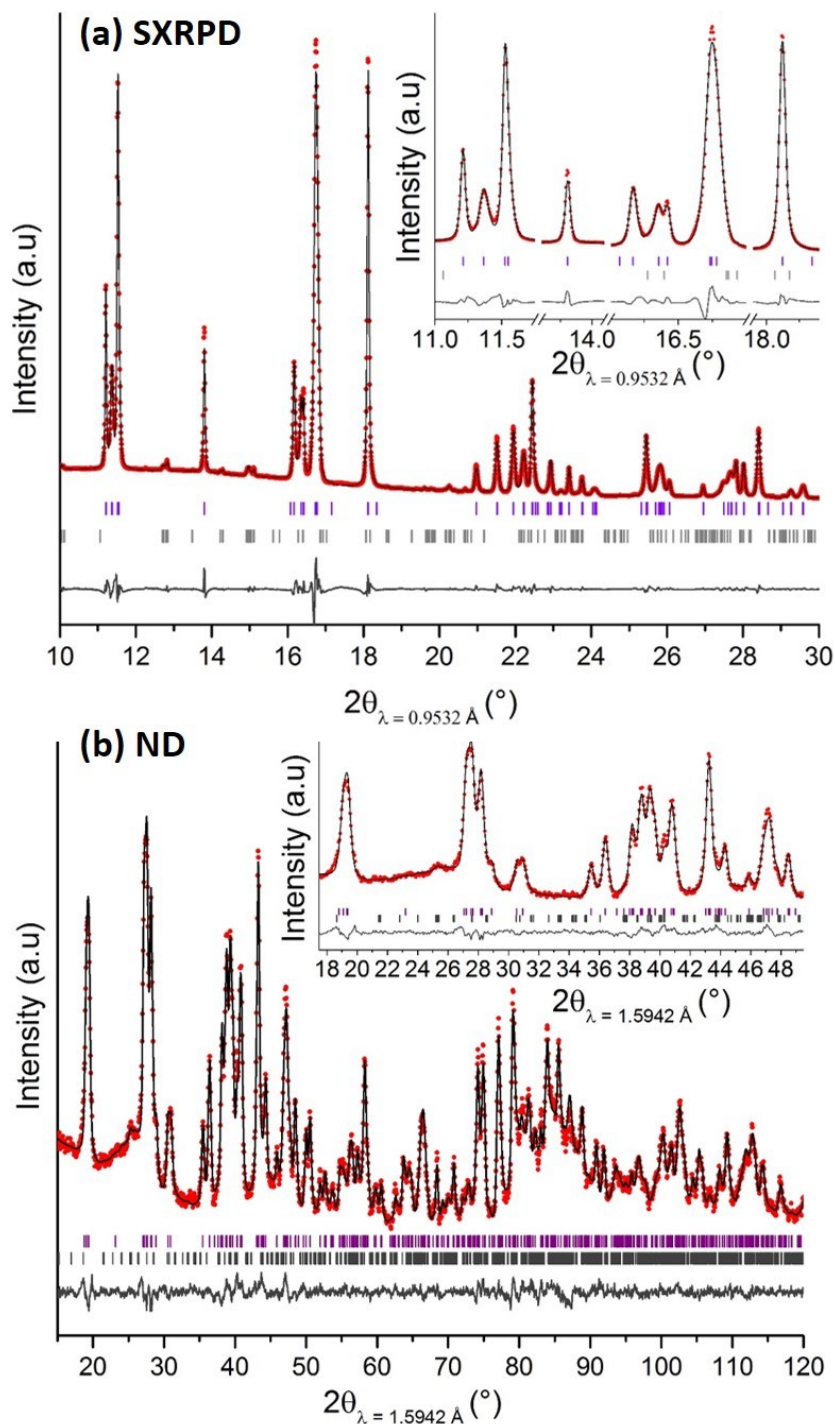


Figure II-32: Rietveld refinement of the structure of $\text{LiVPO}_4\text{F}_{0.45}\text{O}_{0.55}$ based on a combined refinement of Synchrotron X-rays (a) and Neutrons (b) powder diffraction patterns. The observed intensities are plotted as red points, the theoretical Bragg positions are plotted as purple marks for main phase or grey ones for secondary phase (i.e. $\text{Li}_3\text{V}_2(\text{PO}_4)_3$), calculated intensities and the difference between observed and calculated intensities are plotted as black lines.

A comparison between the three solid solution samples and the end-members phases (*i.e.* $\text{LiV}^{\text{III}}\text{PO}_4\text{F}$ and $\text{LiV}^{\text{IV}}\text{PO}_4\text{O}$) is interesting as it allows to understand the nature of the bond observed along the chains of octahedra, depending on the bridging anion (*i.e.* F or O) and the oxidation state of vanadium. In $\text{LiV}^{\text{III}}\text{PO}_4\text{F}$, the distances along the chains of octahedra are almost constant ($1.98\text{-}1.99 \text{ \AA}$)⁹². Conversely, due to the presence of V^{4+} in $\text{LiV}^{\text{IV}}\text{PO}_4\text{O}$, and the formation of the vanadyl bond, an alternation between a short bond (vanadyl bond) at 1.67 \AA and a longer one at 2.19 \AA is observed⁹². This alternation is at the origin of the lower symmetry in $\text{LiV}^{\text{IV}}\text{PO}_4\text{O}$ which must be described in a twice larger cell whereas in the LiVPO_4F -type model, no distortion of octahedra along the d_{z^2} orbitals of vanadium is allowed. So, both V-X distances in a VO_4X_2 octahedron obtained for our solid solutions are symmetrically equivalent. These distances are:

- For $\text{LiVPO}_4\text{F}_{0.25}\text{O}_{0.75}$, $1.937(3)$ and $1.922(3) \text{ \AA}$ with associated BVS of $3.22(1)/3.39(1)$ respectively for V(1) and V(2).
- For $\text{LiVPO}_4\text{F}_{0.45}\text{O}_{0.55}$, $1.963(3)$ and $1.933(3) \text{ \AA}$ with associated BVS of $3.14(1)/3.34(1)$ respectively for V(1) and V(2).
- For $\text{LiVPO}_4\text{F}_{0.65}\text{O}_{0.35}$, $1.972(3)$ and $1.929(3) \text{ \AA}$ with associated BVS of $3.13(1)/3.33(1)$ respectively for V(1) and V(2).

The BVS values associated with vanadium atoms for the three phases discussed here were found to be between 3 and 4, in good agreement with the formation of mixed $\text{V}^{3+}/\text{V}^{4+}$ phases. Nevertheless, some divergences between the average oxidation states of vanadium atoms determined by magnetic measurement and their BVS values exist. Moreover only small differences are observed between the BVS values determined for vanadium atoms in these different phases whereas their average oxidation states were shown to be significantly different. Actually, DFT calculations on $\text{LiVPO}_4\text{F}_{0.96}\text{O}_{0.04}$ predict the local formation of vanadyl ($d(\text{V}^{4+}=\text{O})= 1.70 \text{ \AA}$) in the neighboring of oxygen defect²¹. The $\text{V}^{3+}\text{-F}/\text{V}^{4+}=\text{O}$ disorder present in our materials involved the formation of inhomogeneous distances along the chains, the BVS calculations being performed considering the average description of the structure and thus the average distances is invalid in that case, due to a significant discrepancy between the actual local structure and the average structure.

Table II-12: Significant bond lengths (Å) of LiVPO₄F_{1-y}O_y materials obtained from Rietveld refinement of SXRPD data. Polyhedral distortion is calculated as $\Delta = \frac{1}{N} \sum_{i=0}^N \frac{(d_i - \langle d \rangle)^2}{\langle d \rangle^2}$.

coordination	LiVPO ₄ F _{0.65} O _{0.35}		LiVPO ₄ F _{0.45} O _{0.55}		LiVPO ₄ F _{0.25} O _{0.75}	
	V(1)	V(2)	V(1)	V(2)	V(1)	V(2)
O(1)	/	1.936(8)	/	1.935(9)	/	1.920(9)
O(1')	/	1.936(8)	/	1.935(9)	/	1.920(9)
O(2)	/	1.997(6)	/	1.997(6)	/	2.012(9)
O(2')	/	1.997(6)	/	1.997(6)	/	2.012(9)
O(3)	1.991(6)	/	1.989(6)	/	1.985(9)	/
O(3')	1.991(6)	/	1.989(6)	/	1.985(9)	/
O(4)	1.964(6)	/	1.966(6)	/	1.988(9)	/
O(4')	1.964(6)	/	1.966(6)	/	1.988(9)	/
O(5)/F(1)	1.972(9)	1.929(7)	1.969(9)	1.925(9)	1.937(9)	1.922(9)
O(5')/F(1')	1.972(9)	1.929(7)	1.969(9)	1.925(9)	1.937(9)	1.922(9)
Average	1.976(7)	1.954(7)	1.975(7)	1.953(8)	1.972(9)	1.952(9)
Δ	6.5x10 ⁻⁵	4.8x10 ⁻⁴	5.3x10 ⁻⁵	5.2x10 ⁻⁴	2.8x10 ⁻⁴	9.4x10 ⁻⁴
BVS	3.13(1)	3.33(1)	3.14(1)	3.34(1)	3.22(1)	3.39(1)

The high covalency within phosphate groups generally generates high constancy of the P–O distances¹⁴⁴, ranging here between 1.525(9) and 1.544(9) Å and small tetrahedral distortion ($\Delta = 8.51 \times 10^{-5}$).

The Li site observed in the structure is surrounded by four oxygen atoms belonging to the square plane of VO₄X₂ octahedra and to one bridging anion, X (X=O or F), in a distorted LiO₄X polyhedron. The BVS values associated with Lithium in this site don't correspond to the theoretical value (*i.e.* 0.86(3), 0.89(3) and 0.88(3)) and the Debye-Waller factors (B_{iso}) associated are rather high (6.60, 3.74 and 3.01 respectively for LiVPO₄F_{0.25}O_{0.75}, LiVPO₄F_{0.45}O_{0.55} and LiVPO₄F_{0.65}O_{0.35}). Actually, the lithium position might be impacted by the V³⁺/V⁴⁺ and O/F disorder along the chains. The diffraction techniques, giving an average position, balance the effect of a broad distribution for lithium positions by artificial high atomic displacement parameters which are probably, in that case, a refinement artefact not necessarily correlated to the thermal motion of lithium atoms around their equilibrium positions.

In the absence of modulation peaks, a disordered F-V³⁺/O=V⁴⁺repartition along the chains seems to be formed. Thus, diffraction techniques giving access to an average long range description, no information on the V-F distances neighboring vanadyl bonds (F-(V^{IV}=O)) and V-O upstream to a V-F ones (O-(V^{III}-F)) can be deduced from diffraction data. These distances may have a strong effect on electronic configuration in vanadium's orbitals and *a fortiori* electrochemical properties. Spectroscopy experiments are thus needed to evidence the local vanadyl-type distortions predicted by DFT²¹.

II-3c. Characterization of $\text{V}^{3+}\text{-F}/\text{V}^{4+}\text{=O}$ disorder

i. X-ray absorption spectroscopy

X-ray absorption spectra were recorded at the vanadium K-edge to probe the vanadium oxidation state and local structure around the absorber. **Figure II-33** displays the spectra recorded for the series of $\text{LiVPO}_4\text{F}_{1-y}\text{O}_y$ materials.

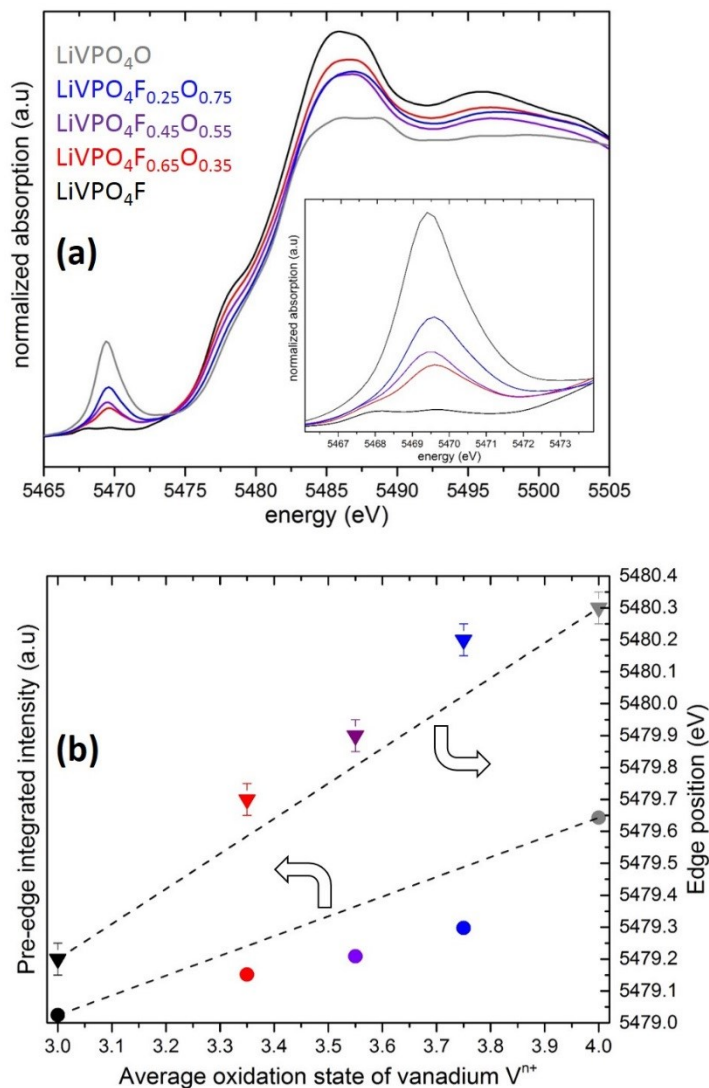


Figure II-33: (a) V K-edge XANES spectra of the whole series of $\text{LiVPO}_4\text{F}_{1-y}\text{O}_y$ with the enlargement of the pre-edge region in inset showing the gradual growth of vanadyl-type environments. (b) Evolution of edge position and pre-edge integrated intensity in function of average oxidation of vanadium.

For these spectra, the Vanadium K-edge XANES in these materials exhibits a pre-edge absorption feature followed by a weak shoulder on a rising absorption curve (the absorption edge) which culminates in a strong peak whose energy position increases with the rise of the

vanadium oxidation state. This strong peak is assigned to the dipole-allowed transition 1s to 4p and the pre-edge feature to the transition 1s to 3d.¹²⁹ This feature is strictly forbidden in perfectly regular Vanadium octahedra but becomes dipole allowed due the distortion of the local symmetry around the absorber leading to a 3d-4p orbital mixing and thus to an overlap of the metal 3d orbitals with the 2p orbitals of the ligand.¹²⁹ A weak contribution at 5468.0 eV, typical for the V³⁺ state, is detected for LiVPO₄F and a second one at 5469.7 eV growing in intensity with the rise of the vanadium oxidation state and thus with the expansion vanadyl-type environments. **Figure II-33b** shows the evolution of the pre-edge intensity as a function of vanadium oxidation state. Its integrated intensity doesn't evolve linearly and significantly below that expected considering a linear evolution between the two end-members phases. The presence of the strongly ionic V-F bond, even in minor proportion, could prevent the formation of "true" vanadyl distortion (O=V⁴⁺--O).

On the same graph, the change in energy position observed for the edge versus the average oxidation state of vanadium is also given and strengthens this hypothesis. Indeed, the edge shift isn't only related to the oxidation state of the transition metal. The ionic-covalent character of the bonds which it forms with its ligands modulates also the position of the 1s to 4p transition.¹⁴⁵ The strong ionicity of the V-F bond tends to increase the edge energy versus the strong covalency of vanadyl one. So, until $n \sim 3.75$, the edge position grows linearly with the rise of oxidation state of vanadium but is systematically overestimated compared to the linear combination of edge position observed for end-member phases. For higher oxidation state, this difference becomes smaller due to the predominance of "true" vanadyl environments (*i.e.* O=V⁴⁺--O). The competition between the formation of strongly ionic V³⁺-F bond at the expense of the strongly covalent V⁴⁺=O one already proposed to explain the offset from Vegard's law could be at the origin of nonlinear phenomena at the electronic level.

At energies above the 1s to 4p transition, absorption features arise from a transition to higher np states (continuum). If the kinetic energy acquired by the ejected photoelectron is great enough to escape from the bound state, the interactions between this photoelectron and other electrons generate the EXAFS oscillations. This phenomenon is a kind of "in situ electron diffraction" in which the absorbing atom is the photoelectron source. The careful treatment of these oscillations allows to determine the nature of the atoms belonging to the coordination sphere of the probed element and the distance between them. In our case, as O²⁻ and F⁻ interact similarly with X-rays, the information about the nature of the atoms belonging to the coordination sphere of vanadium isn't reachable, thus, only the distances between vanadium and its ligands can be probed. The theory of EXAFS is governed by the EXAFS

equation¹⁴⁶ and thus can be fitted using appropriate software (*i.e.* Athena for pre-treatment of the signal and Artemis for the fitting¹⁴⁷). The complexity of the systems studied here (triclinic compounds with defects) doesn't allow us to be fully confident in the fits for far coordination shells. Thus, only the first coordination sphere around vanadium will be discussed here.

The fit of the k^2 -weighted V K-edge EXAFS spectra Fourier transform (k -range: 3.7-11.0 \AA^{-1} , sine window) in the R space and the corresponding fit of the real part of $\chi(q)$ corresponding to the reverse Fourier transform considering only the R -range used for the fit (R range: 1.0 – 2.05 \AA , $dR=0.1$ \AA) are shown in **Figure II-34**.

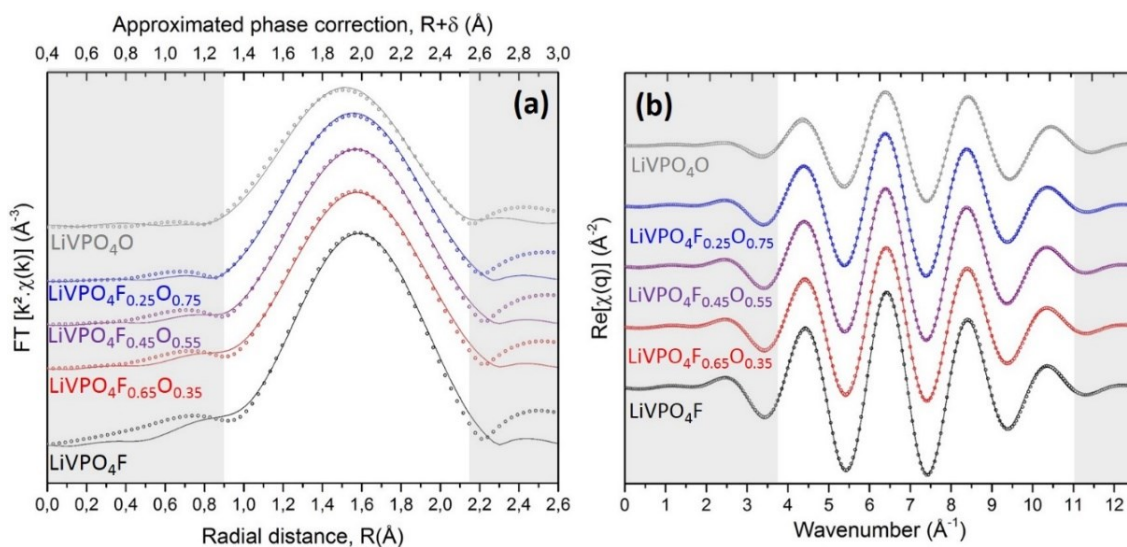


Figure II-34: (a) Fit of the k^2 -weighted V K-edge EXAFS spectra Fourier transform (k -range: 3.7-11.0 \AA^{-1} , sine window) in the R space (R range: 1.0 – 2.05 \AA , $dR=0.1$ \AA , sine window) for the whole series of $\text{LiVPO}_4\text{F}_{1-y}\text{O}_y$ materials (b) the corresponding fit of the real part of $\chi(q)$ corresponding to the back Fourier transform of (a) considering only the R -range used for the fit (R range: 1.0 – 2.05 \AA , $dR=0.1$ \AA). The circles represent the experimental data and the solid lines represent the fits. The parameters thus extracted are provided in Table II-13.

The local environment around vanadium in LiVPO_4F can be described as 6 equivalent ligands located at 1.97(1) \AA away from vanadium atom (vs. 1.971(2) \AA in average for XRD). The tiny amount of defects in this sample doesn't contribute significantly to the EXAFS oscillations contrarily to the vanadyl bond in LiVPO_4O . Actually, for this sample, a 1+4+1 coordination is clearly needed to fit the vanadyl distortion. The shorter $\text{V}^{4+}=\text{O}$ bond length is 1.63(1) (vs. 1.626(3) \AA for XRD) the four following are 1.98(1) (vs. 1.986(3) \AA in average for XRD) and the longest one is 2.32(1) (vs. 2.239(3) \AA for XRD) leading to BVS values of 3.83 from EXAFS against 3.93 from XRD). In both cases, the results obtained from XRD and EXAFS are in good agreement, contrarily to the mixed valence phases in which the higher amount of defects compared to the one observed in LiVPO_4F , involves an inaccurate average long range description, as just described and discussed in the previous section (**section II-3b**).

Models with 3 inequivalent distances with different probabilities to be observed according to the F⁻/O²⁻ substitution ratio (*i.e.* y) have to be used to fit the EXAFS data (see **Figure II-35** and **Table II-13**). In this model, we assume a 6-fold coordination with:

- (i) All V⁴⁺ form a short vanadyl bond with an oxygen with a probability $p_i = y/6$ with y referring to y in LiVPO₄F_{1-y}O_y.
- (ii) Long antagonist V⁴⁺--O bonds are formed along the chains with the following probability: $p_{ii} = (y^2/(2-y))/6$.
- (iii) All the V³⁺-X (X= O or F), V⁴⁺-F and V⁴⁺-O (those belonging to the square plane of VO₄X₂) bonds are equivalent. Indeed, refined independently, their corresponding bond lengths converge towards a similar value. The probability for this distance is $p_{iii} = (6-y-y^2/(2-y))/6$.

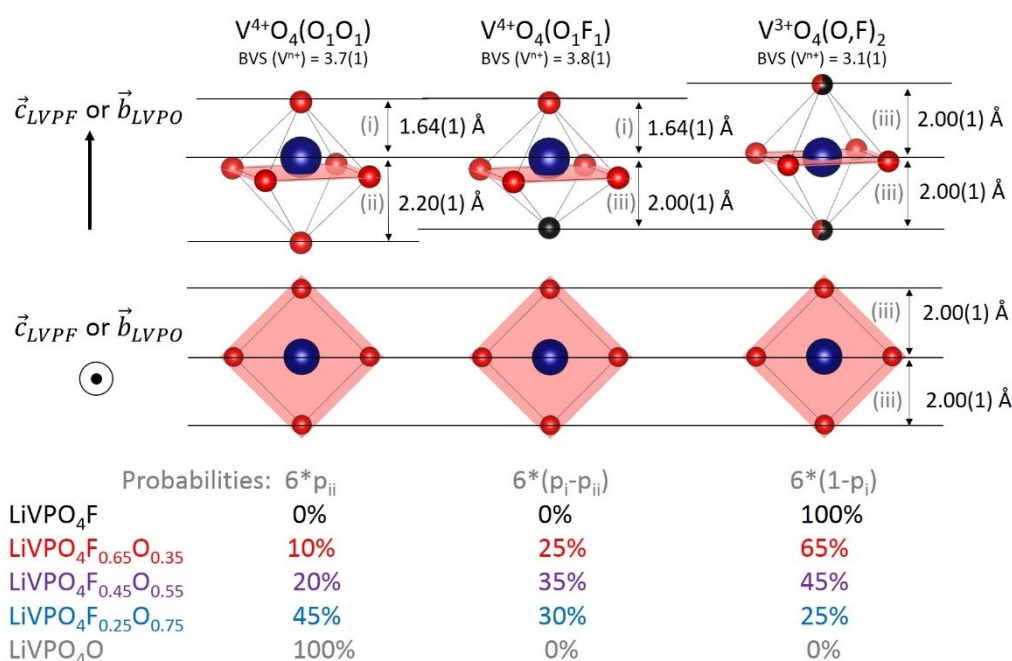


Figure II-35 : Summary of the fit of the k^2 -weighted V K-edge EXAFS spectra Fourier transform explaining the offset from the Vegard's law along the propagation direction of the chains of octahedra. The meaning of (i), (ii) and (iii) and the values of the corresponding probabilities (p_i , p_{ii} , p_{iii}) are specified in the text.

That leads to a coordination such as $[(6 * p_i) v_{4+=O}] + [(6 * p_{iii}) v_{-X}] + [(6 * p_{ii}) v_{4+--O}]$. Thus, 4.8, 5.25 and 5.55 (*i.e.* $6 * p_{iii}$ respectively for LiVPO₄F_{0.25}O_{0.75}, LiVPO₄F_{0.45}O_{0.55} and LiVPO₄F_{0.65}O_{0.35}) ligands are found to be distant of 2.01(1) Å from vanadium. The remaining ligands, to reach a 6-fold coordination for vanadium, are distributed as follows: $(6 * p_i / 6 * p_{ii})$ 0.75/0.45, 0.55/0.20, 0.35/0.1 respectively for LiVPO₄F_{0.25}O_{0.75}, LiVPO₄F_{0.45}O_{0.55} and LiVPO₄F_{0.65}O_{0.35} at 1.64(1) Å and around ~2.20 Å. This description doesn't match with the model found by diffraction which involved centrosymmetric vanadium octahedra. But, even if XRD

failed to describe the local environment for vanadium, the average distances around vanadium obtained from XRD and EXAFS must be similar.

Table II-13 compares the distances around vanadium obtained from EXAFS and XRD and the resulting BVS for all samples discussed here. The distances obtained from EXAFS provide BVS values close to those expected (by magnetic measurements) contrarily to XRD ones.

Table II-13: Structural parameters obtained from the fit of the k^2 -weighted V K-edge EXAFS spectra Fourier transform. The parameters marked by * or # in a same sample have been refined together and fixed to be the same. The XRD distances reported in this table are average ones and are compared to the average distances found by EXAFS. The details for calculation of associated BVS are provided in Table Annex-II-1.

sample	$\text{V}^{n+}\text{-X}$	coordination number, N	R (Å)	σ^2 (10^{-3} Å ²)	BVS
LiVPO_4F $\chi^2=3.85$ $R_f = 3.9 \cdot 10^{-4}$	(i) $\text{V}^{4+}=\text{O}$	/	/	/	
	(ii) $\text{V}^{4+}-\text{O}$	/	/	/	2.92(8)
	(iii) $\text{V}^{4+}-\text{F}$	/	/	/	vs. 3.00
	(iii) $\text{V}^{4+}-\text{F}$	2	2.00(2)*	4.3(3) [#]	theoretically
	(iii) $\text{V}^{3+}-\text{O}$	4	2.00(2)*	4.3(3) [#]	
Average EXAFS		6	2.00(2)	4.3(3)	/
Average XRD		6	1.972(7)	/	3.06(2)
$\text{LiVPO}_4\text{F}_{0.65}\text{O}_{0.35}$ $\chi^2=11.05$ $R_f = 2.1 \cdot 10^{-3}$	(i) $\text{V}^{4+}=\text{O}$	0.35	1.64(1)	5.4(4) [#]	
	(ii) $\text{V}^{4+}-\text{O}$	0.1	2.19(1)	5.4(4) [#]	3.31(8)
	(iii) $\text{V}^{4+}-\text{F}$	0.25	2.01(1)*	5.4(4) [#]	vs. 3.35
	(iii) $\text{V}^{3+}\text{-X}$	1.3	2.01(1)*	5.4(4) [#]	theoretically
	(iii) $\text{V}^{3/4+}\text{-O}$	4	2.01(1)*	5.4(4) [#]	
Average EXAFS		6	1.99(1)	5.4(4)	/
Average XRD		6	1.968(9)	/	3.23(1)
$\text{LiVPO}_4\text{F}_{0.45}\text{O}_{0.55}$ $\chi^2=2.35$ $R_f = 4.3 \cdot 10^{-4}$	(i) $\text{V}^{4+}=\text{O}$	0.55	1.64(1)	4.9(2) [#]	
	(ii) $\text{V}^{4+}-\text{O}$	0.2	2.20(1)	4.9(2) [#]	3.51(8)
	(iii) $\text{V}^{4+}-\text{F}$	0.35	2.01(1)*	4.9(2) [#]	vs. 3.55
	(iii) $\text{V}^{3+}\text{-X}$	0.9	2.01(1)*	4.9(2) [#]	theoretically
	(iii) $\text{V}^{3/4+}\text{-O}$	4	2.01(1)*	4.9(2) [#]	
Average EXAFS		6	1.98(1)	4.9(2)	/
Average XRD		6	1.972(7)	/	3.24(1)
$\text{LiVPO}_4\text{F}_{0.25}\text{O}_{0.75}$ $\chi^2=4.58$ $R_f = 4.4 \cdot 10^{-4}$	(i) $\text{V}^{4+}=\text{O}$	0.75	1.64(1)	4.3(3) [#]	
	(ii) $\text{V}^{4+}-\text{O}$	0.45	2.20(1)	4.3(3) [#]	3.68(8)
	(iii) $\text{V}^{4+}-\text{F}$	0.30	2.01(1)*	4.3(3) [#]	vs. 3.75
	(iii) $\text{V}^{3+}\text{-X}$	0.5	2.01(1)*	4.3(3) [#]	theoretically
	(iii) $\text{V}^{3/4+}\text{-O}$	4	2.01(1)*	4.3(3) [#]	
Average EXAFS		6	1.98(1)	4.3(3)	/
Average XRD		6	1.961(9)	/	3.31(1)
LiVPO_4O $\chi^2=25.49$ $R_f = 3.3 \cdot 10^{-3}$	(i) $\text{V}^{4+}=\text{O}$	1	1.64(1)	4.9(2) [#]	
	(ii) $\text{V}^{4+}-\text{O}$	1	2.25(3)	4.9(2) [#]	3.77(8)
	(iii) $\text{V}^{4+}-\text{F}$	/	/	/	vs. 4.00
	(iii) $\text{V}^{3+}-\text{F}$	/	/	/	theoretically
	(iii) $\text{V}^{4+}-\text{O}$	4	2.00(3)*	4.9(2) [#]	
Average EXAFS		6	1.98(3)	4.9(2)	/
Average XRD		6	1.968(9)	/	3.82(3)

In general, no significant differences for bond lengths found by EXAFS are observed between the three mixed valence materials. Actually, the only difference resides in the probability of the formation of the different kinds of bonds. From the EXAFS point of view, the sequences of octahedra can be described as a sum of 3 kinds of vanadium environments (*i.e.* X-V³⁺O₄-X, F-V⁴⁺O₄=O and O-V⁴⁺O₄=O) whose neighboring octahedra have a negligible impact on it. **Figure II-35** compares schematically the descriptions made from EXAFS and XRD. This model explains the gap from the Vegard's law observed along the propagation direction of the chains of octahedra (along \vec{b}_{LVPO} or \vec{c}_{LVPF}). Indeed, in a conventional solid solution, a mixture of end-member-type environments is expected whereas, in our case, a third environment is detected. Although X-V³⁺O₄-X and O-V⁴⁺O₄=O environments are very similar to LiVPO₄F-type and LiVPO₄O-type ones respectively, the F-V⁴⁺O₄=O octahedra is shrunk along the dz² orbitals of vanadium. The formation of the vanadyl bond is observed but the presence of fluorine prevents the formation of the longer antagonist bond leading to a compaction of the octahedra and a shortening of the b_{LVPO} (or c_{LVPF}) parameter.

EXAFS is in good agreement with DFT calculations performed considering the LiVPO₄F_{0.96}O_{0.04} composition²¹. The local formation of a vanadyl bond (with (F-)V⁴⁺=O at 1.70 Å) occurs close to the oxygen defects and the antagonist (O=)V⁴⁺-F (*i.e.* 2.03 Å) and O-V³⁺-F (*i.e.* 2.06 and 2.07 Å respectively for V-O and V-F) bonds are equivalent to those observed in the -F-V³⁺-F-V³⁺-F- (2.06 Å) sequences. Moreover, the probability of the presence of shrunk F-V⁴⁺O₄=O octahedra (*i.e.* $p = y^2/(2-y)$) fits with a very good agreement the amplitude of the offset from the Vegard's law along \vec{b}_{LVPO} (or \vec{c}_{LVPF}) direction (see **Figure II-30**) as function of the average oxidation state of vanadium in the material. The model proposed for the fit of the EXAFS oscillations describes the local environments of the disordered materials obtained in good agreement with the DFT calculations. However, EXAFS presents some limitations such as the number of independent parameters ($n \sim 2 \cdot \Delta k \cdot \Delta R / \pi$ close to 6 in our case) and the resolution (distances $\pm 0.01 \text{ \AA}$). Vibrational spectroscopy experiments have been conducted in order to further probe the local environments generated.

ii. Vibrational spectroscopy

Mid-Infrared diffuse reflectance spectroscopy and Raman scattering analyses of the whole series of LiVPO₄F_{1-y}O_y compositions were performed, to evidence the absence of the hydroxyl groups and probe the V-O and P-O vibrations. The spectra corresponding to IR are given in **Figure II-36a** and the vanadyl stretching region for Raman scattering in **Figure II-36b**. In the 3000 - 4000 cm⁻¹ region, no contribution was detected except for LiVPO₄O in which a

broad band at 3400 cm^{-1} is assigned to the adsorbed water due to the presence of the corresponding H-O-H bending vibration at 1635 cm^{-1} .¹³⁹ This absence of signal in the O-H stretching vibration region supports the compositions proposed without substitution of fluorine by OH group as sometimes reported for the synthesis of fluorinated compounds.¹⁴⁸ The PO_4 stretching region is located between 950 and 1200 cm^{-1} .^{141,142} A single crystallographic site exists for phosphorus in LiVPO_4F , whereas two sites induced by the lower symmetry (*i.e.* doubling of the unit cell) are identified in LiVPO_4O . That is shown by the increase in the number of components in the PO_4 stretching region with the appearance of 2 peaks around 1165 and 950 cm^{-1} in addition to those observed in LiVPO_4F (around 1110 , 1050 and 1000 cm^{-1}). The PO_4 stretching region signature of the mixed valence samples is similar to the one of LiVPO_4O with broader contributions and weaker satellite peaks. Otherwise, the vanadyl ($\{\text{V}=\text{O}\}^{2+}$) stretching vibration mode, in LiVPO_4O , is located at 915 cm^{-1} .¹⁴¹ This band is not expected in LiVPO_4F which is theoretically a pure V^{3+} -containing material, *i.e.* vanadyl-free composition. Nevertheless, a tiny peak is observed at 874 cm^{-1} , shifted versus the vanadyl stretching observed in LiVPO_4O , which matches with the presence of local vanadyl-type defect in LiVPO_4F . As the average oxidation state of vanadium is increased, a slight shift toward higher wavenumber and an increasing intensity of the vanadyl-type vibration are observed. Moreover, several shoulders are detected around 900 , 865 and 824 cm^{-1} which could be induced by the broad distribution of $\text{V}^{4+}=\text{O}$ environments.

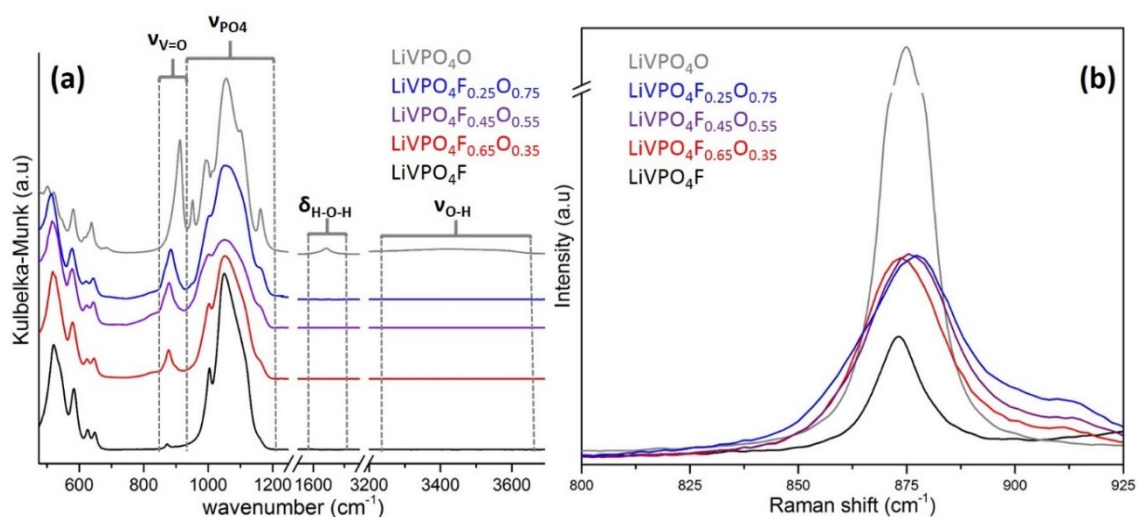


Figure II-36: diffuse reflectance infrared spectra (a) and Raman scattering spectra (b) of LiVPO_4O (grey line), $\text{LiVPO}_4\text{F}_{0.25}\text{O}_{0.75}$ (blue line), $\text{LiVPO}_4\text{F}_{0.45}\text{O}_{0.55}$ (purple line), $\text{LiVPO}_4\text{F}_{0.65}\text{O}_{0.35}$ (red line) and LiVPO_4F (black line).

Raman scattering is a flagship technique to probe vanadyl vibration whose typical region is located between 800 and 940 cm^{-1} .¹⁴⁰ Strong contributions are observed around 875 cm^{-1} (873 , 874 , 875 , 876 and 877 cm^{-1} from $y = 1$ to $y = 0$ in $\text{LiVPO}_4\text{F}_{1-y}\text{O}_y$) and weaker ones

around 910 cm^{-1} (911 , 912 and 913 cm^{-1}) for mixed valence samples. In these materials, as the oxidation state is raised, a weak shift and significant broadening of the vanadyl vibration are observed. This is probably due to the wide distribution of $\text{X-V}^{4+}=\text{O}$ environments which are seen as identical by EXAFS. However, according to the empirical formula allowing to estimate the V-O bond lengths from the wavenumber of its vibration mode taken from ref.¹⁴⁰, that leads to very close $\text{V}^{4+}=\text{O}$ bond lengths (1.66 for 875 cm^{-1} and 1.65 \AA for 910 cm^{-1} vibrations).

Raman scattering reveals itself to be more sensitive than EXAFS to the vanadyl bond lengths which, as suggested by EXAFS, doesn't seem really disrupted by the antagonist ligand (Oxygen or fluorine). MAS NMR has already proved to be a powerful tool to probe vanadyl-type defects and their distributions^{19,21}. As NMR is sensitive to the local electronic structure around the nucleus probed, it could be sensitive to the effect of the antagonist ligand on the vanadyl bond. Thus ^7Li , ^{31}P , ^{19}F MAS NMR experiments were carried out on the whole series of samples.

iii. NMR

Figure II-37 shows the ^7Li MAS NMR spectra recorded for all samples. A rather sharp signal centered at 115 ppm is observed for LiVPO_4F , in agreement with previous publications: it is attributed to the unique Lithium site identified by diffraction^{126,128}.

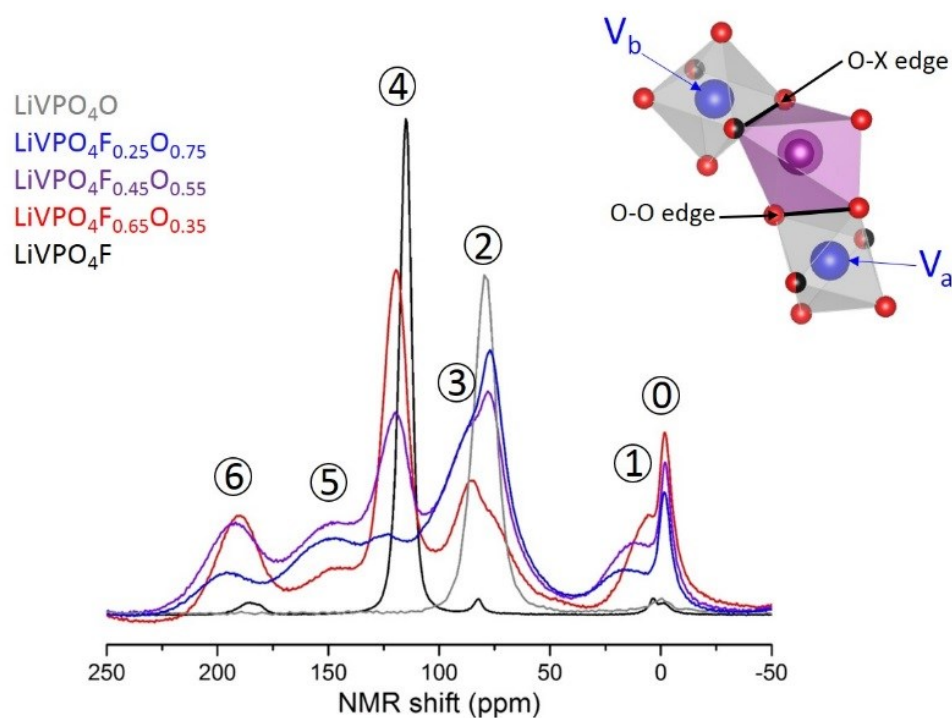


Figure II-37: ^7Li MAS NMR spectra of the whole series of $\text{LiVPO}_4\text{F}_{1-y}\text{O}_y$ compositions. The global intensity of the signal obtained for end members phases have been divided by 10. In inset, a schematic illustration of the lithium environment seen by NMR (only the edge shared with vanadium octahedra are depicted).

The spectrum for the LiVPO_4F sample also exhibits a weak signal at -1 ppm assigned to the presence of residual LiF and other additional signals at 4, 84 and 186 ppm which have been assigned to vanadyl-type defects^{19,21}. The investigation of the NMR spectrum of LVPO shows a single sharp peak at 79 ppm. In LiVPO_4O , there are two crystallographic sites for Lithium⁹². So, two ^7Li MAS NMR peaks would have been expected whereas only one is detected, probably due to their structural similarity between both sites and/or to Lithium mobility between them.

For all Tavorite phases discussed here, the lithium polyhedra share two edges and two corners with the VO_4X_2 octahedra. As the e_g orbitals of vanadium being empty (*i.e.* t_{2g}^2 for V^{3+} and t_{2g}^1 for V^{4+}), the main spin transfer from vanadium to lithium occurs from the t_{2g} orbitals pointing towards common edges between the LiO_4X and VO_4X_2 polyhedra (*i.e.* an O-O one and an O-X one, with bridging anion $\text{X} = \text{O}$ or F). This simplified lithium environment is depicted in the inset of **Figure II-37**.

For LiVPO_4F , both d electrons are homogeneously distributed in the three t_{2g} orbitals whereas for $\text{LiV}^{\text{IV}}\text{PO}_4\text{O}$, the presence of vanadyl bond along the d_{z^2} orbitals induces the destabilization of d_{xz} and d_{yz} .²¹ Therefore the spin transfer provided from t_{2g} orbitals of vanadium to lithium 1s ones for LiVPO_4O occurs only from the d_{xy} through the O-O edge shared with V_a (see **Figure II-37**). For LiVPO_4F the spin transfer is stronger due to, first, the higher number of electron in d orbitals of V^{3+} , and then, the contribution of both vanadium sharing an edge with lithium polyhedra. The mixed valence $\text{V}^{\text{III}}/\text{V}^{\text{IV}}$ samples exhibit very broad contributions basically located in the neighborhood of the signals observed for LiVPO_4F (isotropic peak and defects contributions) and LiVPO_4O . **Table II-14** summarizes the positions of the ^7Li MAS NMR peaks and their relative intensities. Actually 7 components are observed and a quasi-non-shifted one at -2 ppm (denoted as peak#0 in the **Figure II-37**) which is assigned to residual LiF contribution (supported by ^{19}F discussed below).

By analogy with the end member phases, 2 contributions can be assigned to Lithium in interaction with two V^{III} (LiVPO_4F -like environment) around 120 ppm (peak#4) and with two O- $\text{V}^{\text{IV}}\text{O}_4$ -O octahedra ($\text{LiV}^{\text{IV}}\text{PO}_4\text{O}$ -type contribution) around 80 ppm. However, two overlapped peaks appear in the LiVPO_4O region (peak#2 around 75 and peak#3 around 85 ppm) and we aren't able to assign one or the other. Moreover, the remaining signals around 10 (peak#1), 150 (peak#5) and 195 ppm (peak#6) cannot be attributed trivially by analogy with existing phases.

In our group, recent work dealing with the understanding of NMR signatures of vanadyl-type defects in LiVPO₄F predicts, by DFT calculations, the shifts of these contributions²¹. This study reveals that the vanadyl-type defects together with lithium vacancies (same number of lacking lithium atoms than oxygen defects) in the neighboring of these defects could be at the origin of supplementary NMR peaks. In our case, the hypothesis of lithium deficiency is invalidated experimentally (by ICP, ND...) and these results cannot be extrapolated to our system. Similarly to this work, in order to get the shift of NMR contributions for larger vanadyl-type defects' concentrations, several attempts to obtain the relaxed structure of the LiVPO₄F_{0.5}O_{0.5} with a quasi-statistical distribution of V³⁺/V⁴⁺ and O²⁻/F⁻ (involving a Z = 16 supercell instead of Z=2 for the experimental one) didn't converge.

Table II-14: shifts of the ⁷Li, ³¹P and ¹⁹F MAS NMR signals and the corresponding fraction of paramagnetic signal for ⁷Li obtained from the fits of NMR spectra done thanks to origin9 software using a pseudo-Voigt function, and are provided in the Annex part (**Figure Annex-II-3**).

#	NMR shift (ppm) / fraction of paramagnetic signal (%)					assignment	
	LiVPO ₄ F	LiVPO ₄ F _{0.65} O _{0.35}	LiVPO ₄ F _{0.45} O _{0.55}	LiVPO ₄ F _{0.25} O _{0.75}	LiVPO ₄ O		
	0	-2	-2 / -	-2 / -	-2 / -	1	Amorphous LiF
⁷ Li	1	4	9 / 7%	14 / 14%	18 / 6%	-	-
	2	-	73 / 10%	76 / 16%	76 / 23%	79	-
	3	82	86 / 7%	89 / 25%	89 / 37%	-	-
	4	115	119 / 42 %	120 / 21%	124 / 4%	-	LiVPO ₄ F-type
	5	-	147 / 13%	148 / 5%	150 / 21%	-	-
	6	185	191 / 21%	193 / 18%	197 / 9%	-	-
³¹ P	0	-	3	3	51	14	Li ₃ PO ₄ / H ₃ PO ₄
	1	-	1383	1383	1370	1441	LiVPO ₄ O-type
	2	-	1581	1583	1583	1613	LiVPO ₄ O-type
	3	-	2480	2520	2602	-	-
	4	3128	3183	3181	3195	-	-
	5	3871	3949	3923	3872	-	LiVPO ₄ F-type
¹⁹ F	6	-	4461	-	-	-	-
	-	- 125	- 125	- 125	- 125	-	Probe
	-	- 205	- 205	- 205	- 205	-	LiF
-	- 1530	- 1520	- 1520	- 1520	-	Isotropic	

In absence of DFT predictions for larger concentrations of vanadyl-type defects, a probabilistic approach has been used in order to understand the ⁷Li NMR signature of the LiVPO₄F_{1-y}O_y series. Indeed, NMR spectroscopy being a quantitative technique, the area of NMR peaks must be related to the probability of presence of the environments obtained from EXAFS (see **Figure II-35**). Even though, the model built is able to predict the number of NMR contributions observed, it doesn't match with the experimental intensities obtained. The divergences observed between fits of experimental spectra and theoretical relative intensity of NMR peaks could originate from a partial clustering of V⁴⁺-rich and V³⁺-rich domains. In order to detect eventual typical V³⁺/V⁴⁺ sequences along the chains through the interaction of

Lithium atoms with a common Vanadium atom, 2D ^7Li NMR experiments were conducted in similar conditions than those reported by Messinger *et al.* in ref.¹⁹ for the detection of vanadyl type defects in LiVPO_4F . 2D EXSY NMR experiments conducted at CEMHTI (Orléans) in collaboration with Elodie Salager are coherent with this hypothesis with a complex correlation between peaks. However, the complex results of these experiments are still under analysis and won't be discussed in this manuscript.

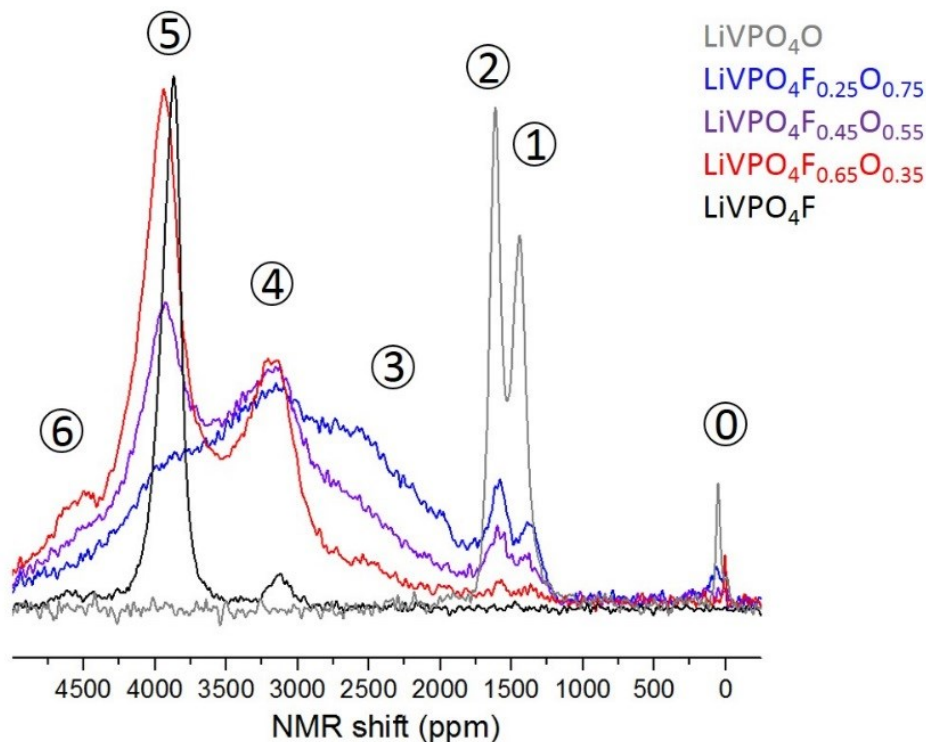


Figure II-38: ^{31}P MAS NMR spectra of the whole series of $\text{LiVPO}_4\text{F}_{1-y}\text{O}_y$ compositions. The global intensity of the signal obtained for end members phases have been divided by 10.

Figure II-38 shows the ^{31}P MAS NMR spectra recorded for the series of composition. In Tavorite-type structures, the PO_4 tetrahedra are connected to four different transition metal octahedra via the oxygen belonging to the VO_4 plane of these octahedra. As discussed by Castets *et al.* for the LiMPO_4OH Tavorite series, in our case (*i.e.* $t_{2g}^2e_g^0$ or $t_{2g}^1e_g^0$) the spin transfer to the 2s (or the sp^3 hybrid) orbital of Phosphorus occurs from the t_{2g} orbitals (via π overlap with a p orbital of oxygen)^{149,150}. For LiVPO_4F a relatively sharp ^{31}P MAS NMR signal is located at 3871 ppm (peak#5 in **Figure II-38**) and another weaker one, overlapped with a spinning side band is located at 3128 ppm (peak#4). That latter isn't expected regarding the unique phosphorous site in the structure and could correspond to the defects' contribution (better seen by ^7Li NMR). The two signals at 1613 ppm and 1441 ppm (peaks#1 and 2) observed for LiVPO_4O confirm the existence of two crystallographic sites in this phase. By analogy with the other vanadium based Tavorite compositions, it is possible to assign the contribution at 3871 ppm (peak#5) to LiVPO_4F -type and at 1441 and 1613 ppm (peak#1 and peak#2) to

LiVPO_4O -type environments respectively. Another contribution is located at 3100 ppm (peak#4) and a very broad one (or maybe several strongly overlapped ones) is located around 2500 ppm (or between 1750 and 2750 ppm, peak#3). The probabilistic approach used to describe the ^7Li NMR signature isn't appropriated for ^{31}P NMR due to the very broad signal obtained, the overlap with spinning side bands and thus the difficulty to obtain a reasonable fit.

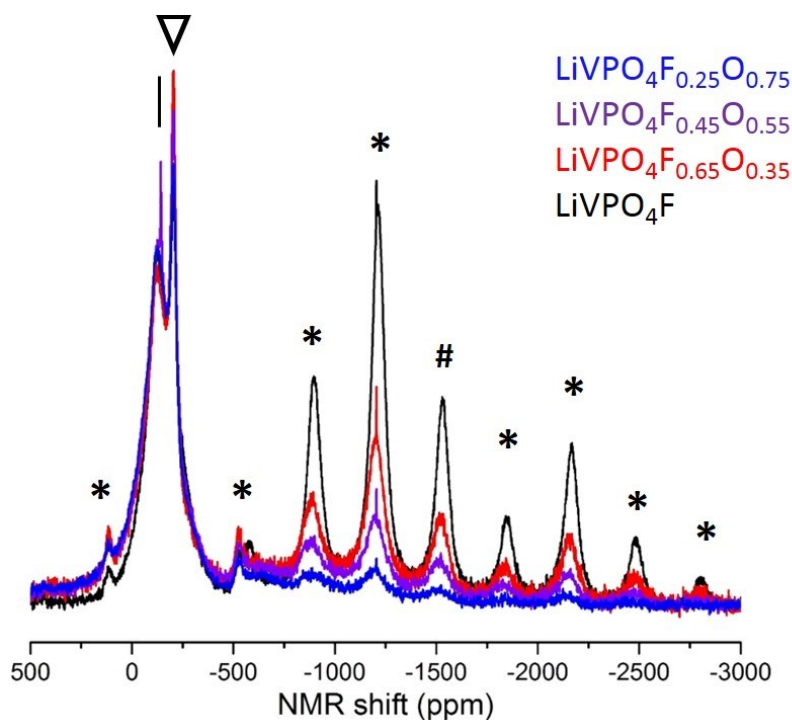


Figure II-39: ^{19}F MAS NMR spectra of the whole series of $\text{LiVPO}_4\text{F}_{1-y}\text{O}_y$ compositions with isotropic peaks highlighted by #, their spinning side bands by * the additional signals assigned to LiF and the probe contribution are marked as ∇ and | respectively.

^{19}F MAS NMR spectra of the $\text{LiVPO}_4\text{F}_{1-y}\text{O}_y$ series are compared in **Figure II-39**. These spectra exhibit a strong parasitic contribution from the probe (which contains Teflon) around -150 ppm and from LiF impurity at -208 ppm. The isotropic peak is located at -1500 ppm for LiVPO_4F and all other contributions regularly separated are assigned to spinning side bands¹²⁶. Surprisingly, no other peak which could be assigned to a Fluorine atom in interaction with V^{4+} cations can be detected for mixed valence samples. The absence of signal cannot be attributed to the absence of fluorine in the neighboring V^{4+} because no signal is seen for V^{4+} -rich phase VPO_4F by ^{19}F NMR¹²⁶. Our hypothesis to explain this absence of contribution is to consider the absence of interaction between V^{4+} and fluorine. Actually, in this compound, as mentioned above the d_{xz} and d_{yz} orbitals of V^{4+} involved in a vanadyl bond are empty. As the fluorine is located on the axis perpendicular to the only the t_{2g} orbital occupied of $\text{V}^{4+}=\text{O}$ (*i.e.* d_{xy}) the spin transfer between the d_{xy} orbitals of vanadium towards fluorine's orbitals can't occur even if

fluorine belongs to the first coordination sphere of vanadium at a short distance from the magnetic center. The global intensity of this signal decreases gradually with the rise of the average vanadium oxidation state due the replacement of oxygen for fluorine. Nevertheless, due to the presence of the probe signal (maybe overlapped with spinning side bands) the integration of the NMR signal can't be precisely performed. However, a slight shift (around 10 ppm) and a slight broadening of the ^{19}F signal for $\text{LiVPO}_4\text{F}_{1-y}\text{O}_y$ series is detected. That is probably due to the wide distribution of Fluorine environments.

II-3d. Summary and prospects

In summary, a one-step synthesis of the mixed valence $\text{LiV}^{3/4+}\text{VPO}_4\text{F}_{1-y}\text{O}_y$ Tavorite phases controlling the substitution rate is reported here. In these materials, the crystal field induces a significant deviation from the Vegard's law correlated to anisotropic strains' effects. EXAFS partially explains this offset from the Vegard's law, predicting the shrinkage of V^{4+} octahedra in a mixed fluorine/oxygen environment leading to a shortening of the cell parameters related to the propagation direction of the chains of octahedra. This behavior has been assigned to the competition between the ionicity of $\text{V}^{3+}\text{-F}$ versus the covalency of the $\text{V}^{4+}=\text{O}$ bonds and has been investigated combining diffraction and spectroscopy techniques. Due to the disorder, both SXRPD and ND predict the presence of purely centrosymmetric vanadium octahedra whereas XANES and Raman clearly highlight local vanadyl-type distortions. MAS NMR revealed that the local environments generated are similar to those of the observed as local defects in LiVPO_4F . The DFT studies conducted to explain these defects have previously predicted that they could originate from a partial substitution of fluorine by oxygen accompanied to lithium vacancy at the neighboring leading to local pairs of V^{4+} inside V^{3+} -rich chains of octahedra. The hypothesis of lithium deficit is invalidated in this work but the partial clustering of V^{4+} domains have been suggested by the results of 2D ^7Li NMR which have to be further confirmed by a careful interpretation of the NMR spectra (1D and 2D). Indeed, currently, the NMR signatures remain unexplained and DFT calculations could be a tool of choice for their interpretation.

The spectroscopic study highlighted that these defects strongly impact the electronic structure of vanadium's orbitals and *a fortiori* the electrochemical behavior. In following part, the influence of vanadyl-type defects' concentration on electrochemical performance of $\text{LiVPO}_4\text{F}_{1-y}\text{O}_y$ materials will be investigated.

II-4. Impact of vanadyl-type defects on electrochemical performance, on phase diagram and on redox mechanisms.

We suspect that all LiVPO₄F reported in literature present various amount of vanadyl-type defects. The electrochemical performance might closely depend on their concentrations/distributions in a similar way than the carbon coating or particles' sizes. In this section we will discuss the influence of the vanadyl environments on the electrochemical properties, on the phase diagrams (through *operando* SXRPD analyses), on the redox mechanisms (through *operando* XANES experiments) and on the local structure (through *operando* EXAFS). The ability of vanadium to be stabilized in various oxidation states allows to play with the V²⁺/V³⁺, V³⁺/V⁴⁺ and V⁴⁺/V⁵⁺ redox couples, by either inserting or extracting lithium into/from LiVPO₄F_{1-y}O_y. The complex processes involved in the two reactions will be investigated separately in the following part.

II-4a. High voltage region, an optimal vanadyl-type defects' concentration

i. Evidence of an optimal vanadyl-type defects' concentration

Figure II-40 gathers the galvanostatic data and the corresponding derivatives obtained for the mixed valence materials cycled in the 3.0 – 4.6 V vs. Li⁺/Li voltage range (involving the V³⁺/V⁴⁺ and V⁴⁺/V⁵⁺ redox couples) at C/10 and at C/50 under GITT conditions. In this voltage region, the lithium extraction from LiVPO₄F corresponds to the oxidation of V^{III} to V^{IV} whereas the V^{IV}/V^V redox couple is involved for LiVPO₄O. The lithium deintercalation from LiVPO₄F occurs at an average voltage of 4.25 V vs. Li⁺/Li while it occurs at a lower potential (3.95 V vs. Li⁺/Li for V^{IV}/V^V) for LiVPO₄O⁹². Actually, for that latter, due to the presence of vanadyl bonds, the redox couple involved is the {V=O}²⁺/{V=O}³⁺ one and the presence of this strongly covalent bond acts as a reverse inductive effect which tends to decrease significantly the voltage of the V⁴⁺/V⁵⁺ redox couple in LiVPO₄O. The phase diagram involved during Lithium extraction from LiVPO₄O is a single biphasic reaction until the VPO₄O composition is reached⁹⁶. For LiVPO₄F, a more complex mechanism occurs with the formation of an intermediate Li_{0.67}VPO₄F composition during charge which isn't observed during discharge²⁰. Similarly to the electrochemical process involved for LiVPO₄F, those associated with LiVPO₄F_{1-y}O_y samples seem to be asymmetric. For instance, three peaks are observed at 4.21, 4.25 and 4.27 V vs. Li⁺/Li on the derivative curve of the first charge of the Li // LiVPO₄F_{0.65}O_{0.35} cell whereas only one asymmetric peak can be detected during the following discharge (at 4.19 V vs. Li⁺/Li). On the GITT profiles, these transitions don't appear as obvious masked by the continuous increase

of the equilibrium voltage suggesting monophasic reactions during lithium extraction. Additional peaks are observed on the derivative curve of $\text{LiVPO}_4\text{F}_{0.45}\text{O}_{0.55}$ (at 3.6, 3.7 and 4.1V vs. Li^+/Li): they correspond to the contribution of the electrochemically active $\text{Li}_3\text{V}_2(\text{PO}_4)_3$ impurity⁶⁵. Moreover, the comparison of dQ/dV curves for the 1st and the 2nd cycles highlights significant differences: a shift and a broadening of the derivative peaks are observed after one cycle. An irreversible reaction seems to occur during the first cycle which could explain the rather large irreversible observed capacity for the first cycle when compared to the following cycles.

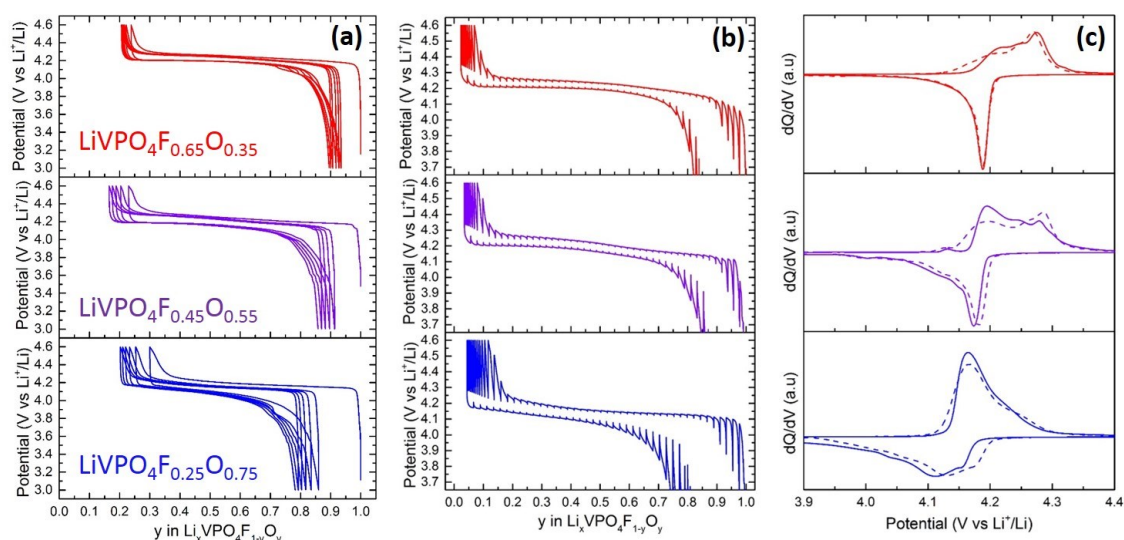


Figure II-40: (a) Galvanostatic profiles obtained versus Lithium at a C/10 rate for $\text{LiVPO}_4\text{F}_{0.25}\text{O}_{0.75}$ (blue line), $\text{LiVPO}_4\text{F}_{0.45}\text{O}_{0.55}$ (purple line) and $\text{LiVPO}_4\text{F}_{0.65}\text{O}_{0.35}$ (red line) in the high voltage domain (*i.e.* between 3.0 and 4.6 V vs. Li^+/Li). (b) GITT profiles of the materials at C/5 (1h pulse and relaxation until $dV/dt < 4\text{mV/h}$). (c) The comparison of dQ/dV curves of the 1st (solid lines) and 2nd (dot lines) cycles.

Figure II-40 reveals, additionally, a clear decrease of the irreversible capacity as the fluorine content in the materials is increased conferring to the fluorine rich materials a higher reversible capacity. Moreover, the polarization tends to decrease (*i.e.* 130mV, 100 mV and 70 mV respectively for $y = 0.75, 0.55$ and 0.35 in $\text{LiVPO}_4\text{F}_{1-y}\text{O}_y$) and the average voltage tends to increase with the rise of fluorine content in the material (*i.e.* 4.13 V, 4.20 V and 4.22V vs. Li^+/Li respectively for $y = 0.75, 0.55$ and 0.35 in $\text{LiVPO}_4\text{F}_{1-y}\text{O}_y$). From these observations, it appears that the fluorine rich solid solution materials deliver the better performance, to be compared with that of LiVPO_4F . **Figure II-41** shows the evolution of the discharge capacity as a function of the cycling number at various C-rates (*i.e.* 5 cycles at C/10, C/5, C/2, C, 2C, C, C/2, C/5, C/10 and then 50 cycles at C) for $\text{LiVPO}_4\text{F}_{1-y}\text{O}_y$ materials (with y between 0 and 0.75). The LiVPO_4F compared in this figure is a quasi-stoichiometric one obtained by a different synthesis (described precisely in the **section II-1**) whose morphology and Carbon coating are very similar

to those of mixed valence phases (see **Figure II-27**). Even if the initial reversible capacity at low rate of LiVPO_4F is the highest of the studied materials (122, 109, 102, 89 mAh/g respectively from $y=0$ to 0.75), its capacity retention and rate capability decrease faster. Indeed after 5 cycles at C/10 a loss of 20% of the reversible capacity is observed for LiVPO_4F whereas no significant decrease is observed for the mixed valence materials. Moreover, as the rate is increased, the reversible capacity delivered by LiVPO_4F decreases strongly until reaching 15mAh/g at 2C whereas at this rate the capacity provided by the $\text{LiVPO}_4\text{F}_{1-y}\text{O}_y$ samples is several times larger (62, 55 and 40 mAh/g respectively for $y = 0.35$ to 0.75). However, the performance delivered by our LiVPO_4F sample are rather poor compared to the better ones reported in literature^{14,15}.

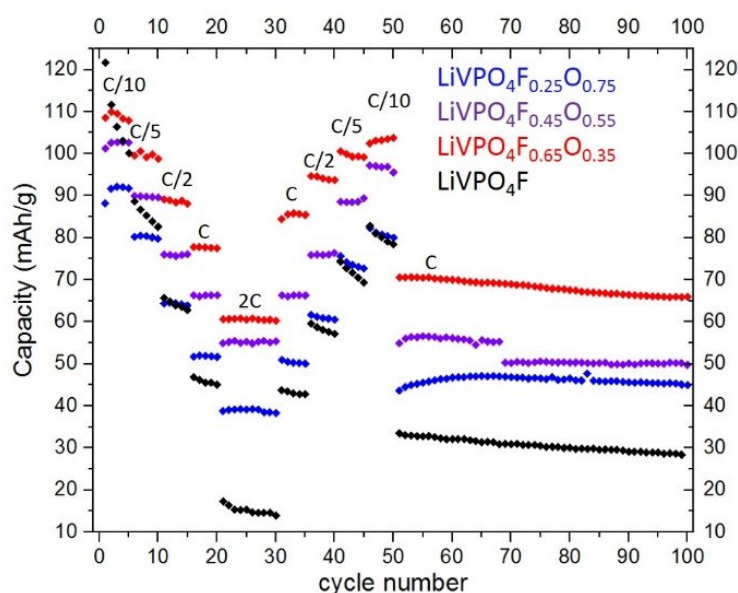


Figure II-41: Evolution of discharge capacity of the $\text{LiVPO}_4\text{F}_{1-y}\text{O}_y$ materials at different C-rates (from C/10 to 2C) in function of cycle number.

The weak amount of defects in our LiVPO_4F materials could participate to these poor performance. But, in such kind of low electronic conductors, the optimization of the carbon coating and the particles' size is essential to provide good performance. There is no doubt that the morphology and carbon coating of our samples aren't optimal regarding the performance that they deliver. However the materials compared in this work present similar coating and particle's sizes and the performance delivered by the solid solution samples are better than those of the stoichiometric material and even better when their fluorine content increases. It would seem that an optimal vanadyl-type defects' concentration (located between the $\text{LiVPO}_4\text{F}_{0.65}\text{O}_{0.35}$ and the LiVPO_4F compositions) exists which would improve the transport properties. Actually, for high voltage materials such as LiVPO_4F , the charge capacity is often limited by the polarization which makes that the cut-off voltage (*i.e.* 4.6 V vs. Li^+/Li , stability

limit of the classical electrolytes) is reached before the reaction is completed. Indeed, many works reported high discharge capacity at high rate after low charge rate^{151,152}. Therefore, the decrease of the polarization and voltage by introducing vanadyl-type defects in the LiVPO_4F structure benefits to the rate capability. The decrease of the polarization can originate from the enhancement of either electronic or cationic mobility. Typically, the mixed valence states of transition metals can increase electronic conductivity by enhancing the hopping process between cations with different oxidation states. Moreover, the distortion of the network due to the competitive formation between $\text{V}^{3+}\text{-F}$ and $\text{V}^{4+}=\text{O}$ (*i.e.* non-Vegard's law behavior) could open new diffusion paths for lithium and thus improve the ionic diffusion

The complex electrochemical signatures observed suggest complex phase diagrams during lithium extraction from $\text{LiVPO}_4\text{F}_{1-y}\text{O}_y$. In order to understand the origin of the optimal vanadyl-type defects' concentration and the irreversible reaction which could occur during the first cycle, the investigation of the phase diagrams is required. Therefore, in the following we will study in details the phase diagram involved by *operando* SXRPD during lithium extraction.

ii. Understanding of the optimal vanadyl-type defects' concentration

Figure II-42 shows the comparison between the patterns of $\text{LiVPO}_4\text{F}_{0.45}\text{O}_{0.55}$ recorded *in situ* (in the electrochemical cell) and in a sealed capillary.

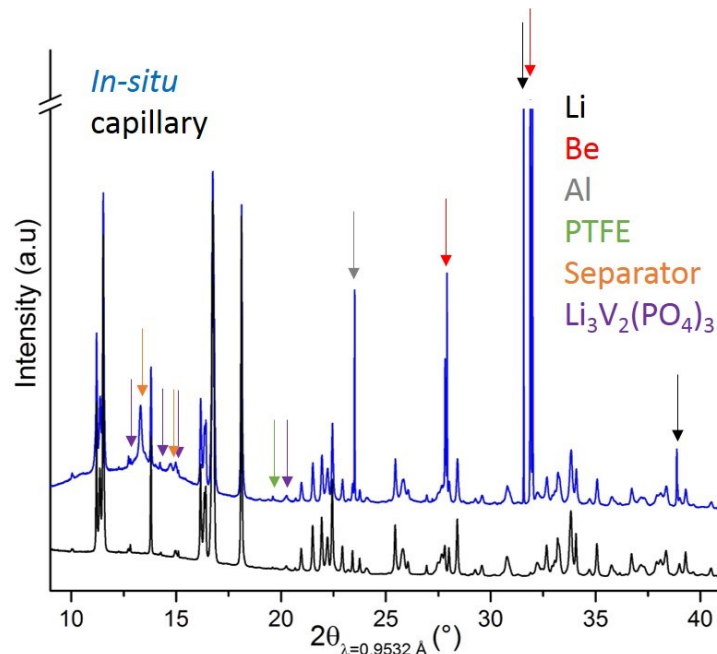


Figure II-42: (a) Comparison of SXR D patterns of the pristine $\text{LiVPO}_4\text{F}_{0.45}\text{O}_{0.55}$ material recorded *in situ* (in the electrochemical cell developed for transmission experiments) (blue) and in a capillary (black). The arrows mark peaks not belonging to the $\text{LiVPO}_4\text{F}_{0.45}\text{O}_{0.55}$ phase, *i.e.* originating from the lithium metal as negative electrode, the Beryllium window, the aluminum collector, the binder PTFE, the separator and a $\text{Li}_3\text{V}_2(\text{PO}_4)_3$ impurity).

The pattern obtained *in situ* presents a series of additional peaks. Indeed, during *in-operando* experiments performed in transmission mode, the beam is going through all the layers of the battery, generating narrow Bragg peaks from lithium (negative electrode), beryllium (two windows one on both sides of the cell stacking), and Aluminum (current collector), as well as broad PTFE (binder) and separator contributions. The refinement of these additional peaks isn't possible due to their different zero shifts. However, a detailed knowledge of the pristine phase allows to exclude the 2θ regions where these peaks appear and to achieve a structural determination very similar to the one described in the **section II-3**. Moreover, due to the setup constraints, the electrode used for this *operando* diffraction experiment has to be self-supported, and the use of PTFE as binder is required (instead of PVDF). This binder being a low electronic conductor, in order to overcome the kinetic limitations generated, the amount of carbon is increased within the electrode, with thus a mass ratio between active material, carbon and binder different to the one use for classical electrochemical tests (*i.e.* 70/20/10 vs. 80/10/10 for galvanostatic curves showed in the previous section). The PTFE/active material ratio has to remain limited. Indeed, an increasing intensity for the main Bragg peaks of the PTFE would lead to a significant overlapping with the reflections of the material, and would thus be highly detrimental to obtain data of good quality. The electrochemical signature obtained in the *in situ* cell differs slightly compared to the one obtained in coin cell. The **Figure II-43** illustrates these differences.

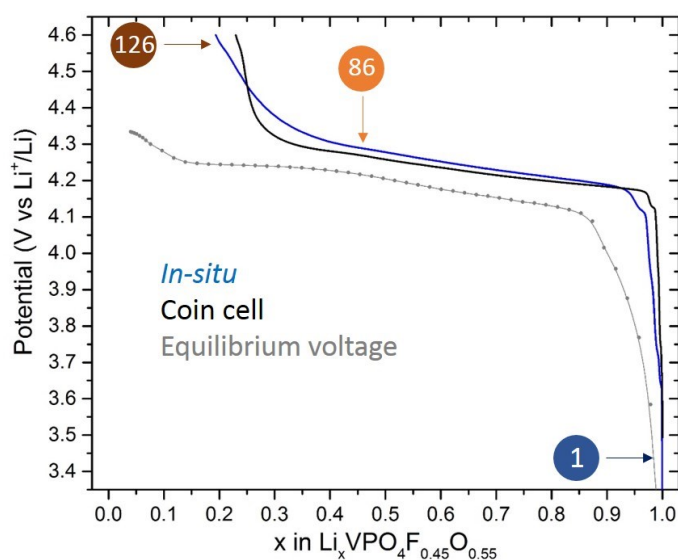


Figure II-43: Comparison between voltage profiles obtained *in situ* in the electrochemical cell and in a classical coin cell. The equilibrium voltage (obtained from GITT, Figure II-40) is also shown in this figure.

Figure II-44 shows the *operando* SXRPD patterns recorded during lithium extraction from $\text{LiVPO}_4\text{F}_{0.45}\text{O}_{0.55}$ and the SXRPD pattern of $\text{VPO}_4\text{F}_{0.45}\text{O}_{0.55}$ obtained *ex situ* (*i.e.* cycled in a

swagelok cell at C/200 until 4.6 V vs. Li⁺/Li, recovered, washed with DMC, dried under vacuum and introduced in a sealed capillary filled under Ar). As suggested by the galvanostatic data, the full delithiation isn't achieved. Indeed, the last pattern recorded corresponds to the Li_{~0.2}VPO₄F_{0.45}O_{0.55} composition and is different than the one of the fully delithiated material (obtained *ex situ*). However, at this point, the final phase has already started to growth. The key patterns, corresponding to specific compositions are also shown in **Figure II-44**.

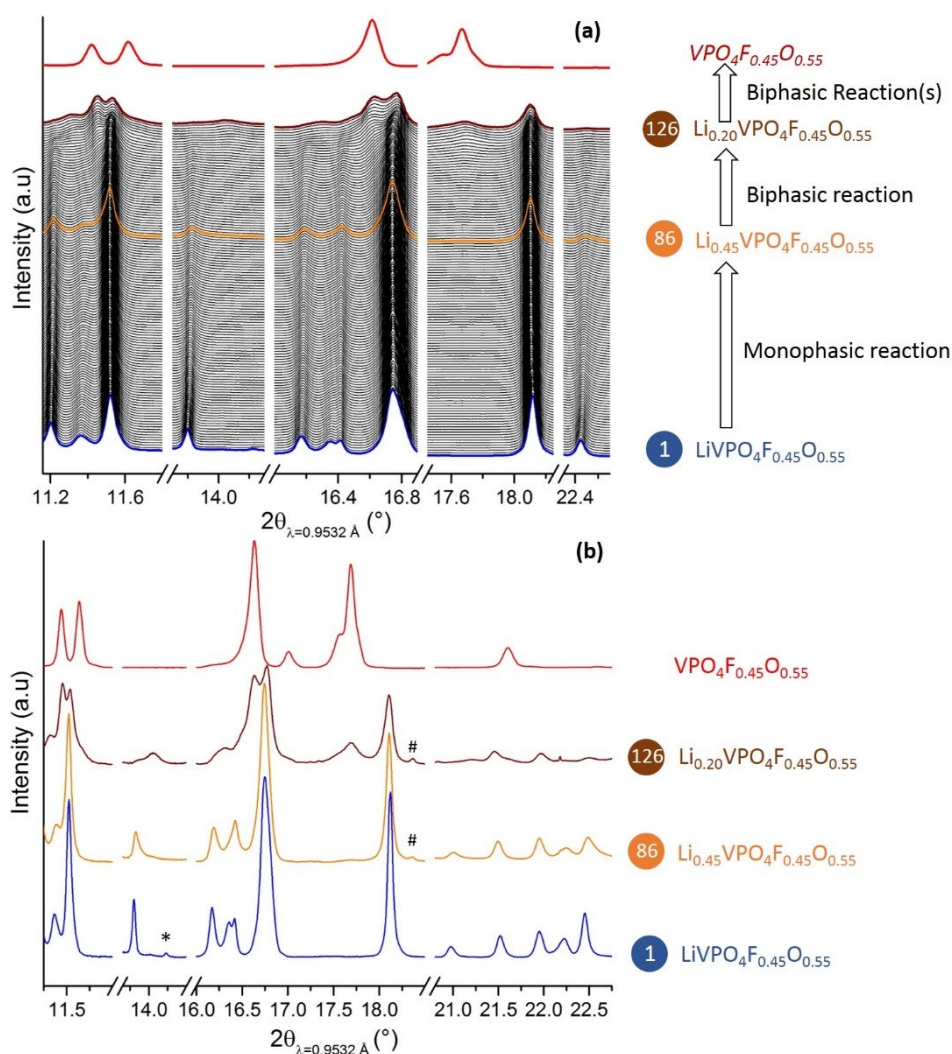


Figure II-44: (a) SXRPD patterns obtained operando during lithium extraction from LiVPO₄F_{0.45}O_{0.55}, the material corresponding to the red pattern has been obtained *ex-situ* (b) Selected SXRPD patterns at specific compositions. The Bragg peak marked as * belongs to the electrochemically active Li₃V₂(PO₄)₃ impurity. Those marked as # belong to partially delithiated LiV₂(PO₄)₃.

During the first step, anisotropic weak shifts of the initial Bragg peaks are observed. Indeed, the *a* and *b* parameters decrease while the *c* parameter weakly increases. That latter is the parameter along which the vanadyl bonds are propagated. Therefore, the V-X distances along the chains don't evolve significantly (from 1.952(9) to 1.953(9) in average on the two

vanadium sites). In parallel, the Bragg peaks related to the electrochemically active $\text{Li}_3\text{V}_2(\text{PO}_4)_3$ impurity disappear (12.8 , 14.3 , 15.0 and 20.5°) and those of the partially delithiated phase (*i.e.* $\text{LiV}_2(\text{PO}_4)_3$) appear at (15.5 and 18.3°)⁶⁵ at the very beginning of the charge. That is in good agreement with the small shoulders seen on the voltage profile at 3.6 , 3.7 and 4.1V vs. Li^+/Li (see **Figure II-44**). Considering these phases as minor impurities and the contributions inherent to the *in situ* experiments in transmission mode (Lithium, Beryllium, Aluminum, PTFE and separator) no additional peaks related to a superstructure have been detected. Therefore, the single Lithium site continuously depopulated is very similar to the one of the starting phase (*i.e.* an LiO_4X environment with distances ranging between $1.93(4)$ and $2.25(3)$ vs. $1.88(4)$ and $2.31(3)$ in $\text{LiVPO}_4\text{F}_{0.45}\text{O}_{0.55}$).

The following delithiation step leads to the appearance of the $\text{Li}_{\sim 0.27}\text{VPO}_4\text{F}_{0.45}\text{O}_{0.55}$ phase according to a pseudo-biphasic mechanism. Indeed, the refinement clearly highlights that the $\text{Li}_{0.45}\text{VPO}_4\text{F}_{0.45}\text{O}_{0.55}$ phase disappears at the expense of the $\text{Li}_{\sim 0.27}\text{VPO}_4\text{F}_{0.45}\text{O}_{0.55}$ one but the cell parameters of each phase still evolve significantly. That latter is characterized by a slightly smaller cell volume ($V/Z = 85.61(1)$) and average distances around vanadium of $1.97(1)$ Å. The fine structural description of this phase is somehow tricky due to (i) the presence of $\text{Li}_{0.45}\text{VPO}_4\text{F}_{0.55}\text{O}_{0.45}$ and $\text{VPO}_4\text{F}_{0.45}\text{O}_{0.55}$ as additional phases in the corresponding SXRPD pattern (**Figure II-45**) (ii) to the small amount of lithium inside the structure which doesn't allow to refine its position and (iii) to the strong anisotropic broadening.

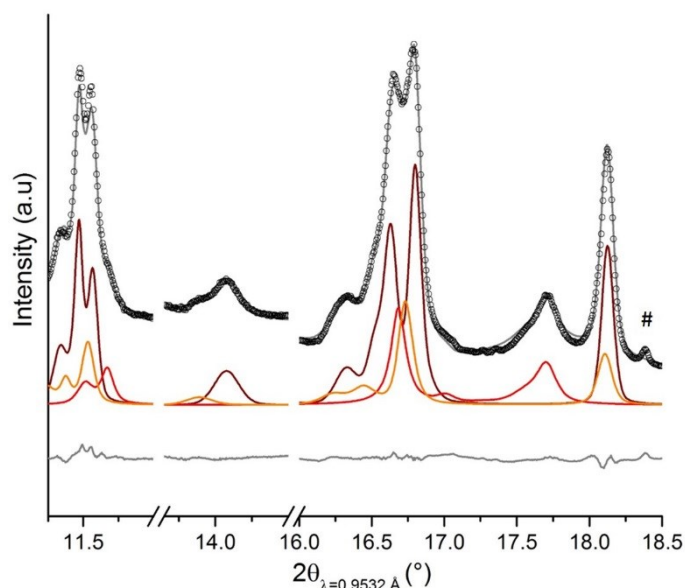


Figure II-45: Rietveld refinement of the last pattern obtained operando (#126, corresponding to an overall composition of $\text{Li}_{0.2}\text{VPO}_4\text{F}_{0.45}\text{O}_{0.55}$) using 3 phases: $\text{Li}_{0.45}\text{VPO}_4\text{F}_{0.45}\text{O}_{0.55}$ (orange), $\text{Li}_{\sim 0.27}\text{VPO}_4\text{F}_{0.45}\text{O}_{0.55}$ (brown) and $\text{VPO}_4\text{F}_{0.45}\text{O}_{0.55}$ (red) with their respective contributions. The peak highlighted by # corresponds to the $\text{LiV}_2(\text{PO}_4)_3$ impurity.

As the full delithiation can't be achieved *operando* (despite the appearance of $\text{VPO}_4\text{F}_{0.45}\text{O}_{0.55}$ at the very end of the experiment), the SXRPD pattern of the fully delithiated material was obtained ex-situ in a standard electrochemical cell. It reveals a complex profile with strong broadening, despite the soft electrochemical extraction conditions used (C/200, *i.e.* conditions theoretically close to the equilibrium). The structure of this phase remains undetermined. Indeed, although the main contributions can be explained in a monoclinic cell (either in a Cc or in $P2_1/c$ or $C2/c$ space group, the corresponding cell parameters are reported in **Table II-15**), some additional peaks are observed (16.2 , 16.6 , 17.9 and 30.0°) (**Figure II-46a**). Even using lower symmetry (triclinic, $P-1$) and bigger cells ($Z = 4$), these peaks remain unexplained despite the additional Bragg positions generated, and only exotic cells have been found to be able to fit all the peaks (triclinic with $V > 1000 \text{ \AA}^3$). However, these additional contributions can be fitted using a secondary phase (**Figure II-46b**).

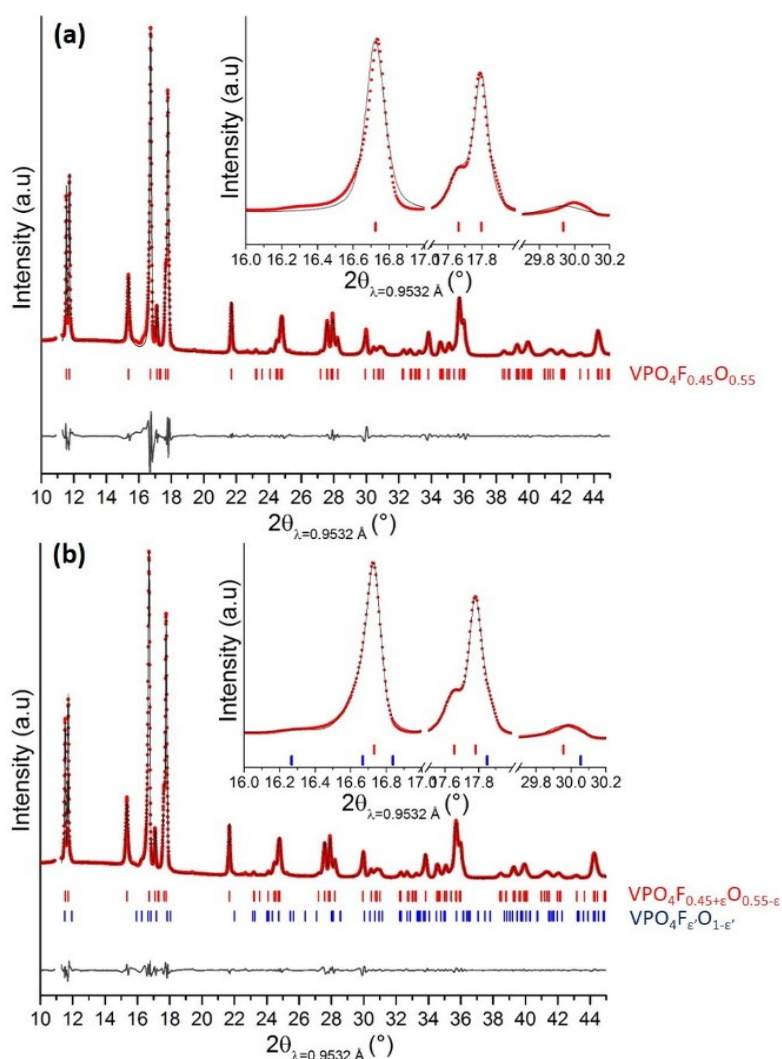


Figure II-46: (a) Rietveld refinements of $\text{VPO}_4\text{F}_{0.45}\text{O}_{0.55}$ phase in the $C2/c$ space group with a single phase and (b) adding the contribution of a secondary phase of VPO_4O -type. The theoretical Bragg positions are plotted as red ($\text{VPO}_4\text{F}_{0.45}\text{O}_{0.55}$ -type phase) and blue (VPO_4O -type phase) marks.

That reveals either the persistence of an intermediate phase (which would grow between the end of the *operando* experiment and the full delithiation) or the “demixing” of VPO₄F_{0.45}O_{0.55} into VPO₄F_{0.45+ε}O_{0.55-ε} and VPO₄F_εO_{1-ε} phases at high voltage, that found its origin by the probable partial clustering of oxygen rich and fluorine rich domains in the starting material. The hypothesis of the “demixing” is the most relevant one. Indeed, the main phase probed within *the ex situ* SXRPD pattern is rather close to the one observed as final phase during the *operando* experiments (*i.e.* $V/Z = 81.09(1) \text{ \AA}^3$ for the VPO₄F_{0.45+ε}O_{0.55-ε} obtained *ex situ* and refined in the *C2/c* space group vs. $81.17(1) \text{ \AA}^3$ for the phase obtained *operando*) whereas the additional minor phase, having a larger cell (*i.e.* *Cc* with $V/Z=81.60(8) \text{ \AA}^3$) is similar to a VPO₄O-type cell (*Cc* with $V/Z=81.98 \text{ \AA}^3$)⁹⁶.

Table II-15: Weight fraction, space group, cell parameters and average Vanadium-Ligand distances of the delithiated phases obtained *ex situ*. In **bold**, the most relevant model retained for the refinement of the whole series of *operando* SXRPD patterns.

Phases	%w	S.G	<i>a</i>	<i>b</i>	<i>c</i>	α	β	γ	V/Z	<V-X>
VPO ₄ F _{0.45+ε} O _{0.55-ε}	92(1)	<i>C2/c</i>	7.1966(3)	7.1303(2)	7.1742(3)	90	118.218(1)	90	81.09(1)	1.89(1)
VPO ₄ F _ε O _{1-ε}	8(1)	<i>Cc</i>	7.3033(9)	6.854(2)	7.222(2)	90	115.46(1)	90	81.60(8)	1.91(1)
VPO ₄ F _{0.45+ε} O _{0.55-ε}	92(1)	<i>P2₁/c</i>	7.1964(2)	7.1295(2)	7.1724(2)	90	118.197(2)	90	81.07(6)	1.90(1)
VPO ₄ F _ε O _{1-ε}	8(1)	<i>Cc</i>	7.299(9)	6.857(9)	7.219(2)	90	115.61(1)	90	81.47(9)	1.91(1)
VPO ₄ F _{0.45+ε} O _{0.55-ε}	92(1)	<i>Cc</i>	7.1963(1)	7.1284(1)	7.1713(1)	90	118.193(2)	90	81.06(3)	1.90(1)
VPO ₄ F _ε O _{1-ε}	8(1)	<i>Cc</i>	7.2963(8)	6.868(1)	7.222(1)	90	115.65(2)	90	81.56(8)	1.91(1)

The strong strains generated by the competition between the covalent V⁵⁺=O and the ionic V⁴⁺-F bonds at interface of oxygen-rich/fluorine-rich domains might even better highlight this phase separation only identified by local probes in the pristine material. That could explain the irreversible reaction which occurs during the first cycle as suggested by the different electrochemical signatures observed during the first and the second cycle (in the **Figure II-40c**). The Rietveld refinement of the structure of the main phase using the *C2/c* space group (*i.e.* VPO₄F-type model, shown in **Figure II-46**) provides constant distances along the chains ($d(V-X) = 1.94(1) \text{ \AA}$) whereas the *Cc* and *P2₁/c* space groups allow the formation of the vanadyl bond and generate an alternation between a short (1.89(2)) and a longer bond (1.98(2)) along the chains. This point is very meaningful for the understanding of the mechanisms involved during lithium extraction from LiVPO₄F_{0.45}O_{0.55} but we aren't able to choose one or the other model based on refinement considerations ($R_{\text{Bragg}} = 4.21, 4.12, 4.18\%$ and $\chi^2 = 56.1, 52.5, 54.2$ for Rietveld refinement performed in the *C2/c*, *Cc* and *P2₁/c* space groups respectively). However, the *C2/c* space group providing constant distances along chains seems more relevant to describe the long range structure of the main phase. Indeed, if the “demixing” aims to relax the strains imposed by the crystal field generating a fluorine-rich

$\text{VPO}_4\text{F}_{0.45+\epsilon}\text{O}_{0.55-\epsilon}$ and an oxygen rich $\text{VPO}_4\text{F}_\epsilon\text{O}_{1-\epsilon}$ phases, the distribution of distances along chains of octahedra in the fluorine enriched phase should, from the XRD point of view, be similar to those observed in VPO_4F . We thus chose the $C2/c$ space group for the refinement of the whole *in-operando* experiment. The evolution of the weight fractions of the different phases and the evolution their cell volumes are given in **Figure II-47**.

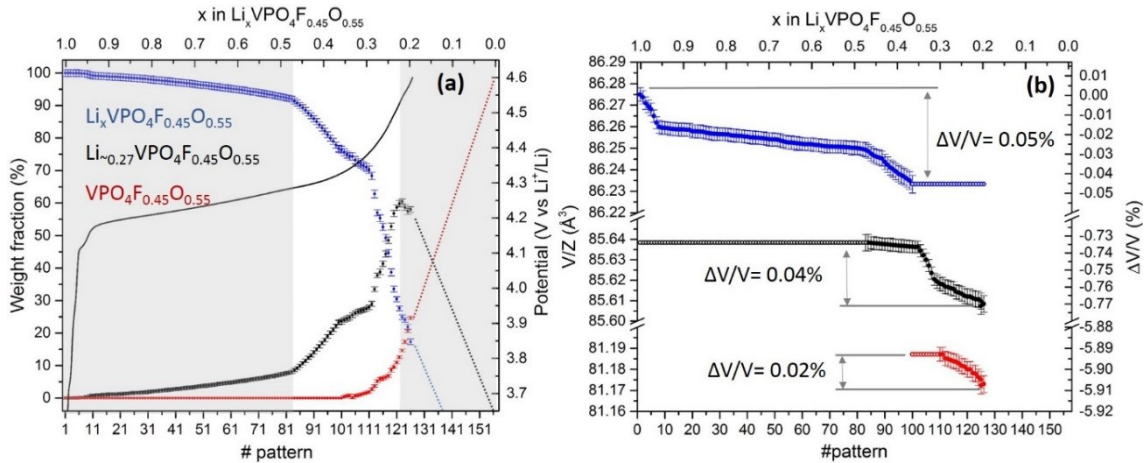


Figure II-47: (a) evolution of the weight fractions and (b) cell volumes of the phases appearing along reaction path.

This figure reveals that the extraction mechanisms (monophasic or biphasic) cannot be clearly defined. Indeed, during the “apparent biphasic processes”, the volume changes of each phase are in the same order of magnitude than those measured during the “apparent monophasic mechanism”. Moreover during the first step of the charge (*i.e.* $1 > x > 0.45$), the intermediate $\text{Li}_{\sim 0.27}\text{VPO}_4\text{F}_{0.45}\text{O}_{0.55}$ phase starts to grow, therefore some thermodynamically forbidden (at least at equilibrium state) tri-phasic domains appear. The disordered O^{2-}/F distribution in the starting phase could induce local inhomogeneous delithiation. This phenomenon is seen from XRD point of view as a combination between monophasic and biphasic reactions whereas it could actually correspond to an infinity of successive biphasic reactions with an unreachable equilibrium state.

Operando SXRPD on the two other compositions (*i.e.* $\text{LiVPO}_4\text{F}_{0.35}\text{O}_{0.65}$ and $\text{LiVPO}_4\text{F}_{0.25}\text{O}_{0.75}$) were also performed in order to investigate the influence of the vanadyl-type defects’ concentration on the nature of phases in presence during lithium extraction. The diffraction patterns obtained during these experiments are shown in the **Figure Annex-II-4** and **Figure Annex-II-5** respectively for $\text{LiVPO}_4\text{F}_{0.35}\text{O}_{0.65}$ and $\text{LiVPO}_4\text{F}_{0.75}\text{O}_{0.25}$ and summarized in the **Figure II-49**. They reveal a similar structural evolution with an apparent solid solution process at the beginning of the charge, whose composition domain depends on the amount of V^{4+} in the starting material. Indeed, this mechanism is observed for $1 > x > 0.25$ and $1 > x > 0.65$

respectively for $y = 0.75$ and $y = 0.35$ (until $\Delta x = y$) in $\text{Li}_x\text{VPO}_4\text{F}_{1-y}\text{O}_y$. Therefore, it could correspond to the activation of the $\text{V}^{4+}=\text{O}/\text{V}^{5+}=\text{O}$ redox couple before the activation of the $\text{V}^{3+}/\text{V}^{4+}$ in a vanadyl-free environment. Moreover, as observed for $\text{Li}_x\text{VPO}_4\text{F}_{0.45}\text{O}_{0.55}$, the structural changes observed during this monophasic process are very weak. **Figure II-48** compares the volume changes ($\Delta V/V$) in function of the state of charge for the three samples studied.

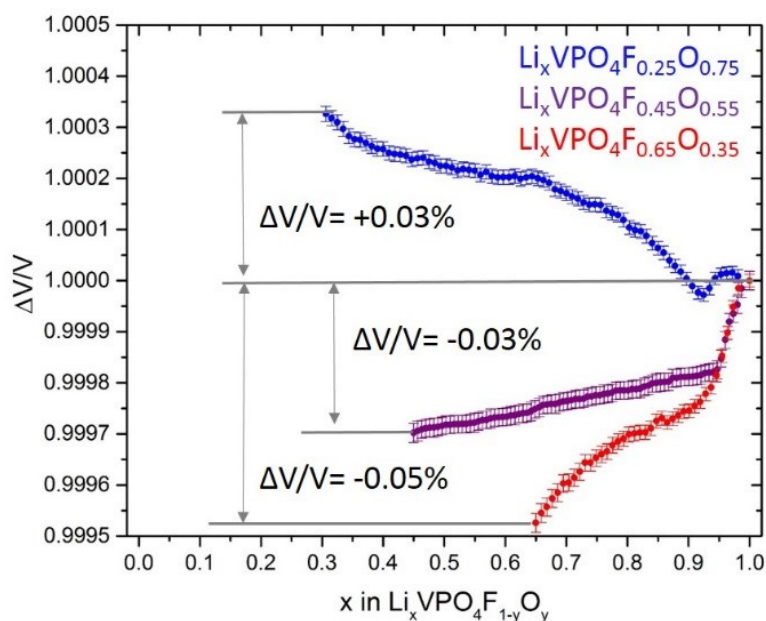


Figure II-48: Evolution of the volume changes of each $\text{Li}_x\text{VPO}_4\text{F}_{1-y}\text{O}_y$ sample as function of x during the first step of the charge (i.e. until $\Delta x = y$).

The volume changes observed are around +0.03%, -0.03% and -0.05% respectively for $y=0.75$, 0.55 and 0.35 in $\text{Li}_x\text{VPO}_4\text{F}_{1-y}\text{O}_y$. The competition between the strong covalency of the growing $\text{V}^{5+}=\text{O}$ entities and the high ionicity of the $\text{V}^{3+}-\text{F}$ bonds could freeze the system. The subsequent lithium depopulation occurs also according to two consecutive pseudo biphasic processes involving the intermediate phases for $x \sim 0.17$ in $\text{Li}_x\text{VPO}_4\text{F}_{0.25}\text{O}_{0.75}$ and $x \sim 0.43$ in $\text{Li}_x\text{VPO}_4\text{F}_{0.65}\text{O}_{0.35}$ (see **Figure II-49**). This phase transition seems to present some similarities with the one observed at the $\text{Li}_{0.67}\text{VPO}_4\text{F}$ composition for LiVPO_4F . Indeed, whatever the oxidation state of vanadium in the starting materials, the phase transition appears at a $\text{V}^{3+}/\text{V}^{4+}$ ratio approximately equivalent to 2 (see **Figure II-49**). Thus, the driving force of the Lithium ordering observed in $\text{Li}_{0.67}\text{VPO}_4\text{F}$ could be the $\text{V}^{3+}/\text{V}^{4+}$ ratio. Nevertheless, even using bright SXRPD source we weren't able to identify the superstructure peaks observed at the $\text{Li}_{0.67}\text{VPO}_4\text{F}$ composition in the $\text{Li}_x\text{VPO}_4\text{F}_{1-y}\text{O}_y$ samples.

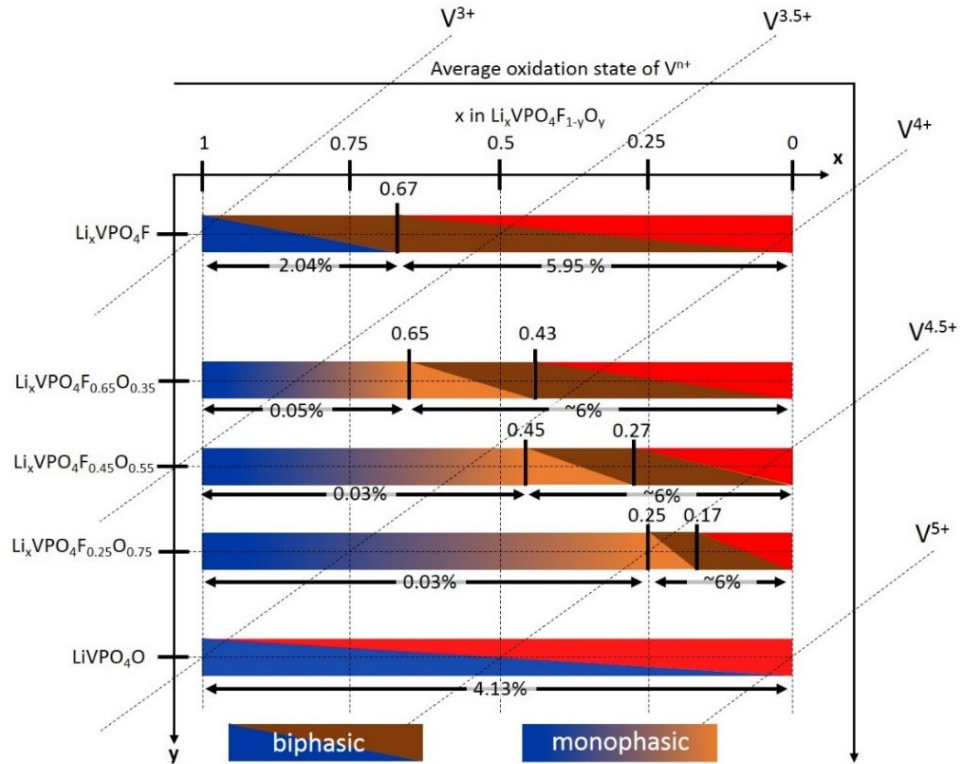


Figure II-49: Schematic phase diagrams observed by X-ray diffraction for the $\text{Li}_x\text{VPO}_4\text{F}_{1-y}\text{O}_y$ system. The “demixing” observed at the end of the charge isn’t represented.

The partial substitution of fluorine by oxygen in $\text{LiVPO}_4\text{F}_{1-y}\text{O}_y$ materials leads to smaller volume changes along the lithium extraction compared to the one observed for the $\text{Li}_x\text{VPO}_4\text{F}^{20}$ (~6% vs. 8.0%) but remaining higher to the one of $\text{Li}_x\text{VPO}_4\text{O}$ (*i.e.* 4.1%)⁹⁶. Although the volume changes observed during electrochemical cycling of LiVPO_4O are smaller, the structural modifications involved by the oxidation of V^{4+} to V^{5+} are strong (*i.e.* from a distorted vanadium octahedron to a pyramid with an elongation of the “anti-vanadyl” $\text{V}^{5+}\text{-O}$ bond and shortening of the V-O bonds belonging to the square plane).

The weaker structural changes for the $\text{Li}_x\text{VPO}_4\text{F}_{1-y}\text{O}_y$ samples seems to be at the origin of their better electrochemical performance compared to the end-member phases ($\text{Li}_x\text{VPO}_4\text{F}$, $\text{Li}_x\text{VPO}_4\text{O}$). Moreover, as (i) the structure seems to be frozen during the first step (solid solution domain until $\Delta x = y$ in $\text{Li}_x\text{VPO}_4\text{F}_{1-y}\text{O}_y$) and as (ii) the further Lithium depopulation to reach the fully delithiated state leads to similar volume changes (~6%) whatever the F^-/O^{2-} substitution ratio, the optimal vanadyl-type defects’ concentration could arise from the balance between the two processes (*i.e.* (i) and (ii)). Indeed, for oxygen-rich materials (characterized by a wide solid solution domain) the structure undergoes major structural modifications in a narrow composition range ($\Delta V/V \sim 6\%$ for $\Delta x = 0.25$ in $\text{Li}_x\text{VPO}_4\text{F}_{0.25}\text{O}_{0.75}$) whereas for the fluorine-rich materials (showing a narrow solid solution domain), these changes are spread on a large composition range ($\Delta V/V \sim 6\%$ for $\Delta x = 0.65$ in $\text{Li}_x\text{VPO}_4\text{F}_{0.65}\text{O}_{0.35}$). That leads to softer structural

changes probably at the origin of the better rate capability and cycling stability of fluorine rich solid solutions.

Operando SXRPD allowed to get an overall view of the system but the average description provided by XRD lacks of details. Indeed, in the case of disordered O/F distribution and considering the lightness of Lithium, the description of the phases obtained during lithium extraction is only partial. However, the composition domains of each mechanism allow to make hypothesis about the redox processes involved: activation of the $\text{V}^{4+}=\text{O}/\text{V}^{5+}=\text{O}$ redox couple in the monophasic domains and of the $\text{V}^{3+}/\text{V}^{4+}$ during the following biphasic reactions. Therefore the inspection of the redox mechanisms thanks to XANES and the local environments around vanadium thanks to EXAFS reveals itself to be essential to get in depth understanding of the phenomena which occur.

iii. The redox processes

Operando XAS was performed at the V K-edge, spectra were recorded during the charge of the $\text{Li} // \text{LiVPO}_4\text{F}_{0.45}\text{O}_{0.55}$ cell at C/15 in the 3.0-4.5 V vs. Li^+/Li voltage range and they are shown in the **Figures II-50a** (1 scan of 5 minutes every 15 minutes leading to 56 spectra).

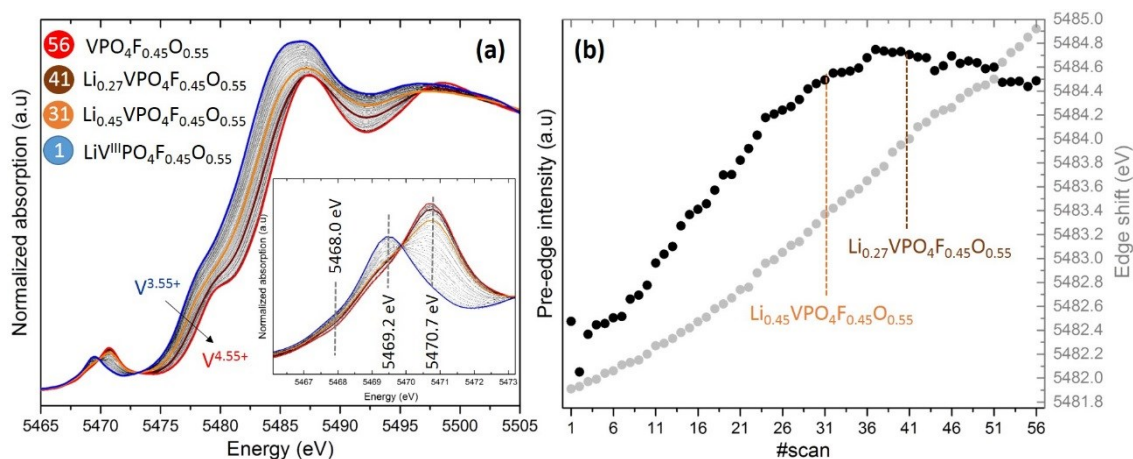


Figure II-50: (a) XANES spectra acquired in operando during Lithium extraction from $\text{LiVPO}_4\text{F}_{0.45}\text{O}_{0.55}$ and in inset the enlargement of the pre-edge region. The colored spectra (#1, #31, #41 and #56) corresponds to the specific compositions highlighted by operando SXRPD experiment (b) The evolution of the pre-edge intensity and the edge position in function of the scan number.

The Vanadium K edge XANES spectra exhibit several features as already largely discussed in this manuscript. The main absorption edge corresponds to the $1s \rightarrow 4p$ dipole-allowed transition. Its position is related to the valence state of the transition metal and to the ionic-covalent character of the bonds formed with its ligands¹⁴⁵. The rather linear shift of the edge towards higher energy from $\text{LiVPO}_4\text{F}_{0.45}\text{O}_{0.55}$ to $\text{VPO}_4\text{F}_{0.45}\text{O}_{0.55}$ (*i.e.* from 5481.9 to 5484.9

eV, see **Figure II-50b**) is consistent with an increase of the vanadium oxidation state during the charge without significant modification of the nature of the bond (ionic or covalent) between vanadium and its ligands. The weaker pre-edge contribution located between 5465-5473 eV arises from the theoretically 1s to 3d forbidden transition which becomes allowed due to distortion of the local environment around Vanadium. The Pre-edge lines are complex to identify and to attribute precisely since there are several contributions all along the electrochemical oxidation of $\text{LiVPO}_4\text{F}_{0.45}\text{O}_{0.55}$. However, as already largely discussed in this manuscript, the use of relevant Tavorite-type references allows to assign the peaks observed at 5468.0 to V^{3+} (Cf $\text{LiV}^{\text{III}}\text{PO}_4\text{F}$), at 5469.2 and 5470.7 eV to $\text{V}^{4+}=\text{O}$ and $\text{V}^{5+}=\text{O}$ contributions respectively (Cf $\text{LiV}^{\text{IV}}\text{PO}_4\text{O}$ and $\text{V}^{\text{V}}\text{PO}_4\text{O}$ see **Figure Annex-I-11**). **Figure II-50b** shows the parallel evolution of the pre-edge intensity and of the edge position. The edge shifts rather linearly during oxidation of vanadium whereas the pre-edge increases strongly until the spectrum 37 and then decreases slightly. This parallel evolution suggests that the whole set of data cannot be described as a simple linear combination of the initial and final spectra. In fact more complex processes seem to occur and therefore the whole data were analyzed using principal component analysis (PCA) combined with multivariate curves resolution (MCR)¹³¹.

The variance plot obtained from PCA given in **Figure II-51a** shows that about 99.74% of the variance of the XANES spectra can be described using three principal components. Although *operando* SXRPD analyses have shown that at least 4 distinct phases are required to explain the phase diagram observed upon Lithium extraction, the addition of a fourth component would only explain 0.05% and would constitute an over interpretation of the signal. Therefore, the residual part is considered as the experimental noise.

The three components thus obtained are shown in **Figure II-51** with the evolution of their relative concentrations along the electrochemical reaction. According to this evolution, these components can be described as follows: component#1 corresponds to the pristine material $\text{LiVPO}_4\text{F}_{0.45}\text{O}_{0.55}$ and the third component to the fully delithiated one $\text{VPO}_4\text{F}_{0.45}\text{O}_{0.55}$. Since component#2 never reaches 100% of the relative quantity, it cannot be found isolated in any spectrum and thus cannot be identified as a measured spectrum. However, its maximum being located at the $\text{Li}_{0.45}\text{VPO}_4\text{F}_{0.45}\text{O}_{0.55}$ composition, this component is assigned to this composition which corresponds to the phase identified at the end of the solid solution domain observed by *operando* SXRPD, when $\Delta x = y$ in $\text{Li}_x\text{VPO}_4\text{F}_{1-y}\text{O}_y$). Comparing the absorption energies of the main edge jump obtained for each component, 5481.9 eV, 5483.6 eV, and 5484.9 eV, it appears that it evolves linearly as a function of the oxidation state of vanadium. Their pre-edges show three main contributions observed at 5468.0, 5469.2 and 5470.7 eV with

different relative intensities along lithium extraction. Between component#1 and component#2, the clear decrease of the $\text{V}^{4+}=\text{O}$ contribution (*i.e.* 5469.2 eV) accompanied to an increase of the $\text{V}^{5+}=\text{O}$ (*i.e.* 5470.7 eV) one is observed, revealing the activation of the $\text{V}^{4+}=\text{O}/\text{V}^{5+}=\text{O}$ redox couple during the first part of the lithium extraction as suggested by *operando* SXRPD. For the component#3, a slight decrease of the V^{3+} contribution (*i.e.* 5468.0 eV) is observed. Therefore, the $\text{V}^{3+}/\text{V}^{4+}$ redox couple seems to be activated at higher voltage compared to the $\text{V}^{4+}=\text{O}/\text{V}^{5+}=\text{O}$ one leading to the formation of mixed valence $\text{V}^{3+}/\text{V}^{5+}$ phase at the end of the first vanadium oxidation step (*i.e.* $\text{Li}_{0.45}(\text{V}^{3+}_{0.45}\text{V}^{5+}_{0.55})\text{PO}_4\text{F}_{0.45}\text{O}_{0.55}$). The $\text{V}^{4+}=\text{O}/\text{V}^{5+}=\text{O}$ couple in LiVPO_4O being located at a lower potential than the $\text{V}^{3+}/\text{V}^{4+}$ couple in LiVPO_4F (*i.e.* 3.95 V for $\text{V}^{4+}/\text{V}^{5+}$ in LiVPO_4O and 4.24 V for $\text{V}^{3+}/\text{V}^{4+}$ in LiVPO_4F), this result is in good agreement with the operating voltages of the end-member phases. The strong covalency of the vanadyl bond acts actually as a reverse inductive effect, decreasing significantly the potential of the redox couple.

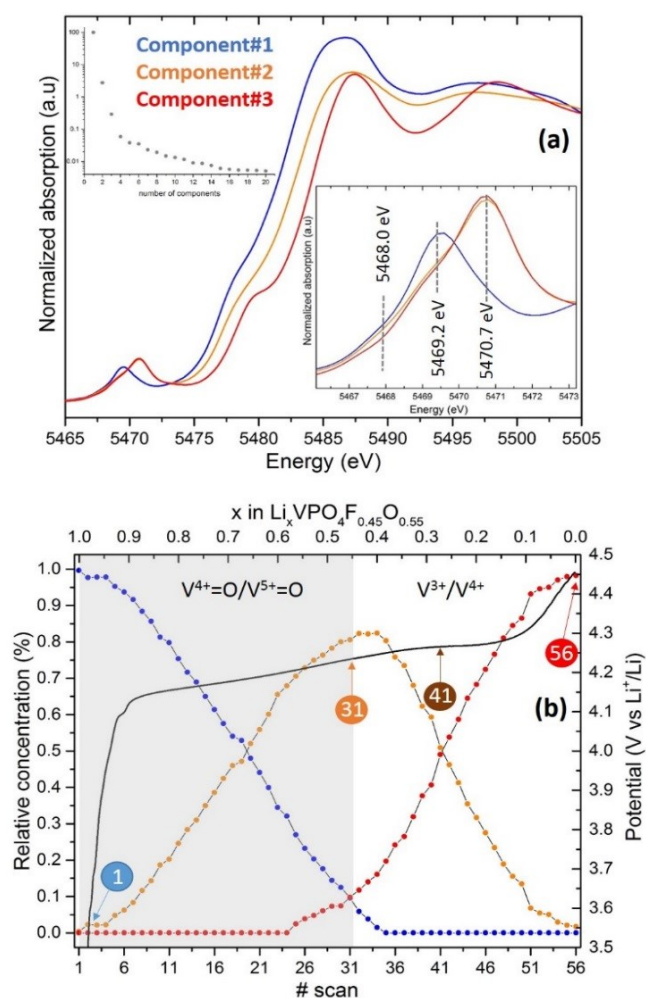


Figure II-51: (a) The components obtained thanks to principal component analysis, the variance plot justifying the use of three components and the enlargement of the pre-edge region are shown in inset. (b) The evolution of the relative concentration of each component in function of the scan number is superimposed to the voltage profile obtained during the *operando* experiment.

Operando SXRPD highlighted that the average structure of the material seems to be frozen during the activation of the $V^{4+}=O/V^{5+}=O$. The treatment of the EXAFS part will allow to know if this structural immobilization persists at the local scale.

iv. The local environments

The k^2 -weighted Fourier transforms of EXAFS spectra (k -range: 3.7 - 11.0 \AA^{-1} , sine windows) of the components extracted from PCA and their corresponding fits (considering only the first shell of ligands: R -range: $1 - 2.05 \text{ \AA}$ with $dR = 0.1 \text{ \AA}$ and a sine window shape) are compared in **Figure II-52**.

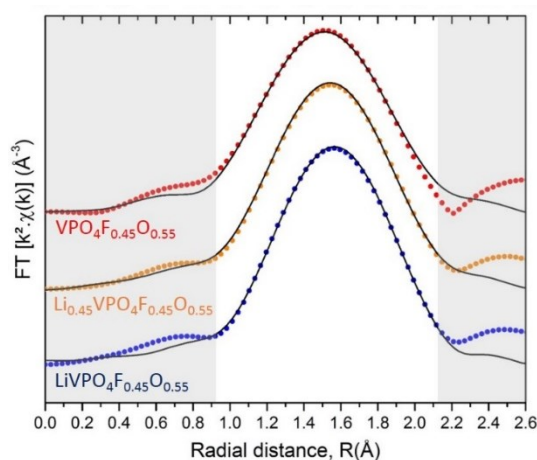


Figure II-52: Fit of the k^2 -weighted V K-edge EXAFS spectra Fourier transform (k -range: 3.7 - 11.0 \AA^{-1} , sine window) in the R space (R range: $1.0 - 2.05 \text{ \AA}$, $dR = 0.1 \text{ \AA}$, sine window) for the components extracted from PCA, $Li_xVPO_4F_{0.45}O_{0.55}$ with $x = 1, 0.45$ and 0 respectively for component#1, 2 and 3.

The model used to describe the starting material has already been described in **section II-3**, as built on 3 populations of bonds around V. During electrochemical cycling, new kinds of environments around V are expected to be generated. Thus, for the fit of the components, a similar model has been used although we refined separately the bond lengths belonging to the square plane of the octahedra and those perpendicular (see **Table II-16** and **Figure II-53**). For the starting material, this model is described as follows:

- (i) the vanadyl $V^{4+}=O$ bonds are formed by all V^{4+} in the material,
- (ii) the “anti-vanadyl” $V^{4+}-O$ bonds are formed only by vanadium involved in a vanadyl bond and having an oxygen as antagonist ligand,
- (iii) all other $V^{n+}-X$ bonds along the propagation direction of octahedra have been considered to be equivalent,
- (iv) all the $V^{n+}-O$ bonds (with $n = 3$ or 4) belonging to the square plane of VO_4X_2 have also been considered to be equivalent,

This leads to 5 parameters refined (4 different kinds of bond lengths and a common Debye Waller factor for all of them) for 6 independent parameters ($2 \cdot \Delta k \cdot \Delta R / \pi \sim 6$). For the composition studied, LiVPO₄F_{0.45}O_{0.55}, the coordination [0.55 + 4 + 1.25 + 0.20] respectively for (i) V⁴⁺=O, (iv) Vⁿ⁺-O, (iii) Vⁿ⁺-X, (ii) V⁴⁺--O has been used. This model provides, for the fit of the component#1, a similar description than the model provided in the **section II-3** with the vanadyl bond V⁴⁺=O (x0.55) at 1.64(1) Å, both Vⁿ⁺-O (x4) and Vⁿ⁺-X (x1.25) at 2.00(1) Å and the V⁴⁺--O at 2.20(1) (x0.20) Å and a common Debye Waller factor of 0.005 Å². The average distances around vanadium obtained from SXRPD and EXAFS are in good agreement. Indeed, the refinement of the SXRPD pattern of the pristine material leads to an average vanadium-ligands distance of 1.972(6) Å in centrosymmetric vanadium octahedra and for EXAFS, the $\langle d_{VL} \rangle_{EXAFS} = 1.97(1)$ Å. The EXAFS model is further supported by the resulting BVS value very close to the theoretical one on the contrary to the one provided from distances calculated from SXRPD (*i.e.* 3.6(1) for EXAFS vs. 3.26(1) in average on the two vanadium sites for SXRPD). The comparison between distances obtained from XRD and EXAFS experiments and associated BVS values are provided in **Table II-16** and the details of BVS calculations are provided in **Table Annex-II-2**.

Table II-16: Structural parameters obtained from the fit of the k^2 -weighted V K-edge EXAFS spectra Fourier transform. The parameters marked by * have been refined together (constrained). The distances calculated from SXRPD data are average ones and are compared to the average distances found by EXAFS. The associated BVS are also compared (The details for BVS calculation are provided in supporting information in Table Annex-II-2)

Sample	V ⁿ⁺ -X	coordination number, N	R (Å)	σ^2 (10 ⁻³ Å ²)	BVS
LiVPO ₄ F _{0.45} O _{0.55} (C#1) $\chi^2 = 1.91$ $R_f = 4.8 \cdot 10^{-4}$	(i) V ⁴⁺ =O	0.55	1.64(1)	0.005(1)*	3.6(1) vs. 3.55 theoretically
	(ii) V ⁴⁺ --O	0.20	2.20(1)	0.005(1)*	
	(iii) V ⁿ⁺ -X	1.25	2.00(1)	0.005(1)*	
	(iv) V ⁿ⁺ -O	4	2.00(1)	0.005(1)*	
	Average EXAFS		6	1.97(1)	0.005(1)
Average XRD		6	1.964(7)	/	3.24(1)
Li _{0.45} VPO ₄ F _{0.45} O _{0.55} (C#2) $\chi^2 = 2.53$ $R_f = 1.3 \cdot 10^{-3}$	(i) V ⁵⁺ =O	0.55	1.63(1)	0.007(1)*	3.9(1) vs. 4.10 theoretically
	(ii) V ⁵⁺ --O	0.20	2.23(1)	0.007(1)*	
	(iii) V ⁿ⁺ -X	1.25	2.03(1)	0.007(1)*	
	(iv) V ⁿ⁺ -O	4	1.95(1)	0.007(1)*	
	Average EXAFS		6	1.95(1)	0.007(1)
Average XRD		6	1.96(1)	/	/
VPO ₄ F _{0.45} O _{0.55} (C#3) $\chi^2 = 0.73$ $R_f = 5.2 \cdot 10^{-4}$	(i) V ⁴⁺ =O	0.55	1.61(1)	0.006(1)*	4.3(1) vs. 4.55 theoretically
	(ii) V ⁴⁺ --O	0.20	2.23(1)	0.006(1)*	
	(iii) V ⁿ⁺ -X	1.25	2.03(1)	0.006(1)*	
	(iv) V ⁿ⁺ -O	4	1.91(1)	0.006(1)*	
	Average EXAFS		6	1.92(1)	0.006(1)
Average XRD		6	1.89(1)	/	/

During the first step of the charge, EXAFS reveals that the $V^{4+}=O$ are oxidized to form $V^{5+}=O$ entities without modification (superior to the relative error) of V-O distances along the propagation direction of the chains and a shortening of the V-O bonds belonging to the equatorial plane. The freezing of the average structure measured by SXRPD partially persists at the local scale as the fluorine in the neighboring of vanadyl entities might give a strong rigidity to the system. The value of the average distances obtained from EXAFS are in good agreement with the XRD refinement results ($\langle d_{V-L} \rangle_{XRD} = 1.97(1) \text{ \AA}$ and $\langle d_{V-L} \rangle_{EXAFS} = 1.95(1) \text{ \AA}$) and the resulting BVS computed thanks to EXAFS distances (3.9(1) vs. 4.10 theoretically) is closer to the theoretical one than the BVS calculated from XRD distances (*i.e.* 3.65(8)). For Component#3, only the bonds belonging to the square plane undergo a significant shortening from 1.95(1)Å to 1.90(1)Å and the other ones remain quasi unchanged conferring a BVS value for vanadium of 4.3(1) (instead of 4.55 theoretically). The EXAFS part is consistent with the XRD results which reveals that no significant changes are observed during the oxidation $V^{4+}=O$ to $V^{5+}=O$ and then, the oxidation of V^{3+} to V^{4+} in a fluorine rich environments leads to an overall shortening of the bonds belonging to the square plane of vanadium octahedra.

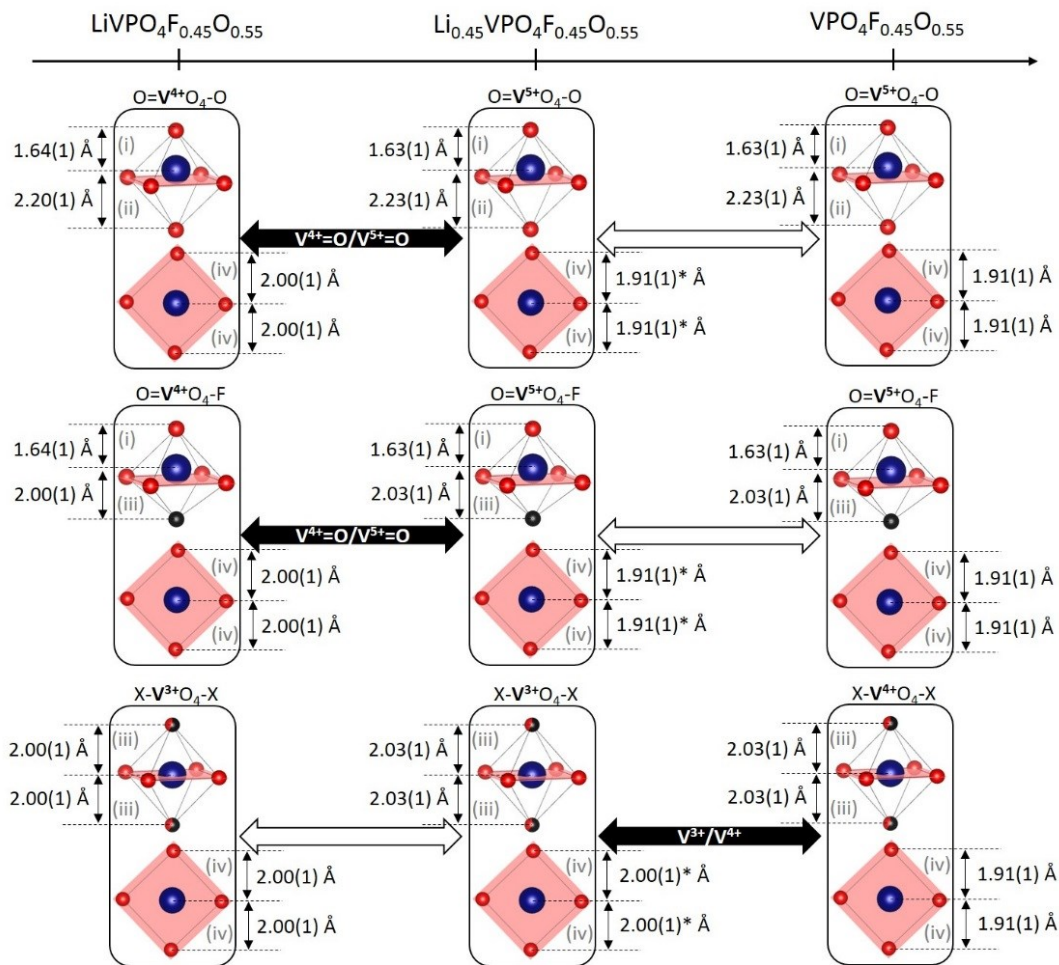


Figure II-53: Schematic representation of the evolution of the local environments around vanadium upon electrochemical cycling. Distances marked with * are extrapolated from the average distance obtained from EXAFS (*i.e.* 1.95(1) Å measured for (iv) $V^{n+}-O$ in $Li_{0.45}VPO_4F_{0.45}O_{0.55}$)

v. Summary and prospects

In summary, the *operando* XAS experiment reveals clearly the activation of V^{4+=O}/V^{5+=O} redox couple during the first step of the charge and then the V³⁺/V⁴⁺ in fluorine rich environment. This first step corresponds to a wide monophasic domain during which the average structure seems to be frozen. The fit of EXAFS oscillation has shown that the structural immobilization persists at the local scale for the bond lengths along the propagation direction of the chains of octahedra (**Figure II-53**) and that a shortening of the equatorial V-O distances is observed. The competitive formation between the strongly covalent vanadyl bond (from V^{4+=O} to V^{5+=O}) and the highly ionic V³⁺-F bond might prevent the structural shrinkage along the Lithium diffusion paths. The further delithiation occurs according to two consecutive pseudo biphasic processes with a phase transition occurring at an approximated V³⁺/V⁴⁺ ratio of 2 whatever the amount of V^{4+=O} defects in the starting material. Therefore, this phase transition suggests similarities with the one observed in LiVPO₄F with the formation of Li_{0.67}(V³⁺_{0.67}V⁴⁺_{0.33})PO₄F. However, the related superstructure peaks observed in Li_{0.67}VPO₄F haven't been detected during the charge of LiVPO₄F_{1-y}O_y materials: *Ex-situ* SXRPD, ND, TEM and ⁷Li MAS NMR experiments could evidence an eventual ordering. Moreover, the PCA applied on the whole series of XAS spectra obtained *operando* during the charge of the Li // LiVPO₄F_{0.45}O_{0.55} cell doesn't allow to reasonably detect this phase transition whereas PCA clearly highlights it for the Li_{0.67}VPO₄F composition (see **section II-1**).

The *ex-situ* SXRPD pattern corresponding to the fully deintercalated state contains two phases. The hypothesis that we propose is to consider a "demixing" between a fluorine-rich phase and an oxygen-rich one. Note that this "demixing" probably results from the partial clustering of the V³⁺/V⁴⁺ (and F⁻/O²⁻) domains in the starting material and the stronger strains imposed by the crystal field at the charge state highlight it even better. However, a complementary *operando* SXRPD experiment is required to confirm our hypothesis and TEM analyses are needed to determine the space group of the final phase (C2/c, P2₁/c or Cc).

In LiVPO₄F_{1-y}O_y, the activation of the V³⁺/V⁴⁺ redox couple leads to an overall shrinkage of the structure reducing thus the size of lithium diffusion pathways. The electrochemical tests have shown that an optimal vanadyl-type defects' concentration could exist for optimized performance (especially, rate capability and cycling stability) of LiVPO₄F_{1-y}O_y. The beneficial effect of vanadyl-type defects on the electrochemical properties could originate from the lower volume change observed in Li_xVPO₄F_{1-y}O_y materials compared to Li_xVPO₄F. Indeed, the structure seems to be frozen during the activation of V^{4+=O}/V^{5+=O} and the further Lithium deintercalation to reach the fully delithiated phase leads to rather similar volume changes

whatever the O^{2-}/F^- substitution ratio. Therefore, for oxygen-rich materials (characterized by a wide solid solution domain involving the $V^{4+}=O/V^{5+}=O$ redox couple) the structure undergoes major structural modifications in a narrow composition range whereas for fluorine-rich materials (showing a narrow solid solution domain), these changes are spread on a large composition range. The softer structural evolution observed in fluorine-rich materials has most probably a beneficial effect on their cycling stability and rate capability. However, the exact composition of this optimal isn't determined yet and further syntheses are also required to optimize the material, *i.e.* the composition, the particles' size and the carbon coating. These syntheses will be undertaken in a near future by Dr. Régnald David, within the development of the prototyping platform of the RS2E network.

$LiVPO_4F$ and $LiVPO_4F_{1-y}O_y$ are competitive with the already commercialized materials playing only with the lithium extraction/insertion in the high voltage domain. Moreover, it's still possible to extract an additional energy density by involving the low voltage region. Indeed, recently $Li_{1\pm x}VPO_4F_{1-y}O_y$ materials have been investigated as multi-electrons systems revealing 800 Wh/kg in the 2.0-4.5 V vs. Li^+/Li voltage window (with $\Delta x = 1.6$)¹⁰⁷. Nevertheless, the activation of several redox couples per transition metals in this material seems to be detrimental to the long life performance (*i.e.* ~50% of capacity fading after 15 cycles C/20)¹⁰⁷. In order to understand these limitations, the low voltage signature was investigated thanks to *operando* SXRPD and XAS.

II-4b. Low voltage region, a probe for the local environments around vanadium

i. Electrochemistry as local probe

In the low voltage region (*i.e.* 3.0 - 1.5 V vs. Li^+/Li), the lithium insertion into LiVPO_4F occurs at 1.8 V according to a biphasic process between LiVPO_4F and $\text{Li}_2\text{VPO}_4\text{F}$ involving the $\text{V}^{\text{III}}/\text{V}^{\text{II}}$ redox couple²⁰. The lithium insertion into LiVPO_4O leads to the reduction of $\text{V}^{\text{IV}}=\text{O}/\text{V}^{\text{III}}$ according to a complex series of phase transitions occurring at 2.48 V, 2.31 V and 2.03 V vs. Li^+/Li , to reach the composition $\text{Li}_2\text{V}^{\text{III}}\text{PO}_4\text{O}$.^{96,98} The **Figures II-54** shows the galvanostatic curves and the corresponding derivative curves of the mixed valence materials cycled in the 3.0 – 1.0 V vs. Li^+/Li voltage range (involving the $\text{V}^{\text{II}}/\text{V}^{\text{III}}$ and $\text{V}^{\text{IV}}=\text{O}/\text{V}^{\text{III}}$ redox couples) at C/10 and in the 3.0 – 1.5 V vs. Li^+/Li voltage range at C/50 under GITT conditions.

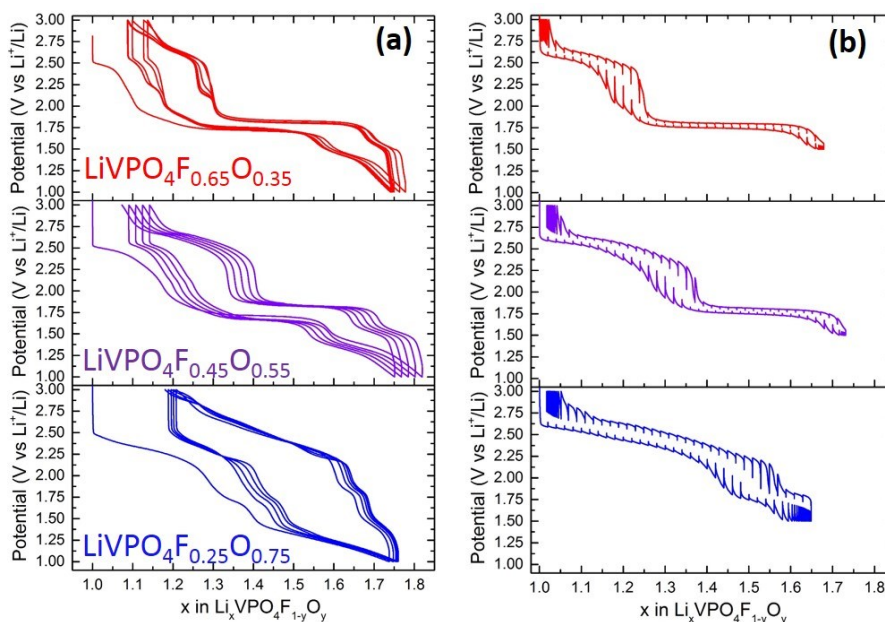


Figure II-54: Galvanostatic profiles obtained versus Lithium at a C/10 rate for $\text{LiVPO}_4\text{F}_{0.25}\text{O}_{0.75}$ (blue line), $\text{LiVPO}_4\text{F}_{0.45}\text{O}_{0.55}$ (purple line) and $\text{LiVPO}_4\text{F}_{0.65}\text{O}_{0.35}$ (red line) in the low voltage domain (*i.e.* between 3.0 and 1.0 V vs. Li^+/Li) (a); Corresponding GITT profiles obtained versus Lithium at C/50 (1h pulse and relaxation until $dV/dt < 4\text{mV/h}$) and in the 3.0-1.5 V voltage window (b).

The voltage profile of the solid solution samples can be described as a combination of an LiVPO_4O -type signature above 1.9 V, an LiVPO_4F -type signature between 1.9 and 1.6 V and a third unknown contribution at lower potential (*i.e.* 1.4 V vs. Li^+/Li , see **Figure II-55**). Moreover, the relative proportions of each contribution evolves as a function of the O^{2-}/F^- ratio. Indeed, by increasing the fluorine content in the materials the lengths of the LiVPO_4F -type pseudo-plateau increases. Regarding the third unknown contribution, it could correspond either to the

further reduction of V^{3+} in an oxygen-rich environment (*i.e.* $O-V^{3+}-O$ to $O-V^{2+}-O$) or to the reduction of V^{3+} in a mixed fluorine-oxygen environment (*i.e.* $O-V^{3+}-F$ to $O-V^{2+}-F$). To the best of our knowledge, the further insertion of lithium into Li_2VPO_4O has never been reported and thus the corresponding voltage is unknown. However, the pseudo-plateau observed for $LiVPO_4F_{1-y}O_y$ samples appears at a voltage close to the one measured for the V^{2+}/V^{3+} redox couple in $Li_{1+x}VPO_4OH$ (*i.e.* ~ 1.4 V against 1.35 V vs. Li^+/Li in $LiVPO_4OH$ ¹⁵³). This contribution cannot be assigned to the presence of OH groups whose absence has already been demonstrated by IR spectroscopy (see **section II-3**). However, the voltage of an eventual reduction of V^{3+} in oxygen-rich environment should be located close to 1.35 V vs. Li^+/Li . Another hypothesis explaining this contribution is to consider the reduction of V^{3+} in a mixed fluorine-oxygen environment whose redox potential is expected to be located at slightly lower voltage than V^{2+}/V^{3+} redox couple in $Li_{1+x}VPO_4F$ (*i.e.* 1.8 V vs. Li^+/Li) due to the lower electronegativity of O^{2-} compared to F^- .

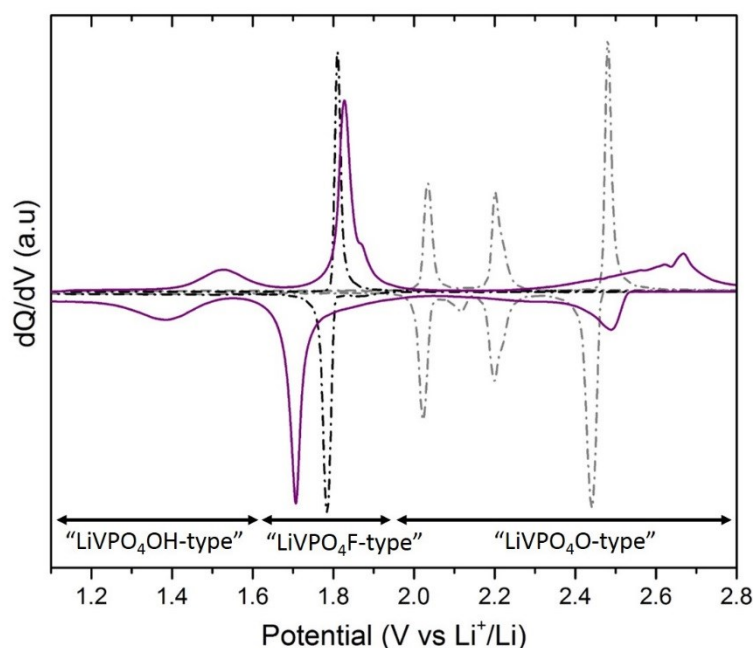


Figure II-55: comparison of the dQ/dV curves calculated for the 1st cycle of $Li/LiVPO_4F_{0.45}O_{0.55}$ cells (purple line), $LiVPO_4F$ (dash black line) and $LiVPO_4O$ (dash grey line).

Although the lithium insertion reaction is less interesting from application's point of view, due to its lower voltage, the corresponding electrochemical signature appears as a local probe, which could support the local description of the materials that we previously made. However the investigation of the phase diagram and the redox mechanisms is required to confirm the visual interpretations made from the shape of the voltage profiles and to elucidate the nature of the contribution below 1.5 V. In the following, only the $LiVPO_4F_{0.45}O_{0.55}$ composition will be investigated using *operando* SXRPD and XAS.

ii. The $\text{Li}_{1+x}\text{VPO}_4\text{F}_{1-y}\text{O}_y$ phase diagram

Figure II-56 shows the XRD patterns recorded during lithium insertion into $\text{LiVPO}_4\text{F}_{0.45}\text{O}_{0.55}$ (at C/12, 13 scans per hour providing 160 diffraction patterns).

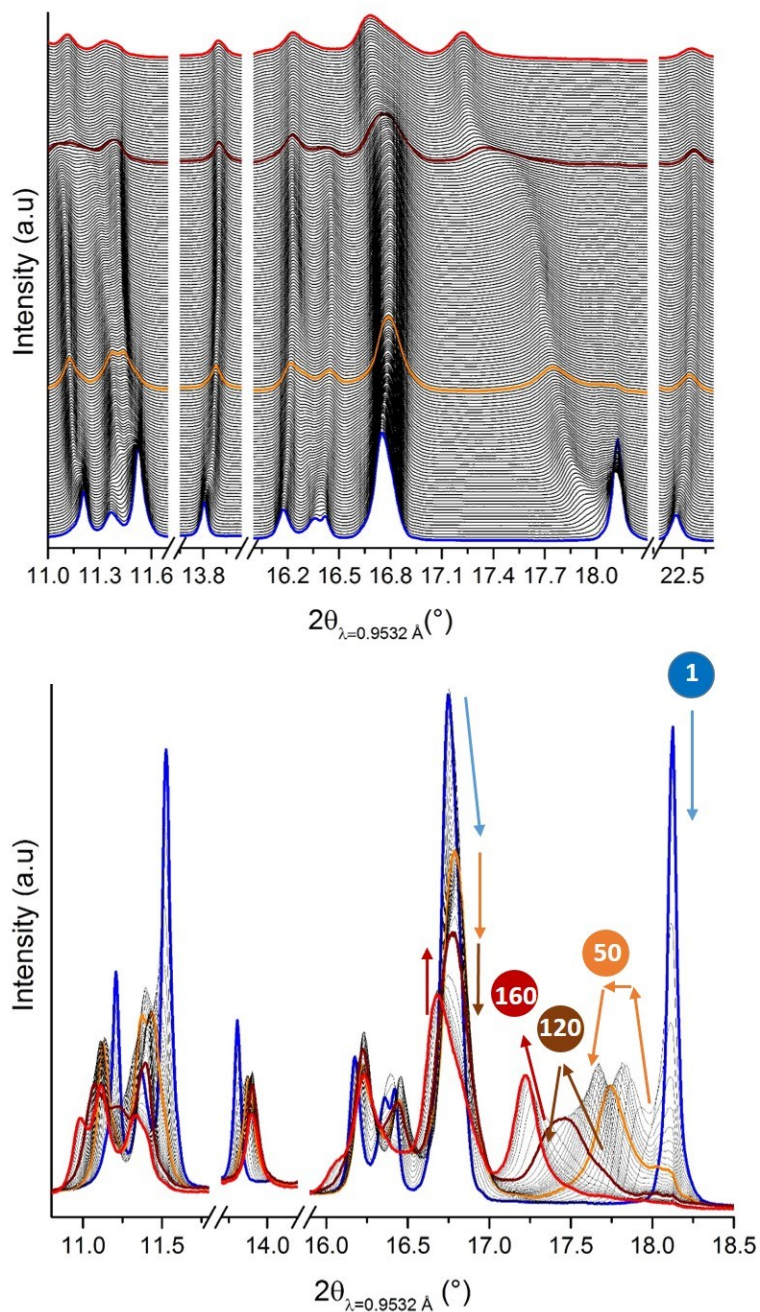


Figure II-56: SXRPD patterns obtained operando during lithium insertion in $\text{LiVPO}_4\text{F}_{0.45}\text{O}_{0.55}$.

The insertion mechanism seems very complex with several biphasic mechanisms associated with significant evolutions of the cell parameters. The **Figure II-56** reveals that the whole series of SXRPD patterns can be indexed using 4 main phases whose evolution of weight fractions and cell volumes during reaction are shown in **Figure II-57**. As the intermediate

phases are never observed as single phases and due to the evolution of their cell parameters, their compositions can only be estimated. However, the assignment of a composition to each phase has been done according to the composition corresponding to the maximum of weight fraction observed for each phase. The first phase is associated with $\text{LiVPO}_4\text{F}_{0.45}\text{O}_{0.55}$ (blue marks in the **Figure II-57**), the second to $\text{Li}_x\text{VPO}_4\text{F}_{0.45}\text{O}_{0.55}$ with $1.17 < x < 1.4$ (orange marks), the third to $\text{Li}_{1.70}\text{VPO}_4\text{F}_{0.45}\text{O}_{0.55}$ (brown marks) and the last one to $\text{Li}_2\text{VPO}_4\text{F}_{0.45}\text{O}_{0.55}$ (red marks).

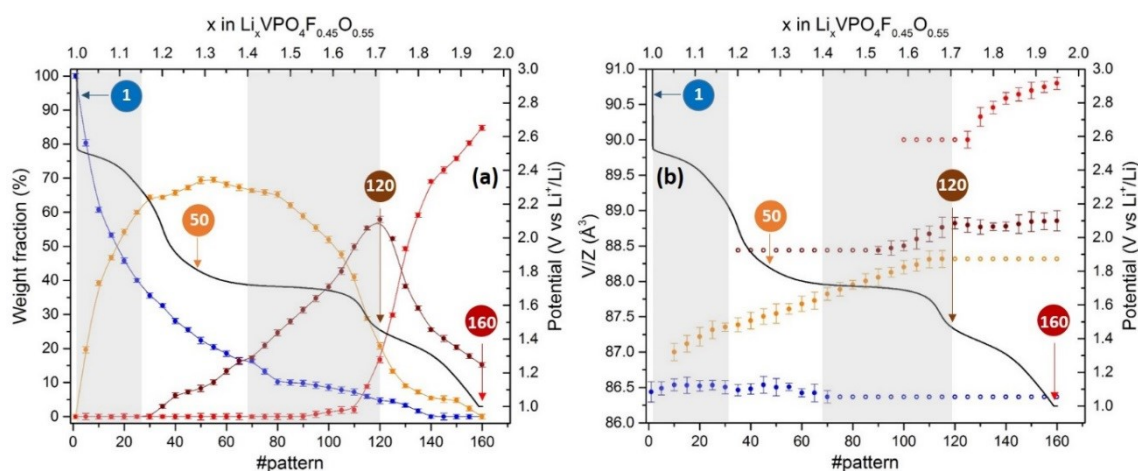


Figure II-57: Evolution of the weight fractions and cell volumes of the phases appearing along the reaction of lithium intercalation in $\text{Li}_{1+x}\text{VPO}_4\text{F}_{0.45}\text{O}_{0.55}$.

Despite the presence of parasitic signals (Lithium, Beryllium, PTFE, separator and $\text{Li}_3\text{V}_2(\text{PO}_4)_3$ as impurity as already discussed in the previous part), the structure of the starting material, obtained from the refinement of the pattern recorded *in situ*, is very similar to the one described in the previous section. During the first part of the charge (corresponding to a $\Delta x \sim 0.17$), the Bragg peaks of the pristine materials undergo a slight shift, a significant broadening and a strong decrease in intensity. In parallel, a first intermediate phase continuously grows and shifts. This phase can be described considering a similar model than that for $\text{LiVPO}_4\text{F}_{1-y}\text{O}_y$ with two centrosymmetric vanadium and probably two lithium sites. Nevertheless, the strong anisotropic broadening of the diffraction lines, the lightness of lithium and the presence of several triclinic phases in the sample don't allow us to precisely locate the Lithium ions. Thus, all along the lithium insertion, their positions were fixed and their occupancies adjusted in function of the composition given by the electrochemistry. Therefore, the lithium environment will not be discussed in this section.

The second lithiation step ($1.17 < x < 1.4$) can be attributed to either a monophasic or a biphasic or two biphasic process(es). Indeed, due the evolution of the cell parameters during the apparent biphasic processes, it's very difficult to assign the exact mechanism to this composition domain:

- Using a single phase to describe the evolution of the SXRPD patterns, the weight fraction of this phase remains quasi constant whereas the intensity of the pristine phase still decreases slowly at the benefit of a third contribution. In parallel, the unit cell volume of stagnant phase (orange marks in **Figure II-57**) is getting closer and closer to the third phase, increasing from $87.4(1) \text{ \AA}^3$ to $88.45(1) \text{ \AA}^3$. This mechanism is unusual and could also be explained as several biphasic processes.
- However, using several phases, their cell parameters converge towards a similar value at the pattern#50 (*i.e.* around $V/Z=87.5(1) \text{ \AA}^3$) suggesting that this domain should actually be explained with a single phase.

In the composition domain corresponding to $1.4 < x < 1.7$ in $\text{Li}_x\text{VPO}_4\text{F}_{0.45}\text{O}_{0.55}$, a biphasic mechanism seems to occur with an obvious increase of the cell parameters of both phases. However, the borders of this domain aren't clear. Indeed the phase corresponding to the $\text{Li}_{1.7}\text{VPO}_4\text{F}_{0.45}\text{O}_{0.55}$ composition (brown marks in **Figure II-57**) has already started to grow since the beginning of the previous step (*i.e.* at the $\text{Li}_{1.17}\text{VPO}_4\text{F}_{0.45}\text{O}_{0.55}$ composition).

The last part of the charge corresponding to the voltage plateau around 1.5V corresponds to a biphasic process between $\text{Li}_{1.7}\text{VPO}_4\text{F}_{0.45}\text{O}_{0.55}$ and $\text{Li}_2\text{VPO}_4\text{F}_{0.45}\text{O}_{0.55}$ (brown and red marks respectively in the **Figure II-57**). Once again the cell parameters of each phase involved in the biphasic reaction still evolve. At the end of the experiment the overall $\text{Li}_{1.94}\text{VPO}_4\text{F}_{0.45}\text{O}_{0.55}$ composition is reached, at this point the corresponding pattern is explained using 85 wt.% of $\text{Li}_2\text{VPO}_4\text{F}_{0.45}\text{O}_{0.55}$ and 15 wt.% of $\text{Li}_{1.7}\text{VPO}_4\text{F}_{0.45}\text{O}_{0.55}$.

All along the lithium insertion process, a succession of phases was detected. All these phases are described using a LiVPO_4F -type model (*i.e.* $P-1$, $Z=2$ generating two centrosymmetric vanadium sites) which differs from those of $\text{Li}_2\text{VPO}_4\text{O}$ and $\text{Li}_2\text{VPO}_4\text{F}$. Indeed, $\text{Li}_2\text{VPO}_4\text{F}$ adopts a $C2/c$ space group involving a single centrosymmetric vanadium site whereas $\text{Li}_2\text{VPO}_4\text{O}$ is described in a $P-1$ space group leading to two non-centrosymmetric vanadium sites. In each case the distances around vanadium are rather homogeneous. In $\text{Li}_2\text{VPO}_4\text{O}$, the vanadium cations are at the V^{3+} state, with shorter V-X distances (1.95 \AA in average) compared to those observed for $\text{Li}_2\text{V}^{\text{IV}}\text{PO}_4\text{F}$ (2.12 \AA in average). In our case, the average distance around vanadium increases gradually from $1.96(1) \text{ \AA}$ in the starting material to $2.09(1)\text{ \AA}$ in $\text{Li}_2\text{VPO}_4\text{F}_{0.55}\text{O}_{0.45}$. It's tricky to further describe with accuracy the structure of the series of phases obtained during lithium insertion due to (i) the strong anisotropic broadening (ii) the presence of several triclinic phases in the SXRPD patterns and (iii) the lightness of lithium which

don't allow us to localized it with accuracy. Moreover, the lattice parameters of each phase still evolve during apparent biphasic processes whereas thermodynamic forbids it (at least in the equilibrium state). The inhomogeneities at the local scale (*i.e.* disordered distribution of O^{2-}/F^-) and/or at the electrode scale (inhomogeneous repartition of active material, carbon and binder) could generate a multitude of consecutive metastable phases. This phenomenon is seen in average by XRD as a combination between monophasic and biphasic mechanisms which could be in fact an infinity of local biphasic reactions in relation with the local domains in these mixed valence materials. So let's probe the redox mechanisms involved as well as the local structure around vanadium by XAS in order to get more relevant insights.

iii. The Redox processes

XAS spectra recorded *operando* at the V K-edge during the discharge of the cell Li//LiVPO₄F_{0.45}O_{0.55} at C/20 in the 3.0-1.3 V vs. Li⁺/Li voltage range are shown in the **Figure II-58**.

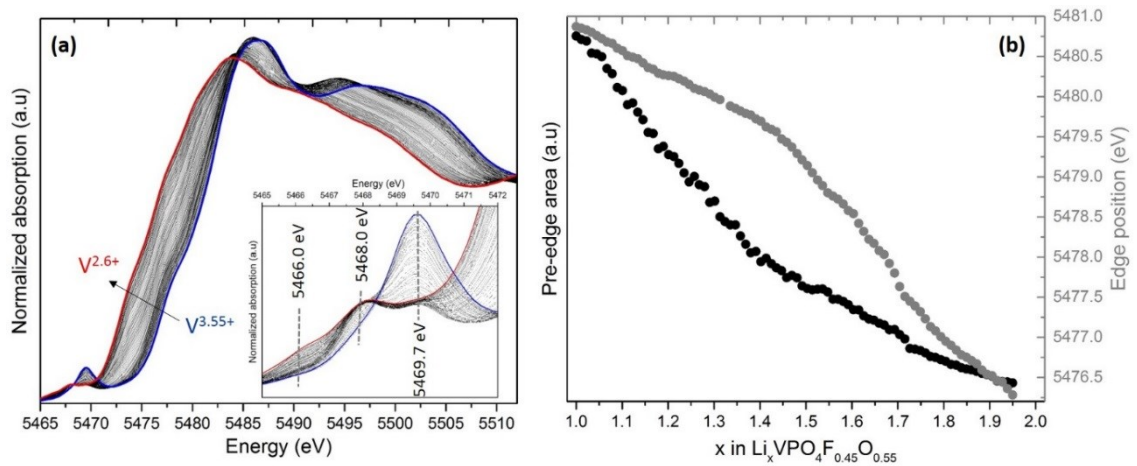


Figure II-58: (a) XANES spectra acquired *operando* during Lithium insertion into LiVPO₄F_{0.45}O_{0.55} and in inset the enlargement of the pre-edge region. (b) The evolution of the pre-edge intensity and the edge position in function x in Li _{x} VPO₄F_{0.45}O_{0.55}.

The Vanadium K edge XANES spectra exhibit several features as already largely discussed in this manuscript. The pre-edge contribution between 5465-5472 eV (shown in inset of **Figure II-58a**) arises from the theoretically 1s to 3d forbidden transition which becomes allowed due to distortion of the local environment around Vanadium. Several contributions appearing all along the electrochemical reduction of LiVPO₄F_{0.45}O_{0.55} observed at 5466.0, 5468.0 and 5469.7 eV are assigned to V²⁺, V³⁺ and V⁴⁺=O respectively (Cf Li₂V^{II}PO₄F, LiV^{III}PO₄F, LiV^{IV}PO₄O respectively, see **Figure Annex-I-11**).

The enlargement of the pre-edge region shows that the $\text{V}^{4+}=\text{O}$ contribution (5469.2 eV) undergoes a strong decrease in intensity and then remains constant during the further reduction of vanadium. In parallel, the contributions at 5468.0 and 5466.0 eV grow one after the other. This two steps evolution reveals that the $\text{V}^{4+}=\text{O}/\text{V}^{3+}-\text{O}$ is activated before the $\text{V}^{3+}/\text{V}^{2+}$ in vanadyl free environments. Indeed, the vanadyl bond being formed only for oxidation states of vanadium strictly superior to 3+, the reduction of V^{4+} to V^{3+} leads to a strong decrease of the distortion around vanadium and thus a strong decrease of the pre-edge intensity during the first step of the discharge, as highlighted by **Figure II-58b**.

The edge position along the reaction, shown in **Figure II-58b**, reveals also a nonlinear evolution with first a smaller shift (from 5480.9 eV to 5479.6 eV, $\Delta E = -1.3$ eV for $\Delta x = 0.45$) and then a larger shift towards lower energies (from 5479.6 eV to 5476.3 eV $\Delta E = -3.3$ eV for $\Delta x = 0.55$). That is in good agreement with the activation of $\text{V}^{4+}=\text{O}/\text{V}^{3+}-\text{O}$ during the first step. Indeed, the shift of the edge doesn't depend exclusively on the oxidation state of vanadium, the iono-covalent character of the bond formed by the absorbing element impacts it substantially¹⁴⁵. In our case, the stronger covalency of the $\text{V}^{4+}=\text{O}$ entity compared to $\text{V}^{3+}-\text{O}$ bond tends to decrease magnitude of the edge shift. Along the reduction of the $\text{V}^{4+}=\text{O}$ entities, the covalency character of the V-O bond is lost which tends to increase the edge shift whereas the reduction of vanadium cations (V^{4+} to V^{3+}) tends to decrease it. Therefore, two competitive phenomena occur during this first step leading to a low shift of the edge until the pure V^{3+} state is reached. The further reduction of vanadium doesn't affect significantly the iono-covalent character of the bond formed by vanadium and thus leads to a stronger edge shift. Strangely, the transition between two steps of the lithium intercalation reaction occurs at the $\text{Li}_{1.45}\text{VPO}_4\text{F}_{0.45}\text{O}_{0.55}$ composition which doesn't correspond to the stoichiometry expected for a pure trivalent state for vanadium (*i.e.* $\text{Li}_{1.55}\text{V}^{3+}\text{PO}_4\text{F}_{0.45}\text{O}_{0.55}$). In fact, the parallel evolution of the edge shift versus the pre edge intensity suggests that complex processes occur, therefore the whole data set were analyzed using PCA combined with MCR¹³¹.

The variance plot obtained from PCA given in **Figure II-59a** shows that about 99.69% of the variance of the XANES spectra can be described using three principal components whereas *operando* SXRPD data analysis has shown that at least 4 distinct phases are required to explain the phase diagram upon Lithium insertion. Although adding another component, a coherent evolution of the weight fractions is obtained, but it would explain only 0.09% of the signal and thus could constitute an over interpretation without improvement of the associated agreement factors ($R_{\text{wp}}=0.018$ and 0.032% for 3 and 4 using components, respectively).

Therefore, we have chosen to use only 3 components and the residual part is considered as experimental noise.

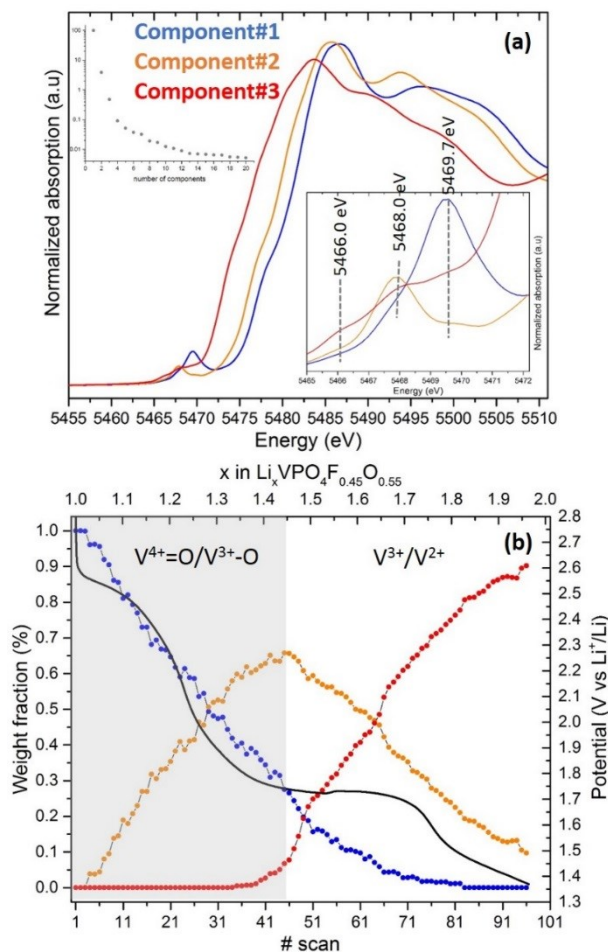


Figure II-59: (a) The components obtained thanks to principal component analysis, the variance plot justifying the use of three components and the enlargement of the pre-edge region are shown in inset. (b) The evolution of the relative concentration of each component in function of the scan number is superimposed to the voltage profile obtained during the operando experiment.

The three components thus obtained are shown in **Figure II-59** with the evolution of their concentrations along the electrochemical reaction. According to the evolution of their relative concentrations, these components can be described as follows: the component#1 corresponds to the pristine material $\text{LiVPO}_4\text{F}_{0.45}\text{O}_{0.55}$ and the third component to the fully delithiated one $\text{Li}_2\text{VPO}_4\text{F}_{0.45}\text{O}_{0.55}$. Since the component#2 never reaches 100% of the relative quantity, it cannot be found isolated in any spectrum. Its maximum contribution corresponds to the $\text{Li}_{1.45}\text{VPO}_4\text{F}_{0.45}\text{O}_{0.55}$ composition, but considering its pre-edge feature, this component would not contain anymore any $\text{V}^{4+}=\text{O}$ contribution and could actually correspond to the pure trivalent phase $\text{Li}_{1.55}\text{V}^{3+}\text{PO}_4\text{F}_{0.45}\text{O}_{0.55}$. Indeed, between component#1 and component#2, a clear decrease of the $\text{V}^{4+}=\text{O}$ contribution (*i.e.* 5469.2 eV) is accompanied an increase of the $\text{V}^{3+}-\text{O}$ (*i.e.* 5468.0 eV) revealing the activation of the $\text{V}^{4+}=\text{O}/\text{V}^{3+}-\text{O}$ redox couple during the first part

of the lithium insertion reaction. However, the rather large intensity of the contribution at 5468.0eV suggests the persistence of the “vanadyl bond” at the V³⁺ state. For The component#3 the rather large V³⁺ contribution has been lost at the benefit of a weak V²⁺ one (at 5466.0eV), in good agreement with the activation of the V³⁺/V²⁺ redox couple. Comparing the absorption energy of the main edge jump obtained for each component at 5480.9 eV, 5479.4 eV, and 5476.1 eV, it appears that it doesn’t evolve linearly as a function of the oxidation state of vanadium. This non-linear evolution has already been assigned to modification of the ionic-covalent character of the bonds around vanadium with the loss of the vanadyl entity.

The XANES study of the low voltage mechanism confirm the observation made from electrochemical tests. Indeed, electrochemistry suggested the activation of the LiVPO₄O-type contribution until $\Delta x \sim 0.5$ that has been confirmed by XANES (activation of the V⁴⁺=O/V³⁺-O redox couple) and then the appearance of LiVPO₄F-type signature at 1.9 and a third one at 1.5 V matching with the reduction of V³⁺ to V²⁺. However the persistence of the “vanadyl bond” at the V³⁺ state has to be confirmed and the nature of the third contribution around 1.5V remains currently undetermined. Therefore, the investigation of the local environments by EXAFS could give more insights.

iv. Local environments

The k²-weighted Fourier transforms of EXAFS spectra (k-range: 3.7-11.0 Å⁻¹, sine windows) of the components extracted from PCA and their corresponding fits (considering only the first shell of ligands: R-range: 1–2.10 Å with dR = 0.1 Å and a sine window shape) are compared in the **Figure II-60**.

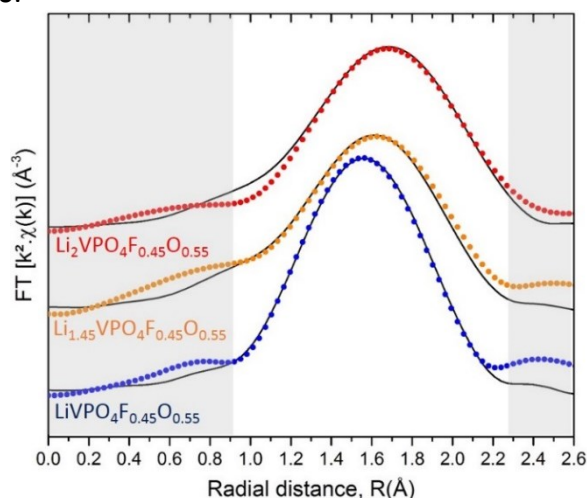


Figure II-60: Fit of the k²-weighted V K-edge EXAFS spectra Fourier transform (k-range: 3.7-11.0 Å⁻¹, sine window) in the R space (R range: 1.0 – 2.20 Å, dR = 0.1 Å, sine window) for the components extracted from PCA, Li_xVPO₄F_{0.45}O_{0.55} with x=1, 1.45 and 2 respectively for component#1, 2 and 3.

The starting material have been previously described in the previous section with a 6-fold coordination. The model provides, for the fit of the component#1, the following bond lengths:

- (i) the vanadyl bond $V^{4+}=O$ (x0.55) at 1.64(1) Å,
- (ii) the “anti-vanadyl” bond $V^{4+}-O$ at 2.23(1) (x0.20) Å
- (iii) the remaining $V^{n+}-X$ (x1.25) along the propagation direction of the chains of octahedra at 2.00(1) Å
- (iv) the $V^{n+}-O$ (x4) belonging to the VO_4 square plane at 2.00(1) Å

with a common Debye Waller factor of 0.005 \AA^2 for all these bond lengths (see **Table II-17**).

Table II-17: Structural parameters obtained from the fit of the k^2 -weighted V K-edge EXAFS spectra Fourier transform. The parameters marked by * have been refined together (constrained). The distances calculated from XRD data are average ones and are compared to the average distances found by EXAFS. The associated BVS are also compared (The details for BVS calculation are provided in supporting information in Table Annex-II-3)

Sample	$V^{n+}-X$	Coordination number, N	R (Å)	σ^2 (10^{-3} \AA^2)	BVS	
LiVPO₄F_{0.45}O_{0.55} (C#1) $\chi^2 = 2.83$ $R_f = 5.6 \cdot 10^{-4}$	(i)	$V^{4+}=O$	0.55	1.64(1)	0.005(1)*	3.6(1) vs. 3.55 theoretically
	(ii)	$V^{4+}-O$	0.20	2.23(1)	0.005(1)*	
	(iii)	$V^{n+}-X$	1.25	2.00(1)	0.005(1)*	
	(iv)	$V^{n+}-O$	4	2.00(1)	0.005(1)*	
	Average EXAFS		6	1.98(1)	0.005(1)	/
	Average XRD		6	1.964(7)	/	3.24(1)
Li_{1.55}VPO₄F_{0.45}O_{0.55} (C#2) $\chi^2 = 16.42$ $R_f = 2.1 \cdot 10^{-3}$	(i)	$V^{3+}-O$	0.55	1.82(1)	0.005(1)*	2.9(1)
	(ii)+(iii)	$V^{3+}-X$	1.45	1.99(1)	0.005(1)*	vs. 3.00
	(iv)	$V^{3+}-O$	4	2.06(1)	0.005(1)*	theoretically
	Average EXAFS		6	2.02(1)	0.005(1)	/
	Average XRD		6	/	/	/
	Li₂VPO₄F_{0.45}O_{0.55} (C#3) $\chi^2 = 8.0$ $R_f = 1.3 \cdot 10^{-3}$	(i)	$V^{3+}-O$	0.55	1.95(1)	0.006(1)*
(ii)+(iii)		$V^{n+}-X$	1.45	2.13(1)	0.006(1)*	vs. 2.55
(iv)		$V^{n+}-O$	4	2.13(1)	0.006(1)*	theoretically
Average EXAFS		6	2.11(1)	0.006(1)	/	
Average XRD		6	2.09(1)	/	/	

The XANES part has highlighted that during the first step of the discharge the $V^{4+}=O$ entities are reduced to form $V^{3+}-O$ ones with a rather strong pre-edge contribution which indicates a strong distortion around the trivalent vanadium ion. The fits of the EXAFS oscillations for the component#2 is consistent with this hypothesis. Indeed, the refinement of distances (keeping the [0.55 + 4 + 1.25 + 0.20] coordination), leads to distances at 1.82(1) Å (x0.55), 2.06(1) Å (x4), 1.99(1) Å (x1.25) and 1.99(1) Å (x0.20) respectively. Even at V^{3+} state, the “vanadyl bond” persist through the formation of rather short bond at 1.82(1) Å which can’t be named as vanadyl bond. Indeed, Clark¹⁵⁴ defined the vanadyl bond as a one which has a

length ranging between 1.57 and 1.68 Å; length shorter than the one observed by EXAFS. The other bond lengths along the chains of the octahedra (V^{3+} -F or V^{3+} -O) are equivalent, at 1.99(1) Å. This is a classical value for the distances around vanadium at the V^{3+} state (*i.e.* 1.99 Å for LiVPO₄F⁹², 2.01 Å for LiVPO₄OH¹⁵³ and 1.95 Å Li₂VPO₄O⁹⁶) whereas the V^{3+} -O bond belonging to the VO₄ square plane of octahedra are rather long for this oxidation state of vanadium (*i.e.* 2.06(1)Å against 1.98 in LiVPO₄F and 2.02 in Li₂VPO₄O for instance). The persistence of the short V^{3+} -O bond might be at the origin of the elongation of the V-O distances in order to satisfy the valence of V^{3+} cations. Indeed, the BVS value computed from distances obtained from EXAFS are in rather good agreement with a vanadium at V^{3+} state (*i.e.* 2.92(6)).

The further lithium insertion leads to the activation of the V^{3+}/V^{2+} redox couple with a significant decrease of the distortion of the vanadium environment highlighted by XANES through the very weak pre-edge intensity for the component#3. The EXAFS results are in good agreement with the decrease of the pre-edge contribution because the short V^{3+} -O bond observed for the component#2 undergoes a significant increase to reach a value close to the one observed in Li₂VPO₄O (from 1.82(1) to 1.95(1) Å (x0.55)) and all remaining bond lengths in the octahedral coordination have been found at 2.13(1) Å (x5.45). This distance is close to those observed in Li₂VPO₄F (*i.e.* 2.12(1) Å in average). The environment around vanadium at the fully lithiated state can thus be described as a combination between Li₂VPO₄O-type and Li₂VPO₄F-type environments. The presence of bond lengths up to 2.1 Å suggests the activation of V^{3+}/V^{2+} in fluorine rich environment around 1.9 V vs. Li⁺/Li (*i.e.* 1.8 V vs. Li⁺/Li in LiVPO₄F). Moreover the decrease of the distortion suggests that the activity of the V^{3+}/V^{2+} of vanadium in oxygen rich environment is involved during the voltage pseudo-plateau around 1.4V vs. Li⁺/Li.

II-4c. Summary and prospects

In summary, *operando* SXRPD highlighted a very complex phase diagram in the low voltage region suggesting an inhomogeneous lithiation of the material at the long range scale whereas *in operando* XAS contrasts with the complex mechanism observed by SXRPD. Indeed, XANES, clearly revealed the reduction of the $V^{4+}=O$ entities to $V^{3+}-O$ during the first step of the lithiation. This leads to the formation of a pure V^{3+} phase at this stage with the persistence a short $V^{3+}-O$ bond which has been detected by both XANES and EXAFS. The further lithiation leads to the activation of the V^{3+}/V^{2+} redox couple with the weakening of the distortion and a strong increase of bond lengths around vanadium.

These conclusions are in good agreement with the observations made from the voltage profile in the low voltage domain with the appearance of the LiVPO_4O -type and at lower voltage the LiVPO_4F -type contributions (see **Figure II-55**). Indeed, electrochemistry acts as a powerful local probe allowing an easy approximation of the amount of vanadyl-type defects in the starting material without requiring the use of heavy techniques which aren't always available for all (especially solid state NMR and XAS). In the future, the authors publishing on performance of LiVPO_4F -type materials should provide the low voltage signature in order to allow the estimation of the part of the defects and the part of the morphology/carbon coating on these performance.

Moreover, recently, $\text{Li}_{1\pm x}\text{VPO}_4\text{F}_{1-y}\text{O}_y$ materials have been investigated as multi-electron systems delivering 800 Wh/kg in the 2.0-4.5 V vs. Li^+/Li potential range (with $\Delta x=1.6$)¹⁰⁷. Nevertheless, the activation of several redox couples per transition metal appeared to be detrimental to the long life performance (*i.e.* ~50% of capacity fading after 15 cycles at C/20)¹⁰⁷. They studied only one composition: $\text{LiVPO}_4\text{F}_{0.25}\text{O}_{0.75}$ (composition claimed by the authors but which reveals to be, based on our study, a composition close to $\text{LiVPO}_4\text{F}_{0.15}\text{O}_{0.85}$). Therefore, It is worth to investigate our $\text{Li}_x\text{VPO}_4\text{F}_{1-y}\text{O}_y$ materials as multi-electron systems playing with the substitution rate (*i.e.* y) and the voltage range in order to control the insertion/extraction reaction (*i.e.* Δx), limit the structural changes and thus stabilize the performance for long life cycling.

This work allows to provide a description of the nature of the defects or of the derived compositions which can be obtained when the synthesis conditions of LiVPO_4F are not perfectly controlled, versus the oxygen content during its synthesis. Furthermore, this study reveals that the versatility of the vanadium chemistry with a large number of stable oxidations states (from V^{2+} to V^{5+}), stabilized in very different environments (from very regular to very distorted ones), opens the road to the formation of new materials, whose strains imposed by the crystal field give attractive electrochemical properties. Therefore, the further substitution of the anionic and alkaline sites could offer interesting properties that we will investigate, in the following chapter, through the study of LiVPO_4OH and NaVPO_4F .

Chapter III: Further investigation of the Tavorite phase diagram

Table of Contents

CHAPTER III: FURTHER INVESTIGATION OF THE TAVORITE PHASE DIAGRAM	153
III-1. A new tavorite-type composition: NaVPO ₄ F	155
<i>III-1a. Syntheses, structure and defects</i>	<i>155</i>
<i>III-1b. Study of electrochemical inactivity</i>	<i>166</i>
<i>III-1c. Summary and prospects</i>	<i>171</i>
III-2. LiVPO ₄ OH, a new type of two electrons system	173
<i>III-2a. Syntheses and structure of LiVPO₄OH</i>	<i>173</i>
<i>III-2b. Electrochemical properties and redox mechanism</i>	<i>189</i>
<i>III-2c. Summary and prospects</i>	<i>199</i>
III-3. A potential high voltage two electrons system: Li ₂ V(H _{0.5} PO ₄) ₂	202
<i>III-3a. Influence of Hydrogen on the Lithium diffusion path</i>	<i>207</i>
<i>III-3b. Summary and prospects</i>	<i>208</i>

III-1. A new tavorite-type composition: NaVPO₄F

The large scale development of batteries requires available and cheap raw materials but the lithium needed for Li-ion batteries applications is essentially located in few countries such as China, Australia, Chili, Bolivia and Argentina. The Lithium resources are estimated at around ten millions of tons (0.002 wt.% of earth's crust ^{155,156}) and could be seen as limited considering the always growing global demand for Lithium-ion batteries. In order to propose alternatives to this technology and to control better possible huge variations of the Lithium price, the Sodium-Ion technology is seriously considered as a solution that will be rapidly mature. Indeed, sodium is one of the most abundant element in the earth's crust and oceans (2.5 wt.% of earth's crust and oceans ^{155,156}), and the material chemistry and electrochemistry required to develop Sodium and Lithium-ion batteries are very similar. Nevertheless, due to the higher electrochemical potential of 0.3V for the Na⁺/Na redox couple compared to that of Li⁺/Li, the energy density stored in Na-ion batteries will remain smaller without the development of high potential positive electrode materials to increase the voltage difference between both electrodes: sodium based polyanionic materials might be a solution. Among these polyanionic compounds, the most investigated positive electrodes for Sodium-ion batteries are vanadium phosphates such as Na₃V^{III}₂(PO₄)₃, Na₃V^{III}₂(PO₄)₂F₃ and Na₃V^{III}_{2-γ}(V^{IV}O)_γ(PO₄)₂F_{3-γ} (or also written Na₃V₂(PO₄)₂F_{3-γ}O_γ).^{13,157-160} The Tavorite materials are excluded from this list whereas the previous section has demonstrated that they show interesting electrochemical properties in Li-ion batteries^{14,98}. In this section, the synthesis, as well as the structural, microstructural and electrochemical properties of the new NaV^{III}PO₄F-type composition crystallizing in Tavorite-like structure will be described in details.

III-1a. Syntheses, structure and defects

ii. Syntheses

The existence of NaVPO₄F was already proposed by several authors¹⁶¹⁻¹⁶⁷, but a careful inspection of the crystallographic data they provided reveals the formation of Na₃V₂(PO₄)₂F₃ or Na₃V₂(PO₄)₃ as major phases. Indeed, the XRD patterns of the compounds published in references ¹⁶¹ (Figure 1a), ¹⁶² (Figure 2), ¹⁶³ (Figure 2b) and ¹⁶⁴ (Figure 1) can be indexed in a Na₃V₂(PO₄)₂F₃-type unit cell and those published in references ¹⁶³ (Figure 2a), ¹⁶⁵ (Figure 5), ¹⁶⁶ (Figure 1b) and ¹⁶⁷ (Figure 1) with a Na₃V₂(PO₄)₃-type unit cell.

By analogy with hydrothermal syntheses already reported for other Vanadium based Tavorite type materials, $\text{HV}^{\text{III}}\text{PO}_4\text{OH}^{168}$, $\text{LiV}^{\text{IV}}\text{PO}_4\text{O}^{169}$ and $\text{LiV}^{\text{III}}\text{PO}_4\text{OH}^{153}$, we obtained the Tavorite-type sodium vanadium (III) fluoride phosphate NaVPO_4F under hydrothermal conditions. The precursors used were vanadium (III) chloride (VCl_3 , Sigma-Aldrich, 97%), sodium phosphate octahydrate ($\text{Na}_3\text{PO}_4 \cdot 8\text{H}_2\text{O}$, Sigma-Aldrich, 97%), phosphoric acid (H_3PO_4 , Sigma-Aldrich, 68% in water) and sodium fluoride (NaF , Sigma-Aldrich, $\leq 99\%$). The precursors were introduced as such in 23mL Teflon vessels filled at $\sim 60\%$. First synthesis trials were attempted by introducing stoichiometric amounts of precursors to get the nominal composition of NaVPO_4F , but this material was actually obtained pure only with the molar ratio $\text{VCl}_3/\text{H}_3\text{PO}_4/\text{Na}_3\text{PO}_4/\text{NaF}$: 1/1.2/0.7/1.2 (*i.e.* Na/V/ PO_4 /F: 3.3/1/1.9/1.2). The reactors were set in a furnace already at the temperature required (240°C for different synthesis durations), and were cooled down naturally to room temperature. The obtained powder was filtered, washed with water (to eliminate the precursors introduced in over-stoichiometry), rinsed with ethanol and dried at 60°C overnight. NaVPO_4F was obtained pure for a synthesis duration of 24h, and the rather large particles obtained have a needle-like shape with a wide size's distribution, as shown in **Figure III-1**. In order to try to decrease the particles' size and thus to improve their electrochemical properties, the reduction of the synthesis duration was attempted (down to 5h). But the materials obtained for shorter reaction times ($< 24\text{h}$) are in fact mixtures of NaVPO_4F and $\text{Na}_3\text{V}_2(\text{PO}_4)_2\text{F}_3$, the weight fraction of the Tavorite phase increasing from 65 wt.% after 5h of reaction time to 100 wt.% after 24h (**Figure III-1a**).

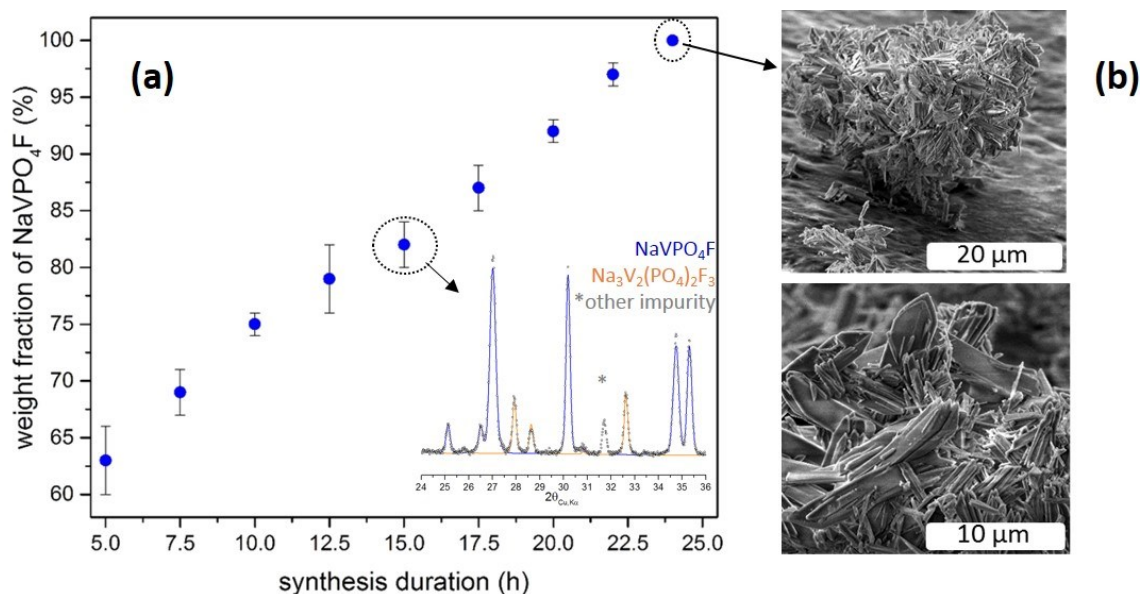


Figure III-1: (a) Evolution of the weight fraction of NaVPO_4F in function of the synthesis duration. In inset the refinement of the XRD pattern of the sample obtained after 15h and (b) SEM images showing a wide distribution of needle-like particles' sizes

The chemical composition in Na, V and P was determined to be 0.97(5):1.03(5):1.00(5) by ICP-OES and thus found to be very close to the expected NaVPO₄F composition. As oxygen and fluorine cannot be distinguished and titrated easily, the determination of the magnetic susceptibility allowed to check for the possible presence of oxygen defects (and thus of V⁴⁺=O vanadyl-type defects for charge compensation). As shown in **Figure III-2**, the magnetic susceptibility determined for NaVPO₄F is 0.905 emu.mol⁻¹ and corresponds to a vanadium average oxidation state of 3.15 according to the theoretical Curie constants of V⁴⁺ (*i.e.* 0.375) and V³⁺ (*i.e.* 1.00). This result suggests a rather large substitution of oxygen for fluorine (~ 15%), and thus the formation of vanadyl-type defects as also already evidenced recently for the lithiated analogue in ref.^{19,21} and in the previous chapter. As it will be highlighted in the following, these defects could be detected by different spectroscopy techniques (Infrared, XAS and NMR) and also indirectly, through their effects on the microstructure.

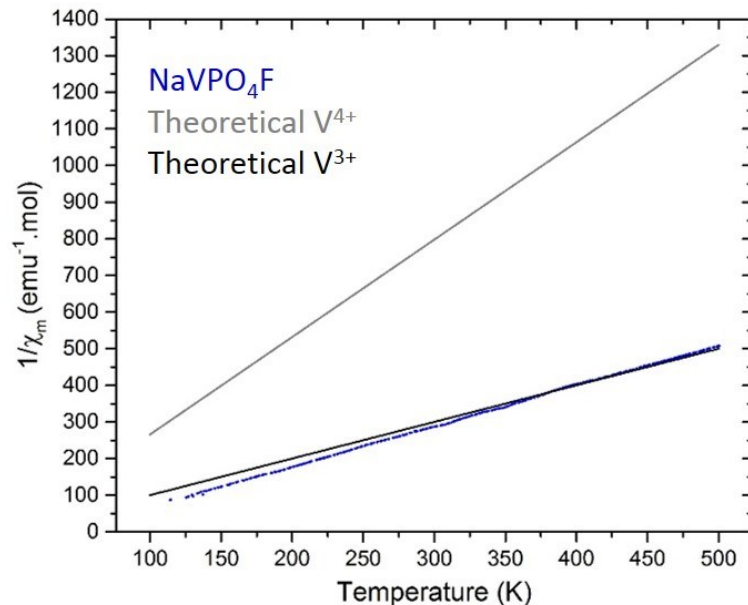


Figure III-2: Temperature dependence of the inverse of the experimental and theoretical magnetic susceptibilities for NaVPO₄F: experimental in blue, theoretical considering vanadium at the trivalent state in black and theoretical considering vanadium at the tetravalent state in grey.

i. Microstructural analysis

The SXRPD pattern of NaVPO₄F can be indexed with a monoclinic cell described in the space group C2/c ($a = 6.5646(1) \text{ \AA}$, $b = 8.4406(1) \text{ \AA}$, $c = 7.3727(1) \text{ \AA}$, $\beta = 117.847(1)^\circ$, $V/Z = 90.302(6) \text{ \AA}^3$). The profile of the diffraction lines is governed by a strong anisotropic broadening, that can be explained by anisotropic size and/or strain effects. Considering the needle shape of the particles, the anisotropic size effect could appear as obvious. Nevertheless, as discussed previously, vanadyl-type defects could also be present in NaVPO₄F and could thus

induce strains as observed for $\text{LiVPO}_4\text{F}_{1-y}\text{O}_y$. In order to precisely calculate the effect of the microstructure, the instrumental contribution of the diffractometer was determined using a standard sample ($\text{Na}_2\text{Ca}_3\text{Al}_2\text{F}_{14}$). The refinements reported in **Figure III-3** were performed considering: (a) an isotropic size and strain model to describe the line profile, (b) an anisotropic size model, and (c) an anisotropic strain model.

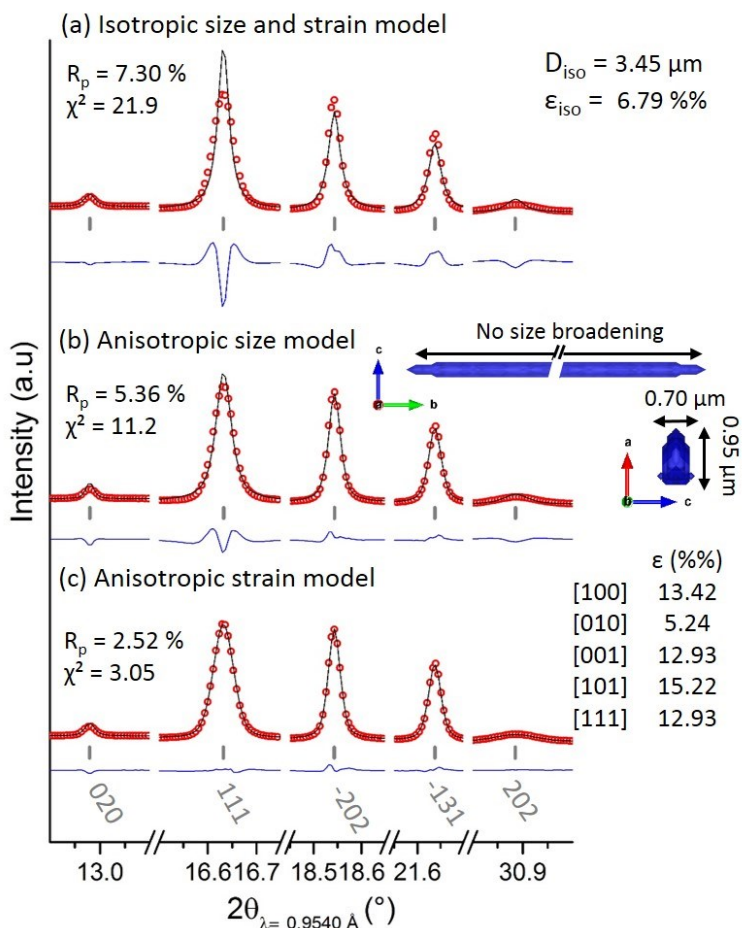


Figure III-3: Profile matching refinements of the diffraction pattern of “ NaVPO_4F ” using an isotropic size and strain model (a), an anisotropic size model (b) and an anisotropic strain model (c) as provided in the FullProf suite. The agreement factors (R_p and χ^2) as well as microstructural parameters, the width of microstrains distribution (ϵ) and/or the crystallites sizes (D), are provided for each refinement.

Obviously, the isotropic model does not allow to take into account the profile of the experimental diffraction lines. The anisotropic size model was used as described in the FullProf suite software for a monoclinic symmetry^{137,138}. It reveals, from the 3D rebuilding of the particles’ shape (made applying the Scherrer’s law to each family of reflections), a size effect that would be associated with a needle-like morphology of the particles. Their calculated sections were close to $0.7 \times 0.95 \mu\text{m}^2$ and their elongation along the direction [010]. Surprisingly, this section is found larger than expected with dimensions corresponding to the

biggest particles observed in **Figure III-1b**, whereas the smallest and more numerous ones should impact more strongly the profile. Considering the anisotropic strain model, it predicts that the strains are maximal along the [101] direction which is the propagation direction of the chains built of VO₄F₂ octahedra. The inspection of the microstructural parameters reveals that the families of reflections which are strongly affected by significant broadening are (h0h), (h00), (00l) and (hhh). It appears difficult to discriminate between the two anisotropic models. Nevertheless, TEM analyses were performed in order to determine the actual elongation direction of the needle-like particles observed by SEM and to examine how extended is the periodicity (**Figure III-4**).

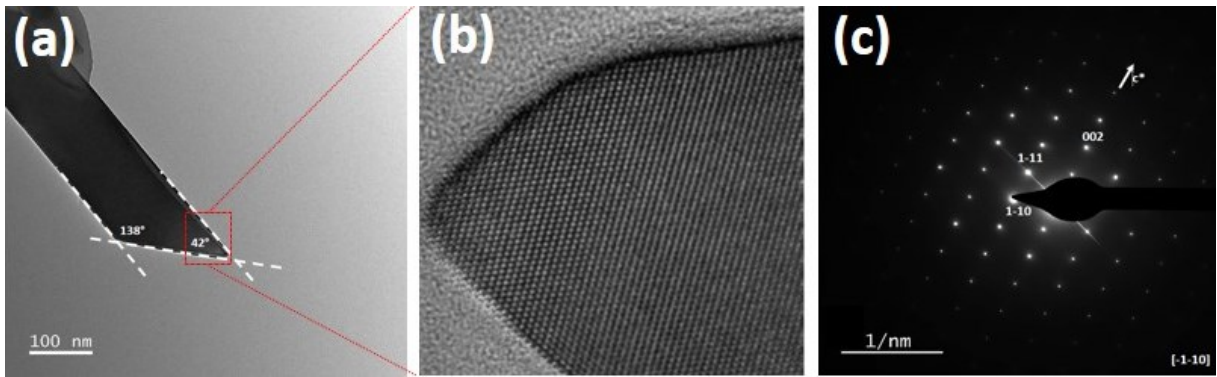


Figure III-4: (a) TEM image of an isolated needle-like particle, representative of the whole sample. The higher magnification picture (b) and the resulting electron diffraction pattern (c).

A TEM image of an isolated needle-like particle, with dimensions of the order of 100 nm width and 1 μ m long, is shown in **Figure III-4a**. The elongation direction of the particles was found to be along the [1-10]. This direction is actually different from the [010] suggested by the microstructural analysis based on the 3D rebuilding of the particles' shape (**Figure III-3**). This result reveals that the anisotropic size model cannot be retained to explain the microstructure, and thus that strains might generate the anisotropic broadening of the diffraction lines. Nevertheless, the high magnification image given in **Figure III-4b** highlights a quasi-perfect long range ordering without any defects in the (-1-10)* plane of the reciprocal space. The electron diffraction pattern reported in **Figure III-4c** can be indexed in the monoclinic space group C2/c with cell parameters in good agreement with those obtained by X-ray diffraction. At least for these small size needles studied by TEM, no diffusion trails or dislocations were observed despite clear anisotropic microstructural effects probably associated with the presence of oxygen in partial substitution for fluorine in NaVPO₄F. Note that similar apparent discrepancies were observed for the lithiated analogue (*i.e.* LiVPO₄F), containing in fact vanadyl-type defects perfectly identified by ⁷Li NMR whereas they were not detected by TEM.¹⁹

Our in-depth analysis of the SXRPD pattern considering different microstructural models, the agreement factors obtained and our previous knowledge of Tavorite systems such as $\text{LiVPO}_4\text{F}_{1-y}\text{O}_y$ ¹⁴ led us to retain the strain broadening model to describe the SXRPD pattern of NaVPO_4F for the Rietveld refinement described here just after.

ii. Structural description

Atomic positions were determined using the *ab-initio* structure solving method provided by the EXPO software.¹⁷⁰ The result of the Rietveld refinement is given in **Figure III-5** and all the structural parameters and reliability factors are listed in **Table III-1**.

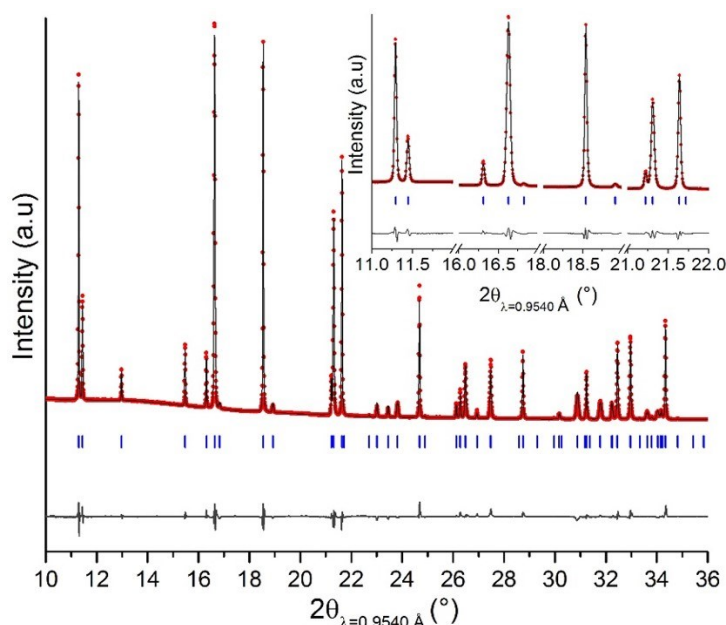


Figure III-5: Rietveld refinement of the structure of “ NaVPO_4F ” using an anisotropic strain broadening model.

Table III-1: Structural parameters obtained by Rietveld refinement of the structure of “ NaVPO_4F ” based on synchrotron XRPD Data.

« NaVPO_4F »							
SG : C2/c		$a = 6.56468(6) \text{ \AA}$					
Z = 4		$b = 8.44060(6) \text{ \AA}$	$\beta = 117.8479(5)^\circ$			$R_{\text{Bragg}} = 3.73\%$	
		$c = 7.37274(6) \text{ \AA}$				$\chi^2 = 22.9$	
		$V = 361.206(6) \text{ \AA}^3$	$V/Z = 90.302(6) \text{ \AA}^3$				
atoms	Wickoff position	x	y	z	occupancy	B_{iso}	BVS
V (1)	4c	$\frac{1}{4}$	$\frac{1}{4}$	0	1	0.78(5)	3.11(2)
P (1)	4e	0	0.0671(4)	$\frac{1}{4}$	1	0.8(1)	4.93(5)
O (1)	8f	0.2163(9)	0.9619(6)	0.3646(8)	1	0.6(1)	1.95(2)
O (2)	8f	0.0333(9)	0.1768(6)	0.0984(8)	1	0.7(1)	1.99(3)
F (1)	4e	0	0.6684(8)	$\frac{1}{4}$	1	1.6(2)	1.34(1)
Na (1)	4e	0	0.4130(6)	$\frac{1}{4}$	1	3.3(2)	1.26(1)

The structural description thus obtained is $(\text{Na})_{4e}(\text{V})_{4c}\{(\text{P})_{4e}[\text{O}_{8f}]_2\}\text{F}_{4e}$, with vanadium on the inversion center of the VO_4F_2 octahedra and both V-F bonds symmetrically equivalent along the chains, on the contrary to what is observed for NaVPO_4O . Indeed, the space group $C2/c$ used to describe $\text{NaV}^{\text{III}}\text{PO}_4\text{F}$ forbids the distortion of the octahedra around vanadium along the dz^2 orbital, whereas the space group $P2_1/c$ used to describe $\text{NaV}^{\text{IV}}\text{PO}_4\text{O}$ allows the distortion required for the formation of the vanadyl bond (*i.e.* the short $\text{V}^{\text{IV}}=\text{O}$ bond).

In order to determine the nature of the bridging anions (*i.e.* oxygen or fluorine, that cannot be distinguished by X-ray or neutron diffraction), bond valence sums (BVS) were calculated according to¹²⁷. The BVS value associated with the bridging anion was found to be smaller (1.34(1)) than those of the two other anions belonging to the equatorial plane of the octahedra (1.97(2), in average). This result is in agreement with the structures already reported for other existing Tavorite-like fluoride phosphate phases, with the fluorine atom bridging adjacent MO_4F_2 octahedra along the chains. Nevertheless, the BVS value determined for the bridging anion is higher than the theoretical value of 1 and the one determined for vanadium is also found to be superior to 3 (*i.e.* $\text{BVS}(\text{V}) = 3.11(2)$). These BVS values are higher than expected assuming the NaVPO_4F composition, but in very good agreement with the magnetic susceptibility measurements (*i.e.* $\text{V}^{3.15+}$). That is explained by the partial replacement of fluorine by oxygen and thus the presence of $\text{V}^{4+}=\text{O}$ vanadyl-type defects in the structure for the charge compensation. Indeed the BVS calculation being based on the average structure determination reveals thus the average oxidation state of “an ion” that can be in fact a distribution of ions in one site, such as here O^{2-} and F^- in the $4e$ anionic site or V^{3+} and V^{4+} in the $4c$ cationic site.

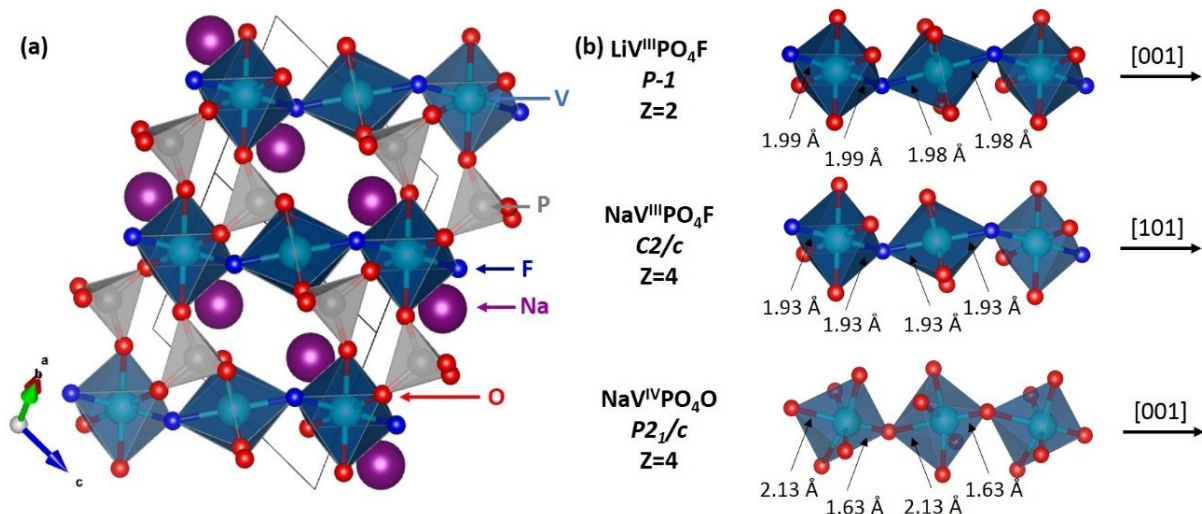


Figure III-6: (a) The structure of “ NaVPO_4F ” (b) a comparison of bond lengths along the chains of vanadium octahedra for the Tavorite-like structures: $\text{LiV}^{\text{III}}\text{PO}_4\text{F}$ (top), “ $\text{NaV}^{\text{III}}\text{PO}_4\text{F}$ ” (middle) and $\text{NaV}^{\text{IV}}\text{PO}_4\text{O}$ (bottom).

The atomic arrangement in “NaVPO₄F” is illustrated in **Figure III-6** and the main distances and angles are summarized in **Table III-2**. This crystal structure is built up by VO₄F₂ octahedra which share common fluorine atoms in such way to form ...V...F...V...F...V... infinite chains running along [101]. These chains of octahedra are connected to each other via PO₄ tetrahedra forming ...V...O...P...O...V... sequences. These corner-sharing polyhedra generate a three-dimensional network within which the sodium ions occupy the tunnels along the [-110] direction. The phosphorus atom lies within a tetrahedron (polyhedron distortion parameters: $\Delta = 8.40 \times 10^{-6}$, whose definition is provided in the caption of the **Table III-2**) with P–O distances in the range of 1.543 – 1.549 Å. Vanadium lies within an octahedral site with a narrow range of V–O distances, 1.974(3) - 2.009(4) Å, a V–F distance of 1.934(6) Å and a rather high distortion of the VO₄F₂ octahedron ($\Delta = 2.61 \times 10^{-4}$) mostly due to the shorter V-F distances along the dz² orbitals of vanadium.

Table III-2: Bond lengths (below the diagonal) and angles (above the diagonal) in the coordination polyhedra of “V³⁺”, Na⁺ and P⁵⁺ in “NaVPO₄F”. The polyhedral distortion is calculated as $\Delta = \frac{1}{N} \sum_{i=0}^N \frac{(d_i - \langle d \rangle)^2}{\langle d \rangle^2}$ with N the number of bond distances considered, d_i the distance between the atom i and the central atom of the polyhedron and $\langle d \rangle$ the average of the distances considered.

VO ₄ F ₂						
	O(1)	O(1')	O(2)	O(2')	F(1)	F(1')
O(1)	2.009(4)	180	88.4(2)	91.6(2)	89.8(2)	90.2(2)
O(1')	4.008(5)	2.009(4)	91.6(2)	88.4(2)	90.2(2)	89.8(2)
O(2)	2.774(4)	2.854(3)	1.974(3)	180	91.0(2)	89.0(2)
O(2')	2.854(6)	2.774(4)	3.952(6)	1.974(3)	89.0(2)	91.0(2)
F(1)	2.774(6)	2.786(5)	2.785(5)	2.735(3)	1.934(6)	180
F(1')	2.786(5)	2.774(6)	2.735(3)	2.785(4)	3.854(3)	1.934(6)
$\Delta = 2.61 \times 10^{-4}$						
PO ₄						
	O(1)	O(1')	O(2)	O(2')		
O(1)	1.549(3)	110.7(3)	109.8(3)	110.1(3)		
O(1')	2.562(6)	1.549(3)	110.1(3)	109.8(3)		
O(2)	2.541(6)	2.545(6)	1.543(4)	106.1(3)		
O(2')	2.545(6)	2.541(6)	2.474(4)	1.543(4)		
$\Delta = 8.40 \times 10^{-6}$						
NaO ₆ F						
	O(1)*2	O(1')*2	O(2)*2	F(1)		
O(1)	2.756(5)	80.2(2)	90.0(2)	67.7(4)		
O(1')	3.342(4)	2.415(4)	73.6(2)	80.4(5)		
O(2)	3.623(5)	2.854(6)	2.352(6)	148.3(5)		
F(1)	2.786(5)	2.960(5)	4.344(9)	2.165(9)		
$\Delta = 6.84 \times 10^{-3}$						

A comparison with similar Tavorite vanadium phosphate compositions is required to fully understand the nature of the bonds observed along the chains of octahedra, depending on the bridging anion. The V³⁺-rich compounds, LiV^{III}PO₄F, LiV^{III}PO₄OH and HV^{III}PO₄OH, show

constant bond lengths along their chains: shorter (1.98-1.99 Å) for V-F⁹², intermediate (2.00-2.03 Å) for V-{OH}¹⁵³, and longer (2.15 Å) for V-{OH₂}¹⁶⁸. Therefore, the shorter V-F distances observed in “NaVPO₄F” (*i.e.* 1.93 Å *vs.* 1.98-1.99 Å in LiVPO₄F) could be explained by the formation of local vanadyl-type (*i.e.* V⁴⁺=O) defects. Indeed, the homeotype NaV^{IV}PO₄O phase exists, with an alternation between short and long bonds along the chains (1.68 and 2.09 Å respectively⁹⁵). As X-ray diffraction is only able to describe an average structure, the partial replacement of ionic V³⁺-F bonds by covalent V⁴⁺=O bonds actually tends to decrease the average distances. However the comparison of The Alkaline-Fluorine distances in NaVPO₄F and LiVPO₄F could offer another explanation. Indeed, it appears that the Na-F distance observed in the sodiated phase (*i.e.* 2.16(1) Å) is rather long compared to the Li-F one observed in LiVPO₄F (*i.e.* 1.90(3) Å). That could also explain, by an antagonist bond effects, the shorter V-F distances in NaVPO₄F compared to that observed in LiVPO₄F.

The unique sodium site observed in “NaVPO₄F” is surrounded by six oxygen and one fluorine, in a distorted NaO₆F polyhedron with Na-X distances ranging between 2.17 and 2.76 Å ($\Delta = 6.84 \times 10^{-3}$) with an isotropic Debye-Waller factor (B_{iso}) associated with sodium of 3.3(2) Å². The associated BVS for Na⁺ cation is also in disagreement with its oxidation state (*i.e.* BVS = 1.26(1)), that could also arise from the partial substitution of fluorine by oxygen.

The diffraction study has thus revealed the formation, for the first time, of a V^{III}-rich NaVPO₄F-type phase crystallizing in the Tavorite-like structure. Magnetic susceptibility measurements and the BVS suggest the formation of a slightly oxidized NaVPO₄F. In this material, strong anisotropic strain effects within the framework have been detected by SXRPD. As observed for the LiVPO₄F_{1-y}O_y materials discussed in a previous section, these strains could arise from the competitive formation between the strongly ionic V^{III}-F bond and the highly covalent V^{IV}=O one along the chains of vanadium octahedra. Nevertheless, they could not be detected by TEM. In order to elucidate this contradiction, further characterization of the local environments around vanadium was conducted by combining ²³Na, ¹⁹F and ³¹P MAS Nuclear Magnetic Resonance, diffuse reflectance infrared and X-ray absorption spectroscopies. However, without the support of a theoretical study by DFT calculations of NaVPO₄F_{1-y}O_y²¹, the interpretation of the NMR spectra was not straightforward, but the presence of vanadyl-type defects cannot be excluded. The NMR spectra recorded are shown and discussed in **Annex-III-1** and hereafter we have thus chosen to focus the discussion on the IR and XAS results.

iii. The nature of the defects

The Mid-IR diffuse reflectance spectrum of “NaVPO₄F” is compared to those of LiVPO₄F and LiVPO₄F_{0.92}O_{0.08} (from part II-2-c) in **Figure III-7**. The absence of signal around 3500 cm⁻¹ evidences the absence of hydroxyl groups,¹³⁹ frequently reported for fluorinated compounds obtained by hydrothermal synthesis.¹⁴⁸ The PO₄ stretching region, between 950 and 1200 cm⁻¹, is characterized by three main bands around 983, 1056 and 1102 cm⁻¹ (as highlighted in inset) and by two additional bands, smaller in intensity, at 950 cm⁻¹ (as a shoulder) and 1185 cm⁻¹. Due to the symmetry of the phosphate group imposed by the C2/c space group of “NaVPO₄F”, only one symmetric and three antisymmetric modes are expected¹⁴² but vanadyl-type defects modify the PO₄ local symmetry and give rise to additional contributions. The signal observed at 881 cm⁻¹ can be assigned to a vanadyl-type bond vibration¹⁴¹ (*i.e.* to a short V^{IV}=O bond), as exists in NaV^{IV}PO₄O described in the P2₁/c space group with alternative long and short distances O---V=O along the chains. The average structure of “NaV^{III}PO₄F” is described in the C2/c space group having constant F--V--F distances along the chains, hence the presence of the vibration at 881 cm⁻¹ is the signature of vanadyl-type local defects. The higher intensity of the V=O stretching contribution detected in our NaVPO₄F-type sample, in comparison with the one observed in LiVPO₄F, highlights a higher concentration of vanadyl-type defects in the sodium phase, estimated to be 15% from the magnetic measurements.

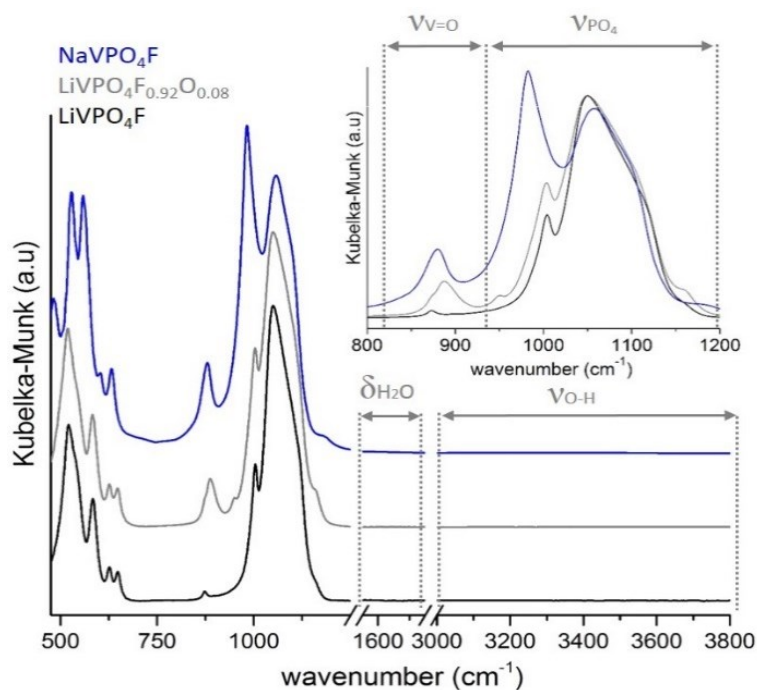


Figure III-7: Diffuse reflectance infrared spectra of “NaVPO₄F” (blue), LiVPO₄F (black) and LiVPO₄F_{0.92}O_{0.08} (grey, taken from part II-2-c). The inset shows an enlarged graph of PO₄ and V^{IV}=O stretching region.

Normalized Vanadium K-edge X-ray absorption near edge structure (XANES) spectra for Tavorite compositions “NaVPO₄F”, LiVPO₄F and LiVPO₄F_{0.92}O_{0.08} are reported in **Figure III-8**. These spectra exhibit a pre-edge absorption feature followed by a rising absorption edge showing a shoulder and culminating in a strong peak at ~5485 eV. This strong peak has been assigned to the dipole-allowed transition 1s to 4p, the lower-energy shoulder as the 1s-4p shakedown transition, and the pre-edge feature as the transition 1s to 3d.¹²⁹ The 1s to 3d transition is strictly forbidden in perfectly regular VO₆ octahedra but becomes dipole allowed when the inversion center is broken. In this case, the distortion of the octahedral local symmetry leads to a V 3d-4p orbital mixing and thus to an overlap of the V 3d orbitals with the 2p orbitals of the ligand¹²⁹. A careful inspection of the pre-edge region reveals weak contributions at 5468.0 and 5469.5 eV for each sample, related to V³⁺ and V⁴⁺ oxidation states respectively.^{85,129} The contribution at 5469.5 eV grows in intensity upon going from LiV³⁺PO₄F to LiVPO₄F_{0.92}O_{0.08} and to “NaVPO₄F”, thus confirming the increase in the vanadium average oxidation state and the formation of local V^{IV}=O vanadyl-type environments.

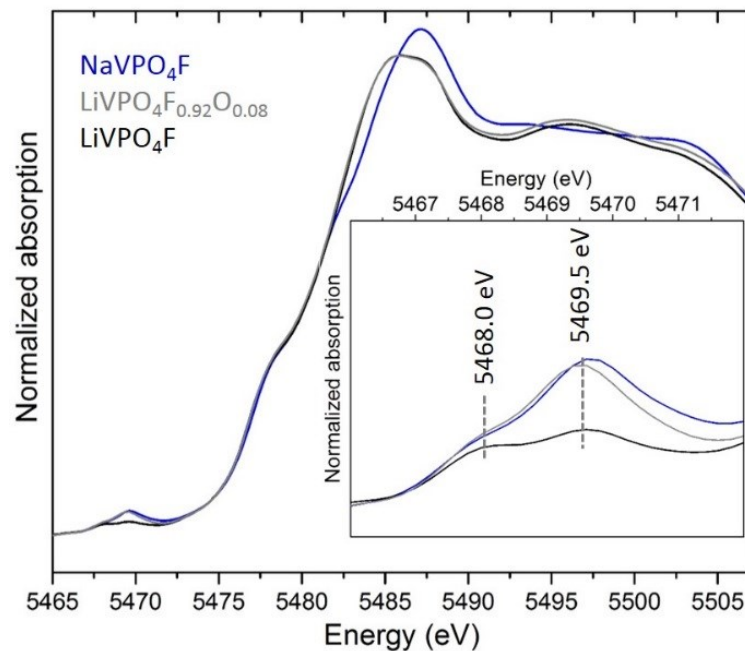


Figure III-8: Vanadium K-edge XANES spectra of “NaVPO₄F” (blue), LiVPO₄F (black) and LiVPO₄F_{0.92}O_{0.08} (grey, taken from part II-2). The inset shows an enlargement of the pre-edge region (5466-5472 eV).

The investigation of the local symmetry around vanadium through IR and XAS evidences the presence of vanadyl-type defects in our NaVPO₄F-type sample. Moreover, magnetic susceptibility measurements and the BVS calculation have already suggested the formation of a partially oxidized material with an average oxidation state for vanadium around 3.15 whereas ICP and SXRPD excluded a charge compensation by Na⁺ vacancies. Therefore, the

approximated $\text{NaV}^{\text{III}}_{0.85}(\text{V}^{\text{IV}}\text{O})_{0.15}(\text{PO}_4)\text{F}_{0.85}$ composition can be proposed for this material. As already demonstrated in the Chapter II, LiVPO_4F delivers interesting electrochemical performance and the vanadyl-type defects enhance even more the transport properties: What about for its sodiated analogue?

III-1b. Study of electrochemical inactivity

i. Electrochemical tests

Electrochemical cells were cycled at C/50 between 2.50 and 4.50 V vs Na^+/Na . As shown in **Figure III-9** the specific capacity obtained during the first charge is limited to 20% of the theoretical one (*i.e.* 30 against 144 mAh/g) and the amount of sodium reinserted is almost negligible. The value of the working potential associated with the $\text{V}^{3+}/\text{V}^{4+}$ redox couple cannot be determined due to the very small reversible capacity, the high polarization and the absence of a clear voltage plateau.

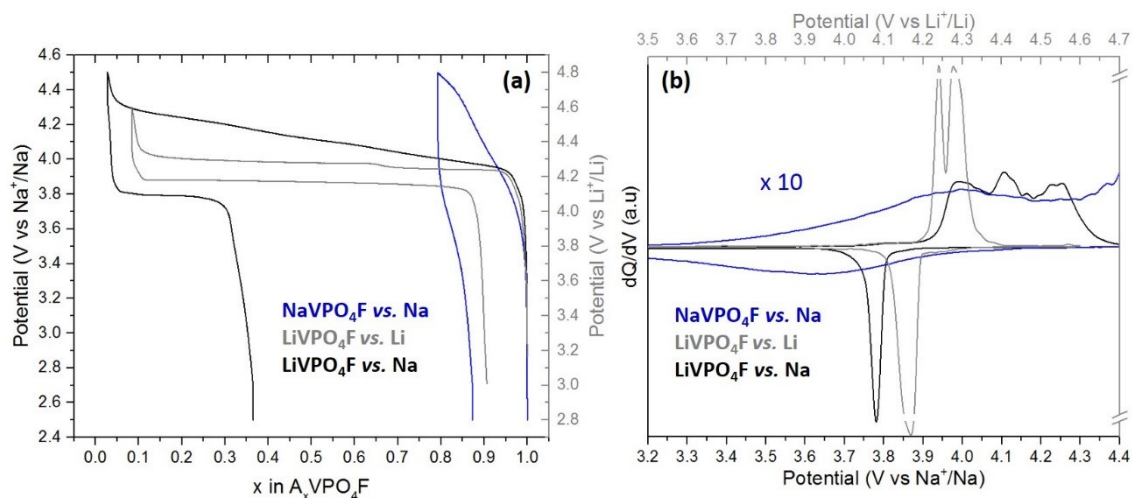


Figure III-9: (a) electrochemical signatures of “ NaVPO_4F ” (blue) and LiVPO_4F (black) obtained in half cells versus Na are compared to that of LiVPO_4F versus Li (grey) at C/50. (b) The corresponding derivative curves. The scales in voltage, vs. Li^+/Li and vs Na^+/Na , were shifted from 0.3 V.

In order to determine if sodium extraction is kinetically or thermodynamically limited, the chemical oxidation of “ NaVPO_4F ” was performed using an excess of NO_2BF_4 in acetonitrile during 7 days. As shown in **Figure III-10**, the SXRPD pattern of the material obtained can be indexed in a unit cell really close to that of the pristine phase NaVPO_4F , with only a small increase in the cell parameters ($a = 6.5691(1)$ Å, $b = 8.4464(1)$ Å, $c = 7.3780(1)$ Å, $\beta = 117.847(1)^\circ$, $V = 361.968(6)$ Å³ against $a = 6.5646(1)$ Å, $b = 8.4406(1)$ Å, $c = 7.3727(1)$ Å,

$\beta = 117.847(1)^\circ$, $V = 361.208(6) \text{ \AA}^3$ for the pristine material) and an occupancy of 0.92(3) for the 4e Na site. That leads to a BVS value for the vanadium slightly higher than that observed in the pristine material (*i.e.* 3.33(1) vs 3.11(2)).

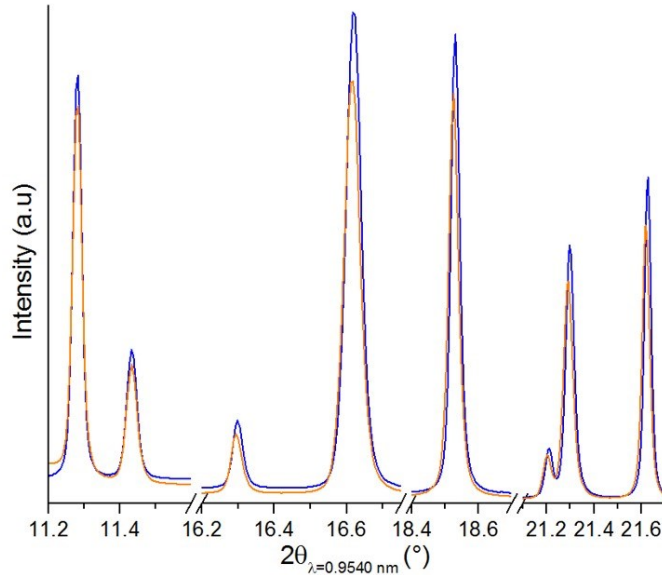


Figure III-10: comparison of selected 2θ angular ranges of SPXRD patterns of pristine “NaVPO₄F” (in blue) and samples which have been in contact with the oxidizing solution (orange).

The closely related lithiated phase, LiVPO₄F, was also cycled in a sodium cell for comparison. Indeed, cycled versus Lithium, the electrochemical performance obtained for this material are excellent with a reversible capacity close to the theoretical one⁹². The electrochemical signature of LiVPO₄F versus sodium is given in **Figure III-9** and appears different from the one observed versus lithium. Indeed, besides a higher average potential, lithium extraction occurs according to a continuous change in the extraction voltage vs. Na⁺/Na whereas two successive plateaus are observed at 4.24 and 4.28 V vs Li⁺/Li. In both cases, one electron is exchanged. During the next discharge vs. Na only 0.3 electron is involved and the intercalation of Na⁺ is limited. At the end of the charge the concentration ratio [Li⁺]/[Na⁺] inside the electrolyte is close to 0.05 (~5 mg of the active material LiVPO₄F vs. 100 μ L of a 1M NaPF₆ solution), and therefore Na⁺ (and not Li⁺) is expected to be the cation reinserted in VPO₄F.

ii. Understanding of the electrochemical inactivity

In order to understand the lithium extraction mechanism from LiVPO₄F into the sodiated electrolyte and to determine the nature of the cation re-inserted during the next discharge, laboratory X-ray diffraction was used to follow the electrochemical reaction under *operando* conditions.

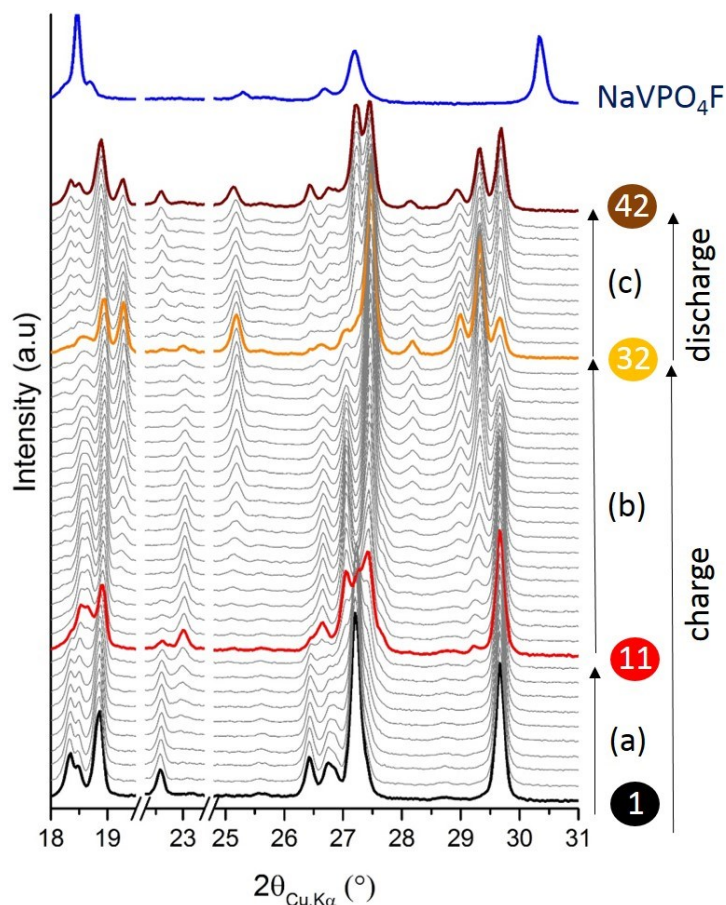


Figure III-11: Selected 2θ region of X-ray diffraction patterns recorded operando during electrochemical cycling of LiVPO_4F vs Na at C/50 (1 pattern/90 minutes). XRD patterns corresponding to each part of the phase diagram $\text{A}_x\text{VPO}_4\text{F}$ ($\text{A} = \text{Li}$ or/and Na) are gathered: (a) biphasic mechanism between LiVPO_4F (black line) and $\text{Li}_{0.67}\text{VPO}_4\text{F}$ (red line), (b) biphasic mechanism between $\text{Li}_{0.67}\text{VPO}_4\text{F}$ and VPO_4F (orange line) and (c) biphasic process between VPO_4F and AVPO_4F ($\text{A} = \text{Li}$ and/or Na). The XRD patterns corresponding to “ NaVPO_4F ” (blue line) acquired under the same conditions is also compared to the patterns obtained operando.

Operando XRD patterns are shown in **Figure III-11**. During the first part of the charge (between patterns #1 and #11), the intensity of the diffraction peaks associated with the pristine phase LiVPO_4F progressively decreases, whereas new lines that can be indexed with the unit cell parameters of $\text{Li}_{0.67}\text{VPO}_4\text{F}$ that continuously grow in intensity. The XRD pattern #11, recorded at 1/3 of the charge (*i.e.* corresponding to a global composition of $\text{Li}_{0.67}\text{VPO}_4\text{F}$), is highlighted in red in **Figure III-11** and can be indexed considering the presence of three phases as reported in **Table III-3**: LiVPO_4F , $\text{Li}_{0.67}\text{VPO}_4\text{F}$ and VPO_4F . Spatial inhomogeneity in the electrode might be at the origin of the coexistence of the 3 phases. Upon further Li^+ extraction (between patterns #11 and #32), a two-phase process occurs between $\text{Li}_{0.67}\text{VPO}_4\text{F}$ and VPO_4F . The fully-oxidized VPO_4F phase was refined in a similar unit cell (*i.e.* S.G: $\text{C2}/c$, $a = 7.1531(9) \text{ \AA}$, $b = 7.1153(6) \text{ \AA}$, $c = 7.220(9) \text{ \AA}$, $\beta = 118.096(4)^\circ$, $V = 319.77(6) \text{ \AA}^3$), close to the previously reported when obtained by Lithium deintercalation from LiVPO_4F in a 1M LiPF_6 electrolyte.^{20,101} No significant difference is observed in the phase diagram stabilized during Lithium extraction

from LiVPO₄F, whatever the nature of the salt (LiPF₆ or NaPF₆) in the electrolyte and the negative electrode (Li or Na) used. The phase diagram itself thus does not provide any information which could explain the difference observed between the first electrochemical charges obtained for the LiVPO₄F//Li and LiVPO₄F//Na cells. Nevertheless, a Li⁺/Na⁺ exchange could occur at the interface between the Li-rich electrode material and the Na-rich liquid electrolyte. The formation of such interphase could modify the potential at the extreme surface of the particles during the lithium deintercalation, and thus explain the different voltage profile observed vs. Na.

Table III-3: Cell parameters and weight fractions of the phases involved in the phase diagram of LiVPO₄F cycled versus Na at specific states of charge (SOC) or of discharge (SOD). The quality of the data obtained does not allow to refine the cell parameters of the minor phases. Consequently, these phases whose cell parameters were fixed according to values reported in literature are noted by *.

Scan# (SOC/SOD)	#1 (0%)	#11 (33%)				#32 (100%)		#42 (30%)		
Phases	LiVPO ₄ F	LiVPO ₄ F	Li _{0.67} VPO ₄ F	VPO ₄ F*	Li _{0.67} VPO ₄ F	VPO ₄ F	LiVPO ₄ F	Li _{0.67} VPO ₄ F*	VPO ₄ F	
S.G.	<i>P-1</i>	<i>P-1</i>	<i>P-1</i>	<i>C2/c</i>	<i>P-1</i>	<i>C2/c</i>	<i>P-1</i>	<i>P-1</i>	<i>C2/c</i>	
<i>a</i> (Å)	5.1673(3)	5.169(1)	5.1687(4)	7.151	5.170(2)	7.1512(9)	5.1666(6)	5.17	7.1531(9)	
<i>b</i> (Å)	5.3075(3)	5.306(1)	5.2208(6)	7.109	5.223(4)	7.1094(6)	5.3074(6)	5.22	7.1153(6)	
<i>c</i> (Å)	7.2628(3)	7.259(2)	7.2711(5)	7.119	7.272(2)	7.1192(9)	7.2648(7)	7.27	7.1220(9)	
α (°)	107.631(6)	107.74(3)	107.467(9)	90	107.53(6)	90	107.70(1)	107.5	90	
β (°)	107.999(6)	108.04(2)	109.480(9)	118.09	109.53(6)	118.096(6)	108.07(9)	109.5	118.096(5)	
γ (°)	98.352(6)	98.26(2)	96.951(1)	90	96.89(9)	90	98.29(7)	96.9	90	
<i>V/Z</i> (Å ³)	174.16(1)	173.97(8)	171.03(1)	319.3	171.06(2)	319.29(7)	174.06(3)	171	319.77(6)	
Weight fraction (%)	100	17(3)	81(4)	2(1)	14(4)	86(4)	39(2)	4(2)	57(4)	

The X-ray diffraction patterns recorded during the next discharge highlight the recovering of the LiVPO₄F phase, and surprisingly not the formation of the phase NaVPO₄F (or Na_xVPO₄F) despite a Na⁺/Li⁺ ratio inside the electrolyte close to 20. Indeed, no Bragg positions related to the monoclinic cell of NaVPO₄F could be detected, whereas other Bragg positions were observed, in good agreement with the cell parameters of LiVPO₄F (comparison given in **Table III-3**, those obtained at the end of the discharge are really close to those of the pristine material LiVPO₄F). These results suggest that no Na⁺ cations could be inserted into VPO₄F during the discharge. The limited discharge capacity and the high polarization are probably due to the lack of Li⁺ cations at the interface electrode/electrolyte and the insertion reaction is thus limited. The poor electrochemical performance delivered by “NaVPO₄F” could arise from the intrinsic low sodium mobility in Tavorite-like structure, therefore, in order to get more insights into the possible pathways for sodium diffusion, the Bond Valence Energy Landscape (BVEL) was calculated thanks to the Bondstr software provided in the Fullprof suite¹⁷¹ and drawn with Vesta¹⁷² (**Figure III-12**). This empirical method uses Bond Valence Sum to determine possible

diffusion pathways considering a given energy to activate the movement of Na^+ ions.¹⁷³ An energy of 1.6 eV is commonly used for alkaline diffusion in polyanionic compounds (**Figure III-12a**).

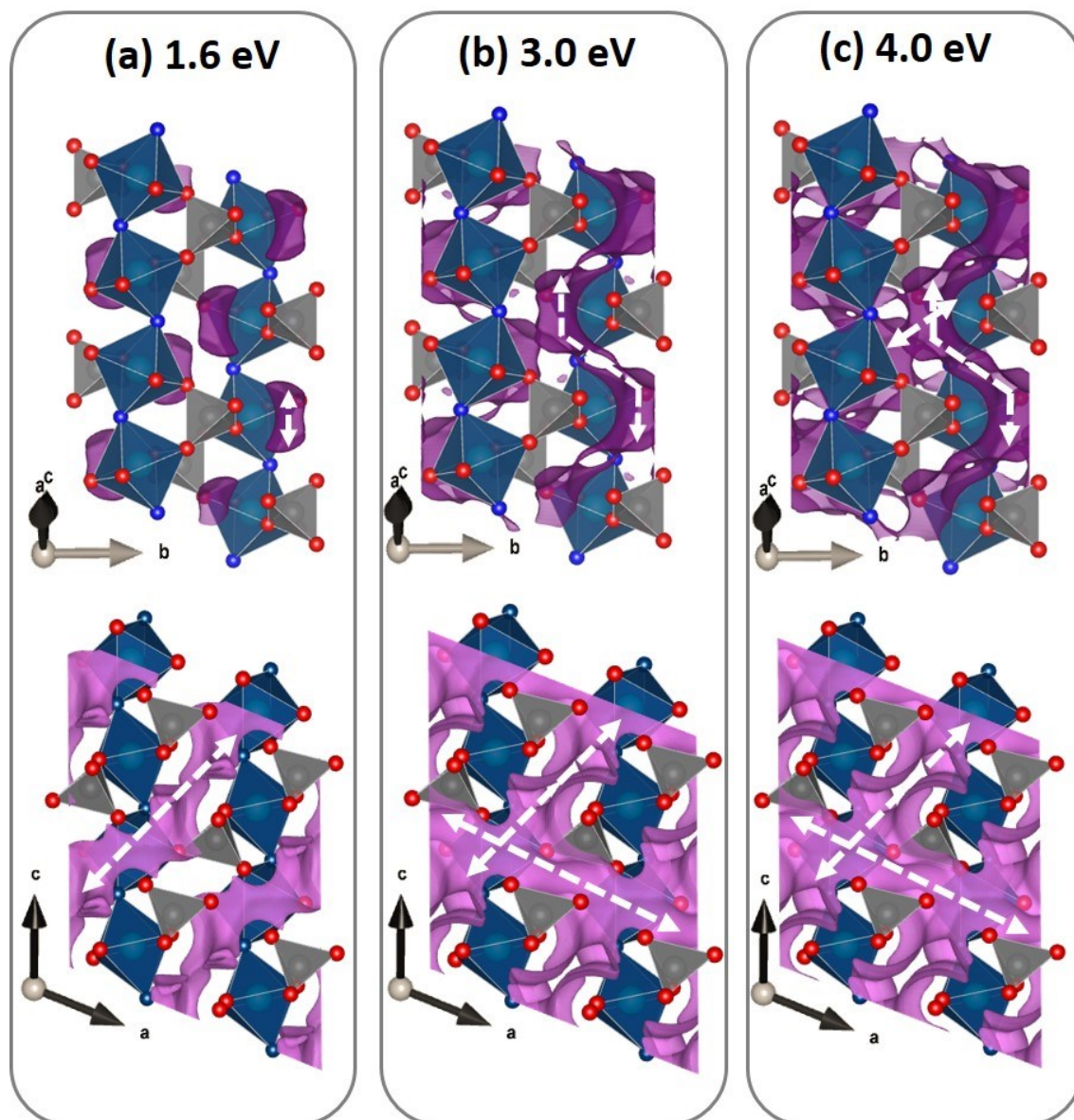


Figure III-12: Sodium (top) and Lithium (bottom) diffusion pathways in “ NaVPO_4F ” and LiVPO_4F respectively calculated thanks to Bond Valence Energy Landscape with an energy of 1.6 eV (a), 3 eV (b) and 4 eV (c).

It appears that in these conditions sodium diffusion is limited inside the structure of “ NaVPO_4F ” whereas at this energy a percolated lithium diffusion path is observed along $[111]$ and $[101]$ in LiVPO_4F . A value of 3 eV is necessary to make possible sodium diffusion from one site to another and to obtain a zig-zag sodium diffusion pathway parallel to the octahedral chains (*i.e.* along the $[101]$ of “ NaVPO_4F ”). As the particle’s shape is needle-like and elongated along $[1-10]$, the direction along $[101]$ (*i.e.* at 75° with $[1-10]$) corresponds to a rather short

diffusion path through the solid for the Na⁺ ions. The needle-like morphology is thus the most appropriate to counterbalance the apparent low intrinsic conductivity, despite the fact that the electrochemical performance of “NaVPO₄F” are really bad compared to those of its lithiated analogue. Indeed, at this energy (*i.e.* 3eV, **Figure III-12b**) a 3D percolated path for Lithium is observed in LiVPO₄F. From an energy value of 4 eV, a second direction for sodium diffusion becomes possible along the [001] which is the direction of the smaller Na-Na distance (3.97 Å) and the preferential direction computed by Ceder and coworkers for lithium diffusion in the Tavorite-type VPO₄F.¹⁷⁴ For LiVPO₄F, this path is activated at an energy below 1.6eV, thus the sodium diffusion in Tavorite structure appears much more difficult than Lithium.

III-1c. Summary and prospects

We report for the first time the synthesis of a Na-based V^{III}-rich phase crystallizing in the Tavorite-like structure. This material was obtained in hydrothermal conditions, showing needle-like shape particles with different sizes. Its crystal structure as well as its electronic properties were fully determined using a combination of several techniques, spanning electron and X-ray powder diffraction as well as Infrared, NMR and X-ray spectroscopy. The BVS calculation and the magnetic susceptibility measurement support an average oxidation state for vanadium slightly higher than V³⁺, suggesting the presence of vanadyl-type defects (close to 15%) and thus the approximated NaVPO₄F_{0.85}O_{0.15} composition. Microstructural effects were identified through the anisotropic broadening of the X-ray lines. Indeed, such strain is consistent with the presence of vanadyl-type environments as defects, which would generate locally a shortening of the V-F(O) distances along the chains of VO₄(F,O)₂ octahedra. Spectroscopic techniques such as IR and XAS were used to investigate the local environments. Indeed, the characteristic features of vanadyl-type contribution have been clearly identified whereas the presence of OH groups have been excluded. This material is electrochemically (quasi) inactive despite a suitable morphology and vanadyl-type defects which are expected to enhance the performance (at least for the lithiated analogue). Indeed, bond valence energy landscape and *operando* X-ray diffraction of LiVPO₄F cycled versus sodium reveal that the electrochemical properties are inhibited by intrinsic low sodium mobility in such Tavorite framework.

To the best of our knowledge, only few Na-based Tavorite compositions have been reported in literature (NaVPO₄O, NaFeSO₄F and now “NaVPO₄F”). It appears that these materials provide poor electrochemical performance compared to their lithiated analogues and thus aren't suitable for application in Na-ion batteries. In a general way, the strategy

aiming to replace the lithiated materials delivering good performance by their sodiated analogues fails. So let's come back to the lithiated Tavorite phase for the investigation of the effect of the further substitution of anionic site by OH groups in LiVPO_4OH .

III-2. LiVPO₄OH, a new type of two electrons system

Up to now the vanadium hydroxyl phosphate with Tavorite structure had never been reported except as a composition mentioned in a patent¹⁷⁵, and despite the existence on one side of vanadium-containing Tavorite-like phases (LiVPO₄F, LiVPO₄O and HVPO₄OH^{92,168}) and on the other side of a series of Tavorite-like hydroxyl phosphates (LiAlPO₄OH, LiFePO₄OH and LiMnPO₄OH^{31,176,177}). In the following, a first report of the synthesis of LiVPO₄OH, its careful structural characterization and an in-depth study of its electrochemical behavior will be given.

III-2a. Syntheses and structure of LiVPO₄OH

iii. Syntheses: influence of vanadium precursors on morphology and composition

By analogy with hydrothermal syntheses already reported for other Tavorite type materials, HVPO₄OH (or VPO₄·H₂O)¹⁶⁸, LiFePO₄OH³¹ and LiVPO₄O¹⁶⁹, we obtained the vanadium (III) hydroxyl phosphate LiVPO₄OH. Three different vanadium precursors were used, V^{III}Cl₃, V^{III}PO₄ and V^V₂O₅, according to the following conditions:

LVPH-a: VCl₃ + 1.40 Li₃PO₄ + 50 H₂O (240°C, 24h)

LVPH-b: C-VPO₄ + 2 CH₃COOLi·2H₂O + 100 H₂O (240°C, 24h)

LVPH-c: V₂O₅ + 1.5 N₂H₄·H₂O + 3 H₃PO₄ + 6 LiOH·H₂O + 200 H₂O (250°C, 24h)

All the precursors used (*i.e.* VCl₃ (Sigma-Aldrich, 97%), V₂O₅ (Sigma-Aldrich, >98%), LiOH·H₂O (Sigma-Aldrich, 97%), CH₃COOLi·2H₂O (Sigma-Aldrich, >98%), Li₃PO₄ (Sigma-Aldrich, 97%), H₃PO₄ (Sigma-Aldrich, 68% in water) and N₂H₄·H₂O (Sigma-Aldrich, 78-82% in water)) are commercially available except VPO₄. It was prepared, as previously reported⁹², through a carbothermal route by ball milling stoichiometric amounts of V₂O₅ and ammonium dihydrogenphosphate (NH₄H₂PO₄, Sigma-Aldrich, >99%) together with an excess of highly divided carbon (Csp) (15 wt%). This carbon acts as reducing agent of V⁵⁺ to V³⁺ and the remaining amount should enhance the electronic conductivity of the final product. Then, performing a thermal treatment under argon flow at 800°C during 8h, C-VPO₄ was obtained. For each sample, the precursors were introduced as such in 23mL Teflon vessels filled at ~60%. The reactors were set in a furnace already at the temperature required for the thermal treatment, and were cooled down naturally until room temperature. The obtained powders were filtered, washed with water, rinsed with ethanol and dried at 60°C overnight.

The reaction leading to LiVPO_4OH is driven by the basic pH of the starting solution (between 8 and 10), whereas moving to acidic solutions leads to the formation of the $\text{VPO}_4 \cdot \text{H}_2\text{O}$ (or HVPO_4OH) Tavorite-like composition. Indeed, that latter can be obtained from VCl_3 by replacing Li_3PO_4 by H_3PO_4 , or from V_2O_5 by replacing $\text{H}_3\text{PO}_4 \cdot \text{LiOH} \cdot \text{H}_2\text{O}$ by H_3PO_4 only. Nevertheless, all our attempts to obtain HVPO_4OH directly from LiVPO_4OH by Li^+/H^+ ionic exchange in HCl aqueous solution failed, as for the reverse reaction (*i.e.* formation of LiVPO_4OH from HVPO_4OH) in LiOH aqueous solution. On the contrary, Marx et al. reported the possibility to obtain Tavorite type $\text{FePO}_4 \cdot \text{H}_2\text{O}$ by a Li^+/H^+ ionic exchange from LiFePO_4OH immersed in a nitric acid aqueous solution and the reverse reaction was shown to occur in LiOH aqueous solution¹⁴².

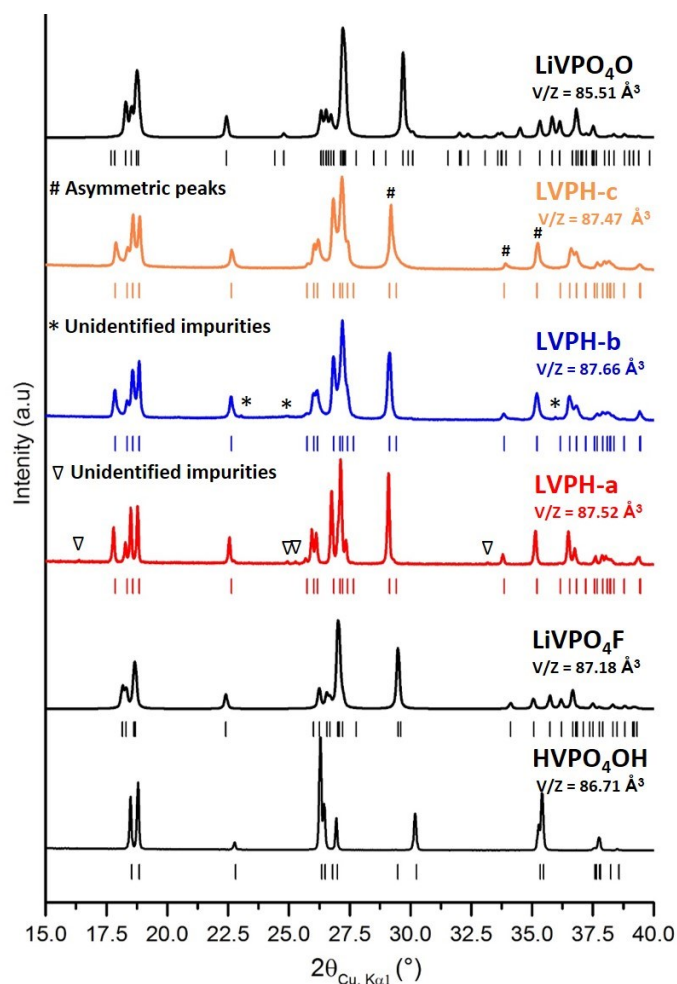


Figure III-13: XRD patterns of the 3 LiVPO_4OH samples (LVPH-a in red, LVPH-b in blue, LVPH-c in orange) and others vanadium based compounds with Tavorite structure (HVPO_4OH , LiVPO_4F and LiVPO_4O plotted as black lines). The theoretical Bragg positions are plotted as black ticks.

The XRD patterns of the three samples thus obtained (LVPH-a, LVPH-b and LVPH-c) are compared in **Figure III-13** to those of other related vanadium based compounds previously studied in our group, LiV^{IV}PO₄O, HV^{III}PO₄OH and LiV^{III}PO₄F. They crystallize in Tavorite type structures described in triclinic (P-1) or monoclinic (C2/c, for HV^{III}PO₄OH) unit cells showing close values for their volume per formula unit (V/Z), and thus similar but easily distinguishable XRD patterns. The XRD pattern of LVPH-a shows narrower diffraction lines than those recorded for LVPH-b and LVPH-c, revealing a higher crystallinity. A careful inspection of these XRD data reveals also the presence of small amounts of impurities in each sample (as highlighted by ∇, * or # in **Figure III-13**). The small intensity peaks observed at $2\theta_{\text{Cu},\text{K}\alpha 1} = 16.3^\circ, 22.7^\circ, 24.9^\circ$ and 33.2° for LVPH-a and at $2\theta_{\text{Cu},\text{K}\alpha 1} = 20.4^\circ, 23.1^\circ$ and 24.9° for LVPH-b cannot be indexed in Tavorite-type unit cells and were attributed to impurities that we haven't been able to identify. Note that for LVPH-c the diffraction lines at $2\theta_{\text{Cu},\text{K}\alpha 1} = 29.1^\circ, 33.8, 35.2$ are obviously asymmetric, which could be explained considering a small amount of Tavorite LiV^{IV}PO₄O-like phase as impurity (as also supported by IR and NMR in the following). The cell parameters determined for the three LiVPO₄OH powders are reported in **Table III-4** and were found to be similar, with unit cell volumes of 175.04(1), 175.32(3) and 174.95(2) Å³ for LVPH-a, LVPF-b and LVPF-c respectively. Thanks to ICP-OES chemical analyses, the molar ratios Li/V/P were determined for the three samples; they are also given in **Table III-4** and are in rather good agreement with the expected LiVPO₄OH stoichiometry (*i.e.* with 1Li:1V:1P), considering the presence of impurities in small amounts

Table III-4: cell parameters determined from pattern matching refinement of XRD patterns, with the corresponding chemical analyses performed by ICP (Li, V and P) or TGA (C).

	LVPH-a	LVPH-b	LVPH-c
Cell parameters, P-1			
a (Å) =	5.1341(2)	5.1369(5)	5.1320(5)
b (Å) =	5.3342(3)	5.3387(6)	5.3286(6)
c (Å) =	7.2833(2)	7.2814 (5)	7.2902(5)
α (°) =	106.557(2)	106.538(5)	106.584(5)
β (°) =	109.216(3)	109.201(6)	109.206(6)
γ (°) =	97.350(2)	97.310(6)	97.335(5)
V (Å ³) =	175.04(1)	175.32(3)	174.95(2)
Chemical analyses (Molar ratio)			
Li/V/P =	0.94/0.96/1	0.95/0.98/1	0.97/1.07/1
C wt% =	/	14.9	/

The SEM images obtained for the three LVPH-a, LVPH-b and LVPH-c powders are given in **Figure III-14**. The primary particles of LVPH-a and LVPH-c are small platelets (smaller than

1.5 and 0.5 μm in diameter respectively), those being agglomerated to form regular spheres of 20 μm in diameter. The morphology of LVPH-b is different with bigger platelet-like primary particles (with a diameter of 1.5 to 3.0 μm and a thickness of 0.5 μm). These primary particles are aggregated in larger agglomerates (50 to 100 μm in diameter), with small grains of carbon (50-100 nm) in the grain boundaries coming from the excess of carbon used during the synthesis of the precursor C-VPO₄. This amount of carbon was determined by TGA analysis to be similar to that initially present in the precursor (*i.e.* around 14.9 wt%). The difference of morphology between LVPH-a, LVPH-b and LVPH-c can be partly explained by a difference of solubility of the precursors used to obtain LiVPO₄OH. Indeed, LVPH-a and LVPH-c are synthesized from VCl₃ or V₂O₅ which are soluble in the alkaline solution whereas the VPO₄ precursor for LVPH-b (with particle size around 50-100 μm) is insoluble at least until 240°C. So, the two former materials are formed by nucleation of species in solution and then growth of small particles which agglomerate. On the contrary, for the latter, as VPO₄ is not soluble, the nucleation of LiVPO₄OH occurs at its surface, then the Li⁺ and HO⁻ ions diffuse inside the particle and the LiVPO₄OH domains grow.

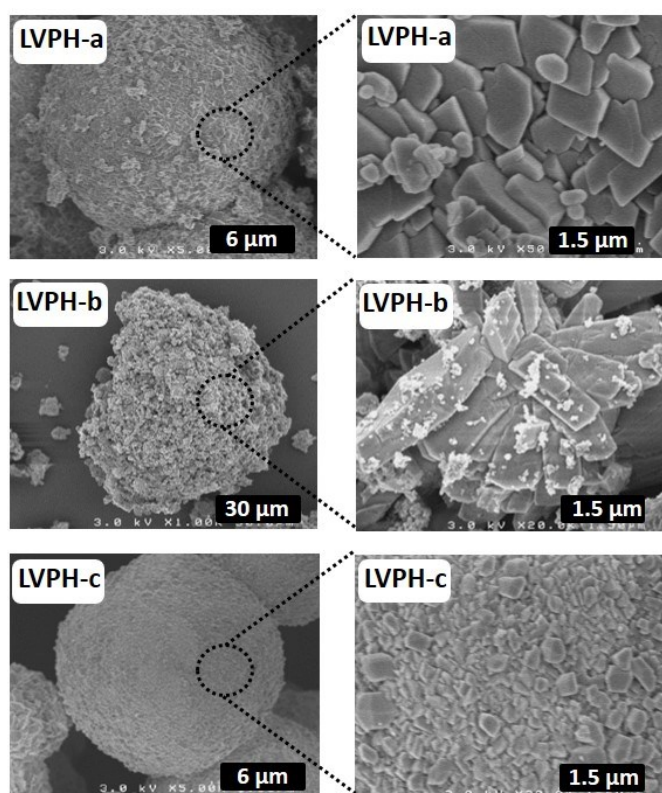


Figure III-14 : SEM images of LVPH-a, LVPH-b and LVPH-c

In the following, in-depth structural characterization from synchrotron and neutron diffraction data (SXRPD and ND) is detailed for LVPH-a, having a better crystallinity.

i. Structure and influence of hydrogen bonds on Li⁺ diffusion paths

The structure of this new LiVPO₄OH Tavorite-like compound was solved using SXRPD and ND combined refinements. Indeed, both diffraction techniques are required because vanadium is a purely incoherent scatterer in ND and light elements such as Lithium and especially Hydrogen weakly scatter in SXRPD. SXRPD pattern of LVPH-a can be indexed with a *P*-1 triclinic unit cell ($a = 5.1335(1) \text{ \AA}$, $b = 5.3334(1) \text{ \AA}$, $c = 7.2824(2) \text{ \AA}$, $\alpha = 106.556(2)^\circ$, $\beta = 109.217(2)^\circ$, $\gamma = 97.352(2)^\circ$, $V/Z = 87.484(6) \text{ \AA}^3$).

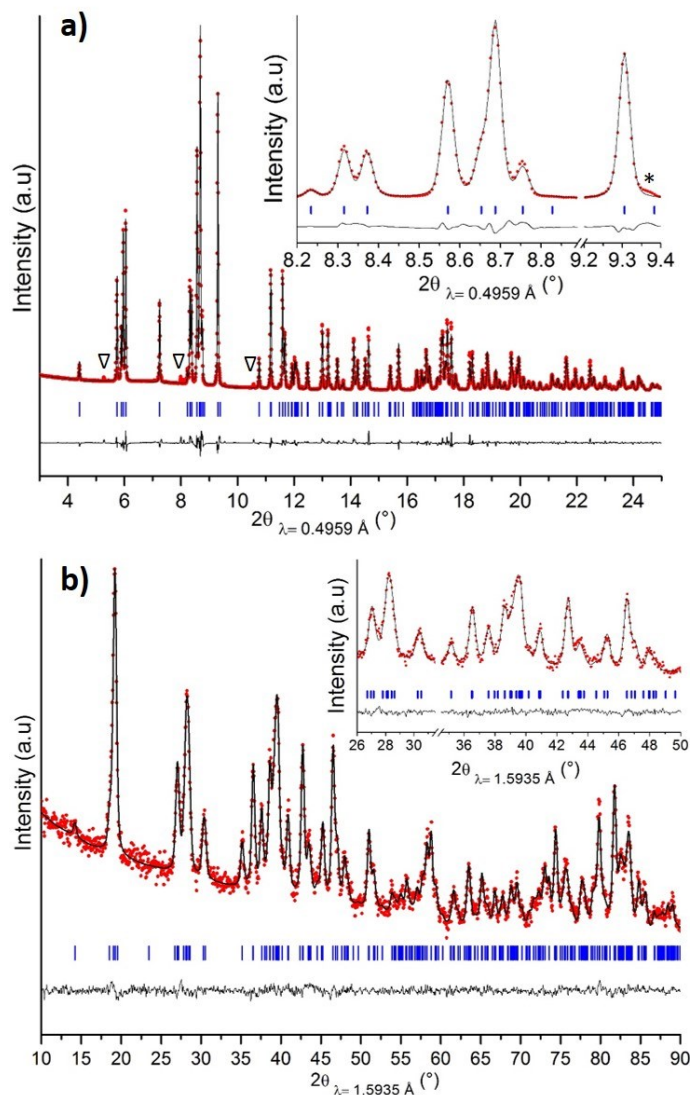


Figure III-15: Rietveld refinement of the structure of LVPH-a combining Synchrotron X-rays (a) and Neutrons (b) diffraction data. The observed intensities are plotted as red points, the theoretical Bragg positions are plotted as blue marks, calculated intensities and the difference between observed and calculated intensities are plotted as black lines. Impurities are spotted by ∇ (unidentified impurity) or * (LiVPO₄O-type impurity).

Combined (ND and SXRPD) Rietveld refinements were performed considering the structural model $(M(1))_{1b}(M(2))_{1c}\{(P)_{2i}[O_{2i}]_4\}O_{2i}$ similar to the one used to describe LiVPO₄F⁹²,

without taking into account lithium and hydrogen atoms. Bond valence sums (BVS) were calculated according to reference¹²⁷. They allowed to determine which oxygen atom is linked to hydrogen to form an OH group: indeed the BVS value associated with the bridging oxygen atom was found to be smaller (0.97) than those of the four others (in average close to 1.75). This result is in agreement with the structure already reported for other existing Tavorite-like hydroxyl phosphate phases, with the hydroxyl groups bridging adjacent MO₆ octahedra along the chains. Moreover, the BVS value determined for the two vanadium atoms was found to be close to 3 (2.93 and 3.00), in good agreement with the formation of a V³⁺-rich phase. In order to determine the lithium and hydrogen atomic positions, Fourier difference maps were calculated, as described in details in reference³¹ for LiFePO₄OH, to localize missing electronic/atomic (for XRD/ND) density: two positions were detected around (0.35, 0.05, 0.85) and (0.25, 0.60, 0.70). The former was attributed to hydrogen since it is close to the bridging oxygen, and the latter to lithium as inside the hexagonal channel of the Tavorite framework. Finally, combined Rietveld refinement was achieved considering the full description of the unit cell with all the atoms, lithium and hydrogen included. The comparison of the experimental and calculated diffraction data is given in **Figure III-15**. The cell parameters, atomic positions and distances thus determined are given in **Table III-5** and in **Table III-6**.

As illustrated in **Figure III-16**, the crystal structure of LiVPO₄OH is built up by VO₆ octahedra which share common oxygen atoms. Each bridging oxygen is also linked to a hydrogen atom so as to form ...V...(OH)...V...(OH)...V... infinite chains running along [001]. These chains of octahedra are connected to each other via PO₄ tetrahedra forming ...V...O...P...O...V... sequences. These corner-sharing polyhedra generate a three-dimensional network within which lithium atoms occupy the hexagonal channels along the [100] direction. The phosphorus atom lies within a tetrahedron with P–O distances in the range of 1.53–1.56 Å and a polyhedron distortion of $\Delta = 3.65 \times 10^{-5}$ (the definition of mathematical of Δ is provided in the legend of **Table III-6**). Vanadium lies within two octahedral sites with a narrow range of V–O distances, 1.99–2.04 Å, V–OH distances being of 2.04 Å and 1.99 Å for the octahedra centered on the V(1) and V(2) atoms respectively. The V(1)O₄(OH)₂ octahedron is slightly less distorted than the V(2)O₄(OH)₂ octahedron ($\Delta = 1.35 \times 10^{-5}$ and $\Delta = 2.73 \times 10^{-5}$ respectively). A comparison with other Tavorite vanadium phosphate compositions is interesting as it allows to fully understand the nature of the bond observed along the chains of octahedra, depending on the bridging anion (or on the bridging anionic group). The V³⁺-rich compounds (LiV^{III}PO₄F, LiV^{III}PO₄OH and HV^{III}PO₄OH) show constant bond lengths along their chains: shorter (1.98–1.99 Å) for V–F, intermediate (2.00–2.03 Å) for V–{OH}, and longer (2.15 Å) for V–{OH₂}, respectively (**Figure III-16b**). Note that for LiV^{IV}PO₄O, due to the presence of {VO}²⁺ vanadyl groups, there is

an alternation between short and long bonds along the chains (1.67 and 2.19 Å respectively). In fact, the more electronegative the bridging anion (or anionic group), the shorter the V-O distance is along the chains. The antagonistic bond to V-O has to be considered as its covalency controls the structure thus stabilized: O-H in ... {HO}-V-{OH} ... for LiVPO₄OH, (O-H)₂ in ...{H₂O}-V-{OH₂}... for HVPO₄OH and V=O in ...{O=V}-O... for LiVPO₄O. Indeed, their increasing covalency explains the increasing length of the antagonistic V-O bond in LiVPO₄OH, HVPO₄OH and LiVPO₄O (2.02, 2.15 and 2.23 Å respectively). Similarly, the length of the V-O bond in these compounds is longer than V-F in LiVPO₄F, even if intrinsically F⁻ is more electronegative than O²⁻ (Figure III-16b).

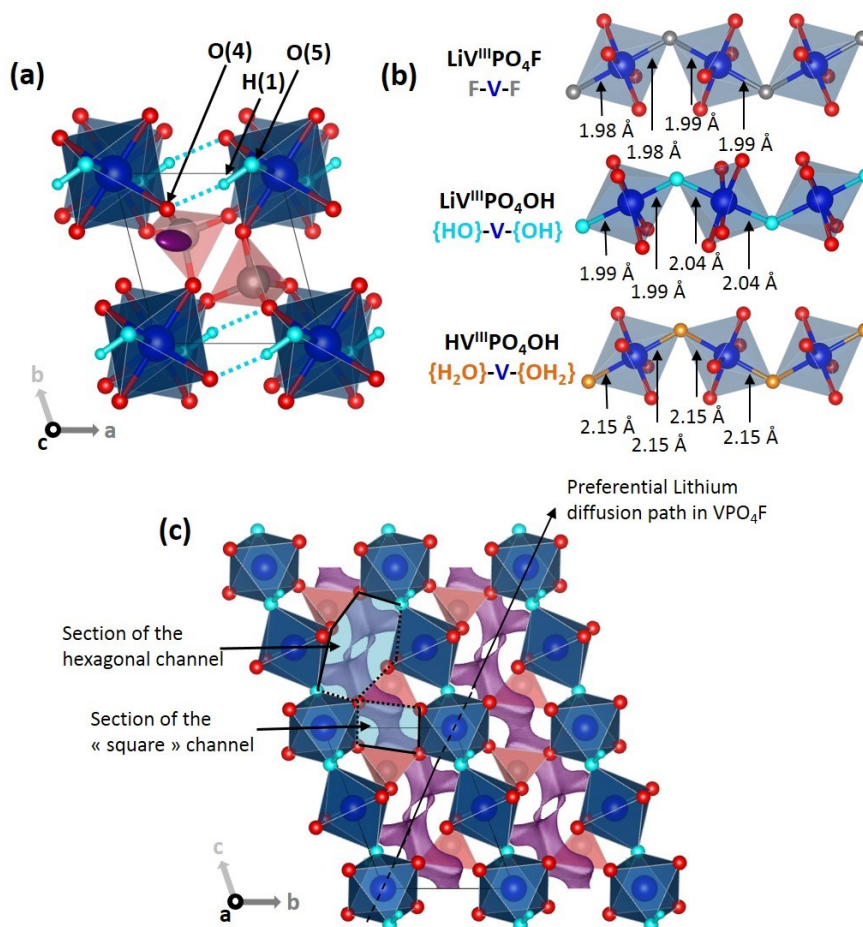


Figure III-16: (a) Structure of LVPH-a along the [001] direction: VO₄(OH)₂ octahedra in blue, PO₄ tetrahedra in red and anisotropic displacement ellipsoids for lithium in purple, dot lines represent the hydrogen bond O(4) ... H; (b) comparison of bond lengths along chains of octahedra for selected Tavorite-type phase; (c) Lithium diffusion pathway calculated thanks to Bond Valence Energy Landscape (with an energy of 1.6 eV above minimum).

The O(5)-H bond length observed in LiVPO₄OH is rather long (*i.e.* 1.06(3) Å) but in the range of those already reported for the other Tavorite-like hydroxyl phosphate compounds (1.09 Å for LiMnPO₄OH¹⁷⁷, 0.97 Å for LiFePO₄OH³¹, and 0.85 Å for LiAlPO₄OH¹⁷⁶). These significant differences of O-H distances could arise from hydrogen bonds formed across the

channel (O(5)-H...O(4)). This hypothesis is supported by the fact that the longer the O(5)-H distance in LiMPO_4OH , the shorter is the distance between H and O(4) across the tunnel (1.68 Å in LiMnPO_4OH , 1.80 Å in LiVPO_4OH , 1.86 Å in LiFePO_4OH and 2.06 Å in LiAlPO_4OH) and thus the stronger is the hydrogen bond.

Table III-5: Structural parameters obtained by combined Rietveld refinement of the structure of LVPH-a based on synchrotron XRD and Neutron Diffraction Data. Oxygen atom spotted by * is the bridging atom which is bound to hydrogen.

LIVPO ₄ OH							
SG : <i>P</i> -1		$a = 5.1335(1) \text{ \AA}$	$\alpha = 106.557(2)^\circ$	Synchrotron: $\chi^2 = 22.9\%$			
$Z = 2$		$b = 5.3334(1) \text{ \AA}$	$\beta = 109.217(2)^\circ$	$R_{\text{Bragg}} = 3.73\%$			
		$c = 7.2824(2) \text{ \AA}$	$\gamma = 97.352(2)^\circ$	neutrons: $\chi^2 = 1.68\%$			
		$V = 174.968(6) \text{ \AA}^3$	$V/Z = 87.484(6) \text{ \AA}^3$	$R_{\text{Bragg}} = 6.56\%$			
atoms	Wyckoff position	x	y	z	occupancy	B iso	BVS
V(1)	1 <i>a</i>	0	0	0	1	0.54(8)	2.93(3)
V(2)	1 <i>b</i>	0	0	1/2	1	0.36(7)	3.00(2)
P(1)	2 <i>i</i>	0.323(1)	0.639(1)	0.268(1)	1	0.16(7)	5.01(6)
O(1)	2 <i>i</i>	0.629(2)	0.751(2)	0.429(1)	1	0.20(5)	2.09(3)
O(2)	2 <i>i</i>	0.111(2)	0.661(2)	0.377(1)	1	0.12(5)	2.03(4)
O(3)	2 <i>i</i>	0.308(2)	0.340(2)	0.159(1)	1	0.31(5)	2.07(3)
O(4)	2 <i>i</i>	0.267(2)	0.790(2)	0.117(1)	1	0.43(6)	2.04(4)
O(5)*	2 <i>i</i>	0.155(2)	0.947(2)	0.772(1)	1	0.16(5)	1.87(3)
H(1)	2 <i>i</i>	0.351(9)	0.063(9)	0.347(7)	1	5.5 (3)	1.14(9)
Li(1)	2 <i>i</i>	0.260(6)	0.605(6)	0.686(5)	1	3.7(7)	0.99(4)
		B_{11}	B_{22}	B_{33}	B_{12}	B_{13}	B_{23}
$B_{\text{anisotropic}}$ of Lithium		0.098	0.036	0.076	0.004	-0.039	-0.020

The unique Li(1) site observed in LiVPO_4OH is surrounded by five oxygen atoms, one of them being bonded to hydrogen, in a distorted $\text{LiO}_4(\text{OH})$ polyhedron with Li-O distances ranging between 1.97 and 2.28 Å ($\Delta = 1.79 \times 10^{-3}$). The BVS value associated with Li(1) is close to 1 (*i.e.* 0.99). The anisotropic Debye-Waller factor (B_{aniso}) for Lithium exhibits an ovoid shape elongated along the [10-1]. In this direction, the $\text{Li}^+ - \text{Li}^+$ distances are huge (*i.e.* 10.2 Å), therefore the diffusion by hopping between sites can't occur along this direction. In order to get more insights into the possible pathways for Lithium diffusion, the Bond Valence Energy Landscape (BVEL) was calculated thanks to the Bondstr software in the Fullprof suite¹⁷¹ and drawn with Vesta¹⁷². With 1.6 eV, BVEL highlights a zig-zag diffusion pathway along the [001] direction with Li^+ ions moving from a large channel defined by an hexagonal section to another, going through intermediate smaller channels, defined by a "square" section (**Figure III-16c**). In fact, the elongation direction of B_{aniso} points towards this "square" channel. Note that these results are different from those predicted by Ceder and coworker¹⁷⁴ for Tavorite compounds, with a preferential diffusion pathway along the [001] direction in VPO_4F (corresponding to the [111] in LiVPO_4F and LiVPO_4OH models). In our case, the hydroxyl group and the possible

hydrogen bond between O(4) and H across the hexagonal channel could hamper Lithium diffusion along the [111] direction, whereas it does not occur along the [001] direction (**Figure III-16c**).

Table III-6 : Bond lengths (below the diagonal) and angles (above the diagonal) in coordination polyhedra of V³⁺, Li⁺ and P⁵⁺ in LiVPO₄OH. The polyhedral distortion is calculated as $\Delta = \frac{1}{N} \sum_{i=0}^N \frac{(d_i - \langle d \rangle)^2}{\langle d \rangle^2}$ with N the number of bond distances considered, d_i the distance between the atom i and the central atom of the polyhedron and $\langle d \rangle$ the average of the distances considered.

V(1)O ₄ (OH) ₂								
	O(3)	O(3')	O(4)	O(4')	O(5)	O(5')	H(1)	H(1')
O(3)	2.01(1)	180	89.6(3)	90.4(3)	86.6(3)	93.4(3)	66.4(3)	113.6(1)
O(3')	4.02(1)	2.01(1)	90.4(3)	89.6(3)	93.4(3)	86.6(3)	113.6(3)	66.4(3)
O(4)	2.82(1)	2.84(1)	1.99(1)	180	86.1(3)	93.9(3)	76.7(3)	103.3(3)
O(4')	2.84(1)	2.82(1)	3.99(1)	1.99(1)	93.9(3)	86.1(3)	103.3(3)	76.7(3)
O(5)	2.77(1)	2.95(1)	2.75(1)	2.95(1)	2.04(1)	180	22.6(3)	157.4(3)
O(5')	2.95(1)	2.77(1)	2.95(1)	2.75(1)	4.08(1)	2.04(1)	157.4(3)	22.6(3)
H(1)	2.57(3)	3.86(3)	2.88(3)	3.62(3)	1.06(3)	4.54(3)	2.59(6)	180
H(1')	3.86(3)	2.57(3)	3.62(3)	2.88(3)	4.54(3)	1.06(3)	5.18(5)	2.59(6)
$\Delta = 1.35 \times 10^{-5}$								
V(2)O ₄ (OH) ₂								
	O(1)	O(1')	O(2)	O(2')	O(5)	O(5')	H(1)	H(1')
O(1)	1.99(1)	180	95.8(3)	84.2(3)	89.8(3)	90.2(3)	66.1(4)	113.9(4)
O(1')	3.98(1)	1.99(1)	84.2(3)	95.8(3)	90.2(3)	89.8(3)	113.9(4)	66.1(4)
O(2)	2.98(1)	2.69(2)	2.02(1)	180	86.5(3)	93.5(3)	86.3(4)	93.8(4)
O(2')	2.69(2)	2.98(1)	4.04(1)	2.02(1)	93.5(3)	86.5(3)	93.8(4)	86.3(4)
O(5)	2.82(1)	2.82(1)	2.75(1)	2.92(1)	1.99(1)	180	23.9(4)	156.0(4)
O(5')	2.82(1)	2.82(1)	2.92(1)	2.75(1)	3.99(1)	1.99(1)	156.0(4)	23.9(4)
H(1)	2.48(3)	3.77(3)	3.10(3)	3.31(3)	1.06(3)	4.41(9)	2.54(6)	180
H(1')	3.77(3)	2.48(3)	3.31(3)	3.10(3)	4.41(9)	1.06(3)	4.99(6)	2.54(6)
$\Delta = 2.73 \times 10^{-5}$								
PO ₄								
	O(1)	O(2)	O(3)	O(4)				
O(1)	1.54(1)	109.5(6)	102.8(5)	110.4(5)				
O(2)	2.53(2)	1.56(1)	110.5(5)	111.4(5)				
O(3)	2.42(1)	2.55(1)	1.55(1)	111.9(6)				
O(4)	2.52(1)	2.55(1)	2.55(1)	1.53(1)				
$\Delta = 3.65 \times 10^{-5}$								
LiO ₄ (OH)								
	O(1)	O(2)	O(2')	O(3)	O(5)	H(1)		
O(1)	2.06(3)	91.7(9)	82.9(9)	71.8(9)	171.3(9)	148.6(9)		
O(2)	3.12(1)	2.28(4)	94.0(9)	140.6(9)	80.4(9)	87.2(9)		
O(2')	2.69(2)	3.13(1)	2.00(4)	115.9(9)	101.3(9)	128.5(9)		
O(3)	2.42(1)	3.67(1)	3.82(1)	2.06(4)	108.2(9)	80.5(9)		
O(5)	4.02(1)	2.75(1)	3.07(1)	3.26(1)	1.97(4)	28.3(6)		
H(1)	4.13(4)	3.11(4)	3.81(4)	2.77(4)	1.06(3)	2.23(4)		
$\Delta = 1.79 \times 10^{-3}$								

This diffraction study reveals the formation of a new LiVPO₄OH phase crystallizing in Tavorite structure. Diffuse reflectance IR and MAS NMR were used to characterize further its local structure and to confirm for instance the presence of a hydroxyl group.

ii. Further evidence of the hydroxyl group

The Mid-IR diffuse reflectance spectra of LVPH-a, LVPH-b and LVPH-c are compared in **Figure III-17**. The assignment of the main vibrational signals is given in **Table III-7**. The first information is the presence of a band at 3300 cm^{-1} matching with the stretching vibration of a hydroxyl group. This signature is clearly different from the O-H stretching mode observed for the H-O-H group in $\text{VPO}_4 \cdot \text{H}_2\text{O}$. For this latter, the water molecule bridges two octahedra along the chains¹⁶⁸ and the IR signature is a very broad band around 3000 cm^{-1} whereas for LiVPO_4OH a narrower band is observed at higher wavenumber. The value of this wavenumber is typical for hydroxyl groups influenced by their environments, in good agreement with a possible hydrogen bond between H and O(4). Indeed, when the OH group is isolated the corresponding vibration appears as an even narrower band at a higher wavenumber (*i.e.* between 3500 and 3700 cm^{-1} ¹³⁹). Nevertheless, the narrow profile of the band despite small difference in width indicates that the hydrogen bonds are quite weak for the three samples.

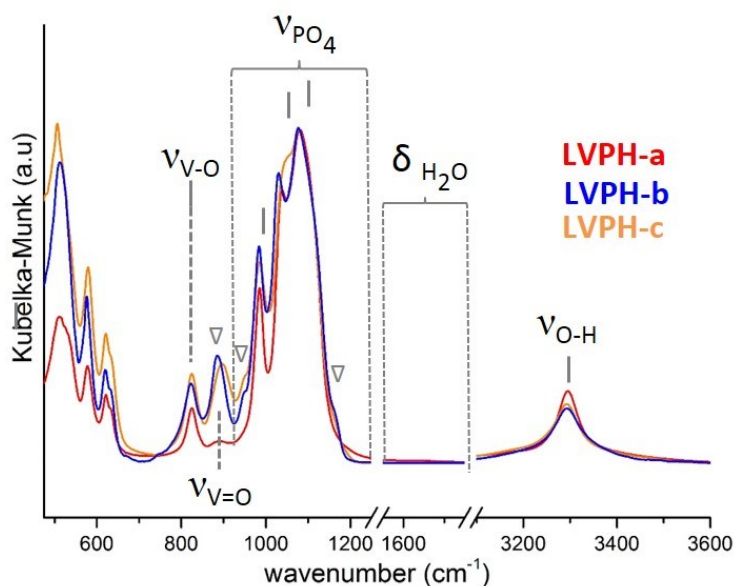


Figure III-17: diffuse reflectance infrared spectra of LVPH-a (red line), LVPH-b (blue line) and LVPH-c (orange line). Typical bands of a LiVPO_4O -type phase are noted by ∇ .

The PO_4 stretching region, between 950 and 1200 cm^{-1} ,^{141,142} is very similar to those of the other vanadium based Tavorite compounds¹⁷, with three main bands around 988 , 1041 and 1085 cm^{-1} . The signature at lower wavenumber is attributed to the symmetric stretching mode of PO_4 groups and the two others to the antisymmetric stretching vibrations. Theoretically, three antisymmetric modes must be observed¹⁴² but the bands overlap does not allow to distinguish them (without Pseudo-Voigt deconvolution of the signal). Two additional

bands, smaller in intensity, are observed at 950 and 1167 cm⁻¹ for LVPH-b and LVPH-c (highlighted by ▽ at the **Figure III-17**). These bands are typical for PO₄ groups in a LiVPO₄O-type structure¹⁴¹.

Table III-7: Wavenumbers of different vibrations observed by diffuse reflectance IR spectroscopy and their assignment.

Wavenumber (cm ⁻¹)			assignment	Ref.
LVPH-a	LVPH-b	LVPH-c		
3305	3300	3303	$\nu_{\text{O-H}}$	139,142
/	1167	1167	ν_{PO_4}	141
1087	1082	1083	ν_{PO_4}	141,142
1042	1034	1048	ν_{PO_4}	141,142
988	988	989	ν_{PO_4}	141,142
/	950	949	ν_{PO_4}	141
891	891	902	$\nu_{\text{V=O}}$	141
829	829	829	$\nu_{\text{V-O}}$	142
636	636	636	?	/
625	623	625	?	/
581	578	582	?	/
513	516	509	?	/

Moreover, a tiny signal is observed at 891 cm⁻¹ for LVPH-a. The same signal exists also for LVPH-b, with a higher intensity. The spectrum of LVPH-c exhibits a more shifted and broader signal at 902 cm⁻¹ whose intensity is slightly larger than that observed for LVPH-b. This contribution around 891-902 cm⁻¹ can be assigned to a vanadyl-type bond vibration¹⁴¹, *i.e.* to a short V=O bond observed only for vanadium with an oxidation state larger than 3+. Typically, for Tavorite LiV^{IV}PO₄O, the corresponding vibration is observed as a narrow peak at 907 cm⁻¹.¹⁴¹ This signature reveals either the presence of a LiVPO₄O-like phase as impurity in the materials (especially in LVPH-b and LVPH-c) or the existence of vanadyl defects in the LiVPO₄OH structure due to some local LiVPO₄O-type arrangement. The weaker wavenumber of the V=O stretching mode (and so the weaker force constant or bond strength) highlights the formation of V=O bonds longer than those observed in ideal LiV^{IV}PO₄O. Furthermore, the broad signal reveals a wide distribution of V=O distances, and so a wide distribution of environments. By analogy with LiFePO₄OH¹⁴², the band located at 829 cm⁻¹ could be assigned to V-O stretching vibration in V-O-H sequences. The region between 500 to 700 cm⁻¹ (and the region below 500 cm⁻¹ which isn't shown here) gathers bending modes of PO₄ and V-O polyhedra, vibrations involving Li-O bonds and lattice modes that we have not been able to assign.

The IR spectroscopy confirms the presence of the hydroxyl group influenced by hydrogen bond and highlights also a vanadyl-type contribution, slightly different for the three

samples. In order to get more insights into the nature (defects or impurity) and the localization of these vanadyl bonds, through their vicinity with ^7Li , ^{31}P and ^1H , MAS NMR spectroscopy experiments were carried out.

iii. Vanadyl-type defects or LiVPO_4O -type impurity?

The ^7Li MAS NMR spectra of the three samples (LVPH-a, LVPH-b and LVPH-c) are compared in **Figure III-18**.

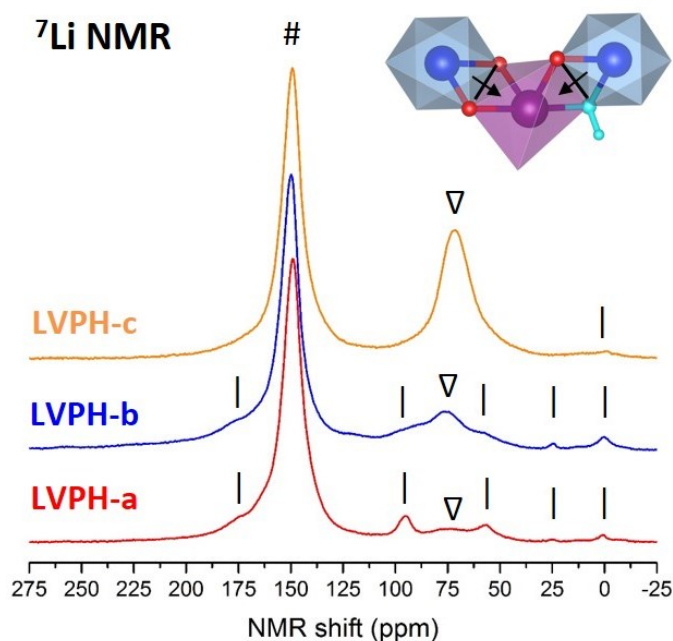


Figure III-18: ^7Li MAS NMR spectra of LVPH samples LVPH-a (red), LVPH-b (blue), LVPH-c (orange). Isotropic signals are noted by # and additional peaks by | or by ∇ (see text). In inset, the simplified Lithium environment and the schematic spin transfer mechanism represented as arrows.

They exhibit a main peak around 149 ppm, highlighted by #, corresponding likely to the Lithium site in LiVPO_4OH . Additional shifted components are observed for the three samples: a series of unidentified small intensity peaks at 180, 97, 58 and 25 ppm (highlighted as | in **Figure III-18**) and a LiVPO_4O -type contribution around 70 ppm (highlighted as ∇ in **Figure III-18**) for the two samples LVPH-a and LVPH-b, the latter being the single additional signal present in the LVPH-c spectrum. The spectra for the two samples LVPH-a and LVPH-b differ only in the intensity ratio of these additional small intensity signals, which are not likely to correspond to the impurities seen by XRD as they are crystallographically different for the two samples. These signals could thus correspond to the contributions of defects in LiVPO_4OH .

2D EXSY-RFDR ⁷Li MAS NMR experiments were conducted on the samples presenting the stronger additional contributions (*i.e.* LVPH-b and LVPH-c), in order to discriminate between impurity and defects. The spectra recorded are shown in **Figure III-19** and do not reveal any obvious dipolar connectivity between these additional signals and the main one at 149 ppm, showing that they correspond to Li ions not present in the same phase. Therefore all samples seem to contain a LiVPO₄O-like impurity and regarding the ⁷Li MAS NMR signal in LiV^{IV}PO₄O, located at 80 ppm¹²⁶ (vs. around 75, 75 and 70 ppm for LVPH-a, LVPH-b and LVPH-c respectively), we thus suggest that structural defects are present in this LiVPO₄O-like impurity.

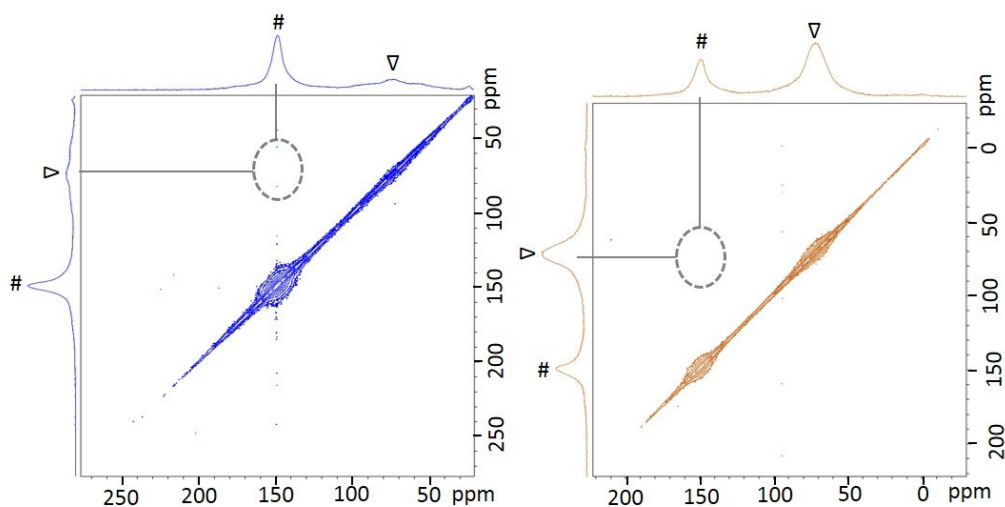


Figure III-19 : 2D ⁷Li{⁷Li} fp-RFDR dipolar correlation NMR spectra of (left) LVPH-b and (right) LVPH-c, acquired using mixing times of 10 ms with a 30 kHz MAS and 7T at 293K. The circles drawn with dot lines represent the regions where cross-peak should appear if the signals are correlated.

Coming back to the main signal of LiVPO₄OH at 149 ppm, it is interesting to compare its position to those reported for other M³⁺ Tavorite-type compounds. All paramagnetic materials (such as vanadium, iron and manganese based Tavorite-like compositions discussed in this section) lead to NMR spectra dominated by interactions between nuclear and electron spins (hyperfine interactions). The Fermi contact shift, which governs the position of the NMR signal of such compounds, corresponds to the presence of some density of electron spin at the nucleus probed. Indeed, the value of the Fermi contact shift is proportional to the spin density at the site of the probed nucleus and to the magnetic susceptibility of the compound¹⁴³. The ⁷Li NMR shifts for LiVPO₄OH, LiVPO₄F¹⁹, LiVPO₄O¹²⁶ LiFePO₄OH¹⁴⁹ and LiMnPO₄OH¹⁵⁰ are given in **Table III-8**. For all these phases, the lithium polyhedra share two edges and two corners with the MO₄X₂ octahedra (with X = O, OH or F). As discussed by Castets et al¹⁵⁰, the spin transfer from vanadium to lithium can occur only from the t_{2g} orbitals for V³⁺ (t_{2g}²) pointing towards the edges of the octahedra, *i.e.* via the common edges between the lithium and vanadium

polyhedra (see inset of **figure III-18**). For the other M^{3+} Tavorite phases, this spin transfer can occur also from the e_g orbitals which are not empty for Mn^{3+} ($t_{2g}^3 e_g^1$) and Fe^{3+} ($t_{2g}^3 e_g^2$), passing through the 2p orbitals of the oxygen atoms shared between the polyhedra. This is fully consistent with the lowest contact shift observed for the V^{3+} phases.

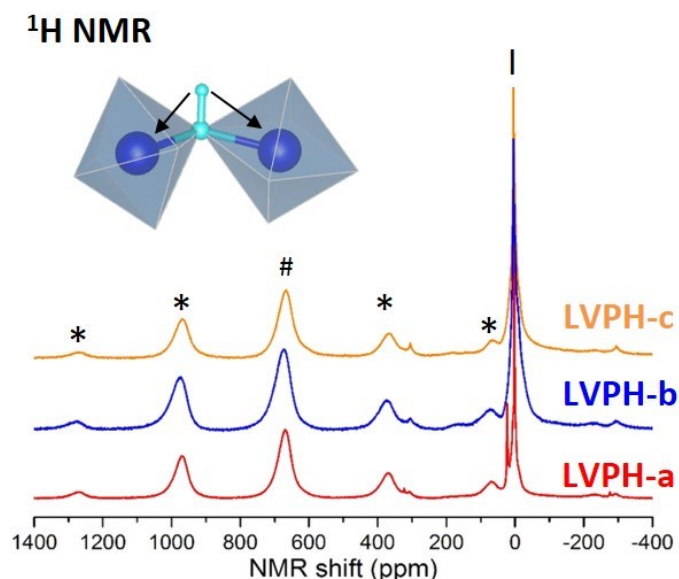


Figure III-20: 1H MAS NMR spectra of LVPH samples LVPH-a (red), LVPH-b (blue), LVPH-c (orange). Isotropic signals are noted by #, their rotational bands by * and additional peaks by | (see text). In inset, the simplified hydrogen environment and the schematic spin transfer mechanism represented as arrows.

The main information given by the 1H MAS NMR spectra is the presence of a shifted signal at 672 ppm (highlighted as # in **Figure III-20**) which may match with the only crystallographic site for the hydrogen atom, thus strengthening the observation made by neutron diffraction. A signal which matches with (diamagnetic) adsorbed water or surface hydroxyl group in the environment of the probe (sample, rotor or probe) is also observed close to 0 ppm (highlighted as | in **Figure III-20**). In the Tavorite structure, hydrogen is bonded to the oxygen which links two transition metal octahedra (inset of **Figure III-20**), and can therefore interact with both of them. As discussed by Castets et al.¹⁴⁹, the spin transfer cannot occur from e_g orbitals of the transition metal to the 1s of hydrogen through the $2p_z$ orbitals of oxygen because the M-O-H angles are far from 180° (*i.e.* 96.7° , 106.5° , and 107.2° for the iron, manganese and vanadium phases respectively). The only transfer possible is via a π overlap of the t_{2g} and the 1s of hydrogen via the 2p of oxygen. However, as shown in **Table III-8**, the 1H shift for $LiVPO_4OH$ is larger than for $LiFePO_4OH$ that has more t_{2g} electron spins. But, as discussed just before, there are significant differences between the hydrogen local environments in Tavorite compounds (especially concerning the strength of the hydrogen bond in which it is involved), therefore, the resulting electron spin transfer needs to be

modeled and analyzed in detail in each case to understand the relative magnitude of the ¹H NMR shifts in the series.¹⁴⁹

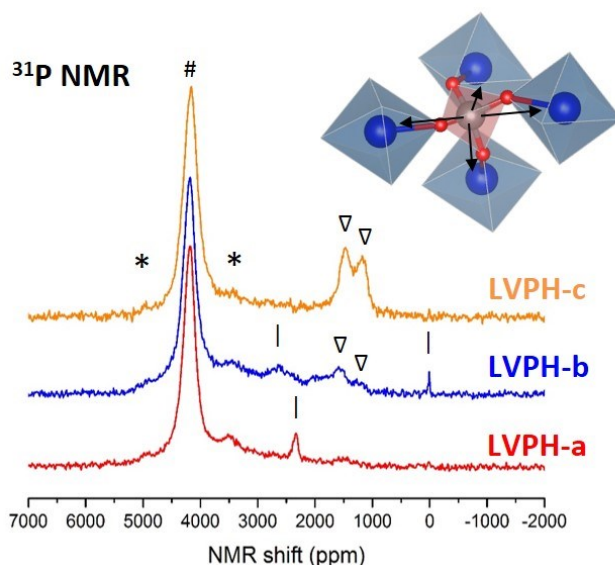


Figure III-21: ³¹P MAS NMR spectra of LVPH samples LVPH-a (red), LVPH-b (blue), LVPH-c (orange). Isotropic signals are noted by #, their rotational bands by * and additional peaks by | or by ∇ (see text). In inset, the simplified Lithium environment and the schematic spin transfer mechanism represented as arrows.

³¹P MAS NMR was also performed and the main signal is located around 4300 ppm for all the samples (highlighted as # in the **Figure III-21**). The spectra however exhibit several other peaks that cannot be attributed to spinning sidebands, mostly one at 2300 ppm for LVPH-a and a pair of peaks at 1480 and 1150 ppm for LVPH-c. That latter appears to be also present but much weaker (and slightly shifted) in LVPH-a and LVPH-b. The ³¹P shifts for the two P sites in LiVPO₄O are 1418 and 1593 ppm¹²⁸. Therefore, following the ⁷Li NMR observation discussed above, the observed signals in LVPH-c might result from the LiVPO₄O-like impurity, although the difference with ideal LiVPO₄O appears to be rather large. Considering the main signal to be that of P in LiVPO₄H, we again compare its position with the Tavorite series in **Table III-8**. As illustrated in **Figure III-21**, in the Tavorite structure, PO₄ tetrahedra are connected to four different transition metal octahedra via the oxygen belonging to the square plane of these octahedra. As discussed by Castets et al.¹⁴⁹, in LiMPO₄OH the spin transfer to the 2s (or the sp³ hybrid) orbital of Phosphorus can occur from the t_{2g} orbitals (via π overlap with a p orbital of oxygen), or from the e_g orbitals via O. Therefore, like in the case of ⁷Li discussed above, the shift for LiVPO₄OH is logically the lowest of the series (LiFePO₄OH: 7498; LiMnPO₄OH: 8483).

Table III-8 : electronic configuration, NMR shift (^7Li , ^1H and ^{31}P) and main spin transfer mechanism of different AMPO_4X Tavorite compounds (with $A = \text{Li}$ or H ; $M = \text{V}^{4+}$, V^{3+} , Mn^{3+} or Fe^{3+} and $X = \text{O}$, F or OH)

^7Li	electronic configuration	isotropic peak position	spin transfer mechanism	Ref.
$\text{LiV}^{4+}\text{PO}_4\text{O}$	$t_{2g}^1e_g^0$	79	t_{2g}	128
$\text{LiV}^{3+}\text{PO}_4\text{F}$	$t_{2g}^2e_g^0$	117	t_{2g}	21
$\text{LiV}^{3+}\text{PO}_4\text{OH}$	$t_{2g}^2e_g^0$	149	t_{2g}	this work
$\text{LiMn}^{3+}\text{PO}_4\text{OH}$	$t_{2g}^3e_g^1$	340	t_{2g}	149
$\text{LiFe}^{3+}\text{PO}_4\text{OH}$	$t_{2g}^3e_g^2$	214	$t_{2g} + e_g$	149
^1H	electronic configuration	isotropic peak position	spin transfer mechanism	Ref.
$\text{LiV}^{3+}\text{PO}_4\text{OH}$	$t_{2g}^2e_g^0$	672	t_{2g}	this work
$\text{LiMn}^{3+}\text{PO}_4\text{OH}$	$t_{2g}^3e_g^1$	815	t_{2g}	149
$\text{LiFe}^{3+}\text{PO}_4\text{OH}$	$t_{2g}^3e_g^2$	162	t_{2g}	149
^{31}P	electronic configuration	isotropic peak position	spin transfer mechanism	Ref.
$\text{LiV}^{4+}\text{PO}_4\text{O}$	$t_{2g}^1e_g^0$	1418 + 1593	t_{2g}	128
$\text{LiV}^{3+}\text{PO}_4\text{F}$	$t_{2g}^2e_g^0$	3998	t_{2g}	128
$\text{LiV}^{3+}\text{PO}_4\text{OH}$	$t_{2g}^2e_g^0$	4300	t_{2g}	this work
$\text{LiMn}^{3+}\text{PO}_4\text{OH}$	$t_{2g}^3e_g^1$	8483	t_{2g}	149
$\text{LiFe}^{3+}\text{PO}_4\text{OH}$	$t_{2g}^3e_g^2$	7498	$t_{2g} + e_g$	149

Thus, MAS NMR has evidenced the expected ^7Li , ^1H and ^{31}P signals for LiVPO_4OH , but also the presence of different additional signals, depending on the sample, the strongest of them being attributed to the presence of LiVPO_4O -type impurities.

The nature of this bridging anion in Tavorite compounds greatly influences the working potential of such kind of material as reported before for iron, titanium and vanadium-containing phases. Electrochemical tests were thus performed in order to demonstrate this influence. In the following, only electrochemical data for LVPH-b are reported as this sample revealed a better activity despite bigger primary particles and aggregates: the presence of carbon most probably improves the electronic percolation within the electrode for this polyanionic material with poor intrinsic transport properties, and the porosity of the aggregates allows their better wettability by the electrolyte.

III-2b. Electrochemical properties and redox mechanism

i. Electrochemical tests

$\text{LiV}^{\text{III}}\text{PO}_4\text{OH}$ was cycled in lithium cells under GITT conditions between 3.0 and 1.2 V vs Li^+/Li (**Figure III-22a**) and under galvanostatic conditions in order to collect *ex-situ* (i.e. recovering electrodes from batteries cycled at C/100 rate) XRD data at different states of (dis)charge (**①**, **②** and **③** in the **Figure III-23**). It is possible to insert almost one lithium per formula unit in $\text{LiV}^{\text{III}}\text{PO}_4\text{OH}$ to form $\text{Li}_2\text{V}^{\text{III}}\text{PO}_4\text{OH}$ (**②** in **Figures III-22a** and **III-23**). A reversible capacity of 136 mAh/g (vs. the theoretical capacity of 158 mAh/g) is reached in the low potential range, with an irreversible capacity of around 10% and LiVPO_4OH recovered at the end of the next charge (**③** in **Figures III-22a** and **III-23**). The insertion of lithium in LiVPO_4OH occurs according to a two-step mechanism: a solid solution process first leads to the formation of an intermediate phase with the composition $\text{Li}_{\sim 1.25}\text{VPO}_4\text{OH}$, and a biphasic reaction is then observed at an average potential of 1.35V vs Li^+/Li between this intermediate phase and the fully lithiated phase $\text{Li}_2\text{V}^{\text{III}}\text{PO}_4\text{OH}$. Note that a careful inspection of the voltage vs. composition data reveals also the presence of several shoulders at 2.45 2.20 and 2.00V vs Li^+/Li (better highlighted considering the derivative curve given in inset of **Figure III-22a**). These values of potentials match with those corresponding to lithium insertion (2.45, 2.20 and 2.00 V) in the Tavorite $\text{LiV}^{\text{IV}}\text{PO}_4\text{O}$, that was indeed revealed, by 2D $^7\text{Li}\{\text{Li}\}$ NMR NMR, as impurity in our samples.

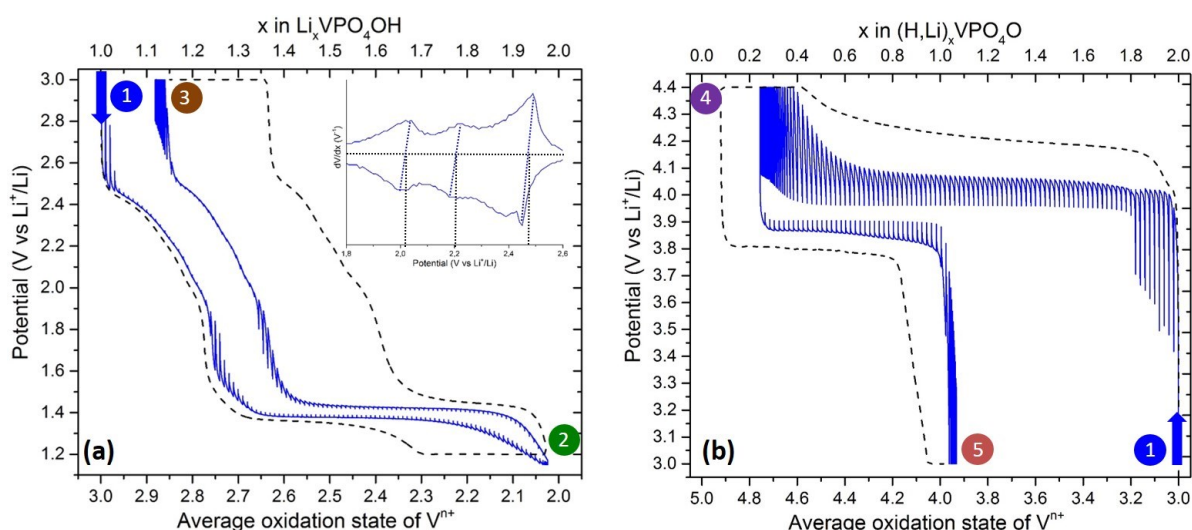


Figure III-22: GITT (blue line) curves of LVPH-b cycled between 3.0 and 1.2 V (a) and between 3.0 and 4.4V (b) vs. Li^+/Li . Dot lines represent the galvanostatic cyclings of LVPH-b used to obtain the *ex-situ* materials whose XRD patterns are shown in the **Figure III-23**.

In the high voltage region, a flat voltage plateau is observed at 3.95 V vs Li⁺/Li during the first charge of Li//LiV^{III}PO₄OH cells in GITT conditions (**Figure III-23b**). The capacity associated with this first charge (280 mAh/g) is almost twice larger than the theoretical one (158 mAh/g), considering only the extraction of lithium. From this result it is thus justified to consider the additional extraction of hydrogen as already observed for HV^{III}PO₄OH by Whittingham and coworkers¹⁷⁸ who showed that it was indeed possible to extract two hydrogens from HVPO₄OH with the formation of the Tavorite-like V^VPO₄O phases at the end of the charge and LiV^{IV}PO₄O at the end of the next discharge. Note also that for LiVPO₄OH, a large irreversible capacity is observed at the end of the discharge at 3 V vs Li⁺/Li: it corresponds to about one electron per vanadium and could thus be associated with the H⁺ extracted and not reinserted.

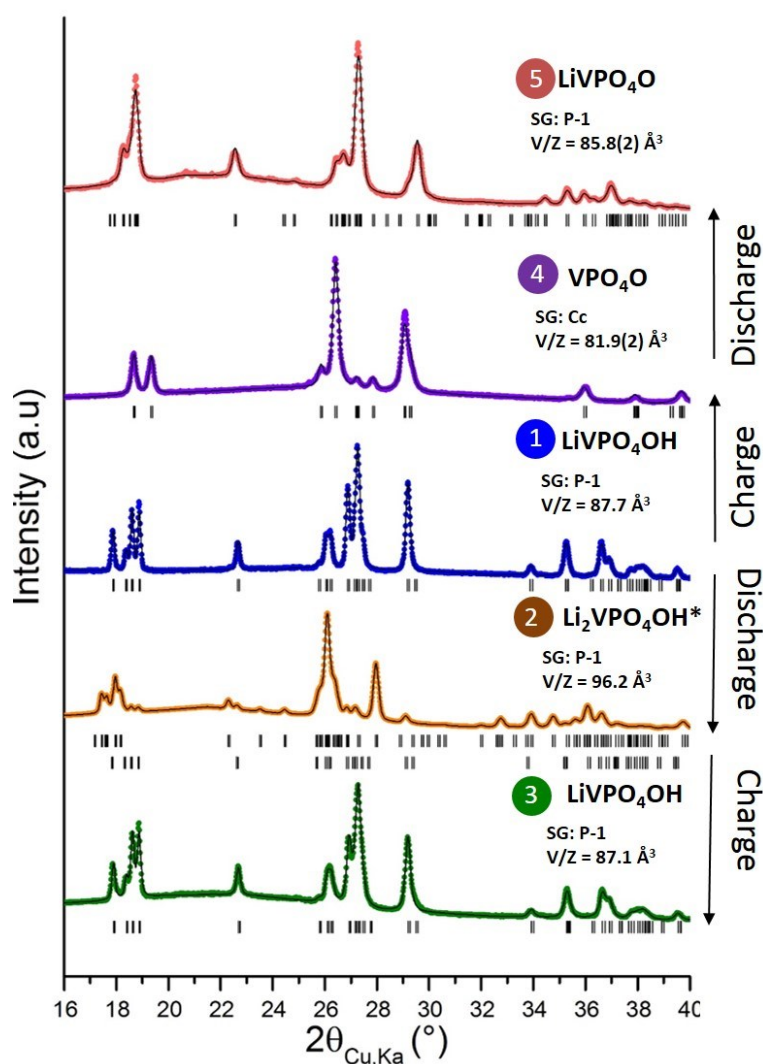


Figure III-23: ex-situ XRD patterns (blue point) of pristine LVPH-b (●), of the end-of-(dis)charge materials obtained after electrochemical cycling in the voltage regions 3.0-1.2 V (● and ●) and 3.0-4.5 V (● and ●) vs. Li⁺/Li. Theoretical Bragg positions (black ticks) and patterns calculated by the Rietveld method are also given.

* A LiVPO₄OH-type phase was added as a secondary contribution.

In order to get more insight into structural modifications and mechanisms involved upon oxidation, XRD experiments were performed *ex-situ* to identify the nature of the phases formed at the end of the charge and at the end of the next discharge (④ and ⑤ respectively, as highlighted in **Figure III-22b**). As shown by the indexation of the XRD patterns given in **Figure III-23** and by the corresponding cell parameters, VPO₄O-type is obtained at the end of the first charge, and LiVPO₄O at the end of the next discharge. Their structures were found to be in good agreement with those already reported in the literature with V/Z values close to 81.98 and 85.51 Å³ for VPO₄O and LiVPO₄O respectively⁹⁶. These results confirm that extraction of both lithium and hydrogen occurs, but surprisingly at the same equilibrium potential of 3.95V vs. Li (and the same as the V⁴⁺=O/V⁵⁺=O redox couple observed in LiVPO₄O). Therefore, we are entitled to ask us: does a V⁴⁺-rich intermediate phase, undetected by GITT, appear during the charge? What is the redox couple involved in this mechanism?

ii. High voltage region: activation of the V³⁺/V⁵⁺=O redox couple?

In order to answer these questions, the study of the phase diagram observed during electrochemical cycling of LiVPO₄OH by means of *operando* SXRPD experiments was conducted with a very fast acquisition duration (5s/scan) at C/10/electron (10h for 1 electron exchanged) in GITT conditions (7 current pulses of 30 minutes followed by 15 minutes of relaxation leading to over 2000 patterns). Selected SXRPD patterns (*i.e.* 1 over 100) are shown in **Figure III-24**. These peculiar conditions were carefully chosen in order to detect an eventual metastable V⁴⁺-rich phase appearing upon charge. Indeed, at the rate applied (*i.e.* C/10), for the low kinetic of the high voltage mechanism of LiVPO₄OH, the patterns are acquired at a non-equilibrium state and the appearance of metastable phase is thus promoted. Then, a relaxation is applied to probe the changes which might occur when the system return to its equilibrium state. The SXRPD patterns are acquired at a high frequency (1 pattern every 5s) providing a kind of “slow motion movie” of the electrode material in order to detect an ephemeral phase eventually formed. Under these conditions the detector must be fixed during acquisition and thus a narrower 2θ region can be scanned (*i.e.* 5-45° vs. 2-72° under classical *operando* conditions). Moreover, due to the architecture of the MYTHEN detector (modules of channel spaced of few millimeters), some narrow 2θ regions cannot be scanned (diffracted X-rays arriving at the junction between two modules).

Despite the presence of parasitic signals inherent to the *operando* SXRPD experiments in transmission mode (Lithium, Beryllium, Aluminum, PTFE, separator and the unidentified impurity already discussed in the previous part) and the narrow 2θ regions where no signal is

recorded (highlighted by ∇ in **Figure III-24**), the cell parameters of the starting materials obtained from refinement of the *in situ* pattern are very similar to those provided in the previous section ($a = 5.1356(3) \text{ \AA}$, $b = 5.3378(3) \text{ \AA}$, $c = 7.2799(3) \text{ \AA}$, $\alpha = 106.533(3)^\circ$, $\beta = 109.189(3)^\circ$, $\gamma = 97.326(3)^\circ$ and $V/Z = 87.64(2) \text{ \AA}^3$ vs. $V/Z = 87.66(3) \text{ \AA}^3$ for LVPH-b in **Table III-4**). **Figure III-24** reveals that the intensities related to starting material decrease and that the only growing contributions arise from the appearance of a VPO_4O -type phase (*i.e.* (-111), (111) and (-202) Bragg reflections of the Cc lattice of VPO_4O are highlighted as red arrows in **Figure III-24**). Therefore, no contribution related to the formation of any V^{4+} -rich phase (even metastable) has been detected and a pure biphasic reaction between $\text{LiV}^{\text{III}}\text{PO}_4\text{OH}$ and $\text{V}^{\text{V}}\text{PO}_4\text{O}$ seems to occur.

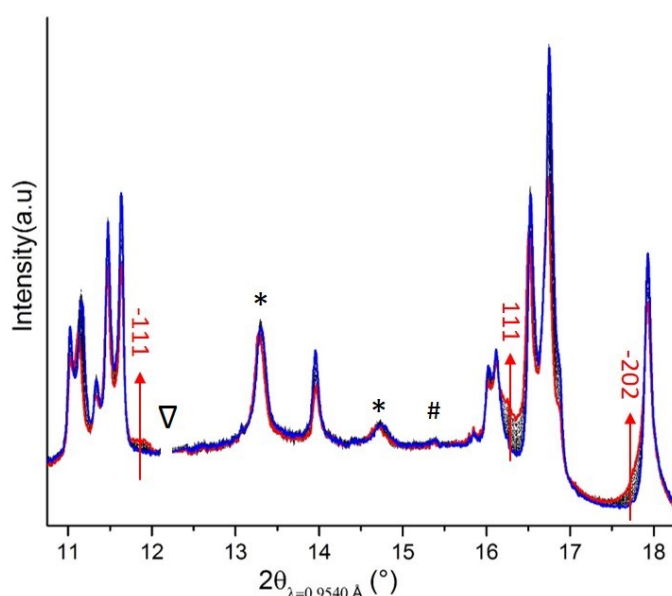


Figure III-24: Selected SXRPD patterns (1 over 100) recorded during the charge of LiVPO_4OH . The first pattern is represented in blue the 2000th in red. The main contributions of the growing phase are highlighted with red arrows. Additional contributions are marked by * (in situ cell contribution) or # (impurity). No signal is recorded in the region highlighted by ∇ .

The whole series of patterns recorded (over 2000 patterns) has been refined with Fullprof in sequential mode fixing all parameters excepted weight fractions of each phase (*i.e.* LiVPO_4OH , VPO_4O) and the cell parameters of LiVPO_4OH . The structural parameters of the VPO_4O have been fixed to those reported in reference⁹⁶. **Figure III-25** shows the evolution of the weight fraction of the growing phase and the cell volume of LiVPO_4OH in function of the pattern number. At each current pulse (corresponding to the exchange of 0.05 electron per vanadium), the weight fraction of VPO_4O increases in good agreement with the mechanism proposed (*i.e.* biphasic mechanism between LiVPO_4OH and VPO_4O) but then decreases during the following relaxation. In parallel, the cell volume of LiVPO_4OH oscillates in function of charge

and relaxation periods. This combination of observations suggests either a self-discharge (*i.e.* re-intercalation of Lithium inside VPO_4O without applying a current) or a more complex relaxation mechanism induced by the presence of V^{5+} in the neighboring of V^{3+} .

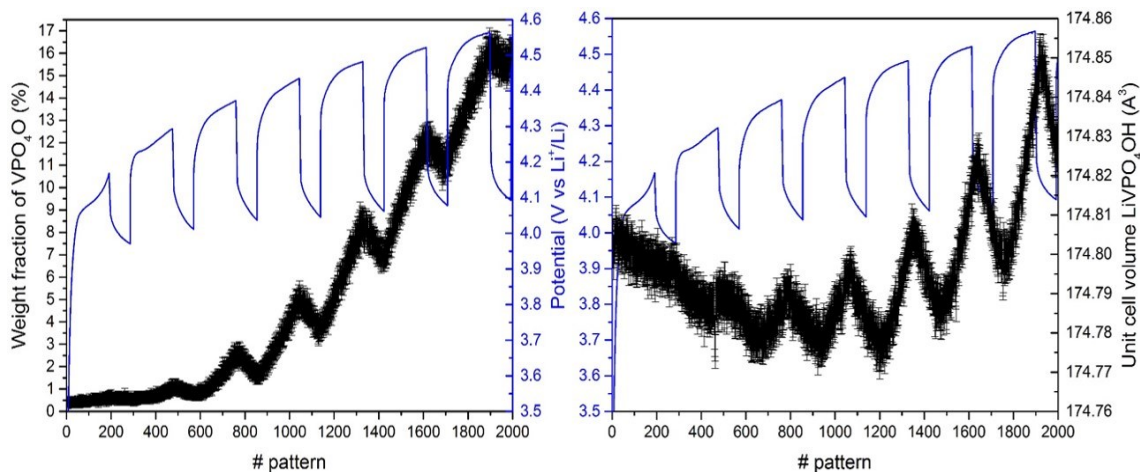


Figure III-25: Weight fraction of VPO_4O (left) and cell volume of LiVPO_4OH (right) as a function of the pattern number. The corresponding voltage profile is represented as blue line. Each current pulse (of 30 minutes) corresponds to the exchange of 0.05 electron per vanadium (*i.e.* 2.5 % of additional VPO_4O according to the mechanism proposed).

Therefore in order to further confirm the mechanism proposed and to probe the redox phenomena during electrochemical cycling and relaxation, an *operando* XAS experiment was conducted (1 scan of 5 minutes every 15 minutes). The spectra were recorded at the V K-edge during charge of LiVPO_4OH at C/5/electron during 5h (*i.e.* until the average overall V^{4+} state is reached) followed by a relaxation of 1h. The spectra are shown in the **Figure III-26**.

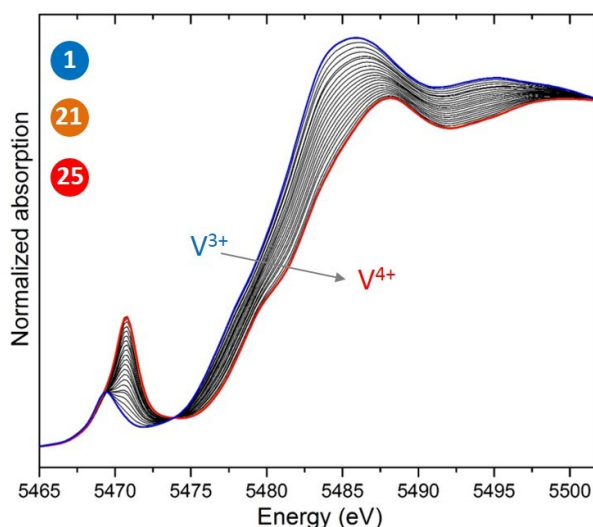


Figure III-26: XANES spectra acquired in *operando* during the charge of LiVPO_4OH (from scan#1 to scan #21) and during relaxation (from scan#21 to scan #25)

Vanadium K-edge XANES exhibits several features as already largely discussed in this manuscript. The main absorption edge corresponds to the $1s \rightarrow 4p$ dipole-allowed transition. The rather linear shift of the edge towards higher energy from $\text{LiV}^{\text{III}}\text{PO}_4\text{OH}$ (*i.e.* $(\text{H,Li})_2\text{V}^{\text{III}}\text{PO}_4\text{O}$) to the overall $(\text{H,Li})\text{V}^{\text{IV}}\text{PO}_4\text{O}$ composition is consistent with an increase of the vanadium oxidation state during the charge. The pre-edge contribution located between 5467 eV and 5474 eV (**Figure III-27a**) arises from the theoretically $1s$ to $3d$ forbidden transition which becomes allowed due to the distortion of the local environment around Vanadium. The tiny peak at 5468.0 eV has already been attributed to a V^{3+} contribution.^{85,129} Moreover, in LiVPO_4OH (*i.e.* LVPH-b sample), a LiVPO_4O -type signature has been previously detected by IR and NMR spectroscopies. This signature has been assigned, thanks to 2D ${}^7\text{Li}\{{}^7\text{Li}\}$ NMR, to the presence of a LiVPO_4O -type impurity (and not vanadyl-type defects). Therefore, the pre-edge contribution seen at 5469.4 eV arises from the contribution of this impurity. Note that the hypothesis of LiVPO_4O -type impurity is strengthened by the very close position for the $\text{V}^{4+}=\text{O}$ pre-edge contribution in LiVPO_4O and LVPH-b (*i.e.* 5469.4 eV in both cases) whereas a slight shift is observed for vanadyl-type defects in $\text{LiVPO}_4\text{F}_{1-y}\text{O}_y$ series, for instance (*i.e.* 5469.2 eV). The fact remains that, although we have previously demonstrated that the pre-edge intensity isn't linear with the amount of vanadyl-type defects (see **section II-3-c**), it is actually proportional in the case of a vanadyl containing impurity. Therefore, an estimation around 7% of LiVPO_4O -type impurity can be made according to the pre-edge intensity observed for LVPH-b compared to LiVPO_4O .

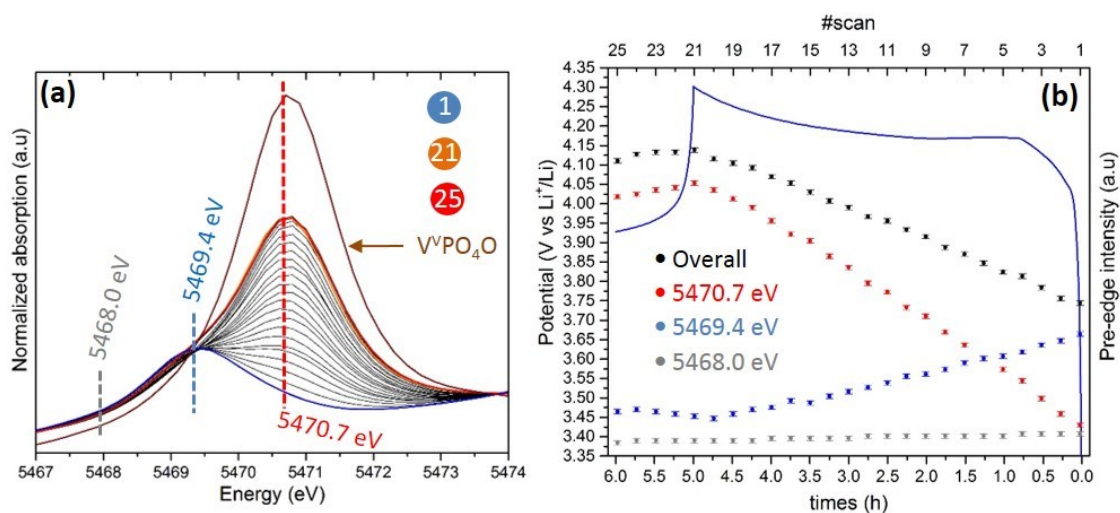


Figure III-27: (a) pre-edge region of the operando XAS spectra (and $\text{V}^{\text{IV}}\text{PO}_4\text{O}$) recorded during the charge of LiVPO_4OH (whose corresponding voltage profile is shown on the right part). The pre-edge feature exhibits 3 main contributions at 5468.0, 5469.4 and 5470.7 eV, the evolution of the intensity of each of these contributions is shown as function of the state of charge (b).

The fits of these 3 pre-edge contributions, performed using a pseudo-Voigt function provided in the Athena Demeter software¹⁴⁷, reveal that this V⁴⁺=O contribution (*i.e.* 5469.4 eV) and the tiny peak at 5468.0 eV (already assigned to V³⁺ contribution) undergo a decrease upon oxidation of vanadium whereas the contribution at 5470.7 eV strongly increases (**Figure III-27b**). Regarding the position of the strong pre-edge intensity observed for VPO₄O (*i.e.* 5470.7eV, spectra shown in **Figure III-27a**), that latter corresponds to the pre-edge contribution of V⁵⁺=O. Therefore, this result suggests the oxidation of V³⁺-O to V⁵⁺=O without detecting any contribution related to a V⁴⁺-rich phase. Moreover, during the relaxation applied during 1h after 5h of charge at C/5/electron, a slight decrease of this V⁵⁺=O contribution (*i.e.* 5470.7 eV) at the benefit of a weak increase of the intensity at 5469.4 eV (*i.e.* V⁴⁺=O contribution) is observed. That is in a good agreement with the decrease of the weight fraction of the VPO₄O phase during relaxation observed by *operando* SXRPD. However, the assignment of this relaxation phenomenon to either a self-discharge or a slow synproportionation of V³⁺ and V⁵⁺ to form a V⁴⁺ phase isn't possible without further investigations.

By a combination of GITT, *operando* SXRPD and XAS experiments, the activation of the V³⁺-O/V⁵⁺=O redox couple has been evidenced. Our hypothesis explaining this phenomenon is to consider a concerted mechanism involving the exchange of two electrons per vanadium (**Figure III-28**).

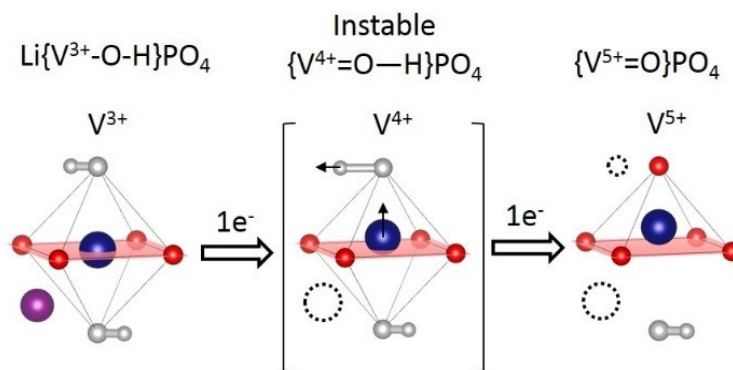


Figure III-28: schematic illustration of the mechanism proposed.

The extraction of lithium should induce the formation of the intermediate phase V^{IV}PO₄OH but this latter appears in fact to be instable and the V^{IV}-O-H sequence is destabilized along the chains due to the competition between the antagonistic bonds: the vanadyl bond V⁴⁺=O on one side and the hydroxyl bond (O-H) on the other side. That leads to a weakening of the latter (V^{IV}-O-H → V^V=O ... H) and thus to the concomitant extraction of Li⁺ and H⁺ at a constant voltage of 3.95 V vs Li⁺/Li.

Regarding the voltage profile in the low voltage region, a more conventional behavior seems to occur with the reversible insertion/extraction of Lithium at 1.40 V vs Li⁺/Li and the formation of Li₂VPO₄OH at the end of the discharge. The structure of these phases will be elucidated in the following part.

iv. Low voltage region: a more conventional V³⁺/V²⁺ redox couple

In order to solve the structure of Li₂V^{II}PO₄OH, the phase was prepared by electrochemical intercalation of Lithium. The powder recovered was then introduced in a sealed capillary for SXRPD analysis. The SXRPD pattern of the reduced phase, Li₂V^{II}PO₄OH, can be refined considering the presence of (i) Li_{1+x}VPO₄OH (11(1) wt%) as an additional phase which could correspond to a remaining amount of the intermediate Li_{1.25}VPO₄OH phase (*P*-1, $a = 5.3520(8)$ Å, $b = 7.4151(9)$ Å, $c = 5.1441(6)$ Å, $\alpha = 111.663(9)^\circ$, $\beta = 82.908(9)^\circ$, $\gamma = 111.713(9)^\circ$, $V = 176.24(3)$ Å³ vs. $V = 175.32(3)$ Å³ for LiVPO₄OH) (ii) the tiny amount of unidentified impurity(ies) in the starting material.

The triclinic unit cell of Li₂V^{II}PO₄OH is described with the following lattice parameters: $a = 7.2835(3)$ Å, $b = 7.5724(3)$ Å, $c = 7.9773(3)$ Å, $\alpha = 89.746(3)^\circ$, $\beta = 88.039(3)^\circ$, $\gamma = 118.675(3)^\circ$, $V = 385.63(3)$ Å³ and $V/Z = 96.17(3)$ Å³. Its cell volume is very large compared to that of the pristine material (*i.e.* $V/Z = 87.66(3)$ Å³, corresponding to a volume expansion of 10.0 %), but it is in rather good agreement with the cell volume already reported for the Tavorite Li₂V^{II}PO₄F with $V/Z = 93.8$ Å³²⁰. Nevertheless, Li₂V^{II}PO₄OH adopting a *P*-1 space group isn't isostructural to Li₂V^{II}PO₄F which crystallizes in a *C2/c* one. Actually, in terms of symmetry, this V²⁺ phase seems to be related to the Li₂V^{III}PO₄O (*P*-1, $V/Z=89.09(3)$ Å³⁹⁶) composition despite the different oxidation states for vanadium in these materials. Indeed, the Rietveld refinement (in a first time, performed without taking into account the Lithium and Hydrogen) reveals that, as previously reported in Li₂V^{III}PO₄O, in Li₂V^{II}PO₄OH, vanadium cations occupy two non-centrosymmetric sites but for that latter the vanadium positions are less distorted (*i.e.* $\Delta = 6.4 \times 10^{-5}$ vs. 1.5×10^{-3} in average on the two vanadium sites respectively for Li₂VPO₄OH and Li₂VPO₄O). Moreover, the distances around vanadium in the hydroxyl phase are significantly larger than those observed in Li₂V^{III}PO₄O (2.14(1) Å for Li₂V^{II}PO₄OH and 2.04(5) in Li₂V^{III}PO₄O in average⁹⁶). They are actually close to the V-O/F bond lengths in Li₂V^{II}PO₄F (2.12(1) Å in average¹⁰¹) leading to BVS in very good agreement with the V²⁺ state (*i.e.* 2.0(1) in average on two vanadium sites). Therefore, the vanadium environment in Li₂VPO₄OH (S.G: *P*-1) is closer to Li₂VPO₄F (S.G: *C2/c*) than Li₂VPO₄O (S.G: *P*-1) whereas Li₂VPO₄OH is isostructural only with Li₂VPO₄O.

Without neutron data, it's challenging to localize lithium cations in the lattice with a high accuracy. However, Fourier difference maps may allow to localize the regions of the real space for which differences between the observed and calculated intensities are significant. In the case of the presence of several phases with a significant overlap of many peaks, the residual intensities arise from the main phase (in which we want to localized Lithium) and also the minor one. Therefore, Fourier difference map will give some additional residual intensities coming from the secondary phase. It's possible to discriminate between relevant and aberrant sites by combining the Fourier Difference Maps with the bond valence map for Li⁺ cations, allowing to get insights into the most stable (at least for the bond valence theory) lithium sites. The bond valence map, calculated with the BondStr software provided in the Fullprof suite¹⁷¹ and drawn with Vesta¹⁷², is shown in **Figure III-29** and suggests several possible Lithium sites (whose approximated positions are listed in **Table III-9**).

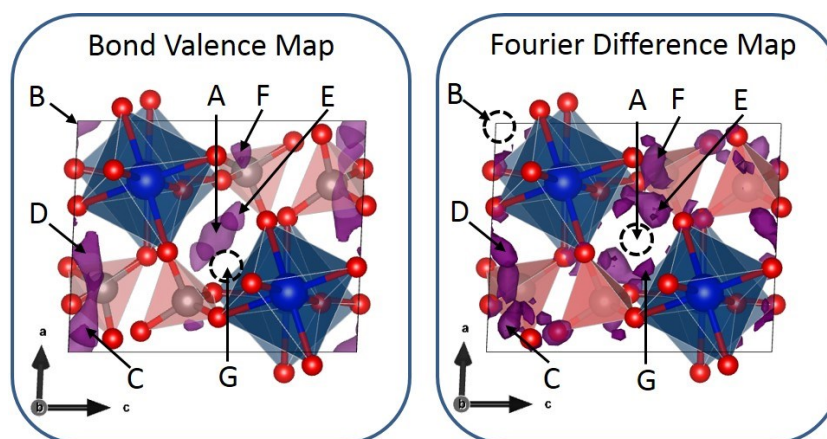


Figure III-29: comparison between bond valence map with a bond valence mismatch of ± 0.15 and Fourier map difference. The position of sites (noted from A to G) marked with arrows are reported in the Table III-9, circles represent empty sites.

Table III-9: approximated position of the most probable lithium sites according to the bond valence theory and the Fourier difference map (see Figure III-29)

site	Bond Valence Map			Fourier Difference Map		
	x	y	z	x	y	z
A	0.5	0.5	0.5	/	/	/
B	0	0.5	0	/	/	/
C	0.95	0.10	0.95	0.90	0.15	0.90
D	0.65	0.35	0.95	0.60	0.30	0.95
E	0.65	0.85	0.50	0.65	0.85	0.50
F	0.80	0.75	0.55	0.80	0.70	0.55
G	/	/	/	0.30	0.95	0.55

The sites A ($\frac{1}{2}$, $\frac{1}{2}$, $\frac{1}{2}$) and B (0, $\frac{1}{2}$, 0) are reported to be fully occupied in $\text{Li}_2\text{VPO}_4\text{O}$ and seem to be in very good agreement with the bond valence theory. Nevertheless, the Fourier difference map (obtained with GFourier software provided in the Fullprof suite¹⁷¹ and drawn with Vesta¹⁷²) clearly reveals the lack of residual density in these regions. Moreover, the Fourier difference map shows a significant residual density in the site G (0.30, 0.95, 0.55) but this site doesn't seem relevant for the bond valence theory. Actually only four $2i$ sites (sites C, D, E and F in **Table III-9**) have been identified to be in agreement with experiment and theory. Therefore, these sites have been chosen as starting model for the refinement of their positions whose result is shown in **Figure III-30** and **31** summarize in **Table Annex-III-1** and **Annex-III-2**.

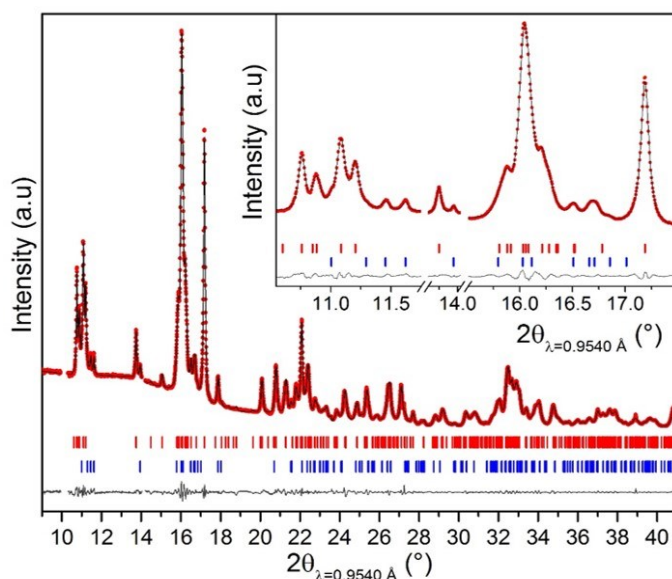


Figure III-30: Rietveld refinement of the structure of $\text{Li}_2\text{VPO}_4\text{OH}$ based on SXRPD considering the 4 fully occupied Lithium sites proposed (i.e. C, D, E and F in the Table III-9). The theoretical Bragg positions are plotted with red and blue marks respectively for $\text{Li}_2\text{VPO}_4\text{OH}$ and $\text{Li}_{1.25}\text{VPO}_4\text{OH}$.

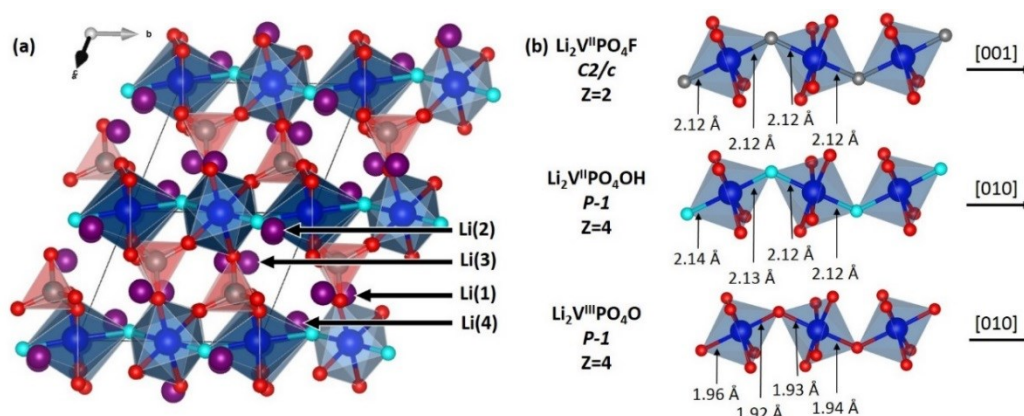


Figure III-31: (a) projection of the crystal structure of $\text{Li}_2\text{VPO}_4\text{OH}$ along the $[\bar{1}01]$ direction: $\text{VO}_4(\text{OH})_2$ octahedra in blue, PO_4 tetrahedra in red and lithium in purple. The oxygen involved in hydroxyl bonds are depicted in turquoise blue. (b) a comparison of bond lengths along the chains of vanadium octahedra for the Tavorite-like structures: $\text{Li}_2\text{V}^{\text{IV}}\text{PO}_4\text{F}$ (top), $\text{Li}_2\text{V}^{\text{IV}}\text{PO}_4\text{OH}$ (middle) and $\text{Li}_2\text{V}^{\text{III}}\text{PO}_4\text{O}$ (bottom).

In Li₂VPO₄OH, the four lithium sites identified are either tetrahedral (Li(1)O₄ and Li(3)O₄ or octahedral (Li(2)O₆ and Li(4)O₆) and rather distorted (from 6.8×10^{-3} to 2.4×10^{-2}). The BVS value associated with each site are in very good agreement with a valence of 1 for Li⁺ cations (1.0(1), 1.0(2) and 0.8(1) for Li(1), Li(2) and Li(4)) except for Li(3) for which the BVS(Li(3))= 1.4(2). This approach gives coherent results, but has to be confirmed by neutron diffraction and ⁷Li NMR experiments.

III-2c. Summary and prospects

In summary, a vanadium based hydroxyl phosphate of Tavorite-type structure, LiVPO₄OH, was obtained for the first time, by hydrothermal route at ~250°C. It could be prepared from at least three different vanadium precursors (VCl₃, V₂O₅ and VPO₄) leading to materials with different morphologies and compositions. The morphology adopted by the samples was partially explained by the solubility of the precursors used leading to different mechanisms of nucleation/growth. Indeed, the materials obtained from soluble precursors (*i.e.* LVPH-a prepared from VCl₃ and LVPH-c obtained from V₂O₅) nucleate from species in solution to form small grains assembled in spherical agglomerates whereas the nucleation of LVPH-b occurs at the surface of the VPO₄ and the LiVPO₄OH domains grow keeping the morphology of the precursors. Nevertheless, whatever the precursors used, impurities with different natures remain. Among them, a Tavorite type impurity, close but different from LiVPO₄O, was also obtained in particular when V₂O₅ was used as precursor despite the large excess of reducer agent in solution.

The crystal structure of LiVPO₄OH was determined thanks to combined ND and SXRPD refinements. Rietveld refinements reveal the formation of a Tavorite phase having a structure very similar to that of LiVPO₄F (replacing F by an OH group) with slightly larger distances around vanadium (*i.e.* 2.00(1) vs 1.975(6) in average on two vanadium sites respectively for LiVPO₄OH and LiVPO₄F) and the formation of a hydrogen bond across the channel. Further proofs of the presence of hydroxyl groups influenced by its environment have been given by diffuse reflectance IR spectroscopy through a broad OH stretching contribution. Despite the great structural similarities of LiVPO₄OH with the LiVPO₄F framework, the BVEL study reveals that this hydrogen bond could hamper the lithium mobility and thus dictate a different lithium diffusion path in LiVPO₄OH. Moreover, solid state MAS NMR (¹H, ⁷Li, ³¹P) appeared to be a tool of choice to discriminate between the presence of LiVPO₄O-type impurity and the formation

of local Vanadyl-type defects. Indeed, bi-dimensional ${}^7\text{Li}\{{}^7\text{Li}\}$ NMR doesn't detect correlation between the LiVPO_4O -type contribution and the peaks assigned to Lithium in LiVPO_4OH .

In the low voltage region, a rather conventional insertion/extraction mechanism occurs in two steps: an apparent solid solution process until the $\text{Li}_{1.25}\text{VPO}_4\text{OH}$ composition is reached and then a biphasic reaction until the $\text{Li}_2\text{V}^{\text{IV}}\text{PO}_4\text{OH}$ phase is formed. Its structure has been solved thanks to SXRPD data. The symmetry in the polyanion framework adopted by $\text{Li}_2\text{VPO}_4\text{OH}$ is related to the one of $\text{Li}_2\text{VPO}_4\text{O}$ whereas the bond lengths around vanadium are close to those observed in $\text{Li}_2\text{VPO}_4\text{F}$ (2.14 vs. 2.13 Å for $\text{Li}_2\text{VPO}_4\text{F}$), in good agreement the common valence for vanadium in these materials. A combination of bond valence and Fourier difference maps allowed to propose four fully occupied Lithium sites in $\text{Li}_2\text{VPO}_4\text{OH}$. However, the Lithium distribution proposed has to be confirmed by ND and ${}^7\text{Li}$ NMR experiments.

In the high voltage region, despite its poor electrochemical performance, this new Tavorite composition reveals an original mechanism. Indeed, *In-operando* XANES at V K-edge has highlighted the continuous growth of a strong $\text{V}^{5+}=\text{O}$ pre-edge contribution suggesting the activation of the $\text{V}^{3+}-\text{O}/\text{V}^{5+}=\text{O}$ redox couple. Moreover, *in-operando* SXRPD has revealed that the oxidation of $\text{LiV}^{\text{III}}\text{PO}_4\text{OH}$ occurs according to a single biphasic process at 3.95 V vs Li^+/Li , leading to the formation of $\text{V}^{\text{V}}\text{PO}_4\text{O}$ at the charged state. Therefore, no V^{4+} -rich phase was detected during electrochemical cycling whereas the extraction of lithium should induce the formation of the intermediate phase, $\text{V}^{\text{IV}}\text{PO}_4\text{OH}$, but we suspect that this latter appears to be instable and thus isn't detected either by SXRPD or XANES. Our hypothesis regarding the instability of $\text{V}^{\text{IV}}\text{PO}_4\text{OH}$ is to consider the competition between $\text{V}^{4+}=\text{O}$ on one side and O-H bond on the other side: The $\text{V}^{\text{IV}}-\text{O}-\text{H}$ sequence is thus destabilized along the chains. In order to satisfy the valence of the Oxygen anion involved in both bonds, a weakening of the O-H occurs leading to the concomitant extraction of Li^+ and H^+ .

Beside the fundamental interest of this mechanism showing new aspects of the fascinating vanadyl bond, this system illustrates a new track to follow to develop two-electron reactions at the same potential (*i.e.* 3.95 V vs Li^+/Li). In LiVPO_4OH , the irreversibility of the mechanism is inherent to the nature of cations extracted and the probable reaction of H^+ with the electrolyte salt. Therefore, it is worth to consider this system either versus reversible exchange of H^+ in aqueous electrolyte or versus reversible bivalent cations extraction-insertion in Mg or Ca-ion batteries. Indeed, if the $\text{V}^{3+}-\text{O}/\text{V}^{5+}=\text{O}$ redox couple is really activated at 3.95 V vs. Li^+/Li upon oxidation of LiVPO_4OH (*i.e.* $(\text{H}^+, \text{Li}^+)_2\text{V}^{\text{III}}\text{PO}_4\text{O}$), the $\text{Mg}^{2+}\text{V}^{\text{III}}\text{PO}_4\text{O}$ or $\text{Ca}^{2+}\text{V}^{\text{III}}\text{PO}_4\text{O}$

could offer the same behavior and an impressive theoretical energy densities (*i.e.* around 1250, 940 and 990 Wh/kg respectively in Li, Mg or Ca-ion batteries).

This study reveals that the prospection towards new Tavorite-like compositions offers materials showing a rich crystal chemistry and original electrochemical properties. The syntheses of other compositions belonging to the LiVPO_4F - LiVPO_4O - LiVPO_4OH ternary phase diagram have been attempted but due to:

(i) The instability of the V^{4+} -O-H sequence, the existence of the mixed valence $\text{LiVPO}_4\text{O}_{1-y}\text{OH}_y$ phases appears as improbable.

(ii) The competition between the basic pH-driven formation of LiVPO_4OH vs. the acid pH-driven formation of $\text{VPO}_4 \cdot \text{H}_2\text{O}$, the direct synthesis of $\text{LiVPO}_4\text{F}_{1-y}\text{OH}_y$ (under similar conditions than those used for obtain LiVPO_4OH in a diluted HF aqueous solution) led systematically to the formation of $\text{Li}_x\text{VPO}_4(\text{OH}, \text{H}_2\text{O}, \text{F})$ -type phases whose the complexity doesn't allow us to characterize them in-depth.

In general, the vanadium hydroxy(hydroxyl) phosphates belong to a large family of materials which is widely investigated in literature for their catalytic, magnetic and electrochemical properties. In the following part, an investigation of the crystal structure and the Lithium diffusion pathways in a new vanadium hydroxy phosphate will be conducted.

III-3. A potential high voltage two electrons system: $\text{Li}_2\text{V}(\text{H}_{0.5}\text{PO}_4)_2$

$\text{Li}_2\text{V}(\text{H}_{0.5}\text{PO}_4)_2$ was obtained by hydrothermal synthesis in similar conditions than those used for the synthesis of the isostructural iron-containing composition¹⁷⁹. The reaction was carried out by mixing VCl_3 (97 %, Sigma-Aldrich), LiH_2PO_4 (> 99 %, Sigma-Aldrich), and $\text{Li}_2\text{B}_4\text{O}_7$ (> 99.9 %, Sigma-Aldrich) with a molar ratio of 1:5:1 in aqueous solution, in a 23 ml Teflon container with a filling rate of 60%. The reactor was introduced in an oven and heated at 220°C for two weeks with heating and cooling rates of 5°C/h. The brown-green powder obtained was filtered, washed with distilled water and then with ethanol and dried at 60°C in an oven overnight. This powder contains both $\text{Li}_2\text{V}(\text{H}_{0.5}\text{PO}_4)_2$ and LiVPO_4OH in a weight ratio 40/60 (**Figure III-32**) and no boron-based impurity was identified, despite the presence of Lithium tetraborate in the starting mixture.

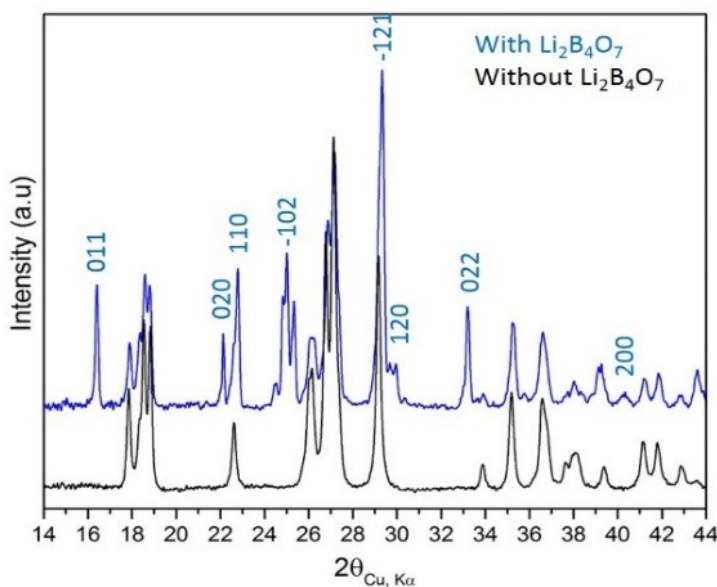


Figure III-32: Powder XRD pattern of the sample containing $\text{Li}_2\text{V}(\text{H}_{0.5}\text{PO}_4)_2$ and LiVPO_4OH (~40:60 wt.%) and obtained as described above (blue), with the indexation of the main Bragg reflections of $\text{Li}_2\text{V}(\text{H}_{0.5}\text{PO}_4)_2$. The powder XRD pattern of LiVPO_4OH is given in black, it was obtained in similar condition but without $\text{Li}_2\text{B}_4\text{O}_7$.

Note that, although the exact role of $\text{Li}_2\text{B}_4\text{O}_7$ in this synthesis is unclear, this precursor might promote the formation of $\text{Li}_2\text{V}(\text{H}_{0.5}\text{PO}_4)_2$ vs. LiVPO_4OH as we observed that without $\text{Li}_2\text{B}_4\text{O}_7$, under similar conditions, a pure LiVPO_4OH was obtained (**Figure III-32**). Single crystals of the new composition $\text{Li}_2\text{V}(\text{H}_{0.5}\text{PO}_4)_2$ were selected from the mixture for its structural characterization.

Single crystal diffraction data were obtained on a Bruker D8 Venture diffractometer equipped with a Photon 100 detector and a Molybdenum micro-source ($\lambda = 0.71073 \text{ \AA}$) at 293K. The crystal used for the diffraction experiment was a green parallelepiped ($0.14 \times 0.09 \times 0.07 \text{ mm}$). The details for the data collection and the refinements are provided in **Table III-10**.

Table III-10: Data collection and refinement details

Data collection	
Diffractometer	Bruker D8 Venture
Radiation type	Mo $K\alpha$ ($\lambda=0.71073 \text{ \AA}$)
Temperature (K)	293
Crystal size (mm)	$0.14 \times 0.09 \times 0.07$
Absorption correction	Numerical (SADABS; Bruker, 2013)
μ (mm^{-1})	2.35
Data collection	APEX3 (BRUKER)
No. of measured, independent and observed [$I > 2\sigma(I)$] reflections	65122, 3250, 2702
$(\sin \theta/\lambda)_{\text{max}}$ (\AA^{-1})	1.116
Refinement	
Cell refinement software	SAINT (BRUKER)
R_{int}	0.059
Data reduction software	SAINT (BRUKER)
Structure solving software	SHELXS97
Structure solving method	Direct method
Structure refinement software	SHELXL (Sheldrick, 2014)
$R[F^2 > 2\sigma(F^2)]$	0.029
$wR(F^2)$	0.067
S	1.10
No. of reflections	3250
No. of parameters	62
$\Delta\rho_{\text{max}}, \Delta\rho_{\text{min}}$ (e \AA^{-3})	1.04, -0.73

$\text{Li}_2\text{V}(\text{H}_{0.5}\text{PO}_4)_2$ crystallizes in a monoclinic unit cell ($a = 4.8093(6) \text{ \AA}$, $b = 8.0070(9) \text{ \AA}$, $c = 7.8485(9) \text{ \AA}$, $\beta = 112.395(6)^\circ$, $V = 279.51(2) \text{ \AA}^3$ and $Z = 2$) described in the $P2_1/c$ (S.G.#14) space group. The crystal structure of $\text{Li}_2\text{V}(\text{H}_{0.5}\text{PO}_4)_2$ (whose atomic positions and cell parameters are listed in **Table III-11** and selected inter-atomic distances in **Table III-12**) is characterized by VO_6 octahedra sharing corners with six PO_4 tetrahedra (**Figure II-33b**) forming a 3-D network while each PO_4 tetrahedron shares three corners with three VO_6 octahedra (**Figure II-33c**). Vanadium is located on the inversion center of VO_6 octahedra and V-O bond distances range from $1.974(2) \text{ \AA}$ to $2.031(2) \text{ \AA}$ forming slightly distorted entities ($\Delta = 1.11 \times 10^{-4}$). The bond valence sum of vanadium is in very good agreement with the formation of a V^{3+} -containing phase (*i.e.* $\text{BVS}(\text{V}) = 2.95(1)$). The PO_4 tetrahedra are quite rigid groups ($\Delta = 2.96 \times 10^{-5}$) in which the distances range from $1.523(2)$ to $1.546(2) \text{ \AA}$, in very good agreement with distances commonly found in phosphate groups¹⁴⁴.

Table III-11: Cell parameters, fractional atomic coordinates, isotropic * or equivalent isotropic displacement parameters (\AA^2) and Bond valence sum obtained from refinement of the crystal structure of $\text{Li}_2\text{V}(\text{H}_{0.5}\text{PO}_4)_2$.

$\text{Li}_2\text{V}(\text{H}_{0.5}\text{PO}_4)_2$							
	$a = 4.8093(6) \text{ \AA}$	$M_w = 255.76 \text{ g.mol}^{-1}$			$R_{\text{int}} = 5.9\%$		
S.G: $P2_1/c$	$b = 8.0070(9) \text{ \AA}$	$V = 279.51(2) \text{ \AA}^3$			$wR(F^2) = 6.7\%$		
$Z = 2$	$c = 7.8485(9) \text{ \AA}$	$\mu = 3.039 \text{ g.cm}^{-3}$			$R[F^2 > 2\sigma(F^2)] = 2.9\%$		
	$\beta = 112.395(6)^\circ$						
Atoms	Wyckoff position	x	y	z	Occupancy	U iso*/Ueq	BVS
V (1)	2a	0	0	0	1.000	0.0046	2.94(1)
H (1)	4e	0.45	0.51	0.01	1/2	0.064*	1.20(1)
P (1)	4e	0.6334(1)	0.65234(6)	0.76519(6)	1.000	0.0048	5.02(1)
O (1)	4e	0.2966(3)	0.6733(2)	0.6506(2)	1.000	0.0078	2.00(1)
O (2)	4e	0.7929(4)	0.8203(2)	0.8116(2)	1.000	0.0092	2.05(1)
O (3)	4e	0.7763(4)	0.5433(2)	0.6605(2)	1.000	0.0087	2.05(1)
O (4)	4e	0.6892(4)	0.5595(2)	0.9480(2)	1.000	0.0102	2.06(1)
Li (1)	4e	0.0466(9)	0.8634(6)	0.6569(9)	1.000	0.0148	1.07(1)

Thanks to Fourier difference map, a residual electronic density was found between the O(4) and its equivalent by centrosymmetry O(4') belonging to two different PO_4 and being unshared with VO_6 . In the following, these oxygen atoms will be called "free" oxygens. The distribution of residual electronic density between these "free" oxygen atoms is peanut-shaped (**Figure III-33c**). Two models can therefore be proposed:

- H atoms are located on a fully occupied $2d$ ($\frac{1}{2}, \frac{1}{2}, 0$) Wyckoff site (on the inversion center of the peanut-shape residual electronic density) leading to two symmetrically equivalent O-H distances ($d_{\text{O}(4)\text{-H}(1)} = d_{\text{O}(4')\text{-H}(1)} = 1.227(2) \text{ \AA}$ and a O(4)-H-O(4') angle of 180°) (**Figure III-33c**),
- H atoms are located on a $4e$ position half occupied site generating two different O-H distances ($d_{\text{O}(4)\text{-H}(1)} = 1.018(2) \text{ \AA}$ and $d_{\text{O}(4)\text{-H}(1')} = 1.466(2) \text{ \AA}$ and an O(4)-H-O(4') angle of $153.4(3)^\circ$) (**Figure III-33c**).

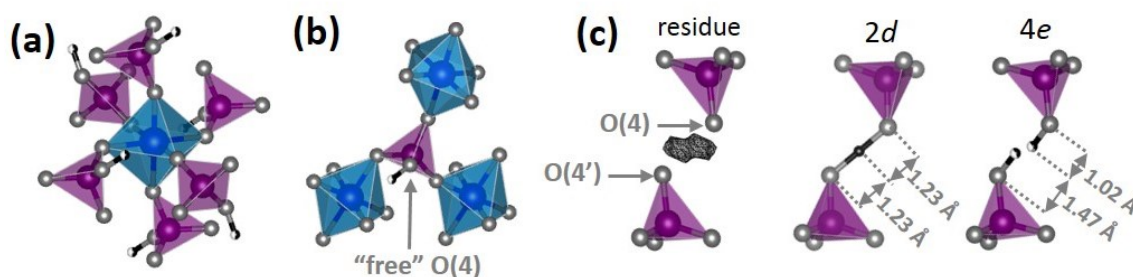


Figure III-33: projection of the structure of $\text{Li}_2\text{V}(\text{H}_{0.5}\text{PO}_4)_2$ along the $[100]$ direction (a) VO_6 octahedra and PO_4 tetrahedra are represented in blue and purple respectively. Li, O and H atoms are depicted by pink, grey and black spheres respectively. The distribution of PO_4 tetrahedra surrounding a VO_6 octahedron is illustrated in (b) and conversely in (c). The residual electronic density located between two "free" oxygens and the two models proposed for hydrogen position are illustrated in (d).

If the hydrogen atom occupies a $2d$ Wyckoff position a three-centers four-electrons bond has to be considered and in the case of $4e$ position a more common hydroxyl group involved in a hydrogen bond would be formed. As it's very difficult to precisely localize H atoms in inorganic materials we weren't able to refine the fractional coordinates of this hydrogen. This latter was thus fixed to the center of each lobe in a $4e$ site (0.45, 0.51, 0.01) half occupied, generating an O-H interatomic distance of 1.018(2) Å commonly observed for hydroxyl group involved in a hydrogen bond. The fact remains that this position is very close to the one found by Jin-Xiao Mi *et al.*¹⁷⁹ for the iron phase (*i.e.* 0.45, 0.52, 0.02) but O-H and O---H distances (*i.e.* 0.86(5) and 1.60(5) respectively) suggest the absence of hydrogen bond in the iron-based material.

In the isostructural iron-containing phase, Jin-Xiao Mi *et al.*¹⁷⁹ described the lithium site as a 4+1 coordination polyhedron. In $\text{Li}_2\text{V}(\text{H}_{0.5}\text{PO}_4)_2$, there are four Li-O bonds close to 2 Å (ranging between 1.952(6) and 2.052(4) Å) and a longer fifth one at 2.357(6) Å. Moreover the four oxygen atoms involved in the short Li-O bonds belong to four different PO_4 groups and form a slightly distorted LiO_4 tetrahedron ($\Delta = 3.69 \times 10^{-4}$). The bond valence sum computed for two coordination models (*i.e.* 4 or 4+1) polyhedra provided slightly different values (*i.e.* BVS = 0.980(5) for LiO_4 and 1.070(5) for LiO_5 polyhedra) hence favorable to the hypothesis of LiO_4 tetrahedra. Actually the fifth distance seems too long to belong to the first coordination sphere of lithium.

Table III-12: Selected bond lengths (Å) and polyhedral distortion calculated as $\Delta = \frac{1}{N} \sum_{i=0}^N \frac{(d_i - \langle d \rangle)^2}{\langle d \rangle^2}$

	V(1) 6 (Oh)	P(1) 4 (Td)	Li(4) 4 (Td)	H(1) 2
O(1)	2.018(2)	1.533(2)	1.952(6)	/
O(1')	2.018(2)	/	/	/
O(2)	2.031(2)	1.523(2)	2.052(4)	/
O(2')	2.031(2)	/	/	/
O(3)	1.974(2)	1.530(2)	1.978(6)	/
O(3')	1.974(2)	/	/	/
O(4)	/	1.546(2)	1.968(5)	1.018(2)
O(4')	/	/	/	1.466(2)
Average	2.008(2)	1.535(2)	1.988(5)	1.242(2)
Δ	1.11×10^{-4}	2.96×10^{-5}	3.69×10^{-4}	/

As mentioned earlier, $\text{Li}_2\text{V}(\text{H}_{0.5}\text{PO}_4)_2$ is isostructural to $\text{Li}_2\text{Fe}(\text{PO}_4)(\text{HPO}_4)$, but is also closely related to the Marinite structure of $\text{Li}_2\text{Fe}^{\text{II}}(\text{SO}_4)_2$.¹⁸⁰ The relations between $\text{Li}_2\text{V}(\text{H}_{0.5}\text{PO}_4)_2$ and $\text{Li}_2\text{Fe}(\text{SO}_4)_2$ are illustrated in **Figure III-34**.

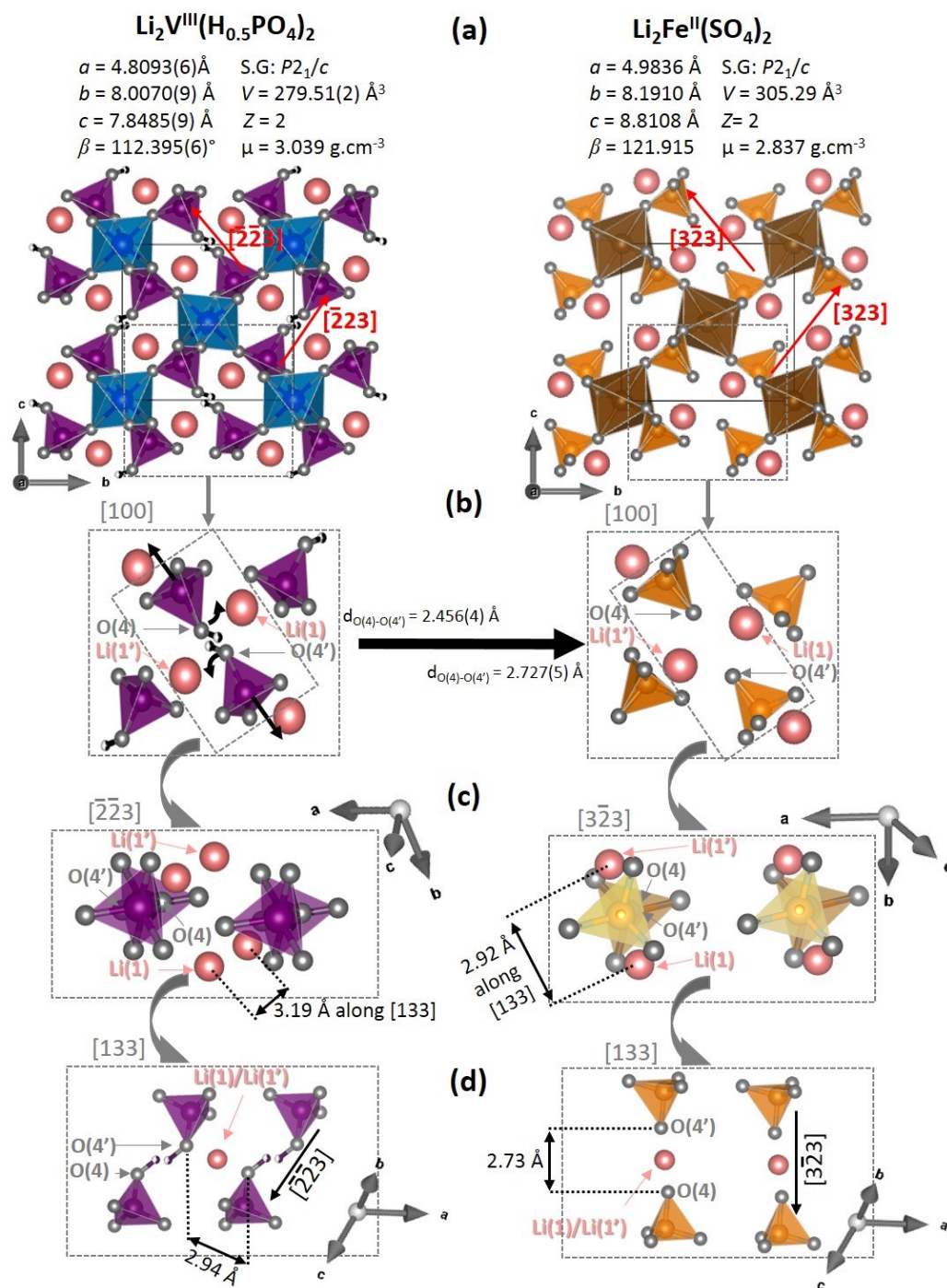


Figure III-34: Structural relationship between $\text{Li}_2\text{V}(\text{H}_{0.5}\text{PO}_4)_2$ (left) and $\text{Li}_2\text{Fe}(\text{SO}_4)_2$ (right). The whole structure in (a) and an enlargement of the $\text{H}(\text{PO}_4)_2$ or $\text{SO}_4)_2$ groups in (b) are projected along [100]. The same groups are projected along the O(4)-O(4') direction in (c) (i.e. $[\bar{2}23]$ and $[3\bar{2}3]$ for $\text{Li}_2\text{V}(\text{H}_{0.5}\text{PO}_4)_2$ and $\text{Li}_2\text{Fe}(\text{SO}_4)_2$ respectively) and along the shorter Li-Li distance in (d) (i.e. [133]). On that latter, the smaller section of the path for lithium hopping between two closest sites is depicted.

The essential differences lie in the orientation of XO_4 groups ($\text{X} = \text{P}, \text{S}$) and in the distance between 2 “free” oxygen atoms. These distances are $2.727(5) \text{ \AA}$ in $\text{Li}_2\text{Fe}(\text{SO}_4)_2$ vs $2.456(2) \text{ \AA}$ in $\text{Li}_2\text{V}(\text{H}_{0.5}\text{PO}_4)_2$. The shorter O(4)-O(4') distance in $\text{Li}_2\text{V}(\text{H}_{0.5}\text{PO}_4)_2$ can be explained by the

presence of hydrogen which screens the electrostatic repulsion between these two “free” oxygen atoms. This shortening leads to a shrinking of the structure and to a decrease of the section of the channel running along [100] in which Li^+ can diffuse. **Figures III-34c and III-34d** illustrate the differences in XO_4 ($\text{X} = \text{P}$ or S) orientations. Indeed the projection along [133] (**Figure III-34d**) corresponding to the direction of shorter Li-Li distances in both materials reveals that the Li(1)-Li(1') path doesn't intersect the O(4)-O(4') segment in $\text{Li}_2\text{V}(\text{H}_{0.5}\text{PO}_4)_2$ whereas it does in $\text{Li}_2\text{Fe}(\text{SO}_4)_2$.

III-3a. Influence of Hydrogen on the Lithium diffusion path

In order to get more insights into the possible pathways for Lithium diffusion, Bond Valence Energy Landscape (BVEL) maps were calculated thanks to the BONDSTR software in the Fullprof suite¹⁷¹ and drawn with VESTA¹⁷² in **Figure III-35**. An energy of 1.6 eV is often used for lithium diffusion in polyanionic compounds¹⁵³ and it is interesting to compare the isosurfaces obtained for $\text{Li}_2\text{Fe}(\text{SO}_4)_2$ and for $\text{Li}_2\text{V}(\text{H}_{0.5}\text{PO}_4)_2$ in order to investigate the influence of the additional hydrogen atom on lithium diffusion. In the iron sulfate phase, this technique highlighted that lithium diffusion occurred along [100], [011] and [0-11] according to a 3D interconnected pathway (see also the figure 8a of reference¹⁸¹).

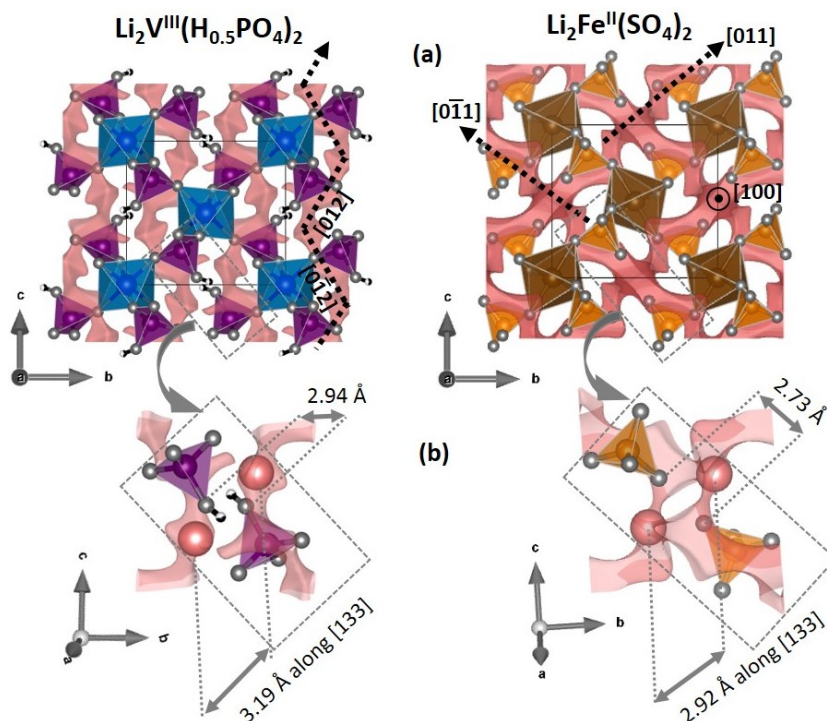


Figure III-35: (a) Projection along [100] of Lithium paths obtained from Bond Valence Energy Landscape (BVEL) with an energy of 1.6 eV above minimum for $\text{Li}_2\text{Fe}(\text{SO}_4)_2$ (right) and $\text{Li}_2\text{V}(\text{H}_{0.5}\text{PO}_4)_2$ (left). (b) Enlargement of the path corresponding to the shorter Li-Li distance (along [133]) showing that a hopping between two Li sites is possible in $\text{Li}_2\text{Fe}(\text{SO}_4)_2$ whereas it isn't allowed in $\text{Li}_2\text{V}(\text{H}_{0.5}\text{PO}_4)_2$.

For $\text{Li}_2\text{V}(\text{H}_{0.5}\text{PO}_4)_2$, lithium diffusion doesn't occur along these directions but via a zig-zag path along [012] and [0-12], hopping between two sites distant of 4.32 Å (**Figure III-35**), and leading to an overall diffusion direction along [001]. The comparison between both structures (**Figure III-35**) illustrates that the presence of hydrogen in $\text{Li}_2\text{V}(\text{H}_{0.5}\text{PO}_4)_2$ enables the diffusion along [100], [011] and [0-11]. At first sight, the inability for Li^+ to diffuse along [011] and [0-11] in $\text{Li}_2\text{V}(\text{H}_{0.5}\text{PO}_4)_2$ comes as a surprise because i) the shorter Li-Li distance (3.19 Å) is found along those axis and ii) the section (2.94 Å) is higher compare to the one found within the Marinite structure (2.73 Å) as depicted in **Figure III-35b**. Actually, in both cases this space is already occupied by oxygen atoms or OH groups and the bypassing of this diffusion obstacle is forbidden in $\text{Li}_2\text{V}(\text{H}_{0.5}\text{PO}_4)_2$ due to the presence of hydrogen that prevents the connection between the two pathways whereas it is possible in Marinite (**Figure III-35b**).

III-3b. Summary and prospects

In summary, a new composition, $\text{Li}_2\text{V}^{\text{III}}(\text{H}_{0.5}\text{PO}_4)_2$, was obtained under hydrothermal conditions and its structure was solved thanks to single crystal X-Ray diffraction. In this structure, VO_6 octahedra share corners with six PO_4 tetrahedra to form a three-dimensional framework. This crystallographic feature is also observed in $\text{LiV}^{\text{III}}\text{P}_2\text{O}_7$ and prevents the formation of vanadyl bonds (*i.e.* of strongly covalent $\text{V}=\text{O}$ bonds for V^{4+} or V^{5+}) in $\text{V}^{\text{IV}}\text{P}_2\text{O}_7$.¹⁸² Interestingly, the voltage of the $\text{V}^{3+}/\text{V}^{4+}$ redox couple in LiVP_2O_7 (4.2V vs Li^+/Li) is much higher than in the vanadyl-rich compound Li_2VOPO_4 (2.3 V)⁹⁸. Moreover, contrarily to LiVP_2O_7 in which the capacity is limited by the lithium content (*i.e.* $\text{Li}/\text{V} = 1$), in $\text{Li}_2\text{V}(\text{H}_{0.5}\text{PO}_4)_2$ the extraction of two Li per V is expected. It would involve first the $\text{V}^{3+}/\text{V}^{4+}$ redox couple (expected to be close to 4.2V as for LiVP_2O_7) and then the $\text{V}^{4+}/\text{V}^{5+}$ redox couple at an higher potential, conferring to this material a very high theoretical energy density (up to 800 Wh/kg against 585 Wh/kg for LiFePO_4). Some attempts to obtain a pure $\text{Li}_2\text{V}^{\text{III}}(\text{H}_{0.5}\text{PO}_4)_2$ powder, especially from LiVP_2O_7 ($\text{LiVP}_2\text{O}_7 + \text{LiOH} = \text{Li}_2\text{V}^{\text{III}}(\text{H}_{0.5}\text{PO}_4)_2$), have been conducted but we never obtained it as a single phase. However, it is worth to carry on these syntheses in order to investigate the electrochemical properties of this theoretical high energy density material even if BVEL study suggests a lower ionic conductivity in this material compared to the Marinite. This lower transport properties have been assigned to hydroxyl group, the hydrogen bond screening the electrostatic repulsion between two "free" oxygen atoms and generating a shrinkage of the Lithium diffusion paths. The substitution of the hydroxyl group by fluorine forming and PO_3F^- - $-\text{OPO}_3$ entities could offer a way to overcome the structural shrinkage. Indeed, in the hypothetic $\text{Li}_2\text{V}^{\text{III}}(\text{F}_{0.5}\text{PO}_4)_2$ material, the expected strong fluorine/oxygen repulsion could lead to a global expansion of crystal structure which could offer larger paths for an easier lithium diffusion.

Conclusion and perspectives

In the introduction of this work we have provided a review of vanadium phosphates as positive electrode materials for Lithium-ion batteries. The recurrent observation made led us to retain a classification of these materials according to their crystal structures which partially predicts their electrochemical properties. Indeed, for this kind of materials, the possibility of formation of the vanadyl bond dictates the working voltage as well as the local structural changes around vanadium upon electrochemical cycling. We therefore conclude:

- For type I materials (e.g. $\text{Li}_3\text{V}_2(\text{PO}_4)_3$), in which the vanadyl bond cannot appear due the involvement of each oxygen atom of VO_6 octahedra in a PO_4 -type entity, the typical evolution of the vanadium environment upon oxidation (from V^{2+} to V^{5+}) follows a quasi-homogeneous shortening of V-O bonds from V^{2+} to V^{4+} and a strong increase of VO_6 distortion to reach the V^{5+} state with corresponding voltages of 1.8V vs Li^+/Li For $\text{V}^{2+}/\text{V}^{3+}$, 3.9 V vs Li^+/Li for $\text{V}^{3+}/\text{V}^{4+}$ and 4.4 V vs Li^+/Li for $\text{V}^{4+}/\text{V}^{5+}$ redox couples (in average on all the type I materials discussed). The activation of that latter appears either irreversible or kinetically limited.
- In type II materials (e.g. LiVPO_4F), the formation of the vanadyl bond is prevented by the presence of fluorine and the vanadium environment follows similar evolution with a slightly higher voltage, in average.
- Type III materials (e.g. LiVPO_4O), in which the vanadyl bond is formed for the oxidation of vanadium at higher degrees than 3+, follow a different mechanism. The V^{3+} environments are quasi undistorted. As the oxidation state of vanadium is increased, vanadium leaves the gravity center of the VO_6 octahedra to get closer to one of its oxygen ligands in order to form the vanadyl bond. The migration of vanadium atom along dz^2 orbitals of vanadium leads to the formation of distorted $\text{V}^{\text{IV}}\text{O}_6$ octahedra (with typical distances ranging between 1.6 and 2.4 Å along dz^2 and quasi equivalent equatorial distances around 2 Å) and then to V^{VO}_5 pyramids (in which the short $\text{V}=\text{O}$ bond is about 1.6 Å and a shortening of the other distances is observed around 1.8-1.9 Å). The corresponding voltages appear completely different to those of type I and type II materials: 2.4 V vs Li^+/Li for the $\text{V}^{3+}\text{-O}/\text{V}^{4+}=\text{O}$ and 3.95 V vs Li^+/Li for the $\text{V}^{4+}=\text{O}/\text{V}^{5+}=\text{O}$ redox couples.

In this work, we have investigated, in particular, two new kinds of mixed type II-type III materials: (i) the $\text{LiVPO}_4\text{F}_{1-y}\text{O}_y$ series of materials in which the partial substitution of a fluorine by oxygen leads to the local formation of the vanadyl-type environments whose behavior during electrochemical cycling is different to those described above and (ii) LiVPO_4OH which behaves as a type II material during insertion of lithium and as type III material upon charge. These systems can supplement the discussion on the electrochemical properties according to the classification provided in the introductory chapter.

$\text{LiVPO}_4\text{F}_{1-y}\text{O}_y$

In $\text{LiVPO}_4\text{F}_{1-y}\text{O}_y$ materials, the $\text{V}^{4+}=\text{O}/\text{V}^{5+}=\text{O}$ redox couple is involved during the first step of the charge and then the $\text{V}^{3+}/\text{V}^{4+}$ in fluorine rich environments is activated. This first step corresponds to a wide monophasic domain during which the structure seems to be frozen. The competitive formation between the strongly covalent vanadyl bond (from $\text{V}^{4+}=\text{O}$ to $\text{V}^{5+}=\text{O}$) and the highly ionic $\text{V}^{3+}-\text{F}$ bond could avoid the structural shrinkage and then the activation of the $\text{V}^{3+}/\text{V}^{4+}$ redox couple leads to significant volume changes. Therefore, an optimal vanadyl-type environments' concentration arises from the balance between both processes. Indeed, for oxygen-rich materials (having a wide domain involving the $\text{V}^{4+}=\text{O}/\text{V}^{5+}=\text{O}$ redox couple during which the structure is quasi-unchanged), the activation of the $\text{V}^{3+}/\text{V}^{4+}$ redox couple induces some strong structural changes in a narrow composition domain whereas for fluorine-rich materials (having a narrow domain involving the $\text{V}^{4+}=\text{O}/\text{V}^{5+}=\text{O}$ redox couple), these changes are spread on a larger composition domain. The softer structural evolution observed in fluorine-rich materials have a beneficial effect on the cycling stability and rate capability.

Even though the $\text{LiVPO}_4\text{F}_{1-y}\text{O}_y$ system is competitive with already commercialized materials (LiFePO_4 and LiCoO_2 for instance) playing only with lithium extraction, it's still possible to extract additional capacity. Indeed, by involving the low voltage processes ($\text{V}^{4+}=\text{O}/\text{V}^{3+}-\text{O}$ and $\text{V}^{3+}/\text{V}^{2+}$ redox couple), $\text{Li}_{1\pm x}\text{VPO}_4\text{F}_{1-y}\text{O}_y$ materials have previously been investigated as multi-electron systems delivering 800 Wh/kg in the 2.0-4.5 V vs. Li^+/Li range (with $\Delta x=1.6$)¹⁰⁷. Nevertheless, the activation of several redox couples per transition metal appeared to be detrimental to the long life performance (*i.e.* ~50% of capacity fading after 15 cycles at a rate of $C/20$)¹⁰⁷. Indeed, the investigation of the phase diagram in the low voltage region reveals strong structural evolution: (i) the reduction of the $\text{V}^{4+}=\text{O}$ to $\text{V}^{3+}-\text{O}$ during the first step of lithiation is observed leading to a pure V^{3+} phase with the persistence of a short $\text{V}^{3+}-\text{O}$ bond, (ii) the further lithiation leads to the activation of the $\text{V}^{3+}/\text{V}^{2+}$ redox couple with the loss of a "vanadyl-type distortion" and a strong increase of bond lengths around vanadium.

However, the authors of ref¹⁰⁷ studied only one oxygen-rich composition. Therefore, it is worth to investigate our $\text{Li}_x\text{VPO}_4\text{F}_{1-y}\text{O}_y$ series of materials as multi-electron systems playing with the substitution ratio (*i.e.* y) and the voltage range in order to control the insertion/extraction reaction (*i.e.* Δx), limit the structural changes and thus stabilize the performance for long life cycling.

Another mixed type II-type III material has already been investigated: $\text{Na}_3\text{V}_2(\text{PO}_4)_2\text{F}_{3-y}\text{O}_y$. It reveals itself to be a high voltage reversible multi-electron system with the exchange of 1.10 electron per vanadium⁸⁸. Some efforts are currently devoted in our group in order to elucidate the phase diagram and the redox mechanisms involved for these materials. Furthermore, many other materials are theoretically able to show similar multi electron properties but they haven't been obtained and studied yet: two strategies can be applied to obtain them (i) the partial substitution of fluorine by oxygen from type II material ($\text{LiVPO}_4\text{F}_{1-y}\text{O}_y$ and $\text{Na}_3\text{V}_2(\text{PO}_4)_2\text{F}_{3-y}\text{O}_y$ being already studied, to the best of our knowledge, the only remaining system could be $\text{Li}_5\text{V}(\text{PO}_4)_2\text{F}_{2-y}\text{O}_y$), and (ii) the fluorination of type III materials. That latter strategy could offer much more possibilities than the former. Indeed, beyond type III materials whose electrochemical properties have already been investigated (reported in **Table I-1**), a huge amount of other vanadium phosphates belonging to the type III family exists (as reported in ref.⁵⁸). A systematic study of their partially fluorinated composition could reveal interesting electrochemical performance.

LiVPO₄OH

The electrochemical oxidation of V^{3+} in LiVPO_4OH occurs according to an original mechanism. Indeed, the activation of the $\text{V}^{3+}\text{-O}/\text{V}^{5+}=\text{O}$ redox couple at a constant equilibrium voltage of 3.95 V vs Li^+/Li , leads to the formation of the tavorite-like $\text{V}^{\text{V}}\text{PO}_4\text{O}$ at the charged state of the battery. Therefore, no V^{4+} -rich phase was detected during electrochemical cycling whereas the extraction of lithium should induce the formation of the intermediate phase, $\text{V}^{\text{IV}}\text{PO}_4\text{OH}$, but we suspect that this latter appears to be instable vs. $\text{LiV}^{\text{III}}\text{PO}_4\text{OH}$ and $\text{V}^{\text{V}}\text{PO}_4\text{O}$. Our hypothesis regarding the instability of $\text{V}^{\text{IV}}\text{PO}_4\text{OH}$ is to consider the competition between $\text{V}^{4+}=\text{O}$ on one side and O-H bond on the other side: the $\text{V}^{\text{IV}}\text{-O-H}$ sequence is thus destabilized along the chains. In order to satisfy the valence of the Oxygen anion involved in both bonds, a weakening of the O-H bond occurs leading to the concomitant extraction of Li^+ and H^+ . This H^+ extraction is also observed for the Tavorite-like $\text{VPO}_4\cdot\text{H}_2\text{O}$ (also called HVPO_4OH or $\text{H}_2\text{VPO}_4\text{O}$) leading also to the formation of $\text{V}^{\text{V}}\text{PO}_4\text{O}$ at the charged state of the battery¹⁸³. The

irreversibility/asymmetry of the mechanism is inherent to the nature of cations extracted and the probable reaction of H^+ with the electrolyte salt. Therefore, it is worth to consider these system versus reversible exchange of H^+ in aqueous electrolyte (310 Wh/kg for $VPO_4 \cdot H_2O$ versus H^+/H^2).

Moreover, the $V^{3+}-O/V^{5+}=O$ redox couple being activated at 3.95 V vs. Li^+/Li upon oxidation of $LiVPO_4OH$ (*i.e.* $(H^+, Li^+)_2V^{III}PO_4O$), the $Mg^{2+}V^{III}PO_4O$ or $Ca^{2+}V^{III}PO_4O$ Tavorite-like materials could offer the same behavior and impressive theoretical energy densities (*i.e.* around 1230, 940 and 990 Wh/kg respectively in Li, Mg or Ca-ion batteries).

Finally, this study reveals that the versatility of the vanadium chemistry with a large number of stable oxidation states (from V^{2+} to V^{5+}), stabilized in very different environments (from very regular to very distorted ones), opens the road towards the formation of new materials, whose strains imposed by the crystal field give attractive electrochemical properties. Even through, in the battery field, the search for new phases shade off since few years, the stabilization of new promising compositions and the in-depth understanding of the mechanisms involved during alkali insertion/extraction have to remain a “hot topic” in the perspective of high voltage two electron systems.

Annex

Table of Contents

ANNEX-I: CHARACTERIZATION OF BATTERY MATERIALS AND EXPERIMENTAL CONDITIONS	219
Annex-I-1. Diffraction techniques	220
Annex-I-2. From Bond Valence Sum to Bond Valence Energy Landscape	230
Annex-I-3. Magnetic measurements	232
Annex-I-4. Solid state MAS NMR spectroscopy.....	234
Annex-I-5. Vibration Spectroscopy, IR vs. Raman	239
Annex-I-6. X-ray absorption spectroscopy	240
Annex-I-7. Electrochemical tests and in-situ everything	245
Annex-I-8. Others techniques: ICP, TGA, SEM, TEM.....	250
ANNEX-II: SUPPLEMENTARY INFORMATION OF CHAPTER II	251
ANNEX-III: SUPPLEMENTARY INFORMATION OF CHAPTER III	258

Annex-I Characterization of Battery materials and experimental conditions

In this manuscript, numerous techniques have been used to characterize in depth the structure of the materials both at the pristine state and during battery operation. Their structural description was undertaken at various scales, ranging:

- from the long range average structure, through diffraction (synchrotron powder X-ray, powder Neutron, single crystal laboratory X-ray and/or electron),
- to local environments by spectroscopy techniques (^1H ^7Li ^{19}F ^{23}Na ^{31}P MAS NMR spectroscopy, diffuse reflectance Infra-red spectroscopy, Raman scattering and X-ray absorption spectroscopy)

The chemical compositions were also carefully monitored by inductively coupled plasma-atomic emission spectroscopy. The morphology of the particles was probed by scanning electron microscopy and the oxidation states around the transition metals via a vibrating sample magnetometer.

The combination of these techniques has allowed a deeper understanding of the electrochemical performance, the structural modifications and the redox mechanisms occurring in the investigated materials.

In this section, we will describe the main techniques as well as the experimental conditions used to study as positive electrodes for Li-ion and Na-ion batteries.

Annex-I-1 Diffraction techniques

i. Bragg's law and symmetry

The wavelengths of X-rays generated from laboratory Cu ($\lambda_{K\alpha_1} = 1.5406 \text{ \AA}$, $\lambda_{K\alpha_2} = 1.5444 \text{ \AA}$), Co ($\lambda_{K\alpha_1} = 1.7890 \text{ \AA}$, $\lambda_{K\alpha_2} = 1.7929 \text{ \AA}$), Mo ($\lambda_{K\alpha_1} = 0.7093 \text{ \AA}$, $\lambda_{K\alpha_2} = 0.7136 \text{ \AA}$) anti-cathodes or from synchrotron sources (and neutrons as well) being in the same order of magnitude than the inter-reticular distances in a crystal, interfere with the electron (or nuclei for neutron). In function of the direction of the real space the flux of X-ray photons will be high for constructive interferences and low for destructive ones. This phenomenon has been discovered by Max Von Laue and further studied by Bragg, father and son. They concluded that the constructive interferences follow the well-known Bragg's law:

$$2d_{hkl} \sin \theta = n\lambda$$

where d_{hkl} is inter-reticular distance, θ the incident beam angle of X-ray deviation, λ the wavelength of the incident beam and n the order of the reflection. The path difference between the diffracted beams from two consecutive reticular planes is $2d_{hkl} \sin\theta$. Thus the constructive interferences appear if the path difference is strictly equal to an integer of the wavelength (*i.e.* $n\lambda$) (**Figure Annex-I-1**).

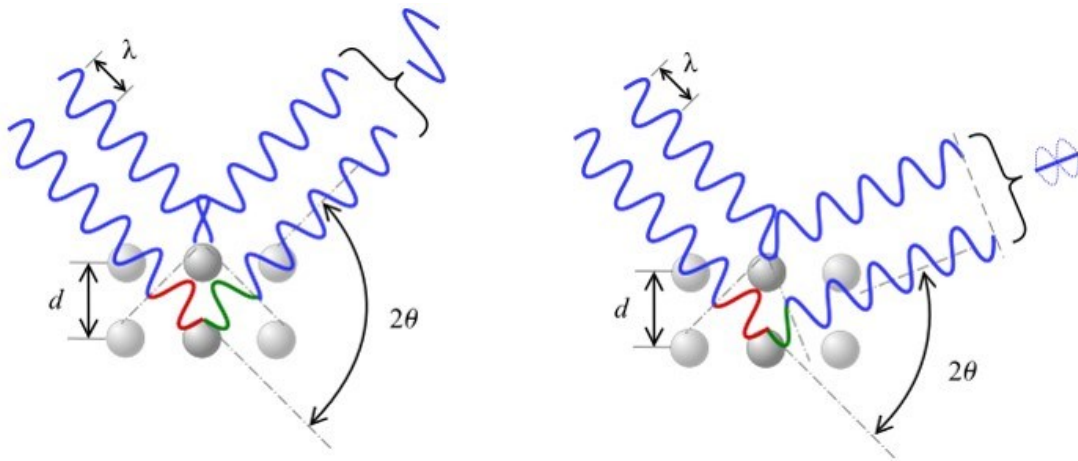


Figure Annex-I-1: Depiction of Bragg's Law. The incident radiation reflects off lattice points, with the path length difference equal to $2d\sin\theta$. If the extra distance travelled by the lower beam is equal to an integer number of wavelengths, constructive interference appears (left) and if not destructive interference occurs (right) adapted from ref. ¹⁸⁴

Even when the Bragg’s law is satisfied some reflections can’t be observed. This phenomenon, called systematic extinctions, is due to specific symmetries within the crystal. Crystals are solids in which the atoms are ordered and can be defined from basic building blocks, known as the unit cell, which continuously repeats in three dimensions. There are only 7 possible unit cell shapes (called crystal systems: triclinic, monoclinic, orthorhombic, tetragonal, rhombohedral, hexagonal and cubic) characterized by relations between a, b, c distances and α, β, γ angles. The distribution of nodes within the repeating units defines the type of lattice: Primitive (P), Body-centered (I), Face-centered (F) and Base-centered (A, B or C). Combining the 7 crystal systems with the 4 types of lattice, 14 Bravais lattices are obtained¹⁸⁵ (Figure Annex-I-2).

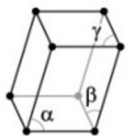
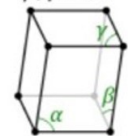
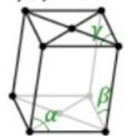
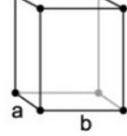
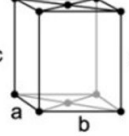
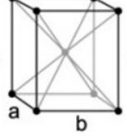
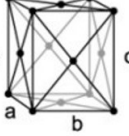
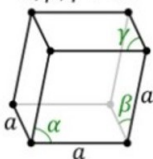
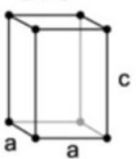
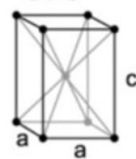
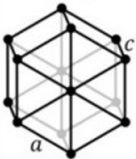
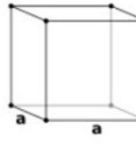
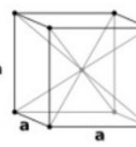
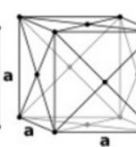
$\alpha, \beta, \gamma \neq 90^\circ$ 	$\alpha \neq 90^\circ$ $\beta, \gamma = 90^\circ$  Simple	$\alpha \neq 90^\circ$ $\beta, \gamma = 90^\circ$  Centered	$a \neq b \neq c$  Simple	$a \neq b \neq c$  Base Centered	$a \neq b \neq c$  Face Centered	$a \neq b \neq c$  Body Centered
Triclinic	Monoclinic		Orthorhombic			
$\alpha, \beta, \gamma \neq 90^\circ$ 	$a \neq c$  Simple	$a \neq c$  Body Centered	$a \neq c$ 	 Simple	 Body Centered	 Face Centered
Rhombohedral	Tetragonal		Hexagonal	Cubic (or isometric)		

Figure Annex-I-2: Combination between the 7 crystal systems with the 4 types of lattices leading to the 14 allowed Bravais lattices in three dimensions.

All non-translational symmetries in a unit cell are gathered in a point group. Only 32 crystallographic point groups are allowed, and when the 14 Bravais lattices are combined with the 32 internal crystal symmetries, 230 space groups (S.G) are defined. These 230 space groups are gathered in the International Tables of Crystallography¹⁸⁶ into which all the systematic extensions involved by the symmetries related to these space groups are listed.

i. Single crystal vs. powder

A single crystal is one single block where all the symmetry operations of the structure are valid for the whole block whereas a polycrystalline material consists of single crystals of very small sizes (usually of the order (sub)micrometer) and randomly oriented (when there is no preferred orientation). Due to this random orientation of the crystal in a powder, the corresponding XRD diagram will show Debye rings rather than Bragg spots for a single crystal. Indeed, to interpret the diffraction pattern of a powder sample we must consider only the magnitude of the momentum transfer (*i.e.* $|\vec{Q}| = 4\pi \sin \theta / \lambda$). Due to random orientation, the information of the vector properties of \vec{Q} has been lost. For single crystal diffraction the vector character of \vec{Q} remains. Therefore in a single-crystal diffraction experiment, the intensity of the spots is measured as a function of the Miller indices hkl whereas in a powder diffraction experiment, all the symmetry-equivalent reflections have the same d spacing and the individual intensities cannot be measured. As battery materials operate at the powder state, in this manuscript the main part of the diffraction experiments have been performed from powder samples. However, sometimes, the use of single crystal diffraction, providing much more informations about symmetries, is required. In that case we used a single crystal Bruker D8 Venture diffractometer equipped with a Photon 100 detector and a Molybdenum micro-source ($\lambda = 0.71073 \text{ \AA}$).

ii. Profile of diffraction lines, size vs. strain effects

Theoretically, in a perfect crystal studied with a perfect instrument, the diffraction patterns are Dirac functions with a null full width at half maximum (FWHM or $H = 0$). Experimentally, the profile of diffraction lines is given by the convolution product of the instrumental resolution function (non-ideal optics, wavelength dispersion, detector resolution...), $G(x)$, by the microstructural function of the sample (finite size and stacking imperfection), $F(x)$:

$$\Phi(x) = G(x) * F(x)$$

The instrumental resolution function which dictates the angular dependency of the FWHM is described by the Caglioti resolution function¹⁸⁷:

$$H^2 = U \tan^2 \theta + V \tan \theta + W$$

where H is the FWHM, U V and W are profile parameters inherent to the instrument. Typically, Silicon, LaB_6 or $\text{Na}_2\text{Ca}_3\text{Al}_2\text{F}_{14}$ (NAC) samples quasi perfectly crystallized are used to

extract these parameters which depend on the wavelength, the diameter of the capillary used, the focalization of the beam, the wavelengths distribution... In this manuscript, several diffractometers were used for diffraction experiments (*i.e.* high resolution D2B and high flux D20 for neutron diffraction at ILL, MSPD for Synchrotron X-ray diffraction at Alba and Panalytical X'pert³ equipped with a copper anticathode at the laboratory). **Figure Annex-I-3** shows the evolution of the FWHM in function of 2θ for all these instruments and **Table Annex-I-1** gathers the experimental conditions used for powder diffraction experiments.

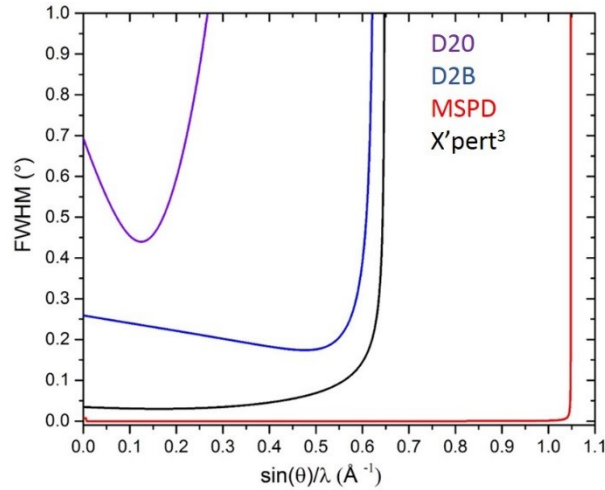


Figure Annex-I-3: Evolution of the FWHM in function of $\sin(\theta)/\lambda$ for the high flux D20 and the high resolution D2B neutron diffractometer @ ILL, the MSPD Synchrotron X-ray diffractometer @ ALBA and for the Panalytical X'pert³ laboratory X-ray diffractometer

Table Annex-I-1: experimental conditions used for diffraction (ND and XRD) experiments

diffractometer	D2B @ ILL	D20 @ ILL	MSPD @ ALBA	PANalytical X'pert3 @ ICMCB	Bruker D8 @ LRCS
Radiation	Neutrons	Neutrons	X-rays	X-rays	X-rays
Wavelength (Å)	1.5935	1.5935	0.9540	Cu, K α	Cu, K α
monochromator	Ge (115)	Ge (115)	Si (111)	/	/
Sample holder (inner diameter)	V cylinder ($\Phi=8\text{mm}$)	V cylinder ($\Phi=8\text{mm}$)	Capillary ($\Phi=0.5\text{ mm}$)	Capillary ($\Phi=0.3\text{ mm}$)	Flat sample ($\Phi=2\text{ cm}$)
reference	NAC	NAC	NAC and Si	Si	/
geometry	Debye-Scherrer	Debye-Scherrer	Debye-Scherrer	Debye-Scherrer	Debye-Scherrer
2θ range (°)	0 – 150°	0 – 150°	1 – 72°	10 – 90°	10 – 90°
2θ step (°)	0.05	0.05	0.006°	0.03	0.03
Counting time	12h	12h	5 min	15 h	15 h

The profiles of diffraction peaks are modelled by Voight-type functions defined by the convolution product Gaussian ($G(x)$) and Lorentzian ($L(x)$) components, $V(x)$. This convolution product can be approximated by the pseudo-Voight function:

$$V(x) = G(x) * L(x)$$

$$\text{With } x = \frac{(2\theta_i - 2\theta_{hkl})}{H_{hkl}}$$

$$pV(x) = (1 - \eta)G(x) + \eta L(x)$$

The diffracting sample also contributes to the broadening of diffraction lines through two ways: the sizes effects and/or the micro-strains effects. The size effect resulting in the finite size of coherent domains, being mainly the Lorentzian part of the broadening is expressed by the Scherrer's law¹⁸⁸:

$$\beta_L = \frac{k \lambda}{D \cos \theta}$$

where k , the Scherrer's constant, usually falls in the 0.8-1 range depending on the shape of particles, β_L is the integral breath (width of the rectangle whose area is equivalent to the one of diffraction peak) and D the diameter of the diffracting domain considered as spherical. The microstrains contribution being mainly the Gaussian component of peaks is governed by the Stokes-Wilson's law¹⁸⁹:

$$\beta_G = 4\varepsilon \tan \theta$$

where ε is the width of the microstrains' distribution ($\varepsilon = \Delta d/d$) generated by local defects such as stacking faults, dislocations, antiphase boundaries, vacancies... The difference in θ dependency for size and strain effects (illustrated at **Figure Annex-I-4**) allows their separation by drawing the so called Williamson-Hall plot¹⁹⁰ (*i.e.* $\beta_{\text{obs}} \cdot \cos \theta$ as function of $\sin \theta$, **Figure Annex-I-4**). In this manuscript we will mainly discuss about vanadyl-type defects and needles-like morphologies whose anisotropic character will generate an inhomogeneous line broadening (depending on the crystallographic directions). This peculiar case can be treated by the Williamson-Hall approach but the low degree of symmetry of the structures discussed in this manuscript (either triclinic either monoclinic) generates strong peaks overlaps (especially at high angles). Thus the extraction of the FWHM of peaks becomes challenging. Fortunately the FullProf suite provides phenomenological models being able to extract the microstructural parameters thanks to refinements by the Le Bail method^{137,138}.

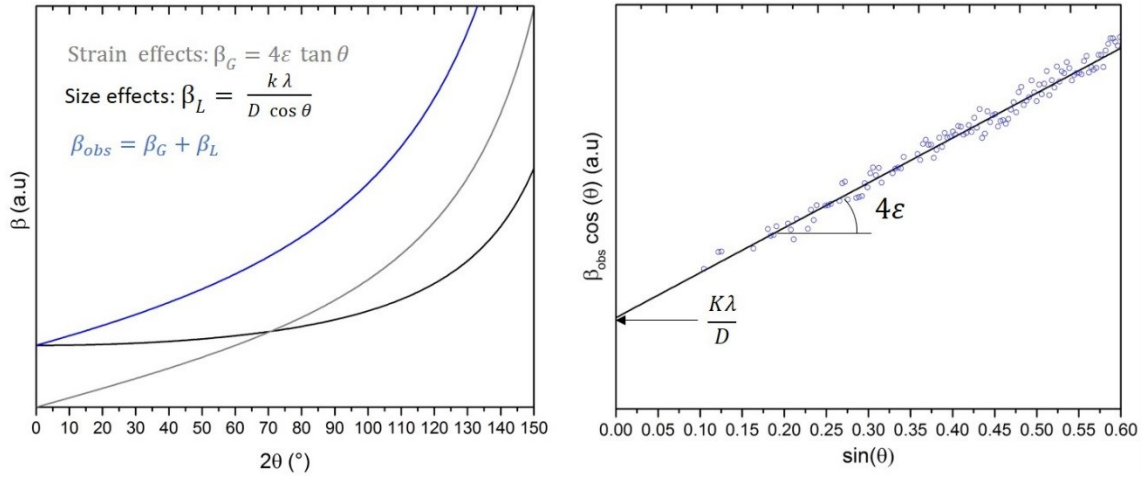


Figure Annex-I-4: Evolution of the integral breaths induced by size effects (black) or by strain effects (grey) and the observed one in function of 2ϑ (left). The Williamson-hall plot allows to separate the size and strain effects from the evolution in 2ϑ of the observed integral breath (right).

Le bail refinements consist in the fit of diffraction patterns considering the profile and the peaks positions without taking into account the atoms in the cell. It allows to obtain the cell parameters (peaks' positions), the space group (systematic extension), the best function describing the profile of peaks (microstructural parameters), the background (air scattering, incoherent scattering ...) and the zero shifts (inherent to the experimental setup). As this approach doesn't consider the elements present in the materials, the integrated intensities of peaks are arbitrary.

ii. Diffracted intensity, X-rays vs. Neutrons

The intensity of a diffraction peaks is proportional to the square of the module of the structural factor ($F(\vec{k})$).

For interaction between the crystal and X-rays the structural factor is defined as follows:

$$F(\vec{k}) = \sum_{j=1}^n f_j \exp(2i\pi \vec{k} \cdot \vec{r}_j)$$

and for the interaction with neutrons:

$$F(\vec{k}) = \sum_{j=1}^n b_j \exp(2i\pi \vec{k} \cdot \vec{r}_j)$$

where \vec{k} is the scattering vector, \vec{r}_j , the atomic position vector of the atom "j". The main difference between X-rays and neutrons thus resides in the f_j and b_j factors.

For X-ray diffraction, f_j , the atomic scattering factor (or form factor or scattering length) of the atom “j”, depends on the number of electrons gravitating around, θ for a given radiation (or $\sin \theta/\lambda$) and the temperature. At $T=0K$, for $\theta = 0$ the scattering amplitude is normally proportional to Z . The X-ray scattering factor (f^0) corresponds to the Fourier transform of the electron density distribution of an atom or ion, which is calculated from theoretical wave functions for free atoms but very often an approximation of f^0 is used:

$$f^0 = \sum_{j=1}^4 a_j \exp\left(\frac{-b_j \sin^2 \theta}{\lambda^2}\right) + c$$

The 9 coefficients a_j , b_j and c are tabulated in ref¹⁹¹. By this approach a precision of 10^{-6} is achieved for the form factors and only few coefficients have to be given for any atom or ion to model the whole $\sin\theta/\lambda$ range.

This expression is true at $T = 0K$ but there will be an additional weakening of the scattering power of the atoms by the so called Debye-Waller factor (B) which is due to thermal motions of atoms around their equilibrium positions. This exponential factor is also angle dependent and affects substantially the high angle reflections.

$$f_{T>0K} = f_{T=0K} \exp\left(\frac{-B \sin^2 \theta}{\lambda^2}\right)$$

where B is related to the mean displacement of a vibrating atom $\langle u \rangle$ by the Debye-Waller equation:

$$B = 8\pi^2 \langle u \rangle^2$$

As u is given in \AA , the unit for B must be \AA^2 . In most structures it suffices to assume the isotropic average displacement. At very high resolution with a sufficient variable to parameter ratio, anisotropic refinements of individual temperature factors may be justified. In that case, u is replaced by a 3x3 tensor u_{ij} .

For Neutron diffraction, b_j , the coherent diffusion length, depends also on the nature of the scattering atom and on the temperature (for that latter, in a similar way than X-ray) but is independent on θ (due to punctual nature of nuclei rather than the finite of electron cloud for X-ray). The real part depends on the neutron-nuclei interaction and can be either positive

(attractive interaction) or negative (repulsive interaction). According to Fermi's pseudo potential, the imaginary part represents the probability that neutron be absorb by the nuclei. The evolution of the coherent diffusion length of neutrons¹⁹² and X-rays¹⁹¹ for main elements of periodic table in function of Z and $\sin(\theta)/\lambda$ are depicted at the **Figure Annex-I-5**.

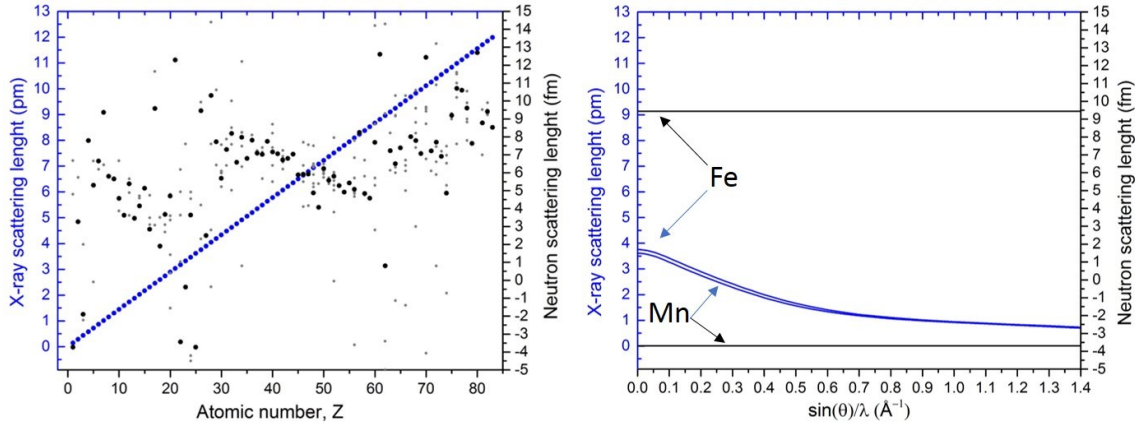


Figure Annex-I-5: Evolution of the scattering lengths for X-rays (blue) and Neutrons (grey for all isotopes and black in average) diffraction in function of the atomic number (left) and in function of $\sin(\theta)/\lambda$ for Iron and Manganese (right) taken from ref. ¹⁹¹ and ¹⁹².

Diffraction experiments using large scale facilities were performed thanks to the technical support and the precious help from Emmanuelle Suard for Neutron diffraction at ILL (Grenoble) and François Fauth for Synchrotron X-rays powder diffraction at ALBA (Barcelona). ND and XRD present complementary features and both techniques are often required to fully describe the crystal structure and the microstructure of the materials investigated. Indeed, as X-rays are scattered by the electronic nuclei around atoms, their diffracted intensity is proportional to Z and thus they aren't very sensitive to the lighter elements of the periodic table. This linear evolution with Z doesn't allow X-rays to distinguish neighboring elements (*i.e.* having a close atomic number). Moreover, the decrease of the diffracted intensity for high θ induces a loss of information compared with neutron diffraction. However, the resolution for X-ray detectors (see **Figure Annex-I-3**) and the high flux of photons provided by synchrotron sources give better resolution and signal/noise ratio compare to neutron diffraction experiments.

iii. Rietveld refinement

Rietveld refinement aims to minimize the residual intensity between the experimental (y_i) and the simulated intensity (y_{ci}) through the following function ¹⁹³:

$$S_y = \sum_i \frac{(y_i - y_{ci})^2}{y_i}$$

Where S_y is the variance y_{ci} is computed thanks to the fundamental equation of Rietveld refinement:

$$y_{ci}(2\theta_i) = \sum_{phases} (S_{phase} \sum_{hkl} (K_{hkl} |F_{hkl}|^{2\Phi_{hkl}}(2\theta_i - 2\theta_{hkl}))) + b_i$$

where the first sum runs over all phases present in the diffraction pattern and the inner sum runs over all hkl of each phase. The scale factor S_{phase} is proportional to the weight fraction of each phase. K_{hkl} is the product of various correction factors (depending on multiplicity of reflections, absorption correction, Lorentz factor and preferred orientation), F_{hkl} is the structure factor, Φ_{hkl} the profile function and b_i the background contribution.

iii. Agreement factors: “how good is good enough?”¹⁹⁴

Numerous agreement factors are calculated by Fullprof¹⁹³. Rietveld refinement, based on the least-square algorithm, aims to minimizing the variance. From the theory of statistics, the expected value of variance should be $N-P+C$ with N is the number of data points, P is the number of fitted parameters, and C is the number of constraints. The quality of the fit is given by the χ^2 parameter:

$$\chi^2 = \frac{\sum_i w_i (y_i - y_{ci})^2}{N - P + C}$$

For a perfect fit, the only source of difference between y_i and y_{ci} is the statistical noise, the χ^2 parameter should be close to 1 and stickily superior to 1. Values of $\chi^2 < 1$ mean that the model fits the noise due to the refinement of too many parameters compared to the number of experimental information. Even if χ^2 is a good indicator, more appropriated factors exist to estimate the quality of a fit. Among them, R_p (profile R-factor) measures the agreement between the calculated and observed patterns:

$$R_p = \frac{\sum_i |y_i - y_{ci}|}{\sum_i y_i}$$

Nevertheless this factor gives more weight to the strong Bragg intensities. The way to solve this problem is to introduce a weighting factor w_i and define the weighted profile R-factor (R_{wp}):

$$R_{wp} = \sqrt{\frac{\sum_i w_i (y_i - y_{ci})^2}{\sum_i w_i y_i^2}}$$

In order to compare refinements from different number of parameters, different powder patterns, or different samples... we have to use the expected weighted profile R-factor (R_{exp}):

$$R_{exp} = \sqrt{\frac{N - P + C}{\sum_i w_i y_i^2}}$$

This factor is called expected because $N-P+C$ is actually the expected value of the variance. All the R-factors described above are based on the difference between the observed and calculated point intensities as recorded in the powder diffraction pattern. Nevertheless, Rietveld refinement doesn't give information about background and its contribution has to be subtracted to the observed intensity in order to give relevant R-factors. Indeed, a powder diffraction pattern with high background will generate artificially low R-factors indicating that the background is well fitted but saying little about how well the crystal structure itself is fitted. Therefore the background corrected R-factors are the correct indicators of the correct fit of Bragg intensities. The Bragg R-factor (R_{Bragg}) is similar to single crystal R-factor based on integrated Bragg intensities of individual reflections hkl obtained by integrating the profile of each reflection hkl after background subtraction.

$$R_{Bragg} = \frac{\sum_{hkl} |I_{hkl}(obs) - I_{hkl}(cal)|}{\sum_{hkl} I_{hkl}(obs)}$$

As it's difficult to estimate the good values of R-factors, to my opinion, the best one is a visual validation of the residual which must always be performed. This inspection allows to know how good is the refinement and also what is going wrong with it. Furthermore, a check on the fitted parameters values (especially profile parameters and Debye-Waller factors) and uncertainties is essential to determine the plausibility of a fit. One has to always make sure that the fitted parameters are consistent with basic crystallographic and chemical principles, and generate a crystal structure which makes sense from the point of view of interatomic distances and coordination polyhedra, as checked for example, by bond-valence sums.

Annex-I-2 From Bond Valence Sum to Bond Valence Energy Landscape

The concept of bond valence is built on the distribution of bond lengths and on the chemical nature of the atoms around a given “central” one. The valence, s_{i-j} of a bond between two atoms i and j is defined by the empirical following expression:

$$s_{i-j} = \exp \left[\frac{R_0 - R}{b} \right]$$

where R is the bond length and b can be considered, to a good approximation, as a constant (*i.e.* $b=0.37 \text{ \AA}$) that doesn't depend on the crystal structure. R_0 is a reference cation-anion distance tabulated in ref.¹²⁷. It has been found empirically that, if a crystal is stable, the bond valence sum BVS_i of each atom i where j runs over all nearest neighbors will be very close to the formal charge of that atom:

$$BVS_i = \sum_j s_{i-j}$$

This approach therefore provides a powerful method for the prediction of the oxidation state of an element and for the differentiation between species quasi-identical from a diffraction point a view. Furthermore, dividing the unit cell into a fine 3D grid and calculating the bond valence sum of a species at each node of this grid (bond valence map), it is possible to localize the most probable sites of some atoms without any experimental information about its position. From this theory, Adams built his own¹⁷³, introducing a penalty term (p_{i-j}) to the bond valence mismatch (difference between bond valence sum and real oxidation state V_i of the specie i):

$$\Delta V_i = \left| \sum_j s_{i-j} - V_i \right| + \sum_j p_{i-j}$$

This penalty function was introduced to discriminate against sites that achieve a matching (*i.e.* ΔV_i inferior to a certain threshold) by strongly asymmetric coordination and to exclude sites close to other cations. Latter, a correlation between this threshold and an energy required for activating the cation migration were added to the model. At a given threshold (or energy) an iso-surface enclosing a volume in which the cations can be located, is obtained. The diffusion pathways thus correspond to a percolating regions, where the bond valence mismatch of the mobile species is below a certain threshold. The value of this threshold significantly influences the volume and the topology of the diffusion pathways in a given

structure. Unfortunately, there is no way to determine the good value of this critical parameter. Thus, in this manuscript, in order to compare the cationic diffusion paths between structures, the energy has been fixed to 1.6eV above the minimum energy. Another limitation of this technique is that it considers the cation diffusion as a continuous phenomenon within the percolated isosurfaces whereas in many cases this diffusion occurs according a discrete mechanism (*i.e.* cation hopping between sites). Thus it's required to consolidate the BVEL results with other techniques such as molecular dynamic (MD) or maximum entropy method (MEM). The **Figure Annex-I-6** compares the results for Na⁺ diffusion obtained from BVEL, MD and MEM in the Nasicon framework.¹⁹⁵

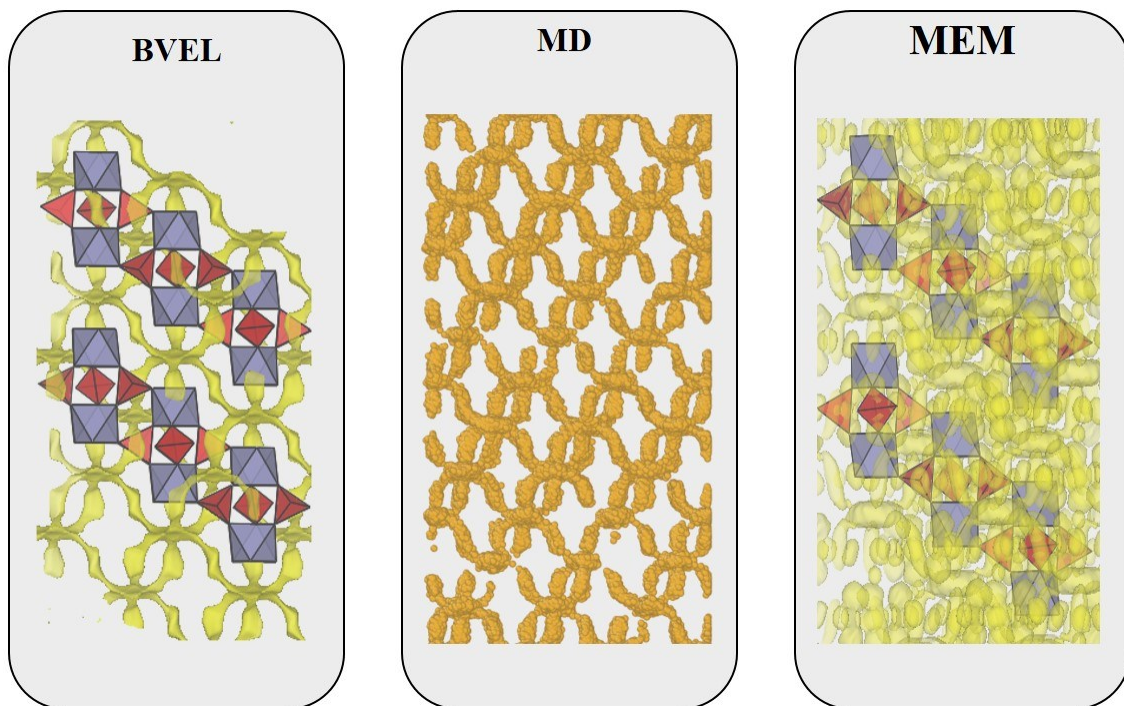


Figure Annex-I-6: Comparison between diffusion paths for Na⁺ cations in the Nasicon framework obtained from Bond Valence Energy Landscape, Molecular Dynamic and Maximum Entropy Method showing the good agreement between the results provided by these techniques, adapted from ref. ¹⁹⁵

Annex-I-3 Magnetic measurements

A vibrating sample magnetometer (VSM) operates on the basis of the Faraday's Law of induction¹⁹⁶, which predicts that the variation of a magnetic field will produce an electric field. This electric field can be measured and provides information on the magnetic behavior of the materials studied. A magnetic sample placed in a constant magnetic field at 78K (*i.e.* liquid nitrogen) will be magnetized by aligning magnetic domains and/or individual magnetic spins. The field and the magnetization are proportional to the applied field strength (*i.e.* 1000 Oe, in our case). The magnetic dipole moment of the sample will generate a magnetic field around it, called the magnetic stray field. Then, a piezoelectric element vibrates carrying with him the sample inducing some magnetic stray field changes as a function of time. The alternating magnetic field generates an electric field in the coil according to Faraday's Law of induction and the current is proportional to the magnetization of the sample. The temperature is then increased in regular increments or continuously (in our case 10K/min until 500K) and magnetization measured at each point. The data collected for a known mass of sample in a field, H , gives the molar magnetization, M_m , which can be converted to the molar magnetic susceptibility, χ_m .

$$\chi_m = \frac{dM_m}{dH} \cong \frac{M_m}{H}$$

The sample holder used was a sealed aluminum capsule in which the powder was immobilized thanks to a plug of glass fibers. The measured magnetic susceptibility was corrected from that of the sample holder (aluminum and glass fiber) based on a blank experiment, as well as from the diamagnetic contribution of materials considering the diamagnetic susceptibility of each constituting ion¹⁹⁷, in order to determine the paramagnetic susceptibility according to:

$$\chi_m = \chi_{para} = \chi_{mes} - \chi_{dia} - \chi_{blank}$$

The linear regions of the temperature-dependent (*i.e.* in paramagnetic domain) data follows the Curie-Weiss law:

$$\chi_m = \frac{C_m}{T - \theta} \cong \frac{C_m}{T}$$

where C_m is the molar Curie constant and θ is the Weiss temperature which become negligible in paramagnetic domain (*i.e.* typically $T > 100K$). The experimental value allows to obtain the effective magnetic moment, μ_{eff} :

$$\mu_{eff}^2 = \frac{3k_B C_m}{N_A \mu_B^2}$$

where k_B is the Boltzmann constant, N_A is Avogadro's constant and μ_B is the Bohr magneton. The effective magnetic moment is directly related to the electronic configuration of the paramagnetic cations as follow:

$$\mu_{eff} = g\sqrt{S(S+1)}$$

where g is the Landé factor ($g = 2$) and S , the spin quantum number of the magnetic cations. For transition metal ions, in the paramagnetic domain, the spin-orbit coupling can be assumed to be negligible. In this manuscript we will only discuss about oxidation state of vanadium cations: the electronic spins of V^{2+} (t^2g^3), V^{3+} (t^2g^2), V^{4+} (t^2g^1) and V^{5+} (t^2g^0) are $3/2$, 1 , $1/2$ and 0 respectively and thus their corresponding theoretical Curie's constants are 1.875 , 1 , 0.375 and 0 respectively.

Annex-I-4 Solid state MAS NMR spectroscopy

iv. NMR principle

The nucleus consists of elementary particles (*i.e.* neutrons and protons). As electrons, the spin of a nucleus can be described using a quantum number, I (and m for the spin in a magnetic field). The value of I depends on the parity of A and Z , indeed, nuclei with even numbers of protons and neutrons haven't spin and all the other atoms with odd numbers have a non-zero spin. All species with a non-zero nuclear spin have a magnetic moment, μ ($\mu = \gamma I$ with γ is the gyromagnetic ratio, specific to each nucleus). The magnetic moment of the spin can be conceptualized by be arrows randomly oriented in the absence of external magnetic field. During the NMR experiment, a magnetic field (B_0) is applied, these arrows react as little magnet and are now aligned parallel (low energy, $m = -I$) or anti-parallel (high energy, $m = +I$) to the field that leads to a splitting of energy levels (Zeeman effects, **Figure Annex-I-7** depicted the case where $I = \frac{1}{2}$).

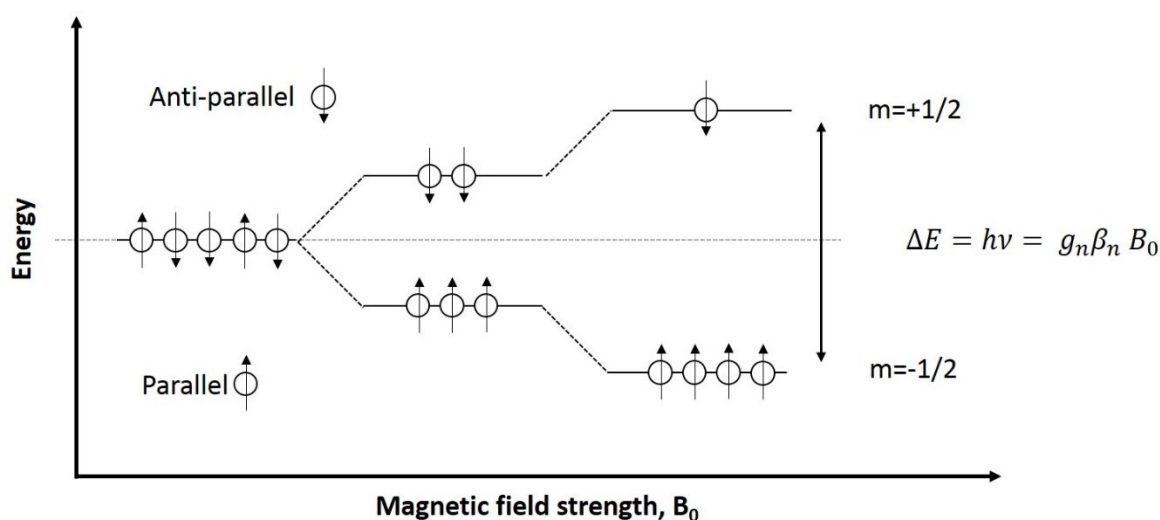


Figure Annex-I-7: Schematic representation of the Zeeman effect.

The number of energy levels available is thus equal to $2I+1$. During NMR experiments some spin flip of the magnets occurs which require exact quanta of energy (ΔE):

$$\Delta E = g_n \beta_n B_0 = \gamma \hbar B_0$$

$$\nu = \frac{\Delta E}{h} = \frac{\gamma B_0}{2\pi}$$

These exact amounts of energy thus depends of the nuclear magneton, β_n , (or Planck constant, \hbar) and the Landé factor, g_n , (or gyromagnetic factor, γ) intrinsic to each nucleus. This energy is generated by applying a secondary alternative magnetic field (B_1) perpendicularly to B_0 with a frequency ν (Larmor frequency) during a short time which will tend to equilibrate the spins' population (parallel and anti-parallel) and move the macroscopic magnetization away from its equilibrium positions. The length of the B_1 pulse (τ), tilting the magnetization with an angle, $\alpha = \gamma B_1 \tau$, is about few μs . The NMR signal observed following an initial excitation pulse induced by B_1 decays with time due to both spin lattice relaxation process (T1-type, the time taken for the spins to return to the B_0 direction after a pulse is applied) and spin-spin relaxation (T2-type, the time constant of the signal decay). This decreasing of magnetization is called free induction decay (FID) and the Fourier Transform of the FID gives a NMR spectrum defined in the frequency space (Hz) often compare with a reference frequency to obtain a signal expressed in ppm.

i. The NMR experiments

As the FID must be measured by the coil which apply the B_1 field, a dead time between the end of excitation and the beginning of detection has to be used leading to a loss of information. Nevertheless, peculiar sequences can be applied to counteract this setup constraint. Indeed, Spin echo (or Hahn echo, **Figure Annex-I-8**) refocuses the spin magnetization applying an alternation between B_1 pulse (during τ and then 2τ) and relaxation (during t)¹⁹⁸.

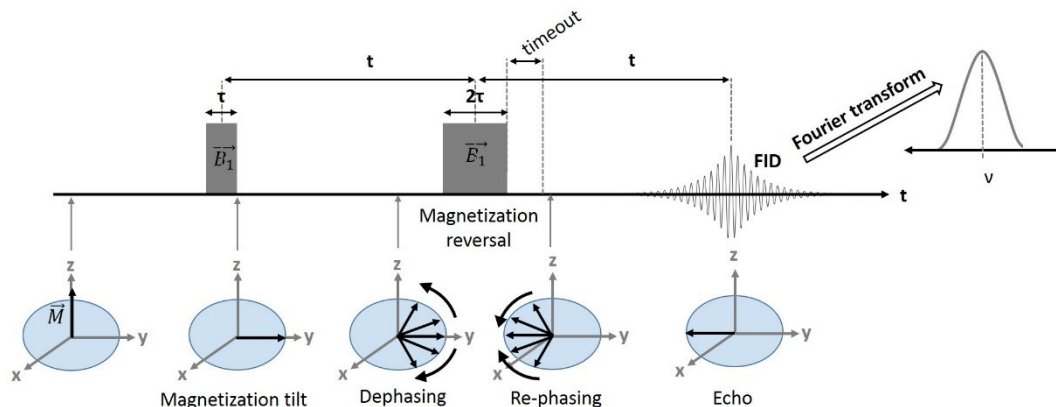


Figure Annex-I-8: Principle of the Hahn echo MAS NMR sequence

The inhomogeneous dephasing can be removed by applying after the excitation pulse ($\pi/2$ -pulse) a 180° inversion pulse (*i.e.* π -pulse) that inverts the magnetization vectors. If the inversion pulse is applied after a period t of dephasing, the inhomogeneous evolution will

rephase to form an echo at time $2t$. In simple cases, the intensity of the echo relative to the initial signal is given by e^{-2t/T_2} where T_2 is the time constant for spin-spin relaxation.

A typical solid-state NMR spectrum as compared to a liquid-state NMR one consist of broad and featureless lines (**Figure Annex-I-9**).

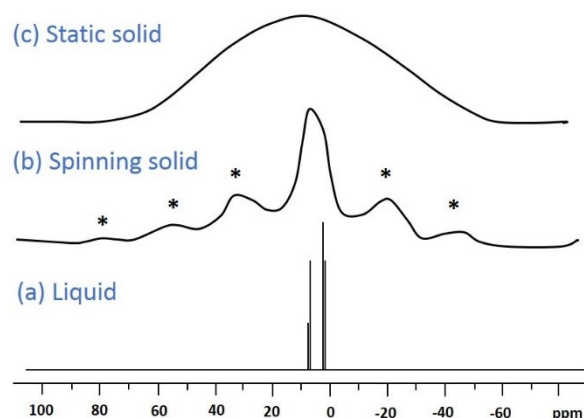


Figure Annex-I-9: ^1H NMR spectra of the same organic compound acquired at liquid state (a) or solid state (b, c) and in spinning (b) with their spinning side bands highlighted as * or static (c) mode.

This is due to many concurrent strong interactions of a nuclear spins that are dependent on spins' mutual orientation and their orientation with respect to the external magnetic field such as: dipole-dipole interactions, chemical shift anisotropy (CSA), dipolar ($I=1/2$) and quadrupolar ($I>1/2$) coupling. In fact, these anisotropic orientation-dependent interactions are also present in liquid-state spectra but, in solution, they are averaged due to rapid random molecular motions and reorientations that lead to narrow well-defined lines. For solid state matter, the chemical shift anisotropy and the dipolar coupling significantly broaden the lineshape (compare to liquid). By inspecting the Hamiltonians of the dipolar interaction, the " $3 \cos \theta - 1$ " term appears. If this term was set to zero (*i.e.* $\theta=54.44^\circ$ vs. B_0 field, the magic angle) the dipolar coupling would go to zero. Moreover fast rotation around this angle avoids the chemical shift anisotropy and thus would lead to a purely isotropic lineshapes. Furthermore, the rotation of the sample during FID acquisition leads to the appearance of spinning side bands (highlighted as * in **Figure Annex-I-9**) which can be conceptualized as measurement artefacts located in each side of the isotropic peak at a frequency corresponding to the rotation speed of the sample.

The NMR experiments presented in this manuscript have been performed by Dr Tahya Bamine-Abdessalam and thanks to the precious advises from Dany Carlier and Michel Ménétrier. The **Table Annex-I-2** summarizes the NMR experimental setup used in this work.

Table Annex-I-2: experimental conditions used for 1D MAS NMR experiments.

Probed nuclei	^1H	^7Li	^{19}F	^{31}P
Nuclear Spin	$\frac{1}{2}$	$\frac{3}{2}$	$\frac{1}{2}$	$\frac{1}{2}$
Spectrometer	Bruker Avance	Bruker Avance	Bruker Avance III	Bruker Avance III
Probe	Bruker 2.5 MAS	Bruker 2.5 MAS	Bruker 2.5 MAS	Bruker 2.5 MAS
Spinning frequency	30kHz	30kHz	30kHz	30kHz
0 ppm reference	H_2O	LiCl	CFCl_3	H_3PO_4
Temperature (K)	298	298	298	298
B_0 strength (Tesla)	7	7	2.35	2.35
Sequence type	Hahn echo	Hahn echo	Hahn echo	Hahn echo
B_1 pulse (ν , τ)	300 MHz, 1.2 μs	116 MHz, 1.2 μs	93.4 MHz, 1 μs	40.6 MHz, 1.2 μs
Recycle delay	1s	100s	1s	1s

v. 2D NMR

In one-dimensional NMR experiment, the signal is recorded as a function of one time variable and then Fourier transformed to give a spectrum which is a function of one frequency variable. In two-dimensional NMR the signal is recorded as a function of two time variables, t_1 and t_2 , and the resulting data Fourier transformed twice to yield a spectrum which is a function of two frequency variables¹⁹⁹. First, the sample is excited by a B_1 pulse (preparation time). The resulting magnetization is allowed to evolve during t_1 (evolution time). Then another period follows, called the mixing time, which consists of a further pulse (or pulses). After the mixing period the signal is recorded as a function of the second time variable, t_2 . The signal is not recorded during the evolution time (*i.e.* t_1), but only during the time t_2 and the principle of 2D NMR is to vary t_1 by Δt_1 increments from one sequence to another and to measure the impact of t_1 length on the FID (measured during t_2). The exact nature of the preparation and mixing periods determines the kind of experiment COSY, EXSY, NOEXSY ... and the information contain in a spectrum. In this manuscript 2D EXSY-RFDR ^7Li NMR experiments were carried out in similar conditions than those described in ref ¹⁹ The RFDR sequence corresponds to a train of π -pulses of duration, τ_p , applied during the mixing time, τ_m , and every rotor period, τ_R .

ii. Interpretation of NMR spectra of paramagnetic materials

In paramagnetic compounds, such as materials discussed in this manuscript, the hyperfine interaction governs the NMR signature¹⁴³. This coupling is very sensitive to the interaction between nuclei and lone electrons and leads to the shift and the broadening of NMR signals. The Hamiltonian describing the hyperfine interaction depends on a term called Fermi contact coupling which is due to the presence of lone electrons at the probed atom site. The shift of NMR signal is thus dictated by the Fermi contact which depends, among other, on the spin density around the nucleus probed and the magnetic susceptibility of the sample. DFT calculation is thus essential for in-depth understanding of the NMR signature, as it allows to get insight into the localization of the electrons around probed atoms through the rebuilding of 3D spin density maps needed to elucidate the spin transfer mechanisms between the orbitals of the paramagnetic atoms and those of the nucleus probed. In this manuscript, DFT calculations have been performed by Tahya Bamine who defended her PhD in 2017 at the university de Bordeaux supervised by Dr Michel Ménétrier and Dr Dany Carlier. More details about calculations are provided in refs ²¹ and ¹²⁸.

Annex-I-5 Vibration Spectroscopy, IR vs. Raman

Infra-Red (IR) absorption and Raman scattering are related and complementary vibrational spectroscopies for characterizing matter. Matter is investigated through its interaction with an electromagnetic radiation (especially with the electric part) usually defined by its wavenumber (cm^{-1}). Due to the energy range of vibrations, most spectra are recorded in the mid-infrared region, from 400 to 4000 cm^{-1} (*i.e.* from 50 meV to 500 meV). Depending on the crystal symmetry, some vibrations can be IR or Raman active, that's why these techniques are complementary. The factors that determine whether a vibration can be detected by Raman or IR are called selection rules²⁰⁰. An IR active vibration must cause a change in the dipole moment whereas a Raman active vibration must involve a change of polarizability. In both cases, the intensity of the corresponding signal is proportional to the amplitude of the variations. In other terms, IR probes the separation between positive and negative charge during vibrational motion (basically the ionic character of a bond) whereas Raman probes the tendency of electron's cloud to be distorted from its equilibrium shape by an external electric field (basically the covalent character of a bond). If a bond is strongly polarized, a small change in its length such as that occurs during a vibration, will have only a small additional effect on polarization. Vibrations involving strongly polar bonds (O-H bond, for instance) produce usually weak Raman signals but strong IR bands due to the large dipole moment change during the vibrational motion.

The vibrational spectroscopy experiments were carried at the Institute of Molecular Sciences (Molecular Spectroscopy Group) under the technical direction and the valuable advices of Dr Lydie Bourgeois. In this manuscript, diffuse reflectance infrared measurements were performed in the range of 400–4000 cm^{-1} (mid-IR) using a Nicolet 6700 Fourier Transform spectrometer (Thermo Scientific) equipped with a DTGS detector and a diffuse reflectance accessory. The samples were finely ground in a mortar with dried KBr, the mass ratio between active material and KBr being approximately 1:50. Finally, reflectance spectra were treated with the Kubelka-Munk law, which converts the reflectance to a signal proportional to the absorption coefficient. Raman scattering measurements were performed with a Horiba Jobin Yvon Labram HR-800 micro-spectrometer. Spectra were recorded with a 514.5 nm excitation wavelength of an Ar⁺ laser, with a power adjusted to ca. 50 μW in order to avoid any degradation of the sample. No specific sample preparation was needed.

Annex-I-6 X-ray absorption spectroscopy

X-ray Absorption Spectroscopy (XAS) is a site selective and a local probe technique and is well suited for the characterization of not only crystals but also materials that possess or a short-range translational order. It is based on the absorption: when a sample is exposed to X-rays, it will absorb part of the incoming photon beams. The absorption coefficient μ is strongly depending on both the atomic number Z and the incident energy E . In the hard X-rays regimes (3–50 KeV), the absorption coefficient $\mu(E)$ is mainly generated by the photoelectric effect.

Following the Fermi's golden rule, the incident X-ray photon can promote a core atomic electron to the final state close to the Fermi level, by creating an excited state with a core hole. The so generated photoelectron will be ejected in the continuum. This electronic transition must obey to the dipole selection rules²⁰⁰, $\Delta\ell = \pm 1$, $\Delta j = \pm 1$, $\Delta s = 0$, with the primary transition being from a core s orbital to an empty p orbital (K edge for a $1s$ electron, L1 for a $2s$ electron, L2,3 for a $2p$ electron, etc.).

Depending on the kinetic energy of the photoelectron, two different regions of the XAS spectrum can be distinguished: the X-ray Absorption Near Edge Structure (XANES) region close to the absorption edge and the Extended X-ray Absorption Fine Structure (EXAFS) region for energy above the edge position (Figure **Annex-I-10**). The XANES part provides details on the local geometry, the electronic structure and the oxidation state of the absorbing element. On the other hand, the analysis of the EXAFS region will give access to the local structural distribution of the nearest-neighboring atoms around the absorber, *i.e.* the coordination number, the distances and the fluctuations of the bonds.

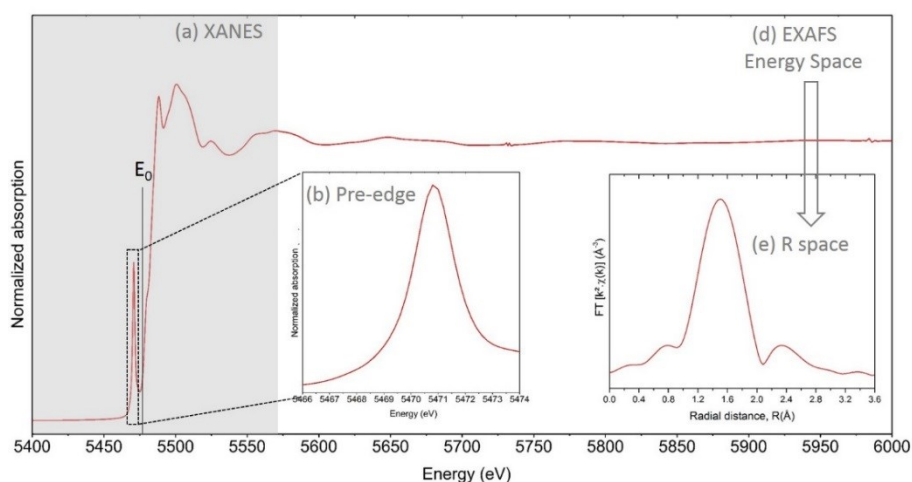


Figure Annex-I-10: (a) XANES region of the V K-edge XAS spectrum of a vanadyl phosphate compound (b) zoom on the pre-edge region. The EXAFS part in the energy space (d) the magnitude of the Fourier transform of the k^2 -weighted EXAFS oscillations in the R space (e).

The V K-edge XAS spectrum of a vanadyl phosphate compound is shown at the **Figure Annex-I-10**. Typically, the absorption threshold E_0 associated with the 1s to 4p transition is taken as the inflection point of the rising V K main edge and it is an indicator of the V oxidation state. In fact, the position of the main edge is shifted at higher energy for higher oxidation state, as shown in **Annex-I-11**. Moreover, the value of E_0 is also related to the ionic-covalency degree of bond formed by the absorbing atom with its ligands, with the edge shifting to higher energy with increasing ionicity.¹⁴⁵ In our case, a pre-peak feature below the main edge energy is observed. The presence of this feature can have different explanations, as already reported in V oxides¹²⁹ XAS studies. For transition metals a pre-edge feature is observed corresponding to the theoretically forbidden 1s \rightarrow 3d transition ($\Delta l = 2$) caused by mixing with 4p orbitals¹²⁹. For a centro-symmetric undistorted octahedra, no 4p-3d orbital mixing occurs and the pre-edge feature is not observed, whereas for distorted octahedra the intensity of this feature increases with increasing distortion of the local environment around absorbing element. The tetrahedral environment will have the strongest intensity pre-edge feature as the coordination causes a strong 3d-4p orbital hybridization.

If we consider the shape of the absorption edge, it reflects the empty density of states. For this reason, a quantitative analysis of the XANES region needs careful DFT calculations. In order to get information from XANES spectra without such heavy computations, it is necessary to compare them with relevant references. The **Figure Annex-I-11** shows the V-K edge XANES spectra of Tavorite-type materials used as references: $\text{Li}_2\text{V}^{\text{II}}\text{PO}_4\text{F}$, $\text{LiV}^{\text{III}}\text{PO}_4\text{F}$, $\text{LiV}^{\text{IV}}\text{PO}_4\text{O}$ and $\text{V}^{\text{V}}\text{PO}_4\text{O}$.

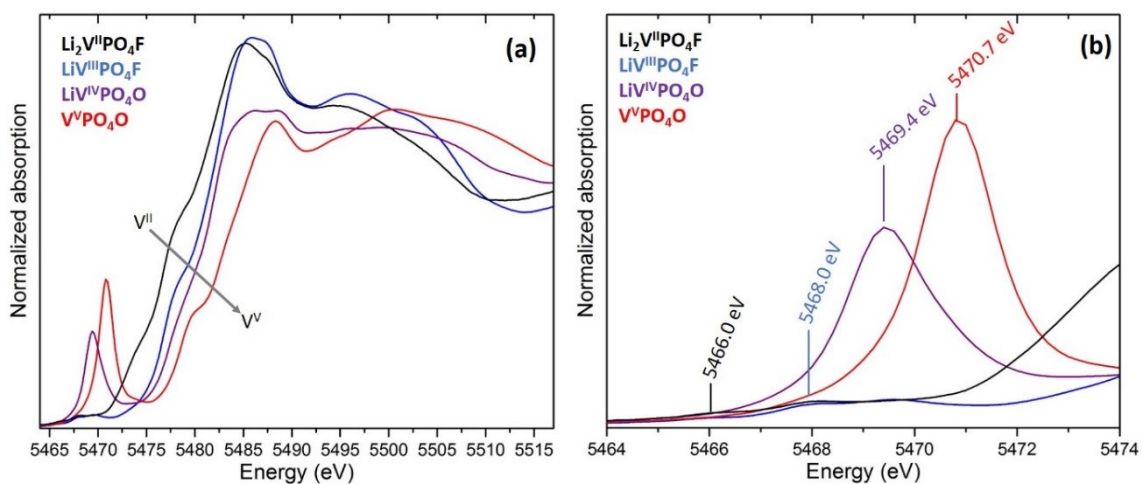


Figure Annex-I-11: (a) V K-edge XANES spectra of several Tavorite-type references: $\text{Li}_2\text{V}^{\text{II}}\text{PO}_4\text{F}$ (black line), $\text{LiV}^{\text{III}}\text{PO}_4\text{F}$ (blue line), $\text{LiV}^{\text{IV}}\text{PO}_4\text{O}$ (purple line) and $\text{V}^{\text{V}}\text{PO}_4\text{O}$ (red line). (b) The enlargement of the pre-edge region with the typical energy position of each contribution.

All along this manuscript we will mainly discuss about vanadyl-type (*i.e.* $V^{4+}=O$) defects or activation of V^{2+}/V^{3+} , V^{3+}/V^{4+} , $V^{3+}/V^{4+}=O$ and $V^{4+}=O/V^{5+}=O$ redox couples during battery operation. The covalent vanadyl bond observed in $LiV^{IV}PO_4O$ (*i.e.* $V^{4+}=O$ at 1.64 Å) and V^VPO_4O (*i.e.* $V^{5+}=O$ at 1.59 Å) leads to a strong pre-edge contribution respectively at 5469.4 eV and 5470.7 eV which are typical for $V^{4+}=O$ and $V^{5+}=O$ state. The pre-edge features observed for $Li_2V^{II}PO_4F$ and $LiV^{III}PO_4F$ are weaker due to the lower distortion of the vanadium environment observed in these structures. Indeed, tiny peaks are observed in the pre-edge region respectively at 5466.0 and 5468.0 eV respectively. Moreover, the spectrum of $LiVPO_4F$ presents an additional tiny contribution at 5469.7 eV (close to the typical signature of $V^{4+}=O$) due to the presence of a weak amount fluorine substituted by oxygen leading to the local formation of $V^{4+}=O$ vanadyl-type defects for the charge compensation. These pre-edge contributions have been used as signatures of the activation of the corresponding redox couple and the distortion of the environments around vanadium.

When the kinetic energy of the ejected photoelectron is great enough to escape to the bound state, the photoelectron can be modelled as a plane wave propagating in the medium and with wave-number k , corresponding to:

$$k = \sqrt{\frac{2m(E - E_0)}{h^2}}$$

where E_0 is the absorption edge, m is the electron mass and h is the Planck constant.

When other atoms are located in the vicinity of the absorber (the central atom), the photoelectron is scattered by the neighbours. The interference between the out-going and the back-scattered waves is a function of the energy of the X-ray beam. Therefore, the modulations in the absorption coefficient $\mu(E)$ are expected to vary periodically as a function of the energy. The total absorption coefficient $\mu(E)$ can be expressed as the isolated atomic absorption $\mu_0(E)$, modulated by a correction factor $\chi(E)$, the oscillation, which is also defined as the EXAFS signal:

$$\chi(E) = \frac{\mu(E) - \mu_0(E)}{\Delta\mu_0(E_0)}$$

where the denominator $\Delta\mu_0(E_0)$ is the atomic absorption evaluated at the edge energy E_0 . $\chi(k)$ can be considered as the fractional change in absorption coefficient induced by the presence

of neighboring atoms. The EXAFS oscillations contain important information on the local atomic distribution around the absorber atom. This phenomenon is a kind of “*in situ* electron diffraction” in which the absorbing atom is the photoelectron source, without any requirement on the crystallinity. The EXAFS oscillations are described and modelled according by the following equation¹⁴⁶ :

$$\chi(k) = S_0^2 \sum_j \frac{N_j f_j(k) e^{-2k^2 \sigma_j^2} e^{-2R_j/\lambda}}{k R_j^2} \sin(2kR_j + \delta_j(k))$$

where j represents the individual coordination shell of identical atoms at the same distance from the absorber, $f(k)$ and $\delta(k)$ are scattering amplitude and phase-shift respectively, S_0^2 is the amplitude of the reduction factor (due to the passive electrons), N is the number of neighboring atoms, R is the distance between the absorber and the neighboring atom, and σ^2 is the mean-square displacements in the distance R representing the intrinsic disorder. The EXAFS equation allows us to determine N , R , and σ^2 knowing the scattering amplitude $f(k)$ and phase-shift $\delta(k)$. Furthermore, since the scattering factor $f(k)$ depends on the atomic number Z of the neighboring atom, EXAFS is also sensitive to the atomic species of the neighboring atom. To amplify the oscillations at high k , $\chi(k)$ is often weighted by a power of k typically k^2 or k^3 . The different frequencies contributions in the oscillations in $\chi(k)$ correspond to different near-neighbor coordination shells. Fourier transformation is used to decompose a frequency-space signal into its different constituent frequencies, in order to move from the k -space to the R -space. Since the Fourier transform operation is defined in the infinite k -range, we have to introduce a window function $W(k)$ to extend the EXAFS signal, which is defined in a finite k -range.

$$FT(R) = \frac{1}{\sqrt{2\pi}} \int_{-\infty}^{+\infty} k^n \chi(k) e^{2ikR} W(k) dk$$

Using the appropriate softwares calculating the scattering amplitudes and phases the EXAFS oscillations can be fitted in order to extract N , R and σ^2 . Nevertheless, the number of independent points is limited by the Nyquist criterion as reported in the following equation:

$$n = \frac{2\Delta k \Delta R}{\pi}$$

With Δk is the k -range used for the Fourier transform from k space to the R space (k_{\max} - k_{\min}) and ΔR is the radius of the sphere around the absorbing atom which is taking into account for the fit of the EXAFS oscillations.

Vanadium K-edge X-ray absorption spectroscopy (XAS) spectra were acquired at the ROCK beamline in SOLEIL Synchrotron (France), thanks the technical support and the numerous advises from Dr. Antonella Iadecola. The spectra were recorded at room temperature in transmission mode using a vanadium foil as a reference for the energy calibration. A Si (111) channel-cut quick-XAS monochromator with an oscillation frequency of 2 Hz and an energy resolution of 0.2 eV at V K-edge energy was used for this experiment. Powder samples were mixed uniformly in a cellulose matrix and pressed into pellets of 13 mm diameter, to obtain edge step close to 1. Several X-ray absorption scans were collected to ensure the reproducibility of the spectra and to obtain a high signal to noise ratio. The normalization and background subtraction were performed using the Demeter package.¹⁴⁷

Annex-I-7 Electrochemical tests and *in-situ* everything

To determine the electrochemical properties of the materials studied in this manuscript, laboratory lithium coin cells were assembled (**Figure Annex-I-12**). The positive electrodes were prepared using 80 wt% of active material, 10 wt% of carbon (Super P) and 10 wt% of polyvinylidene fluoride (PVDF). First, N-methyl pyrrolidinone was added to this mixture and the resultant slurry was cast on an Al foil and dried at 60°C during 24h. Discs (diameter 12 mm) cut in this foil were cycled in coin cells vs. metallic Lithium. The electrolyte used was a 1M solution of LiPF₆ in ethylene carbonate and dimethyl carbonate in a 1:1 volume ratio (LP30) which soaks the separators (Cell gard and Viledon).

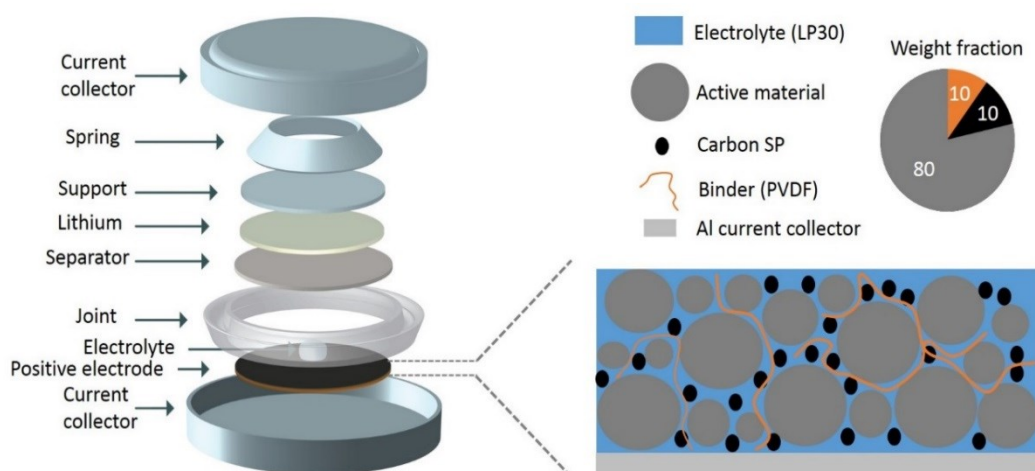


Figure Annex-I-12: Schematic of a coin cell (left) and the positive electrode material (right) adapted from ref ²⁰¹

The most commonly used technique in this thesis is galvanostatic electrochemical cycling of coin cells which allows the capacity, working voltage, efficiency and cycle life to be assessed. A cell is rested for few hours and the open circuit voltage recorded (OCV). A constant current is then applied at rates varying from C/100 to 2C (*i.e.* extraction or insertion of 1 Li⁺ per unit formula in 100h and 2h respectively) until a pre-set voltage limit is reached, at which point the current is reversed.

Galvanostatic intermittent titration technique (GITT) was also used to complement classical galvanostatic cycling. GITT provides information on the energetics of the electrochemical reactions occurring. The measurement consists of a series of short galvanostatic pulses (typically 1h at C/50) each followed by a relaxation time where no current is applied. The rest period is characterized by a short, sharp change in potential due to internal resistance (the iR drop), followed by a gradual decrease until the material reaches a quasi-equilibrium state (*i.e.* $dV/dt < 4mV/h$). Once the cell returns to its OCV the difference between

this value and the voltage at the end of the galvanostatic step is observed, and is termed polarization (or overpotential). This polarization corresponds to the extra energy required for the reaction to occur. Large overpotentials suggest either large electrical resistance of the electrode (arising either from active material or cell), or large ionic resistance (high activation energies for ion movement). As GITT gives insight into kinetic of ion movements, the ionic diffusion coefficient can be extracted at each step of a monophasic domain. If sufficient small currents are applied for short time, the ionic diffusion coefficient, D (cm^2/s), can be expressed as follows²⁰²:

$$D = \frac{4}{\pi\tau} \left(\frac{n_m V_m}{S} \right)^2 \left(\frac{\Delta E_s}{\Delta E_t} \right)^2$$

Where, τ is the duration of the current pulse (s), n_m is the number of moles of active material (mol); V_m is the molar volume of the electrode (cm^3/mol), S is the electrode/electrolyte contact area (cm^2), ΔE_s is the steady-state voltage change, due to the current pulse and ΔE_t is the voltage change during the constant current pulse, eliminating the iR drop (**Figure Annex-I-13**).

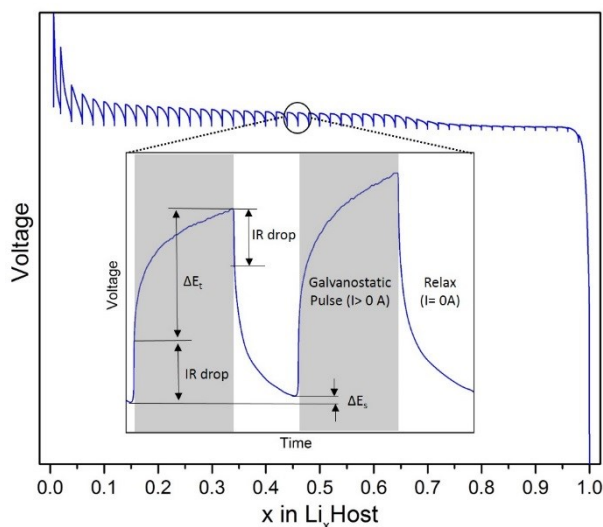


Figure Annex-I-13: Schematic representation of the GITT mode: evolution of the voltage of a Li battery as a function of time

For *operando* measurements (*i.e.* XRD, SXRPD or XAS during battery operation) either in classical galvanostatic or in GITT modes, the preparation of the electrode material is slightly different. In this case, a self-supported composite electrode with the active material, carbon and PTFE as binder (with mass ratio specified in **Table Annex-I-3**) is used. Indeed, due to setup constraints the electrode must be self-supported²⁰³ in order to avoid the use of a thick Al foil (500 μm) as current collector which strongly absorbs the X-ray beam. Indeed, either for

laboratory *in-operando* XRD, in reflection mode, or for experiments using synchrotron X-ray source, in transmission mode, the beam has to span this component (see **Figure Annex-I-14**). Although, Beryllium is a poor electronic conductor compare to Al (and much more toxic...), this light (therefore low X-ray absorber) metal is the most appropriate to be used as current collector. Nevertheless, due to the electrochemical instability of Beryllium at high voltage (*i.e.* $E > 3.6V$) a thin Al foil (10 μm) has to be used to protect it against oxidation.

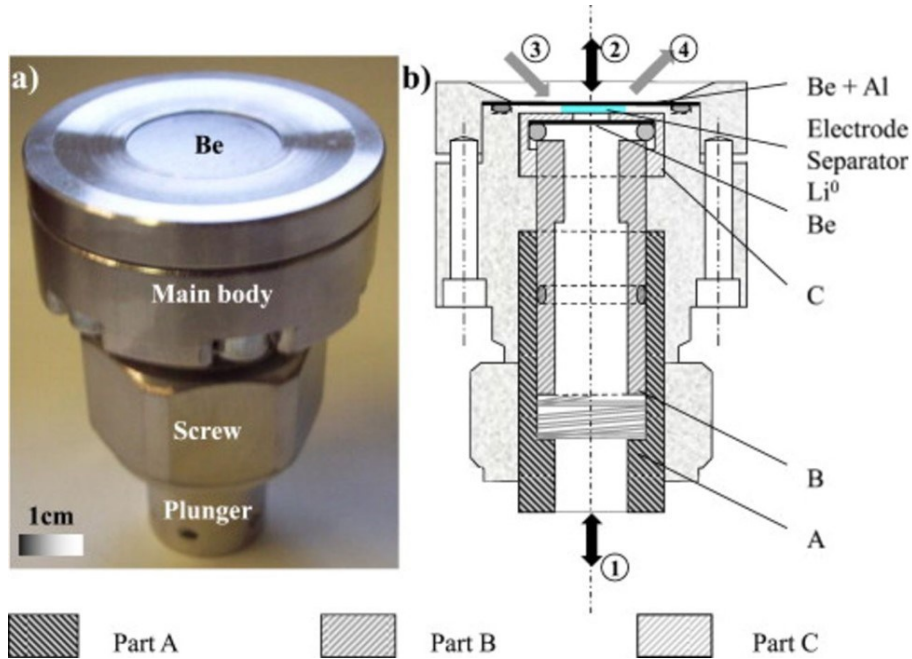


Figure Annex-I-14: Electrochemical cell for operando measurements, from ref. ²⁰³ (a) Photo and (b) detailed view of the cell with incoming and outgoing beam paths in transmission (① and ②) and reflection mode (③ and ④).

Table Annex-I-3: experimental conditions used for *in operando* XRD and XAS experiments.

<i>In operando</i> ...	Laboratory XRD	Synchrotron XRD	X-ray absorption spectroscopy
Beam line / diffractometer	Bruker D8	MSPD @ ALBA	ROCK @ SOLEIL
Wavelength (Å)	Cu, K α	0.9532 or 0.9540	1.9680 < λ < 2.3263
Monochromator	/	Si (111)	Si (111)
Mode	reflection	transmission	transmission
reference	/	NAC and Si	V foil
range (° or eV)	17 – 41°	1 - 50	5330 - 6300
step (° or eV)	0.03°	0.006°	0.2eV or 1eV
Φ beam (mm ²)	100	7.5	2
Φ electrode (mm ²)	133	133	50
Electrode loading (AM/C/PTFE)	80/10/10	85/10/5	50/45/5
Rate (nC)	0.02	0.05 < n < 0.1	0.05
Counting time	2h	5s or 5 min	5 min

The huge amount of data obtained during *operando* experiment was analyzed by specific tools. The XRD data were refined thanks to sequential Rietveld refinements with the Fullprof program¹⁹³. The sequential mode aims to refine the pattern n from the refinement results of the pattern $n-1$ and then automatically refines the pattern $n+1$ from the results of n ...

The normalized *operando* XANES spectra were globally analyzed using a chemometric approach based on principal components analysis (PCA) and multivariate curve resolution using alternative least square (MCR-ALS) reconstruction, available in a commercial software package (MATLAB 2015b, The MathWorks Inc., Natick, **Massachusetts**, US). This approach is widely used for the interpretation of *in-situ* XAS experiments and is carefully described and discussed in refs.^{132–134,204} We will give in the following a brief description of this mathematical tool.

PCA is a chemometric factor analysis tool generally used to determine the number of independent components contributing to the whole series of collected spectra during the electrochemical cycling. This method allows to consider each spectrum as a vector having n -dimensions (n is equal to the number of measured points). The combination of all these vector (spectra) constitutes a matrix whose dimension can be reduced from n to k through Singular Value Decomposition (SVD) method which describes the data matrix into orthogonal vectors. The k parameter is determined when no significant variation of the variance is observed over the reconstruction of the whole series of spectra. The k orthogonal components considered as the minimal number of components necessary for satisfactory rebuilding the experimental data should be significantly larger than the experimental noise. The so called variance plot showing the variance explained as function of the number of components allows to select the more relevant value of k .

Since the principal components are purely mathematical functions, they could have no chemical meaning. Therefore, the number of principal components determined by PCA was then used as the basis for MCR-ALS method which allows to reconstruct the corresponding real XAS components as well as their relative contribution to each spectrum. The experimental data are first represented in a matrix form, called D ($N_{\text{snapshots}}, N_{\text{energy}}$), in which the $N_{\text{snapshots}}$ are the XAS spectra recorded at the energies (N_{energy}) during the experiment. A bilinear decomposition of the matrix D is done into the matrix containing pure concentration profiles C ($N_{\text{snapshots}}, k$) and the matrix containing pure XAS spectra S^T (k, N_{energy}) of the k components of the unknown mixtures according to the following relation:

$$D = CS^T + E$$

where the matrix E ($N_{\text{snapshots}}, N_{\text{energy}}$) contains the residual variation of the data (typically the experimental noise). MCR techniques do not require information concerning the data for resolving C and S^T , except the estimation of the number of pure constituents in the system given by PCA analysis.

In this manuscript, the MCR-ALS analysis was performed applying the following constraints for both spectral components and their respective concentrations, in order to reproduce a physically and chemically meaningful behavior: (i) non-negativity of the concentrations of the components, (ii) unimodality (only a single highest value of concentration), and (iii) closure (sum of the three components always equal to 100% of the intensity).

The MCR-ALS method relies on the iterative ALS optimization of matrices C and S^T : iterations are carried out alternatively on C or S^T in order to minimize the $\|D - CS^T\|^2$ function, according the following steps:

- i) Given D and the initial estimate of S^T , an optimization of C is carried out by the least square calculation and the constraints for C .
- ii) Given D and the so-calculated C matrix, an optimization of S^T is carried out by the least square calculation and the constraints for S^T .
- iii) Then the reproduction of D using matrices C and S^T determined in steps (i) and (ii) is done. If the convergence criterion is fulfilled, the process is finished. If not, the program goes back to step (i)

Annex-I-8 Others techniques: ICP, TGA, SEM, TEM

In order to obtain the chemical compositions of the samples, the Li, V, and P contents were determined using an Inductively Coupled Plasma / Optical Emission Spectrometry (**ICP-OES**) spectrometer (Varian 720-ES Optical Emission Spectrometer) after complete dissolution of the powders into a mixture of hydrochloric and nitric acids. Elemental analyses of C and H were performed using a gas chromatography spectrometer, an Elementar Vario Micro Cube **CHNS** analyser. A certain mass of the sample was introduced in a tin capsule. In this technique, a sample is burned in an excess of oxygen and various traps, collecting the combustion products: carbon dioxide, water, and nitric oxide... The masses of these combustion products is then used to calculate the composition the sample

The thermogravimetric analysis (**TGA**) sometimes coupled with mass spectroscopy (**TGA-MS**) of the materials studied in this work have also been performed in order to get insights in the chemical compositions (Carbon volatilization, Hydroxyl group or Fluorine losses). TGA-MS experiments wer done on a STA449C Jupiter thermo-microbalance coupled with a QMS Aëolos 32 spectrometer commercialized by Netzsch with a continuous heating rate for the first experiment. In order to separate the different weight losses and overpass the kinetics phenomena, in a second experiment, several plateaus were performed with TGA-MS at the characteristic temperatures defined by the first one. The specific conditions used (gaz flux, temperature rate, temperature plateaus and their duration and m/z channels for MS...) depending on the materials studied are specified in the text.

The investigation of the morphology was performed by Scanning Electron Microscopy (**SEM**) using either a Hitachi S-4500 microscope either FEI Quanta 200F operating at 20 kV. The powders were previously metallized by gold deposition. Electron diffraction (**ED**) patterns and Transmission electron microscopy (**TEM**) images were obtained with a Tecnai G2 electron microscope operated at 200 kV. Samples were prepared by grinding the crystalline powder in a mortar in anhydrous ethanol and depositing drops of the suspension on a copper grid.

Annex-II Supplementary information of chapter II

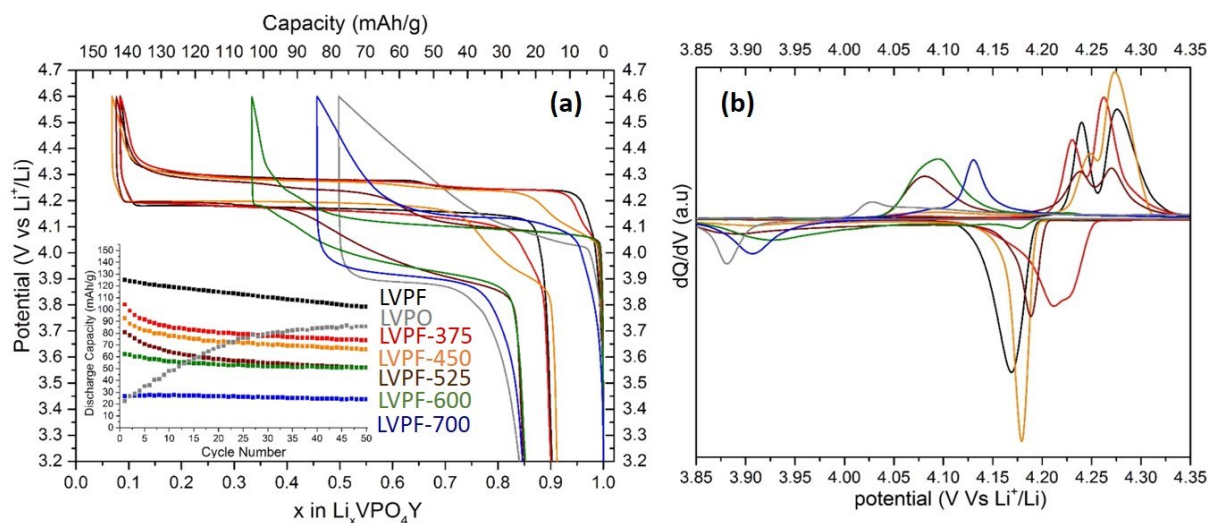


Figure Annex-II-1: (a) Galvanostatic curves obtained versus Lithium at a C/50 rate for all the annealed samples in the high voltage domain (i.e. between 3.0 and 4.6 V vs Li⁺/Li) with evolution of the discharge capacity at C/10 given in inset. (b) The corresponding derivative curves are given in (b).

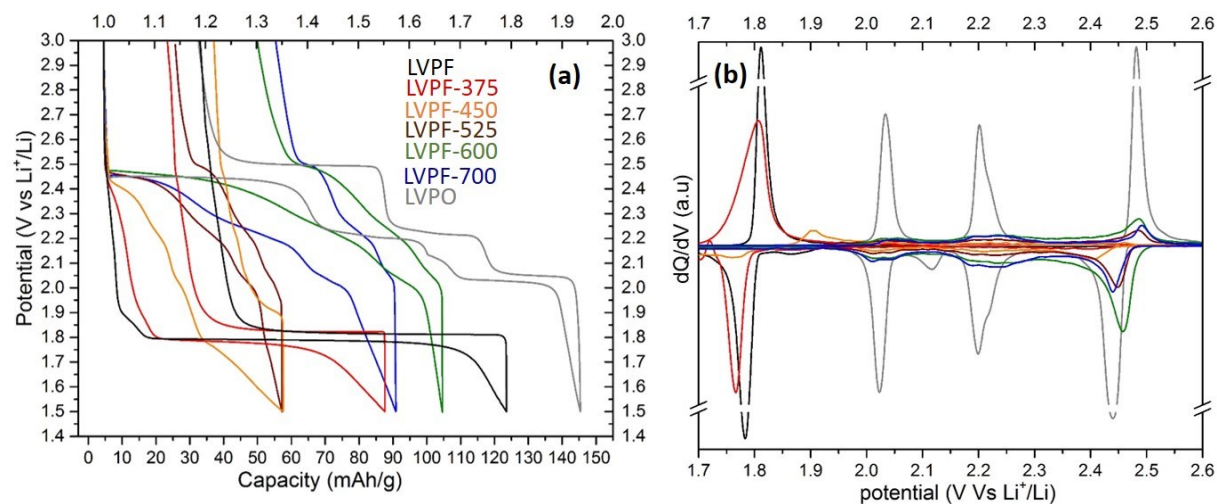


Figure Annex-II-2: (a) Galvanostatic curves obtained versus Lithium at a C/50 rate for all the annealed samples in the high voltage domain (i.e. between 3.0 and 1.5 V vs Li⁺/Li). (b) The corresponding derivative curves are given in (b).

Table Annex-II-1: details of BVS calculation for the $\text{LiVPO}_4\text{F}_{1-y}\text{O}_y$ series of material.

	Octahedra	%	$\text{V}^{3+}\text{-O}$	$\text{V}^{3+}\text{-O}$	$\text{V}^{3+}\text{-F}$	$\text{V}^{4+}\text{-O}$	$\text{V}^{4+}\text{-O}$	$\text{V}^{4+}\text{-O}$	$\text{V}^{4+}\text{-F}$	BVS	Overall
			$d_0=1.749 \text{ \AA}$	$d_0=1.749 \text{ \AA}$	$d_0=1.702 \text{ \AA}$	$d_0=1.735 \text{ \AA}$	$d_0=1.780 \text{ \AA}$	$d_0=1.780 \text{ \AA}$	$d_0=1.700 \text{ \AA}$		
$\text{LiVPO}_4\text{F}_{0.65}\text{O}_{0.35}$	$\text{O-(V}^{4+}\text{O}_4)\text{-O}$	10%	/	/	/	1.64(1)*1	2.01(1)*4	2.19(1)*1	/	3.7(1)	3.4(1) vs.
	$\text{F-(V}^{4+}\text{O}_4)\text{-O}$	25%	/	/	/	1.64(1)*1	2.01(1)*4	/	2.01(1)*4	3.9(1)	3.35
	$\text{X-(V}^{3+}\text{O}_4)\text{-X}$	65%	2.01(1)*0.4	2.01(1)*4	2.01(1)*1.6	/	/	/	/	3.1(1)	theoretically
$\text{LiVPO}_4\text{F}_{0.45}\text{O}_{0.55}$	$\text{O-(V}^{4+}\text{O}_4)\text{-O}$	20%	/	/	/	1.64(1)*1	2.01(1)*4	2.20(1)*1	/	3.7(1)	3.5(1) vs.
	$\text{F-(V}^{4+}\text{O}_4)\text{-O}$	35%	/	/	/	1.64(1)*1	2.01(1)*4	/	2.03(1)*4	3.9(1)	3.55
	$\text{X-(V}^{3+}\text{O}_4)\text{-X}$	45%	2.01(1)*0.75	2.01(1)*4	2.01(1)*1.25	/	/	/	/	3.1(1)	theoretically
$\text{LiVPO}_4\text{F}_{0.25}\text{O}_{0.75}$	$\text{O-(V}^{4+}\text{O}_4)\text{-O}$	45%	/	/	/	1.64(1)*1	2.01(1)*4	2.20(1)*1	/	3.7(1)	3.7(1) vs.
	$\text{F-(V}^{4+}\text{O}_4)\text{-O}$	30%	/	/	/	1.64(1)*1	2.01(1)*4	/	2.01(1)*4	3.9(1)	3.75
	$\text{X-(V}^{3+}\text{O}_4)\text{-X}$	25%	2.01(1)*1.2	2.01(1)*4	2.01(1)*0.8	/	/	/	/	3.1(1)	theoretically

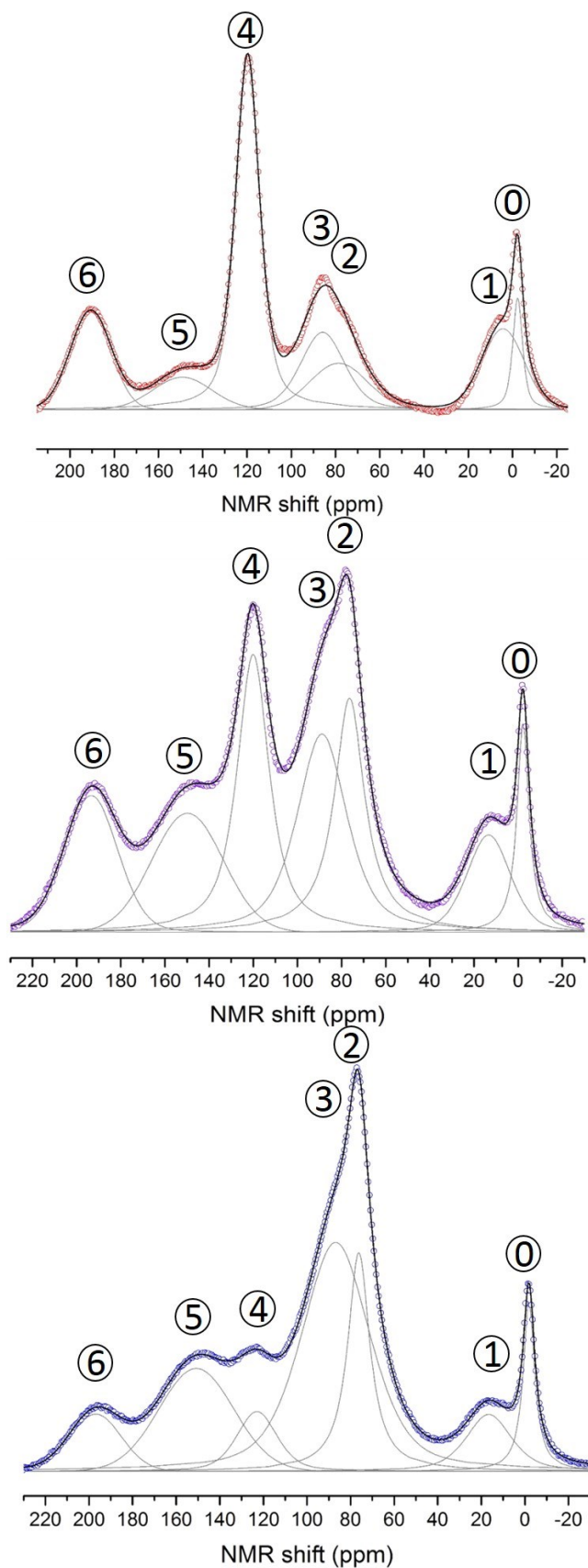


Figure Annex-II-3: fits of ${}^7\text{Li}$ MAS NMR spectra of the whole series of $\text{LiVPO}_4\text{F}_{1-x}\text{O}_x$ compositions thanks to a pseudo-Voigt function.

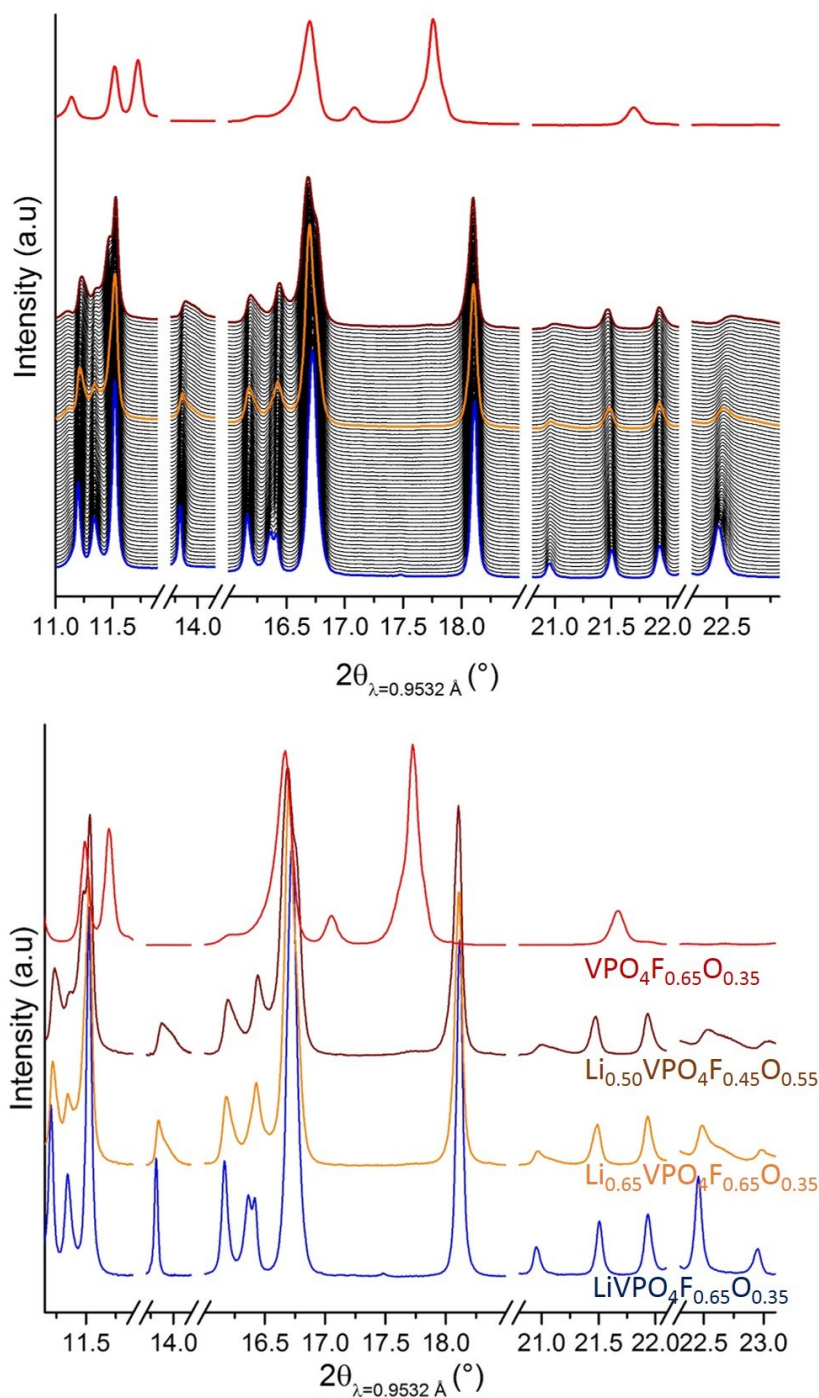


Figure Annex-II-4: SXRPD patterns recorded in-operando during lithium extraction from $\text{LiVPO}_4\text{F}_{0.65}\text{O}_{0.35}$ (top) the material corresponding to the red pattern have been obtained ex-situ. Selected SXRPD at specific compositions (bottom).

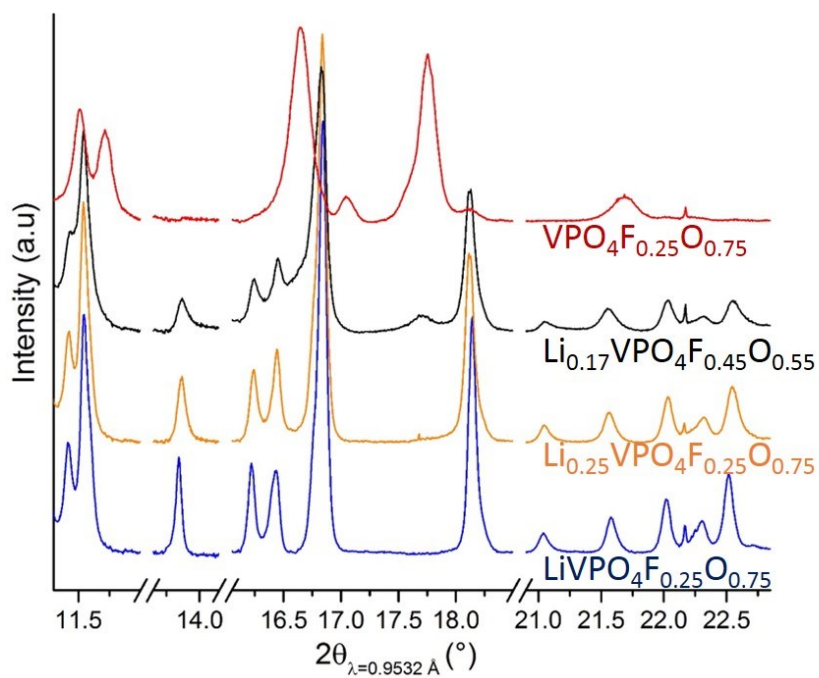
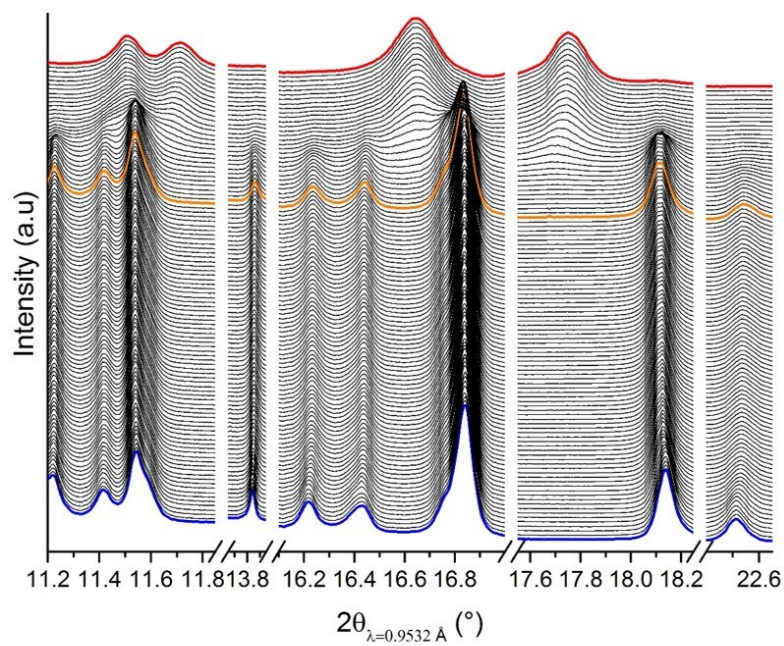


Figure Annex-II-5: SXRPD patterns obtained in-operando during lithium extraction from $\text{LiVPO}_4\text{F}_{0.25}\text{O}_{0.75}$ (top) Selected SXRPD at specific compositions are shown (bottom).

Table Annex-II-2: details of BVS calculation for the $Li_{1-x}VPO_4F_{0.45}O_{0.55}$ series of material

sample	octahedra	%	$V^{3+}O$ $d_0=1,749 \text{ \AA}$	$V^{3+}O$ $d_0=1,749 \text{ \AA}$	$V^{3+}F$ $d_0=1,702 \text{ \AA}$	$V^{4+}O$ $d_0=1,735 \text{ \AA}$	$V^{4+}O$ $d_0=1,780 \text{ \AA}$	$V^{4+}O$ $d_0=1,780 \text{ \AA}$	$V^{4+}F$ $d_0=1,700 \text{ \AA}$	$V^{5+}O$ $d_0=1,735 \text{ \AA}$	$V^{5+}O$ $d_0=1,799 \text{ \AA}$	$V^{5+}O$ $d_0=1,799 \text{ \AA}$	$V^{5+}F$ $d_0=1,700 \text{ \AA}$	BVS	Overall
$LiVPO_4F_{0.45}O_{0.55}$	$O-(V^{4+}O_4)=O$	20%	/	/	/	$1.64(1)^*1$	$2.00(1)^*4$	$2.20(1)^*1$	/	/	/	/	/	3.8(1)	3.6(1) vs. 3.35 theoretically
	$F-(V^{4+}O_4)=O$	35%	/	/	/	$1.64(1)^*1$	$2.00(1)^*4$	/	$2.00(1)^*1$	/	/	/	/	4.0(1)	
	$X-(V^{4+}O_4)X$	45%	$2.00(1)^*0,75$	$2.00(1)^*4$	$2.00(1)^*1,25$	/	/	/	/	/	/	/	/	3.2(1)	
$Li_{0,45}VPO_4F_{0,45}O_{0,55}$	$O-(V^{5+}O_4)=O$	20%	/	/	/	$1.63(1)^*1$	/	/	/	$1.63(1)^*1$	$1.95(1)^*4$	$2.23(1)^*1$	/	4.4(1)	3.9(1) vs. 4.10 theoretically
	$F-(V^{5+}O_4)=O$	35%	/	/	/	$1.63(1)^*1$	/	/	/	$1.63(1)^*1$	$1.95(1)^*4$	/	$2.03(1)^*1$	4.5(1)	
	$X-(V^{5+}O_4)X$	45%	$2.03(1)^*0,75$	$1.95(1)^*4$	$2.03(1)^*1,25$	/	/	/	/	/	/	/	/	3.1(1)	
$VPO_4F_{0,6}O_{0,55}$	$O-(V^{5+}O_4)=O$	20%	/	/	/	$1.61(1)^*1$	/	/	/	$1.61(1)^*1$	$1.91(1)^*4$	$2.23(1)^*1$	/	4.7(1)	4.3(1) vs. 4.55 theoretically
	$F-(V^{5+}O_4)=O$	35%	/	/	/	$1.61(1)^*1$	/	/	/	$1.61(1)^*1$	$1.91(1)^*4$	/	$2.03(1)^*1$	4.8(1)	
	$X-(V^{5+}O_4)X$	45%	/	/	/	/	$1.91(1)^*4$	$2.03(1)^*0,75$	$2.03(1)^*1,25$	/	/	/	/	3.7(1)	

Table Annex-II-3: details of BVS calculation for the $Li_{1+x}VPO_4F_{0.45}O_{0.55}$ series of material

sample	Octahedra	%	V^{2+} -O			V^{3+} -O			V^{4+} -O			BVS	Overall		
			$d_0=2,160 \text{ \AA}$	$d_0=2,160 \text{ \AA}$	$d_0=2,16 \text{ \AA}$	$d_0=1,749 \text{ \AA}$	$d_0=1,749 \text{ \AA}$	$d_0=1,749 \text{ \AA}$	$d_0=1,702 \text{ \AA}$	$d_0=1,735 \text{ \AA}$	$d_0=1,780 \text{ \AA}$			$d_0=1,780 \text{ \AA}$	$d_0=1,700 \text{ \AA}$
$LiVPO_4F_{0.45}O_{0.55}$	$O-(V^{4+}O_4)=O$	20%	/	/	/	/	/	/	/	/	/	/	3,8(1)	3,6(1)	
	$F-(V^{4+}O_4)=O$	35%	/	/	/	/	/	/	/	1,64(1)*1	2,00(1)*4	2,23(1)*1	2,00(1)*1		3,9(1)
	$X-(V^{3+}O_4)X$	45%	/	/	/	/	/	/	/	/	/	/	/		3,2(1)
	$O-(V^{3+}O_4)=O$	20%	/	/	/	1,82(1)*1	2,06(1)*4	1,99(1)*1	/	/	/	/	/		3,1(1)
$Li_{1.55}VPO_4F_{0.45}O_{0.55}$	$F-(V^{3+}O_4)=O$	35%	/	/	/	1,82(1)*1	2,06(1)*4	/	1,99(1)*1	/	/	/	/	3,0(1)	2,9(1)
	$X-(V^{3+}O_4)X$	45%	/	/	/	1,99(1)*0,75	2,06(1)*4	/	1,99(1)*1,25	/	/	/	/	2,8(1)	
	$O-(V^{3+}O_4)=O$	20%	/	/	/	1,95(1)*1	2,13(1)*4	2,13(1)*1	/	/	/	/	/	2,3(1)	
$Li_2VPO_4F_{0.65}O_{0.55}$	$F-(V^{3+}O_4)=O$	35%	/	/	/	1,95(1)*1	2,13(1)*4	/	2,13(1)*1	/	/	/	/	2,3(1)	2,1(1)
	$X-(V^{2+}O_4)X$	45%	2,13(1)*0,75	2,13(1)*4	2,13(1)*1,25	/	/	/	/	/	/	/	/	1,9(1)	

Annex-III Supplementary information of Chapter III

The ^{23}Na MAS NMR spectra of NaVPO_4F is provided at **Figure Annex-III-2**. The spectrum of NaVPO_4F exhibits several very asymmetric broad signals, typical for NMR signature of quadrupolar nuclei. Indeed, the spin of ^{23}Na Nucleus is superior to $\frac{1}{2}$ (*i.e.* $I = 3/2$) and so the quadrupolar interaction might influences greatly the NMR spectrum. A first asymmetric contribution is located around 164 ppm and others negatively shifted components are observed at -27 and -74 ppm. The main observation is that, although one single Na crystallographic site is expected, several NMR resonances are observed. Thus, DFT calculation is essential to understand the NMR signature of NaVPO_4F . We performed these calculations for two main objectives:

- i) Identify the Na isotropic signal that correspond to the unique site in this structure
- ii) Understand the spin transfer mechanisms from the magnetic transition metal ions to the Na nucleus.

In fact, the sodium coordination polyhedra in NaVPO_4F shares four edges with four VO_4F_2 octahedra. The e_g orbitals of V^{3+} (t_{2g}^2) being empty, the spin transfer from vanadium to sodium can occur only from the t_{2g} orbitals pointing toward these edges. The calculation of ^{23}Na NMR shift by the GGA+U approach give a closer value to those observed experimentally compared to the GGA one due to the stronger localization of the d electrons on the transition metal induced by the Hubbard term $U=4.5\text{eV}$ (GGA+U: 171 ppm vs GGA: 248 ppm and 164 ppm experimentally). The unique computed contribution obtained suggests a unique spin transfer mechanism from the transition metal to the sodium orbitals. Indeed, the 3D spin density map around the sodium nucleus reveals that the two d electrons of the V^{3+} ions are distributed uniformly in the 3 t_{2g} orbitals. The four vanadium belonging to the local environment of Na participate to the spin transfer with the orbital lobes pointing between O/F ligands. Each V thus exhibits a lobe pointing directly toward the Na site through the common edge between the NaO_6F and VO_4F_2 polyhedra. Therefore we consider that the extra signals at -27 and -74 belong either to the same material (local defects) or to traces of separate phases present as impurities (not detected by diffraction due to the limited extent of their domain coherence). Indeed the possibility of having a partial oxidation defect in this material is highly probable, as it was reported for several similar materials^{19,21}.

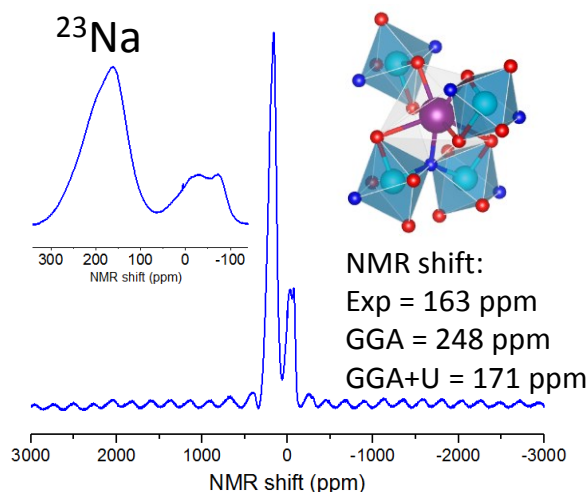


Figure Annex-III-1: ^{23}Na NMR spectrum of NaVPO_4F . In inset the local environment of the probed atom and value of NMR shifts computationally (GGA and GGA+U) and experimentally obtained.

^{31}P MAS NMR (**Figure Annex-III-2**) was also performed and the only signal is located at 3452 ppm. Contrarily to ^{23}Na NMR, The large width of this contribution cannot be attributed to the quadrupolar interaction because the spin of ^{31}P is $\frac{1}{2}$. That suggests the presence of defects which may affect greatly the ^{31}P NMR signature. As illustrated in **Figure Annex-III-2**, in the Tavorite structure, PO_4 tetrahedra are connected to four different transition metal octahedra via the oxygen belonging to the square plane of these octahedra. As discussed by Castets et al.^{149,150}, in tavorite materials the spin transfer to the 2s (or the sp^3 hybrid) orbital of Phosphorus can occur from the t_{2g} orbitals (via π overlap with a p orbital of oxygen), or from the e_g orbitals via O. Nevertheless, the e_g orbitals of V^{3+} (t_{2g}^2) being empty, the second spin transfer mechanism proposed cannot be at the origin of the NMR shift. A comparison of ^{31}P NMR shifts (experimental and computed) in the Tavorite series is provided in **Figure Annex-II-2**. The V-P distances are 3.21 and 3.37 Å in NaVPO_4F whereas they are ranging between 3.20 and 3.32 Å in LiVPO_4F . The shorter V-P distances in LiVPO_4F promotes the spin transfer between their orbitals and the shift of the signal is thus higher compare to the ^{31}P NMR shift for NaVPO_4F . This is confirm by the calculated shift for NaVPO_4F (*i.e.* GGA = 6249 ppm, GGA+U = 3192 ppm for NaVPO_4F vs GGA = 6265 ppm, GGA+U = 2983 ppm for LiVPO_4F ¹²⁸ once again the GGA+U approach gives a better approximation of the shift compare to GGA one.

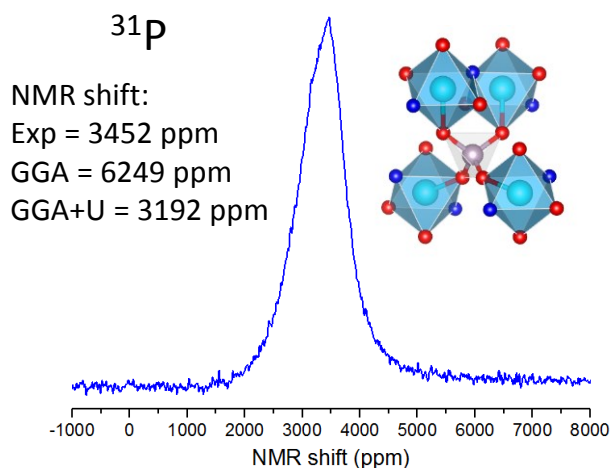


Figure Annex-III-2: ^{31}P NMR spectrum of NaVPO_4F . In inset the local environment of the probed atom and value of NMR shifts computationally (GGA and GGA+U) and experimentally obtained.

^{19}F MAS NMR spectrum of NaVPO_4F is compared to those of LiVPO_4F at the **Figure Annex-III-3**. These spectra exhibit a strong parasitic contribution from the probe (which contains Teflon) around 150 ppm and several more shifted signals. Among them, by analogy with the LiVPO_4F 's signature, the isotropic peak is assigned to the signal at -1309 ppm and the others to their spinning side bands. Nevertheless, DFT calculations give a ^{19}F shift located at -498 ppm with GGA+U and 96 ppm with GGA approach. The strong difference between experimental and computed shifts might be due to the strong difference between the experimentally and computationally obtained V-F bond lengths (1.93 Å vs 2.01 Å). This difference is probably due to the presence of vanadyl-type defects which might impact the antagonist V-F leading to a shortening of the average bond lengths measured by diffraction. The presence of local vanadyl-type environment should have been highlighted by the presence of a signal assigned to fluorine in interaction with V^{4+} but this kind of contribution was not observed. The absence of signal cannot be assigned to the absence of fluorine in interaction with V^{4+} because no signal is seen for V^{4+} -rich phase VPO_4F by ^{19}F NMR^{126,128}. Our hypothesis to explain this absence of contribution is to consider a too strong interaction between fluorine and V^{4+} nuclei. Actually, in this compound fluorine belongs to the first coordination sphere of vanadium and the proximity between orbitals of probed atom and magnetic center (1.92 Å in $\text{V}^{\text{IV}}\text{PO}_4\text{F}$ versus 2.01 Å in $\text{NaV}^{\text{III}}\text{PO}_4\text{F}$ (DFT) vs 1.99 Å in $\text{LiV}^{\text{III}}\text{PO}_4\text{F}$) leads to a strong dipolar interaction which would induce an extremely broad contribution doesn't discernible to the background.

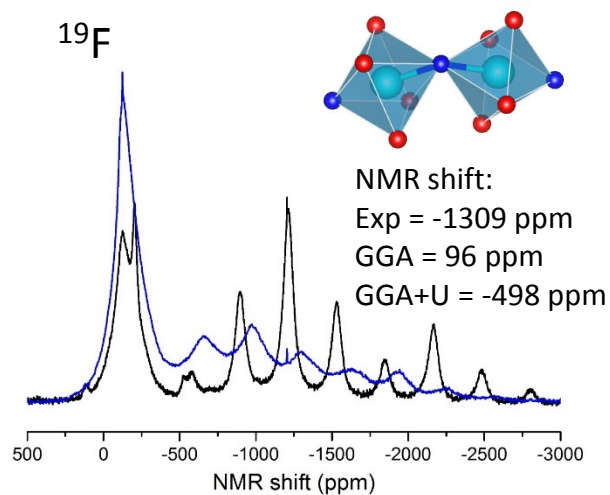


Figure Annex-III-3: ^{19}F NMR spectra of NaVPO_4F (blue) and LiVPO_4F (black). In inset the local environment of the probed atom and value of NMR shifts computationally (GGA and GGA+U) and experimentally obtained.

Table Annex-III-1: Structural parameters obtained by Rietveld refinement of the structure of $\text{Li}_2\text{VPO}_4\text{OH}$ based on synchrotron XRD and Neutron Diffraction Data. Oxygen atom note by * is the bridging atom which is bound to hydrogen.

$\text{Li}_2\text{VPO}_4\text{OH}$						
SG : $P-1$		$a = 7.2835(3) \text{ \AA}$		$\alpha = 89.746(3)^\circ$		
$Z = 4$		$b = 7.5724(3) \text{ \AA}$		$\beta = 88.039(3)^\circ$		$\chi^2 = 12.3$
$\text{Li}_2\text{VPO}_4\text{OH}$: 89(1) w%		$c = 7.9773(3) \text{ \AA}$		$\gamma = 118.675(3)^\circ$		$R_{\text{Bragg}} = 4.65\%$
$\text{Li}_{1.25}\text{VPO}_4\text{OH}$: 11(1) w%		$V = 385.68(3) \text{ \AA}^3$		$V/Z = 96.17(3) \text{ \AA}^3$		
atoms	Wickoff position	x	y	z	occupancy	B iso
V(1)	$2i$	0.741(3)	0.988(3)	0.246(3)	1	1.08(9)
V(2)	$2i$	0.752(4)	0.500(3)	0.251(3)	1	1.08(9)
P(1)	$2i$	0.223(3)	0.765(3)	0.405(3)	1	0.49(9)
P(2)	$2i$	0.277(3)	0.259(3)	0.109(3)	1	0.49(9)
O(1)	$2i$	0.568(9)	0.067(8)	0.674(5)	1	0.35(8)
O(2)	$2i$	0.087(7)	0.668(7)	0.255(6)	1	0.35(8)
O(3)	$2i$	0.736(7)	0.395(7)	0.504(7)	1	0.35(8)
O(4)	$2i$	0.149(6)	0.894(6)	0.515(6)	1	0.35(8)
O(5)*	$2i$	0.207(9)	0.731(9)	0.862(9)	1	0.35(8)
O(6)	$2i$	0.061(9)	0.079(8)	0.160(7)	1	0.35(8)
O(7)	$2i$	0.225(8)	0.404(8)	0.006(8)	1	0.35(8)
O(8)*	$2i$	0.699(9)	0.722(9)	0.371(9)	1	0.35(8)
O(9)	$2i$	0.584(7)	0.646(7)	0.740(6)	1	0.35(8)
O(10)	$2i$	0.364(7)	0.146(5)	0.993(6)	1	0.35(8)
Li(1)	$2i$	0.69(1)	0.35(1)	0.92(1)	1	2.3(2)
Li(2)	$2i$	0.64(2)	0.83(2)	0.48(1)	1	2.3(2)
Li(3)	$2i$	0.87(1)	0.76(1)	0.52(1)	1	2.3(2)
Li(4)	$2i$	0.93(2)	0.17(1)	0.92(1)	1	2.3(2)

Table Annex-III-2: Significant bond length distances of $\text{Li}_2\text{VPO}_4\text{OH}$ obtained from Rietveld refinement of SXRPD data. Only distances shorter than 2.6 Å are considered. V–O distances along the chains are highlighted in **bold**.

Polyhedral distortion is calculated as $\Delta = \frac{1}{N} \sum_{i=0}^N \frac{(d_i - \langle d \rangle)^2}{\langle d \rangle^2}$.

coordination	V(1) 6 (Oh)	V(2) 6 (Oh)	P(1) 4 (Td)	P(2) 4 (Td)	Li(1) 4 (Td)	Li(2) 6 (Oh)	Li(3) 4 (Td)	Li(4) 6 (Oh)
O(1)	2.153(6)	/	1.547(7)	/	/	2.40(3) / 2.56(2)	/	/
O(2)	/	2.145(8)	1.535(8)	/	2.10(3)	/	/	1.91(3)
O(3)	/	2.152(7)	1.556(7)	/	/	2.44(4)	2.47(3)	/
O(4)	2.115(9)	/	1.582(9)	/	/	1.90(3)	1.77(4)	/
O(5)	2.143(7)	2.119(6)	/	/	2.12(3)	/	/	2.25(3)
O(6)	2.173(6)	/	/	1.548(7)	/	/	/	2.04(3) / 2.41(3)
O(7)	/	2.153(8)	/	1.552(7)	1.77(3)	/	/	2.17(4)
O(8)	2.125(8)	2.120(7)	/	/	/	1.53(3)	1.87(3)	/
O(9)	/	2.149(7)	/	1.539(8)	/	2.38(3)	2.50(3)	/
O(10)	2.154(6)	/	/	1.577(9)	2.23(4)	/	/	2.40(3)
distorsion	8.1×10^{-5}	4.6×10^{-5}	1.2×10^{-4}	8.2×10^{-5}	7.0×10^{-3}	2.7×10^{-2}	2.4×10^{-2}	6.8×10^{-3}
BVS	2.0(1)	2.0(1)	4.7(2)	4.9(2)	1.0(1)	1.4(2)	1.0(2)	0.8(1)

Bibliography

- (1) Mizushima, K.; Jones, P. C.; Wiseman, P. J.; Goodenough, J. B. Li_xCoO_2 ($0 < x < 1$): A New Cathode Material for Batteries of High Energy Density. *Solid State Ionics* **1981**, *4*, 171–174.
- (2) Guilmard, M.; Pouillier, C.; Croguennec, L.; Delmas, C. Structural and Electrochemical Properties of $\text{LiNi}_{0.70}\text{Co}_{0.15}\text{Al}_{0.15}\text{O}_2$. *Solid State Ionics* **2003**, *160*, 39–50.
- (3) Koyama, Y.; Tanaka, I.; Adachi, H.; Makimura, Y.; Ohzuku, T. Crystal and Electronic Structures of Superstructural $\text{Li}_{1-x}[\text{Co}_{1/3}\text{Ni}_{1/3}\text{Mn}_{1/3}]\text{O}_2$ ($0 \leq x \leq 1$). *J. Power Sources* **2003**, *119-121*, 644–648.
- (4) Bang, H. J.; Joachin, H.; Yang, H.; Amine, K.; Prakash, J. Contribution of the Structural Changes of $\text{LiNi}_{0.8}\text{Co}_{0.15}\text{Al}_{0.05}\text{O}_2$ Cathodes on the Exothermic Reactions in Li-Ion Cells. *J. Electrochem. Soc.* **2006**, *153* (4), 731–737.
- (5) Manthiram, A.; Goodenough, J. B. Lithium Insertion into $\text{Fe}_2(\text{SO}_4)_3$ Frameworks. *J. Power Sources* **1989**, *26*, 403–408.
- (6) Padhi, A. K.; Nanjundaswamy, K. S.; Goodenough, J. B. Phospho-Olivines as Positive-Electrode Materials for Rechargeable Lithium Batteries. *J. Electrochem. Soc.* **1997**, *144* (4), 1188–1194.
- (7) Andersson, A. S.; Thomas, J. O.; Kalska, B.; Häggström, L. Thermal Stability of LiFePO_4 -Based Cathodes. *Electrochem. solid state Lett.* **2000**, *3* (2), 66–68.
- (8) Andersson, A. S.; Kalska, B.; Haggstrom, L.; Thomas, J. O. Lithium Extraction/insertion in LiFePO_4 : An X-Ray Diffraction and Mossbauer Spectroscopy Study. *Solid State Ionics* **2000**, *130*, 41–52.
- (9) Yamada, A.; Chung, S. C.; Hinokuma, K. Optimized LiFePO_4 for Lithium Battery Cathodes. *J. Electrochem. Soc.* **2001**, *148* (3), 224–229.
- (10) Huang, H.; Yin, S.; Nazar, L. F. Approaching Theoretical Capacity of LiFePO_4 at Room Temperature at High Rates. *Electrochem. solid state Lett.* **2001**, *4* (10), 170–172.
- (11) Recham, N.; Chotard, J.-N.; Jumas, J.-C.; Laffont, L.; Armand, M.; Tarascon, J.-M. Ionothermal Synthesis of Li-Based Fluorophosphates Electrodes. *Chem. Mater.* **2010**, *22*, 1142–1148.
- (12) Barpanda, P.; Ati, M.; Melot, B. C.; Rouse, G.; Chotard, J.-N.; Doublet, M.-L.; Sougrati, M. T.; Corr, S. a; Jumas, J.-C.; Tarascon, J.-M. A 3.90 V Iron-Based Fluorosulphate Material for Lithium-Ion Batteries Crystallizing in the Triplite Structure. *Nat. Mater.* **2011**, *10*, 772–779.
- (13) Masquelier, C.; Croguennec, L. Polyanionic (phosphates, Silicates, Sulfates) Frameworks as Electrode Materials for Rechargeable Li (or Na) Batteries. *Chem. Rev.* **2013**, *113*, 6552–6591.
- (14) Huang, H.; Faulkner, T.; Barker, J.; Saidi, M. Y. Lithium Metal Phosphates, Power and Automotive Applications. *J. Power Sources* **2009**, *189*, 748–751.
- (15) Kim, M.; Lee, S.; Kang, B. Fast-Rate Capable Electrode Material with Higher Energy Density than LiFePO_4 : $4.2\text{V LiVPO}_4\text{F}$ Synthesized by Scalable Single-Step Solid-State Reaction. *Adv. Sci.* **2015**, 1–9.

- (16) Li, P.; Ma, R.; Lin, X.; Shao, L.; Wu, K.; Shui, M.; Long, N.; Shu, J. Impact of H₂O Exposure on the Structure and Electrochemical Performance of LiVPO₄F Cathode Material. *J. Alloys Compd.* **2015**, *637*, 20–29.
- (17) Ma, R.; Shao, L.; Wu, K.; Shui, M.; Wang, D.; Long, N.; Ren, Y.; Shu, J. Effects of Oxidation on Structure and Performance of LiVPO₄F as Cathode Material for Lithium-Ion Batteries. *J. Power Sources* **2014**, *248*, 874–885.
- (18) Zhou, F.; Zhao, X.; Dahn, J. R. Reactivity of Charged LiVPO₄F with 1M LiPF₆ EC:DEC Electrolyte at High Temperature as Studied by Accelerating Rate Calorimetry. *Electrochem. commun.* **2009**, *11*, 589–591.
- (19) Messinger, R. J.; Ménétrier, M.; Salager, E.; Boulineau, A.; Duttine, M.; Carlier, D.; Ateba Mba, J.-M.; Croguennec, L.; Masquelier, C.; Massiot, D.; Deschamps, M. Revealing Defects in Crystalline Lithium-Ion Battery Electrodes by Solid-State NMR: Applications to LiVPO₄F. *Chem. Mater.* **2015**, *27*, 5212–5221.
- (20) Ateba Mba, J.-M.; Croguennec, L.; Basir, N. I.; Barker, J.; Masquelier, C. Lithium Insertion or Extraction From/into Tavorite-Type LiVPO₄F: An In Situ X-Ray Diffraction Study. *J. Electrochem. Soc.* **2012**, *159* (8), 1171–1175.
- (21) Bamine, T.; Boivin, E.; Boucher, F.; Messinger, R. J.; Salager, E.; Deschamps, M.; Masquelier, C.; Croguennec, L.; Ménétrier, M.; Carlier, D. Understanding Local Defects in Li-Ion Battery Electrodes through Combined DFT/NMR Studies: Application to LiVPO₄F. *J. Phys. Chem. C* **2017**, *121* (6), 3219–3227.
- (22) Alexander, L. V.; Allen, S. K.; Nathaniel L. Bindoff, F.-M. B.; Church, J. A.; Cubasch, U.; Emori, S.; Forster, P.; Friedlingstein, P.; Gillett, N.; Gregory, J. M.; Hartmann, D. L.; Jansen, E.; Kirtman, B.; Knutti, R.; Krishna Kumar Kanikicharla, P. L.; Marotzke, J.; Valérie Masson-Delmotte, G. A. M.; Mokhov, I. I.; Piao, S.; Plattner, G.-K.; Dahe, Q.; Venkatachalam Ramaswamy, D. R.; Rhein, M.; Rojas, M.; Sabine, C.; Shindell, D.; Stocker, T. F.; Talley, L. D.; Vaughan, D. G.; Xie, S.-P. *Climate Change 2014: Synthesis Report of International Panel on Climate Change (IPCC)*; 2014.
- (23) Agency international energy. *Key World Energy Statistic*; 2016.
- (24) Campbell, colin J. *Campbell's Atlas of Oil and Gas Depletion*; 2013.
- (25) tesla energy for business.
- (26) Troiano, J. How do Lithium Ion Batteries Work?
- (27) Larcher, D.; Tarascon, J.-M. Towards Greener and More Sustainable Batteries for Electrical Energy Storage. *Nat. Chem.* **2015**, *7*, 19–29.
- (28) Grey, C. P.; Tarascon, J. M. Sustainability and in Situ Monitoring in Battery Development. *Nat. Mater.* **2017**, *16*, 45–56.
- (29) Tarascon, J.-M.; Armand, M. Issues and Challenges Facing Rechargeable Lithium Batteries. *Nature* **2001**, *414*, 359–367.
- (30) Manthiram, A.; Goodenough, J. B. Lithium Insertion into Fe₂(MO₄)₃ Frameworks: Comparison of M = W with M = Mo. *J. Solid State Chem.* **1987**, *71*, 349–360.
- (31) Marx, N.; Croguennec, L.; Carlier, D.; Wattiaux, A.; Le Cras, F.; Suard, E.; Delmas, C. The Structure of Tavorite LiFePO₄(OH) from Diffraction and GGA + U Studies and Its Preliminary Electrochemical Characterization. *Dalt. Trans.* **2010**, *39*, 5108–5116.
- (32) Ben Yahia, M.; Lemoigno, F.; Rouse, G.; Boucher, F.; Tarascon, J.-M.; Doublet, M.-L. Origin of the 3.6 V to 3.9 V Voltage Increase in the LiFeSO₄F Cathodes for Li-Ion Batteries. *Energy Environ. Sci.* **2012**, *5*, 9584–9594.

- (33) Gao, J.; Shi, S.; Li, H. Brief Overview of Electrochemical Potential in Lithium Ion Batteries. *Chinese Phys. B* **2016**, *25* (1), 1–24.
- (34) Xu, W.; Wang, J.; Ding, F.; Chen, X.; Nasybulin, E.; Zhang, Y.; Zhang, J.-G. Lithium Metal Anode for Rechargeable Batteries. *Energy Environ. Sci.* **2014**, *7*, 513–537.
- (35) Peled, E.; Menkin, S. Review - SEI : Past , Present and Future. *J. Electrochem. Soc.* **2017**, *164* (7), 1703–1719.
- (36) Lin, X.; Pan, F.; Wang, H. Progress of $\text{Li}_4\text{Ti}_5\text{O}_{12}$ Anode Material for Lithium Ion Batteries. *Adv. Funct. Mater.* **2014**, *29*, 82–87.
- (37) Zhao, B.; Ran, R.; Liu, M.; Shao, Z. A Comprehensive Review of $\text{Li}_4\text{Ti}_5\text{O}_{12}$ -Based Electrodes for Lithium-Ion Batteries: The Latest Advancements and Future Perspectives. *Mater. Sci. Eng. R* **2015**, *98*, 1–71.
- (38) Ting-Feng, Y.; Shuang-Yuan, Y.; Ying, X. Recent Advances of $\text{Li}_4\text{Ti}_5\text{O}_{12}$ as Promising next Generation Anode Material for High Power Lithium-Ion Batteries. *J. Mater. Chem. A* **2015**, *3* (11), 5750–5777.
- (39) Croguennec, L.; Palacin, M. R. Recent Achievements on Inorganic Electrode Materials for Lithium-Ion Batteries. *J. Am. Chem. Soc.* **2015**, *137* (9), 3140–3156.
- (40) Luo, F.; Liu, B.; Zheng, J.; Chu, G.; Zhong, K.; Li, H.; Huang, X.; Chen, L. Review - Nano-Silicon/Carbon Composite Anode Materials Towards Practical Application for Next Generation Li-Ion Batteries. *J. Electrochem. Soc.* **2015**, *162* (14), 2509–2528.
- (41) Zhang, S. S. A Review on Electrolyte Additives for Lithium-Ion Batteries. *J. Power Sources* **2006**, *162*, 1379–1394.
- (42) Manthiram, A.; Yu, X.; Wang, S. Lithium Battery Chemistries Enabled by Solid State Electrolytes. *Nat. Rev.* **2017**, *2*, 1–16.
- (43) Kamaya, N.; Homma, K.; Yamakawa, Y.; Hirayama, M.; Kanno, R.; Yonemura, M.; Kamiyama, T.; Kato, Y.; Hama, S.; Kawamoto, K. A Lithium Superionic Conductor. *Nat. Mater.* **2011**, *10*, 682–686.
- (44) Dahn, J. R.; Von Sacken, U.; Juzkow, M. W.; Al-Janaby, H. Rechargeable $\text{LiNiO}_2/\text{Carbon}$ Cells. *J. Electrochem. Soc.* **1991**, *138* (8), 2207–2211.
- (45) Dahn, J. R.; Von Sacken, U.; Michal, C. A. Structure and Electrochemistry of $\text{Li}_{1\pm y}\text{NiO}_2$ and a New Li_2NiO_2 Phase with the $\text{Ni}(\text{OH})_2$ Structure. *Solid State Ionics* **1990**, *44*, 87–97.
- (46) Ohzuku, T.; Ueda, A.; Nagayama, M. Electrochemistry and Structural Chemistry of LiNiO_2 (R-3m) for 4 Volt Secondary Lithium Cells. *J. Electrochem. Soc.* **1993**, *140* (7), 1862–1870.
- (47) Xu, J.; Lin, F.; Doeff, M. M.; Tong, W. A Review of Ni-Based Layered Oxides for Rechargeable Li-Ion Batteries. *J. Mater. Chem. A* **2017**, *5*, 874–901.
- (48) Lu, Z.; Dahn, J. R. Understanding the Anomalous Capacity of In Situ X-Ray Diffraction and Electrochemical Studies. *J. Electrochem. Soc.* **2002**, *147* (7), 815–822.
- (49) McCalla, E.; Artem M. Abakumov, Matthieu Saubanère, D. F.; Berg, E. J.; Rouse, G.; Doublet, M.-L.; Gonbeau, D.; Novák, P.; Tendeloo, G. Van; Dominko, R.; Tarascon, J.-M. Visualization of O-O Peroxo-like Dimers in High-Capacity Layered Oxides for Li-Ion Batteries. **2015**, *350* (6267), 1516–1521.
- (50) Rozier, P.; Marie, J. Review - Li-Rich Layered Oxide Cathodes for Next-Generation Li-Ion Batteries : Chances and Challenges. *J. Electrochem. Soc.* **2015**, *162* (14), 2490–2499.

- (51) Thackeray, M. M.; Johnson, P. J.; Picciotto, L. A.; Bruce, P. G.; Goodenough, J. B. Electrochemical Extraction of Lithium from LiMn_2O_4 . *Mat. Res. Bull.* **1984**, *19*, 179–187.
- (52) Jang, D. H.; Shin, Y. J.; Oh, S. M. Dissolution of Spinel Oxides and Capacity Losses in 4 V $\text{Li}/\text{Li}_x\text{Mn}_2\text{O}_4$. *J. Electrochem. Soc.* **1996**, *143* (7), 2204–2211.
- (53) Thackeray, M. Manganese Oxides for Lithium Batteries. *Prog. Solid State Chem.* **1997**, *25*, 1–71.
- (54) Patoux, S.; Daniel, L.; Bourbon, C.; Lignier, H.; Pagano, C.; Le Cras, F.; Jouanneau, S.; Martinet, S. High Voltage Spinel Oxides for Li-Ion Batteries : From the Material Research to the Application. *J. Power Sources* **2009**, *189*, 344–352.
- (55) Yamada, A.; Chung, S. Crystal Chemistry of the Olivine-Type $\text{Li}(\text{Mn}_y\text{Fe}_{1-y})\text{PO}_4$ and $(\text{Mn}_y\text{Fe}_{1-y})\text{PO}_4$ as Possible 4 V Cathode Materials for Lithium Batteries. *J. Electrochem. Soc.* **2001**, *148* (8), 960–967.
- (56) Delacourt, C.; Laffont, L.; Bouchet, R.; Wurm, C.; Leriche, J.-B.; Morcrette, M.; Tarascon, J.-M.; Masquelier, C. Toward Understanding of Electrical Limitations (Electronic, Ionic) in LiMPO_4 (M = Fe, Mn) Electrode Materials. *J. Am. Chem. Soc.* **2005**, *127* (5), 913–921.
- (57) Lv, D.; Bai, J.; Zhang, P.; Wu, S.; Li, Y.; Wen, W.; Jiang, Z.; Mi, J.; Zhu, Z.; Yang, Y. Understanding the High Capacity of $\text{Li}_2\text{FeSiO}_4$: In Situ XRD/XANES Study Combined with First-Principles Calculations. *Chem. Mater.* **2013**, *25* (10), 2014–2020.
- (58) Boudin, S.; Guesdon, A.; Leclaire, A.; Borel, M. Review on Vanadium Phosphates with Mono and Divalent Metallic Cations : Syntheses, Structural Relationships and Classification, Properties. *Int. J. Inorg. Chem.* **2000**, *2*, 561–579.
- (59) Whittingham, M. S. Ultimate Limits to Intercalation Reactions for Lithium Batteries. *Chem. Rev.* **2014**, *114* (23), 11414–11443.
- (60) Yabuuchi, N.; Kubota, K.; Dahbi, M.; Komaba, S. Research Development on Sodium-Ion Batteries. *Chem. Rev.* **2014**, *114* (23), 11636–11682.
- (61) Jian, Z.; Hu, Y.; Ji, X.; Chen, W. NASICON-Structured Materials for Energy Storage. *Adv. Mater.* **2017**, *29* (20), 1–16.
- (62) Anantharamulu, N.; Rao, K. K.; Rambabu, G.; Kumar, B. V.; Radha, V.; Vithal, M. A Wide-Ranging Review on Nasicon Type Materials. *J. Mater. Sci.* **2011**, *46* (9), 2821–2837.
- (63) Huang, B. H.; Yin, S.; Kerr, T.; Taylor, N.; Nazar, L. F. Nanostructured Composites: A High Capacity, Fast Rate $\text{Li}_3\text{V}_2(\text{PO}_4)_3/\text{Carbon}$ Cathode for Rechargeable Lithium Batteries. *Adv. Mater.* **2002**, *14* (21), 1525–1528.
- (64) Patoux, S.; Wurm, C.; Morcrette, M.; Rousse, G.; Christian, M. A Comparative Structural and Electrochemical Study of Monoclinic $\text{Li}_3\text{Fe}_2(\text{PO}_4)_3$ and $\text{Li}_3\text{V}_2(\text{PO}_4)_3$. *J. Power Sources* **2003**, *121*, 278–284.
- (65) Yin, S.-C.; Grondy, H.; Strobel, P.; Anne, M.; Nazar, L. F. Electrochemical Property : Structure Relationships in Monoclinic $\text{Li}_{3-y}\text{V}_2(\text{PO}_4)_3$. *J. Am. Chem. Soc.* **2003**, *125* (11), 10402–10411.
- (66) Rui, X.; Yan, Q.; Skyllas-kazacos, M.; Mariana, T. $\text{Li}_3\text{V}_2(\text{PO}_4)_3$ Cathode Materials for Lithium-Ion Batteries : A Review. *J. Power Sources* **2014**, *258*, 19–38.
- (67) Yin, S.-C.; Strobel, P. S.; Grondy, H.; Nazar, L. F. $\text{Li}_{2.5}\text{V}_2(\text{PO}_4)_3$: A Room-Temperature Analogue to the Fast-Ion Conducting High-Temperature γ -Phase of $\text{Li}_3\text{V}_2(\text{PO}_4)_3$. *Chem. Mater.* **2004**, *16*, 1456–1465.

- (68) Kang, J.; Mathew, V.; Gim, J.; Kim, S.; Song, J.; Im, W. Bin; Han, J.; Lee, J. Y.; Kim, J. Morphology for Advanced Li-Ion Batteries. *Sci. Rep.* **2014**, *4* (4047), 1–9.
- (69) Saïdi, M. Y.; Barker, J.; Huang, H.; Swoyer, J. L.; Adamson, G. Performance Characteristics of Lithium Vanadium Phosphate as a Cathode Material for Lithium-Ion Batteries. *J. power source* **2003**, *119* (121), 266–272.
- (70) Kim, S.; Zhang, Z.; Wang, S.; Yang, L.; Cairns, E. J.; Penner-hahn, J. E.; Deb, A. Electrochemical and Structural Investigation of the Mechanism of Irreversibility in $\text{Li}_3\text{V}_2(\text{PO}_4)_3$ Cathodes. *J. Phys. Chem. C* **2016**, *120*, 7005–7012.
- (71) Rui, X. H.; Yesibolati, N.; Chen, C. H. $\text{Li}_3\text{V}_2(\text{PO}_4)_3/\text{C}$ Composite as an Intercalation-Type Anode Material for Lithium-Ion Batteries. *J. Power Sources* **2011**, *196*, 2279–2282.
- (72) Gaubicher, J.; Wurm, C.; Goward, G.; Masquelier, C.; Nazar, L. Rhombohedral Form of $\text{Li}_3\text{V}_2(\text{PO}_4)_3$ as a Cathode in Li-Ion Batteries. *Chem. Mater.* **2000**, *12*, 3240–3242.
- (73) Delmas, C.; Olazcuaga, R.; Cherkaoui, F.; Brochu, R.; Leflem, G. New Family of Phosphates with Formula $\text{Na}_3\text{M}_2(\text{PO}_4)_3$ (M= Ti,V,Cr,Fe). *C. R. Seances Acad. Sci.* **1978**, *287*, 169–171.
- (74) Chotard, J.-N.; Rouse, G.; David, R.; Mentré, O.; Courty, M.; Masquelier, C. Discovery of a Sodium-Ordered Form of $\text{Na}_3\text{V}_2(\text{PO}_4)_3$ below Ambient Temperature. *Chem. Mater.* **2015**, *27*, 5982–5987.
- (75) Lalère, F.; Seznec, V.; Courty, M.; David, R.; Chotard, J. N.; Masquelier, C. Improving the Energy Density of $\text{Na}_3\text{V}_2(\text{PO}_4)_3$ -Based Positive Electrodes through V/Al Substitution. *J. Mater. Chem. A* **2015**, *3* (31), 16198–16205.
- (76) Jian, Z.; Yuan, C.; Han, W.; Lu, X.; Gu, L.; Xi, X.; Hu, Y.; Li, H.; Chen, W.; Chen, D.; Ikuhara, Y.; Chen, L. Atomic Structure and Kinetics of NASICON $\text{Na}_x\text{V}_2(\text{PO}_4)_3$ Cathode for Sodium-Ion Batteries. *Adv. Funct. Mater.* **2014**, *24* (27), 1–8.
- (77) Golalal Krishnan, J.; Kasthuri Rangan, K. NASICON-Type Vanadium Phosphate Synthesized by Oxidative. *Chem. Mater.* **1992**, *4* (4), 746–749.
- (78) C. W. Mason, I.; Gocheva, H. E.; Hostera, D. Y. W. Y. Activating Vanadium's Highest Oxidation State in the NASICON Structure. *ECS Trans.* **2014**, *58* (12), 41–46.
- (79) Aragón, M. J.; Lavela, P.; Ortiz, G. F.; Tirado, J. L. Benefits of Chromium Substitution in $\text{Na}_3\text{V}_2(\text{PO}_4)_3$ as a Potential Candidate for Sodium-Ion Batteries. *chem electro chem* **2015**, *2* (7), 1–9.
- (80) Zhou, W.; Xue, L.; Gao, H.; Li, Y.; Xin, S.; Fu, G.; Cui, Z.; Zhu, Y.; Goodenough, J. B. $\text{MV}(\text{PO}_4)_3$ (M= Mn, Fe, Ni) Structure and Properties for Sodium Extraction. *nano Lett.* **2016**, *16*, 7836–7841.
- (81) Le Meins, J.; Crosnier-Lopez, M.-P.; Hemon-Ribaud, A.; Courbion, G. Phase Transitions in the $\text{Na}_3\text{M}_2(\text{PO}_4)_3$ Family (M= Al^{3+} , V^{3+} , Cr^{3+} , Fe^{3+} , Ga^{3+}): Synthesis, Thermal, Structural, and Magnetic Studies. *J. Solid State Chem.* **1999**, *148*, 260–277.
- (82) Bianchini, M.; Brisset, N.; Fauth, F.; Weill, F.; Elkaim, E.; Suard, E.; Masquelier, C.; Croguennec, L. $\text{Na}_3\text{V}_2(\text{PO}_4)_2\text{F}_3$ Revisited: A High-Resolution Diffraction Study. *Chem. Mater.* **2014**, *26*, 4238–4247.
- (83) Shakoor, R. A.; Seo, D.-H.; Kim, H.; Park, Y.-U.; Kim, J.; Kim, S.-W.; Gwon, H.; Leec, S.; Kang, K. A Combined First Principles and Experimental Study on $\text{Na}_3\text{V}_2(\text{PO}_4)_2\text{F}_3$ for Rechargeable Na Batteries. *J. Mater. Chem.* **2012**, *22*, 20535–20541.

- (84) Bianchini, M.; Fauth, F.; Brisset, N.; Weill, F.; Suard, E.; Masquelier, C.; L. Croguennec. Comprehensive Investigation of the $\text{Na}_3\text{V}_2(\text{PO}_4)_2\text{F}_3\text{-NaV}_2(\text{PO}_4)_2\text{F}_3$ System by Operando High Resolution Synchrotron X-ray Diffraction. *Chem. Mater.* **2015**, *27*, 3009–3020.
- (85) Broux, T.; Bamine, T.; Fauth, F.; Simonelli, L.; Olszewski, W.; Marini, C.; Ménétrier, M.; Carlier, D.; Masquelier, C.; Croguennec, L. Strong Impact of the Oxygen Content in $\text{Na}_3\text{V}_2(\text{PO}_4)_2\text{F}_{3-y}\text{O}_y$ ($0 \leq y \leq 0.5$) on Its Structural and Electrochemical Properties. *Chem. Mater.* **2016**, *28*, 7683–7692.
- (86) Broux, T.; Bamine, T.; Simonelli, L.; Stievano, L.; Fauth, F.; Ménétrier, M.; Carlier, D.; Masquelier, C.; Croguennec, L. Solid-, VIV Disproportionation Upon Sodium Extraction From $\text{Na}_3\text{V}_2(\text{PO}_4)_2\text{F}_3$ Observed by Operando X-ray Absorption Spectroscopy and State NMR. *J. Phys. Chem. C* **2017**, *121*, 4103–4111.
- (87) Park, Y.; Seo, D.; Kim, H.; Kim, J.; Lee, S.; Kim, B.; Kang, K. A Family of High-Performance Cathode Materials for Na-Ion Batteries, $\text{Na}_3(\text{VO}_{1-x}\text{PO}_4)_2\text{F}_{1+2x}$ ($0 \leq x \leq 1$): Combined First-Principles and Experimental Study. *Advanced Funct. Mater.* **2014**, *24* (29), 1–12.
- (88) Park, Y.; Seo, D.; Kwon, H.; Kim, B.; Kim, J.; Kim, H.; Kim, I.; Yoo, H.; Kang, K. A New High-Energy Cathode for a Na-Ion Battery with Ultrahigh Stability. *J. Am. Chem. Soc.* **2013**, *135*, 13870–13878.
- (89) Serras, P.; Alonso, J.; Sharma, N.; Miguel, J.; Kubiak, P.; Gubieda, M.-L.; Rojo, T. Electrochemical Na Extraction/Insertion of $\text{Na}_3\text{V}_2\text{O}_{2x}(\text{PO}_4)_2\text{F}_{3-2x}$. *Chem. Mater.* **2013**, *25*, 4917–4925.
- (90) Morimoto, H.; Ito, D.; Ogata, Y.; Suzuki, T.; Sakamaki, K.; Tsuji, T.; Hirukawa, M.; Matsumoto, A.; Tobishima, S. Charge/discharge Behavior of Triclinic LiTiOPO_4 Anode Materials for Lithium Secondary Batteries. *Electrochem. Soc. Japan* **2016**, *84* (11), 878–881.
- (91) Barker, J.; Saidi, M. Y.; Swoyer, J. L. Electrochemical Insertion Properties of the Novel Lithium Vanadium Fluorophosphate, LiVPO_4F . *J. Electrochem. Soc.* **2003**, *150* (10), 1394–1398.
- (92) Ateba Mba, J.-M.; Masquelier, C.; Suard, E.; Croguennec, L. Synthesis and Crystallographic Study of Homeotypic LiVPO_4F and LiVPO_4O . *Chem. Mater.* **2012**, *24*, 1223–1234.
- (93) El Badraoui, A.; Pivan, J. Y.; Maunaye, M.; Pena, O.; Louer, M.; Louer, D. Order-Disorder Phenomena in Vanadium Phosphates. Structures and Properties of Tetragonal and Monoclinic $\text{VPO}_4 \cdot \text{H}_2\text{O}$. *Ann. Chim. Sci. Mat.* **1998**, *23*, 97–101.
- (94) Lii, K. H.; Li, H.; H, C. C.; L, W. S. Synthesis and Structural Characterization of Sodium Vanadyl (IV) Orthophosphate NaVOPO_4 . *Zeitschrift für Krist.* **1991**, *197*, 352–359.
- (95) Song, J.; Xu, M.; Wang, L.; Goodenough, J. B. Exploration of NaVOPO_4 as a Cathode for a Na-Ion Battery. *Chem. Commun.* **2013**, *49*, 5280–2282.
- (96) Bianchini, M.; Ateba-Mba, J. M.; Dagault, P.; Bogdan, E.; Carlier, D.; Suard, E.; Masquelier, C.; Croguennec, L. Multiple Phases in the $\epsilon\text{-VPO}_4\text{O-LiVPO}_4\text{O-Li}_2\text{VPO}_4\text{O}$ System: A Combined Solid State Electrochemistry and Diffraction Structural Study. *J. Mater. Chem. A* **2014**, *2*, 10182–10192.
- (97) Lee Harrison, K.; Bridges, C.; Segre, C.; Varnado, D.; Applestone, D.; Bielawski, C.; Paranthaman, M.; Manthiram, A. Chemical and Electrochemical Lithiation of LiVOPO_4 Cathodes for Lithium-Ion Batteries. *Chem. Mater.* **2014**, *26* (10), 3849–3861.

- (98) Lin, Y.; Wen, B.; Wiaderek, K.; Sallis, S.; Liu, H.; Lapidus, S.; Borkiewicz, O.; Quackenbush, N.; Chernova, N.; Karki, K.; Omenya, F.; Chupas, P.; Piper, L.; Whittingham, S.; Chapman, K.; Ong, S. Thermodynamics, Kinetics and Structural Evolution of ϵ -LiVOPO₄ over Multiple Lithium Intercalation. *Chem. Mater.* **2016**, *28*, 1794–1805.
- (99) Barker, J.; Saidi, M. Y.; Swoyer, J. L. A Comparative Investigation of the Li Insertion Properties of the Novel Fluorophosphate Phases, NaVPO₄F and LiVPO₄F. *J. Electrochem. Soc.* **2004**, *151* (10), 1670–1677.
- (100) Barker, J.; Gover, R. K. B.; Burns, P.; Bryan, A.; Saidi, M. Y.; Swoyer, J. L. Structural and Electrochemical Properties of Lithium Vanadium Fluorophosphate, LiVPO₄F. *J. Power Sources* **2005**, *146*, 516–520.
- (101) Ellis, B. L.; Ramesh, T. N.; Davis, L. J. M.; Goward, G. R.; Nazar, L. F. Structure and Electrochemistry of Two-Electron Redox Couples in Lithium Metal Fluorophosphates Based on the Tavorite Structure. *Chem. Mater.* **2011**, *23*, 5138–5148.
- (102) Piao, Y.; Qin, Y.; Ren, Y.; Heald, S. M.; Sun, C.; Zhou, D.; Polzin, B. J.; Trask, S. E.; Amine, K.; Wei, Y.; Chen, G.; Bloom, I.; Chen, Z. A XANES Study of LiVPO₄F: A Factor Analysis Approach. *Phys. Chem. Chem. Phys.* **2014**, *16*, 3254–3260.
- (103) Zhong, S.; Chen, W.; Li, Y.; Zou, Z.; Liu, C. Synthesis of LiVPO₄F with High Electrochemical Performance by Sol-Gel Route. *Trans. Nonferrous Met. Soc. China* **2010**, *20*, 275–278.
- (104) Xiong, Z.; Zhang, G.; Mo, L.; Zhong, M. Electrochemical Performance of LiVPO₄F Synthesized by Ball Milling Assisted Sol – Gel Method. *Russ. J. Electrochem.* **2014**, *50* (10), 1003–1007.
- (105) Li, Y.; Zhou, Z.; Gao, X. P.; Yan, J. A Novel Sol–gel Method to Synthesize Nanocrystalline LiVPO₄F and Its Electrochemical Li Intercalation Performances. *J. Power Sources* **2006**, *160*, 633–637.
- (106) Rangaswamy, P.; Shetty, V. R.; Suresh, G. S.; Mahadevan, K. M.; Nagaraju, D. H. Enhanced Electrochemical Performance of LiVPO₄F/f-Graphene Composite Electrode Prepared via Ionothermal Process. *J. Appl. Electrochem.* **2016**, *47*.
- (107) Kim, M.; Lee, S.; Kang, B. High Energy Density Polyanion Electrode Material ; LiVPO₄O_{1-x}F_x (x ≈ 0.25) with Tavorite Structure. *Chem. Mater.* **2017**, *29* (11), 4690–4699.
- (108) Wurm, C.; Morcrette, M.; Rousse, G.; Loic, D.; Masquelier, C. Lithium Insertion/Extraction Into/from LiMX₂O₇ Compositions (M= Fe , V; X = P, As) Prepared via a Solution Method. *Chem. Mater.* **2002**, *14*, 2701–2710.
- (109) Barker, J.; Gover, R. K. B.; Burns, P.; Bryan, A. LiVP₂O₇: A Viable Lithium-Ion Cathode Material? *Electrochem. Solid-State Lett.* **2005**, *8* (9), 446–448.
- (110) Deng, C.; Zhang, S. 1D Nanostructured Na₇V₄(P₂O₇)₄(PO₄) as High-Potential and Superior-Performance Cathode Material for Sodium-Ion Batteries. *Appl. Mater. interfaces* **2014**, *6*, 9111–9117.
- (111) Kovrugin, V.; Chotard, J.-N.; Fauth, F.; Jamali, A.; David, R.; Christian, M. Structural and Electrochemical Studies of Novel Batteries. *J. Mater. Chem. A* **2017**, *5*, 14365–14376.
- (112) Kuang, Q.; Xu, J.; Zhao, Y.; Chen, X.; Chen, L. Layered Monodiphosphate Li₉V₃(P₂O₇)₃(PO₄)₂: A Novel Cathode Material for Lithium-Ion Batteries. *Electrochim. Acta* **2011**, *56*, 2201–2205.

- (113) Deng, C.; Zhang, S.; Zhao, B. First Exploration of Ultra Fine $\text{Na}_7\text{V}_3(\text{P}_2\text{O}_7)_4$ as a High-Potential Cathode Material for Sodium-Ion Battery. *Energy Storage Mater.* **2016**, *4*, 71–78.
- (114) Makimura, Y.; Cahill, L. S.; Iriyama, Y.; Goward, G. R.; Nazar, L. F. Layered Lithium Vanadium Fluorophosphate, $\text{Li}_5\text{V}(\text{PO}_4)_2\text{F}_2$: A 4 V Class Positive Electrode Material for Lithium-Ion Batteries. **2008**, No. 6, 4240–4248.
- (115) Barker, J.; Saidi, M. Y.; Swoyer, J. L. Electrochemical Properties of $\beta\text{-LiVOPO}_4$ Prepared by Carbothermal Reduction. *J. Electrochem. Soc.* **2004**, *151* (6), 796–800.
- (116) He, G.; Kan, W.; Manthiram, A. $\beta\text{-NaVOPO}_4$ Obtained by a Low-Temperature Synthesis Process: A New 3.3 V Cathode for Sodium-Ion Batteries. *Chem. Mater.* **2016**, *28*, 1503–1512.
- (117) He, G.; Bridges, C.; Manthiram, A. Crystal Chemistry of Electrochemically and Chemically Lithiated Layered $\alpha_1\text{-LiVOPO}_4$ Crystal. *Chem. Mater.* **2015**, *27* (19), 6699–6707.
- (118) Kishore, M. S.; Pralong, V.; Caignaert, V.; Malo, S.; Hebert, S.; Varadaraju, U. V.; Raveau, B. Topotactic Insertion of Lithium in the Layered Structure $\text{Li}_4\text{VO}(\text{PO}_4)_2$: The Tunnel Structure $\text{Li}_5\text{VO}(\text{PO}_4)_2$. *J. Solid-State Chem.* **2008**, *181*, 976–982.
- (119) Kim, J.; Kim, H.; Lee, S. With Open Framework for Na Ion Batteries New High Power Cathode Material $\text{Na}_4\text{VO}(\text{PO}_4)_2$ with Open Framework for Na Ion Batteries. *Chem. Mater.* **2017**, *29* (8), 3363–3366.
- (120) Kishore, M. S.; Pralong, V.; Caignaert, V.; Varadaraju, U. V.; Raveau, B. A New Lithium Vanadyl Diphosphate $\text{Li}_2\text{VOP}_2\text{O}_7$: Synthesis and Electrochemical Study. *Solid State Sci.* **2008**, *10*, 1285–1291.
- (121) Zhang, B.; Dugas, R.; Rouse, G.; Rozier, P.; Abakumov, A. M.; Tarascon, J.-M. Insertion Compounds and Composites Made by Ball Milling for Advanced Sodium-Ion Batteries. *Nat. Commun.* **2016**, *7*, 1–9.
- (122) Tang, A.; Shen, J.; Hu, Y.; Xu, G.; He, D.; Yi, Q. Electrochemical Performance of A- LiVOPO_4 /Carbon Composite Material Synthesized by Sol-Gel Method. *J. Electrochem. Soc.* **2014**, *161* (1), 10–13.
- (123) Lu, J.; Nishimura, S.; Yamada, A. Polyanionic Solid-Solution Cathodes for Rechargeable Batteries. *Chem. Mater.* **2017**, *29*, 3597–3602.
- (124) Po, V. RSC Advances A High Rate and Stable Electrode Consisting of. *RSC Adv.* **2017**, *7*, 21820–21826.
- (125) Saravanan, K.; Mason, C. W.; Rudola, A.; Wong, K. H.; Balaya, P. The First Report on Excellent Cycling Stability and Superior Rate Capability of $\text{Na}_3\text{V}_2(\text{PO}_4)_3$ for Sodium Ion Batteries. *Adv. energy Mater.* **2013**, 444–450.
- (126) Ateba Mba, J.-M. PhD Thesis. *Univ. Bordeaux*, **2013**.
- (127) Brown, I. D.; Altermatt, D. Bond-Valence Parameters Obtained from a Systematic Analysis of the Inorganic Crystal Structure Database I. *Acta Cryst B* **1985**, *41*, 244–247.
- (128) Bamine, T. PhD Thesis. *Univ. Bordeaux* **2017**.
- (129) Wong, J.; Lytle, F. W.; Messmer, R. P.; Maylotte, D. H. K-Edge Absorption Spectra of Selected Vanadium Compounds. *Phys. Rev. B* **1984**, *30* (10), 5596–5610.
- (130) Bianchini, M. PhD Thesis. *Univ. Picardie Jules Vernes, Amiens* **2015**.

- (131) Jaumot, J.; Gargallo, R.; Juan, A.; Tauler, R. A Graphical User-Friendly Interface for MCR-ALS: A New Tool for Multivariate Curve Resolution in MATLAB. *Chemom. Intell. Lab. Syst.* **2005**, *76*, 101–110.
- (132) Tauler, R. Multivariate Curve Resolution Applied to Second Order Data. *Chemom. Intell. Lab. Syst.* **1995**, *30*, 133–146.
- (133) Juan, A.; Tauler, R. Chemometrics Applied to Unravel Multicomponent Processes and Mixtures Revisiting Latest Trends in Multivariate Resolution. *Anal* **2003**, *500*, 195–210.
- (134) Ruckebusch, C.; Blanchet, L. Multivariate Curve Resolution: A Review of Advanced and Tailored Applications and Challenges. *Anal. Chim. Acta* **2013**, *765*, 28–36.
- (135) Boucher, F.; Gaubicher, J.; Cuisinier, M.; Guyomard, D.; Moreau, P. Elucidation of the Na₂/3FePO₄ and Li₂/3FePO₄ Intermediate Superstructure Revealing a Pseudouniform Ordering in 2D. *J. Am. Chem. Soc.* **2014**, *136* (25), 9144–9157.
- (136) Onoda, M.; Ishibashi, T. Phase Transition and Spin Dynamics of the LiVFPO₄ Insertion Electrode with the S = 1 Linear Chain and the Development of F – O Mixed System. *J. Physiol. Soc. Japan* **2015**, *84*, 1–5.
- (137) Stephens, P. Phenomenological Model of Anisotropic Peak Broadening in Powder Diffraction. *J. Appl. Crystallogr.* **1999**, *32*, 281–289.
- (138) Rodríguez-Carvajal, J.; Roisnel, T. Line Broadening Analysis Using FullProf: Determination of Microstructural Properties. *Mater. Sci. Forum* **2004**, *443*, 123–126.
- (139) Nakamoto, K. *Infrared and Raman Spectra of Inorganic and Coordination Compounds.*; John Wiley & Sons, Inc., 1997.
- (140) Hardcastle, F.; Wachs, I. Determination of Vanadium-Oxygen Bond Distances and Bond Orders by Raman Spectroscopy. *J. Phys. Chem.* **1991**, *95* (13), 5031–5041.
- (141) Harrison, K.; Manthiram, A. Microwave-Assisted Solvothermal Synthesis and Characterization of Various Polymorphs of LiVOPO₄. *Chem. Mater.* **2013**, *25*, 1751–1760.
- (142) Marx, N.; Croguennec, L.; Carlier, D.; Bourgeois, L.; Kubiak, P.; Le Cras, F.; Delmas, C. Structural and Electrochemical Study of a New Crystalline Hydrated Iron(III) Phosphate FePO₄·H₂O Obtained from LiFePO₄(OH) by Ion Exchange. *Chem. Mater.* **2010**, *22*, 1854–1861.
- (143) Bertini, I.; Luchinat, C.; Parigi, G. Magnetic Susceptibility in Paramagnetic NMR. *Prog. Nucl. Magn. Reson. Spectrosc.* **2002**, *40* (3), 249–273.
- (144) Huminicki, D.; Hawthorne, C. The Crystal Chemistry of the Phosphate Minerals. *Rev. Mineral. Geochemistry* **2002**, *48*, 123–253.
- (145) Ghatikar, M. N.; Padalia, B. D. Empirical Relations and the X-Ray Absorption Edge-Shifts. *J. Phys. Chem. C* **1978**, *11*, 1941–1955.
- (146) GAUR, A.; Shrivastava, B. D.; NIGAM, H. L. X-Ray Absorption Fine Structure (XAFS) Spectroscopy – A Review. *Proc. Indian Nat. Sci. Acad.* **2013**, *79* (4), 921–966.
- (147) Ravel, B.; Newville, M. ATHENA, ARTEMIS, HEPHAESTUS: Data Analysis for X-Ray Absorption Spectroscopy Using IFEFFIT. *J. Synchrotron Radiat.* **2005**, *12*, 537–541.
- (148) Ellis, B.; Nazar, L. Anion-Induced Solid Solution Electrochemical Behavior in Iron Tavorite Phosphates. *Chem. Mater.* **2012**, *24*, 966–968.
- (149) Castets, A.; Carlier, D.; Zhang, Y.; Boucher, F. A DFT-Based Analysis of the NMR Fermi Contact Shifts in Tavorite-. *J. Phys. Chem. C* **2012**, *116*, 18002–18014.

- (150) Castets, a; Carlier, D.; Zhang, Y.; Boucher, F.; Marx, N.; Gautier, R.; Le Fur, E.; Le Pollès, L.; Croguennec, L.; Ménétrier, M. NMR Study of the LiMnPO_4OH and $\text{MPO}_4\cdot\text{H}_2\text{O}$ (M = Mn, V) Homeotypic Phases and DFT Calculations. *Solid State Nucl. Magn. Reson.* **2012**, *42*, 42–50.
- (151) Xiao, P. F.; Lai, M. O.; Lu, L. Transport and Electrochemical Properties of High Potential Tavorite LiVPO_4F . *Solid State Ionics* **2013**, *242*, 10–19.
- (152) Wang, Y.; Zhao, H.; Ji, Y.; Wang, L.; Wei, Z. Long-Life and High-Rate $\text{LiVPO}_4\text{F}/\text{C}$ Nanocrystals Modified with Graphene as Cathode Material for Lithium-Ion Batteries. *Solid State Ionics* **2014**, *268*, 169–173.
- (153) Boivin, E.; Chotard, J.-N.; Ménétrier, M.; Bourgeois, L.; Bamine, T.; Carlier, D.; Fauth, F.; Suard, E.; Masquelier, C.; Croguennec, L. Structural and Electrochemical Studies of a New Tavorite Composition LiVPO_4OH . *J. Mater. Chem. A* **2016**, *4*, 11030–11045.
- (154) Clark, R. J. H. *The Chemistry of Titanium and Vanadium*; 1968.
- (155) Alekseenko, V.; Alekseenko, A. The Abundances of Chemical Elements in Urban Soils. *J. Geochemical Explor.* **2014**, *147*, 245–249.
- (156) V. M. Goldschmidt. The Principles of Distribution of Chemical Elements. *J. Chem. Soc.* **1937**, 655–673.
- (157) Xiang, X.; Zhang, K.; Chen, J. Recent Advances and Prospects of Cathode Materials for Sodium-Ion Batteries. *Adv. Mater.* **2015**, *27*, 5343–5364.
- (158) Ponrouch, A.; Dedryvère, R.; Monti, D.; Demet, A. E.; Ponrouch, A.; Marcel, J.; Mba, A.; Croguennec, L.; Masquelier, C.; Johansson, P.; Palac, M. R. Environmental Science Towards High Energy Density Sodium Ion Batteries through Electrolyte Optimization. *Energy Environ. Sci.* **2013**, *6*, 2361–2369.
- (159) Dugas, R.; Zhang, B.; Rozier, P.; Tarascon, J. M. Optimization of Na-Ion Battery Systems Based on Polyanionic or. *J. Electrochem. Soc.* **2016**, *163* (6), 867–874.
- (160) Jian, Z.; Han, W.; Lu, X.; Yang, H.; Hu, Y.; Zhou, J.; Zhou, Z.; Li, J.; Chen, W.; Chen, D.; Chen, L. Superior Electrochemical Performance and Storage Mechanism of $\text{Na}_3\text{V}_2(\text{PO}_4)_3$ Cathode for Room-Temperature Sodium-Ion Batteries. *Adv. energy Mater.* **2013**, *3*, 156–160.
- (161) Barker, J.; Saidi, M. Y.; Swoyer, J. L. A Comparative Investigation of the Li Insertion Properties of the Novel Fluorophosphate Phases, NaVPO_4F and LiVPO_4F . *J. Electrochem. Soc.* **2004**, *151* (10), A1670.
- (162) Barker, J.; Saidi, M. Y.; Swoyer, J. L. A Sodium-Ion Cell Based on the Fluorophosphate Compound NaVPO_4F . *Electrochem. solid state Lett.* **2003**, *6* (1), 1–4.
- (163) Zhao, J.; He, J.; Ding, X.; Zhou, J.; Ma, Y.; Wu, S.; Huang, R. A Novel Sol–gel Synthesis Route to NaVPO_4F as Cathode Material for Hybrid Lithium Ion Batteries. *J. Power Sources* **2010**, *195*, 6854–6859.
- (164) Ruan, Y.; Wang, K.; Song, S.; Han, X.; Cheng, B. Electrochimica Acta Graphene Modified Sodium Vanadium Fluorophosphate as a High Voltage Cathode Material for Sodium Ion Batteries. *Electrochim. Acta* **2015**, *160*, 330–336.
- (165) Lu, Y.; Zhang, S.; Li, Y.; Xue, L.; Xu, G.; Zhang, X. Preparation and Characterization of Carbon-Coated NaVPO_4F as Cathode Material for Rechargeable Sodium-Ion Batteries. *J. Power Sources* **2014**, *247*, 770–777.
- (166) Jin, T.; Liu, Y.; Li, Y.; Cao, K.; Wang, X.; Jiao, L. Electrospun $\text{NaVPO}_4\text{F}/\text{C}$ Nanofibers as Self-Standing Cathode Material for Ultralong Cycle Life Na-Ion Batteries. **2017**.

- (167) Law, M.; Balaya, P. NaVPO₄F with High Cycling Stability as a Promising Cathode for Sodium-Ion Battery. **2018**, *10* (April 2017), 102–113.
- (168) Vaughey, J. T.; A, W. T.; Jacobson, A. Synthesis, Structure and Properties of Two New Vanadium (III) Phosphates : VPO₄-H₂O and V_{1.23}(PO₄)(OH)_{0.69}(H₂O)_{0.31}.0.33H₂O. *Inorg. Chem.* **1994**, *23*, 2481–2487.
- (169) Ren, M. M.; Zhou, Z.; Gao, X. P.; Liu, L.; Peng, W. X. LiVOPO₄ Hollow Microspheres : One-Pot Hydrothermal Synthesis with Reactants as Self-Sacrifice Templates and Lithium Intercalation Performances. *J. Phys. Chem. C* **2008**, *112*, 13043–13046.
- (170) Altomare, A.; Cuocci, C.; Giacovazzo, C.; Moliterni, A.; Rizzi, R.; Corriero, N.; Falcicchio, A. EXPO2013 : A Kit of Tools for Phasing Crystal Structures from Powder Data. *J. Appl. Crystallogr.* **2013**, *46*, 1–5.
- (171) Rodriguez-carvajal, J. Recent Advances in Magnetic Structure Determination by Neutron Powder Diffraction. *Phys. B* **1993**, *192*, 55–69.
- (172) Momma, K.; Izumi, F. VESTA 3 for Three-Dimensional Visualization of Crystal, Volumetric and Morphology Data. *J. Appl. Crystallogr.* **2011**, *44* (6), 1272–1276.
- (173) Adams, S. From Bond Valence Maps to Energy Landscapes for Mobile Ions in Ion-Conducting Solids. *Solid State Ionics* **2006**, *177*, 1625–1630.
- (174) Mueller, T.; Hautier, G.; Jain, A.; Ceder, G. Evaluation of Tavorite-Structured Cathode Materials for Lithium-Ion Batteries Using High-Throughput Computing. *Chem. Mater.* **2011**, *23*, 3854–3862.
- (175) Barker, J.; Saidi, Y.; Swoyer, J. L. Alkali/insertion Metal Halo- and Hydroxy Phosphates and Related Electrode Active Materials, 2004.
- (176) Groat, A.; Chakoumakos, B. C.; Brouwer, D. H.; Hoffman, C. M.; Fyfe, C. A.; Morell, H.; Schultz, A. J. The Amblygonite (LiAlPO₄F) -Montebrasite (LiAlPO₄OH) Solid Solution : A Combined Powder and Single-Crystal Neutron Diffraction and Solid-State 6 Li MAS, CP MAS, and REDOR NMR Study. *Am. Mineral.* **2003**, *88*, 195–210.
- (177) Yang, Y.; Hirayama, M.; Yonemura, M.; Kanno, R. Synthesis, Crystal Structure, and Electrode Characteristics of LiMnPO₄(OH) Cathode for Lithium Batteries. *J. Solid State Chem.* **2012**, *187*, 124–129.
- (178) Song, Y.; Zavalij, P.; Whittingham, S. ε-VOPO₄: Electrochemical Synthesis and Enhanced Cathode Behavior. *J. Electrochem. Soc.* **2005**, *152* (4), 721–728.
- (179) Mi, J.-X.; Borrmann, H.; Zhang, H.; Huang, Y.-X.; Schnelle, W.; Zhao, J.-T.; Kniep, R. Synthesis, Magnetism, and Crystal Structure of Li₂Fe[(PO₄)(HPO₄)] and Its Hydrogen Position Refinement. *Zeitschrift für Anorg. und Allg. Chemie* **2004**, *630*, 1632–1636.
- (180) Reynaud, M.; Ati, M.; Melot, B.; Sougrati, M.; Rouse, G.; Chotard, J.-N.; Tarascon, J.-M. Li₂Fe(SO₄)₂ as a 3.83V Positive Electrode Material. *Electrochem. commun.* **2012**, *21*, 77–80.
- (181) Lander, L.; Reynaud, M.; Carrasco, J.; Katcho, N.; Bellin, C.; Polian, A.; Baptiste, B.; Rouse, G.; Tarascon, J.-M. Unveiling the Electrochemical Mechanisms of Li₂Fe(SO₄)₂ Polymorphs by Neutron Diffraction and Density Functional Theory Calculations. *Phys. Chem. Chem. Phys.* **2016**, *18*, 14509–14519.
- (182) Gwenaelle, R.; Wurm, C.; Morcrette, M.; Rodriguez-carvajal, J.; Gaubicher, J.; Masquelier, C. Crystal Structure of a New Vanadium (IV) Diphosphate: VP₂O₇, Prepared by Lithium Extraction from LiVP₂O₇. *Inorg. Mater.* **2001**, *3*, 881–887.

- (183) Song, Y.; Zavalij, P. Y.; Whittingham, M. S. ϵ -VOPO 4 : Electrochemical Synthesis and Enhanced Cathode Behavior. *J. Electrochem. Soc.* **2005**, *152* (4), 721–728.
- (184) Bragg's law, wikipédia.
- (185) Bravais, B. On the Systems Formed by Points Regularly Distributed on a Plane or in Space Auguste Bravais 1850. *J. Ec. Polytech* **1850**, *19*, 1–128.
- (186) Hahn, T. *International Tables for Crystallography. Volume A: Space-Group Symmetry*; 2002.
- (187) Caglioti, C.; Ricci, F. Resolution and Luminosity of Crystal Spectrometers for Neutron Diffraction. *Nucl. Instruments Methods* **1962**, *15*, 155–163.
- (188) Scherrer, P. Bestimmung Der Größe Und Der Inneren Struktur von Kolloidteilchen Mittels Röntgenstrahlen. *Nachrichten von der Gesellschaft der Wissenschaften zu Göttingen, Math. Phys. Klasse* **1918**, 98–100.
- (189) Stokes, A. R. A Numerical Fourier-Analysis Method for the Correction of Widths and Shapes of Lines on X- Ray Powder Photographs. *Proc. Phys. Soc.* **1948**, *61*, 382–391.
- (190) Williamson, K.; Hall, H. X-Ray Line Broadening from Filled Aluminium and Wolfram. *acta Metall.* **1953**, *1*, 22–31.
- (191) Brown, P. J.; Fox, A. G.; Maslen, E. N.; Keefe, M. A. O.; Willis, B. T. M.; Maslen, B. E. N.; Fox, A. G.; Keefe, M. A. O.; Fox, Ê. À.; Keefe, O. Intensity of Diffracted Intensities. *Int. Tables Crystallogr.* **2006**, Vol. C (section 6.1.1), 554–590.
- (192) Varley, F. S. Neutron Scattering Lengths and Cross Sections. *Neutron news* **1992**, *3* (3), 29–37.
- (193) Rodríguez-carvajal, J. *An Introduction to the Program FullProf 2000*; 2001.
- (194) Toby, B. R Factors in Rietveld Analysis: How Good Is Good Enough? *Powder Diffr.* **2006**, *21* (01), 67–70.
- (195) Deng, Y. PhD Thesis. *Univ. Picardie Jules Vernes, Amiens* **2016**.
- (196) Foner, S. Versatile and Sensitive Vibrating Sample Magnetometer. *Rev. Sci. Instrum.* **1959**, *30* (7), 548–557.
- (197) Bain, G.; Berry, J. Diamagnetic Corrections and Pascal's Constants. *J. Chem. Educ.* **2008**, *85* (4), 532–536.
- (198) Hahn, E. Spin Echoes. *Phys. Rev.* **1950**, *80* (4), 580–602.
- (199) Aue, W. P.; Bartholdi, E.; Ernst, R. R. Twodimensional Spectroscopy . Application to Nuclear Magnetic Resonance. *J. Chem. Phys.* **1976**, *64* (5), 2229–2246.
- (200) Harris, D.; Bertolucci, M. *Symmetry and Spectroscopy: An Introduction to Vibrational and Electronic Spectroscopy*; 1978.
- (201) Skare, M. O. PhD Thesis. *Nor. Univ. Sci. Technol.* **2016**.
- (202) Ma, R.; Shu, J.; Shao, L.; Lin, X.; Wu, K.; Shui, M.; Li, P.; Long, N.; Ren, Y. Determination of Lithium Ion Diffusion Behaviors in Tavorite LiVPO₄F by Galvanostatic Intermittent Titration Technique. *Ceram. Int.* **2014**, *40*, 15113–15119.
- (203) Leriche, J. B.; Hamelet, S.; Shu, J.; Morcrette, M.; Masquelier, C.; Ouvrard, G.; Zerrouki, M.; Soudan, P.; Belin, S.; Elkaïm, E.; Baudelet, F. An Electrochemical Cell for Operando Study of Lithium Batteries Using Synchrotron Radiation. *J. Electrochem. Soc.* **2010**, *157* (5), 606–610.
- (204) Cassinelli, W. H.; Martins, L.; Passos, A. R.; Pulcinelli, S. H.; Santilli, C. V; Rochet, A.; Briois, V. Multivariate Curve Resolution Analysis Applied to Time-Resolved

Synchrotron X-Ray Absorption Spectroscopy Monitoring of the Activation of Copper Alumina Catalyst. *Catal. Today* **2014**, 229, 114–122.

Résumé

Ce travail de thèse a pour but d'explorer de nouveaux matériaux de type structural Tavorite et de revisiter certains déjà bien connus. Dans un premier temps, les synthèses de compositions ciblées ont été réalisées selon des procédures variées (voies tout solide, hydrothermale, céramique assistée par sol-gel, broyage mécanique) afin de stabiliser d'éventuelles phases métastables et d'ajuster la microstructure impactant fortement les performances électrochimiques de tels matériaux polyanioniques. Ces matériaux ont ensuite été décrits en profondeur, dans leurs états originaux, depuis leurs structures moyennes, grâce aux techniques de diffraction (diffraction des rayons X sur poudres ou sur monocristaux et diffraction des neutrons) jusqu'aux environnements locaux, en utilisant des techniques de spectroscopie (résonance magnétique nucléaire à l'état solide, absorption des rayons X, infra-rouge et Raman). Par la suite, les diagrammes de phases et les processus d'oxydoréduction impliqués pendant l'activité électrochimique des matériaux ont été étudiés grâce à des techniques *operando* (diffraction et absorption des rayons X). La compréhension des mécanismes impliqués pendant le cyclage permet de mettre en évidence les raisons de leurs limitations électrochimiques : La synthèse de nouveaux matériaux (composition, structure, microstructure) peut maintenant être développée afin de contrepasser ces limitations et de tendre vers de meilleures performances.

Mots clés : batteries Li-ion et Na-ion, cathode à haut potentiel, nouvelles phases Tavorites, cristallographie, défauts de type Vanadyle, RMN du solide, DRX *operando*, XAS *operando*

Abstract

This PhD work aims at exploring new Tavorite-type materials and at revisiting some of the well-known ones. The syntheses of targeted compositions were firstly performed using various ways (all solid state, hydrothermal, sol-gel assisted ceramic, ball milling) in order to stabilize eventual metastable phases and tune the microstructure impacting strongly the electrochemical performances of such polyanionic compounds. The materials were then described in-depth, at the pristine state, from their average long range structures, thanks to diffraction techniques (powder X-rays, single crystal X-rays and neutrons diffraction), to their local environments, using spectroscopy techniques (solid state Nuclear Magnetic Resonance, X-rays Absorption Spectroscopy, Infra-Red and/or Raman). Thereafter, the phase diagrams and the redox processes involved during electrochemical operation of the materials were investigated thanks to *operando* techniques (SXRPD and XAS). The in-depth understanding of the mechanisms involved during cycling allows to highlight the reasons of their electrochemical limitations: the synthesis of new materials (composition, structure and microstructure) can now be developed to overcome these limitations and tend toward better performance.

Keywords : Li-ion et Na-ion batteries, high voltage cathode, new Tavorite phases, crystallography, vanadyle-type defects, MAS NMR, *operando* XRD, *operando* XAS